AM-68-1
May 1, 1968

Final Report

Lunar Module (LM) Soil Mechanics Study

Volume I

GPO PRICE $ _____

CFSTI PRICE(S) $ _____

Hard copy (HC) 3.00

Microfiche (MF) .65

ff 653 July 65

FACILITY FORM 602

N68-31324 (ACCESSION NUMBER)	(THRU)
456 (PAGES)	1 (CODE)
CR-92208 (NASA CR OR TMX OR AD NUMBER)	30 (CATEGORY)

NASA CR 92208

May 1, 1968

Bendix Report #AM-68-1

FINAL REPORT

LUNAR MODULE (LM)

SOIL MECHANICS STUDY

Prepared for

NASA, Manned Spacecraft Center
NASA Road 1, Houston, Texas 77058

Under Contract #NAS 9-5759

Prepared by

The Bendix Corporation
Energy Controls Division
Analytical Mechanics Engineering Department
717 North Bendix Drive
South Bend, Indiana 46620

PRECEDING PAGE BLANK NOT FILMED.

FOREWORD

This document represents the final report of technical work accomplished by the Energy Controls Division of The Bendix Corporation under Contract NAS 9-5759, entitled "A Lunar Module (LM) Soil Mechanics Study." The work was performed for the Manned Spacecraft Center of NASA, during the period from May, 1966 to February, 1968. Mr. D. L. Brown and, later, Mr. B. Holder were designated as NASA Technical Representatives for the contract. At Bendix, Mr. R. E. Schmidt was assigned as Project Manager and Mr. R. J. Black was assigned as Technical Director for the program.

Other members of the Bendix team who contributed significantly to the program and to the preparation of this report are Messrs. H. K. Winters, R. G. Alderson, J. Y. Woo, W. D. Chambers, F. P. Mackrill, P. W. Seder, D. A. Kobb, R. E. Mikel, A. J. Kasak, and W. Avery.

The success of a complex and extensive program such as this entails teamwork and the collective talents of many individuals. Although the Bendix team provided the mainstream effort throughout the study, the assistance of various other participating personnel and organizations is also gratefully acknowledged. These include the IIT Research Institute-particularly, Dr. E. Vey and Dr. J. D. Nelson - at Chicago, Illinois; the Missile Systems Division of Bendix at Mishawaka, Indiana; and the McDonnell Automation Company, at St. Louis, Missouri.

It is particularly appropriate to acknowledge the helpful contributions of our Soil Mechanics technical consultants, Prof. M. E. Harr of Purdue University, and Prof. B. B. Schimming, formerly of the University of Notre Dame. In addition, we also wish to acknowledge the assistance and contributions of Prof. R. M. Brack and Prof. L. H. N. Lee

of the University of Notre Dame. Finally, the guidance and assistance provided by Messrs. D. Brown, B. Holder, H. Benson, and G. Zupp of the NASA Manned Spacecraft Center is gratefully acknowledged. Their diligence and ours was further enhanced by the critical reviews conducted by Dr. L. Reiffel of NASA Headquarters and his Soil Consultants group, including Prof. G. A. Leonards of Purdue University; Prof. F. E. Richart, Jr., of the University of Michigan, Prof. R. N. Scott of the California Institute of Technology, and Prof. H. B. Seed of the University of California.

TABLE OF CONTENTS

Section		Page
	FOREWORD	iii
I	INTRODUCTION	1-1
II	SOIL SELECTION AND CONTROL	2-1
2.1	Introduction	2-1
2.1.1	Abbreviations of Units and Names in Soil Testing	2-1
2.2	Soil Properties Affecting Dynamic Strength of Dry Soils	2-4
2.2.1	Boundary Conditions	2-5
2.2.2	Field Equations	2-5
2.2.3	Equation of State	2-5
2.3	Estimations of the Properties of the Lunar Soil	2-11
2.4	Selection of the Test Soils	2-13
2.5	Test Procedures Used to Determine Soil Properties	2-15
2.5.1	Types of Tests	2-15
2.5.2	Basic Soil Tests	2-18
2.5.3	Sonic Velocity Test	2-52
2.6	Bearing Strength Test	2-52
2.6.1	Test Apparatus	2-56
2.6.2	Test Procedure	2-57
2.6.3	Load-Penetration Test Results	2-59
2.7	Soil Bed Control Tests	2-88
2.7.1	Dynamic Penetrometer Test	2-88
2.7.2	Static Penetrometer Test	2-94
2.7.3	Grain Size Analysis	2-94
2.7.4	Minimum-Maximum Density Test	2-98
2.7.5	In-Place Density Measurements	2-99
2.7.6	Evaluation of Soil Control Tests	2-101
2.8	Soil Test Bed Preparation Procedures	2-101
2.8.1	Preparation of Loose Soil Test Beds	2-103
2.8.2	Preparation of Intermediate Soils	2-109
2.8.3	Preparation of Dense Soils	2-113
2.9	Summary of Main Results of "Soil Selection and Control" Phase of Program	2-113

TABLE OF CONTENTS (Continued)

Section		Title	Page
III		CONTROLLED MOTION TEST EQUIPMENT FOR SOIL/FOOTPAD DYNAMICAL INTERACTIONS	3-1
	3.1	Introduction	3-1
	3.2	Subscale Drag Test Equipment	3-2
	3.2.1	General Purpose	3-2
	3.2.2	Equipment Modifications	3-4
	3.2.3	Equipment Arrangement and Operation	3-5
	3.2.4	Instrumented Strut (Load Cell) Design	3-9
	3.2.5	Instrumented Footpad Design	3-13
	3.2.6	Recording Instrumentation	3-16
	3.3	Subscale Oblique Impact Test Equipment	3-17
	3.3.1	Purpose and General Description	3-17
	3.3.2	Equipment Modifications	3-19
	3.3.3	Equipment Description and Operation	3-20
	3.3.4	Instrumented Load Cell and Footpad	3-22
	3.3.5	Recording Instrumentation	3-23
	3.4	Full-Scale Oblique Impact Test Equipment	3-27
	3.4.1	Purpose and General Description	3-27
	3.4.2	Equipment Design and Operation	3-27
	3.4.3	Instrumented Load Cell and Footpad	3-32
	3.4.4	Recording Instrumentation	3-35
	3.5	Full-Scale Drag Test Facility Design	3-35
	3.5.1	Purpose and General Description	3-35
	3.5.2	The Hydraulic Power/Control Unit	3-38
	3.5.3	The Carriage and Gantry Structure	3-41
	3.5.4	The Instrumented Strut and Footpad	3-42
	3.6	Vacuum/Atmosphere Impact Tester and Subgravity Simulator	3-44
IV		DEVELOPMENT OF SOIL/FOOTPAD INTERACTION MODEL	4-1
	4.1	Introduction	4-1
	4.2	Description of Drag Test Program	4-3
	4.3	Description of Impact Test Program	4-7
	4.4	Analysis of Subscale Drag Test Data	4-22
	4.5	Analysis of Impact Phenomena	4-47
	4.6	Description of Soil Model	4-61
	4.7	Comments on Soil Properties Appearing in the Interaction Force Laws	4-92
V		SUBSCALE MODEL LANDING PROGRAM	5-1
	5.1	Introduction	5-1
	5.2	Description of Model, Instrumentation, and Drop Test Facility	5-2
	5.2.1	Modification-General Design and Instrumentation	5-4
	5.2.1.1	Accelerometer Installation	5-4
	5.2.1.2	Load and Stroke Measurement-Secondary Struts	5-7

TABLE OF CONTENTS (Continued)

Section		Title	Page
	5.2.1.3	Load Measurement-Primary Status	5-9
	5.2.1.4	Stroke Measurements-Primary Struts	5-13
	5.2.2	Energy Absorbing Capsules	5-13
	5.2.3	Geometric and Physical Characteristics of LM Models	5-18
	5.2.4	Model Drop Test Facilities	5-22
	5.2.5	Instrumentation Recording System	5-25
	5.3	Listing of LM Model Drops	5-25
	5.4	Rigid Surface Landing of the LM Model	5-25
	5.4.1	Model Setup	5-33
	5.4.2	Rigid Surface Landing Test Site	5-33
	5.4.3	Rigid Surface Model Drop Tests	5-35
	5.5	Detailed Correlation Tests and Results	5-38
	5.5.1	Instrumentation and Footpad Load Resolution	5-38
	5.5.2	Data Handling for Detailed Correlation Studies	5-41
	5.5.3	Soil Description for Detailed Correlation Studies	5-43
	5.5.4	Detailed Correlation Drop Tests	5-44
	5.5.5	Detailed Correlation Test Results	5-46
	5.6	Cross Correlation Tests and Results	5-67
	5.6.1	Test Setup and Instrumentation	5-67
	5.6.2	Test Soils and Soil Bed Preparation	5-67
	5.6.3	Cross Correlation Drop Tests and Results	5-69
	5.7	Exploratory Tests-Investigation of Secondary Tension	5-73
	5.7.1	Test Setup for Exploratory Drops	5-73
	5.7.2	Exploratory Drop Test Results and Discussion	5-77
VI		CORRELATION STUDIES	6-1
	6.1	Introduction	6-1
	6.2	LM Landing Dynamics Computer Program	6-1
	6.3	LM Toppling Stability Comparison	6-3
	6.4	Detail Correlation Study	6-14
VII		CONCLUSIONS AND RECOMMENDATIONS	7-1
	7.1	Introduction	7-1
	7.2	Conclusions Related to Semi-Empirical Soil Model	7-1
	7.3	Recommendations for Utilization of the Analytical Soil Model	7-6
	7.4	Secondary Conclusions and Recommendations	7-8
APPENDIX A		SOIL SPECIMENS	
APPENDIX B		DETERMINATION OF THE TANGENT MODULUS	
APPENDIX C		DIRECT SHEAR TEST DATA	
APPENDIX D		FULL-SCALE DRAG TEST FACILITY DESIGN	
APPENDIX E		VACUUM/ATMOSPHERIC IMPACT TESTER AND SUBGRAVITY SIMULATOR	

LIST OF ILLUSTRATIONS

Figure	Title	Page
1-1	Schematic and Nomenclature for Dynamic Model	1-8
2-1	Factors Considered in Two Forms	2-6
2-2	General Force-Equilibrium Relationships for Dynamic Loading	2-6
2-3	Schematic of Dry Particulate Soil	2-8
2-4	Idealized Stress-Strain Curve	2-8
2-5	Factors Influencing Stress-Strain Behavior of Soil	2-9
2-6	Magnified View of Volcanic Scoria Grains	2-9
2-7	Flow Chart Illustrating Separation of Soil Property Effects	2-17
2-8	Sieve Shaker	2-19
2-9	Constant Temperature Oven	2-20
2-10	Triple Beam Balance	2-21
2-11	Sample Splitter	2-21
2-12	Grain Size (Sieve) Analysis	2-23
2-13	Grain Size Curve for Example Data in Figure 2-5	2-25
2-14	Average Curve for Six Basic Test Soils	2-27
2-15	Unit Weight vs. Relative Density Graph	2-31
2-16	Vibrating Tool and Proctor Mold	2-32
2-17	Average Density vs. Relative Density Curves for Six Basic Soil Types	2-36
2-18	LM Soil Mechanics Study Time of Compaction Study	2-39
2-19	Direct Shear Test Measurement	2-41
2-20	Schematic Drawing of Direct Shear Test Equipment	2-42
2-21	Direct Shear Test Data	2-43
2-22	Failure Envelope	2-44
2-23	Angle of Internal Friction vs. Relative Density	2-46
2-24	Photomicrograph of RS Soil	2-48
2-25	Hypothetical Failure Envelopes for Shear Failure Due to Breaking of Soil Particles	2-50
2-26	Triaxial Shear Test Machine	2-51
2-27	Penetrometer Test Fixture (LPT)	2-53
2-28	Load-Penetration Test (LPT) Setup	2-54
2-29	Load-Penetration Test (RS Dense)	2-55
2-30	Load-Penetration Test (LPT) Setup	2-58
2-31	Bearing Capacity Factors	2-62
2-32	Load-Penetration Curves for Two-Inch Diameter Cylinder in Soil No. 1 (RS Loose) ($D_r \approx 0.0$)	2-63
2-33	Load-Penetration Curves in RS Dense ($D_r \approx 0.94$)	2-64
2-34	Load-Penetration Curves for Four-Inch Cylinder in Soil No. 9 ($D_r \approx 0.76$)	2-65
2-35	Load-Penetration Curves for Four-Inch Cylinder in RS Dense ($D_r \approx 0.97$)	2-67
2-36	Load-Penetration Test Results in RS Soil Pressure Parameter vs. Relative Depth	2-70
2-37	Pressure Parameter vs. Relative Depth in Intermediate and Dense RS Soil	2-71

LIST OF ILLUSTRATIONS (Continued)

Figure	Title	Page
2-38	Load-Penetration Test Results in SS Soil Pressure Parameter vs. Relative Depth	2-72
2-39	Load-Penetration Test Results in PS Soil Pressure Parameter vs. Relative Depth	2-73
2-40	Load-Penetration Curves for Four-Inch Cylinder in RS Loose at Different Rates of Penetration	2-75
2-41	Load-Penetration Curves for Four-Inch Cylinder in RS Intermediate at Different Rates of Penetration	2-76
2-42	Load-Penetration Curves for Four-Inch Cylinder in RS Dense at Different Rates of Penetration	2-77
2-43	Load-Penetration Curves for Two-Inch Cylinder in RS Intermediate at Different Rates of Penetration	2-78
2-44	Load-Penetration Curves for Four-Inch Cylinder in RS Dense Soil in Bins of Various Sizes	2-79
2-45	Load-Penetration Curves in Soil No. 1 (RS Loose) ($D_r \approx 0.0$)	2-81
2-46	Load-Penetration Curves in Soil No. 3 (RS Intermediate) ($D_r \approx 0.29$)	2-82
2-47	Load-Penetration Curves in Soil No. 4 (RS Dense) ($D_r \approx 0.69$)	2-83
2-48	Load-Penetration Curves for Four-Inch Cylinder and Four-Inch Footpad in Soil No. 9 (SS Dense) ($D_r \approx 0.76$)	2-84
2-49	Comparison of Footpad and Cylinder Load-Penetration Tests Pressure Parameter vs. Relative Depth in RS Soil	2-85
2-50	Load-Penetration Test Results Using Footpad in SS Soil Pressure Parameter vs. Relative Depth	2-86
2-51	Mechanical Strength Coefficient From Subscale Drag Test Analysis, C_{MS}	2-87
2-52	Pressure Parameter at a Relative Depth of 0.2 vs. Dynamic Penetrometer Test Results	2-89
2-53	Dynamic Penetrometer (DPT) and Schematic	2-91
2-54	Typical DPT Signatures	2-92
2-55	LM Soil Mechanics Study Dynamic Penetrometer Test Correlation	2-93
2-56	Grain Size Analysis Curves - LS SMS	2-95
2-57	PS Soil Used in Subscale Drag Tests	2-96
2-58	RSM Soil Used in Subscale Drag Tests	2-97
2-59	Mass Density Scoop	2-100
2-60	LM SMS Density vs. Test Numbers - SS Drag Tests	2-102
2-61	Subscale Drag Test Hopper	2-105
2-62	Soil Removal System (Front View)	2-106
2-63	Full-Scale Impact and Model Test Bed Soil Preparation Equipment	2-108
2-64	Air Operated Chipping Hammer and Plate	2-111
2-65	Soil Densifying Roller	2-112

LIST OF ILLUSTRATIONS (Continued)

Figure	Title	Page
3-1	Subscale Drag Test Equipment	3-3
3-2	Subscale Drag Test Setup	3-6
3-3	Rear View of Drag Test Equipment (Before Modification) Showing Acceleration Device	3-8
3-4	Close Up View of Constant Velocity Drive Mechanism	3-8
3-5	Idealized Three-Dimensional Load Cell	3-10
3-6	Operational Principle of the Three-Dimensional Load Cell	3-10
3-7	Schematic Diagram of Three-Dimensional Load Cell for Subscale Drag Test System	3-12
3-8	Effect of Drag Load on Vertical Sensor	3-14
3-9	Effect of Vertical Load on Drag Load Sensors	3-14
3-10	Subscale Instrumented Footpad for Drag Test	3-15
3-11	Diagram of Subscale Drag Test Data Recording Instrumentation	3-16
3-12	Subscale Oblique Impact Test Fixture	3-18
3-13	Subscale Oblique Impact Test Equipment	3-21
3-14	Three-Dimensional Load Cell for Subscale Oblique Impact Tests	3-24
3-15	Subscale Instrumented Footpad for Oblique Impact Tests	3-24
3-16	Effect of Drag Load on Vertical Load Sensor	3-25
3-17	Effect of Side Load on Vertical Load Sensor	3-26
3-18	Effect of Vertical Load on Drag Load Strain	3-26
3-19	Diagram of Subscale Oblique Impact Test Recording Instrumentation	3-26
3-20	Full-Scale Impact Test Fixture	3-28
3-21	Full-Scale Impact Test Rig	3-29
3-22	Oblique Impact Test Structure - Assembly	3-30
3-23	Full-Scale Load Cell and Footpad	3-33
3-24	Effect of Vertical Load on Drag Load Sensors	3-34
3-25	Effect of Drag Load on Vertical Load Sensors	3-34
3-26	Simulated LM Footpad	3-36
3-27	Full-Scale Oblique Impact Test Recording Instrumentation	3-37
3-28	Perspective View of the Full-Scale LM Footpad Drag Test Facility	3-39
3-29	General Arrangement Hydraulic Power/Control Unit	3-40
3-30	Strut and Footpad - Full-Scale Drag Test System	3-43
4-1	Impact Phase Division	4-2
4-2	Subscale Drag Test Parameter Values	4-5
4-3	Number of Subscale Drag Tests for Each Soil Studied	4-5
4-4	Nomenclature for Constant Penetration Drag Tests	4-6
4-5	Drag Test Record Run No. 2-20	4-6
4-6	Subscale Drag Test Results - Soil No. 1 - RS Loose	4-8
4-6	Subscale Drag Test Results - Soil No. 1 - RS Loose	4-9
4-6	Subscale Drag Test Results - Soil No. 1 - RS Loose	4-10
4-7	Subscale Drag Test Results - Soil No. 2 - PS Loose	4-11
4-8	Subscale Drag Test Results - Soil No. 3 - RS Intermediate	4-12
4-9	Subscale Drag Test Results - Soil No. 4 - RS Dense	4-13
4-10	Subscale Drag Test Results - Soil No. 5 - RSM_a Loose	4-14

LIST OF ILLUSTRATIONS (Continued)

Figure	Title	Page
4-11	Subscale Drag Test Results - Soil No. 6 - RC2 Loose	4-15
4-12	Subscale Drag Test Results - Soil No. 7 - SS Loose	4-16
4-13	Subscale Drag Test Results - Soil No. 8 - SS Intermediate	4-17
4-14	Subscale Drag Test Results - Soil No. 9 - SS Dense	4-18
4-15	Subscale Drag Test Results - Soil No. 10 - LSM Intermediate	4-19
4-16	Subscale Drag Test Results - Soil No. 11 - LSM Dense	4-20
4-17	Oblique Impact Test Parameter Values	4-21
4-18	Number of Impact Tests for Each of the Soils Studied	4-22
4-19	Force and Displacement vs. Time for Impact Tests on Various RS Soils	4-23
4-20	Force vs. Displacement for Vertical Impact Tests on Various RS Soils	4-24
4-21	Force vs. Displacement for Vertical Impact Tests on RS Loose Soil	4-25
4-22	Force vs. Displacement for Vertical Impact Tests Using 6.17 and 37-Inch Diameter Footpads	4-26
4-23	Drag Force Parameter vs. Velocity Parameter - Soil No. 1 - RS Loose	4-28
4-24	Numerical Results of Statistical Estimation of Coefficients in the Drag Force Equation	4-35
4-25	Drag Force Parameter vs. Velocity Parameter - Soil No. 1 - RS Loose	4-38
4-26	Drag Force Parameter vs. Velocity Parameter - Soil No. 2 - PS Loose	4-39
4-27	Drag Force Parameter vs. Velocity Parameter - Soil No. 3 - RS Intermediate	4-39
4-28	Drag Force Parameter vs. Velocity Parameter - Soil No. 4 - RS Dense	4-40
4-29	Drag Force Parameter vs. Velocity Parameter - Soil No. 5 - RSM_a Loose	4-40
4-30	Drag Force Parameter vs. Velocity Parameter - Soil No. 6 - RC2 Loose	4-41
4-31	Drag Force Parameter vs. Velocity Parameter - Soil No. 7 - SS Loose	4-41
4-32	Drag Force Parameter vs. Velocity Parameter - Soil No. 8 - SS Intermediate	4-42
4-33	Drag Force Parameter vs. Velocity Parameter - Soil No. 9 - SS Dense	4-42
4-34	Drag Force Parameter vs. Velocity Parameter - Soil No. 10 - LSM Intermediate	4-43
4-35	Drag Force Parameter vs. Velocity Parameter - Soil No. 11 - LSM Dense	4-43
4-36	Mechanical Strength Coefficient vs. tan ϕ for Zero Relative Density Soils	4-45
4-37	$C_{MS}/29 \tan \phi$ vs. D_r for All Soils Based Upon Drag Test Results	4-46
4-38	Schematic of Dynamic Model	4-48
4-39	Normalized Footpad Geometry	4-51
4-40	Preliminary Values of Coefficients	4-53
4-41	Comparison of Experimental and Computed Force vs. Time Histories	4-54
4-42	Comparison of Experimental and Computed Force vs. Penetration Histories	4-54
4-43	Comparison of Experimental and Computed Force vs. Time Histories	4-55
4-44	Comparison of Experimental and Computed Force vs. Penetration Histories	4-55
4-45	Comparison of Experimental and Computed Force vs. Time Histories	4-56

LIST OF ILLUSTRATIONS (Continued)

Figure	Title	Page
4-46	Comparison of Experimental and Computed Force vs. Penetration Histories	4-56
4-47	Comparison of Experimental and Computed Force vs. Time Histories	4-57
4-48	Comparison of Experimental and Computed Force vs. Penetration Histories	4-57
4-49	Sample Analog Computer Output	4-58
4-50	Variation of Normalized Dynamic Mechanical Strength With Relative Density - Drag and Impact Test Results	4-60
4-51	Finalized Values of Coefficients - 1/6 Scale Footpad	4-62
4-52	Comparison of Experimental and Computed Force vs. Penetration Histories	4-64
4-53	Comparison of Experimental and Computed Force vs. Penetration Histories	4-64
4-54	Comparison of Experimental and Computed Force vs. Penetration Histories	4-65
4-55	Comparison of Experimental and Computed Force vs. Penetration Histories	4-65
4-56	Coefficients Applicable to Reduced Gravity Test - 1/6 Scale Footpad	4-66
4-57	Schematic and Nomenclature for Dynamic Soil Model	4-67
4-58	Variation of Normalized Dynamic Mechanical Strength with Relative Density - Drag and Impact Test Results	4-72
4-59	Static Load vs. Penetration Curves for RS Type Soils	4-73
4-60	Dynamic and Mechanical Strength Coefficients vs. D_r	4-75
4-61	Normalized Static Mechanical Strength Coefficients vs. D_r	4-76
4-62	Dynamic Impact Test Results and Comparison of Pre and Post Impact Static Strength	4-78
4-63	Normalized Momentum Transfer Drag Coefficient vs. D_r	4-80
4-64	Effect of Path Angle, θ, on the Normalized Drag Coefficient	4-81
4-65	Effect of the Local Acceleration of Gravity on the Normalized Drag Coefficient - SS Dense Results with $D_r \simeq 0.75$ to 0.85	4-83
4-66	Ratio of Experimentally Determined η Values to Conical Soil Wedge Values vs. Relative Density	4-83
4-67	Effective Elastic Modulus vs. Sonic Modulus at Four psi Confining Pressure	4-85
4-68	Footpad Pitch Angle vs. Dimensionless Depth - Velocity Parameter	4-87
4-69	Axial Pressure vs. Normal Pressure for Subscale Drag Tests Using RS Soils	4-88
4-70	ψ vs. Depth of Penetration for Full-Scale Impact Tests At Various Values of θ in SS Loose Soil	4-90
4-71	Ratio of Axial Force to Normal Force vs. Path Angle For Various Depths of Penetration	4-91

LIST OF ILLUSTRATIONS (Continued)

Figure	Title	Page
5-1	Langley-Grumman 1/6-Scale Dynamic Model of LM Before Modification	5-3
5-2	Modified LM Model	5-5
5-3	General View of Partly Assembled Modified Model	5-6
5-4	Exploded View of Leg Assemblies	5-8
5-5	LM Model - Leg and Footpad Identification	5-10
5-6	Instrumentation to Measure Pad Forces, Moments, and Angular Displacement on Dynamic Model	5-11
5-7	Nomenclature of Pad Moment and Force Resolution Equations	5-12
5-8	Pad Instrumented to Measure Forces, Moments and Angles	5-14
5-9	Comparison of Modified 1/6-Scale Model With Present LM Configuration	5-15
5-10	Comparison of 1/6-Scale Model and Present LM Loads vs. Strokes	5-16
5-11	LM Coordinate System	5-19
5-12	Sketch of Six Degree of Freedom Drop Test System and Soil Bed	5-23
5-13	Six Degree of Freedom Drop Test Rig	5-24
5-14	LM Model Drop Test Instrumentation	5-26
5-15	Magnetic Tape to Oscillograph Reproduction	5-27
5-16	Spiked Footpad Assembly-Rigid Surface Tests	5-34
5-17	Spiked Footpad Assembly	5-36
5-18	Rigid Surface Test Bed	5-36
5-19	Rigid Surface Landing Stroboscopic Photo Drop No. 53	5-36
5-20	Stability Profile - Rigid Surface Tests	5-37
5-21	Flow Chart - Data Reduction Program	5-42
5-22	Absolute Footpad Velocity vs. Time (NASA Test No. 1)	5-47
5-23	Footpad Heading With Respect to Vertical (θ) vs. Time (NASA Test No. 1)	5-48
5-24	Footpad Penetration Depth vs. Time (NASA Test No. 1)	5-49
5-25	Strut Axial Load vs. Time (NASA Test No. 1)	5-50
5-26	CG Vertical Acceleration vs. Time (NASA Test No. 1)	5-51
5-27	CG Vertical Velocity vs. Time (NASA Test No. 1)	5-52
5-28	CG Vertical Displacement vs. Time (NASA Test No. 1)	5-53
5-29	Absolute Footpad Velocity vs. Time (NASA Test No. 1)	5-54
5-30	Footpad Heading With Respect to Vertical (θ) vs. Time (NASA Test No. 2)	5-55
5-31	Footpad Penetration Depth vs. Time	5-56
5-32	Strut Axial Load vs. Time (NASA Test No. 2)	5-57
5-33	CG Vertical Acceleration vs. Time (NASA Test No. 2)	5-58
5-34	CG Vertical Velocity vs. Time (NASA Test No. 2)	5-59
5-35	CG Vertical Displacement vs. Time (NASA Test No. 2)	5-60
5-36	CG Horizontal Velocity vs. Time (NASA Test No. 2)	5-61
5-37	CG Horizontal Displacement vs. Time (NASA Test No. 2)	5-62
5-38	Vehicle Pitch Velocity vs. Time (NASA Test No. 2)	5-63
5-39	Vehicle Pitch Angle vs. Time (NASA Test No. 2)	5-64
5-40	Stability Profile For Model Landings in RS Dense Soil, 2-2 Downhill	5-70
5-41	Stability Profile For Model Landings in RSM-b Soil, 2-2 Downhill	5-71
5-42	Stability Profile For Model Landings in RS Dense Soil, 22 1/2° Yaw Downhill	5-72

LIST OF ILLUSTRATIONS (Continued)

Figure	Title	Page
5-43	Exploratory Model Drop No. 2	5-75
5-44	Exploratory Model Drop No. 3	5-75
5-45	Exploratory Model Drop No. 4	5-75
5-46	Exploratory Model Drop No. 5	5-76
5-47	Exploratory Model Drop No. 6	5-76
6-1	Block Diagram For Typical Landing Dynamics Computer Program	6-2
6-2	Flow Diagram For Subroutine SOIL	6-4
6-3	Flow Diagram For Subroutine BEN	6-5
6-4	Rigid Surface LM Model Drops	6-7
6-5	Stability Profile For Model Landing on Wooden Surface	6-8
6-6	LM Model Drops on RS Dense Soil	6-9
6-7	Stability Profile For Model Landings on RS Dense Soil, 2-2 Downhill	6-10
6-8	LM Model Drops For RSM-b Soil	6-12
6-9	Stability Profile For Model Landing in RSM-b Soil, 2-2 Downhill	6-13
6-10	LM Model Drops For Detail Correlation Studies	6-15
6-11	Detail Correlation Results For LM Model Drop No. 2	6-17
6-12	Computer Results For LM Model Drop No. 2	6-22
6-13	Detail Correlation Results For LM Model Drop No. 1	6-26
6-14	Detail Correlation Results For LM Model Drop No. 3	6-30
6-15	Detail Correlation Results For LM Model Drop No. 4	6-34
6-16	Detail Correlation Results For LM Model Drop No. 5	6-38
6-17	Detail Correlation Results For LM Model Drop No. 6	6-42
6-18	Detail Correlation Results For LM Model Drop No. 7	6-46
6-19	Detail Correlation Results For LM Model Drop No. 8	6-50
6-20	Computer Program For LM Model Drop No. 1	6-54
6-21	Computer Program For LM Model Drop No. 3	6-58
6-22	Computer Program For LM Model Drop No. 4	6-62
6-23	Computer Program For LM Model Drop No. 5	6-66
6-24	Computer Program For LM Model Drop No. 6	6-70
6-25	Computer Program For LM Model Drop No. 7	6-74
6-26	Computer Program For LM Model Drop No. 8	6-78
6-27	Comparison of Computed and Experimental Footpad Penetration Depths	6-82

LIST OF TABLES

Table	Title	Page
1-1	Test Soils and Properties	1-6
2-1	Estimated Lunar Soil Properties	2-12
2-2	Potential Test Soils and Preliminary Evaluation	2-14
2-3	Test Soils and Properties	2-16
5-T1	Basic Model Scale Factors	5-2
5-T2	List of Model Drop Tests	5-28
5-T3	Detailed Correlation Drops	5-45

SECTION I

INTRODUCTION

The basic purpose of the Lunar Module (LM) Soil Mechanics Study was to develop soil force laws which give the interrelationships between footpad motions and the resultant forces acting on the footpad during the brief period of the LM touchdown. Knowledge of this force/motion interaction is important since the soil reactive forces and the footpad motion control the overall landing dynamics of the vehicle. The landing dynamics includes such items as the vehicle translational and rotational velocities and accelerations during touchdown, landing gear shock strut stroking, vehicle toppling stability, and final vehicle orientation.

A considerable amount of study has been carried out dealing with the landing dynamics of LM using a rigid model of the lunar surface. Experimental model studies show, however, that there is a sizable difference in landing performance on a soil surface in comparison to rigid surface landings. Thus an accurate analysis of the landing performance and landing capabilities of the LM spacecraft requires an analytical force/motion model that accounts for the interaction of the lunar soil and the LM footpads.

To be used for analytical studies of vehicle performance, the soil/footpad force laws must relate instantaneous, three-dimensional footpad accelerations, velocities, and positions to the instantaneous soil forces - also three-dimensional. Angular pitching motion of the footpad must also be accounted for since the footpad is attached to the main leg of the landing gear system via a spherical pin joint. This type of force law is necessary because the analytical determination of vehicle performance during touchdown is carried out by a step-by-step numerical integration of the translational and rotational equations of motions of both the footpads and the main vehicle mass, with the footpad

forces determined from their motion conditions at the particular instant of time under consideration.

The approach taken in this program to develop the force relationships for the LM footpads is of a semi-empirical nature. A primarily analytical approach backed up by a minimum of experimental soil load/deformation data is not feasible because of the current state-of-the-art in soil dynamics. A purely experimental approach is not feasible because of the large number of parameters involved in the problem. The semi-empirical approach outlined below is believed to represent a practical compromise between these two extremes.

Briefly stated the approach taken consists of the following:

First, sufficient dynamic testing is conducted on a variety of soils and soil preparations to permit the nature of the soil response to be categorized.

Second, the data is carefully examined and a preliminary mathematical model is formulated using the principles of mechanics and factors known to affect soil response.

Third, dynamic soil testing equipment and procedures are evolved. These must allow for the controlled motion of a footpad into a (carefully) prepared soil test bed such that the force response of the soil can be studied as a function of the acceleration, velocity, penetration, and angular orientation of the footpad.

Fourth, a set of test soils is selected for more extensive experimentation. The soils chosen must satisfy two basic requirements; first, they must encompass the expected characteristics of the lunar soil, and second, they must display a sufficient range of basic soil properties to permit a quantitative assessment of the factors influencing soil response.

Fifth, dynamic tests are conducted on the selected soils using the controlled-motion test equipment mentioned in Step No. 3.

Analysis of the resulting data constitutes the sixth step in the procedure. The analysis centers on verification or improvement of the preliminary model introduced in Step No. 2. This includes the development of dimensionless force law coefficients in terms of the soil properties for the particular soils selected in Step No. 4.

The seventh and final step in the procedure consists of verification of the derived force law by independent tests.

Steps Nos. 1, 2, and 3 (exploratory testing, formulation of a preliminary mathematical model of the soil interaction, and evolving controlled motion dynamic soil testing equipment, respectively) were, to a large extent, accomplished in previous studies (References 1 and 2). Most of the dynamic soil testing equipment had been developed and used in these previous studies. The present study begins, essentially, with Step No. 4, the soil selection studies.

Selection of test soils for a program with the stated aims of the LM Soil Mechanics Study involves several key considerations. The first of these concerns the basic question of what set of soil properties will provide an adequate parametric definition of a soil for the purpose of predicting the forces acting on a spacecraft footpad. That is, if the soil/footpad interaction is treated as a "system" composed of an input, a transfer mechanism, and an output, the input would consist of the footpad translational accelerations, velocities, and displacements, and the angular orientation of the footpad. The transfer mechanism would consist of the geometric properties of the footpad and its articulation and the physical properties (or descriptors) of the soil. The output would consist of the forces acting on the footpad from the soil.

An adequate definition of the relationship between the input and the output requires a careful definition of the system. An inadequate definition can result in a variation in output force being related to a coincidental variation of a particular soil property rather

than being ascribed to the actual property causing that variation. While this may seem to be somewhat academic, it should be noted that there is a tendency in soil mechanics literature to define static resistance to penetration of the soil in terms of only three parameters of the soil (References 3, 4, 5, and 6 for example). These parameters are the "cohesive shear strength," c; the "soil angle of internal friction," ϕ; and the "weight density" of the soil, γ. A relatively minor amount of experimentation shows that two soils having identical values of these parameters can exhibit markedly different resistance levels to penetration depending on their degree of looseness. This is not a new finding. Terzaghi and Peck (page 124, Reference 7) in their equations for static bearing capacity differentiate between the force law coefficients to be used for dense soils exhibiting a "general shear" failure and those to be used for a loose soil exhibiting "local shear" failure --- with an extrapolation recommended for soils of intermediate degrees of compaction.

As a result of the initial studies associated with the soil selection phase of the program a total of seven soil properties or descriptors was chosen to represent the soil system. Later studies, utilizing the data from the controlled motion dynamic soil tests, reduced the number of significant parameters to four. The final set consisted of the mass density of the soil, $\rho = \gamma/g$, where g is the gravitation constant; the angle of internal friction of the soil, ϕ; the soil relative density, D_r (which quantifies degree of compactiveness of the soil); and an effective elastic modulus of the soil, E_e. The studies were limited to soils with nearly zero values of the cohesive strength parameter, c.

The second key consideration in the selection of the test soils for the LM Soil Mechanics Study consists of the selection of the range of soil properties which must be covered in the test program. As previously noted in Step No. 4, the range and nature of the properties must consider reasonable estimates of the lunar soil characteristics, and further, must include a broad enough range of these so that the influence of the chosen parameters is clearly evident from the test data trends.

Best estimates of the lunar soil properties, based primarily on the data of References 8 and 9, are as follows: The angle of internal friction, ϕ, is estimated to be in the range of 35 to 45 degrees depending on the relative density assumed for the soil. The relative

density, D_r, is estimated to be greater than 50 percent. The cohesive component of shear strength, c, is small with estimates putting it in the range of 0.02 to 0.10 psi. The mass density of the soil, ρ, is estimated to be between 1.0 and 2.0 grams/cubic centimeter, with a "most likely" value in the vicinity of 1.5 grams/cubic centimeter.

Eleven test soils were used in the semi-empirical determination of the force laws for the LM footpads. The properties of these soils are given in Table 1-1 along with the properties of soil No. 12 which was used in the final analytical/experimental correlation studies to be discussed below. It can be seen from Table 1-1 that the properties of the test soils covered a broad enough range such that parametric effects, within the general range of lunar soil property estimates, can be established.

A third key consideration in the selection of the test soils is the ease with which the soils can be handled and placed in the test beds. A large number of dynamic tests are required to provide data for the semi-empirical determination of the force laws. Since each test requires a completely new undisturbed soil surface, it is important to be able to prepare the soil test beds quickly. In addition, the test bed properties must be consistent from test to test.

A considerable amount of effort was carried out first to select soils which met all of these considerations and then to develop soil placement and handling equipment which would allow rapid preparation of the test beds - and would yield consistent soil properties for a given test bed preparation.

The dynamic soil/footpad testing equipment, mentioned in Step No. 3 of the approach discussion, was readied for the experimental studies during the soil selection phase of the program. This equipment consisted of two oblique impact testers (one adaptable to a full-scale LM footpad and one for a 1/6th-scale LM footpad), and a drag test machine. The drag test machine used was sized for the 1/6th-scale LM footpad. A drag test machine for a full-scale footpad was carried through the design phase, but, because of expense, it was not constructed. The decision was made to rely primarily on the oblique impact test equipment for investigation of scaling effects from the 1/6th- to full-scale

TABLE 1-1. TEST SOILS AND PROPERTIES

No.	Bendix Designation	Description	Relative Density D_r	Unit Weight γ pcf	Friction Angle ϕ	Elastic Modulus E,psi*	Grain Size Parameters: Mean Size $\mu_w$mm	Uniform Coeff. C_μ	% -200**	D_{95}*** mm
1	RS Loose	Red Crushed Volcanic Scoria (narrowly graded)	0	41.4	40°	5,500	1.8	1.7	<3%	2.7
2	PS Loose	White Crushed Pumice (narrowly graded)	0	23.8	43°	4,500	1.8	1.7	<3%	2.7
3	RS Inter.	Red Crushed Volcanic Scoria (narrowly graded)	.45	45.9	44.5°	8,600	1.8	1.7	<3%	2.7
4	RS Dense	Red Crushed Volcanic Scoria (narrowly graded)	.80	50.5	47.3°	10,900	1.8	1.7	<3%	2.7
5	RSM-a Loose	Mixture of RS and Crushed Marble (MS) (narrowly graded)	0	58.2	37°	7,800	2.4	1.6	<3%	2.7
6	RC2 Loose	Red Crushed Volcanic Scoria (Broadly graded)	0	61.4	43°	8,000	1.1	17.0	11%	4.7
7	SS Loose	White Silica Sand (Wedron 4040-narrowly graded)	0	94.7	29°	10,000	0.4	1.3	0%	0.52
8	SS Inter.	White Silica Sand (Wedron 4040-narrowly graded)	.53	104	36.8°	18,000	0.4	1.3	0%	0.52
9	SS Dense	White Silica Sand (Wedron 4040-narrowly graded)	.69	107	39°	24,000	0.4	1.3	0%	0.52
10	LSM Inter.	Mixture of RC and Air-Floated Clay	.50	77.5	42°	4,000	.07	large	51%	4
11	LSM Dense	Mixture of RC and Air-Floated Clay	.70	82	42°	6,000	.07	large	51%	4
12	RSM-b Dense	Mixture of RS and Crushed Marbel (MS) (narrowly graded)	.75	85	48°	20,000	2.15	1.87	<1%	2.9

*Measured by sonic means at 4 psi confining pressure.
**Percent of material (by weight) passing thru a No. 200 sieve (ACS).
***Diameter at 95% "smaller than" point in standard sieve analysis.

range. However, some investigation of scaling effects was carried out on the subscale drag test equipment using 4.10 and 6.17 inch diameter footpads.

The full-scale and subscale oblique impact testers were similar in operation. Each consisted of an instrumented LM shape footpad attached to the lower end of a moving mass. The mass was guided on a set of bearings so that the velocity vector angle was fixed during footpad impact and penetration into the soil. Propulsion of the moving mass was provided by an air-powered piston which disengaged prior to footpad impact. Impact velocity, angle of impact, and the total mass of the impacting system could be varied to study the variation of the soil reaction as a function of the footpad's motion variables.

The subscale drag test equipment consisted of an instrumented strut-footpad system attached to a movable carriage. The carriage ran along a set of fixed horizontal guide rails, and its initial acceleration, and running velocity (constant over approximately 1/3 of the total running distance) could be varied. In addition, the footpad penetration could be varied. These variations allowed study of the vertical and horizontal footpad forces under the conditions of low penetration velocities.

In addition to the above test equipment, which was used to obtain the bulk of the test data used in the development of the semi-empirical force laws, a separate set of 1/6th-scale footpad impact tests, similar to those using the oblique impact test equipment were conducted to study the effects of pore air and gravitational acceleration on the resultant footpad reactions. These studies were made by the IIT Research Institute under a subcontract of the main program. Pore air effects were evaluated by conducting identical tests in both a normal atmosphere and in an induced vacuum. Gravitational acceleration effects were evaluated by repeating certain of the atmospheric tests on an accelerating soil test bed. The acceleration (which varied from approximately 1/6th earth g's to 1.0 earth g's) was obtained by using a partially counterbalanced platform mounted in a drop-test tower.

Analysis of all test data indicated that the soil reaction on the footpad could be represented by a nonlinear, second-order system, the components of which are shown schematically in Figure 1-1. The mass of the soil system was the result of a "stagnation mass" which formed in the soil immediately below the footpad and moved with the footpad except for

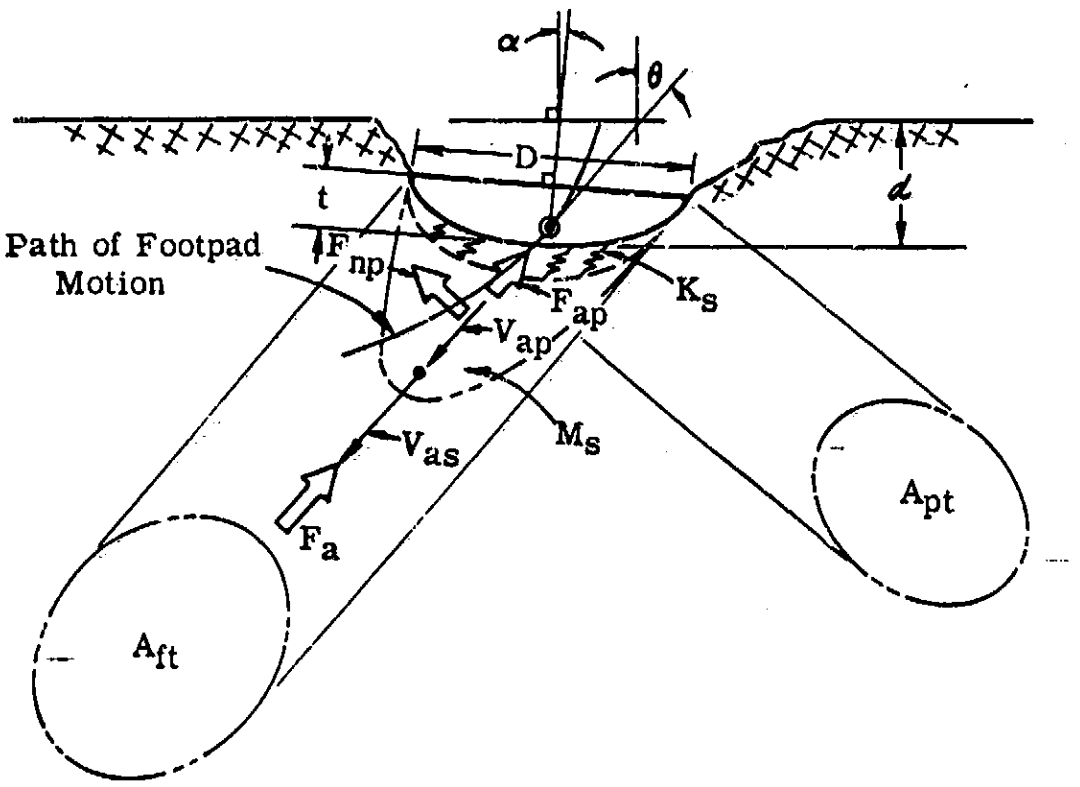

Figure 1-1. Schematic and Nomenclature for Dynamic Soil Model

the relative deflection of an idealized elastic spring located between the footpad and the soil mass. The reaction on the footpad was divided into two components. The first, F_{ap} (termed the footpad axial force), was aligned with the instantaneous velocity vector of the footpad, and the second, F_{np} (termed the footpad normal force), was perpendicular to the first.

The footpad normal force, F_{np}, was found to be equal to the axial force multiplied by a dimensionless factor. The factor was, in turn, found to be related to the instantaneous angle between the footpad velocity vector and the surface normal (θ), the depth of penetration of the footpad (d), and the area ratio between the footpad frontal area (A_{ft}) and the area obtained by a projection in the direction of the normal force (A_{pt}).

The footpad axial force, F_{ap}, was related primarily to the axial force acting on the stagnation mass (the force F_a in Figure 1-1). F_a, in turn, could be represented by an expression made up of two terms: the "mechanical strength," and the "momentum transfer force." The mechanical strength portion of the resistance is related to the strength parameters of the soil (ϕ and D_r) and the depth of penetration of the footpad (d). The momentum transfer force was found to be related to the velocity of the penetrating footpad. Analysis of the reduced gravity tests and the regular oblique impact tests showed that the magnitude of the momentum transfer term was dependent on the local acceleration of gravity and the strength parameters of the soil. It reflects a more complex phenomena than simply the acceleration of the soil particles up to the velocity of the footpad.

To account for variations in the soil resistance with the direction of penetration, both the mechanical strength and the momentum transfer portions of F_a were made functions of the angle θ (shown in Figure 1-1). The experimental results from the oblique impact tests and drag tests were used to determine the function as well as the force law coefficients.

The technique selected for the verification of the derived semi-empirical force laws (Step No. 7) consisted of comparisons of computer-simulated landing performance with the performance of a scale model LM when it was landed (drop tested) onto a prepared

soil bed. The computed performance was obtained using the NASA-MSC Lunar Module Landing Dynamics computer program with the semi-empirical force laws incorporated into its footpad dynamical equations. Two types of comparison were carried out. The first compared computed and experimental footpad penetrations, velocities, velocity angles, and ground reactions, while the second compared computed and experimental toppling stability profiles. Both types of comparisons showed good correlation between the experimental and computed results.

The principal output of the LM Soil Mechanics Study was a workable, experimentally verified, LM footpad-soil interaction model. Through the efforts of Manned Spacecraft Center personnel, this model has been incorporated into the Lunar Module Landing Dynamics computer program at NASA, MSC. The real-soil landing simulations made possible by the resulting program will enable considerably more realistic evaluation of the landing performance of the Lunar Module Spacecraft than was previously obtainable.

In addition, the techniques used in this study can, with appropriate modification, be adapted to the study of real-soil landings of other spacecraft landing on lunar or planetary soils. Application to the Surveyor Alightment Dynamics Computer Program (currently planned) will enhance the analysis of telemetered data received from the five successfully landed spacecraft. Application of developed procedures to landing system studies of other planned lunar and interplanetary spacecraft can be of considerable benefit in establishing more realistic landing performance data and landing gear design criteria for these vehicles.

The following sections discuss pertinent details of each of the major segments of the LM Soil Mechanics Study and are arranged in the approximate sequence of the technical approach steps outlined in this Introduction. Section II describes the efforts associated with selection of the test soils, identification of their properties, and development of equipment and procedures for soil test bed preparation and control. Section III describes the controlled motion dynamic test equipment used to obtain the data from which the soil interaction model was developed.

Section IV discusses the controlled motion footpad tests, the analysis of data, and development of the semi-empirical soil interaction model. Section V and VI describe the scaled-model landing equipment and test program and details of the correlation studies. Conclusions and recommendations, based on evaluation of the overall program results, are covered in Section VII. Certain applicable portions of the documentation are covered in Appendices A through E.

SECTION II

SOIL SELECTION AND CONTROL

2.1 INTRODUCTION

This section of the report discusses the selection of the test soils for the LM soil mechanics study, the test procedures used to measure the properties of the soils, and the methods used to prepare the soils in the test beds to obtain repeatable soil properties for multiple test bed preparations. The development of methods of monitoring the soil properties of the test beds throughout the program are also discussed.

Two preliminary questions must be answered before making any attempts at soil selection. The first of these is, "What are the soil properties which contribute to the soil dynamic strength?" This question is important since the essential aim of the study is to define the footpad reaction in terms of these properties. The second question is, "What are the estimated values of these properties for the lunar soil?"

The first two parts of this section of the report discuss the effort carried out to answer these two questions.

A summary of the main results of the "Soil Selection and Control" phase of the program is given at the end of this section.

2.1.1 Abbreviations of Units and Names in Soil Testing

BC - Black crusher run volcanic scoria.

C.E.C. - Consolidated Electrodynamics Corporation (refers to manufacturer of strain-gauge type accelerometer used in Dynamic Penetrometer).

Dense (i.e. describing a soil in a dense state of compaction; a soil for which $0.7 \leq D_r \leq 1.0$).

DD - Density Determination (refers to a determination of soil unit weight or density made in a weighed test bin of known volume and weight).

DPT - Dynamic Penetrometer Test.

DST - Density Scoop Test (refers to in In-Place Density Test done with a density scoop apparatus designed by E.T. Selig).

fps - feet per second.

fps^2 - feet per second per second.

FSIT, FSIMP Test - Full Scale Oblique Impact Test.

g., G. - gravitational constant (earth = 32.2 fps^2; moon = 5.3 fps^2).

G.S.A. - Grain Size Analysis.

INTER - Intermediate; describing a soil in an intermediate state of compaction; a soil for which $0.3 \leq D_r \leq 0.7$.

ksi, KSI --Kips per square inch.

ksf, KSF - Kips per square foot.

LOOSE - Loose; describing a soil in a loose state of compaction; a soil for which $0.0 \leq D_r \leq 0.3$.

LM SMS - Lunar Excursion Module Soil Mechanics Study.

LPT - Load-Penetration Test; a test for determination of bearing strength of a soil.

LSM - A basic test soil type used in the LM SMS; a mixture of crushed volcanic scoria (RC2) and air-floated clay designed to simulate certain features of the lunar soil as indicated by the Surveyor I photographs.

mm - millimeter(s).

MMDT - Minimum-Maximum Density Test; test used to establish relative density of granular soil.

ms, msec - millisecond(s); 1 ms = 0.001 sec.

pcf, PCF - pounds per cubic foot.

PFT - Passive Failure Test; a model retaining wall test used to determine angle of internal friction of a soil.

PS - White narrowly graded crushed pumice; a basic test soil type used in the LM SMS.

psi, PSI - pounds per square inch.

psf, PSF - pounds per square foot.

RC - Red broadly-graded "crusher run" andesitic volcanic scoria; one of the basic soil types investigated for use in the LM SMS. It was later replaced with the RC2 since it was not available in the amounts needed for the program.

RC2 - Red broadly-graded "crusher run" andesitic volcanic scoria; one of the basic soil types used in the LM SMS. It was obtained from the same source as the RS material.

RS - Red narrowly-graded crushed volcanic scoria; one of the basic soil types used in the LM SMS.

RSM-a - A narrowly-graded mixture of five parts of RS material and seven parts of crushed marble by weight; one of the basic soil types used in the LM SMS.

RSM-b - A narrowly-graded mixture of one part of RS material and three parts of crushed marble by weight; one of the basic soil types used in the LM SMS.

SSDT, SSDRAG Test - Subscale Drag Test; one of the tests made with a scaled-down LEM footpad used in the development of the soil-footpad force laws in the LM SMS.

SSIT, SSIMP Test - Subscale Oblique Impact Test; one of the tests made with a scaled-down LEM footpad used in the development of the soil-footpad force laws in the LM SMS.

tsf, TSF - Tons per square foot.

VPT - Visual Penetration Test; a type of Load-Penetration Test utilizing a half-cylinder against a glass plate for the purpose of viewing soil movement or failure during penetration.

2.2 SOIL PROPERTIES AFFECTING DYNAMIC STRENGTH OF DRY SOILS

As previously stated in the Introduction, the central purpose of this program is to find an interrelationship between soil descriptors and the resulting forces acting on the LM footpads for a prescribed motion of the footpads. Before attempting this, however, considerable care is required to establish a realistic set of descriptors. The form the force laws will take, their range of applicability, and their accuracy all depend on the initial set of descriptors. The selection of descriptors must be given particular attention in this program in that none of the various test soils used to establish empirical constants for the force laws is likely to be identical to the actual lunar surface. Interpolations and extrapolations will eventually be necessary, and this is only possible when the variable actually causing the change in resistance functions from soil to soil has been pinpointed.

There are two extremes possible in the initial selection of descriptors. An overly conservative approach, in which too many descriptors are investigated, will result in a wasteful expenditure of time and resources. On the other hand, the exclusion of significant descriptors will result in either complete confusion or in ascribing variation in forces to incidental variation in soil properties; that is, an erroneous force law.

At the outset a reasonable compromise between too few and too many descriptors is to include those that are known to affect the response with a subsequent sensitivity analysis, possibly reducing the initial selection.

A rational guide to the initial selection of experimental variables is the examination of variables necessary for a formal analysis. Common to all solid mechanics problems, the following requirements must be considered:

1. Boundary conditions.
2. Field equations.
3. Equation of state.

Each of these factors will now be considered, as summarized in Figure 2-1, in relation to the particular problem of the prediction of the LM landing performance of the lunar surface.

2.2.1 Boundary Conditions

In a broad sense, boundary conditions may be considered synonymous with environmental conditions. In particular, the lunar environment can be characterized as a vacuum, having extreme temperature variations with a reduced gravitational constant, compared to that of the earth.

These conditions immediately comment on the exclusion of certain soil parameters which would ordinarily be of importance in the earth environment. All moisture factors, such as moisture content, degree of saturation, permeability, pore fluid pressure, etc., are nonexistent and can thus be eliminated from consideration.

2.2.2 Field Equations

The description of the behavior of a material mass subjected to dynamic forces involves the satisfaction of the equations of motion, as stated in Figure 2-2, and a continuity or compatibility requirement. This requirement can be stated in a number of ways, but it basically involves kinematic requirements and functions of the material density.

It can be seen that the bulk density (γ) of the material must be known from an analytical point of view and thus must be included in an empirical study.

2.2.3 Equation of State

To transform the stresses in the equations of motion into displacements, an equation of state relating stresses to strain and/or strain rates for the material under consideration must be stated. This element of the analysis is precisely the reason this problem is so complex.

For a dry particulate material, schematically shown in Figure 2-3; the strain mechanism involves the deformation of the individual grains and the rolling, sliding, interlocking action of one grain relative to another.

ENVIRONMENT
(boundary conditions)

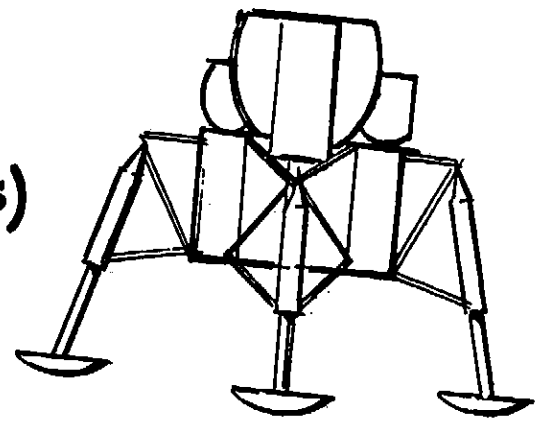

FIELD EQUATIONS
(eqs. of motion-continuity)

EQUATION OF STATE
(stress-strain law)

Figure 2-1. Factors Considered in Two Forms (Analysis)

$$\frac{\partial \sigma_x}{\partial x} + \frac{\partial \tau_{yx}}{\partial y} + \frac{\partial \tau_{zx}}{\partial z} = \frac{\gamma}{g}\frac{\partial^2 u}{\partial t^2}$$

$$\frac{\partial \tau_{xy}}{\partial x} + \frac{\partial \sigma_y}{\partial y} + \frac{\partial \tau_{zy}}{\partial z} = \frac{\gamma}{g}\frac{\partial^2 v}{\partial t^2}$$

$$\frac{\partial \tau_{xz}}{\partial x} + \frac{\partial \tau_{yz}}{\partial y} + \frac{\partial \sigma_z}{\partial z} + \gamma = \frac{\gamma}{g}\frac{\partial^2 w}{\partial t^2}$$

Figure 2-2. General Force-Equilibrium Relationships for Dynamic Loading

If the discipline of soil mechanics could provide a functional relationship describing a typical stress-strain curve as shown in Figure 2-4, in terms of the aforementioned strain mechanism, the issue would be greatly simplified. Unable to do this, it is only possible to state qualitatively which soil properties control the stress-strain behavior of the material under study. This qualitative relationship is summarized in Figure 2-5.

For conventional cohesionless earth soils the magnitude of the deformation of individual grains is usually small compared to the relative motion between grains. The magnitude of this deformation may not be negligible for highly vesicular volcanic lunar simulants. Figure 2-6 shows a magnified view of individual grains of a volcanic scoria used as one of the test soils in this study. It can be seen that the grain structure differs drastically from that of more typical terrestial soils.

A measure of the stress-strain behavior or individual grains is provided by the slope (elastic or Young modulus) of the approximately linear portion of the overall stress-strain curve at very small (recoverable) strain values. Relative grain motion is essentially nonrecoverable (16)*; thus the above criterion is a fairly reliable estimate of individual grain elasticity. This tends to be substantiated by BARKAN (10) in view of the insensitivity of E, the elastic modulus, to certain variables, such as porosity, which are known to influence relative grain motion in conventional sands.

The factors which influence the relative movement between individual grains as a function of stress level have not received much attention, with one outstanding exception, namely, the ultimate stress level. Obviously, this particular point of the stress-strain curve has been studied intensively by the foundation engineer because of his interest in stability calculations. Basically, the argument concerning relative grain motion at all stress levels will rest on conclusions made at the peak or maximum point of the stress-strain curve.

---

* Numbers in parentheses indicate References.

Figure 2-3. Schematic of Dry Particulate Soil

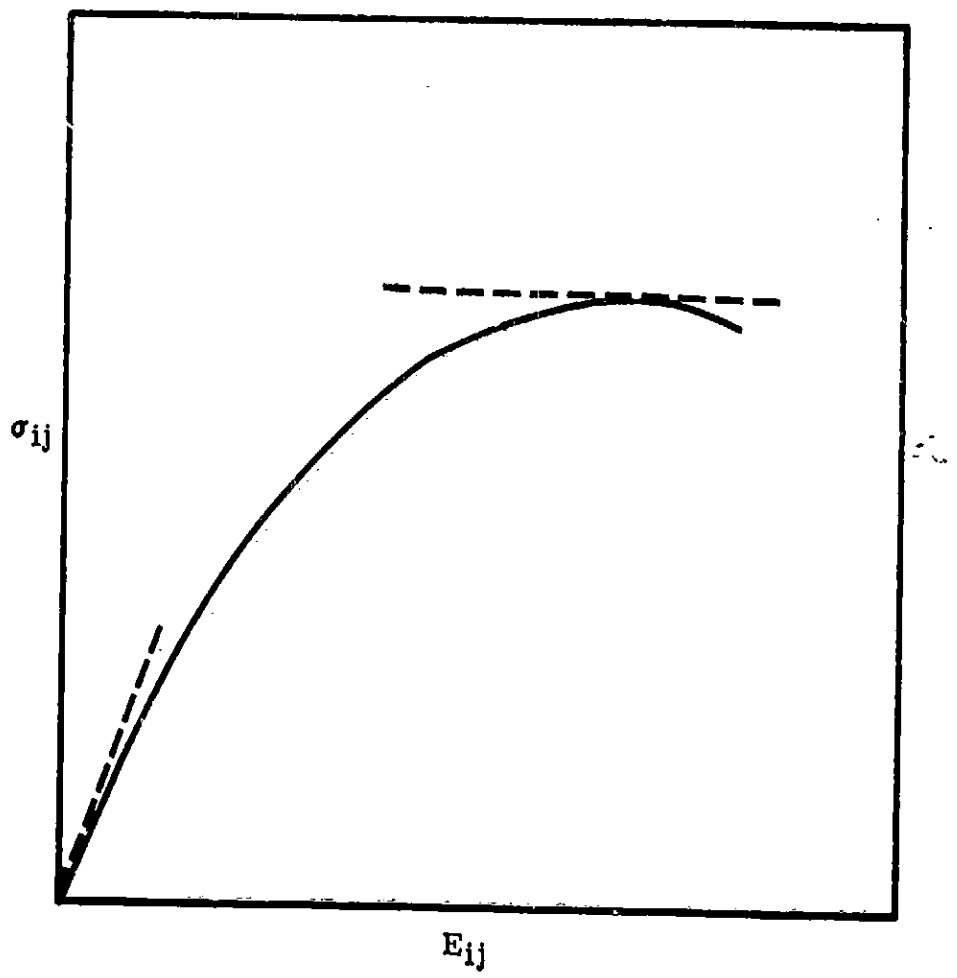

Figure 2-4. Idealized Stress-Strain Curve

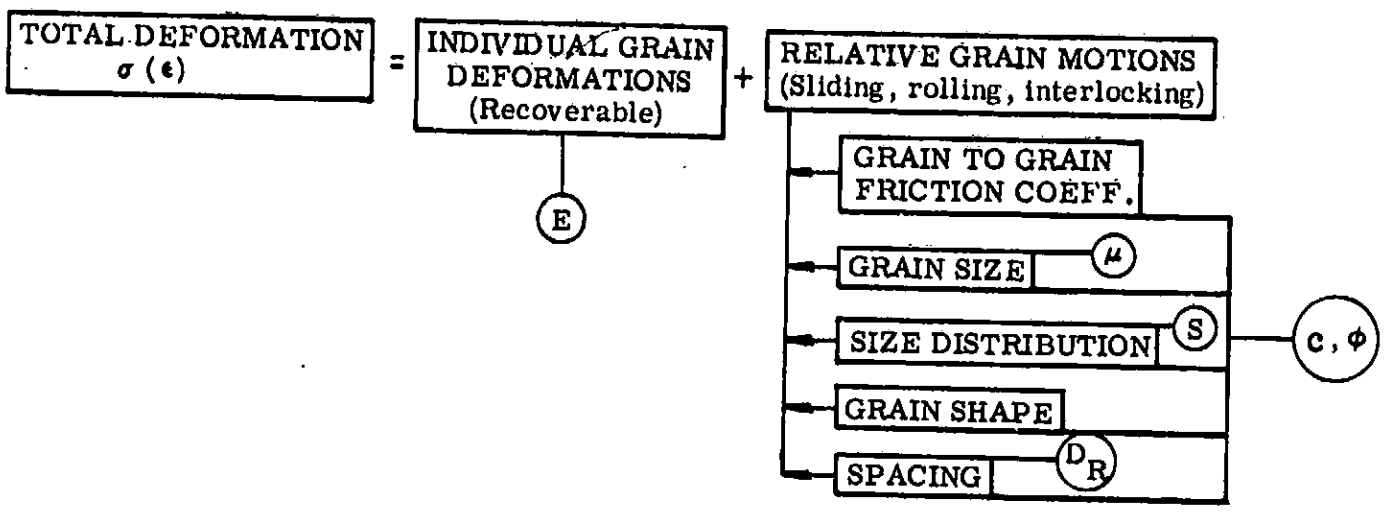

Figure 2-5. Factors Influencing Stress-Strain Behavior of Soil

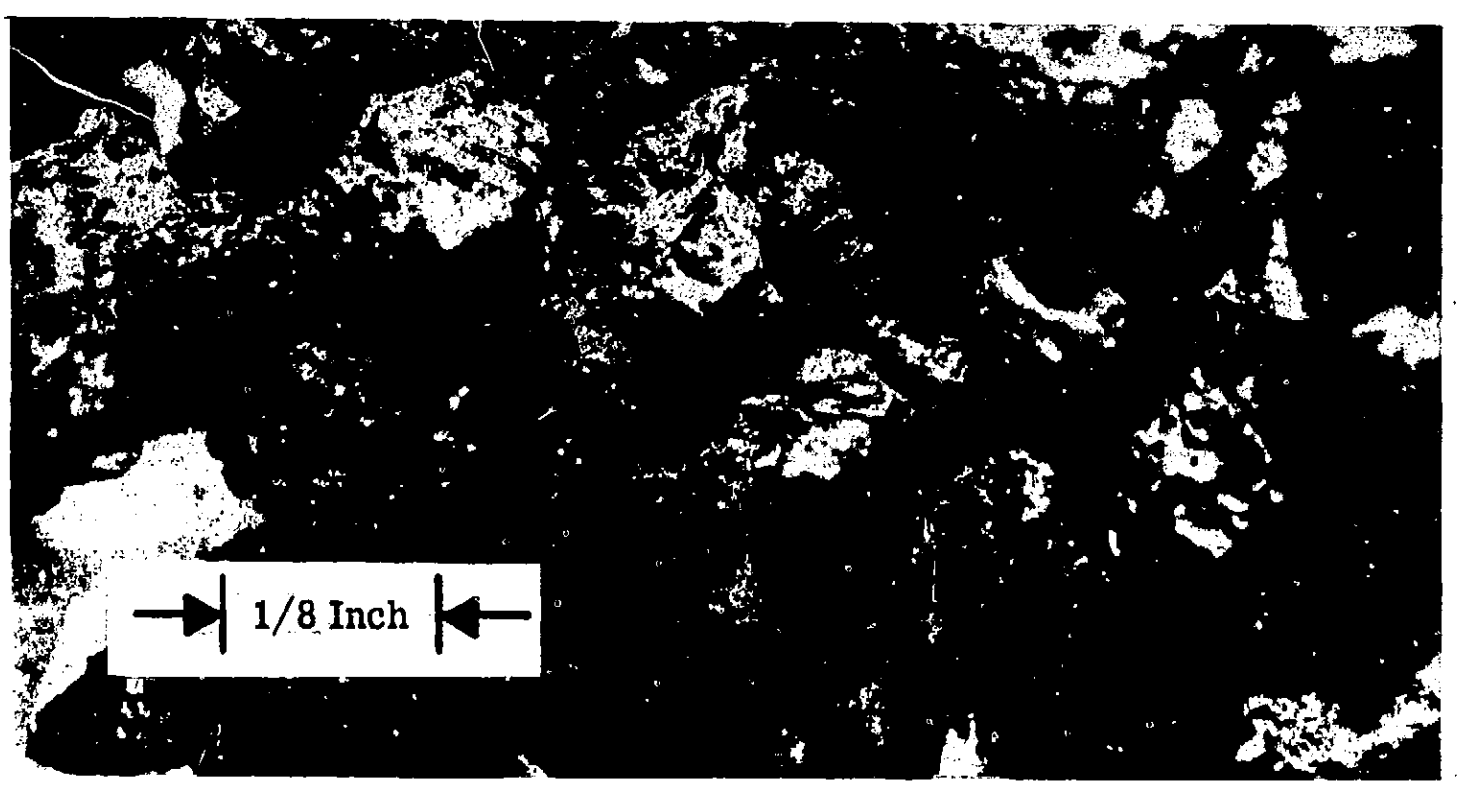

Figure 2-6. Magnified View of Volcanic Scoria Grains

There is general agreement (12, 15) regarding those factors which control the "strength" of dry granular soils and thus the ability of one grain to move with respect to another while offering maximum resistance. These factors are the grain-to-grain frictional resistance (dictated by the texture of individual grain surfaces), grain shape, grain size, grain size distribution, and spacing between grains. Each of these variables must be quantitively described for the subsequent experimental investigation. Size and spacing effects are conveniently handled with the following descriptors:

grain size - mean grain size (μ)

grain size distribution - standard deviation of size distribution (S) or uniformity coefficient (C_u)

spacing - relative density (D_r).

Grain shape and grain-to-grain frictional resistance are not as easily described and, in fact, must be measured indirectly. The strength of a soil is typically described in terms of the intercept, C (cohesion), and slope, ϕ (internal friction angle), of the envelope of maximum shearing resistance versus normal stress on the failure plane. Thus if size and spacing effects (μ, S, D_r) are held constant, the "angle of internal friction" would provide a relative measure of grain shape and grain-to-grain friction for two different soils. The cohesion for lunar simulants would reflect "cementation" between particles.

No viscous or strain rate dependent properties have been considered for inclusion in the equation of state. This omission is based on the findings of a considerable amount of recent soil dynamics research which is summarized in reference (14) and indicates the insensitivity of the strength of dry granular material to strain rate variations.

Hence, in conclusion, the force displacement relation for a footpad as a function of soil parameters can be stated as shown below:

$$F(\delta) = f(\gamma, \mu, S, D_r, E, C, \phi)$$

Soil Parameters

where, F = force on footpad (F)

δ = displacement of footpad (L)

γ = soil density (F/L^3)

μ = mean grain size (L)

S = standard deviation in size (L)

D_r = relative density ($F^\circ\ L^\circ\ T^\circ$)

E = elastic (Young's) modulus (F/L^2)

C = cohesive strength parameter (F/L^2)

ϕ = angle of internal friction ($F^\circ\ L^\circ\ T^\circ$)

f = function of

2.3 ESTIMATIONS OF THE PROPERTIES OF THE LUNAR SOIL

In order for the test results and analysis to be meaningful, the test soils used in the LM Soil Mechanics Study must have property values which include those of the lunar soil. When the final set of soils was being selected for the test work of this study, the lunar soil property estimation had to be made on the basis of Luna 9, Luna 13, and Surveyor I results, combined with postulations based on visual observations and theories on the origin of the surface topography of the moon. Since that time Surveyors III, V, VI and VII landed successfully on the moon and have provided considerably more information on surface properties so that more precise estimates could be made on the soil properties of concern here.

Table 2-1 shows the initial and present estimation of the lunar soil properties and a comparison with the soil properties of the test soils used in the LM Soil Mechanics Study. The initial estimates of the lunar soil properties were based on studies covered in References 17 through 29. The present estimates were based on studies covered in these references plus the Surveyor III report (Reference 9).

TABLE 2-1. ESTIMATED LUNAR SOIL PROPERTIES AND COMPARISON WITH RANGE OF APPLICABILITY OF FORCE LAWS FROM LM SOIL MECHANICS STUDY (TARGET)

	Estimated Lunar Soil Characteristics From Various Sources*	Range of Applicability of Force Laws (Target)	Present Estimates
Density	40 to 100 lb./ft.^{3} (if on earth)	20 to 110 lb./ft.^{3}	60 to 130
Relative Density	30% to 85%	0 to <100%	50% to 100%
Angle of Internal Friction	25° to 50°	25° to 50°+	35° to 45°
Cohesive Shear Strength	0 to <200 lb./ft.^{2}	0 to < 100 lb./ft.^{2}	.02 to .10 psi
Mean Grain Size	10μ to 100μ	< 70μ to 2000μ	10μ to 100μ
Gradational Uniformity	Wide	Uniform to Very Wide	WIDE
Elastic Modulus (Recoverable Strains)	Probably Roughly Comparable to Earth Soils		LOW
Grain Shape	Angular	Smooth to Highly Angular	ANGULAR
Uniformity with Depth	Uniform to Approximately 3 ft. Depths	Uniform	Uniform in composition to at least 3 feet. Possible higher compaction below 2-3 inches of surface.

*References 17 through 29.

It can be seen that the properties of the test soils generally encompass the estimates of the lunar soil properties. The one exception to this is mean grain size which overlaps only the higher region of the lunar soil mean grain size estimated range. This was found to be necessary since the fine grain size would exhibit considerable pore air effects in atmospheric tests.

Fortunately, analyses of the test results indicate that grain size and grain size distribution do not appear explicitly in the resistance equations for a soil in a vacuum. Therefore atmospheric tests on a soil having a large enough grain size that pore air effects are insignificant is a good simulation of the performance of a similar fine grain soil in a vacuum test.

2.4 SELECTION OF THE TEST SOILS

The basic requirements governing the types of soils to be used to develop the force interaction model were modified several times in the early stages of the program. This was primarily a result of Surveyor I and subsequent data narrowing the somewhat broad speculations of possible lunar surface characteristics that, in turn, had influenced the initial program requirements. The modifications resulted, eventually, in limiting the study to dry particulate materials of relatively small grain size that would fail, essentially, by particle displacement or compaction in combination with particle displacement.

The initial requirements, in comparison, were quite broad and called for a selection of relatively low bearing strength materials that would fail only or predominantly under each of several specified failure mechanisms. These included particle displacement, compaction, crushing or compression, and perimeter-shear type failure. These and other requirements led to initial consideration of a relatively large number and variety of both natural and artificial materials as potential soil candidates.

Table 2-2 lists materials that were obtained in small sample lots for preliminary evaluation purposes. Many of these materials were eliminated from further consideration when it was determined that the lunar surface was a soil-like material as opposed to a weak rock-like structure, and some reasonable estimates were made of its bearing and cohesive strengths.

TABLE 2-2. POTENTIAL TEST SOILS AND PRELIMINARY EVALUATION

Material	Description	Approx. Density (#/Cu.Ft.)	Approx. Strength Range	Failure Type	Comments	Final Select.
Silica Sand	AGSCO #4, White	100-107	2-15 psi	Particle Displ. and Compaction	Satisfactory	
Silica Sand	WEDRON 4040, White	100	2-15 psi	Particle Displ. and Compaction	Satisfactory	Used
Salt - Coarse		72-82	2-15 psi	Particle Displ. and Compaction	Satisfactory	
Salt - Fine	200 Mesh	40-85	0-15 psi	Particle Displ. and Compaction	Satisfactory	
Aluminum Oxide	100 and 80 Mesh, Powdered	110-140	5-15 psi	Particle Displ. and Compaction	Satisfactory, Very Expensive	
Air Floated Clay	Dry-200 Mesh	80-100	0-15 psi		Entrapped Air Effects, Potential Use Mixed With Other Materials	Used
Petroleum Coke	Graded, 0-5/32" Particle, Some Moisture	50	---	Particle Displ. and Compaction	Excessive Moisture, Costs to Dry	
Charcoal	#10 Granular, Commercial	14-20	---	Particle Displ. and Compaction		
Pumice-Powdered	White, Screened, 200 + Mesh	20-35	0-20 psi		Entrapped Air Effects, Potential Use as Mix	
Pumice-Navajo and Grey Crushed	Approximately 1/4" to 5/8" Irregular Lumps	25	3-10 psi	Particle Displ. and Compaction	Particles Too Large	
Pumice-Grey Crushed Fine	Narrowly Graded, Approximately 1/8" to 1/4" Particle Size	25-30	3-10 psi	Particle Displ. and Compaction	Satisfactory	Used
Pumice-Block Grey and Black	"Featherock," Sawed, Black Is Highly Vesicular	35	100-200 psi	Compaction	Strength Too High, Similar to Rigid Surface	
Pumice-Charcoal	Grey-1/8" to 1/4" Broadly Graded Lumps	25	3-10 psi	Particle Displ. and Compaction	Potentially Satisfactory	
Microballoons	Bakelite No. BJO-0930 .0002" to .005" Diameter Hollow Spheres	12	Very Low	Particle Displ. and Compaction	Air Effects May Be Large	
Dylite-Unexpanded	Polystyrene Plastic Beads, "ISO-Balls"	40	---	Particle Displ. and Compaction	Particles Highly Elastic	
Dylite-Expanded	Made From Above, Vary From 8-40 Mesh, Can Be Tailored to Densities Between 1 and 10 #/Cu.Ft.	1 to 10	Very Low	---------	Highly Elastic-Trapped Air	
CAB-O-SIL 2.2 CAB-O-SIL M-7, M-D-7 CAB-O-SIL M-5	Fumed Silica, White	2-7 7 5	Extremely Low	Compaction	Extremely Low Strength, Entrapped Air Effects Predominate	
Pearlite	Granular, Commercial	Low	Low	Particle Displ. and Compaction	Spongy-Excessive Particle Breakdown	
Vermiculite	Granular, Commercial	Low	Low		Particle Breakdown	
Pelaspan	Foamed Polystyrene	1-10	10 psi up	Compaction and Compression	Highly Elastic	
Foamglas	Low Density Cellular Glass Insulation	9	50 psi	Compaction-Brittle Fracture of Cell Walls	Strength Too High, Similar to Rigid Surface	
Foamthane	Foamed Polyurethane	2	25	Compaction and Compression	Highly Elastic, Strength Too High	
Foamthane (S.E.)	Self-Extinguishing Foamed Polyurethane	2	25	Compaction and Compression	Strength Too High, Material Elastic but More Brittle Than Regular	
Polylite	Foamed Polystyrene	---	10 psi up	Compaction and Compression	Highly Elastic	
Marble Chips	Narrowly Graded #10 Georgia, White Crushed	100	2-15 psi	Particle Displ. and Compaction	Satisfactory	Used
Volcanic Cinders-Black	Crush, Screened, Dust to 1/4" Particle Size	50-65	2-15 psi	Particle Displ. and Compaction	Satisfactory	
Volcanic Cinders-Red	Crushed, Screened, Dust to 1/4" Particle Size	55-90	2-15 psi	Particle Displ. and Compaction	Satisfactory	Used
Volcanic Cinders-Black	Crushed, Narrowly Graded, Approximately 1/8" to 1/4" Particle	40-55	2-15 psi	Particle Displ. and Compaction	Satisfactory	
Volcanic Cinders-Red	Crushed, Narrowly Graded, Approximately 1/8" to 1/4" Particle	40-55	2-15 psi	Particle Displ. and Compaction	Satisfactory	Used
Aluminum Oxide Crust	Artificially Formed Top Surface Crust	130	10 psi up	Perimeter Shear, Then Compaction and Particle Displ.		
Sugar Bonded Silica, Low Cohesion	Uniformly Permeated With Weak Solution of Sugar Water, Then Cured	100	5 psi up	Particle Displacement and Compaction	Extremely Difficult to Prepare in Large Quantities	
Sugar Bonded Silica, High Cohesion		100	25 psi up			
Sugar Bonded Aluminum Oxide		130	15 psi up			

In addition to the requirement that the test soils must have properties which encompass the estimated properties of the lunar soil, the test soils must also have a large enough range of each soil descriptor that specific soil property effects can be identified. Ideally, the test soils should allow evaluation of a particular parameter effect by selecting several soils which are identical except for a single property. In practice this is extremely difficult and often impossible to achieve since a variation in one property usually results in variations of several of the other soil properties. This factor compounds the complexity of the analysis of the test data.

The soils selected for the LM Soil Mechanics Study and details of their properties are given in Table 2-3. It can be seen that they consist of various preparations or combinations of volcanic cinders, crushed pumice, silica sand, crushed marble and air-floated kaolin clay. Detailed description of each of these 12 soils is given in Appendix A.

The chart given in Figure 2-7 illustrates schematically how these soils may be evaluated in various ways to yield specific soil property effects. For example, the PS loose soil and RS loose soil are similar in all respects except for the bulk density. Therefore by examining the differences in test results for both the oblique impact tests and the drag tests the effect of bulk density can be identified. Knowing the effect of bulk density, the PS loose and RS loose, intermediate and dense results then allows the separation of relative density and angles of internal friction effects. Proceeding in this manner each of the various property effects can be categorized.

2.5 TEST PROCEDURES USED TO DETERMINE SOIL PROPERTIES

2.5.1 Types of Tests

The soil testing for this project falls into three categories.

a. Tests to determine the basic properties of the test soils used

b. Bearing strength tests

c. Control tests to determine the properties and uniformity of the soil beds for the drag, impact, and model drop tests.

TABLE 2-3. TEST SOILS AND PROPERTIES

No.	Bendix Designation	Description	Relative Density D_r	Unit Weight γ pcf	Friction Angle Φ	Elastic Modulus E,psi*	Grain Size Parameters: Mean Size $\mu_w$mm	Uniform Coeff. C_μ	%** -200	D_{95}*** mm
1	RS Loose	Red Crushed Volcanic Scoria (narrowly graded)	0	41.4	40°	5,500	1.8	1.7	<3%	2.7
2	PS Loose	White Crushed Pumice (narrowly graded)	0	23.8	43°	4,500	1.8	1.7	<3%	2.7
3	RS Inter.	Red Crushed Volcanic Scoria (narrowly graded)	.45	45.9	44.5°	8,600	1.8	1.7	<3%	2.7
4	RS Dense	Red Crushed Volcanic Scoria (narrowly graded)	.80	50.6	47.3°	10,900	1.8	1.7	<3%	2.7
5	RSM-a Loose	Mixture of RS and Crushed Marble (MS) (narrowly graded)	0	58.2	37°	7,800	2.4	1.6	<3%	2.7
6	RC2 Loose	Red Crushed Volcanic Scoria (Broadly graded)	0	61.4	43°	8,000	1.1	17.0	11%	4.7
7	SS Loose	White Silica Sand (Wedron 4040-narrowly graded)	0	94.7	29°	10,000	0.4	1.3	0%	0.52
8	SS Inter.	White Silica Sand (Wedron 4040-narrowly graded)	.53	104	36.8°	18,000	0.4	1.3	0%	0.52
9	SS Dense	White Silica Sand (Wedron 4040-narrowly graded)	.69	107	39°	24,000	0.4	1.3	0%	0.52
10	LSM Inter.	Mixture of RC and Air-Floated Clay	.50	77.5	42°	4,000	.07	large	51%	4
11	LSM Dense	Mixture of RC and Air-Floated Clay	.70	82	42°	6,000	.07	large	51%	4
12	RSM-b Dense	Mixture of RS and Crushed Marbel (MS) (narrowly graded)	.75	85	48°	20,000	2.15	1.87	<1%	2.9

*Measured by sonic means at 4 psi confining pressure.
**Percent of material (by weight) passing thru a No. 200 sieve (ACS).
***Diameter at 95% "smaller than" point in standard sieve analysis.

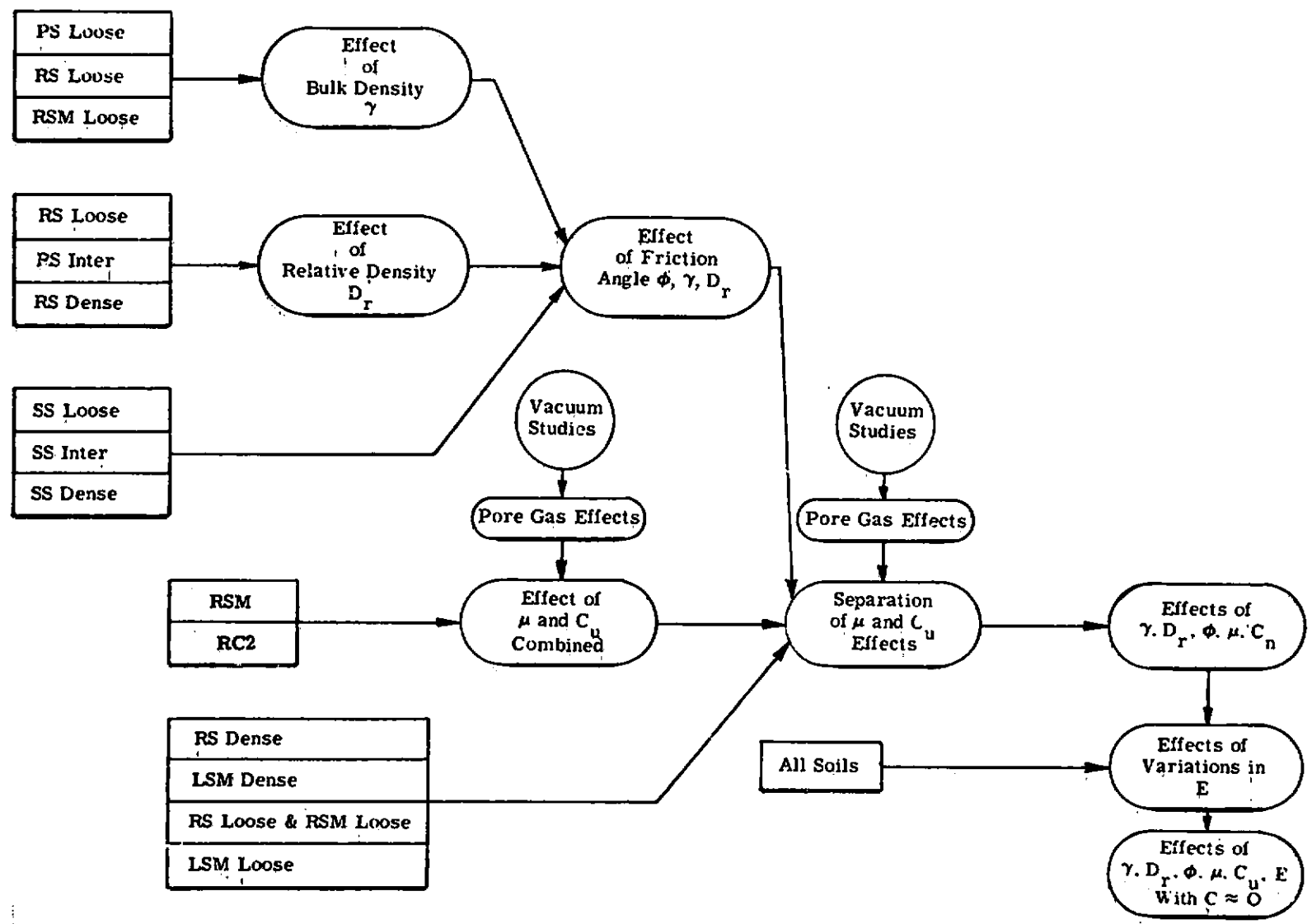

Figure 2-7. Flow Chart Illustrating Separation of Soil Property Effects

2.5.2 Basic Soil Tests

By basic soil tests are meant those performed on previously unused samples of the soil, that is, prior to any changes induced by testing or handling procedures. They include the minimum-maximum density test, grain size analysis, the direct shear test, and the sonic velocity test. Table 2-3 summarizes the results of these tests and a detailed description of the procedures is given below.

2.5.2.1 Grain Size Analysis

Grain size analysis was performed in a manner similar to that outlined by Lambe (30, pp. 29-42)* and ASTM** (31, pp. 95-105).

Figure 2-8 shows the shaker used (Soiltest, Inc., Model No. CL 370C [32, p. 31]). Mounted on top of this shaker is a holder fabricated by Bendix for 8-inch diameter sieves. The large shaker holds five 20-inch by 20-inch sieve trays and a pan and is used for analysis of large soil samples (up to one cubic foot).

The 8-inch diameter sieves were used for smaller soil samples ranging from 0.01 to 0.03 cubic foot. The 8-inch diameter sieves were used for most of the analyses done for this program.

The other basic equipment required for grain size analysis is a thermostatically-controlled, constant-temperature drying oven (Figure 2-9), a beam balance scale with a sensitivity of 0.10 gram (Figure 2-10)***, and a sample splitter (Figure 2-11)****.

---

*The numbers in brackets refer to the keyed references given in the Bibliography and the page numbers in the referenced publication.

**American Society for Testing and Materials.

***The beam balance scale shown is Model No. L-415 in the Soiltest, Inc., Catalog (33, p. 244).

****The sample splitter shown is Model No. S2512 in the Testlab Corporation Catalog (34, p. 32).

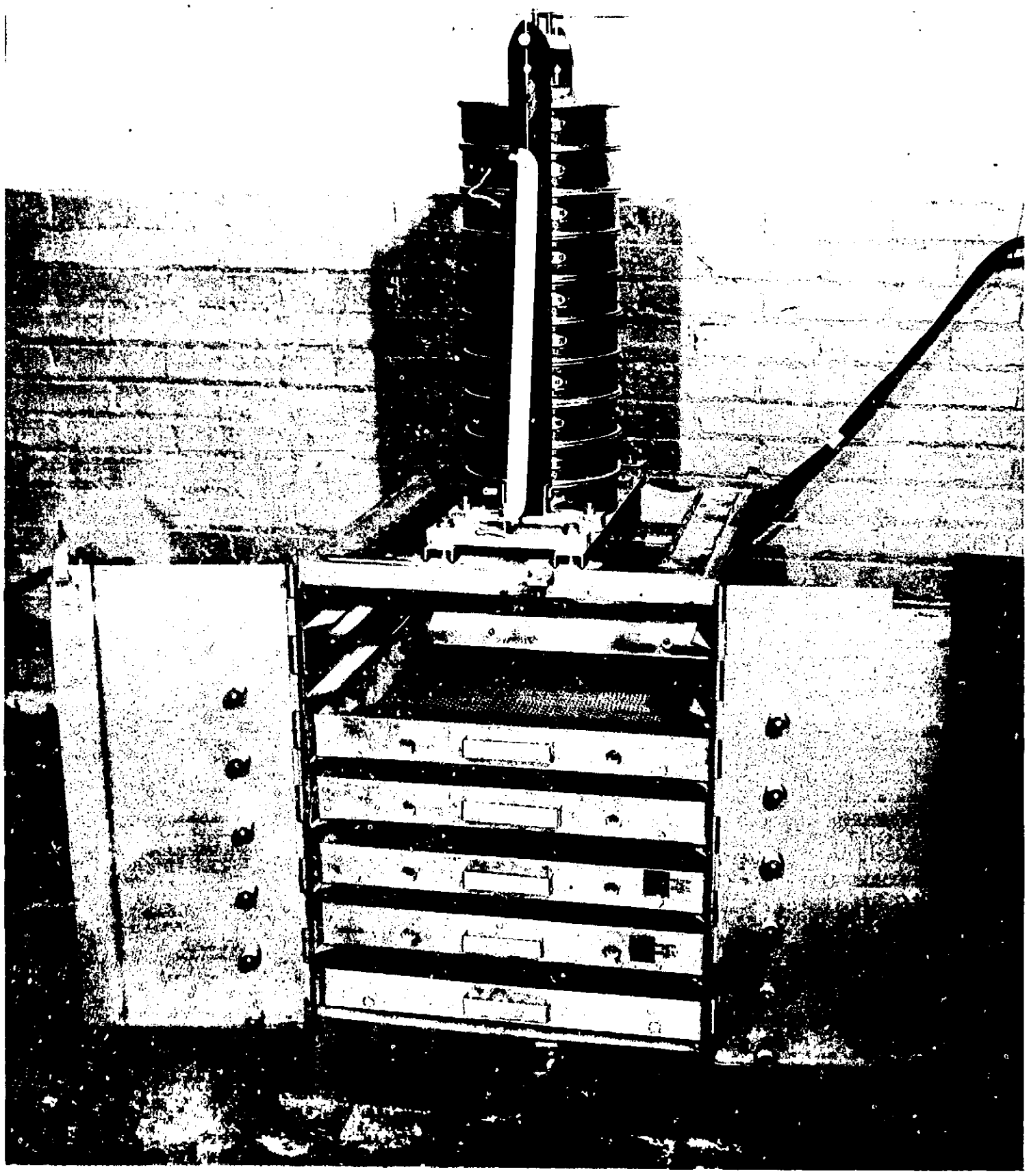

Figure 2-8. Sieve Shaker

Figure 2-9. Constant Temperature Oven

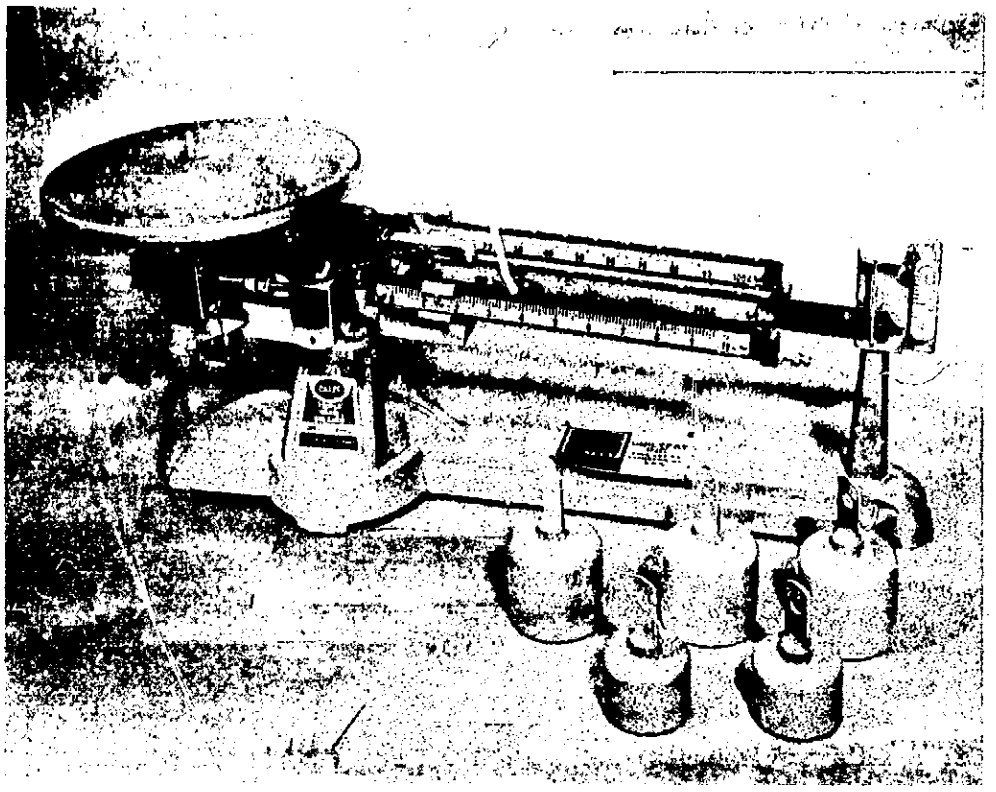

Figure 2-10. Triple Beam Balance

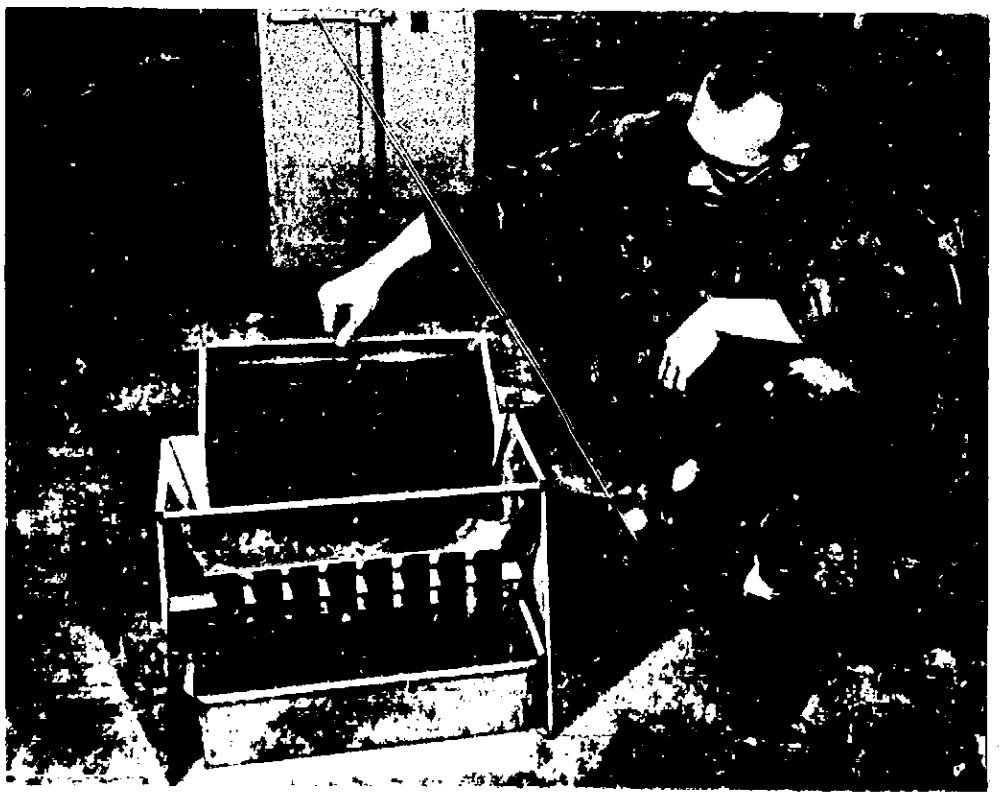

Figure 2-11. Sample Splitter

The grain size analysis is determined in the following manner.

a. A large sample (i.e., on the order of one cubic foot) is taken from a test bin or other batch of soil and successively halved in the sample splitter until a sample of convenient size is obtained.

b. The small sample is weighed (to the nearest 0.1 g), oven-dried (at 110°C, 230°F) and then reweighed. Figure 2-12 shows a typical grain size analysis data sheet for this study. Lines 1 and 2 show the values obtained for the operations described above. Line 3 shows the difference between these two weighings, the weight of water in the sample, and the computation to the right of line 3 shows the determination of moisture content (M.C.).

c. The oven-dried sample is placed in a #200* sieve and the material finer than the #200 sieve openings (called the "minus #200 material" or the "silt and clay" portion) washed out of the sample through the sieve (wet sieving).** The washed sample is oven-dried and weighed. This weight is recorded on line 4. The tare weight (weight of the pan the soil is in) is recorded on line 6 and this value is subtracted from the weight recorded on line 4 to obtain the weight of the grain size analysis sample for the dry sieving operation (line 8).

d. An appropriate set of sieves*** is placed together (in our example, those indicated by the symbol + on the data sheet) with the coarsest sieve at the top and a pan at the bottom beneath the finest sieve (a #200 sieve in our example).

---

*The sieves used in this study are referred to by the number applied to them by the U.S. Bureau of Standards. The numbers are related to the size of the sieve openings (30, p. 31) and are commonly called the "U.S. Standard Sieve Numbers."

**Normally, removing the silt and clay portion from a sample by wet sieving prior to dry sieving is not considered necessary for soil containing less than about 10% finer than the #200 sieve. However, our studies indicated that prior washing resulted in doubling the amount of soil retained on the #40 and finer sieves even for soils containing only 1-2% "-#200" material.

***The uppermost sieve in the series should be the finest sieve through which all the samples will pass. The following sieves are generally chosen such that each succeeding sieve has openings half the size of the previous one.

GRAIN SIZE (SIEVE) ANALYSIS

Project: LM Soil Mechanics Study Date: 2-6-67 Perf. By: J.M.

Soil Type: RC2 used for test bed for SS Drag Test #6-1

Soil Symbol: RS (RC2) RSM / PS ~~SS~~ LSM

Soil Preparation: Washed through #200 sieve; dried

1. Total weight soil plus tare = 655.2
2. Total OD* weight soil plus tare = 653.7
3. Weight water (1 - 2) = 1.5
4. Weight OD washed soil plus tare = 595.2
5. Weight - 200 material (2 - 4) = 58.5
6. Weight tare = 121.8
7. Total OD weight soil (2 - 6) = 531.9
8. OD weight SA sample (4 - 6) = 473.4

All weights in (Grams) Lbs. (circle)

$$M\,C = \frac{100\,(3)}{(7)} = 0.3\%$$

$$\%\ \text{Sieve Loss} = \frac{[(8) - ((9) - (5))]\ 100}{(8)} = ____$$

$$= 0.2\%$$

SIEVE NO. (U.S. STD.)	SIEVE SIZE (MM)	WGT. RET. "W"	% WGT. RET. 100W/(9)	CUM. % RET.	% PASSING	
3 8" (+)	9.52	0.0	0.00	0.00	100.00	
3	6.35					
4 (+) +	4.76	32.1	6.05	6.05	93.95	
6 (+) +	3.36	77.7	14.63	20.68	79.32	
8 (+) +	2.38	62.7	11.80	32.48	67.52	
10 +	2.00					
12 (+) +	1.68	44.9	8.46	40.94	59.06	
16 (+) +	1.19					
20 (+) +	0.84	64.7	12.19	53.13	46.87	
40 (+) +	0.42	54.5	10.27	63.40	36.60	
60 (+)	0.25	42.5	8.01	71.41	28.59	
80	0.177					
100 (+) +	0.149	40.3	7.59	79.00	21.00	
120	0.125					
200 (+) +	0.074	48.9	9.21	88.21	11.79	
PAN		4.1				
(5)		58.5				
TOTAL - 200		62.3	11.79	100.00	0.00	
TOTAL WGT. ((9))		530.9				

* OD - Oven-Dried at 110 C (230 F)

(+) For Broadly-Graded Soils (e.g., RC2, LSM)

\+ For Coarse, Narrowly-Graded Soils (e.g., RS, PS, RSM)

Figure 2-12 Grain Size (Sieve) Analysis

The soil sample is placed in the top of the set of sieves and the shaker put in operation for 10 minutes.*

e. After the shaking operation, the weight of soil retained on each sieve and the pan is recorded on the data sheet (the third column in our example). The amount of -#200 material previously washed out (line 5) is added to that obtained in the pan ** to obtain the total weight of -#200 material. These weights are then converted to "% weight retained" as shown in the fourth column in our example (computed as a percentage of the total weights used in the "weight retained" column - line 9)***. The sum of the "% weight retained" values should be 100 per cent. The "% passing" can then be computed by successively subtracting the "% weight retained" figure from the preceding "% passing" figure (starting with 100%), or, subtracting the "cumulative % weight retained" from 100% for each sieve.

f. The resulting "% passing" or "percent finer than by weight" is then plotted versus sieve size or grain size on a graph similar to that shown in Figu 2-13. (The data points shown are those from the data sheet example.) T "% passing" is shown on the ordinate of this graph to a linear scale. Th U.S. Standard Sieve Size is shown on the upper abscissa. Also shown, be the bottom abscissa, is the ASEE (American Society for Engineering Education) definitions of soil components as reported by D. M. Burmister in his article "Suggested Methods of Test for Identification of Soils" (31, pp. 222-223).

---

*For finer-grained soils, the time is increased to 15 minutes (30, p. 31).

**Note that the amount retained in the pan will be a function of how well the sample was washed and/or the amount of particle breakdown during sieving.

***The "% Sieve Loss" is computed as shown in the upper right-hand corner of our example. If this figure is greater than 1%, the procedure or computations should be examined for the source of error or loss.

GRAIN SIZE ANALYSIS CURVES - LM SMS

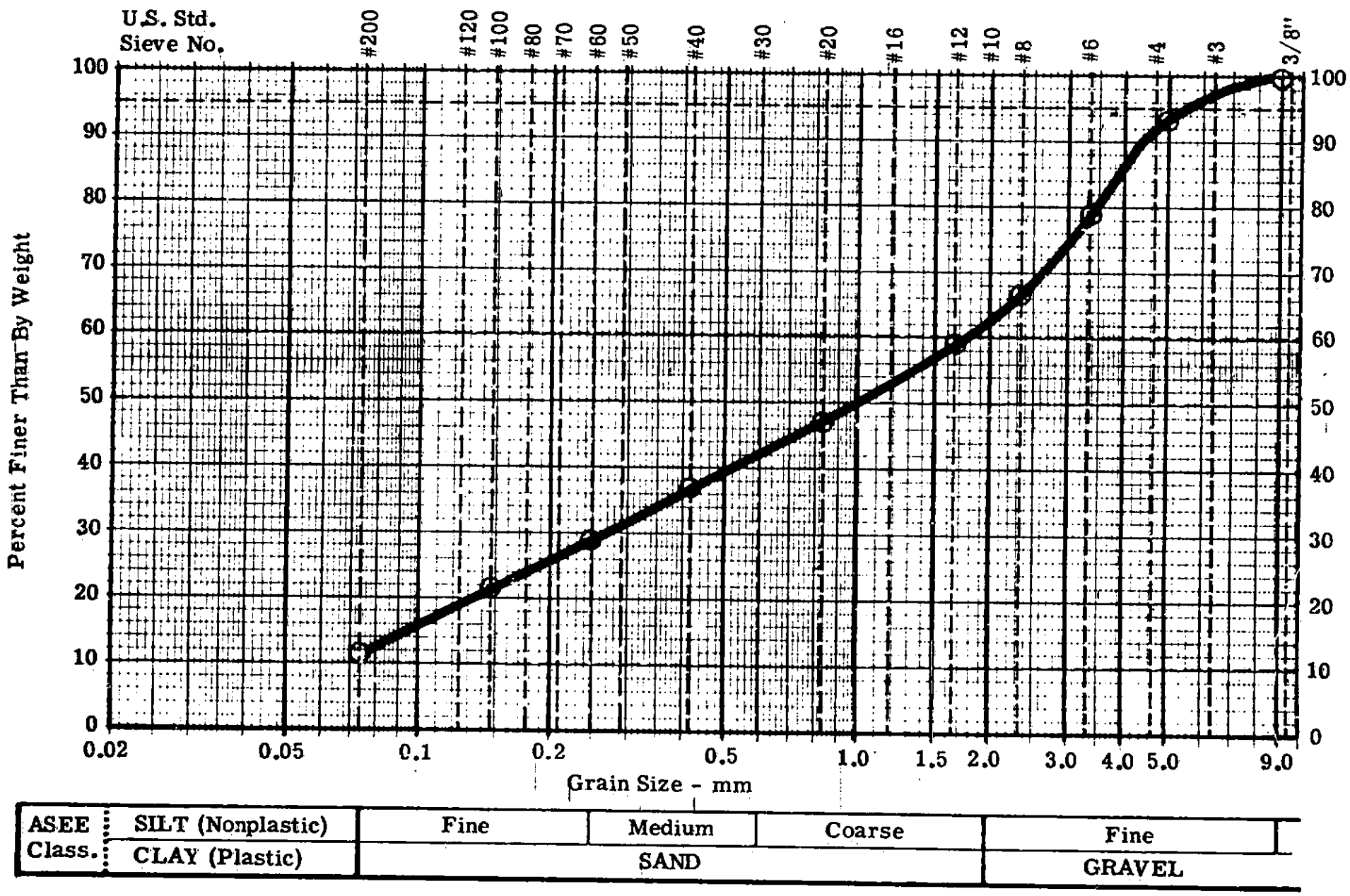

Figure 2-13. Grain Size Curve for Example Data in Figure 2-12

The major grain size parameters used in this study are mean grain size (by weight), D_{50}* (μ, μ_s) and the coefficient of uniformity, C_u, which is defined as the ratio of D_{60} to D_{10}, these values being taken from the grain size curve. Other grain size parameters which further define the grain size curve are effective size, D_{10}; the "%-#200,"** and the value of D_{95}. Knowledge of all these values will allow a fairly accurate reproduction of the grain size curve.

Other quantities describing characteristics of the grain size distribution curve are described in the referenced literature (35, pp. 21-25; 46, pp. 25-27). These other grain size curve characteristics were not used because they were considered either redundant or of unproven value to the present study, or represented a degree of refinement not warranted by the scope of this study.

The values for the grain size curve characteristics described above for our example data are:

Mean Grain Size, D_{50},	=	1.0 mm
Coefficient of Uniformity, C_u, = D_{60}/D_{10} = 1.8/0.064**'	=	28
Effective Size, D_{10},	=	0.064 mm***
Percent by weight of clay and silt size particles, "% -#200"	=	11%
D_{95}	=	5.5 mm

The grain size curves on the graph in Figure 2-14 show the results of the averaging of several grain size analyses run on each of the six basic soil types being used in the LM

*"D_x" indicates the grain size or sieve opening corresponding to the "X% finer than by weight" point on the grain size curve.

**"% -#200" is the value of "Percent Finer Than by Weight" at the point where the grain size curve crosses the #200 sieve line and represents the percentage (by weight) of clay and silt size particles in the soil.

***Note that the value of D_{10} is interpolated since the last data point corresponds to about D_{11}.

GRAIN SIZE ANALYSIS CURVES - LM SMS

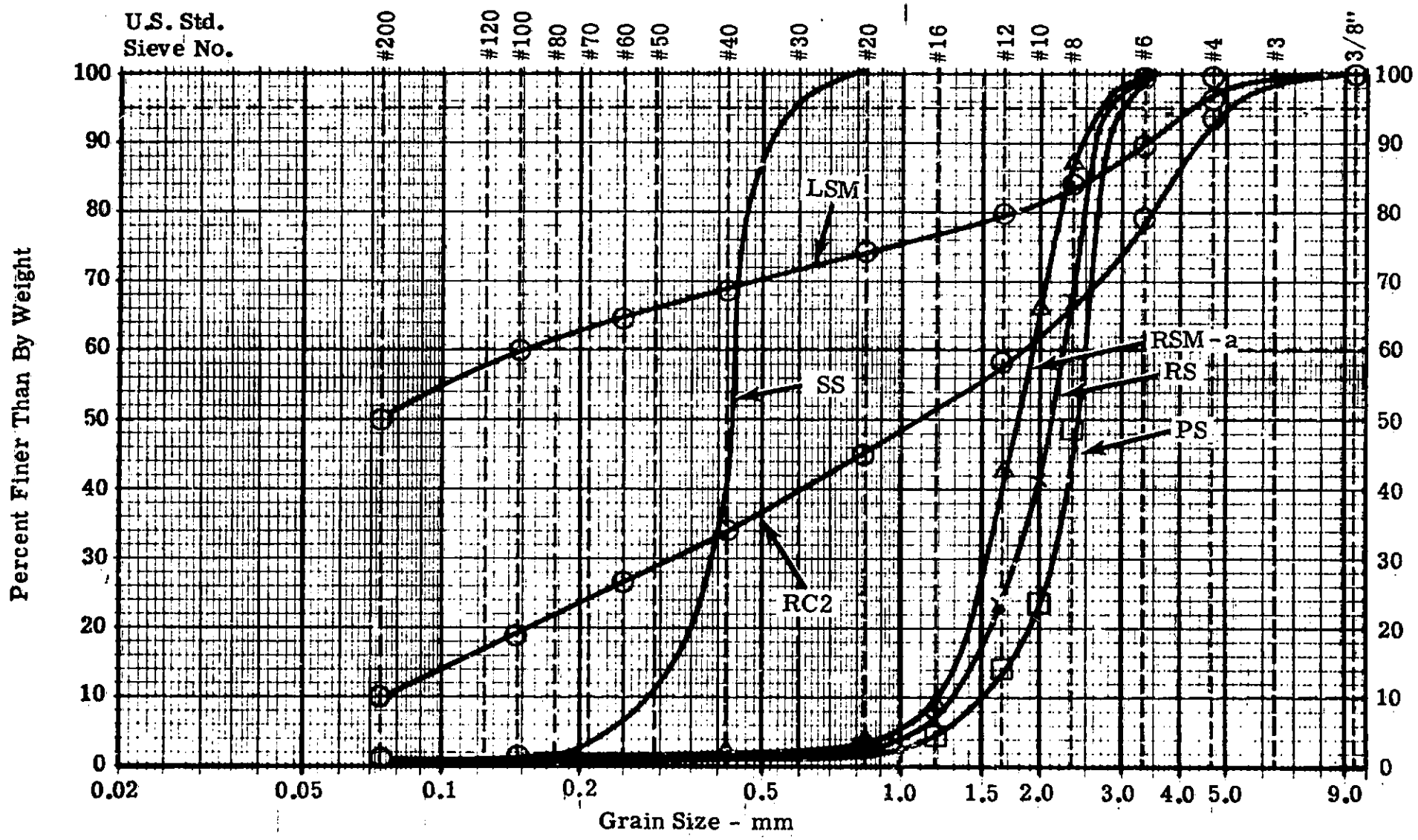

ASEE Class.	SILT (Nonplastic)	Fine	Medium	Coarse	Fine
	CLAY (Plastic)	SAND			GRAVEL

Figure 2-14. Average Curve for Six Basic Test Soils

soil mechanics study.* Table 2-3 summarizes the grain size distribution parameters derived from the curves shown in Figure 2-14.

Since the finest size that sieve analysis measures is 0.074 mm (i.e., that material passing the #200 sieve), any size measurement in the clay and silt size range necessary to determine a grain size distribution parameter is not available except, possibly, by extrapolation. Note that extrapolation is necessary to get the value of D_{10} for our example curve in Figure 2-13 and the value of D_{50} for the LSM soil in Figure 2-14.

Since these interpolated values are relatively close to the last data points they are fairly reliable. An estimate of D_{10} for the LSM soil, however, could not be made with any great degree of confidence, and, hence, no definite quantitative values are given for these parameters in Table 2-3.

It can be seen that movement of a curve upward and to the left on the grain size analysis graph indicates increasing fineness (decreasing D_{50}) of the soil and movement downward and to the right increasing coarseness (increasing D_{50}). The slope of the central portion of the curve indicates the broadness of gradation-a steep slope indicating a narrowly-graded soil (C_u approaching one) and a flat slope indicating a broadly-graded soil (C_u large).

Samples of the soil beds were taken from the drag and impact test bins periodically for grain size analysis and minimum-maximum density tests to provide a check on possible grain size distribution changes taking place throughout a test series. The periodic check tests provide quantitative information about these changes, and these values can be incorporated into the overall analysis of the force law investigation.

2.5.2.2 Minimum-Maximum Density Test

The minimum-maximum density test established the relative density scale for a given soil. Minimum density is that unit weight representing the least compact condition of a soil. In this state the soil possesses its maximum void ratio (i.e., ratio of volume of

*The results shown are for tests run on previously unused, undegraded samples of soil.

voids to volume of solids) and has, by definition, a relative density equal to zero. Maximum density is the unit weight of the soil in its most compact condition when it has its smallest possible void ratio and a relative density equal to one.

The concept of relative density was originally expressed in terms of void ratio as shown:

$$D_r = \frac{e_{max} - e}{e_{max} - e_{min}} \qquad (2\text{-}1)$$

where: D_r = relative density

e = void ratio

$= \frac{V_v}{V_s}$

V_v = volume of voids or pore spaces in a soil mass of unit volume

V_s = volume of soil grains in a soil mass of unit volume

e_{max} = maximum possible value of "e" for a given soil

e_{min} = minimum possible value of "e" for a given soil.

Void ratio is related to the dry unit weight of a soil by the expression:

$$e = \frac{G\gamma_w}{\gamma} - 1$$

where:

G = specific gravity of the soil grains

γ_w = unit weight of water

γ = dry unit weight or density of the soil.

If we replace this expression for "e" in the equation for "D_r" given above, we obtain:

$$D_r = \frac{\gamma - \gamma_{min}}{\gamma_{max} - \gamma_{min}} \cdot \frac{\gamma_{max}}{\gamma} \qquad (2\text{-}2)$$

where:

γ_{min} = minimum density or unit weight (corresponding to e_{max})

γ_{max} = maximum density or unit weight (corresponding to e_{min}).

As can be seen from equation (2-2) above, there is a linear relationship between D_r (relative density and the reciprocal of unit weight (i.e., $1/\gamma$)). Hence, a plot of density or unit weight on a linear scale allows one to join minimum and maximum density with a straight line to represent the relationship between D_r and γ .

Figure 2-15 shows a graphical solution of equation (2-2) for a density range of 55-115 pcf. The slanting line on this graph represents a hypothetical soil having a minimum density of 64.0 pcf and a maximum density of 78.0 pcf which represents relative densities of 0.0 and 1.0, respectively, for this soil as shown. The relative density of this soil having a density between the minimum and maximum densities can be found by noting the value of relative density corresponding to the given density along the line joining the minimum and maximum density points.

Figure 2-16 illustrates some of the equipment used in the performance of the minimum-maximum density test. This apparatus includes a standard compaction mold* (volume:

*Available from Soiltest, Inc., Model No. CN404 (33, p. 38).

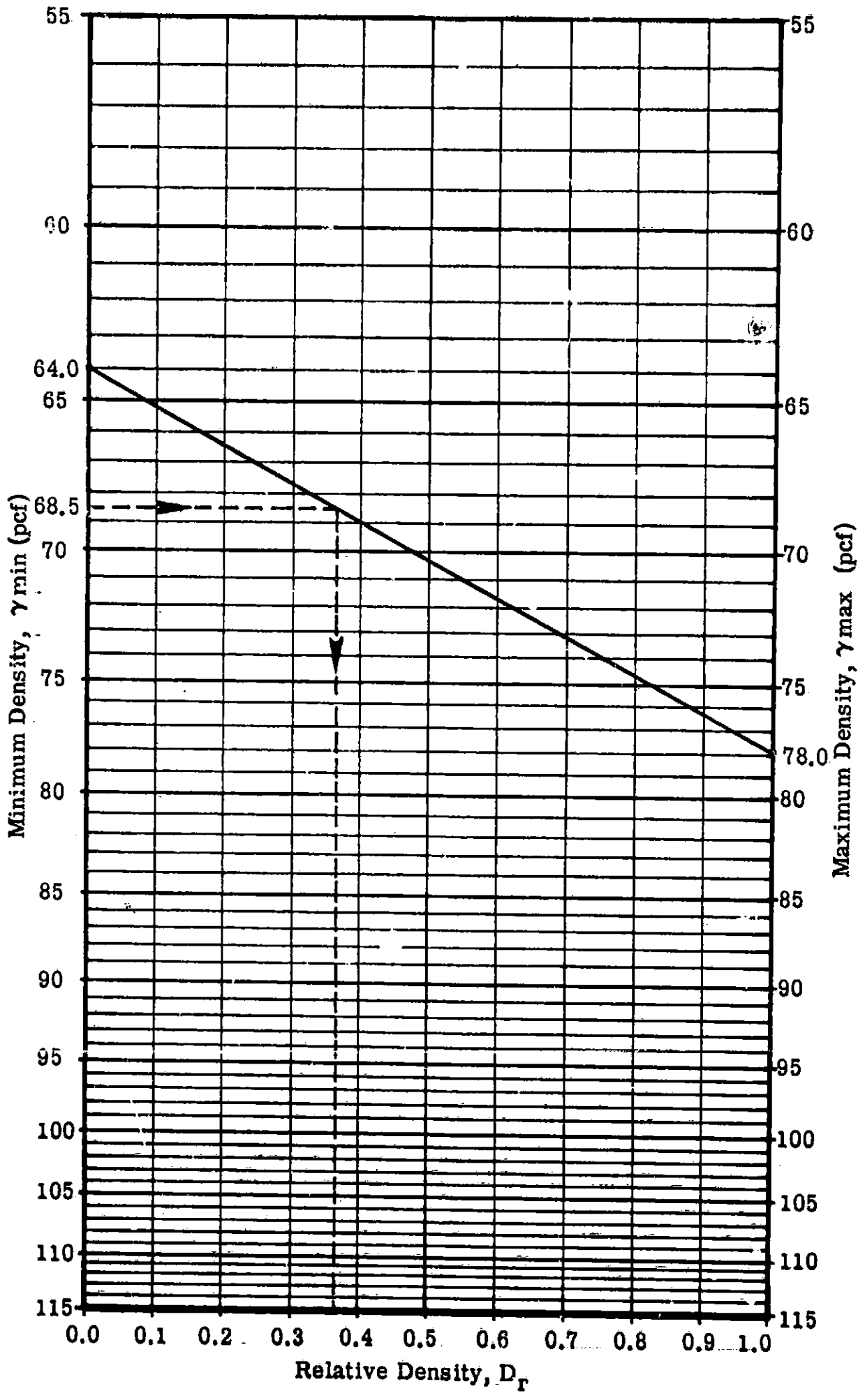

Figure 2-15. Unit Weight vs. Relative Density Graph

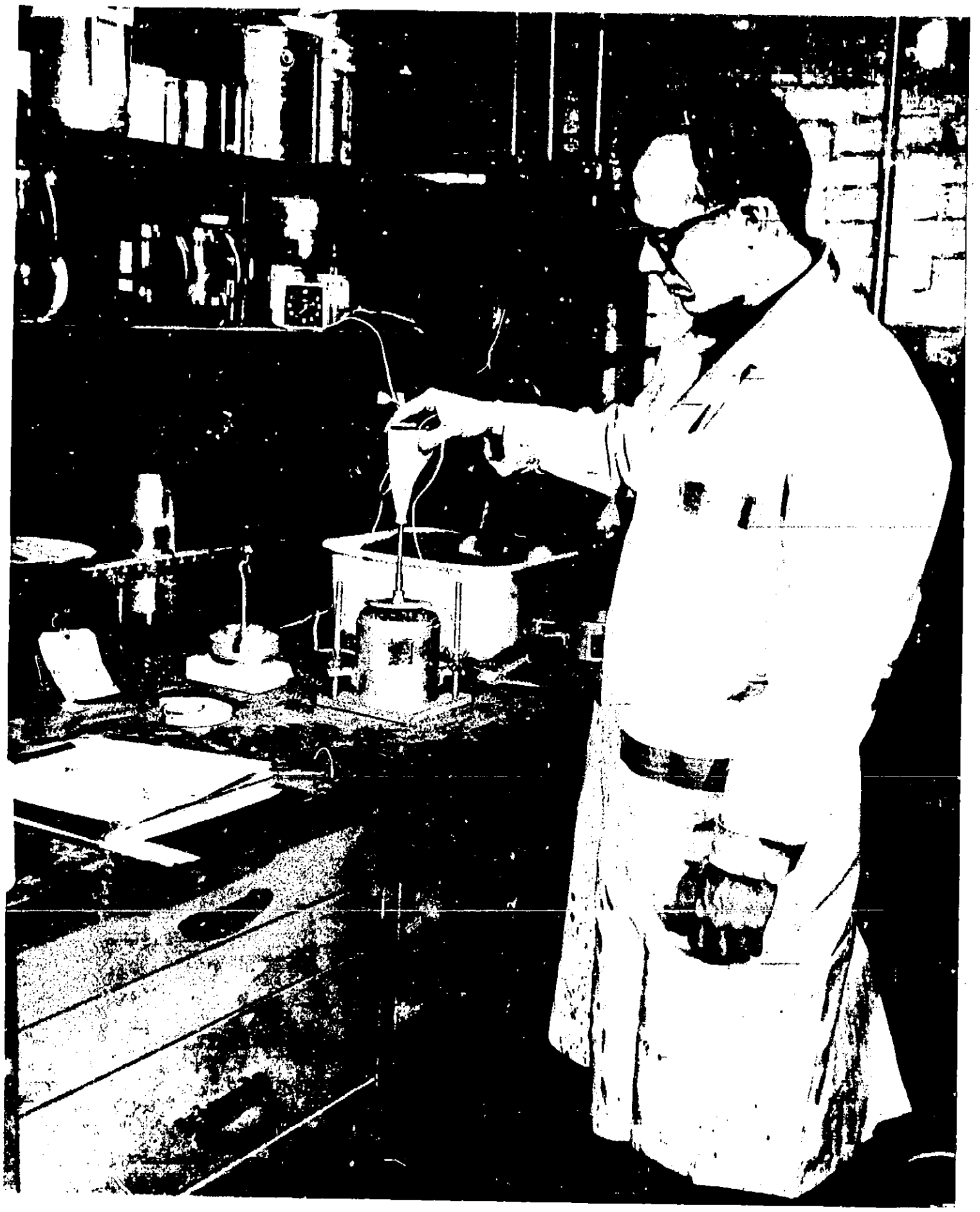

Figure 2-16. Vibrating Tool and Proctor Mold

1/30 cu. ft.), a small vibratory compactor*, a pound scale (sensitivity: 0.01 lb.)**, a sample splitter***, a funnel, various scoops, brushes, and pans.

The method used for determining minimum and maximum density of the test soils is that developed by D. M. Burmister (31, pp. 175-177). To determine the minimum density, obtain a representative sample of air-dried soil sufficient to make 3 or 4 determinations without reusing material (about 1/6 cu. ft.). Mix soil thoroughly before each determination to minimize segregation effects****.

Deposit soil into mold through a funnel***** such that the distance from the bottom of the funnel and the soil already placed is the minimum necessary to allow the flow of the soil through the funnel. The soil is placed by moving the funnel in a concentric motion from side to center of the mold, bringing the soil level up in more or less horizontal layers.

---

*The small vibratory compactor pictured is an electrically-operated engraving tool which has been modified to hold a tamping foot (the one shown is 3-1/2 inches in diameter). The engraving tool is commercially available as the "Vibro-graver," Model V-73, manufactured by Burgess Vibrocrafters, Inc., Grayslake, Illinois.

**Available from Soiltest, Inc., Model No. L-770 (33, p. 49).

***Available from Testlab Corp., Model No. S2512 (34, p. 32).

****Variation in test results due to segregation of grain sizes is especially noticeable with broadly-graded soils. This variation can be substantially reduced if the test sample is quartered in the sample splitter and each quarter used to determine a test point.

*****A funnel with an inside diameter of 5/8 inches was used in this study. Too large a diameter will allow the soil to flow from the funnel too quickly and cause higher values of minimum density. Too small a diameter will not allow the soil to flow. The appropriate diameter for a given soil is the minimum that will allow free flow of the soil.

When soil is placed to overflowing in mold, screed off excess level with top of mold with a straight edge*.

Determine the weight of the soil and divide this by the volume of the mold (1/30 cu.ft.) to obtain value of minimum density.

Make three or four determinations of minimum density to obtain average and range of values for several different samples of soil.

The maximum density test is performed with soil used for minimum density test using same precautions for ensuring uniformity of sample.

Place 1.0-inch thick layer of soil in mold and tamp with vibratory compactor for two minutes**.

Place successive layers (compacting each for the specified time) until the soil extends over the top of the mold.

Screed off excess soil level with top of mold; weigh mold and soil as previously described for minimum density test, and determine the value for maximum density.

Make three or four determinations of maximum density in this manner on several different samples of the soil to obtain the average and range of values for the soil.

---

*At no time during the filling process and final screeding should the mold be subjected to vibration or impact as this will tend to densify the soil.

**The thickness of layer and time required for compaction of each layer to achieve maximum density depends on the type of soil and type of compactor used. Studies by Bendix indicated that 1/2-inch layers compacted with the small vibratory compactor (fitted with a 1-1/4-inch diameter tamping foot) for 1-1/2 minutes produced a satisfactory value for maximum density. Subsequent investigations showed that use of a 3-1/2-inch diameter tamping foot on the vibratory compactor, placement of 1-inch layers, and a time of compaction (per layer) of two minutes produced equivalent values of maximum density. Since the latter method is much less time-consuming its use is preferable.

11

The minimum-maximum density test data was evaluated using the following criteria:

> Those values of minimum or maximum density obtained from a series of tests on a given sample which varied more than 3% from the overall average were eliminated from the final computation of the average reported.
>
> The minimum requirement for the number of tests run on a given soil sample was that at least 75% of the test results fall within 3% of the reported average.

The average minimum and maximum densities obtained by the test procedures described above and using the evaluation criteria outlined are then plotted on a graph similar to that shown in Figure 2-15. Figure 2-17 shows the results of tests done on several different samples of each of the six basic soil types being used in the LM soil mechanics study. The values shown were obtained on previously unused, undegraded soil materials or on soils that did not suffer appreciable degradation.

Considerable variation in test results can be obtained if the conditions leading to such variation are not recognized and eliminated in the test procedures used. Basically, such variation results from variation of the soil material and inadequate control of the test procedures and apparatus.

Variation of the Soil - This type of variation is due to nonuniformity of the grain size distribution and the material comprising the soil grains which occurs at the source of supply of the soil material. The use of proper sampling techniques to choose the samples to be tested from the soil material supplied will ensure that statistical analysis of the test results incorporate the influence of such nonuniformity.

Inadequate Control of Test Procedures - Certain variations in test results are bound to occur such that the results fall above and below some "true" value which can adequately be described by the average value. Such variation can be defined by statistical analysis. However, inadequate control over the test procedure can introduce variation

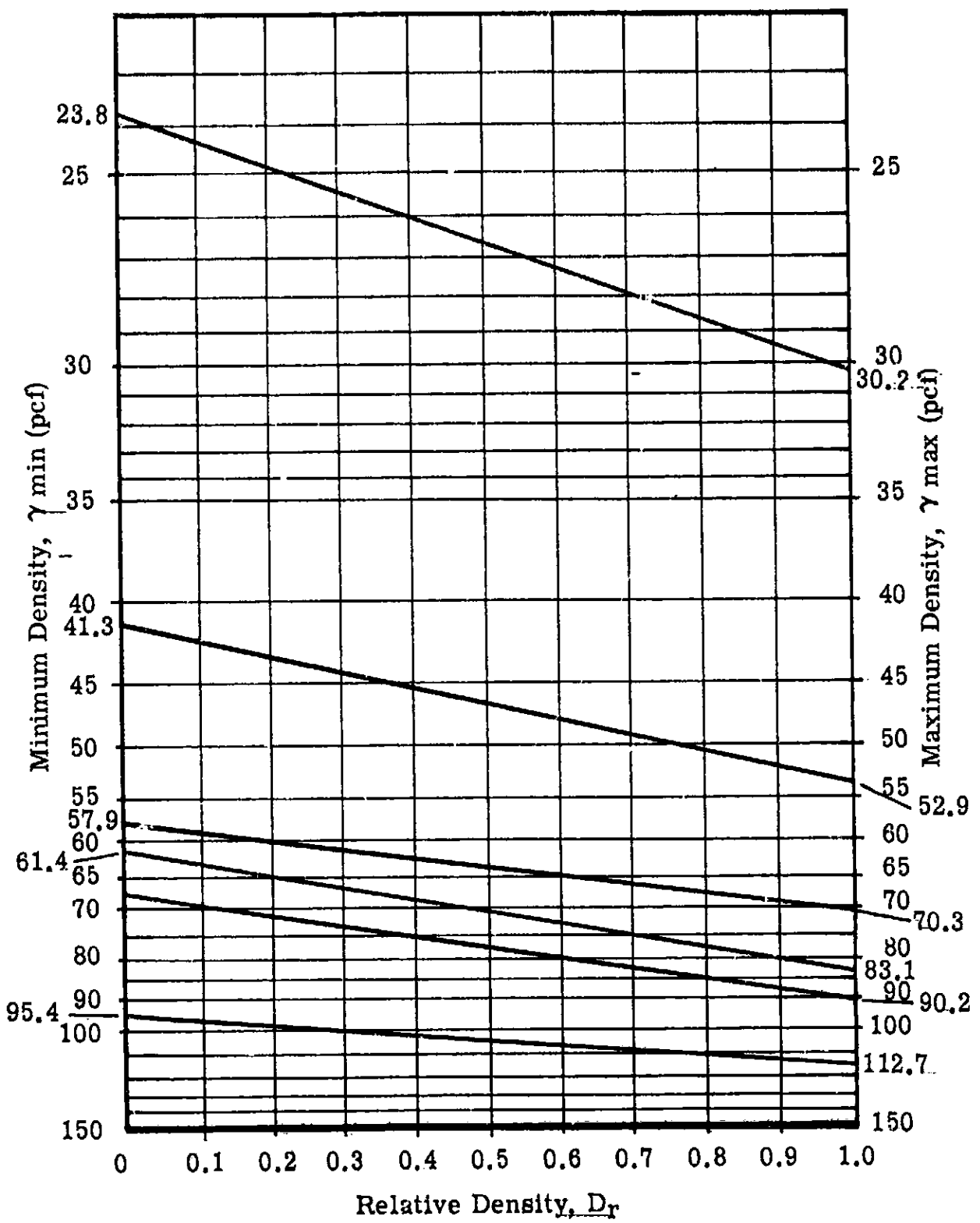

Figure 2-17. Average Density vs. Relative Density Curves for Six Basic Soil Types

which is more or less consistently above or below the "true" value and the average of these values is not an adequate representation of the "true" value. These effects and the procedures used to eliminate or minimize them are discussed below.

Variation in Grain Size Distribution - The density of a given soil depends primarily on the width of the grain size distribution and distribution of particle sizes within that range. A well graded soil is a broadly-graded soil whose particle sizes are distributed in such a manner that an optimum unit weight can be achieved. A poorly graded soil is one in which the majority of soil particles fall into a narrow range of sizes and the unit weight of the soil falls below the optimum mentioned above to a degree dependent on the width of gradation and the distribution of particle sizes.

If a soil sample which is being tested is poorly mixed (i.e., nonuniform in terms of grain size distribution, or, particle sizes are segregated) the soil placed in the test mold will not be representative of the sample and, thus, the unit weight achieved will not be representative. This type of variation will be especially acute with broadly-graded soils (e.g., the RC2 soil, in this study). The variations due to such nonuniformity can be minimized by splitting the sample down into size units close to that required for one test determination.

Nonuniformity of grain size distribution can also occur during placement of the soil into the mold if the soil is placed in such a manner that the soil particles are allowed to roll down a slope. This can be prevented by placing the soil from the funnel in a concentric circling motion from the side of the mold to the center such that the soil is built up in relatively level layers.

If the soil grains are relatively weak the compaction process used to achieve maximum density may produce a change in grain size distribution which has a significant effect on the value of maximum density achieved. Grain size analysis of the soil before and after being tested for maximum density will indicate whether or not such a change is taking place.

Variation in Soil Placement - If the soil is not placed in the mold with the minimum free fall from the funnel, higher densities will be produced.

Allowing the soil to flow too quickly from the funnel will also tend to produce higher values for minimum density.

Vibration of Loose Soil - Vibration or impact of the mold during performance of the minimum density test will tend to produce high values of density.

Variation in Compactive Effort - Since vibratory compaction has been found to be the most effective way to compact dry, granular materials, this method was used to determine the maximum density of the soils used in this study*. The degree of compaction achieved is a function of the thickness of the layer being compacted, the time taken to compact each layer and the size of the tamping foot. In practice, if a given size of layer is specified and a tamping foot of given size is used, maximum density can be expressed as that density at which additional compactive effort will effect no significant increase in density. A study was made by Bendix in which 1/2-inch layers of RS soil were compacted for various time increments using the small vibratory compactor, previously described, fitted with a 1-1/4-inch diameter tamping foot. Figure 2-18 shows the results of these tests. These graphs indicate that very little increase in density was obtained after 1-1/2 minutes of compaction per layer. Subsequently, it was found that similar maximum densities were achieved using 1-inch layers compacted for two minutes using a 3-1/2-inch diameter tamping foot. Since this configuration allowed for quicker determinations, this was the standard technique adapted for the latter part of our study.

As discussed previously, it was found that the compaction process can result in some breakdown of the cinder soil particles and, thus, the maximum densities reported for these soils might tend to be slightly higher than the "true" value for these soils. Care should be taken that these soils are not compacted for greater periods of time than

*The vibratory methods also produce much less breakage of the particles of the cinder soils used in this study than the standard "impact" compaction methods.

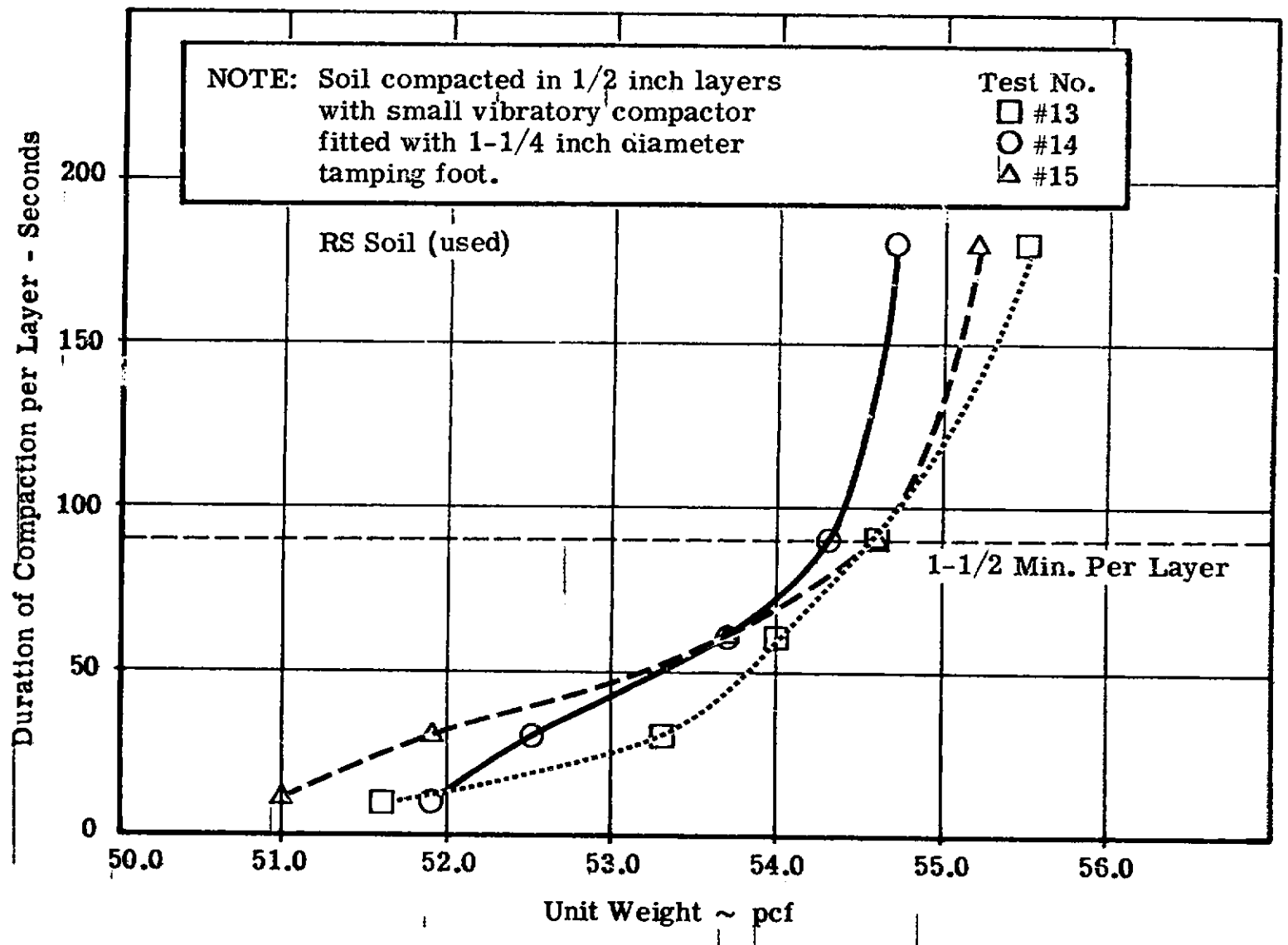

Figure 2-18. LM Soil Mechanics Study- Time of Compaction Study

those suggested. Conversely, Figure 2-18 illustrates that periods of compaction lower than those specified can result in values of "maximum density" significantly lower than "true" values.

2.5.2.3 Direct Shear Test

The angle of internal friction reported for the test soils was determined by Direct Shear Tests performed by the Civil Engineering Department of the University of Notre Dame. A photograph and schematic drawing of the test apparatus used is shown in Figures 2-19 and 2-20*.

Soil at a specified state of relative density is placed in the shear box and a normal load applied to the soil. The 2-1/2-inch diameter shear box is split horizontally and the bottom element slowly pulled away laterally from the upper element inducing a shear surface along the horizontal plane defined by the two elements of the shear box. Readings are taken of shear load, shear strain and volume change of the sample until about ten percent shear strain has occurred. The test is repeated using several different values of normal load on samples of the same soil at the same initial relative density. Figure 2-21 shows a plot of these measurements on samples of RS soil having a relative density of about 0.50 to 0.57.

The maximum shear stress achieved at each normal stress level is then plotted and the best straight line drawn through these data points as shown in Figure 2-22. This straight line is called the "failure envelope," and the angle the failure envelope makes with the normal stress axis is defined as the angle of internal friction. This relationship is derived from the Coulomb Equation for shear strength of a soil:

$$S = C + \sigma_n \tan \phi \qquad (3\text{-}1)$$

*A detailed description of the Direct Shear Test is given in the reference (31, pp. 354-356; 30, pp. 88-97).

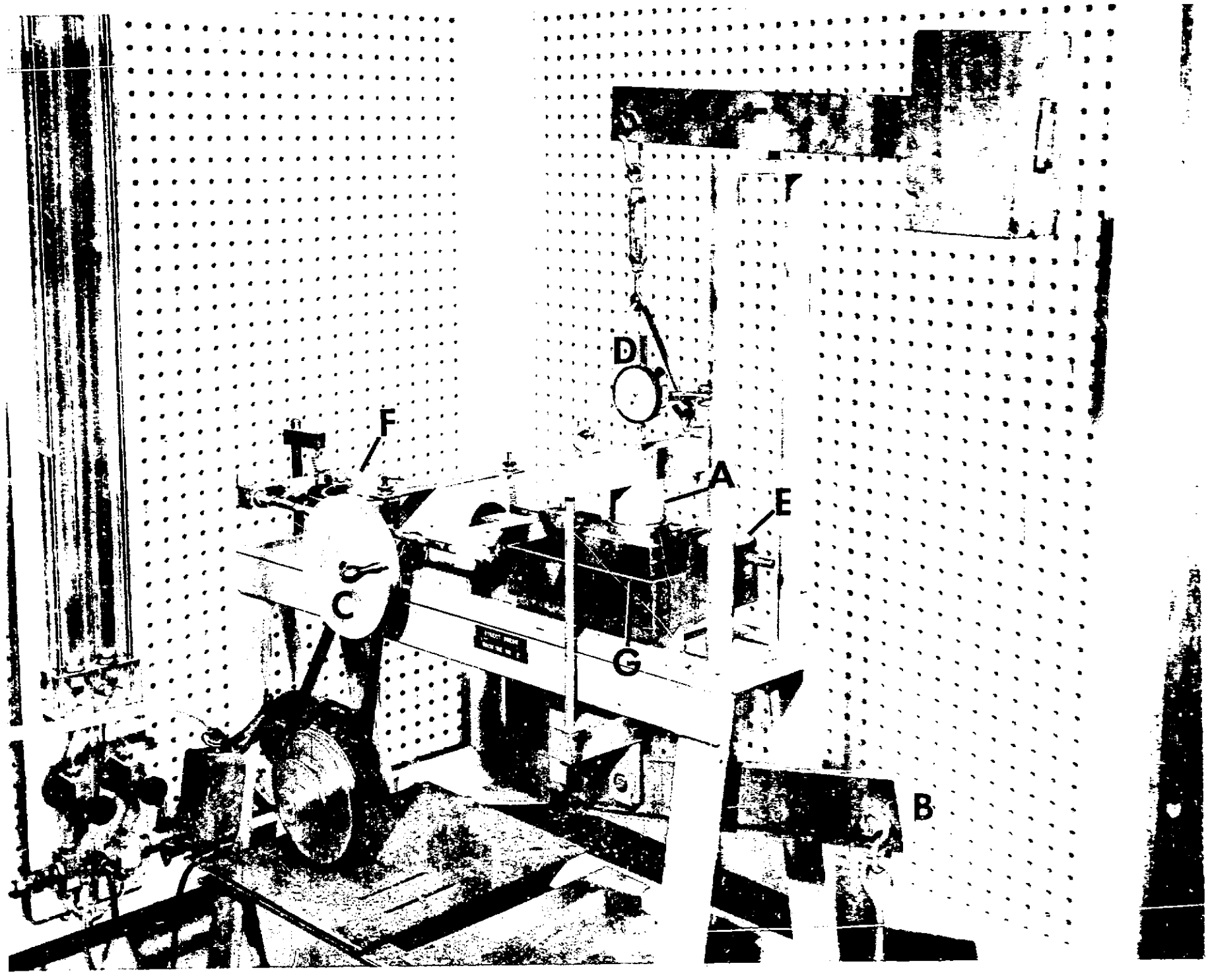

Figure 2-19. Direct Shear Test Measurement

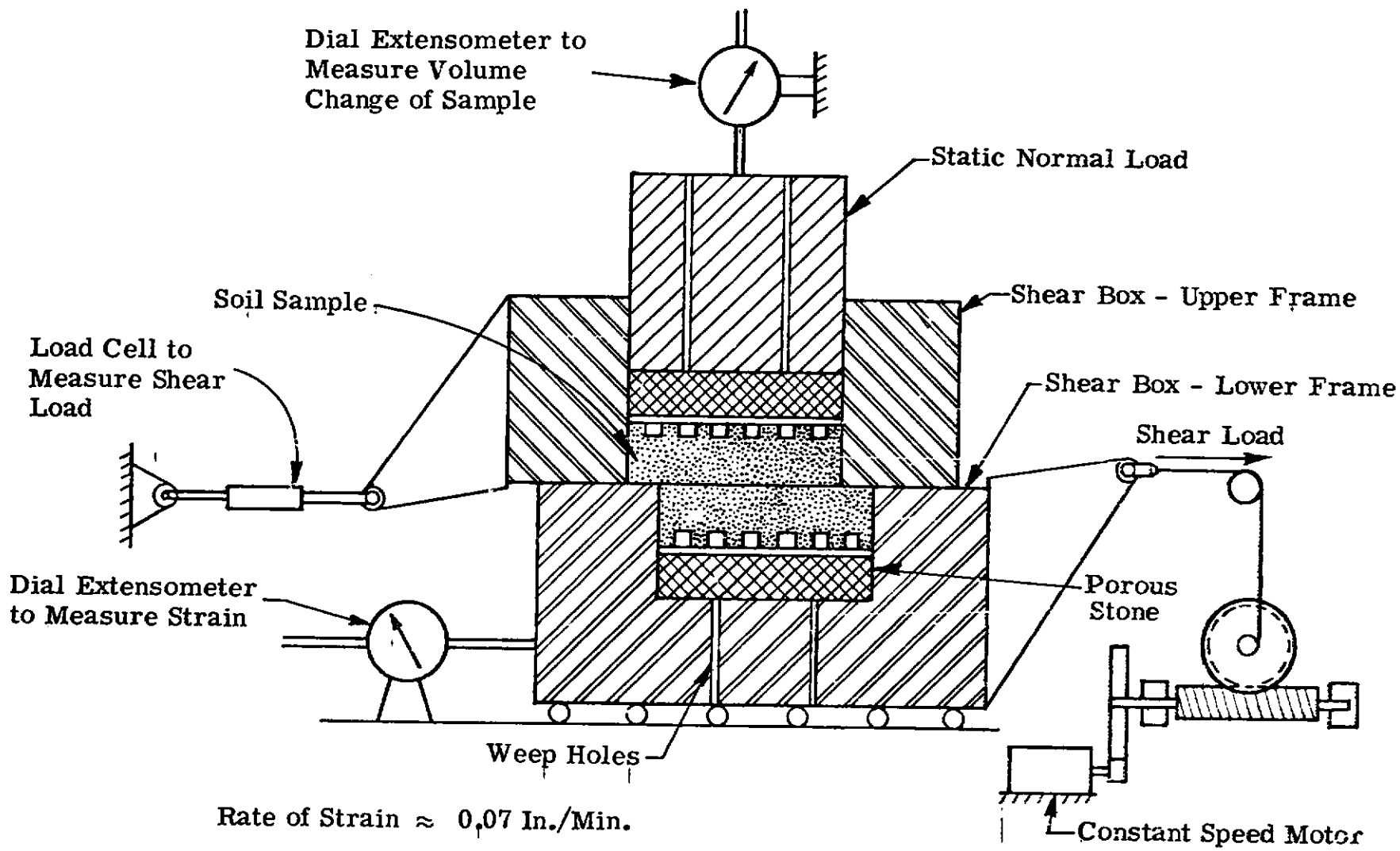

Figure 2-20. Schematic Drawing of Direct Shear Test Equipment

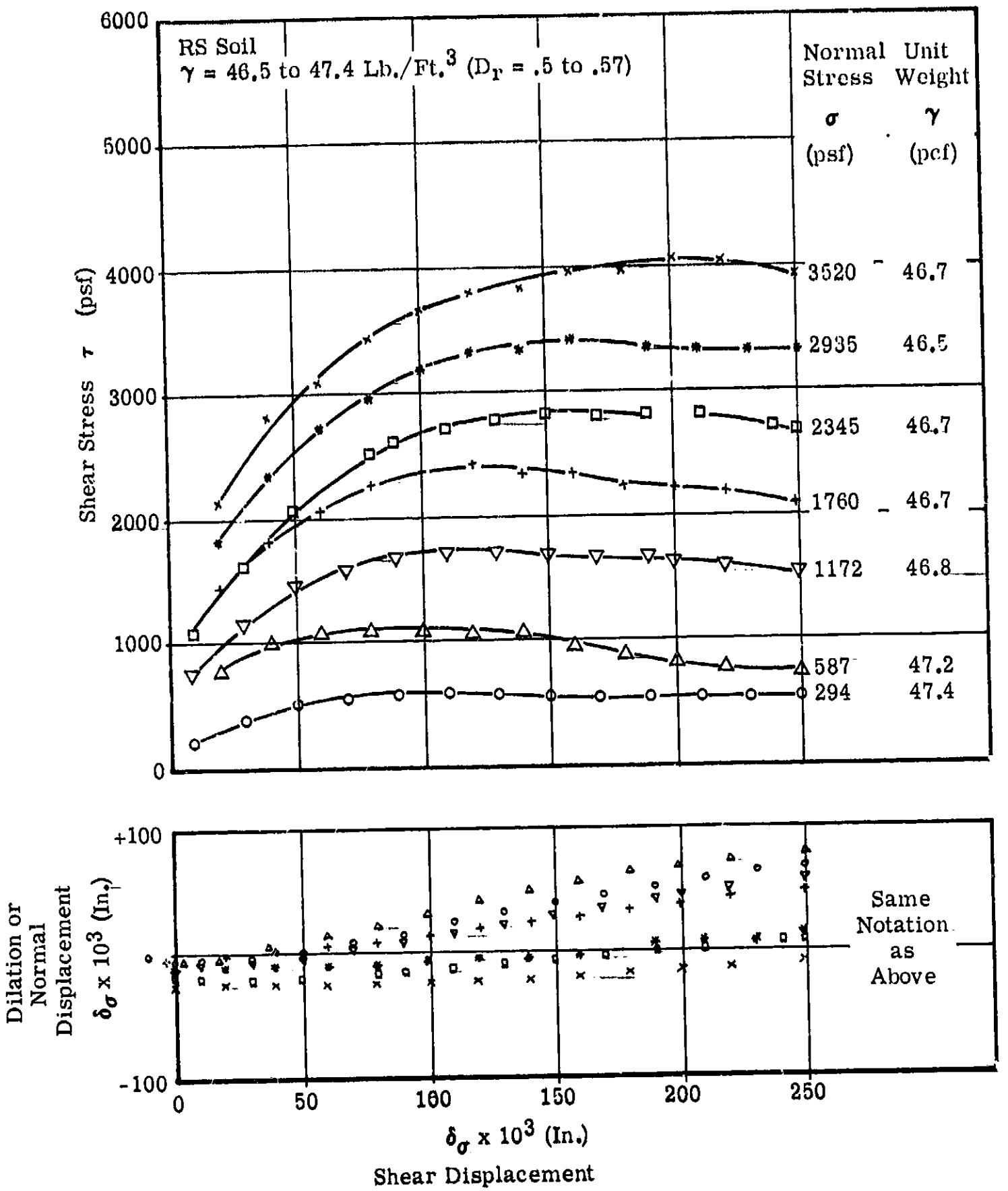

Figure 2-21. Direct Shear Test Data

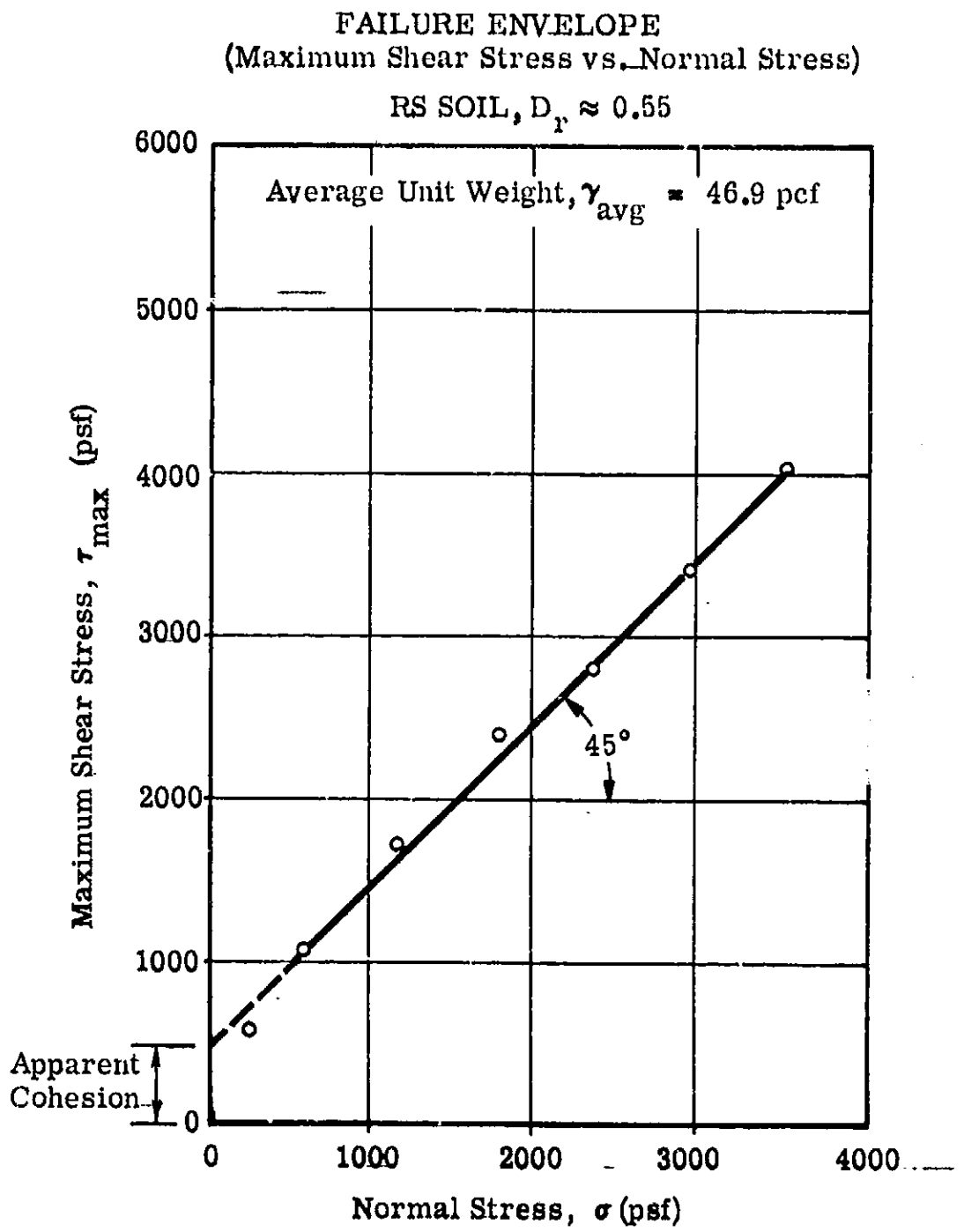

Figure 2-22. Failure Envelope

S = Shear resistance or strength of the soil (or, the maximum shear stress recorded in a direct shear test, τ_{max}).

C = Cohesion; shear strength due to cohesion.

σ_n = Normal stress on plane of shear.

ϕ = Angle of internal friction.

Solving this equation for ϕ yields:

$$\phi = \tan^{-1} \frac{S - C}{\sigma_n} = \text{slope of failure envelope}$$

All of the direct shear test data and failure envelopes obtained on the test soils is presented in Appendix C. Figure 2-23 summarizes the average relationship found between angle of internal friction and relative density* for all the test soils except soil number 10 as determined by the direct shear tests.

Examination of the failure envelopes obtained for the test soils (see Appendix C) and the relationships between ϕ and D_r shown in Figure C-1b reveals the following noteworthy characteristics:

> The values of angle of internal friction for the cinder soils are substantially higher than those for the silica sand (which values are more or less typical of earth-type granular noncohesive soils). The failure envelopes indicate appreciable values of "cohesion" for the cinder soils. The curves for the cinder soils tend to be relatively flat.
>
> The data for the LSM soil indicates no change of ϕ with D_r and, at least nominally, shows a higher value of ϕ for the test run at the lower relative density.

The relatively high value for angle of internal friction obtained for the cinder soils can be explained by the difference in particle surface characteristics between the cinder particles and earth-type soils such as silica sand. Although it has been found that

*The value of relative density used is the value existing prior to application of the normal load.

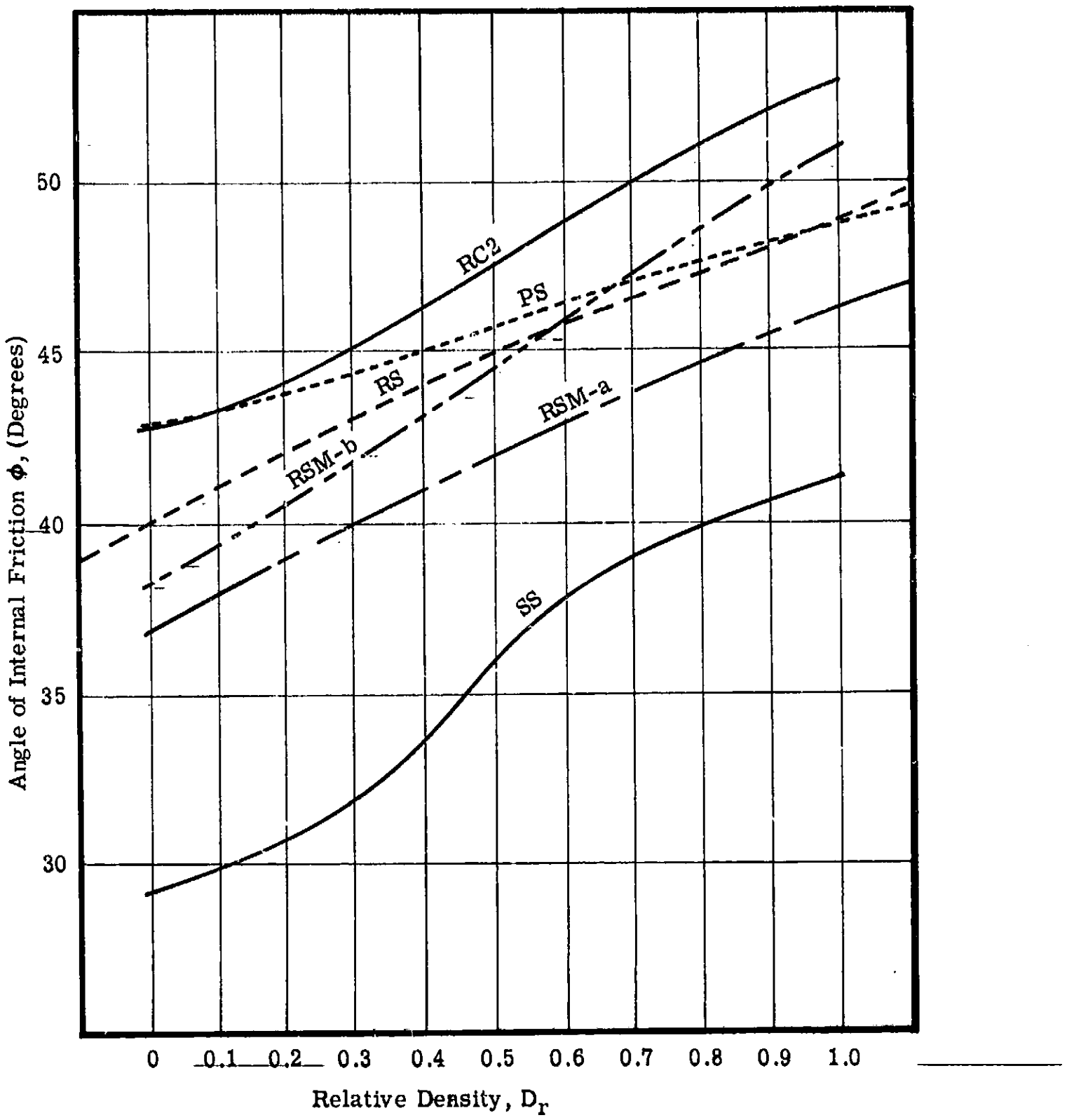

Figure 2-23. Angle of Internal Friction (as Determined by the Direct Shear Test) Versus Relative Density

angle of internal friction is predominantly a function of the compactness or relative density of a soil, it is known that there are other secondary factors affecting this value (12, pp. 217-219). Angle of internal friction has been found to increase with increasing grain coarseness, angularity and roughness and the degree to which the soil is well graded. The changes in the value of angle of internal friction caused by changes in these secondary soil properties were found to be quite small (i.e., 2° - 4°) and the assumption of a direct correlation between relative density and angle of internal friction (39, p. 39*) has been found adequate for most design purposes.

The cinder soils are significantly different from the common silica-feldspar soils. Each grain is a mineral assemblage and they are not solid but have a highly crenulate surface as shown in the photomicrograph of the RS soil in Figure 2-24. It is likely that the significantly higher value of angle of internal friction obtained for the cinder soils is the result of the appreciably higher particle angularity and surface roughness.

The crenulate character of the cinder particles may also contribute some "apparent cohesive strength" to these soils. An examination of the failure envelopes obtained for the cinder soils (Appendix C) indicates appreciable values for "apparent cohesion." However, studies made by Bendix of bearing strength tests performed on these soils (the load-penetration test) indicates that inclusion of the values of "apparent cohesion" obtained in the direct shear and triaxial tests on the cinder soils in Terzaghi's bearing capacity equation yield higher values of bearing strength than observed in bearing strength tests**.

"True cohesion" is regarded as that shear strength possessed by a fine-grained soil due to attractive forces of a physiochemical nature between particles (37, pp. 199-203). This type of shearing resistance is stress-independent.

---

*Of chart in Figure 2-2 of the reference.

**It has been found that a small value of "C" (on the order of 0.1 psi) is needed to explain some of the size effects observed in the load-penetration test. The values of "apparent cohesion" obtained in the direct shear tests were about 50 times greater than this value.

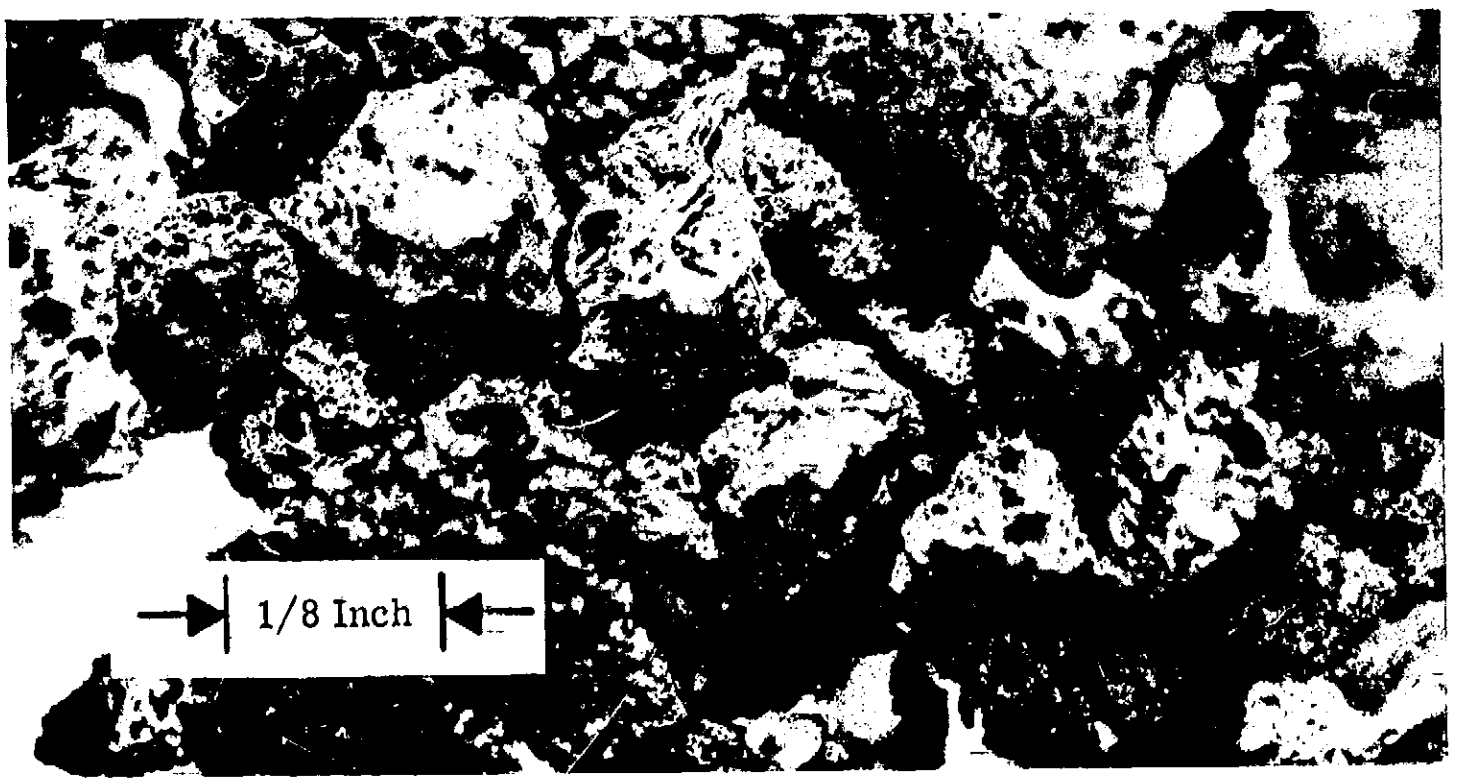

Figure 2-24. Photomicrograph of RS Soil; Note Pronounced Angularity and Vesicularity

It has been suggested that the interlocking of soil particles can also contribute an "apparent cohesion." This might be a possible explanation of the apparent cohesion value exhibited on the failure envelope graphs for the cinder soils in Appendix C.

Another possible explanation for the apparent cohesion value exhibited by these soils postulates that shear failure occurs by the rolling and sliding of soil grains on the failure plane at low stress levels and by crushing of soil particles at higher stress levels. If such behavior did take place failure envelopes such as those shown in Figure 2-25 would tend to be produced. In this figure, σ_{ncr} represents the normal stress at which some of the soil particles will crush before achieving the rolling and sliding phase, thus limiting the maximum shear stress that can be achieved. If most of the data points are in the range of normal stress above σ_{ncr}, the "best" straight line through the data points will be that having the slope ϕ' and interpolated back to the σ axis (as shown by the dashed lines) will exhibit an apparent cohesion as shown. The limiting effect of the breaking strength of the particles might also tend to make the value of ϕ' for both loose and dense soils similar, thus explaining the relatively small range of values of angle of internal friction reported for the PS soil. The distribution of the data points on the failure envelopes for the cinder soils tends to exhibit such an effect, but the scatter of these points does not permit a definite conclusion.

Bendix performed a limited number of triaxial tests on the cinder soils using the apparatus shown in Figure 2-26. In the triaxial test a cylindrical prism of soil is subjected to a constant hydrostatic confining stress while a steadily increasing axial stress is applied until the sample fails in shear. Mohr's circle analysis of the tests, run at various confining pressures, yields a failure envelope similar to that described for the direct shear tests. Triaxial tests were performed on the RS soil in intermediate and dense states. The apparent cohesion obtained was on the same order of magnitude as that obtained in the direct shear tests and the value for angle of internal friction was about 38° in both cases. When the data was re-examined for the effects illustrated in Figure 2-25 (crushing of grains and a lower value of ϕ at higher confining pressures) it was found that this interpretation of the tests did yield values of ϕ of 39° and 43° for the RS intermediate and RS dense soils, respectively, at low confining pressures, and values of 36° for both soils at high confining pressures.

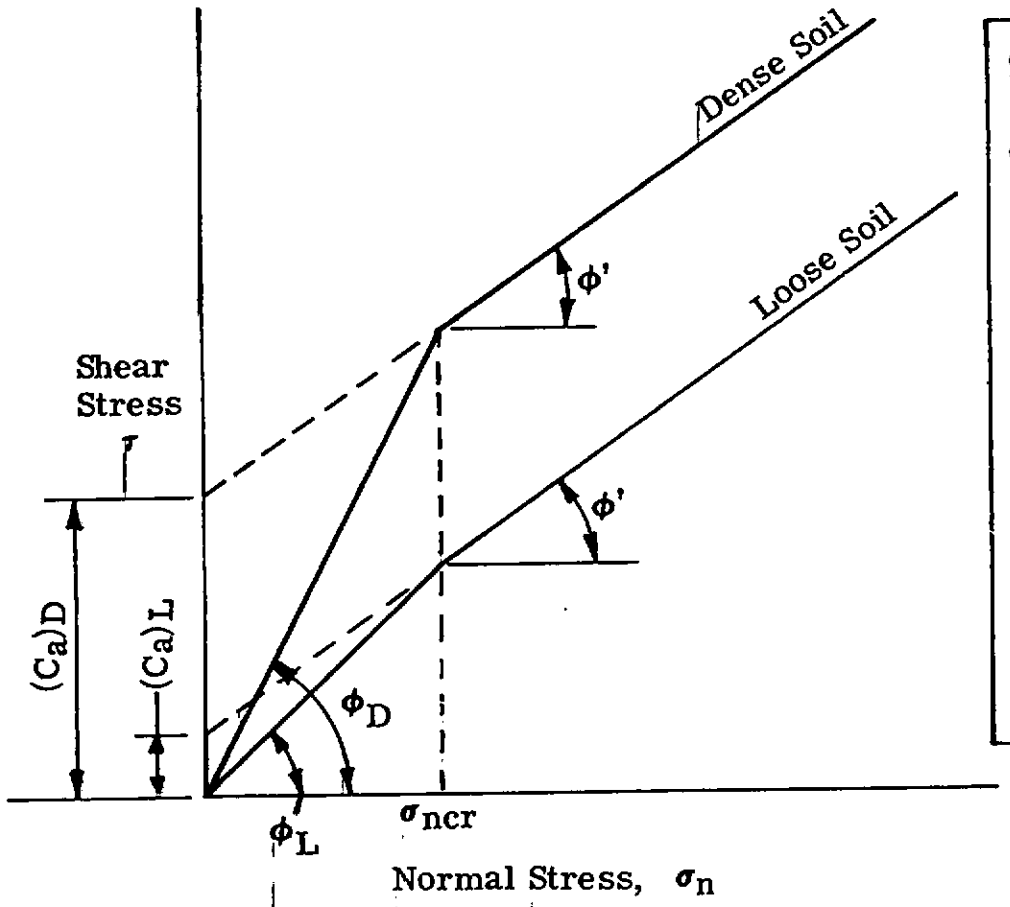

ϕ_L	=	Angle of Internal Friction for loose soil
ϕ_D	=	Angle of Internal Friction for dense soil
ϕ'	=	Angle of Internal Friction due to crushing of particles ($\sigma_n > \sigma_{ncr}$)
σ_{ncr}	=	Critical Normal Stress (Normal stress above which particles tend to break rather than roll and slide)
$(C_a)_D$	=	Apparent cohesion for dense soil
$(C_a)_L$	=	Apparent cohesion for loose soil

Figure 2-25. Hypothetical Failure Envelopes for Shear Failure Due to Breaking of Soil Particles

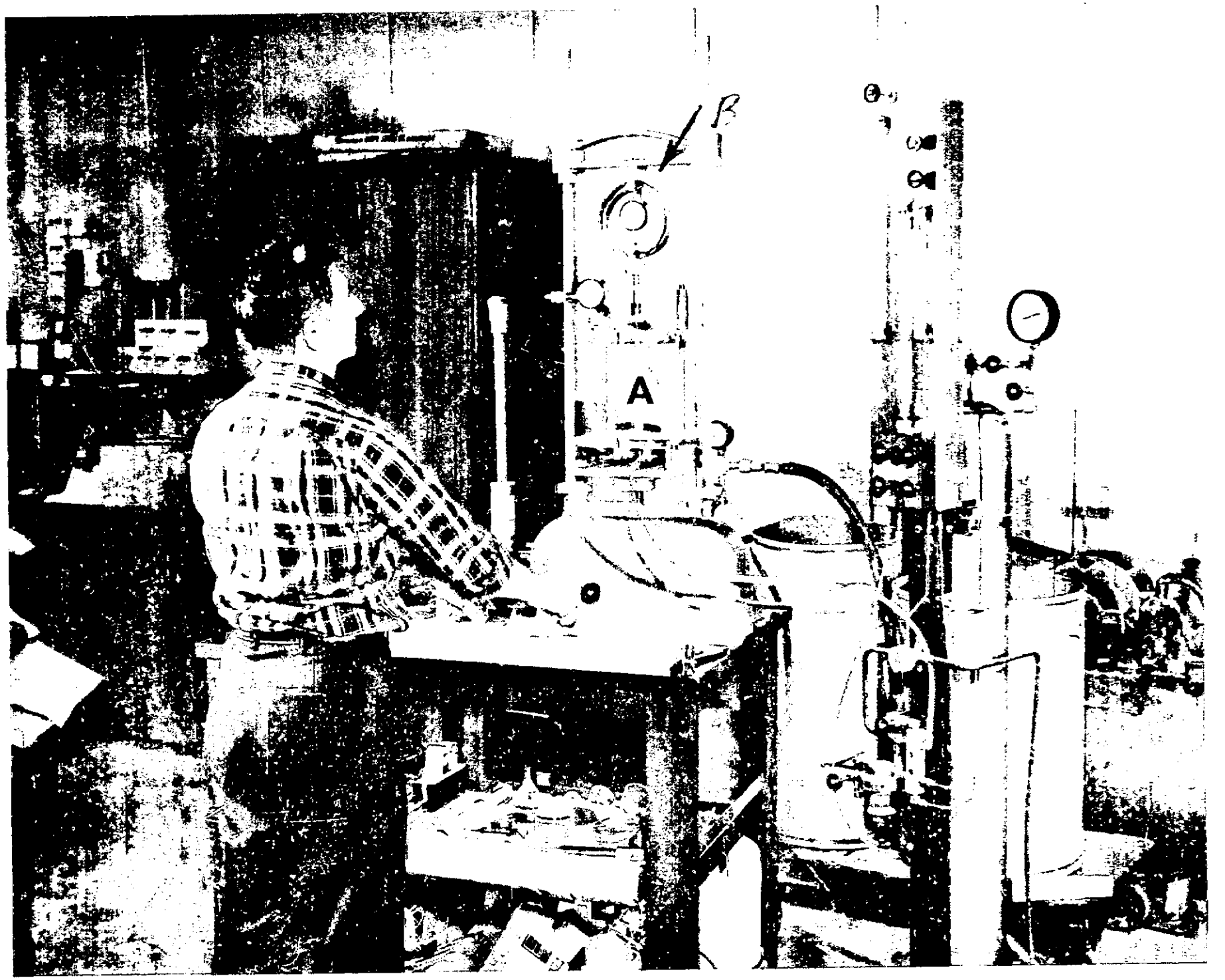

Figure 2-26. Triaxial Shear Test Machine

The scope of the present program did not allow for a detailed investigation of the various aspects of the direct shear test results. In view of the lack of correlation between the apparent cohesion intercept data for the cinder soils and the resulting static and dynamic strength levels, the apparent cohesion was not used as a soil descriptor.

The fact that the direct shear test data for the LSM soil does not indicate any significant change in ϕ with D_r can be explained, in part, by density changes occurring in the soil during the progress of the test. Examination of the normal displacement readings ("Dilation") for the loose LSM soil indicates that the soil densified upon the application of the normal load prior to the actual shearing operation. For the higher normal loads, the densification produced is about equal to the density of the dense LSM soil. The ϕ relationship shown for the LSM soil in Figure 2-23 is based on a failure envelope constructed using the lowest values of normal load used in the direct shear test on the loose LSM soil.

2.5.3 Sonic Velocity Test

The sonic velocity tests used to determine the modulus of elasticity or initial tangent modulus of the test soils were conducted by IITRI. Their report of the tests is given in Appendix B.

2.6 BEARING STRENGTH TEST

Tests to determine the bearing strength or bearing capacity of the test soils were performed in the load-penetration test (LPT) apparatus shown in Figures 2-27 and 2-28. A test cylinder or subscale footpad is advanced into the soil under hydraulic pressure at a specific rate of penetration and a record made on an x-y plotter of the load-penetration history of the test. An example of such a plot is shown in Figure 2-29.

In addition to using the LPT as a direct measurement of bearing strength of the soil, the LPT data was compared to the value of bearing strength obtained by using Terzaghi's bearing capacity equation (38, pp. 124-134) in conjunction with the values of angle of internal friction obtained from the direct shear tests performed on the test soils. Finally various methods of soil placement were investigated for use in the development of soil placement procedures for the drag, impact, and drop tests.

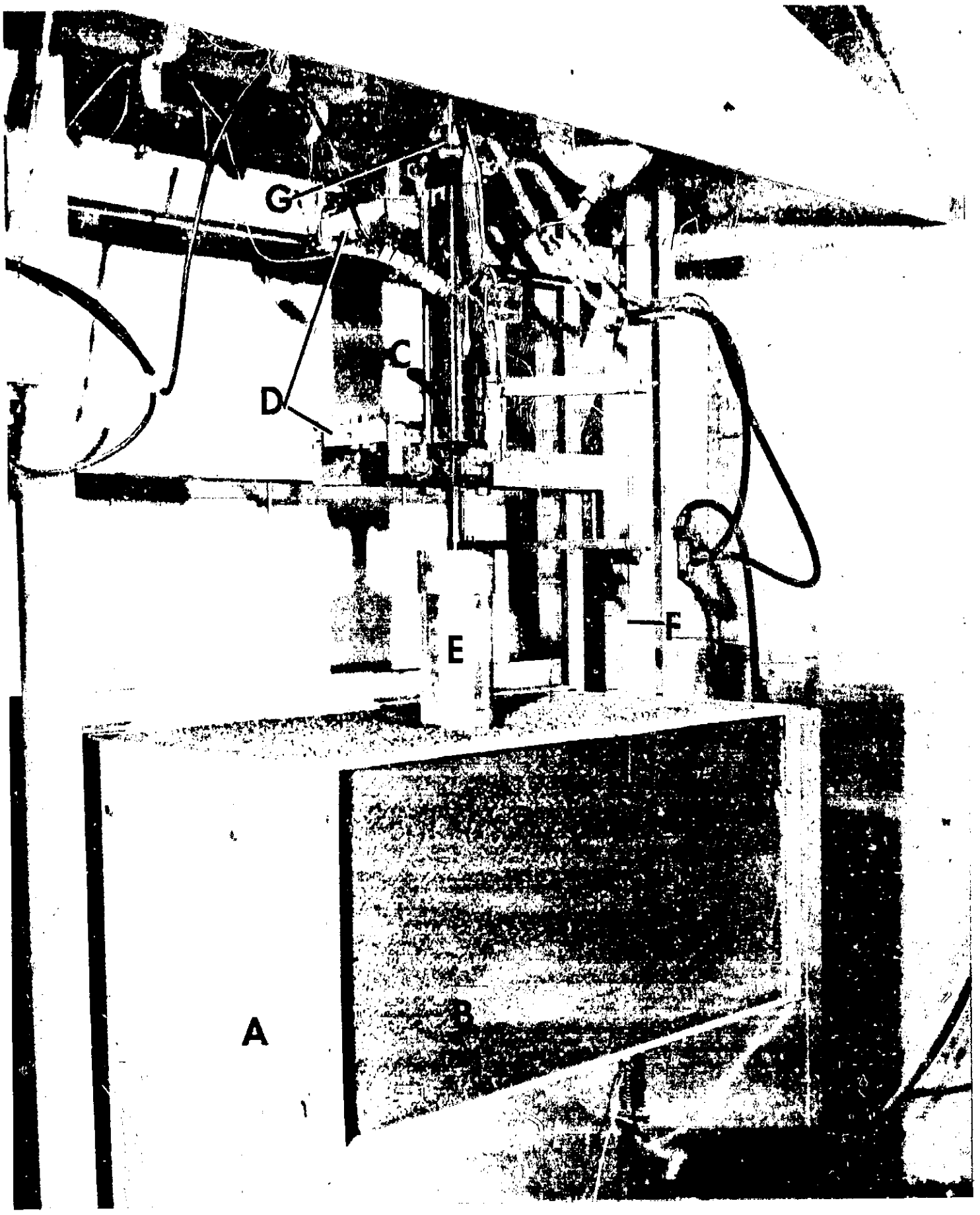

Figure 2-27. Penetrometer Test Fixture (LPT)

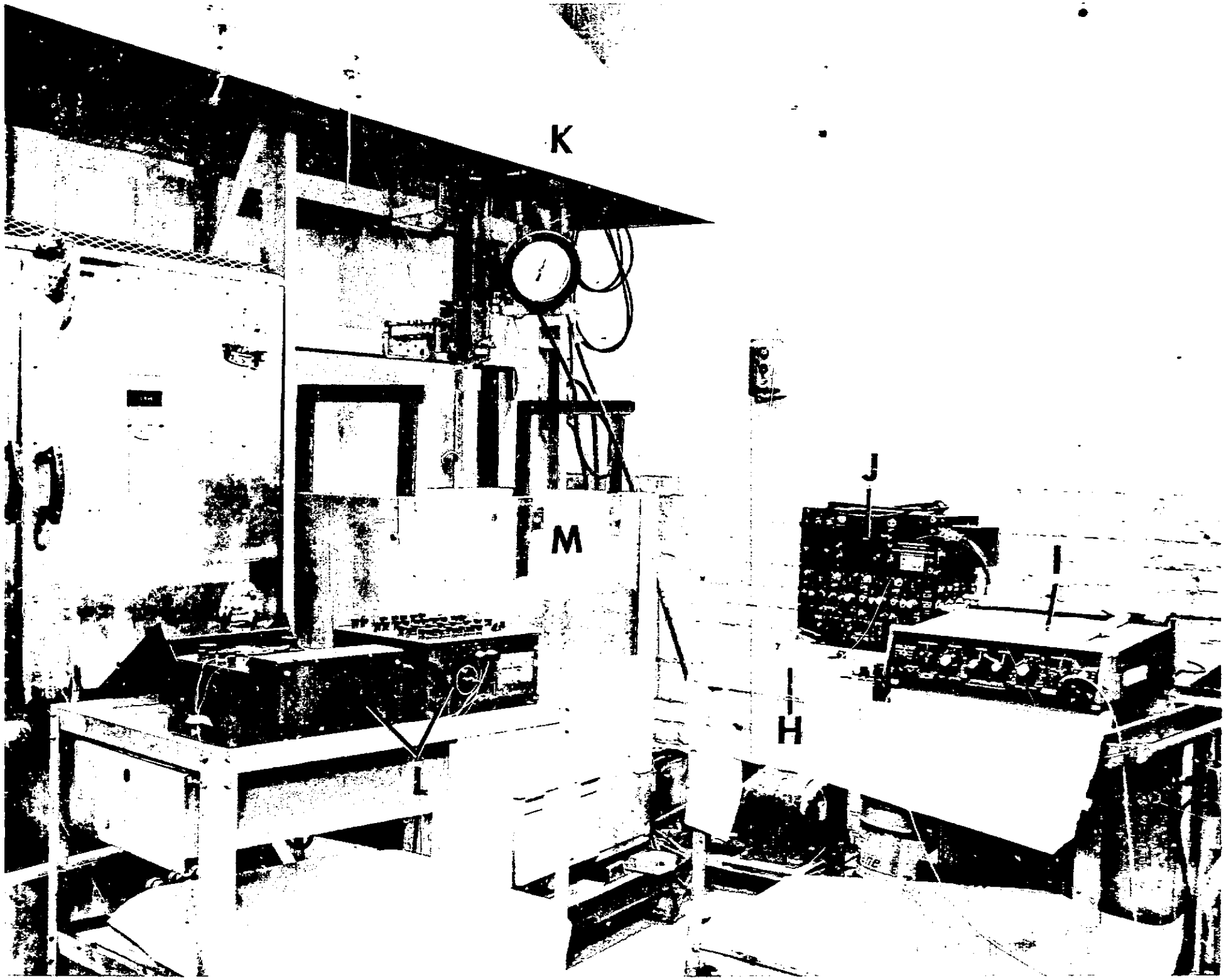

Figure 2-28. Load-Penetration Test (LPT) Setup

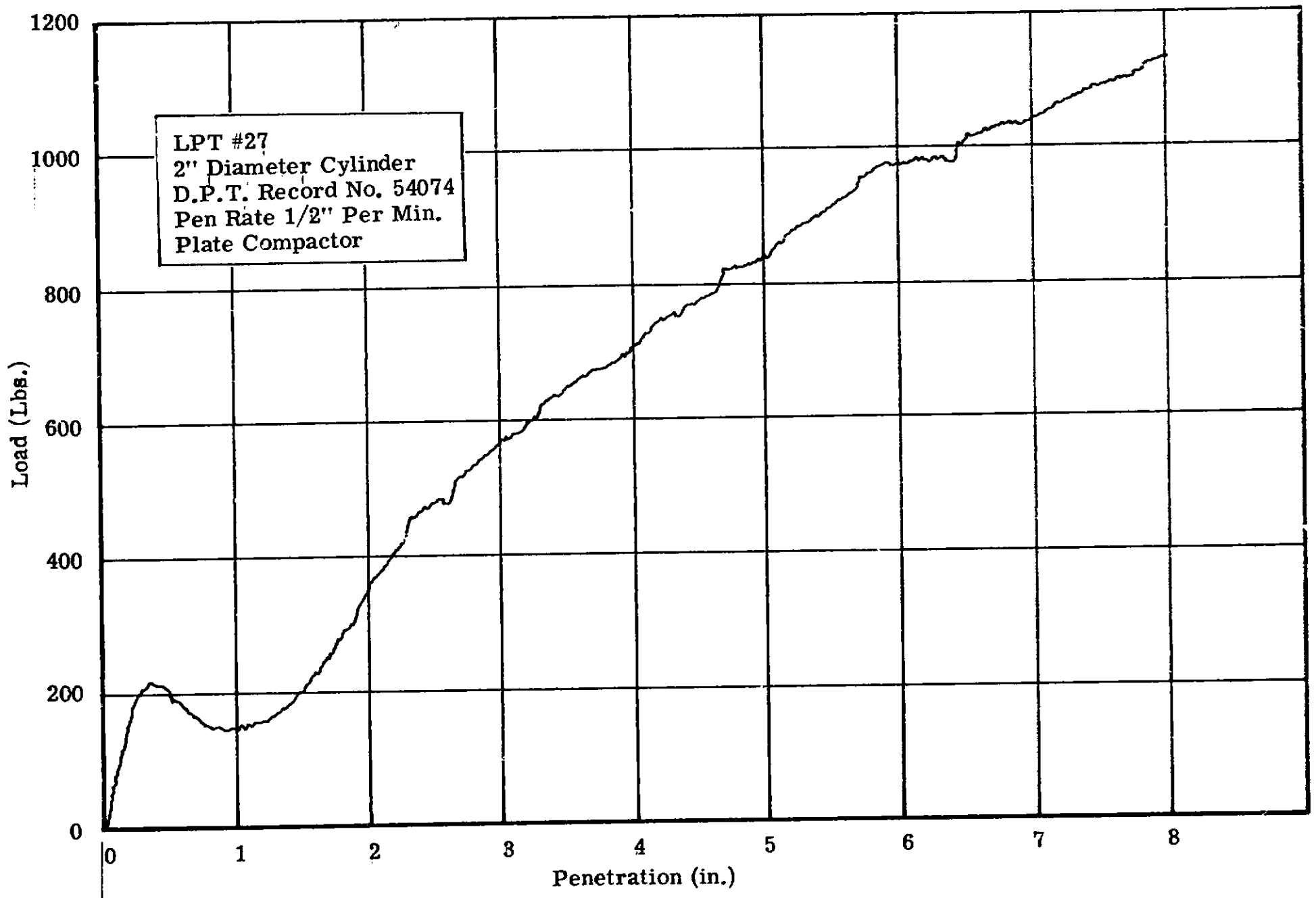

Figure 2-29. Load-Penetration Test (RS Dense)

2.6.1 Test Apparatus

Two views of the load-penetration test apparatus are shown in Figures 2-27 and 2-28. The labeled parts are described below.

A. Soil Container-A wooden box constructed of 1.0" plywood, 18" wide, 36" long and 36" deep. This box is supported on four instrumented load cells (not shown) for soil weight measurements.

B. Glass Front-1" thick plate glass, 18" deep.

C. Hydraulic Cylinder-Used to force test cylinder into soil.

D. Support Hinges-Hinges supporting hydraulic cylinder which take bending and transverse loads during loading of test cylinder.

E. Test Cylinder-The test cylinder shown is 4" in diameter. Other test cylinders used are 1", 2", and 8" in diameter.

E. Resistance Wire-Stroke wire for measuring penetration of test cylinder on x-y plotter.

G. Test Load Cell-Instrumented load cell used to record force on x-y plotter.

H. X-Y Plotter-Used to measure load versus penetration of test cylinder.

I. X-Y Plotter-Used to measure and regulate rate of penetration of test cylinder.

J. Amplifiers driving x-y plotters.

K. Exhaust Hood-Used to remove dust produced during soil handling.

L. SR4 Box and Switching Unit-Used to read load rings supporting test bin for soil weight measurements.

Figure 2-30 shows an adaptation of the LPT apparatus made to fit the subscale impact test bin so that the effect of container size might be investigated and that LPT might be run in the bin used in the subscale impact tests in soil prepared in the same manner as for for the impact tests. This test setup was also used to perform LPT using the 4-inch and 6.17-inch diameter subscale footpads used in the impact tests. The equipment and procedures used for these tests are essentially the same as those used for the other test setup. The labeled parts are described below.

1. Test Load Cell-Instrumented load cell used to record force on x-y plotter.

2. Hydraulic Cylinder-Used to force test cylinder into soil.

3. Test Cylinder-The test cylinder shown is 2" in diameter with the 6.17" diameter subscale footpad attached.

4. Support Hinges-Hinges supporting hydraulic cylinder which take bending and transverse-loads during loading of test cylinder.

2.6.2 Test Procedure

Soil Bed Preparation: The soil box is marked off in volume increments of 4, 6, 8, 10, 12, and 13.78 cubic feet (full box). As the soil placed in the box reaches each level, a weight determination is made. The unit weight of the soil was computed for each increment to check on the uniformity of the soil bed (i.e., the variation of unit weight from layer to layer) and for the full box to provide the value of average unit weight of the soil bed. The relative density of the soil beds is determined utilizing the relationships found for the various test soils by the minimum-maximum density test (2.5.2.2 of this section). A description of the various methods of soil placement investigated and used in the load-penetration test is given in Appendix C.

Test Operation: At the completion of test bed preparation and measurement, a test cylinder is affixed to the bottom of the hydraulic cylinder and pressure admitted to the top of the hydraulic cylinder. Load versus penetration is recorded on one x-y plotter and the rate of penetration regulated by a plot of penetration versus time on the second

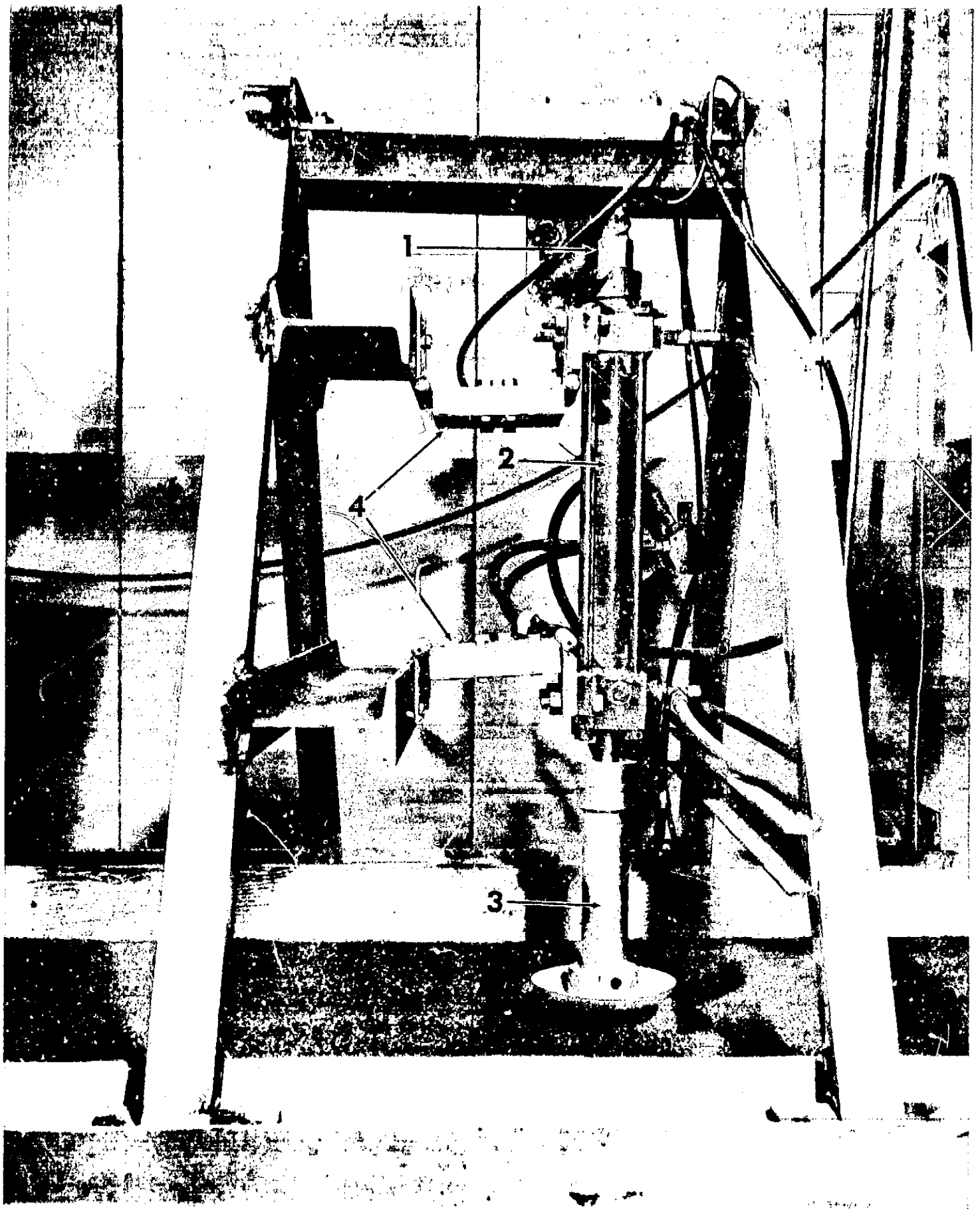

Figure 2-30. Load-Penetration Test (LPT) Setup

x-y plotter. The pressure to the cylinder is controlled so that the plotting pen follows a predetermined line on the penetration versus time graph corresponding to the desired rate of penetration. The cylinder is forced into the soil a distance of 8 inches or until the capacity of the hydraulic power supply has been reached.

2.6.3 Load-Penetration Test Results

Bearing strength or bearing capacity represents the summation of shear strength on a failure plane whose shape and size is a function of the size of the footing or test cylinder, its depth below the soil surface and the relative density of the soil. Thus, one aspect of the determination of the bearing capacity of the test soils was to investigate the effect of size of cylinder or footing on the bearing capacity of a given soil at a given depth. The standard method for determining bearing capacity generally involves the progressive application of load increments, each increment being added only after the settlement occasioned by the previous load increment had ceased (e.g., ASTM Designation D1194-57) (31, pp. 517-520). Since the performance of the LPT involves advancing the test cylinder into the soil continuously and at some specified rate of penetration, tests were run to determine the relationship between the LPT and the standard type of bearing test and to determine the effect of changing the rate of penetration of the cylinder on the load-penetration curve.

A bearing capacity failure (i.e., application of that unit force on the soil which exceeds the bearing strength of the soil) is generally envisioned as causing the soil to undergo a transition from a state of elastic equilibrium to plastic equilibrium. This generally results in displacements, laterally and upward, of wedges of soil below and beside the footing (38, p. 119-121). Terzaghi reports that small-scale model tests indicate that the greatest heave of the ground surface around a loaded circular area with a radius R occurs within 3R of the center of the loaded area, and that, beyond 5R from the center, the heave is imperceptible (38, p. 134). Since the closest boundary of the LPT bin for the 4-inch diameter cylinder is 9 inches (i.e., 4.5R) from the center of the cylinder, this size of bin would appear to satisfy the condition that the bin be large enough to eliminate significant boundary effects. However, it was noticed during an LPT in dense SS soil that a failure plane did intersect the glass face of the LPT bin and that this resulted in a noticeable upward displacement of a large portion of the soil. This observation

suggested that there could be a significant boundary effect for such soils in this size of bin and hence tests were made in larger bins to check this possibility.

Some tests were run with subscale footpads to investigate the effect of the footpad shape on the LPT curve. Both 4-inch diameter and 6-inch diameter footpads were used so that the size effect might also be investigated for each footpad shape.

Finally, an attempt was made to relate a bearing capacity factor determined from the LPT to soil strength coefficients developed in the analysis of the drag and impact tests.

The most common method of analysis employs the bearing capacity equation formulated by Karl Terzaghi (38, p. 118-134) given below:

$$q = D_f \gamma N_q + 0.3D\gamma \; N_\gamma + 1.3c \; N_c \qquad (3\text{-}1)$$

where:

q	=	bearing capacity of footing (FL^{-2} units)
γ	=	unit weight of soil (FL^{-3} units)
D_f	=	surcharge depth; depth of soil above bottom of footing (L units)
D	=	diameter of circular footing (L units)
C	=	cohesive strength (FL^{-2} units)
N_q, N_γ, N_c	=	bearing capacity factors dependent solely on the angle of internal friction, ϕ, of the soil (dimensionless)

For loose or very compressible soils, the bearing capacity factors given as applicable by Terzaghi are N_q', N_γ', and N_c*.

*Terzaghi distinguishes between general shear, the massive lateral displacement of soil during a bearing capacity failure, and local shear, a failure condition whereby lateral compression of the soil is of such magnitude that the failure surface cannot extend to the soil surface laterally and, hence no heave is observed. The bearing capacity factors for local shear were computed using the relationship: $\tan\phi' = 2/3 \tan\phi$ where ϕ is the angle of internal friction for a loose soil. For soils of intermediate relative density, interpolation between the general shear and local shear values may be used.

Figure 2-31 gives the values of the bearing capacity factors versus angle of internal friction. The values of N_q, N_q' and N_c shown were computed using the equations given by Terzaghi (38, p. 127). The values of N_γ and N_γ' shown were interpolated using the values given in the Navdocks Design Manual, DM-7 (39, p. 7-11-2).

Since the soils used in this study are essentially cohesionless soils, the cohesion term in Equation 3-1 was eliminated. Solving the remaining part of this equation for load or force on the footing at failure we obtain:

$$Q = A\gamma N_q D_f + 0.3AD\gamma N_\gamma \qquad (3\text{-}2)$$

where: γ, N_q, D_f, D, N_γ are defined as for Equation 3-1.

Q = load on footing at failure (F units)

A = area of bottom of footing (L^2 units)

On a graph of load versus penetration (Q versus D_f), Equation 3-2 would plot as a straight line with a Q intercept of $0.3AD\gamma N_\gamma$ and a slope of $A\gamma N_q$.

Figures 2-32 through 2-34 summarize the comparison of the bearing capacity equation to the LPT results. Since the bearing capacity equation predicts only a point of failure rather than the continuous penetration of a footing, LPT were performed starting at the surface and one or two positions below the surface. A straight line was passed through the various points of failure observed and the slope and load intercept value used to evaluate ϕ in the corresponding terms of the bearing capacity equation. The values of ϕ obtained in this manner were then compared to the values of ϕ obtained in the direct shear tests (see Figure 2-23).

Figure 2-32 showed the results of this for LPT in soil No. 1 (RS loose) using the 2-inch diameter cylinder. The comparison between the values of ϕ obtained using the bearing capacity equation (ϕ = 40° for the slope requirement and ϕ = 39.5° for the load intercept value) compare quite well with the value of ϕ = 38.5° in the direct shear tests.

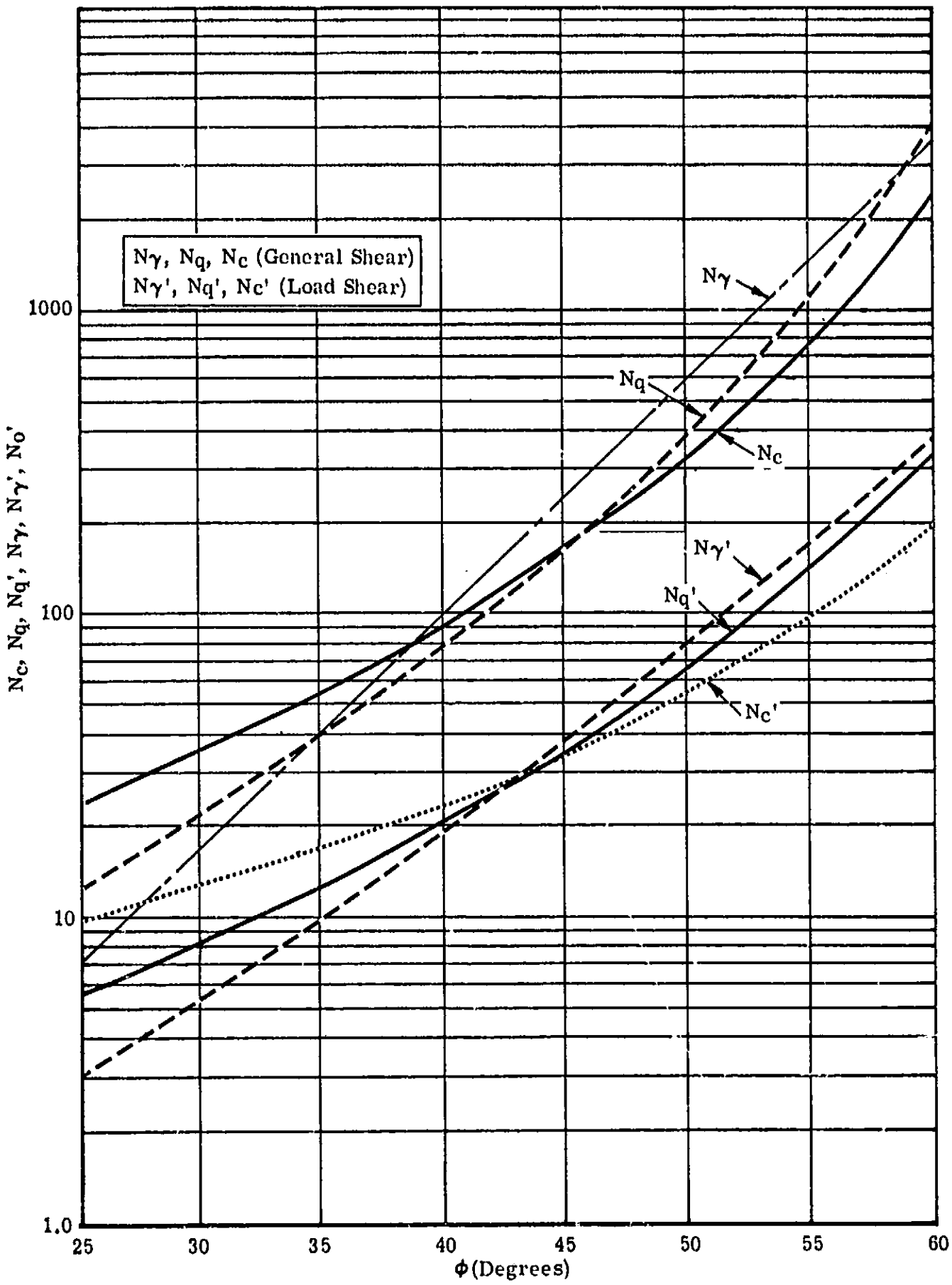

Figure 2-31. Bearing Capacity Factors

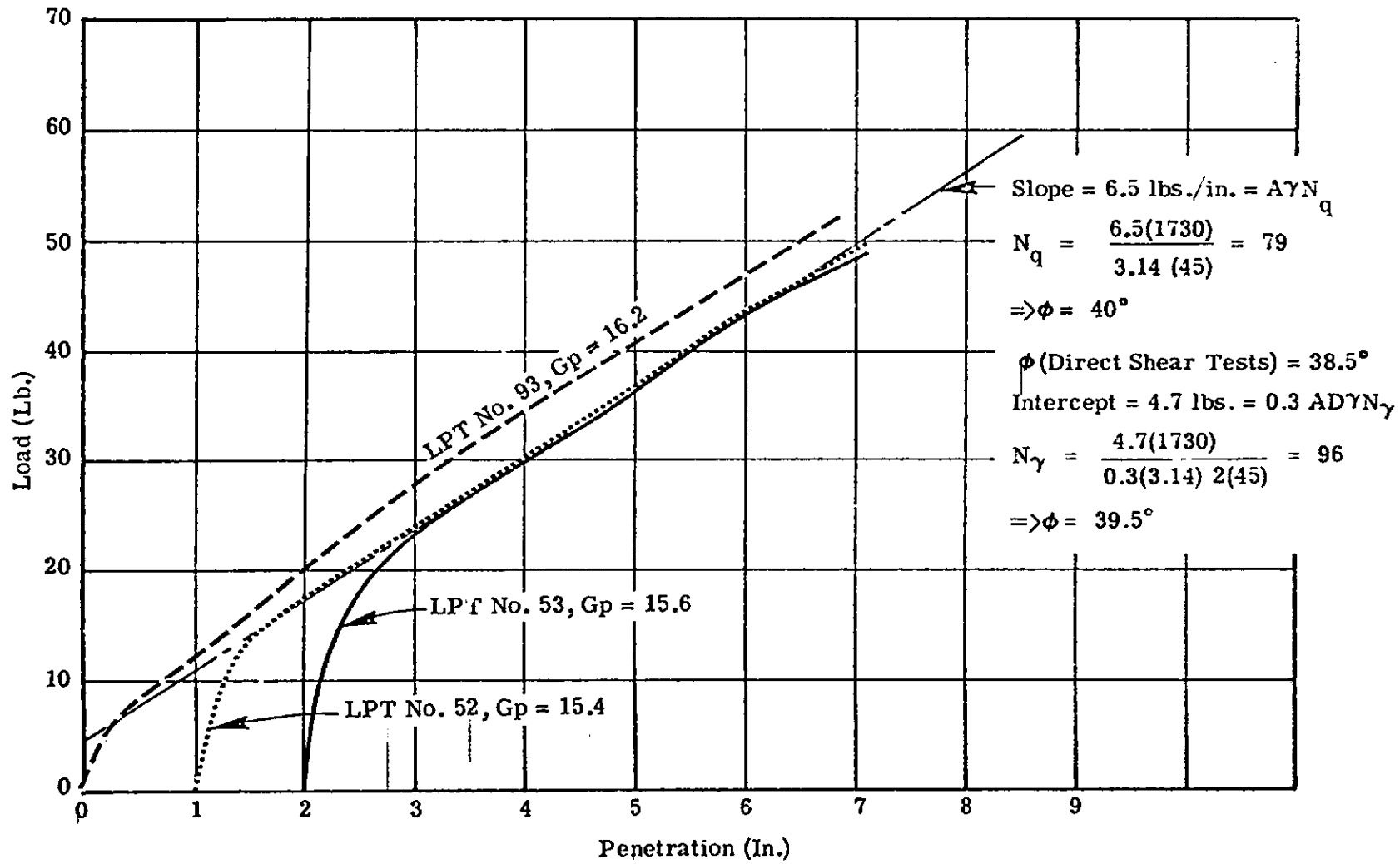

Figure 2-32. Load-Penetration Curves for Two-Inch Diameter Cylinder in Soil No. 1 (RS Loose) ($D_r \approx 0.0$)

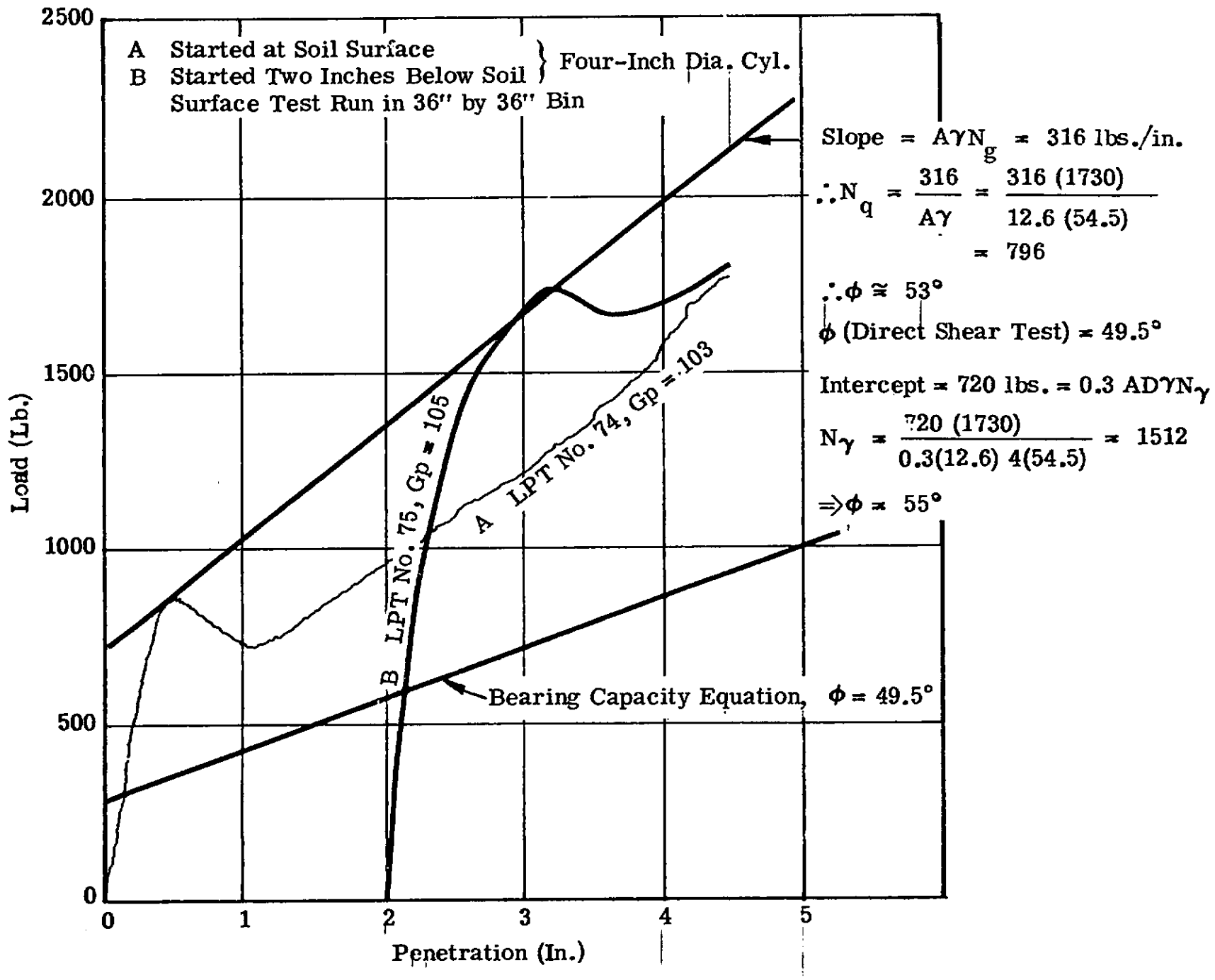

Figure 2-33. Load-Penetration Curves in RS Dense ($D_r \approx 0.94$)

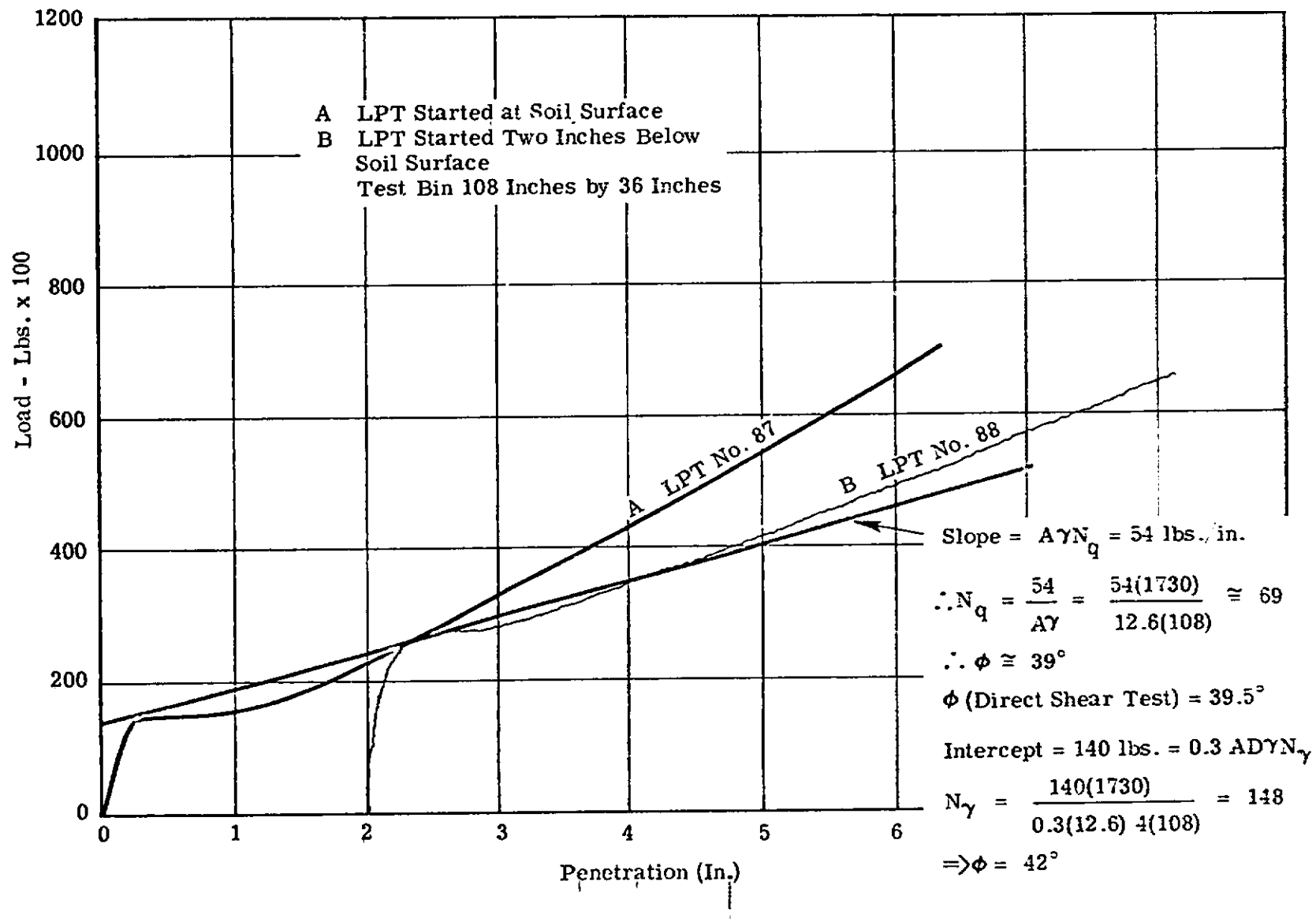

Figure 2-34. Load-Penetration Curves for Four-Inch Cylinder in Soil No. 9 ($D_r \approx 0.76$)

Note also that the line joining the failure points of the three LPT more or less follows the straight line portion of the LPT curves*.

Figure 2-33 shows the results of a similar analysis on LPT run in dense RS soil (note that this soil is much more dense than soil No. 4 which is also designated as RS dense) using a 4-inch diameter cylinder. Although it might not appear that the values of ϕ obtained by use of the bearing capacity equation are not appreciably higher than that obtained by the direct-shear test (i.e., 49.5°), it can be seen that the difference is appreciable when the straight line obtained from the LPT data is compared to the line representing the solution of the bearing capacity equation for ϕ = 49.5°**.

Note that the line joining the failure points has a slope similar to that of the LPT curve after the initial failure point.

Figure 2-34 shows the results of analysis of the LPT curves obtained using a 4-inch cylinder in soil No. 9 (SS dense). Here, the results yielded by the bearing capacity equation compare quite favorably with the results obtained by the direct shear test.

Figure 2-35 shows the results of the previously described analysis on LPT curves obtained using a 4-inch cylinder in dense RS soil in a smaller bin than that used for the tests of Figure 2-33. It can be seen that the value of ϕ obtained from the slope term in the bearing capacity equation is higher than that obtained in the larger bin. Note that

*Note that, even though soil No. 1 is very loose and would appear to require the use of the bearing capacity factors relating to local shear failure, the values of ϕ obtained using these local shear values are unrealistically high (i.e., ϕ = 51° for the slope requirement, and ϕ = 51° for the intercept value).

**It should be pointed out, however, that one series of direct shear tests on dense RS soil ($D_r \approx 1.0$) yielded a value of ϕ = 52.6°. The value of ϕ = 49.5° used above represents the average of several direct shear tests on dense RS soil. It has also been previously pointed out that the direct shear tests may provide low values of ϕ for the cinder soils (i.e., the RS, PS, RC2, and RSM soils) if crushing of particles occurs at higher normal stresses which are appreciably higher than those actually present on a failure plane during a bearing capacity failure.

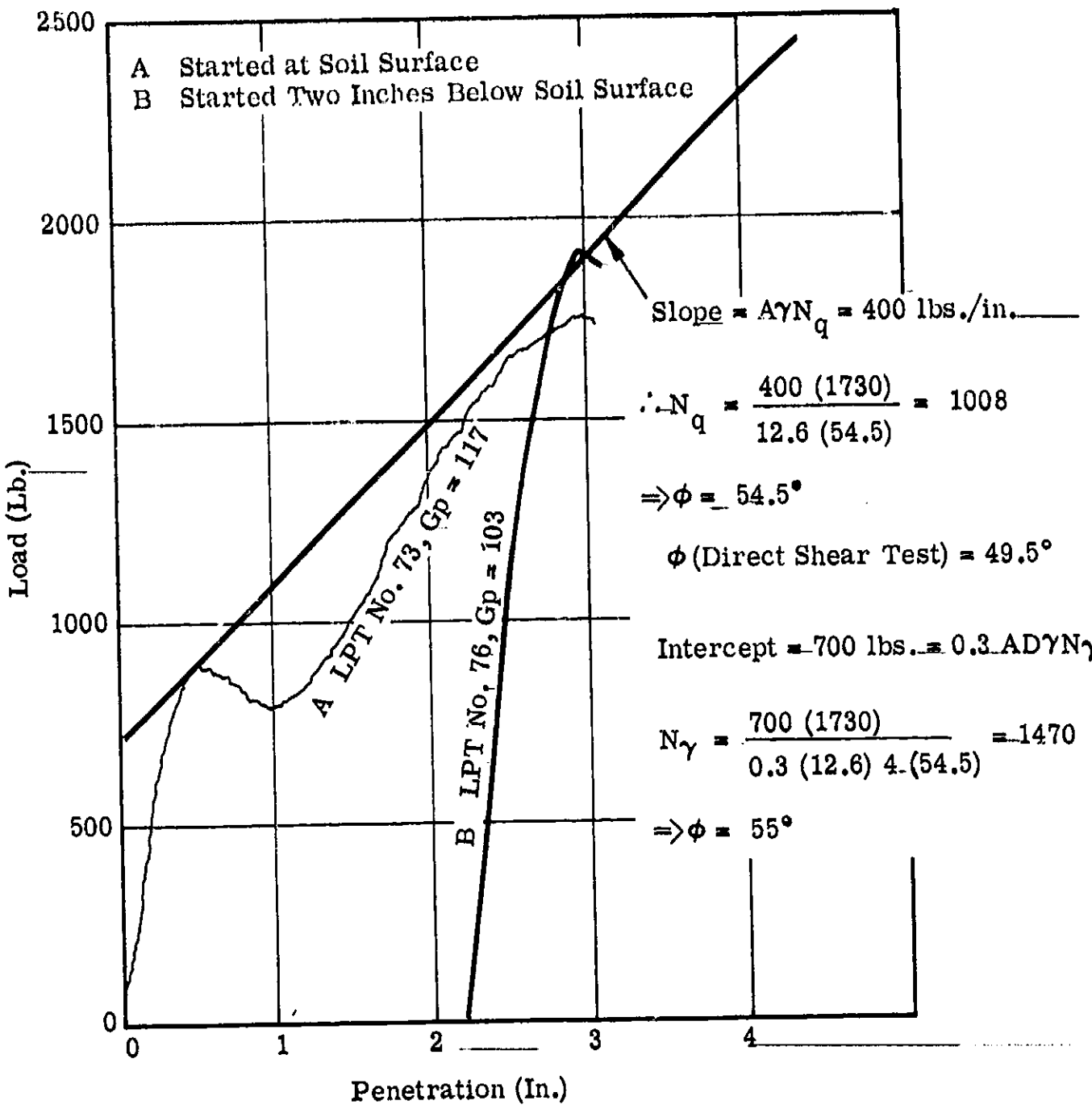

Figure 2-35. Load-Penetration Curves for Four-Inch Cylinder in RS Dense ($D_r \approx 0.97$); Bin Size : 18 Inches by 36 Inches

although the value of ϕ is only increased by 1.5° in the smaller bin, the corresponding value of N_q obtained is about 50% larger than that obtained in the larger bin.

The scope of this program did not permit an intensive investigation of the bearing capacity equation. However, the results described above indicate that the bearing capacity equation and direct shear test values of ϕ do compare approximately to the LPT results. Where the discrepancy is fairly large, such as in the results obtained for the LPT in dense RS soil, it is uncertain whether this discrepancy is due to the lack of applicability of the bearing capacity equation or error in the determination of ϕ in the direct shear tests. As has been pointed out previously, even small differences in the value of ϕ can have a pronounced effect on the values yielded by the bearing capacity equation, especially for values of ϕ greater than 50°.

It is believed that the poor success of the bearing capacity equation using the bearing capacity factors for local shear to provide realistic values of ϕ (e.g., the analysis for local shear of the LPT in Figure 2-32) is due to the fact that in loose soils excessive settlement takes place before failure is reached. Thus, the bearing capacity factors for local shear are probably intended to yield allowable bearing values to limit excessive settlements prior to bearing capacity failure.

If the bearing capacity equation (Equation 3-1) is divided through by the quantity $D\gamma$ and the cohesion term dropped, the result is:

$$\frac{q}{D\gamma} = N_q \frac{D_f}{D} + 0.3\, N_\gamma \qquad (3\text{-}3)$$

where the symbols used are as previously described for Equation 3-1.

This form of the bearing capacity equation indicates that for any size of footing or test cylinder in a given soil a plot of the dimensionless pressure parameter, $q/D\gamma$ versus relative depth D_f/D, will fall on the same line regardless of the size of the footing.

Figures 2-36, 2-38, and 2-39 show the results of load-penetration tests in the RS, PS, and SS soil using 2-inch and 4-inch diameter test cylinders. The results are generally averaged from several tests done in 18" x 36" bin and are plotted as the dimensionless pressure parameter versus relative depth. Figure 2-37 is a plot of several tests done in RS soil in several sizes of bin with 1-inch, 2-inch, and 4-inch test cylinders.

Figures 2-36 and 2-37 indicate that the size effect predicted by the bearing capacity equation (i.e., that a plot of the pressure parameter $q/D\gamma$, versus relative depth, D_f/D will plot as the same line for any size footing in a given soil) does tend to be confirmed in the loose and intermediate RS soil (i.e., with $0.0 \leq D_r \leq 0.7$). There is not sufficient data to determine whether the tendency for results for the large test cylinder to plot above those for the smaller cylinder is a characteristic due to size effect or due to the slight differences noted in relative density determinations.

It is possible that the pronounced dip observed in the curve obtained for the smaller cylinder below that for the larger cylinder in Figure 2-36 for the intermediate soil (i.e., $D_r \approx 0.46$) is a result of the method used to produce an intermediate soil (in this instance, screeding). When intermediate density was produced by a roller, as for the bottom pair of curves on Figure 2-37, this pronounced dip is not observed.

In the tests performed in dense RS soil (in Figures 2-36 and 2-37, those tests for which $D_r \leq 0.83$), the 2-inch cylinder tests generally exhibit significantly higher values of the pressure parameter for a given relative depth than the 4-inch cylinder tests. A similar but much more pronounced, tendency is exhibited by the test with the 1-inch cylinder (Figure 2-37) in the RS soil with a relative density of 0.69. In this soil, however, the curve for the 2-inch cylinder falls below that of the 4-inch cylinder. It appears that the size effect implied in the bearing capacity equation does not hold for small diameter cylinders penetrating a dense soil. The differences increase with increasing relative density and decreasing size of cylinder.

Figures 2-38 and 2-39 representing plots of the pressure parameter versus relative depth for the SS and PS soils, respectively, indicate conclusions similar to those given for the RS soil.

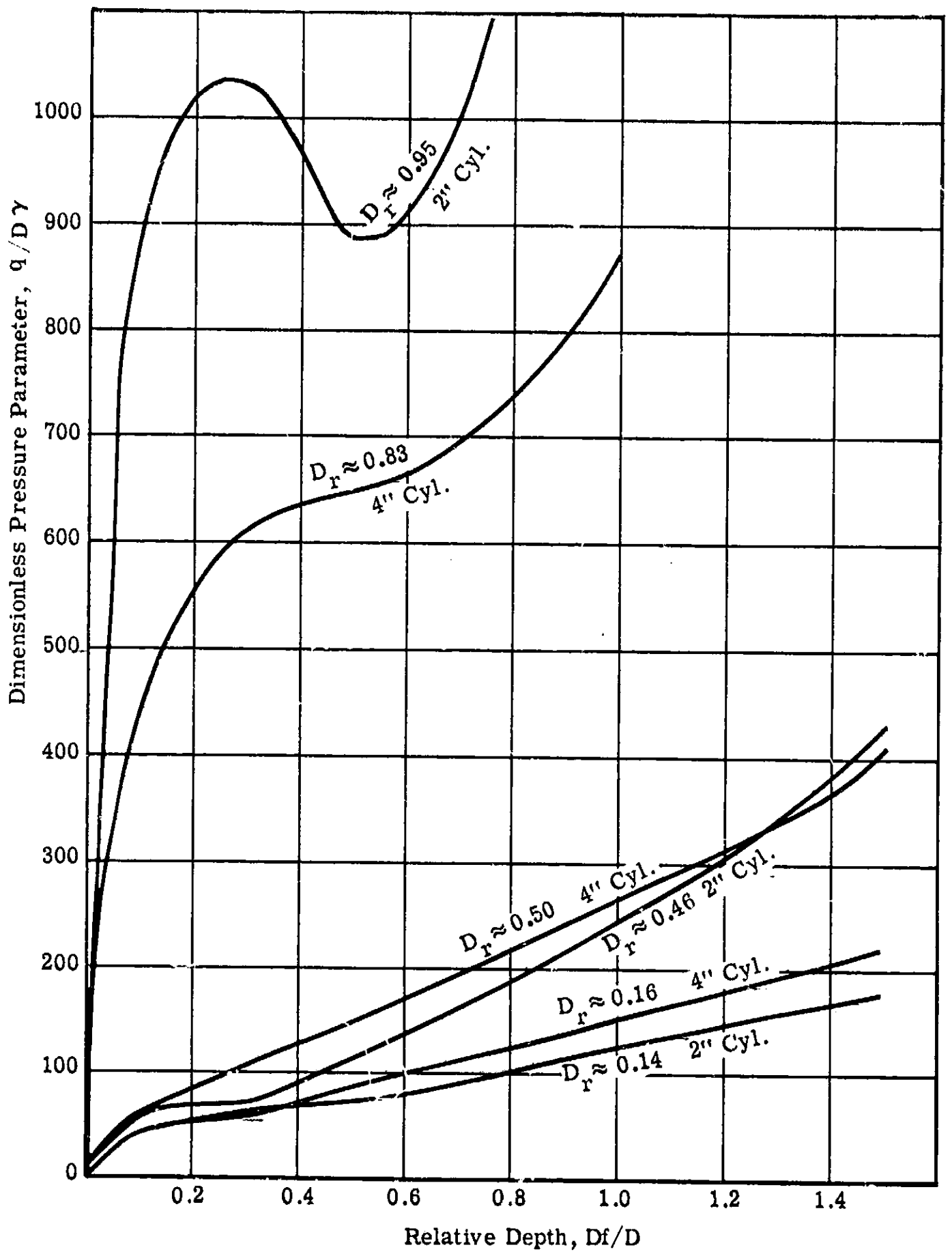

Figure 2-36. Load-Penetration Test Results in RS Soil
Pressure Parameter vs. Relative Depth

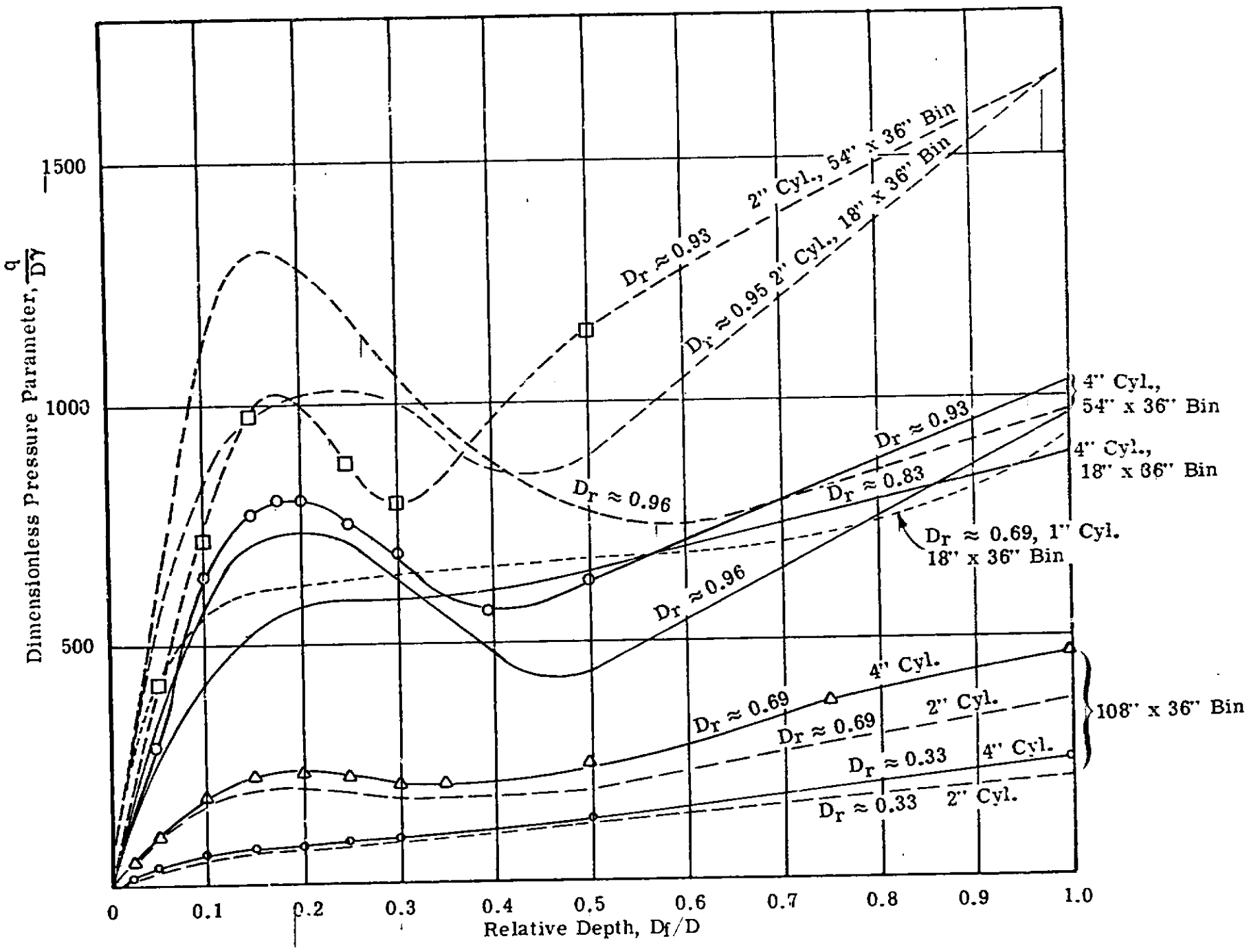

Figure 2-37. Pressure Parameter vs. Relative Depth in Intermediate and Dense RS Soil

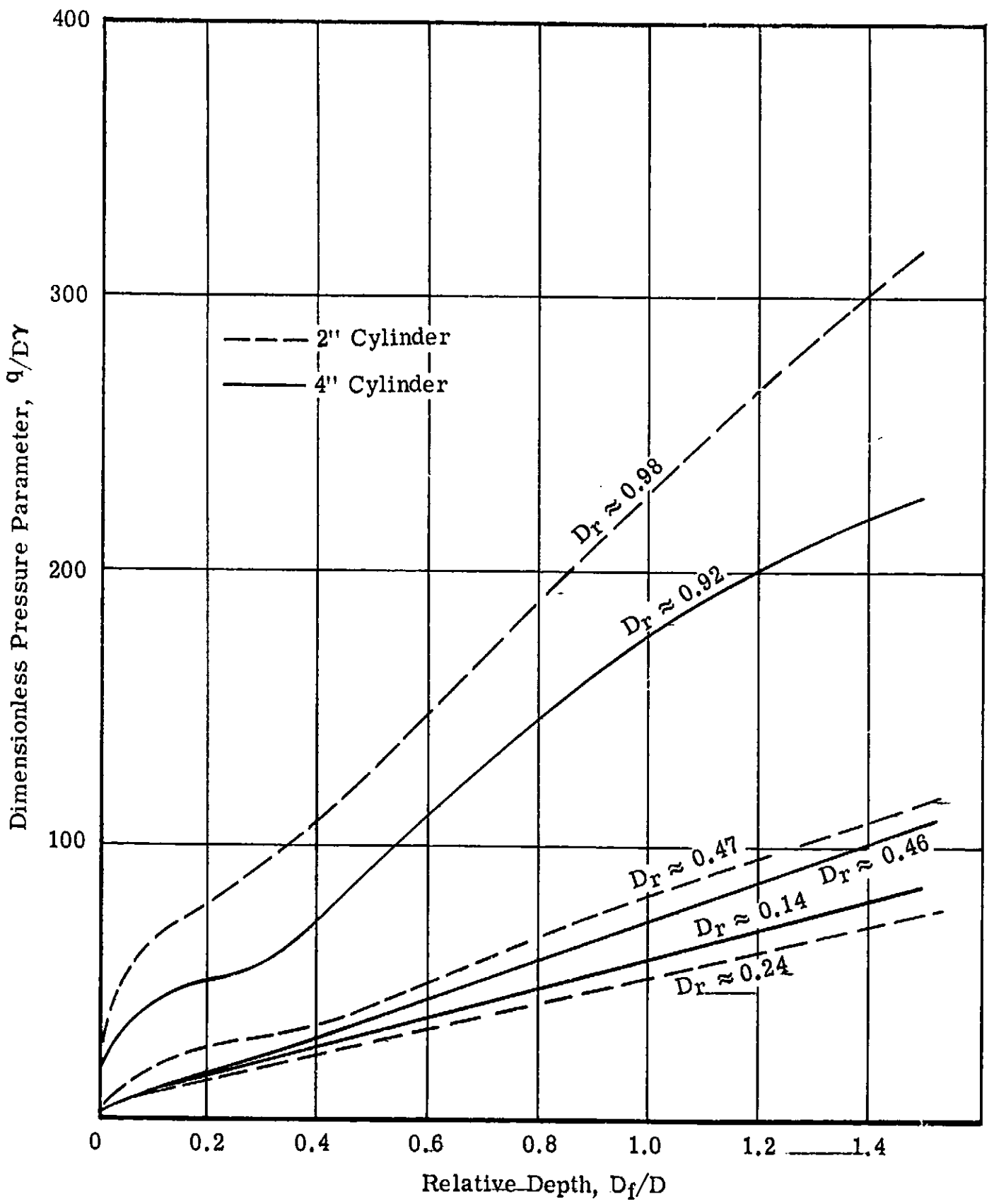

Figure 2-38. Load - Penetration Test Results in SS Soil
Pressure Parameter vs. Relative Depth

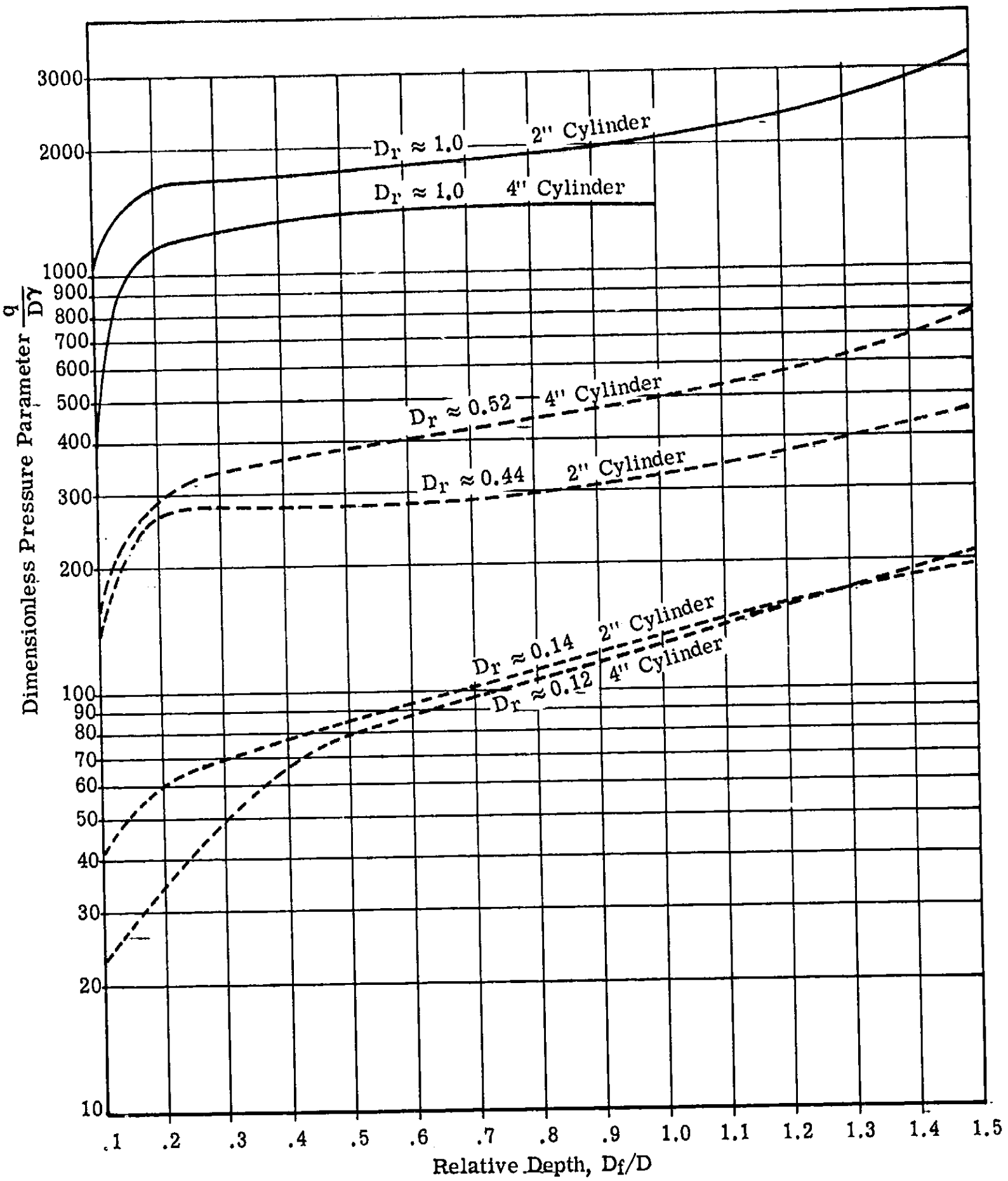

Figure 2-39. Load-Penetration Test Results in PS Soil Pressure Parameter vs. Relative Depth

Figures 2-40 through 2-43 show the results of LPT performed to investigate the effect of rate of penetration on the magnitude and shape of the LPT curve.

Figure 2-40 shows LPT performed in the 36" x 18" bin with a 4-inch cylinder in loose RS soil ($D_r \approx 0.15$). Penetration rates vary from 1 inch per minute to 4 inches per minute, and an attempt was made to perform a "static" load test (i.e., load applied in increments and each increment added after no further penetration is produced by the previous increment) to provide a comparison of the magnitude and shape of a static load penetration curve with one produced by advancing the cylinder into the soil continously at some specified rate of penetration. Curve A represents the static load-penetration curve, and the remaining curves are those obtained for the rates of penetration noted on the figure. These curves indicate that the continous rate of penetration tests give quite good approximations of the static test, and that the LPT curves are relatively insensitive to rate of penetration up to the rate of 4 inches per minute which was the highest rate used.

Figures 2-41, 2-42, and 2-43, show similar results in RS soils of different relative density and using a different size of cylinder.

Figure 2-44 summarizes the results of a brief investigation into the effects of bin size (Boundary Effects) on the shape of LPT curve 5. The tests shown were run in three different sizes of bin, as noted, in dense RS soil having an average relative density of about 0.96. Although the relative density of each soil bed is about the same, the dynamic penetrometer readings (G_p) have been given to indicate possible variation between them. These curves indicate that there is a tendency for the tests in the larger bins to have higher values of load at failure (i.e., the magnitude of the peak in the curve) and lower slopes in the approximate straight line portion after failure. As pointed out previously in the discussion of the bearing capacity equation, tests in the smallest bin tend to give higher apparent values of equivalent angles of internal friction than tests run in the same soil with the same test cylinder in a larger bin. If this tendency is valid it would explain at least in part, why the smaller cylinders tend to give higher values for the dense soils (e.g., Figures 2-36 through 2-39), since a bin of a given size would be larger, relative to the size of the cylinder, for the smaller cylinders than for the large cylinders.

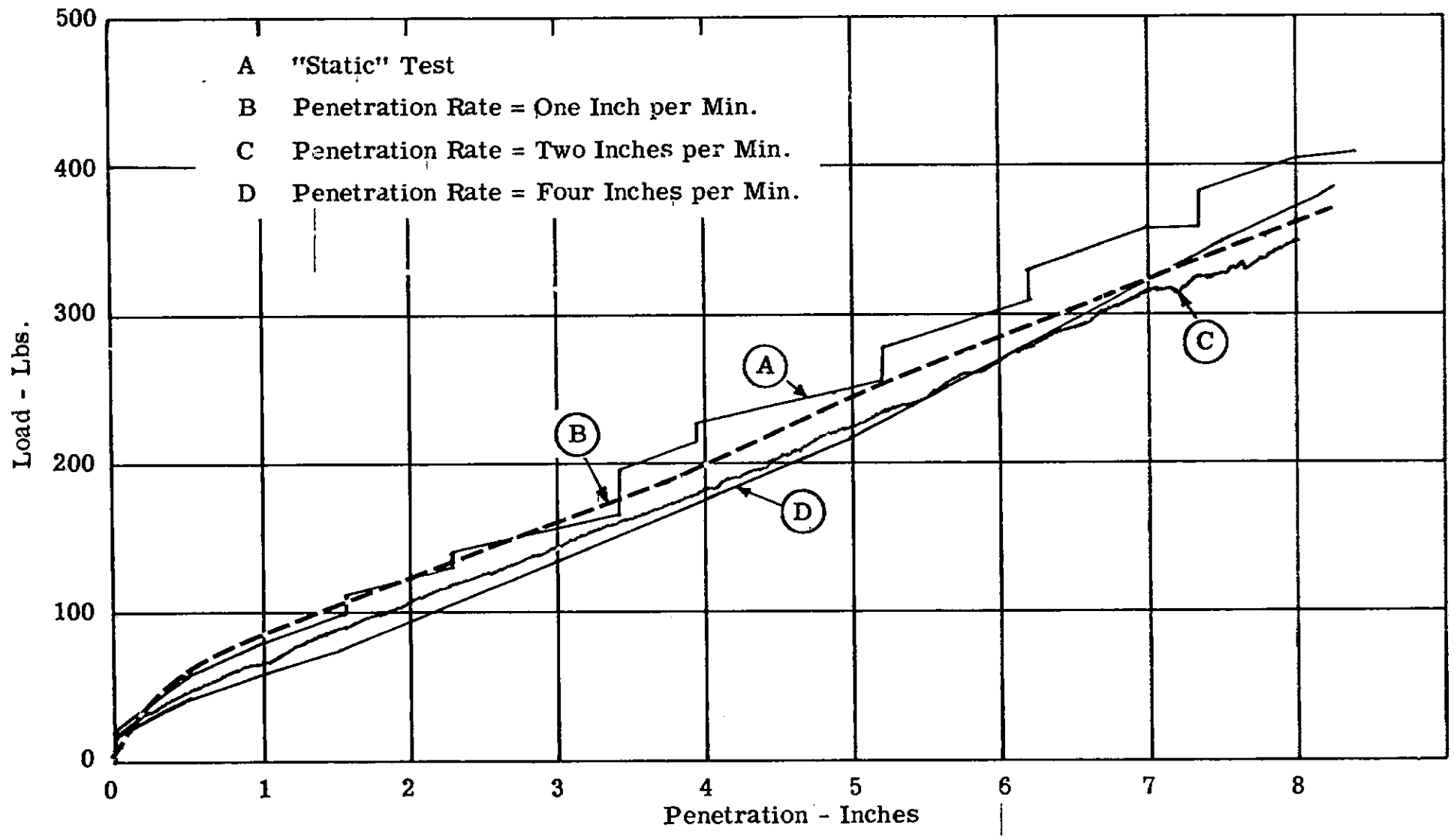

Figure 2-40. Load-Penetration Curves for Four-Inch Cylinder in RS Loose at Different Rates of Penetration

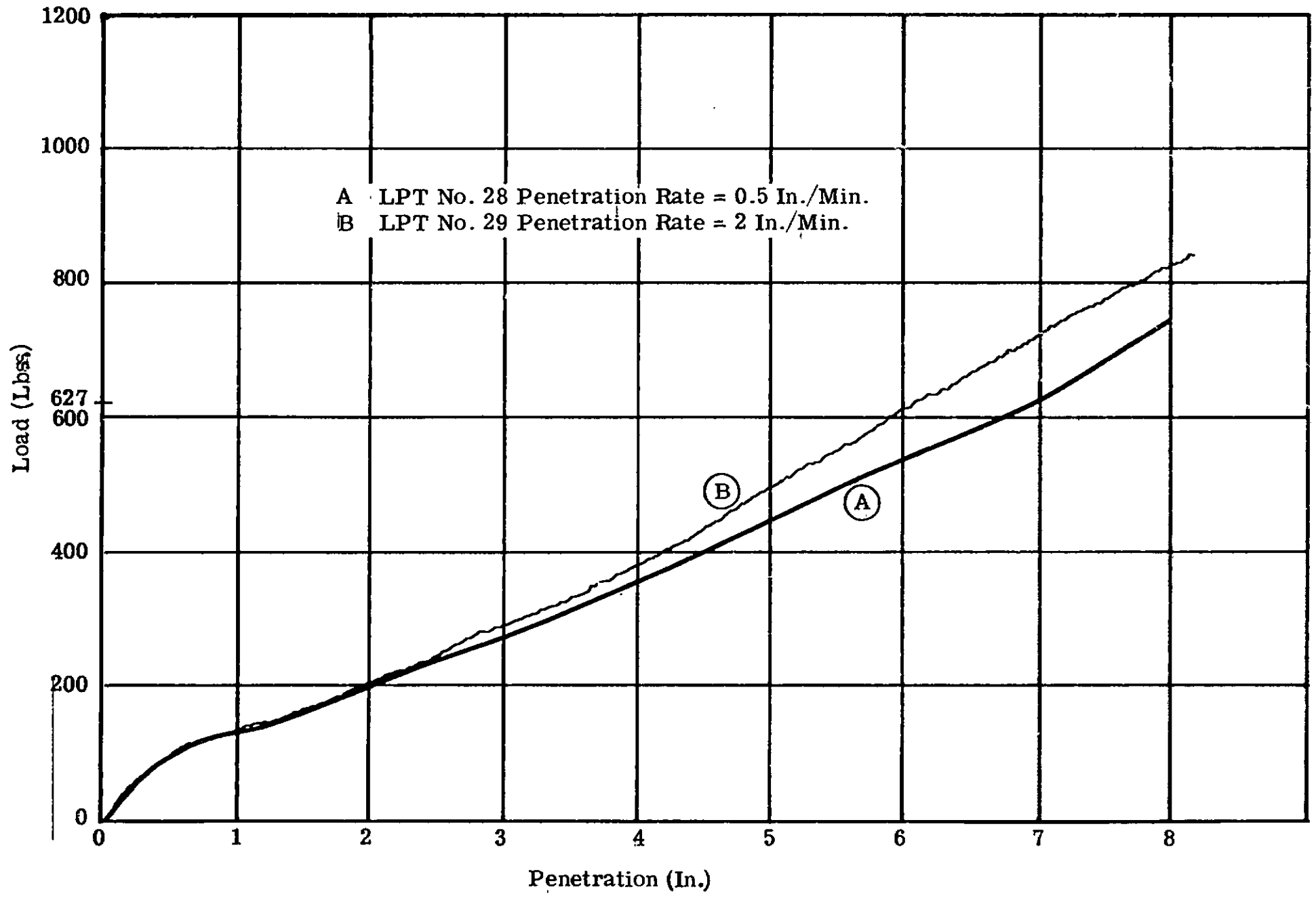

Figure 2-41. Load-Penetration Curves for Four-Inch Cylinder in RS Intermediate at Different Rates of Penetration

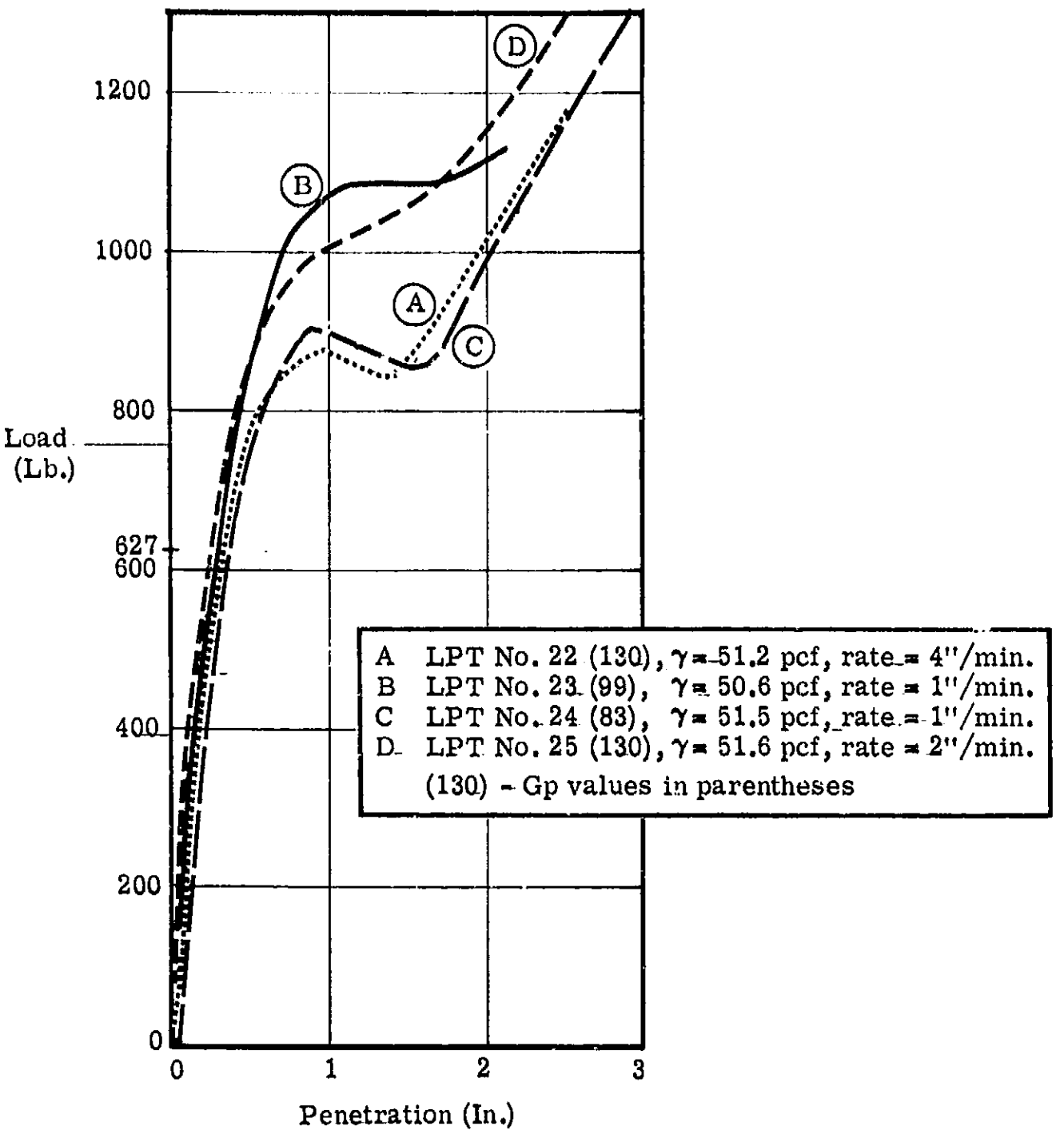

Figure 2-42. Load-Penetration Curves for Four-Inch Cylinder in RS Dense at Different Rates of Penetration

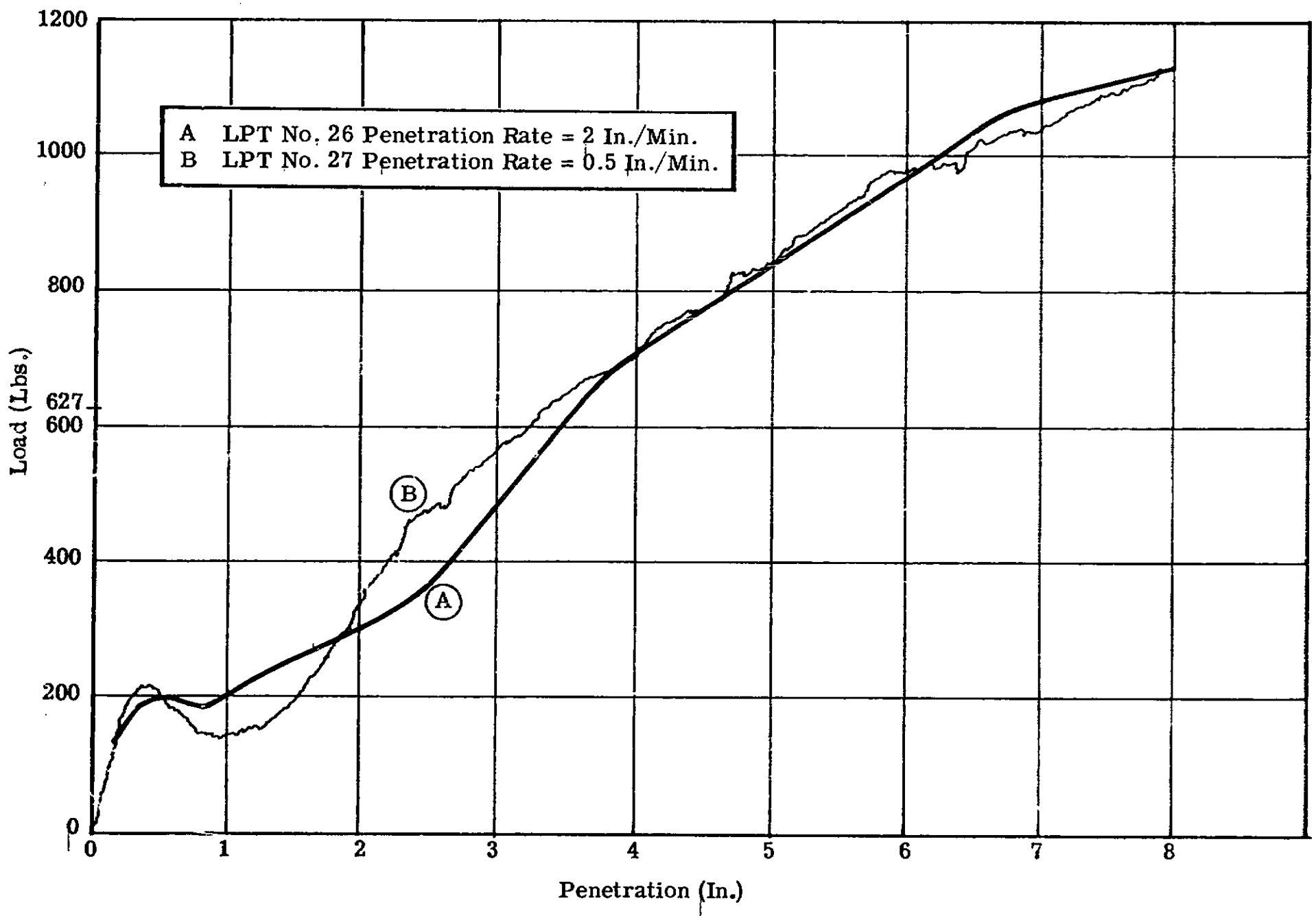

Figure 2-43. Load-Penetration Curves for Two-Inch Cylinder in RS Intermediate at Different Rates of Penetration

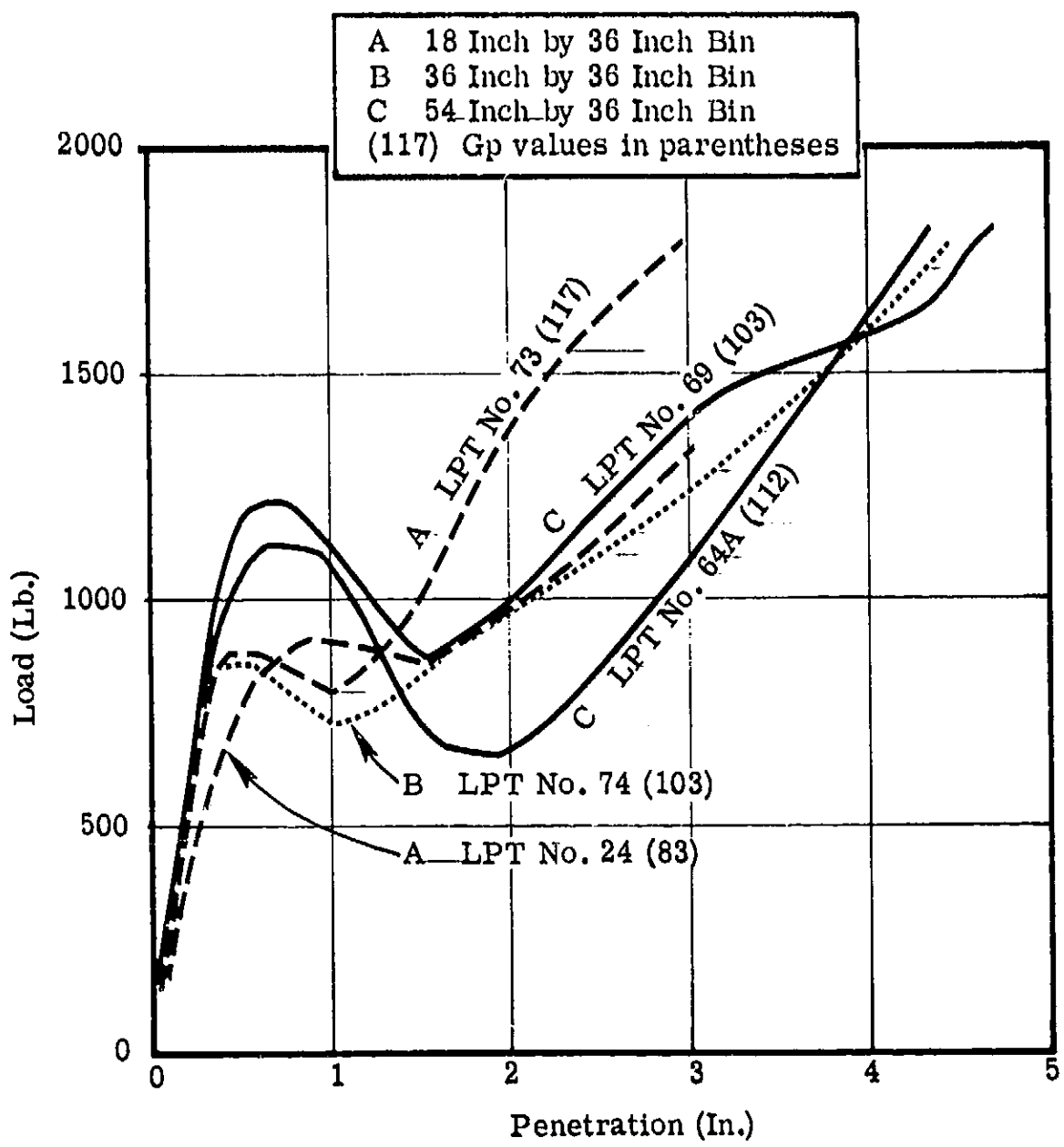

Figure 2-44. Load-Penetration Curves for Four-Inch Cylinder in RS Dense Soil in Bins of Various Sizes

The effect of footpad shape versus flat cylinder was studied and Figures 2-45 through 2-48 were prepared to show the results of LPT performed in four of the test soils (Nos. 1, 3, 4, and 9) using the 4-inch cylinder and 4-inch subscale footpad. It will be observed that the LPT curve for the footpad generally lies appreciably below the LPT curve for the cylinder. Part or all of this difference can be explained by the following:

a. At any given depth the average force on the bottom of the footpad will tend to be less than that on the bottom of the cylinder since the outer portion of the footpad is at a lesser depth and, hence, has a lower pressure exerted against it than the inner portion at the central lowermost part of the footpad.

b. With increasing penetration, the sides of the cylinder would tend to provide some resistance due to friction forces between the soil and the sides of the cylinder. Since there are no vertical sides on the footpad, there should be no side friction added. This effect would tend to make the LPT curve for the cylinder rise at a faster rate than that for the footpad.

c. Since there is open space above the footpad, when it is penetrating part of the soil would tend to fall in above the top of the footpad thus decreasing the amount of soil resisting soil failure and the force necessary to cause failure.

Figures 2-49 and 2-50 show plots of LPT results using 4-inch and 6-inch subscale footpads in the RS and SS soils (soils Nos. 1, 3, and 4; and soils Nos. 7, 8, and 9 respectively). Also shown are LPT results for a 4-inch cylinder in soils Nos. 1, 3, 4, and 9.

The analysis of the subscale drag test results has yielded an expression for the forces on a footpad as a function of mass, velocity and soil properties. One of the terms of this expression is called the "mechanical strength coefficient" of the soil, a term related to soil strength. Figure 2-51 shows a plot of the pressure parameter, $q/D\gamma$, derived from LPT performed using a 4-inch cylinder, 4-inch footpad and 6-inch footpad, versus the mechanical strength coefficient, C_{ms}, derived from the analysis of the subscale drag tests.

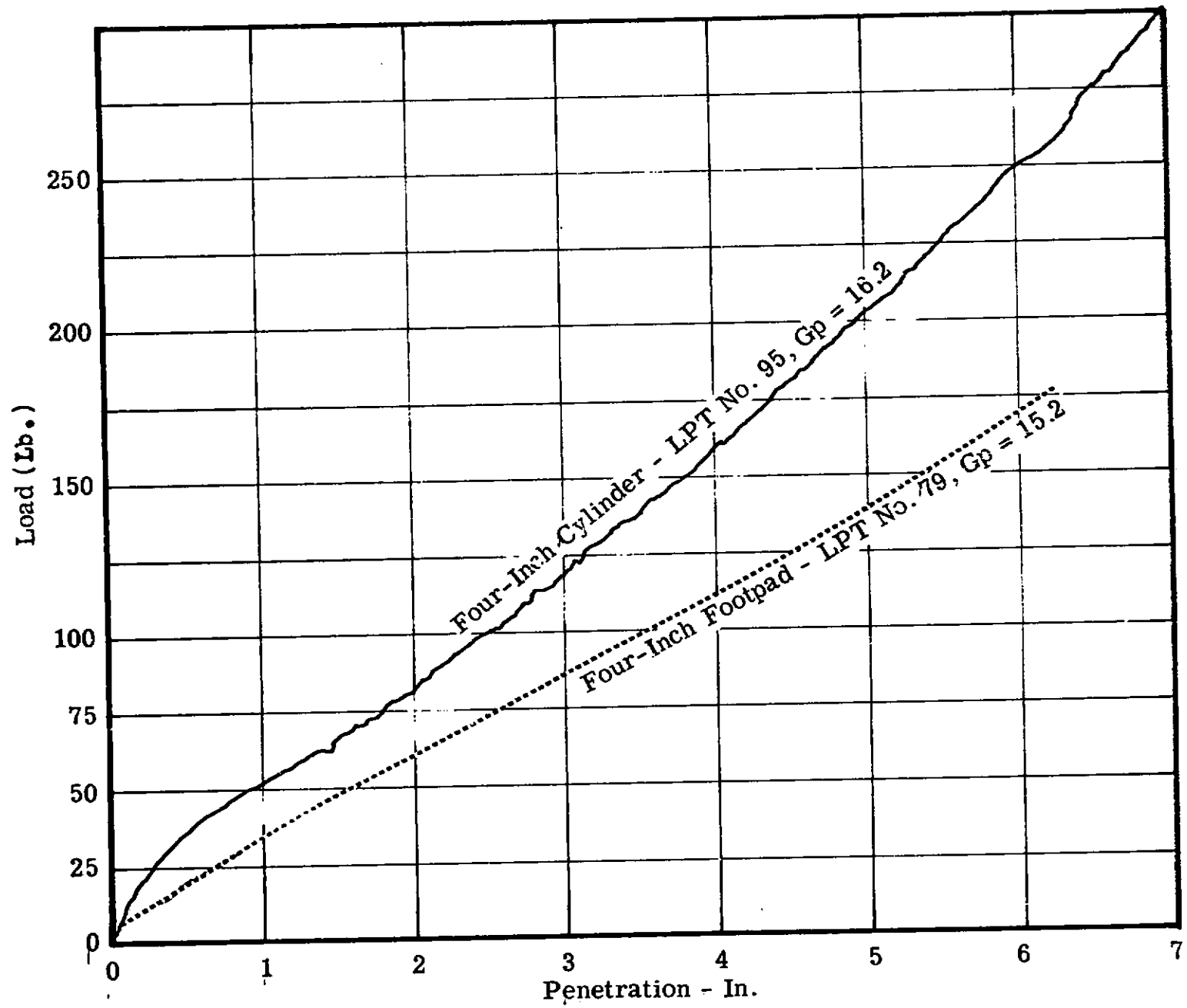

Figure 2-45. Load-Penetration Curves in Soil No. 1 (RS Loose) ($D_r \approx 0.0$)

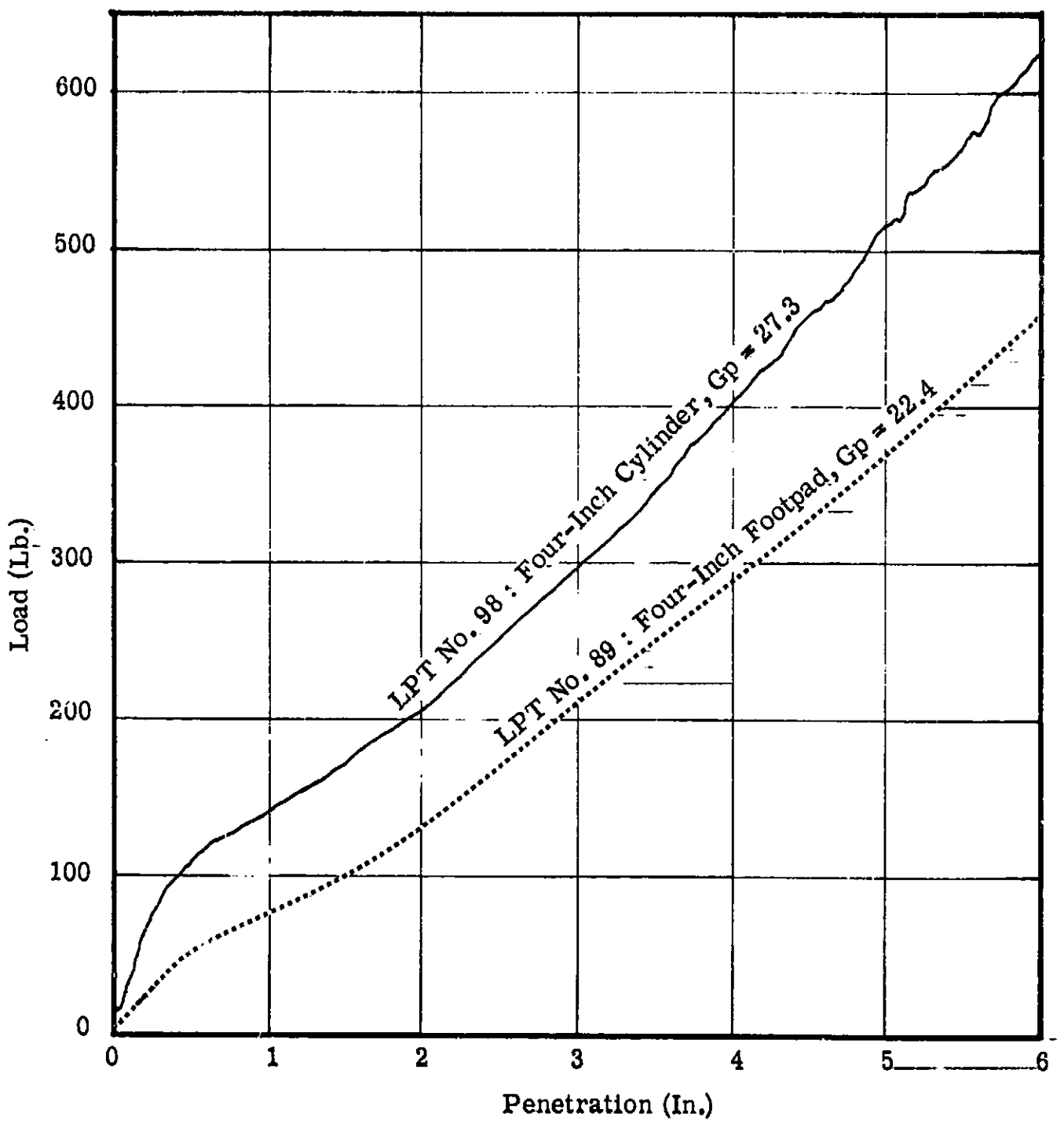

Figure 2-46. Load-Penetration Curves in Soil No. 3 (RS Intermediate) ($D_r \approx 0.29$)

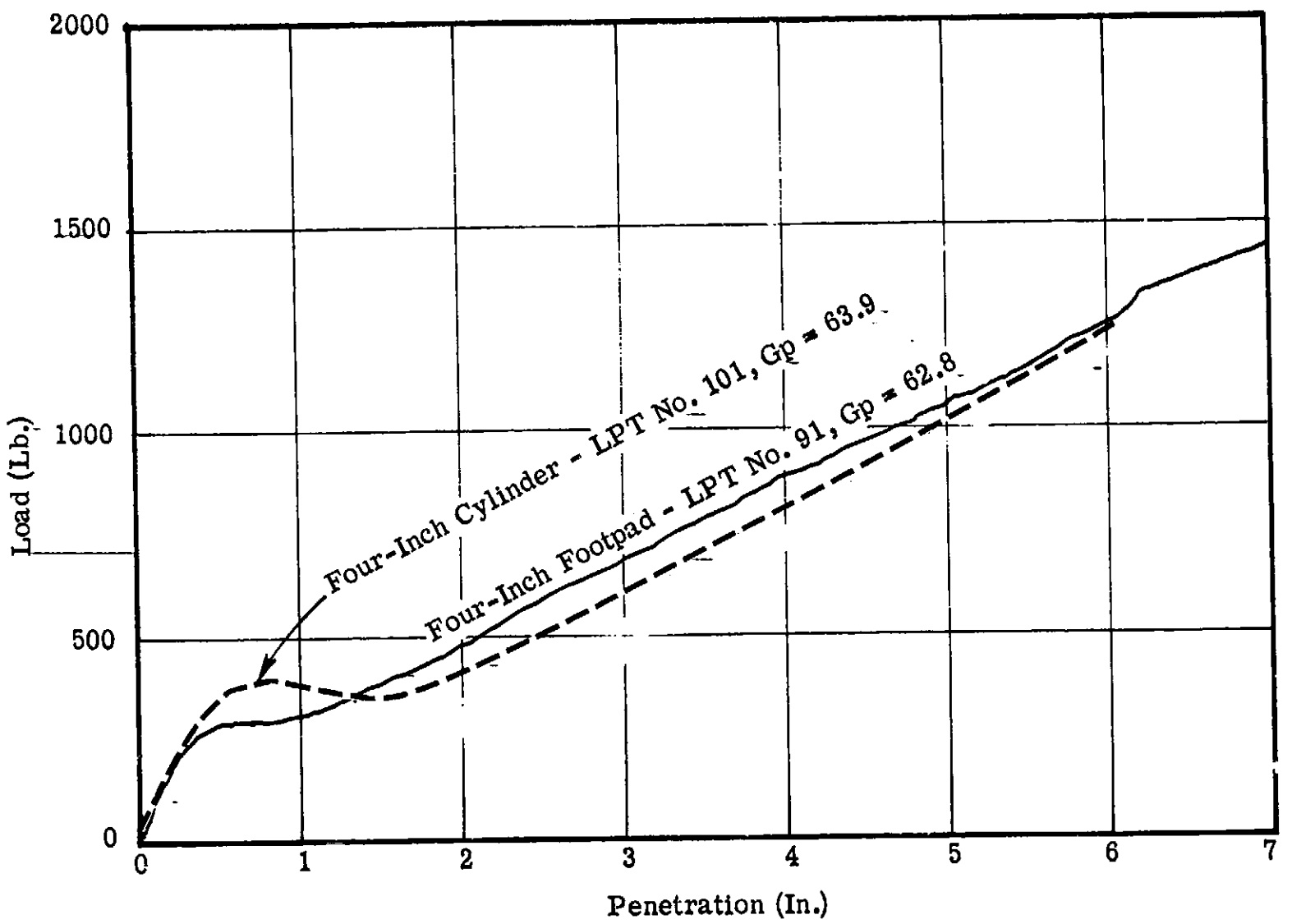

Figure 2-41. Load-Penetration Curves in Soil No. 4 (RS Dense) ($D_r \approx 0.69$)

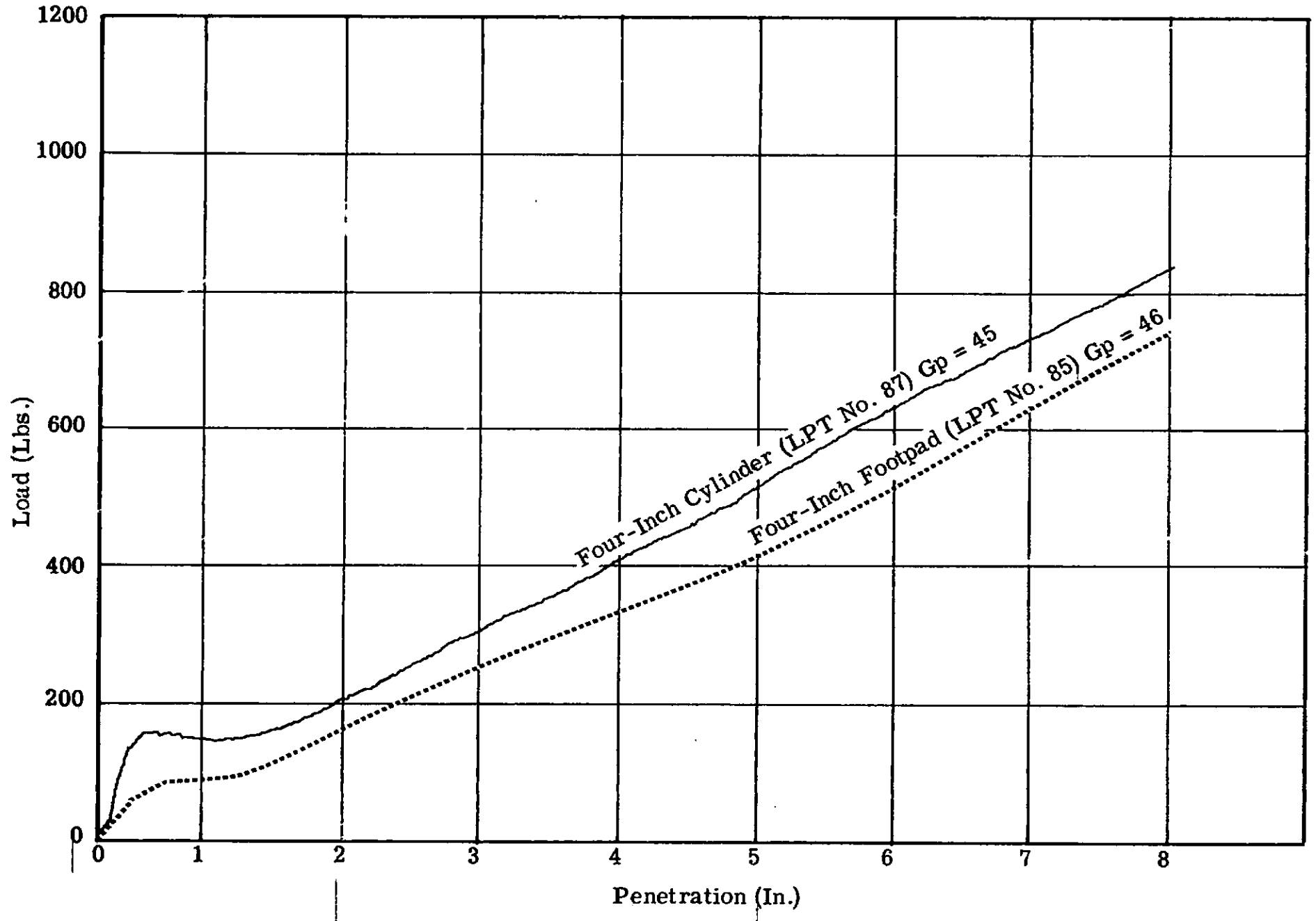

Figure 2-48. Load-Penetration Curves for Four-Inch Cylinder and Four-Inch Footpad in Soil No. 9 (SS Dense) ($D_r \approx 0.76$)

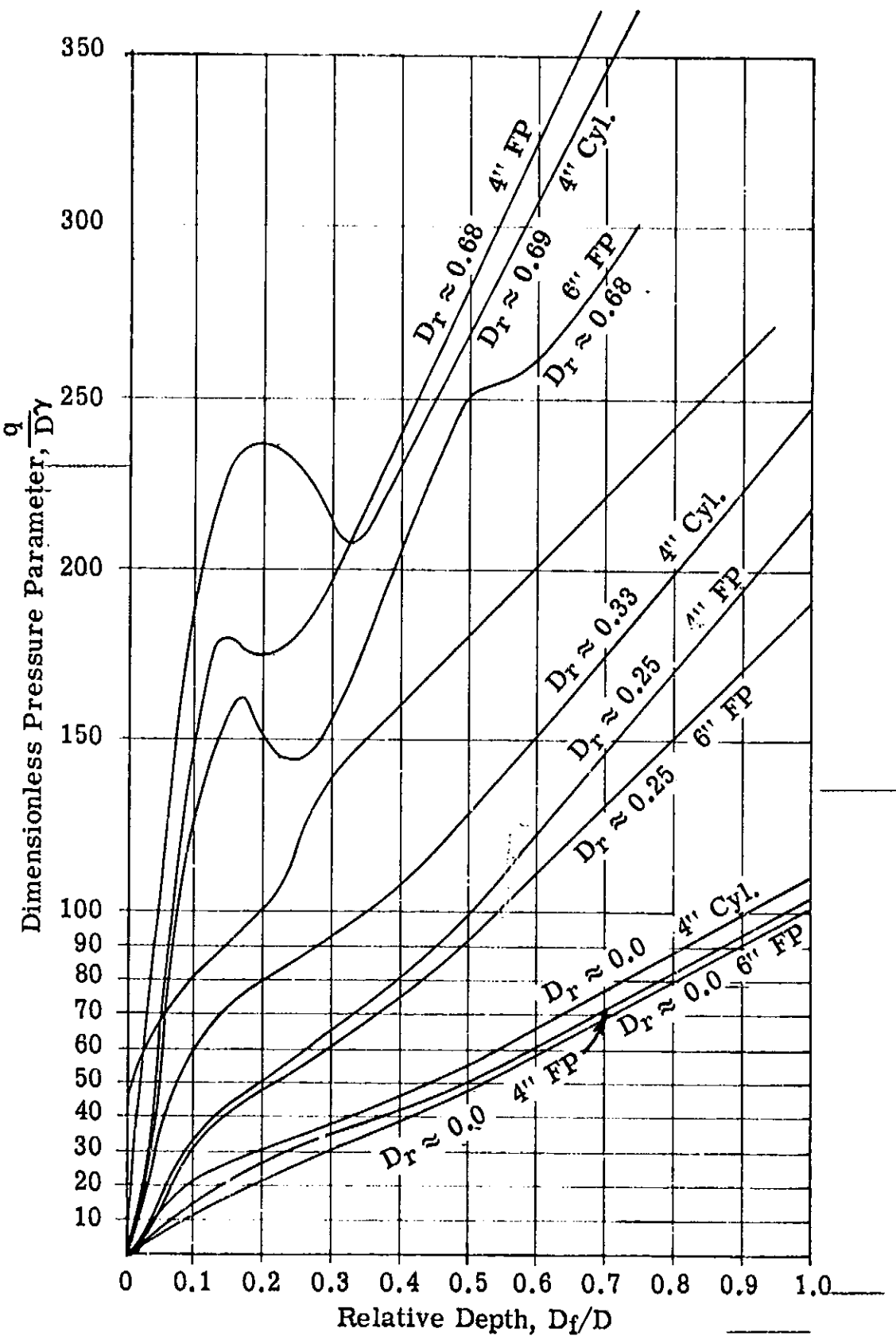

Figure 2-49. Comparison of Footpad and Cylinder Load-Penetration Tests Pressure Parameter vs. Relative Depth in RS Soil

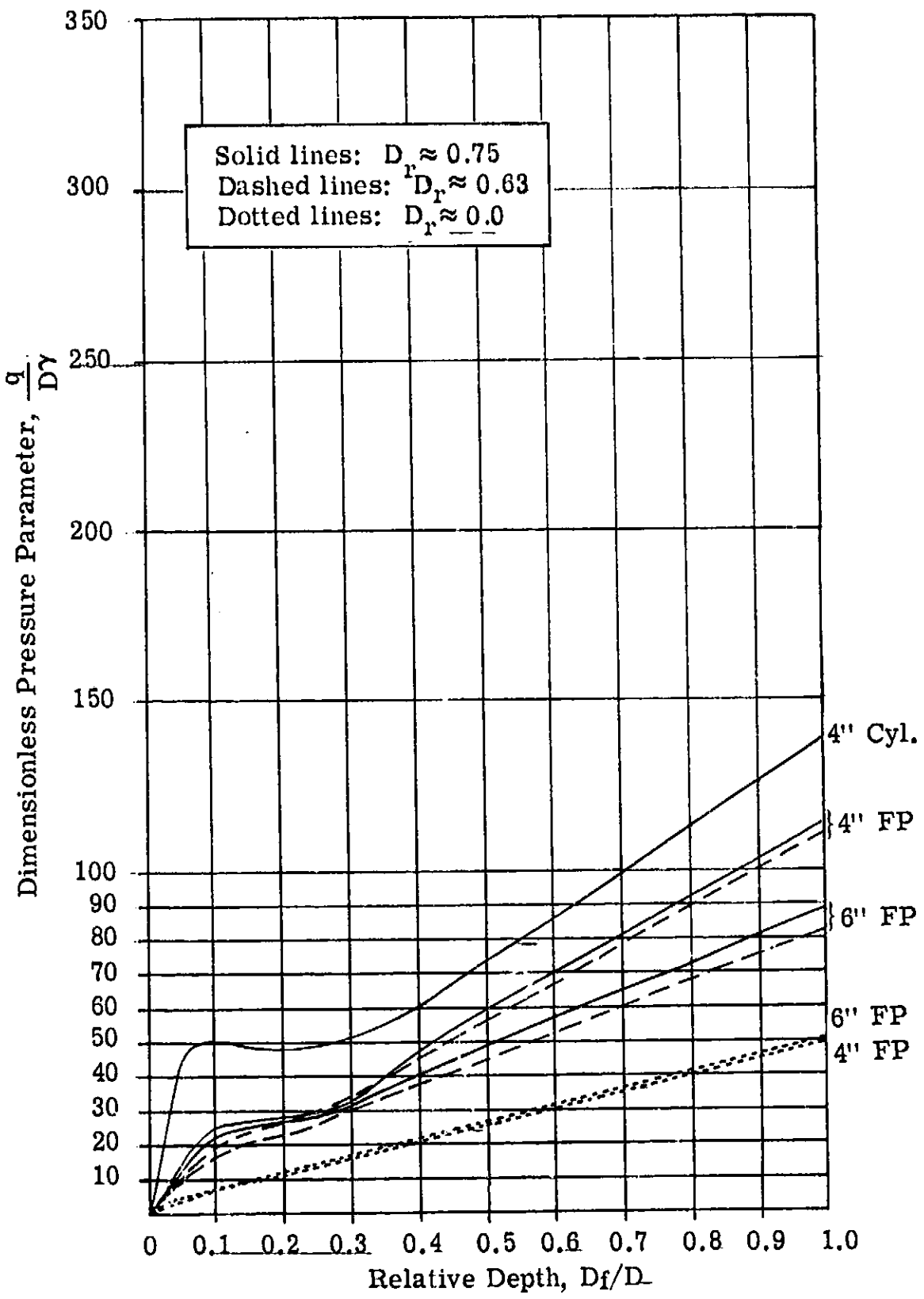

Figure 2-50. Load-Penetration Test Results Using Footpad in SS Soil Pressure Parameter vs. Relative Depth

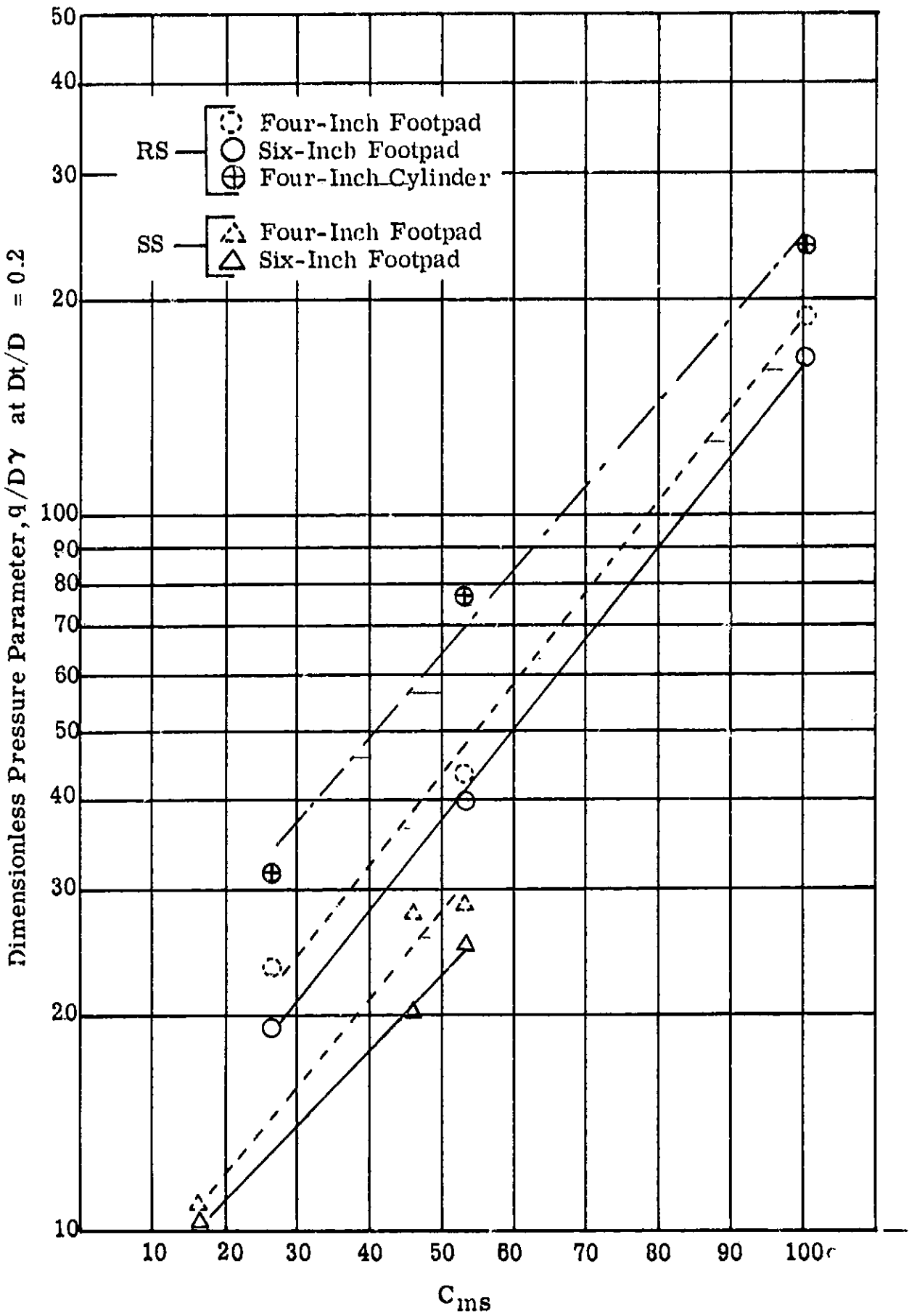

Figure 2-51. Mechanical Strength Coefficient from Subscale Drag Test Analysis, C_{ms}

Figure 2-52 shows a plot of the pressure parameter, $q/D\gamma$, at a relative depth of 0.2 versus the peak magnitude of deceleration measured in the dynamic penetrometer test, G_p.

2.7 SOIL BED CONTROL TESTS

Five types of tests were used to measure and control the soil properties of the test beds used for the drag, impact and model drop tests:

Dynamic Penetrometer Test,

Static Penetrometer Test,

Grain Size Analysis,

Minimum-Maximum Density Test,

In-Place Density Measurement.

In addition, a limited number of load-penetration tests (LPT) were performed in some of the test soils using different sizes of cylinder and subscale footpads as penetrating devices. The performance and results of these tests have already been described in Section 2.6.

2.7.1 Dynamic Penetrometer Test

The Dynamic Penetrometer Test (DPT) is used primarily as an index of the relative density and uniformity of a soil bed. It has been found that the peak deceleration experienced by a body of fixed mass falling freely from a fixed height can be correlated with the relative density of a given soil type. The correlation studies were run in soil beds whose relative density was determined by direct weight-volume measurements. Correlation curves were plotted of the peak magnitude of deceleration observed versus the measured relative density. These correlation curves were then used to determine the relative density of the soil beds by means of the DPT in these soil beds where the relative density could not be measured directly.

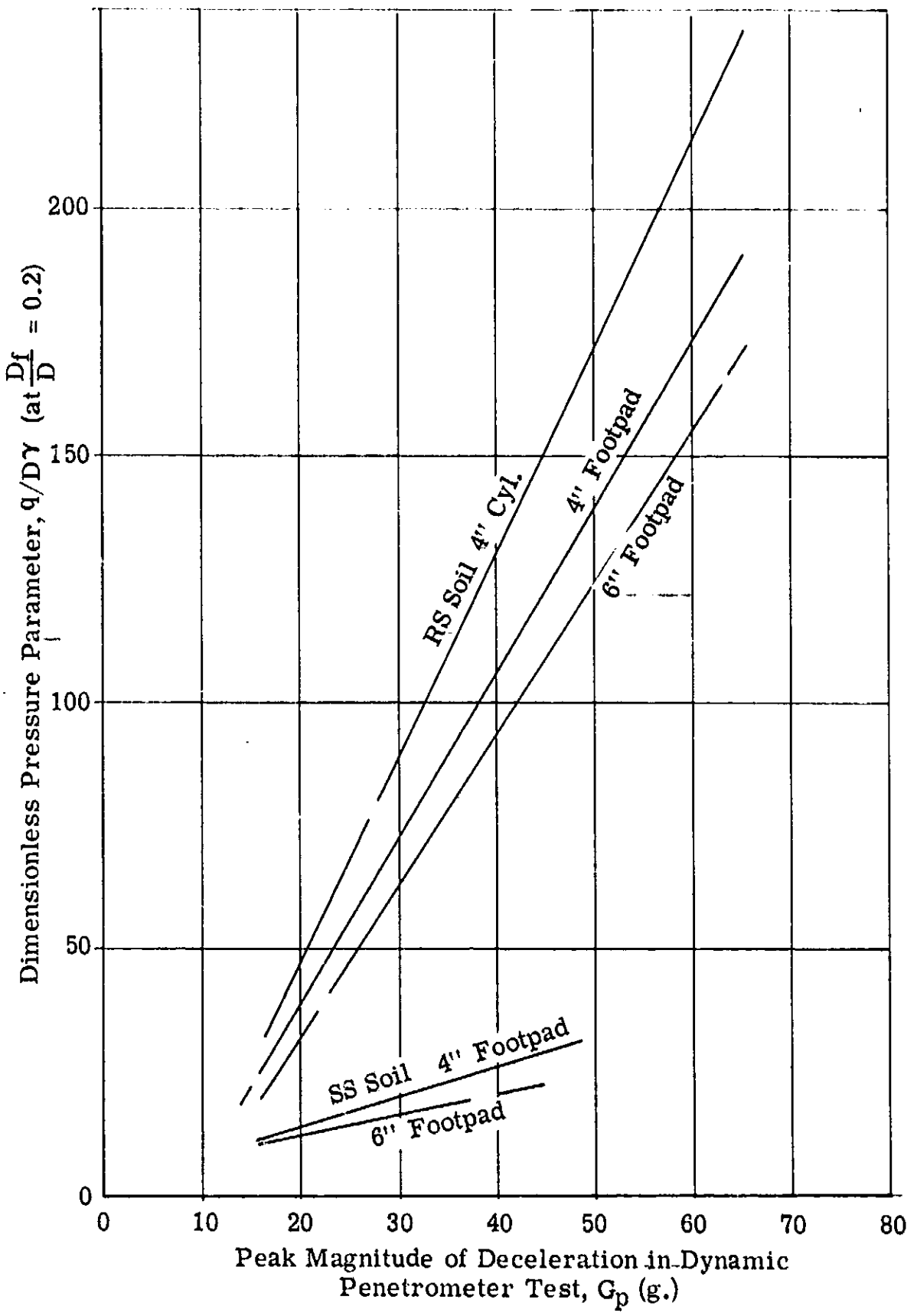

Figure 2-52. Pressure Parameter at a Relative Depth of 0.2 vs. Dynamic Penetrometer Test Results

Figure 2-53 shows a photograph and schematic drawing of the dynamic penetrometer used in this study. It was designed and fabricated by Bendix. The body consists of a solid piece of aluminum 2-3/4 inches in diameter with a full radius nose. The top is recessed to hold a CEC direct current strain gage accelerometer having a range of 100 g. The total weight of the penetrometer is 1.59 lbs.

The test consists of dropping the penetrometer through a fiberglass tube (to maintain vertical alignment of the penetrometer) from a fixed height (25.4 inches). A record of the acceleration-time history of the drop is made on an oscillograph. The results of peak magnitude of deceleration on the acceleration-time signatures are averaged for all penetrometer drops on a particular soil bed, and this value used to determine the average relative density of the soil bed using the correlation curves previously described. An examination of the average results obtained in a number of soil beds prepared using the same placement procedure gives an indication of the uniformity and examination of the range of results in a particular soil bed gives an indication of uniformity of the soil bed.

Figure 2-54 shows typical acceleration-time records (DPT) signatures for RS soil in the loose, intermediate and dense condition. Correlation curves showing peak acceleration (G_p) versus relative density (D_r) for the six basic soil types used in the study are presented in Figure 2-55. These curves were developed from the results of penetrometer drops on soil beds prepared to yield relative densities ranging from near zero to near 100 percent.

A statistical analysis was done on the first 49 tests performed on Soil No. 1 (RS loose) in the subscale drag test bin to obtain a relative measure of the uniformity of the soil beds. Four DPT were run in each of the 49 soil beds. The mean G_p value was computed for each soil bed and then the standard deviation and 95 percent confidence interval for these means. The mean of these values, with no extreme values rejected from the computation, was 11.76 ± 0.14 g's. The small confidence interval associated with the means indicates that the uniformity from soil bed to soil bed is good.

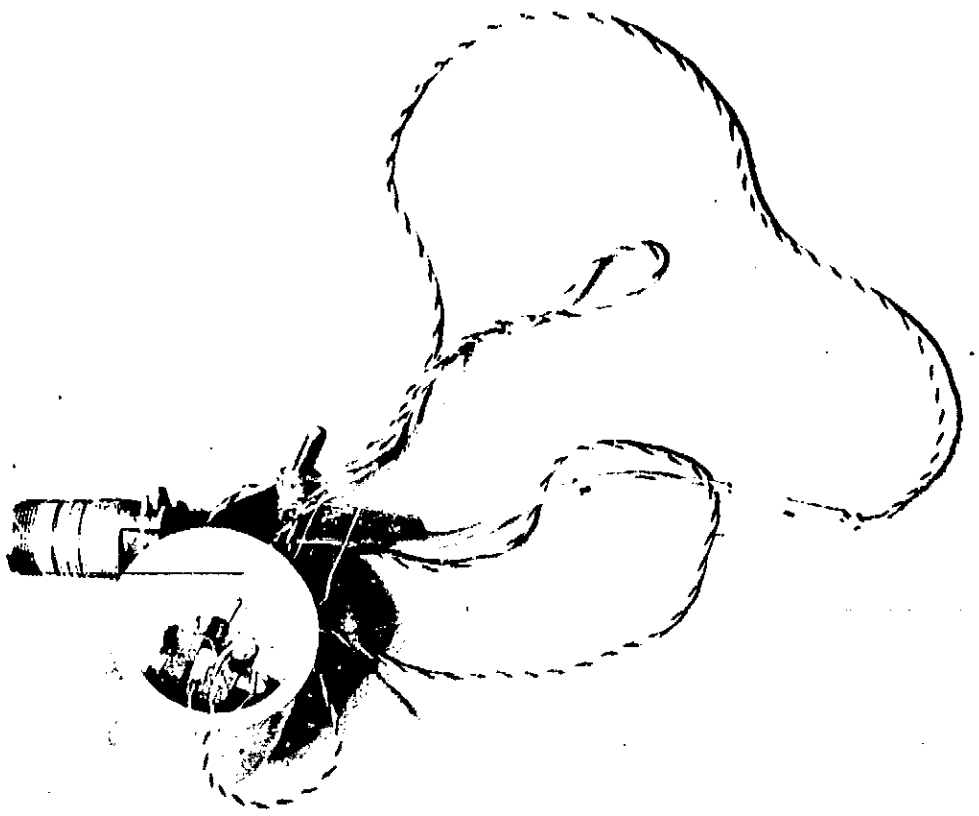

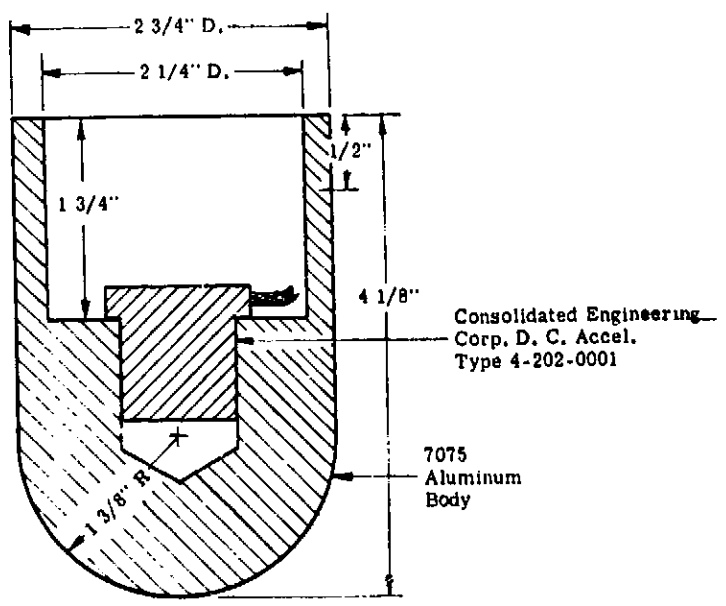

Figure 2-53. Dynamic Penetrometer (DPT) and Schematic

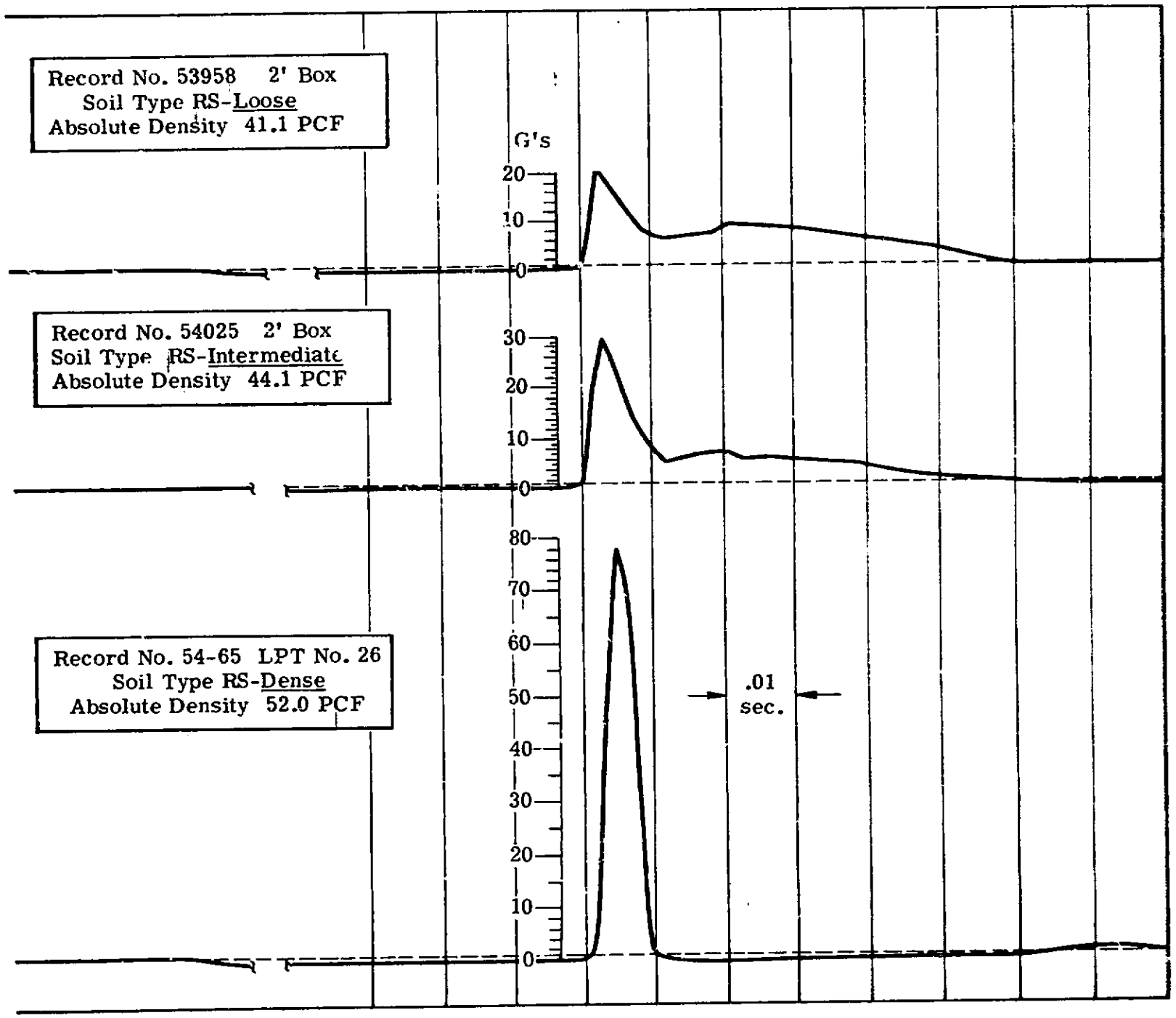

Figure 2-54. Typical DPT Signatures

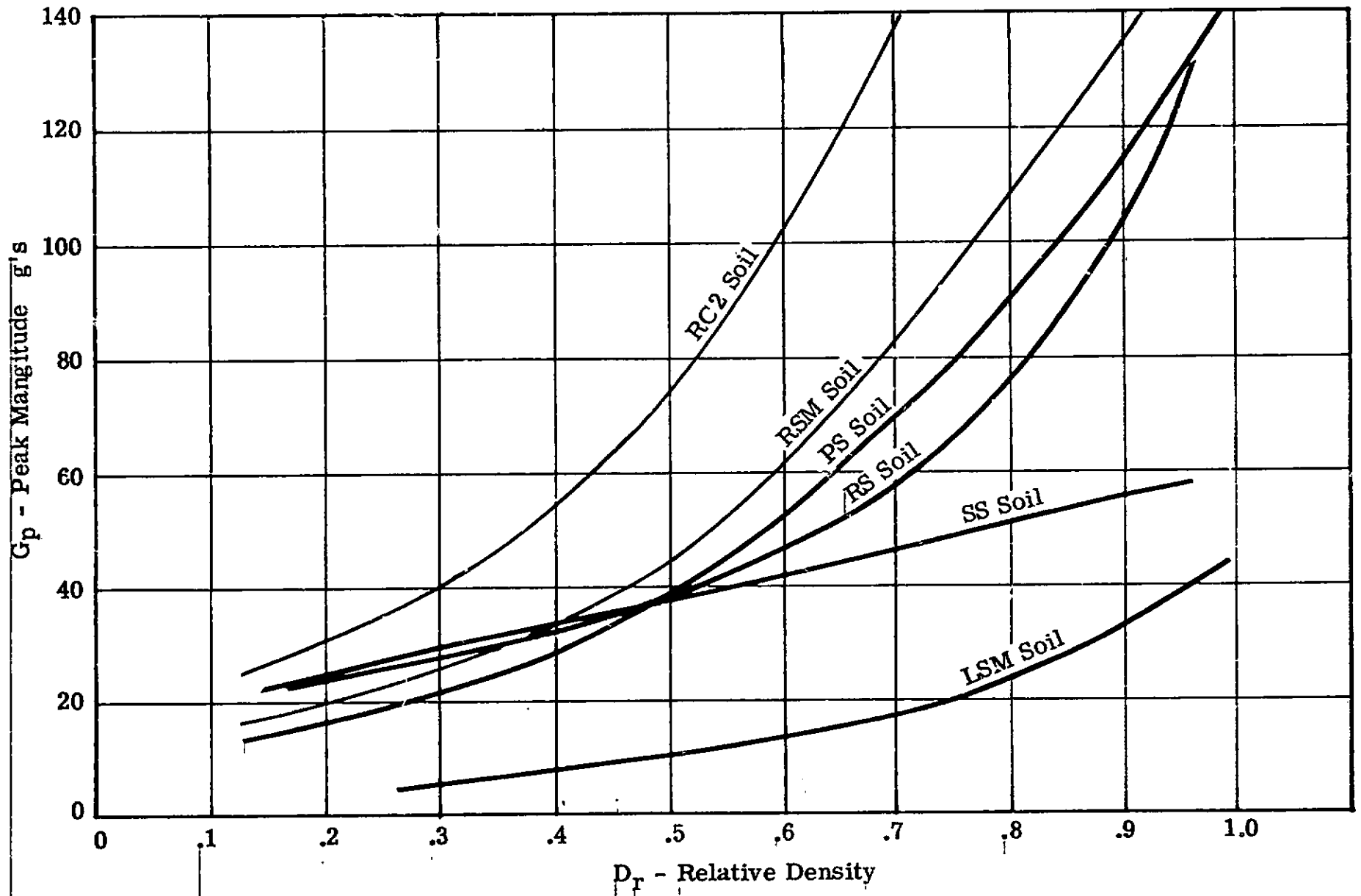

Figure 2-55. LM Soil Mechanics Study Dynamic Penetrometer Test Correlation

In the correlation studies done to determine the relationship between G_p and D_r in the calibrated test bins, it was not found possible to achieve G_p values as low as those obtained in the drag and impact test bins even when the calibrated bins used in the correlation study were filled using the same procedure used to establish the minimum density of the soil. This would suggest that the hopper system used to place the RS loose soil in the drag and impact test bins created a looser soil condition than that employed for the minimum density test. It is also possible that this difference is due to boundary effects in the correlation study not present in the larger bins. Similar results were obtained for the other test soils used in the loose condition.

2.7.2 Static Penetrometer Tests

Two types of manually-operated static penetrometer were investigated as methods of measuring and controlling the soil test bed properties-a modified "pocket penetrometer,"* and a cone-type proving ring penetrometer**. Both of these devices were found unsuitable for control or measurement of soil properties, primarily because the results they gave varied a great deal from operator to operator even for the same soil.

2.7.3 Grain Size Analysis***

Soil samples were taken from the drag and impact test bins periodically to check on possible grain size distribution changes due to degradation of soil grains caused by handling and testing. A portion of each of these samples was used for grain size analysis and the remainder of each sample used for a minimum-maximum density test.

Figures 2-56 through 2-58 show the results of several grain size analyses on the RS, PS, and RSM soils used in the subscale drag test. Basically, these soils were handled by a vacuum hose system**** or by shoveling. The legend on each figure describes

*Soil Test Model No. CL-700 (33, p. 43).

**Soil Test Model No. CN-970 (33, p. 43).

***Section 2.5.2.1.

****See Section 2.8.1.3 for a description of this system.

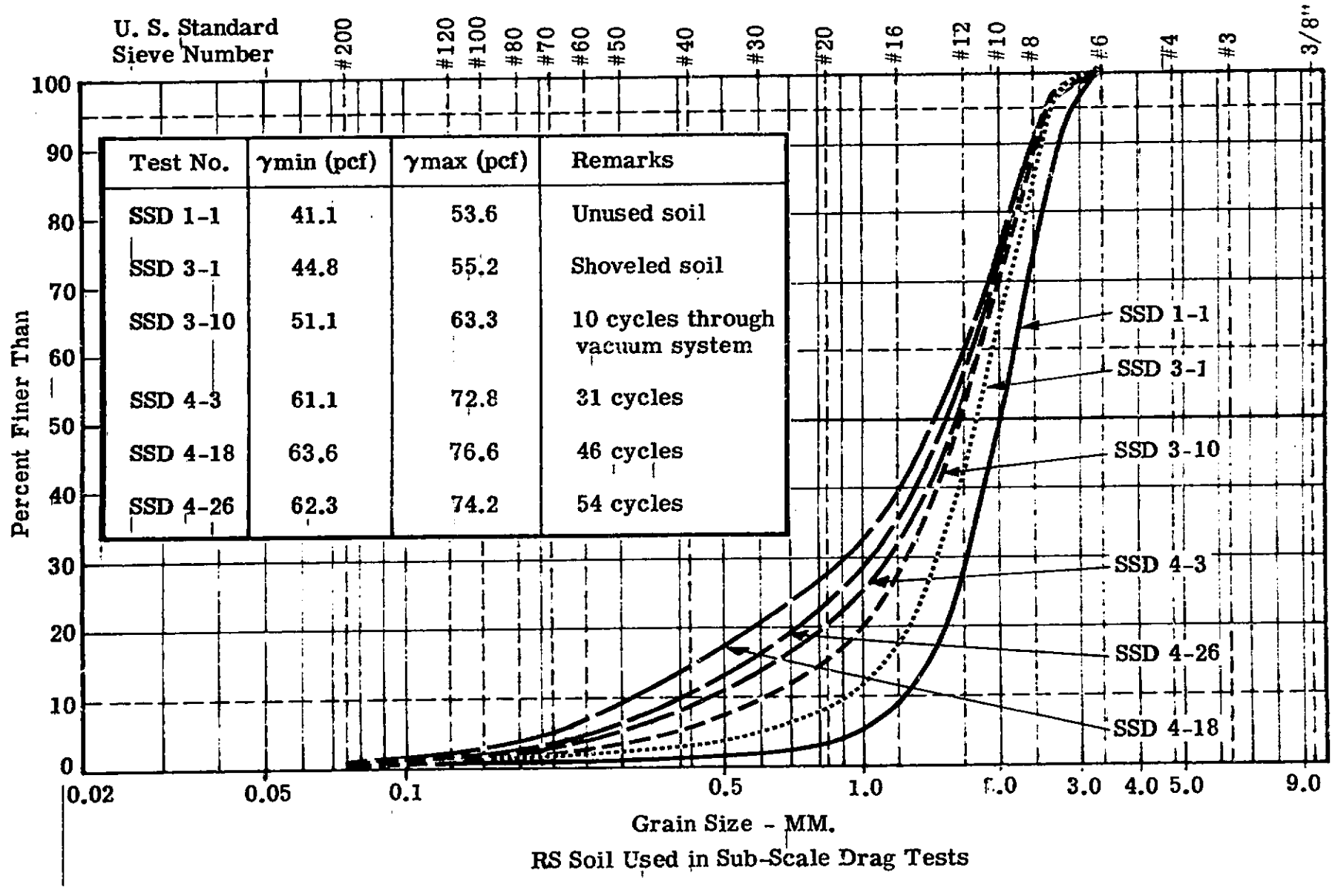

Test No.	γmin (pcf)	γmax (pcf)	Remarks
SSD 1-1	41.1	53.6	Unused soil
SSD 3-1	44.8	55.2	Shoveled soil
SSD 3-10	51.1	63.3	10 cycles through vacuum system
SSD 4-3	61.1	72.8	31 cycles
SSD 4-18	63.6	76.6	46 cycles
SSD 4-26	62.3	74.2	54 cycles

RS Soil Used in Sub-Scale Drag Tests

Figure 2-56. Grain Size Analysis Curves - LM SMS

GRAIN SIZE ANALYSIS CURVES - LM SMS

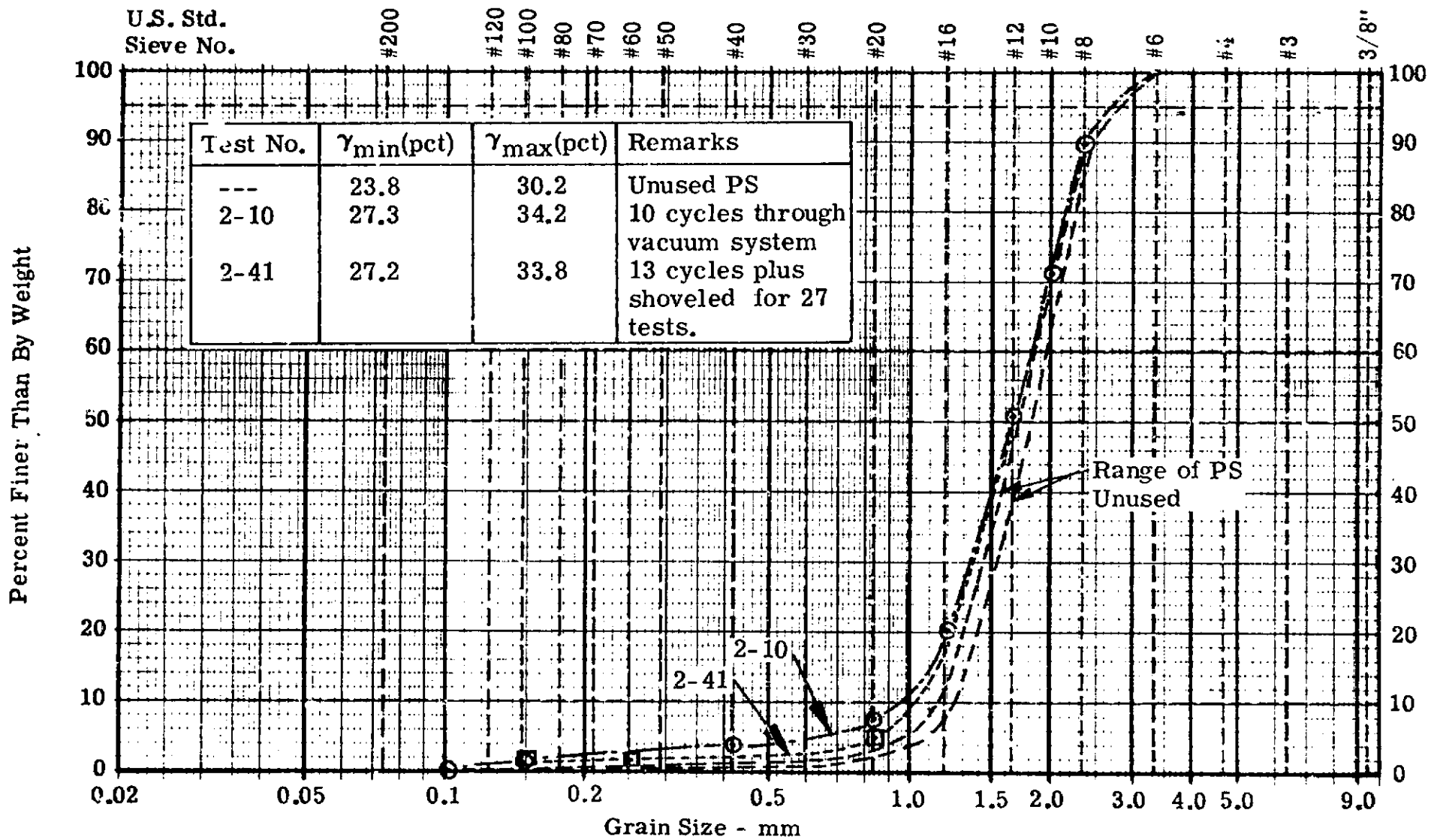

Test No.	γ_{min}(pct)	γ_{max}(pct)	Remarks
---	23.8	30.2	Unused PS
2-10	27.3	34.2	10 cycles through vacuum system
2-41	27.2	33.8	13 cycles plus shoveled for 27 tests.

ASEE Class.					
SILT (Nonplastic)	Fine	Medium	Coarse	Fine	
CLAY (Plastic)	SAND			GRAVEL	

Figure 2-57. PS Soil Used in Subscale Drag Tests

GRAIN SIZE ANALYSIS CURVES - LM SMS

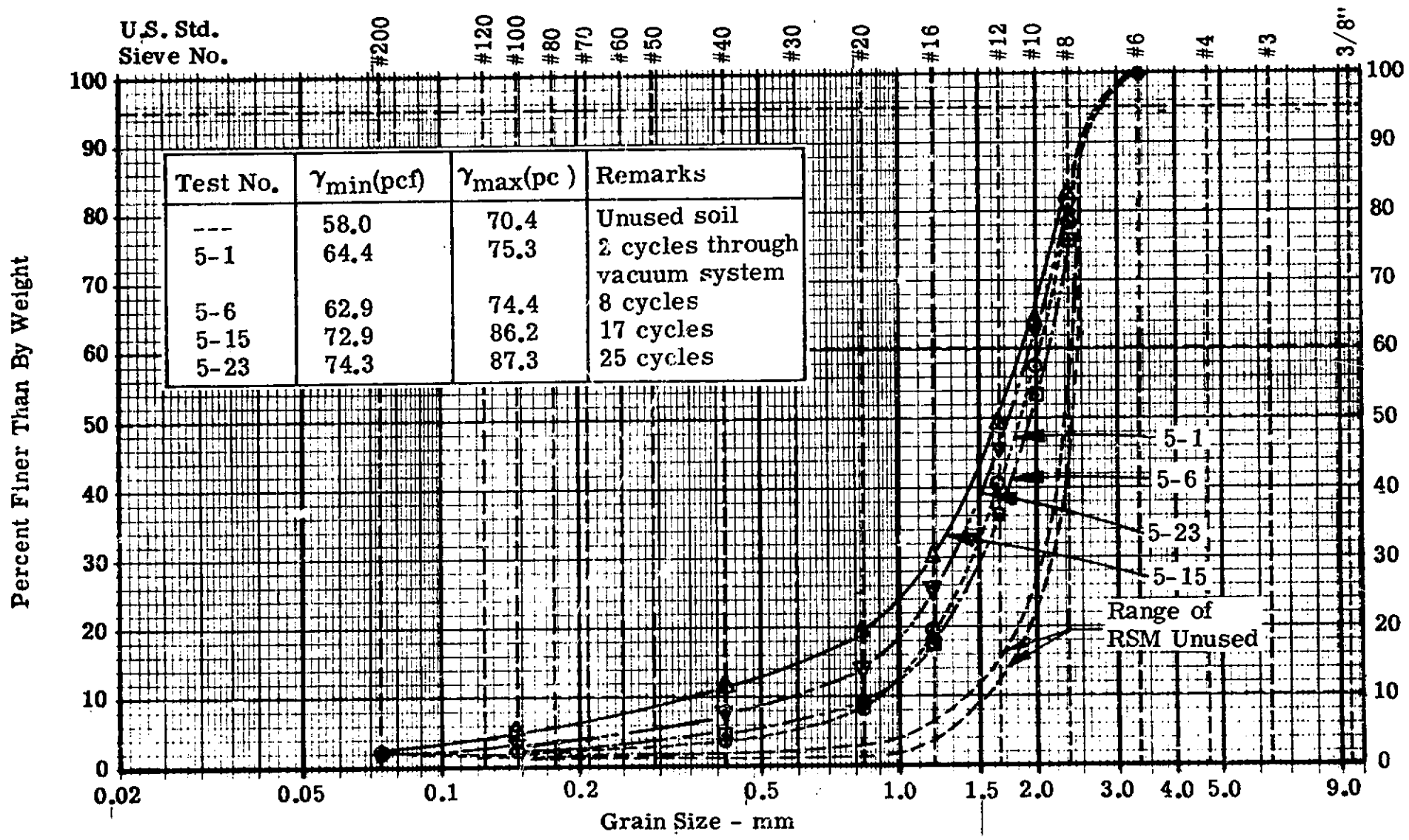

Test No.	γ_{min}(pcf)	γ_{max}(pc)	Remarks
---	58.0	70.4	Unused soil
5-1	64.4	75.3	2 cycles through vacuum system
5-6	62.9	74.4	8 cycles
5-15	72.9	86.2	17 cycles
5-23	74.3	87.3	25 cycles

ASEE Class.					
	SILT (Nonplastic)	Fine	Medium	Coarse	Fine
	CLAY (Plastic)	SAND			GRAVEL

Figure 2-58. RSM Soil Used in Subscale Drag Tests

how the soil was handled and how many cycles it experienced through the vacuum system. Also indicated is the average or range of the grain size distribution for the unused soil. These figures show that the RS and RSM soil particles experienced a significant degree of breakdown or degradation in passing through the vacuum system. The PS soil exhibits some breakdown but not to the degree indicated for the RS and RSM soils. The data also indicates that the degradation caused by shoveling was relatively small. Although the SS soil was also handled by the vacuum system, the grain size analyses of samples taken from the drag and impact test bins did not reveal any significant variation outside the limits shown for the SS soil in Figure 2-14.

Since the LSM and RC2 soils contain appreciable fine particles, they were handled by shovel only (since the vacuum system would have tended to remove most of the fine particles from these soils). The grain size analyses of the sample of these soils taken from the drag and impact test bins also indicated no significant variation outside the limits shown for the unused soils in Figure 2-7.

2.7.4 Minimum-Maximum Density Test*

As mentioned in the preceding section of grain size analysis, minimum-maximum density tests were also done on the periodic samples taken from the drag and impact test bins. A complete resume' of this data is presented in the part of this report dealing with the analysis of the drag and impact test data. The tables in Figures 2-56 through 2-58 show the results of these tests for the RS, PS, and RSM soils in the subscale drag tests corresponding to the grain size analysis previously discussed.

The conclusions indicated by this data are similar to those described for the grain size analyses. The data exhibits increasing values of minimum and maximum density with an increasing number of cycles through the vacuum loading system and shows a positive correlation with the soil degradation indicated by the grain size analyses. Analysis of the data obtained for the RC2, RSM, LSM, and SS soils indicates that these values also tend to be within the limits established for the unused soils as shown in Figure 2-17.

*Section 2.5.2.2 Apparatus and Procedures.

2.7.5 In-Place Density Measurements

Several types of in-place density measuring devices were used in this study. All of the methods consist of removing a measured weight of soil from the soil bed and measurement of the volume occupied by the soil removed. The weight to volume ratio gives the unit weight or density of the soil. Knowing the minimum-maximum density relationships for the soil, this density measurement allows determination of the relative density of the soil.

The first attempts to measure in-place density of the soil beds utilized the sand cone method*. An amount of soil is carefully removed from the soil bed and weighed. The volume of the hole created is measured by weighing the amount of sand known unit weight required to fill the hole. It was found that although this method worked fairly well in some intermediate and dense soils, gross errors were encountered in loose soils and in the SS soil in any state of density. These errors were eventually traced at least in part to the fact that the weight of the apparatus was causing failure of the sides of the hole.

A modification of the sand cone method using water to measure the volume of the hole created by the soil removal eliminated the slope failure problem, but the correction required to compensate for the folds in the material lining the hole (Saran wrap or thin plastic sheet), and other factors, produced considerable undesirable variation in the results.

A third device for measuring in-place density is a "density scoop" developed by E. T. Selig of Illinois Institute of Technology Research Institute (IITRI). Bendix fabricated their own version of this device and it is shown in Figure 2-59. This device scoops out a fixed volume of soil determined by the radius of the scoop (0.0118 cu.ft.). The weight of the soil scooped out divided by this volume yields a value for unit weight of the soil.

---

*ASTM Designation D1556-64 (31, pp. 418-422).
The equipment used in this study: Soil Test Model No. CN-992, CN-994, and L-770 (33, pp. 47, 49). The sand used was Wedron 4040 (SS soil).

Figure 2-59. Mass Density Scoop

A comparison of the results obtained with the density scoop and the weight-volume measurements in the LPT bin indicates an error ranging from 0 to 3.2 percent and an average error for eight tests of 1.0 percent. The results obtained with the density scoop tend to be lower than the "true" values obtained in the LPT bin measurements.

2.7.6 Evaluation of Soil Control Tests

Figure 2-60 illustrates the results of the periodic minimum-maximum density tests, the in-place density measurements, and the dynamic penetrometer tests in the sub-scale drag tests performed on the RS soil. The minimum density determinations are shown as circles; the maximum density determinations as squares. A dashed line joins these points to show the trend of the values and to provide interpolated values between tests. The in-place density measurements are plotted as dots. The solid line joins the plotted points of soil unit weight as determined by the dynamic penetrometer test (the G_p value provides a value of relative density; the value of relative density used in conjunction with the interpolated or measured values of minimum and maximum density provides a value for unit weight).

The prominent increase in slope after test Number 1-75 indicates where the vacuum loading system was started in use. This slope shows the significant increase in the rate of soil degradation that occurred when this system went into operation. The solid line, indicating the DPT results, shows that despite the changes in unit weight occurring due to soil degradation the relative densities in the test bin were relatively uniform. The dots, indicating the in-place density measurements, exhibit a considerable amount of scatter and generally tend to be noticeably lower than the densities determined by the DPT. The scatter probably indicates the necessity for a greater number of in-place density measurements for a reliable average value to be obtained. However, the number of such measurements is limited by the amount of disturbance that can be tolerated in the test bed.

2.8 SOIL TEST BED PREPARATION PROCEDURES

The primary consideration in the preparation of soil test beds is to produce a uniform bed of soil in such a manner that the soil properties are consistent from test to test (i.e., that the placement procedure produces a uniform density and relative density,

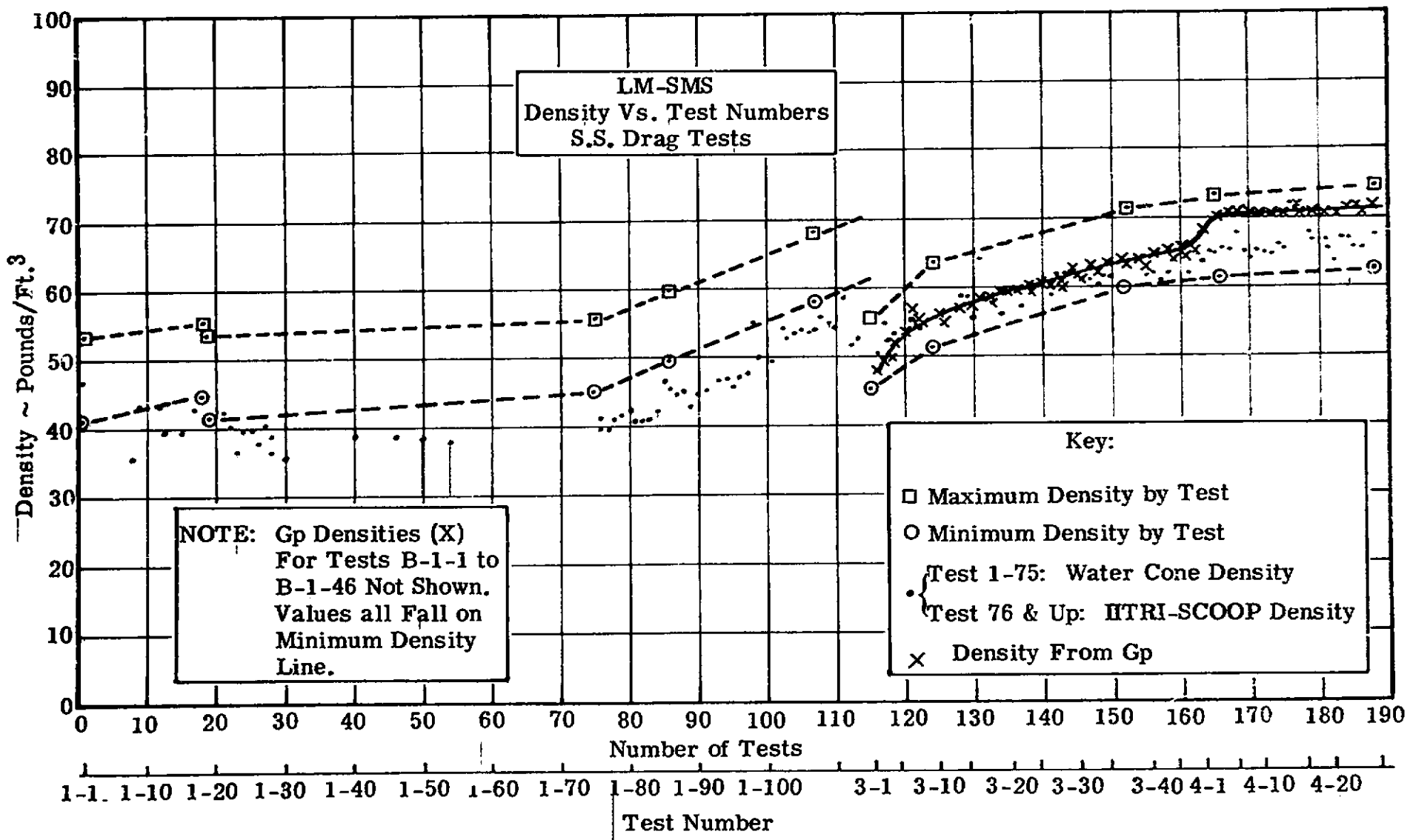

Figure 2-60. LM SMS Density versus Test Numbers - SS Drag Tests

both laterally and vertically, within the test bin, and prevention of segregation of grain sizes (i.e., nonuniformity of grain size distribution). Since a great many tests must be performed in a relatively short time to fulfill the testing schedule, the placement procedure must also be optimized in terms of the minimum time necessary for filling and emptying the test bin and the performance of control tests. Finally, the method used should preferably be such that excessively dusty conditions are not created.

All the soils used in this study were tested in an air-dried condition. Moisture content determinations on the air-dried soils (measurement of the percentage water removed by drying in an oven at 230° F) varied from 0.2 to 0.3 percent and, occasionally as high as 0.6 percent.

2.8.1 Preparation of Loose Soil Test Beds.

Three methods of placing soil in the "loose" state (i.e. $0 \leq D_r \leq 0.3$) were investigated: a slope-filling method, a scoop-placing method, and deposition from a hopper.

2.8.1.1 Slope-Filling Method.

This method consists of raising a hopper up one side of the test bin (the hopper being as long as the side of the bin) sufficiently slowly that the soil pours out the bottom without appreciable free-fall. The soil spreads across the bin by rolling down the slope formed, and the slope is periodically leveled as the bin is filled. This procedure tends to produce a density at or near the minimum density of the soil (i.e., $D_r \approx 0$) as established by the standard laboratory test described in Section 2.5.2.2. The uniformity of density vertically is generally good, however, a noticeable segregation of coarse and fine particles takes place during that phase of the filling when the soil is rolling down the slope, the coarse grains tending to roll to the bottom and the finer tending to stay near the top. This would tend to produce lateral nonuniformity of density and would probably influence other soil properties due to nonuniform grain size distribution. Also, the periodic leveling done in the bin would tend to produce higher densities in that portion of the soil screeded and, thus, would probably produce some vertical nonuniformity of density.

2.8.1.2 Scoop-Placing Method

This method consists of filling the test bin with a scoop or shovel such that the soil is placed rather than dropped on the existing surface. The surface is brought up in more or less level fashion to minimize segregation due to rolling of particles. This procedure tends to produce a moderately loose soil condition ($D_r \approx 0.15$) which is fairly uniform and repeatable, however, it is a relatively slow procedure for filling large test bins.

2.8.1.3 Hopper Method.

This method was conceived to overcome the slowness associated with the scoop-placing method and consists of filling the test bin from a hopper such as that shown in Figure 2-61 ("A" is the shutoff gate in the open position; "B" is the bottom opening of the hopper, and "C" is a guide rail for the hopper). The hopper is placed so that the bottom edge is slightly above the existing surfaces, and, after the gate has been opened, the hopper is pulled along so that the bottom edge of the opening is the leading edge. It can be seen that the trailing edge of the bottom opening of the hopper will be level with or slightly above the surface of the soil being deposited. This aspect of the design of the hopper was derived from observation that screeding a loose soil surface (i.e., leveling it with a straight edge) tends to densify the soil, and this design feature was intended to eliminate the screeding effect and, thus, produce greater vertical uniformity. Density and relative density measurements on the soil bed produced in this manner indicate that the soil has a density at or close to minimum density (i.e., $D_r \approx 0$), is very uniform laterally and vertically and is repeatable within very narrow limits.

Initially, the hopper was loaded by shovel. To reduce the time consumed by unloading the test bin and loading the hopper with shovels (and, also, to reduce the dusty conditions produced by shoveling) a vacuum hose system and storage hopper was developed and fabricated by Bendix as shown in Figure 2-62. (The hopper shown in Figure 2-61 is shown here placed over the subscale drag test bin and mounted in the frame used to support and carry it along the test bin). The labeled components of the vacuum soil handling system are as follows:

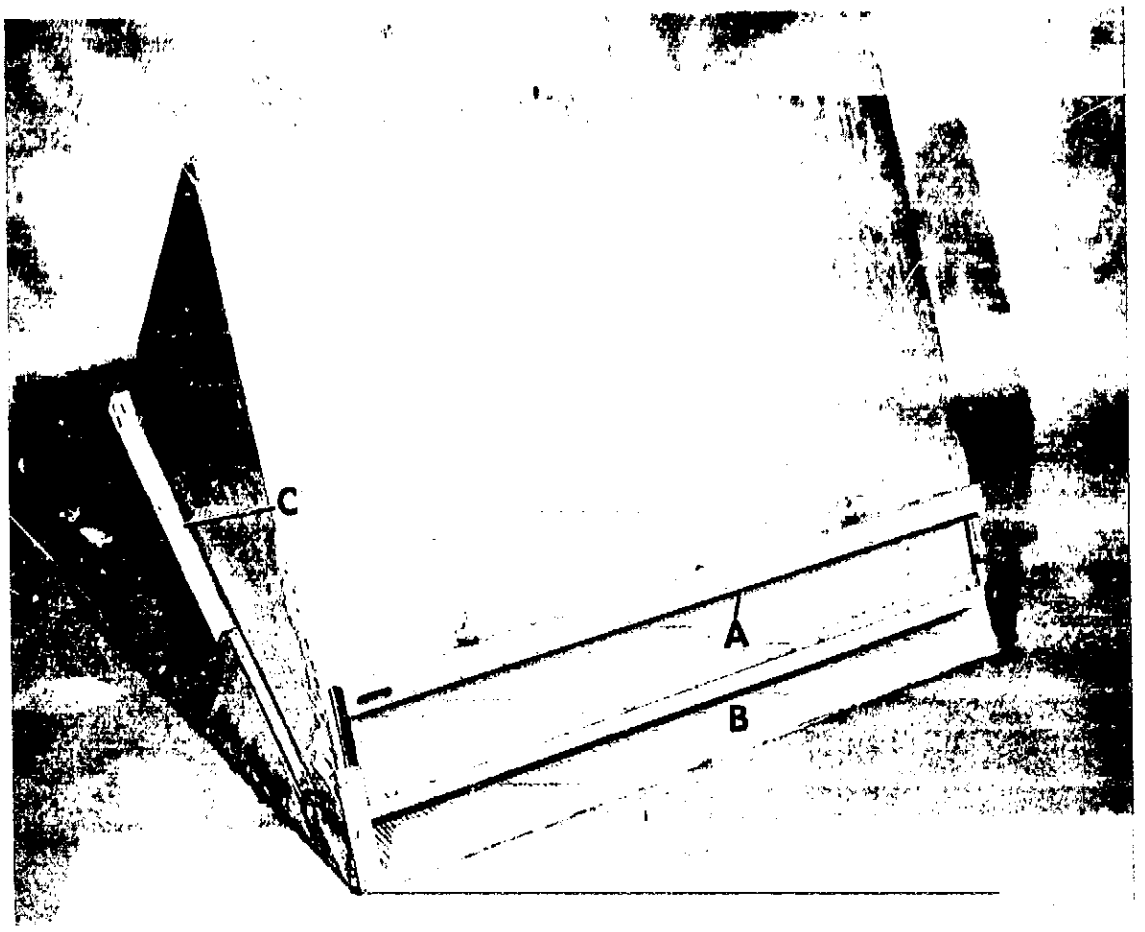

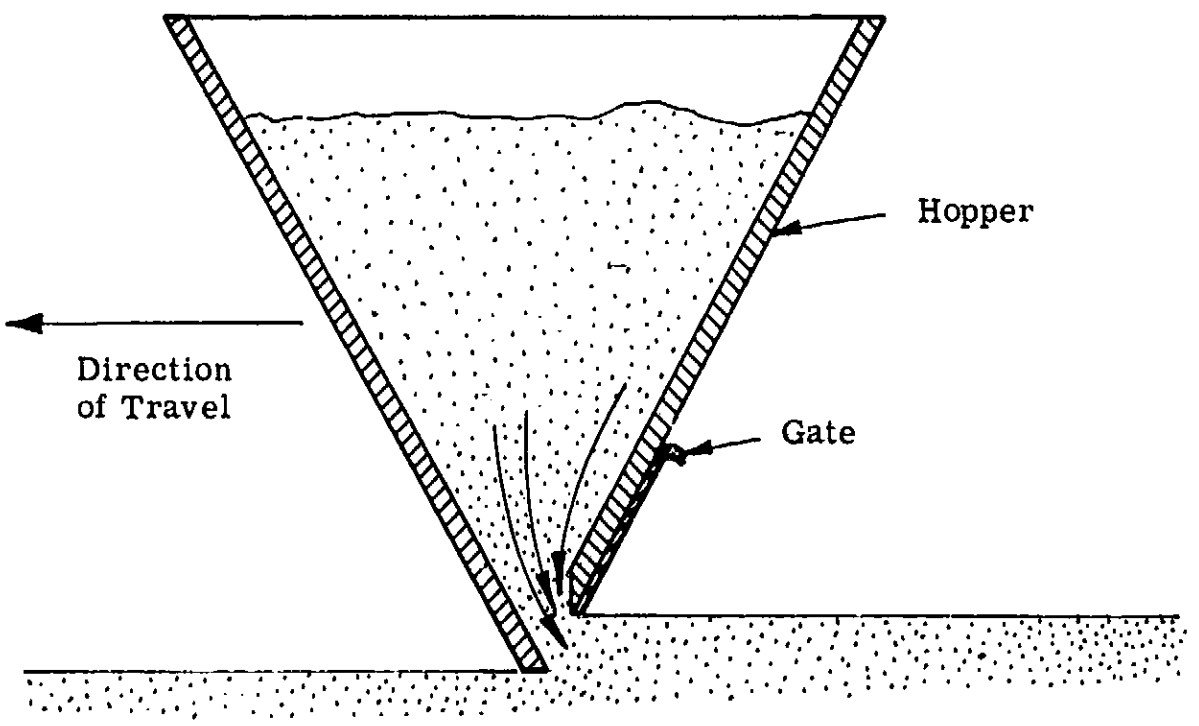

Figure 2-61. Subscale Drag Test Hopper

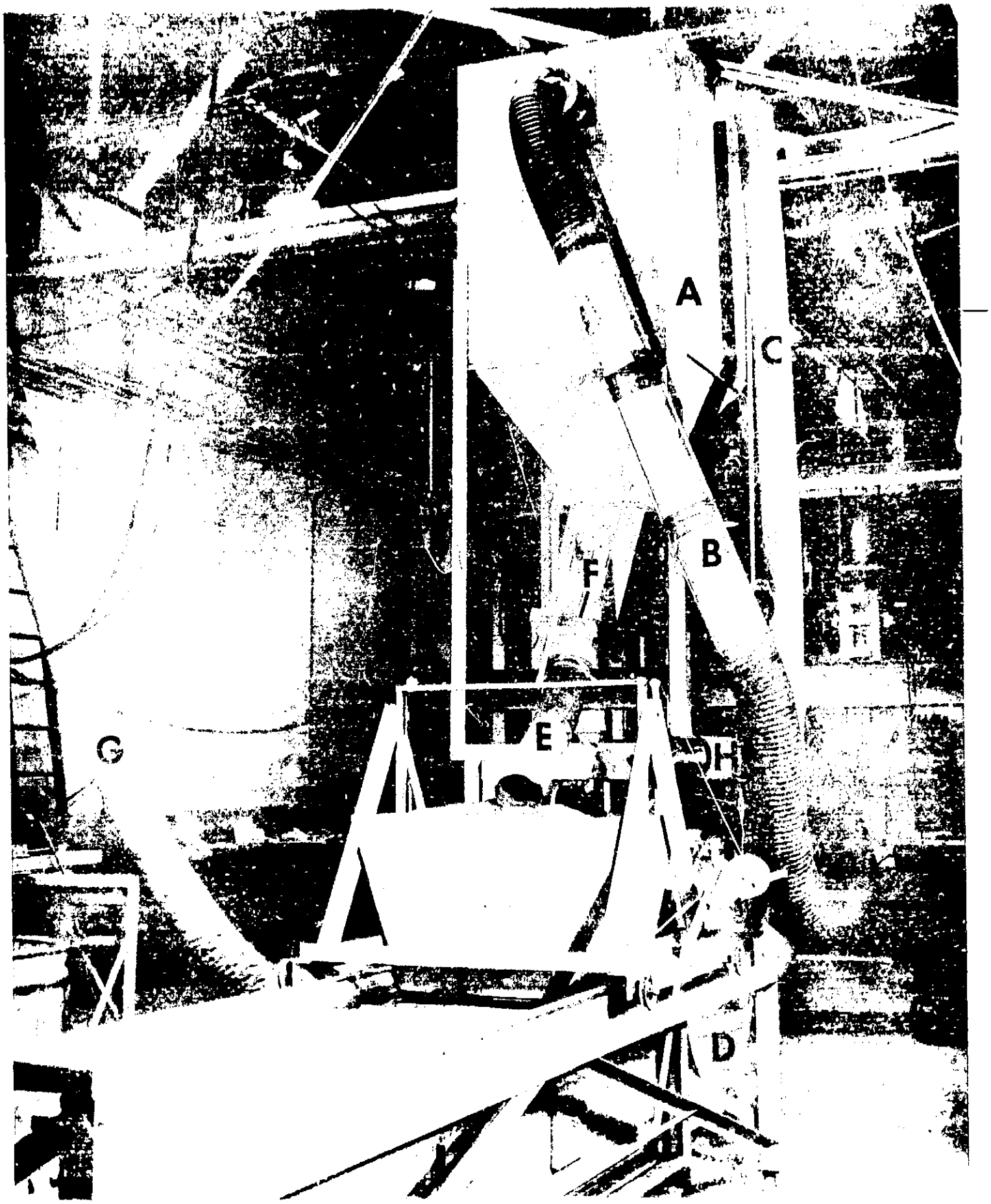

Figure 2-62. Soil Removal System (Front View)

A - A 36 cu. ft. wooden storage hopper.

B — Vacuum hose soil intake pipe.

C - Suction pipe; applies partial vacuum in storage hopper and intake pipe.

D - A 25 HP turbine fitted to a 3500 rpm, 30 HP direct drive 440 volt electric motor. The turbine produces a partial vacuum of 6 inches of mercury at a flow of 1000 cu. ft. of air per minute.

E - Pipe for emptying storage hopper into soil placement hopper.

F - Cutoff knife valve for regulating flow of soil from storage hopper.

G - Exhaust pipe.

H - Exhaust port of suction pipe "C."

Although this system allows for rapid soil handling (it will move 400 pounds of soil per minute), it has been found that soil losses through the exhaust system, degradation of soil particles, and hose and turbine impeller damage from abrasion are inordinately high. The addition of more filters and increase of hose diameters (to reduce air velocity) reduced but did not eliminate the problem.

Since the exhaust system tends to remove the fine particles from the soil being handled, this system could not be used for the LSM and RC2 soils.

These soils were handled by shovel. The cinder soils (RS, PS and RSM) that were handled using this system underwent pronounced degradation due to abrasion in passing through the intake hose, and careful periodic sampling of the soils was necessary to keep track of these effects so that their influence could be included in the analysis of the drag and impact tests. Predictably, no significant degradation effects were noted for the SS soil since the silica particles constituting this soil are relatively resistant to breakdown.

Figure 2-63 shows the large soil placement hopper developed and fabricated by Bendix for the full-scale impact test and model drop test bin. The labeled elements of this figure are as follows:

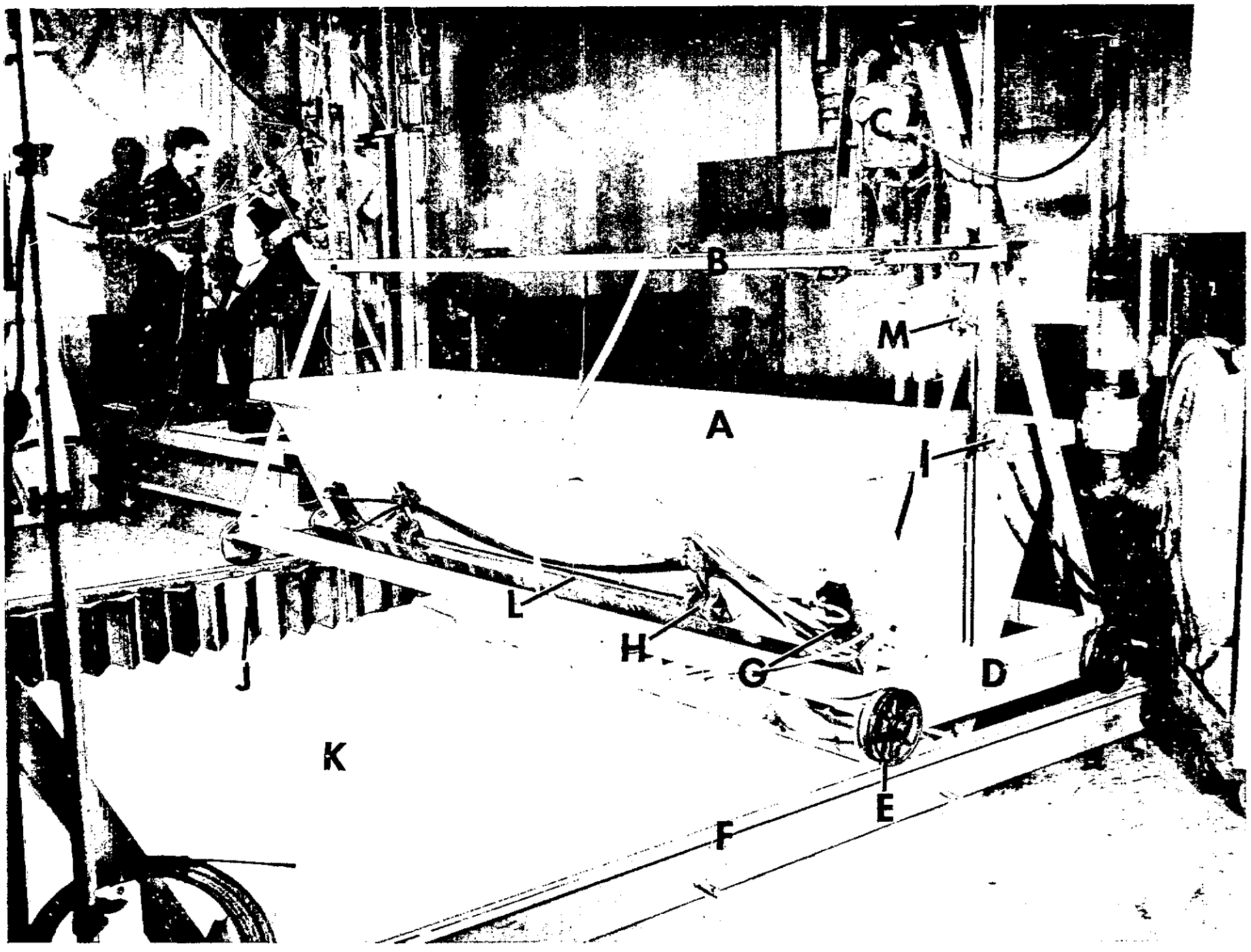

Figure 2-63. Full-Scale Impact and Model Test Bed Soil Preparation Equipment

A - Soil placement hopper.

B - Cables and winch chain supporting hopper in frame and used to move it up and down.

C - One ton capacity electric winch.

D - Support frame for hopper.

E - Grooved wheels on which hopper is moved along bin.

F - Rails at sides of bin on which wheels ride.

G - One of two pneumatic cylinders used to operate shutoff gate on hopper.

H - Rack and pinion gears used to synchronize movement of pneumatic cylinders.

I - Air pressure regulator for gate cylinders (G).

J - Soil bin walls.

K - Soil test bed (SS soil shown).

L - Shaft connecting rack and pinion gears (H).

M - Two-way valve for air pressure to pneumatic cylinders (G).

2.8.2 Preparation of Intermediate Soils.

Several methods of producing intermediate densities (i.e. $0.3 \leq D_r \leq 0.7$) in the test soils have been investigated. These include deposition by free-fall from a fixed height, screeding, and mechanical compaction utilizing both static and vibratory methods.

2.8.2.1 Free-Fall Method.

A range of loose through intermediate densities can be obtained in a granular soil bed by varying the distance through which the soil falls in being deposited. Loose soils are obtained by keeping the distance of free-fall to a minimum, and successively higher densities are produced by increasing the distance of free-fall. This method was used in the small Load-Penetration Test (LPT) bin and, when the height of drop was carefully controlled, fairly uniform intermediate densities were obtained. However, this method

created much dust and produced significant segregation of soil particle sizes when the broadly-graded soils such as the RC2 were used.

2.8.2.2 Screeding.

It was found that screeding of a loose soil (i.e., leveling with a straight edge) tended to densify the soil and this behavior was utilized in producing intermediate densities in the LPT bin. Small piles of soil sufficient to produce a layer about one-inch thick were placed in the bin and then screeded to form a level surface. This method appeared to work fairly well when the resulting layers were relatively thin (i.e., about one inch) but produced visible nonuniformity and lower densities when thicker layers were used (because the lower part of these layers tended to remain in a loose condition). Although this method yielded fairly good results in the relatively small LPT bin, time considerations precluded using it in the larger test bins.

2.8.2.3 Mechanical Compaction.

Both static (i.e., dead weight) and dynamic (i.e., vibratory) methods have been used to obtain intermediate density soil beds. In both cases a two-to four-inch layer is laid down by the hopper as described for the loose soils, and each layer is compacted before the next is placed. The vibratory compactor used is an air-powered chipping hammer fitted with an eight-inch square plate (see Figure 2-64). One quick "pass" was made on each layer. Density measurements and dynamic penetrometer tests indicated that intermediate densities were obtained, but there was considerable scatter in the data, in part due to variations in air pressure delivered to the compactor. A lawn roller was then tried (see Figure 2-65). Only the RS, SS and LSM soils were used in the intermediate condition (i.e., Soils Nos. 3, 8, and 11, respectively), and it was found that a different number of passes of the roller was required for each type of soil. Soil No. 3 was obtained by rolling each layer two times (one pass back and forth in the bin). This produced an average relative density of about 0.4. Soil No. 8 was obtained by rolling each layer eight times (4 passes back and forth), producing an average relative density of about 0.6. Soil No. 10 was obtained by rolling each layer two times while the layer was covered with a section of cardboard. The cardboard strip was found necessary because the roller has a tendency to plow the soil during the rolling phase producing nonuniform densities. The average relative density produced by this procedure was about 0.5.

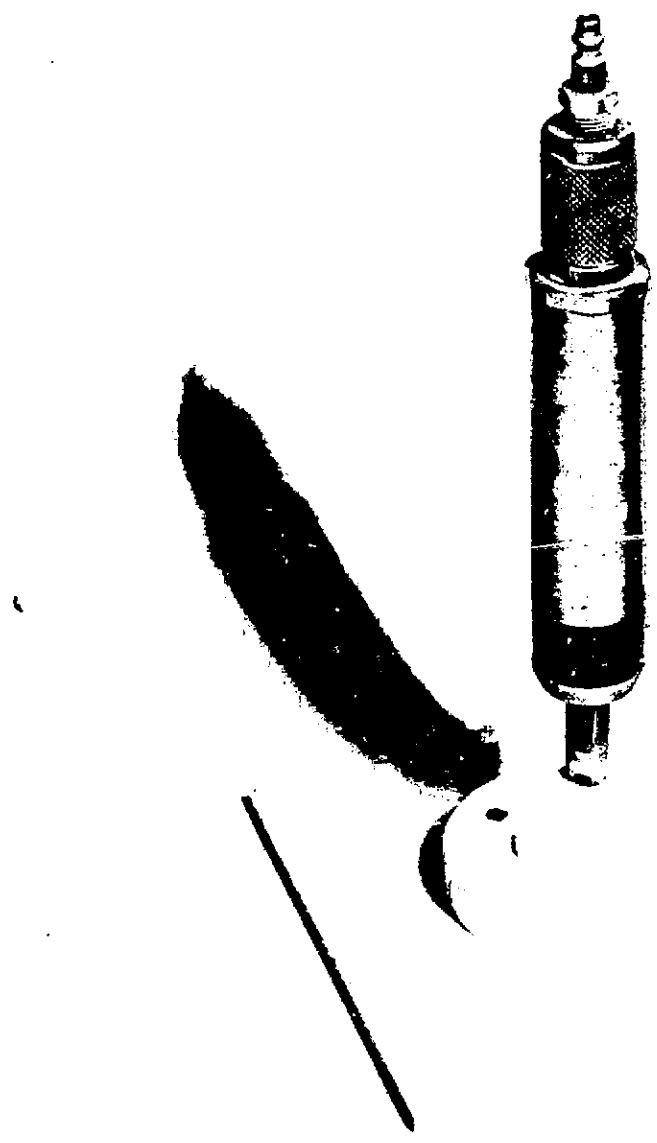

Figure 2-64. Air Operated Chipping Hammer and Plate

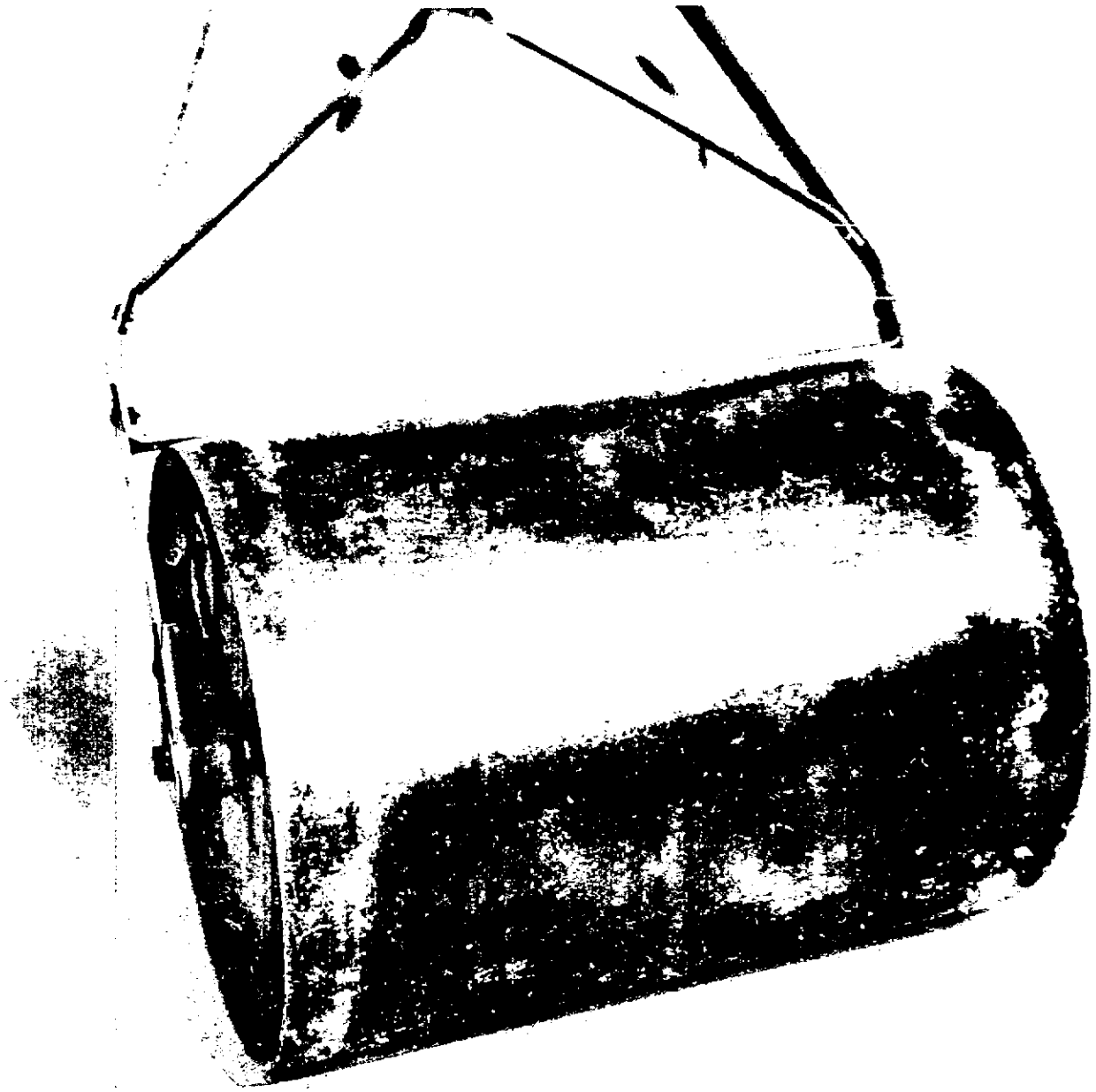

Figure 2-65. Soil Densifying Roller

2.8.3 Preparation of Dense Soils.

Dense soils prepared for the Load-Penetration Tests were produced by the vibratory plate compactor described above (see Figure 2-64). Generally, three passes per layer (about three inches thick) produced relative densities between 0.85 and 0.95, depending on the thickness of the layer.

However, as with the intermediate soils, this method was not found convenient in the larger drag and impact test bins. Here, the dense soils, Soils Nos. 4 (RS Dense), 9 (SS Dense), 11 (LSM Dense), and 12 (RSM-b Dense) were obtained using the lawn roller compactor. Soil No. 4 was obtained by rolling each layer sixteen times (eight passes back and forth) producing an average relative density of about 0.7. Soil No. 9 was obtained by making twenty-four passes on each layer, producing an average relative density of about 0.75 to 0.8. Soil No. 11 was obtained by rolling each layer (covered by a strip of cardboard, as described for Soil No. 10) six times, producing an average relative density of about 0.7. Soil No. 12 was obtained by making twenty-four passes on each layer, producing an average relative density of about 0.78.

2.9 SUMMARY OF MAIN RESULTS OF "SOIL SELECTION AND CONTROL" PHASE OF PROGRAM.

In view of the many facets of the "Soil Selection and Control" phase of the subject program and the resultant length of this particular section of the final report, it was felt that a summary of the main results of the soil selection and control studies would be helpful.

1. A set of soil properties which could contribute to the dynamic strength of the soil were developed. The set is made up of the following soil properties:

   γ, bulk density

   D_r, relative density

   ϕ, angle of internal friction

   C, cohesive shear strength parameter

μ_w, mean grain size

C_u, coefficient of grain size uniformity

E, sonic elastic modulus

2. Twelve tests soils were selected for the dynamic soil tests for the development of the semi-empirical model. The range of properties of the test soils encompass the best estimates of the lunar soil properties. In addition sufficient range is covered in the properties that effects of individual properties on the soil force response may be classified.

3. The above properties were carefully measured for each of the test soils wherever possible using standard testing procedures.

4. Various soil-bed preparation procedures were attempted. Quite a few resulted in inconsistent soil properties, grain size segregation, nonuniform strength, nonuniform soil composition with depth, and other faults. However, satisfactory methods of soil test bed preparation were developed for each of the twelve test soils. Soil placement and handling equipment was the[illegible] and built for use in the dynamic soil testing program.

5. A considerable number of bearing strength tests (LPT's) were conducted in the various tests soils. The objectives of these tests were:

   a. Examination of failure mode and static strength characteristics of the soil.

   b. Examination of the consistency of the static strength characteristics- a screeding procedure for the test bed preparation techniques mentioned in item (4) above.

   c. Examination of the applicability of traditional bearing strength relationships (that of Terzaghi for example) for definition of the load-penetrations relationship of the LM footpad.

With regard to each of the above objectives, the following summary is given:

a. The failure modes of the soil ranged from the "local shear" failure for soils of low relative density and low angle of internal friction (< 35°), to an intermediate combination of "local shear and general shear" for soils of low relative density and higher angles of internal friction (> 35°), and also for soils of intermediate relative density and low angle of internal friction (< 35°), to general shear failure for soils of high relative density.

b. The use of the LPT's for determination of the consistency of various preparation techniques proved quite valuable since nonuniform preparation of the soil from one LPT test to another was readily apparent from comparison of the resultant load vs. penetration curves.

c. A mixed degree of success was achieved in using Terzaghi's bearing strength relationship for defining the load vs. penetration curve for a given soil. Since the equation was developed to give the failure load of a soil rather than the resistance of a constantly penetrating footing, it would be a fortunate coincidence if the relationship proved applicable to the definition of the penetration dependent portion of the total soil resistance.

   Because of the mixed degree of success in the attempt at application of Terzaghi's relationship, the static and dynamic penetration dependent portion of the soil resistance was developed in a semi-empirical manner as a function of the soil strength properties of γ , D_r, and ϕ . This development is covered in Section 4 of the report.

6. Methods of monitoring the test bed soil properties were developed so that adequate control of the soil properties could be achieved. These methods consisted of five types of tests:

   a. Dynamic Penetrometer Test

   b. Static Penetrometer Test

c. Grain Size Analysis

d. Minimum-Maximum Density Test

e. In-Place Density Measurements

The static penetrometer test later proved to be somewhat unreliable due to the type of penetrometer used. It was therefore abandoned in the later stages of the controlled motion dynamic soil-test program since the remaining four tests gave an adequate indication of the test bed properties.

SECTION III

CONTROLLED MOTION TEST EQUIPMENT FOR SOIL/FOOTPAD DYNAMICAL INTERACTIONS

3.1 INTRODUCTION

Successful development of the LM soil interaction model depended largely upon the detailed analysis of experimental data resulting from controlled motion tests of simulated LM footpads moving through selected soils. This section discusses the five (5) equipment/instrumentation systems that were devised to obtain the specific data required, and an additional* system that was designed for possible future use. These six test systems are:

At Bendix: Subscale Drag Test Equipment (SSD)
Subscale Oblique Impact Test Equipment (SSOI)
Full-scale Oblique Impact Test Equipment (FSOI)
*Full-scale Drag Test Equipment (FSD)

At IITRI: Vacuum/Atmospheric Impact Tester (subscale)
Subgravity Simulator (subscale)

Each system was designed to measure footpad motion and/or the forces acting on the footpad while it is moved in a precisely controlled manner through the soil. The full-scale equipment utilizes a full-scale simulated LM footpad, while each of the subscale systems accommodates up to 1/6-scale LM footpads.

The first two subscale systems listed (e.g., SSD and SSOI) were developed by Bendix during earlier studies and modified during this program to accommodate the specific loading and instrumentation requirements. Two counterpart full-scale systems (FSD and

FSOI) were designed during the program; however, for various reasons, only the oblique impact system was fabricated and used to obtain test data.

The Vacuum/Atmospheric Impact Tester and Subgravity Simulator were developed by IIT Research Institute to meet technical requirements established by Bendix. Details of this equipment presented in this report are reproduced from the IITRI final report that was submitted to Bendix at the conclusion of this subcontracted effort.

3.2 SUBSCALE DRAG TEST EQUIPMENT

3.2.1 General Purpose

The subscale drag test equipment shown in Figure 3-1 is used to measure the dynamic soil resistance forces acting on an instrumented footpad moving horizontally through the soil at a constant velocity, with the footpad maintained either at a constant depth of penetration, or under conditions of constant vertical load. The equipment is designed to facilitate individual control of vertical and horizontal displacement, horizontal velocity, acceleration, attitude, and loading of the instrumented footpad.

In Figure 3-1, the instrumented footpad (B) and instrumented strut (C) are shown in operating position over one of two soil test bins. The strut is supported from a traveling carriage which rides between two parallel support rails (A), rigidly mounted over the soil bin.

After acceleration, constant velocity movement of the carriage is effected by drive system (D) through cam rod (H), one end of which is fastened to the carriage. The cam rod is pulled by a friction wheel (E), which is powered by an electric motor (F) through a speed regulator (G). The drive system frame (J) is mounted on rollers (K) to aid movement from one test bin to the other. Soil test bed preparation equipment (see Section II) is shown straddling the second test bin, to the right in Figure 3-1.

The subscale drag test system was originally developed by Bendix while conducting lunar landing systems engineering studies under contract to Bellcomm, Inc., and is described in detail in Bendix Final Report No. MM-65-2.

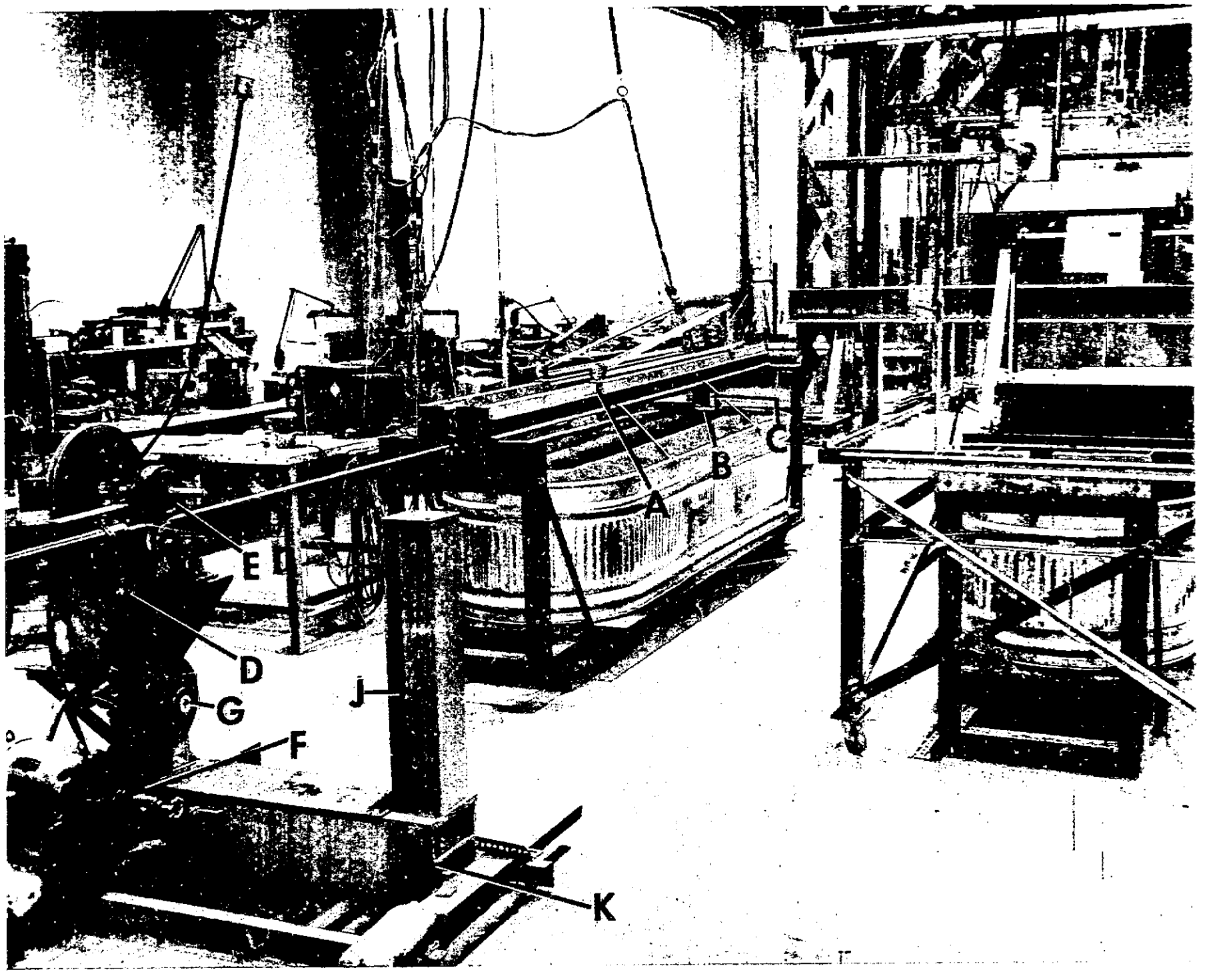

Figure 3-1. Subscale Drag Test Equipment

3.2.2 Equipment Modifications

To accommodate the requirements of the LM Soil Mechanics Study, various modifications were made to increase the power and structural capabilities of this equipment and to improve instrumentation and instrumentation response characteristics.

Figure 3-1 actually depicts the system after incorporating these changes. The more significant features of the modifications are summarized below.

1. Steel channels were added to the carriage support rails to increase both lateral and vertical rigidity of the rails and the structural steel frames which support the rails at each end were considerably stiffened. The frame was also redesigned to facilitate rapid portability from one test bin to the other.

2. Steel guide wheels on the carriage were replaced with Teflon sliding blocks, or slippers, to reduce instrumentation noise.

3. A new instrumented strut was designed that measured forces on the footpad in three dimensions. This equipment, discussed in detail in Section 3.2.4, replaced the two dimensional measurement system originally used.

4. The air bearing and gravity loading system originally used to provide vertical load to the instrumented strut was replaced by a gas loading system to remove uncertainties of air bearing friction load effects during constant vertical load drag tests.

5. The new subscale LM footpad incorporates special instrumentation to measure footpad pitch and roll attitude with respect to the strut. This equipment is further described in paragraph 3.2.5 of this report.

6. Originally, the friction drive wheel was roller chain driven from a variable speed changer powered by a 1/4-horsepower AC electric motor. This system was replaced by a 3-horsepower motor and belt driven speed regulator which,

with the addition of a heavy flywheel, substantially increased both power and velocity control of the equipment. The original cam rod was also replaced with a new rod, precision machined from solid steel.

3.2.3 Equipment Arrangement and Operation

Figure 3-2 is a schematic diagram of the modified drag test equipment. The soil bin is approximately 10 feet long and 3 feet wide with a built-in false bottom that provides soil depths of 11 to 12 inches. During the test program two identical bins were used, located side by side to facilitate soil bed preparation in one while tests were being conducted in the other.

The composite steel and wood carriage support rails are securely positioned above the bin by a rigid framework at each end. A parallel steel track is attached to the bottom face of the support rails, and the carriage - to which the instrumented strut and footpad is attached - slides on the steel track on Teflon slippers. Insert A is a cross section of the rig showing general arrangement of the rails, carriage, and instrumented strut and footpad.

The carriage is instrumented to measure acceleration (accelerometer), velocity (rate generator), and horizontal displacement (slide wire potentiometer), as well as vertical displacement of the footpad (linear potentiometer). Measurement of vertical, horizontal, and lateral forces acting on the footpad, in addition to pad angular position, are provided by the instrumented strut and footpad which are described later.

The motion of the carriage consists of an acceleration phase, a constant speed phase, and a deceleration phase, with each phase controlled separately. All three phases occur within a nine-foot length within the soil bed, six feet of which is used for the actual (constant speed) test run.

Acceleration is accomplished by first pulling the carriage back against the force of heavy rubber bungee cords and then releasing it. The ends of the rubber cords are firmly anchored to the upper surface of the carriage support rails, and the cord centers loop

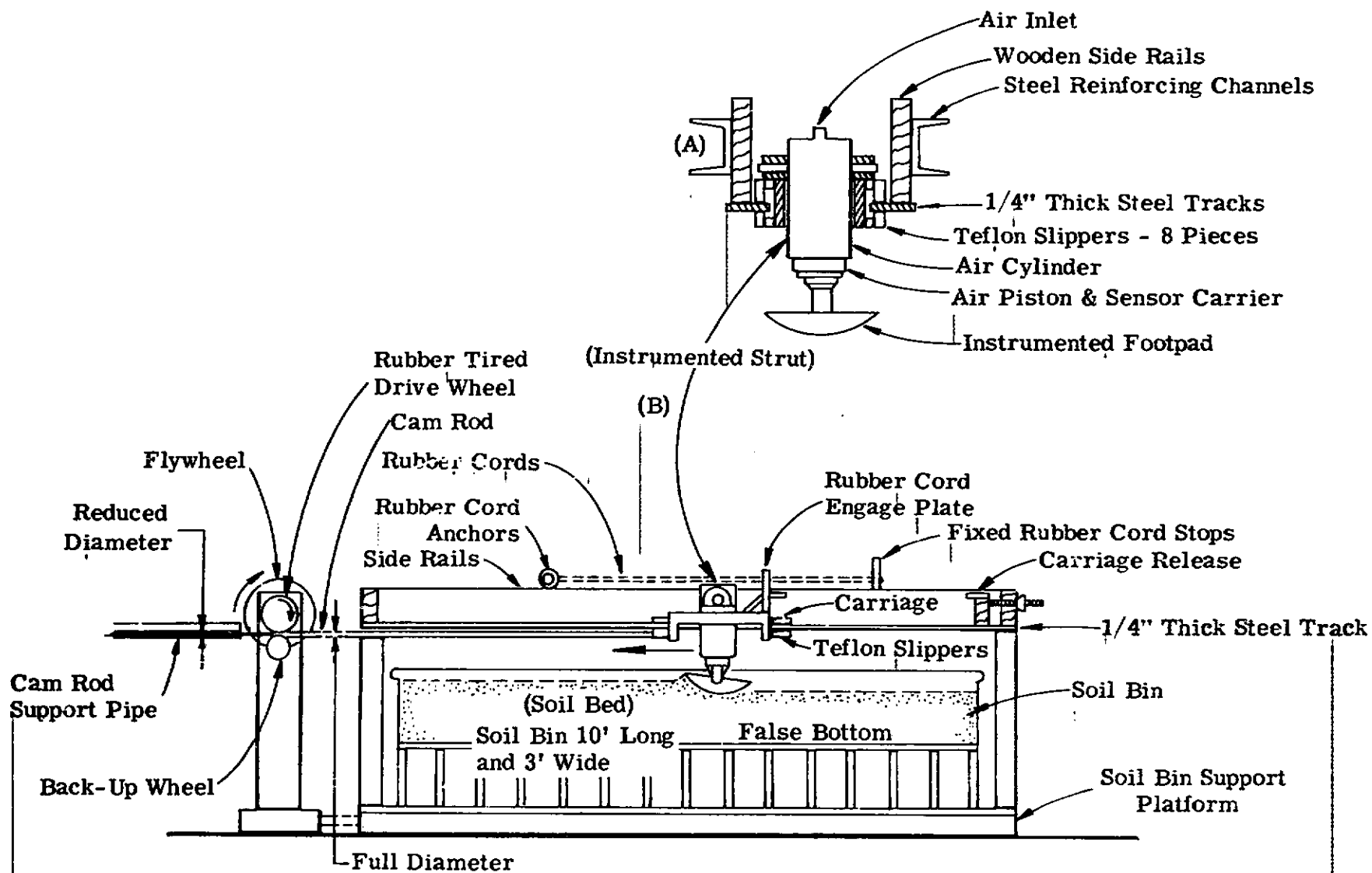

Figure 3-2. Subscale Drag Test Setup

around an "engage plate" on the rear of the carriage (see Figure 3-3). A hand-operated winch and manual latch/release mechanism is used to "cock" and "fire" the system, and fixed rubber cord stops limit the acceleration distance as desired. Carriage acceleration is controlled by varying the number of rubber cords used and the distance traveled before the cords engage the fixed stops.

The constant-velocity phase of carriage motion is controlled by the cam rod and friction drive wheel arrangement. One end of the cam rod passes through a vibration damper and is attached to the carriage. The other (free) end passes between the grooved surfaces of a rubber-tired drive wheel and steel backup wheel (see Figure 3-4). The backup wheel is adjusted vertically to provide positive power transfer to the rod (e.g., by negative clearance between wheels and rod OD), except for two sections of the rod which have a reduced diameter to provide clearance with the drive wheels. One of these reduced diameter sections, the last two feet of length at the free end, permits prerotation of the drive wheel to the exact desired speed before and during carriage acceleration. The other reduced diameter section allows power disengagement during carriage deceleration.

In operation, the carriage is accelerated over distance "a" (Figure 3-2) to the desired speed by the rubber cords. At the end of the acceleration phase, as the carriage "engage plate" passes the fixed cord stops, the full diameter of the cam rod engages the rotating drive wheel and the carriage is pulled through the constant velocity portion of the test cycle. At the end of the constant speed phase the power drive disengages, and the carriage is decelerated by springs and a damper cylinder.

The system provides rapid acceleration with essentially linear velocity control, and by proper selection of drive wheel speeds and number and tension of bungee cords, smooth transitions from acceleration to constant velocity phases can be obtained. With the 1/6-scaled LM footpad installed, the modified system provides accelerations up to 3 g's, constant velocities up to 18 feet/second, and decelerations up to about 6 g's. The system will accommodate footpad vertical and drag forces up to 250 pounds and footpad penetration up to six inches.

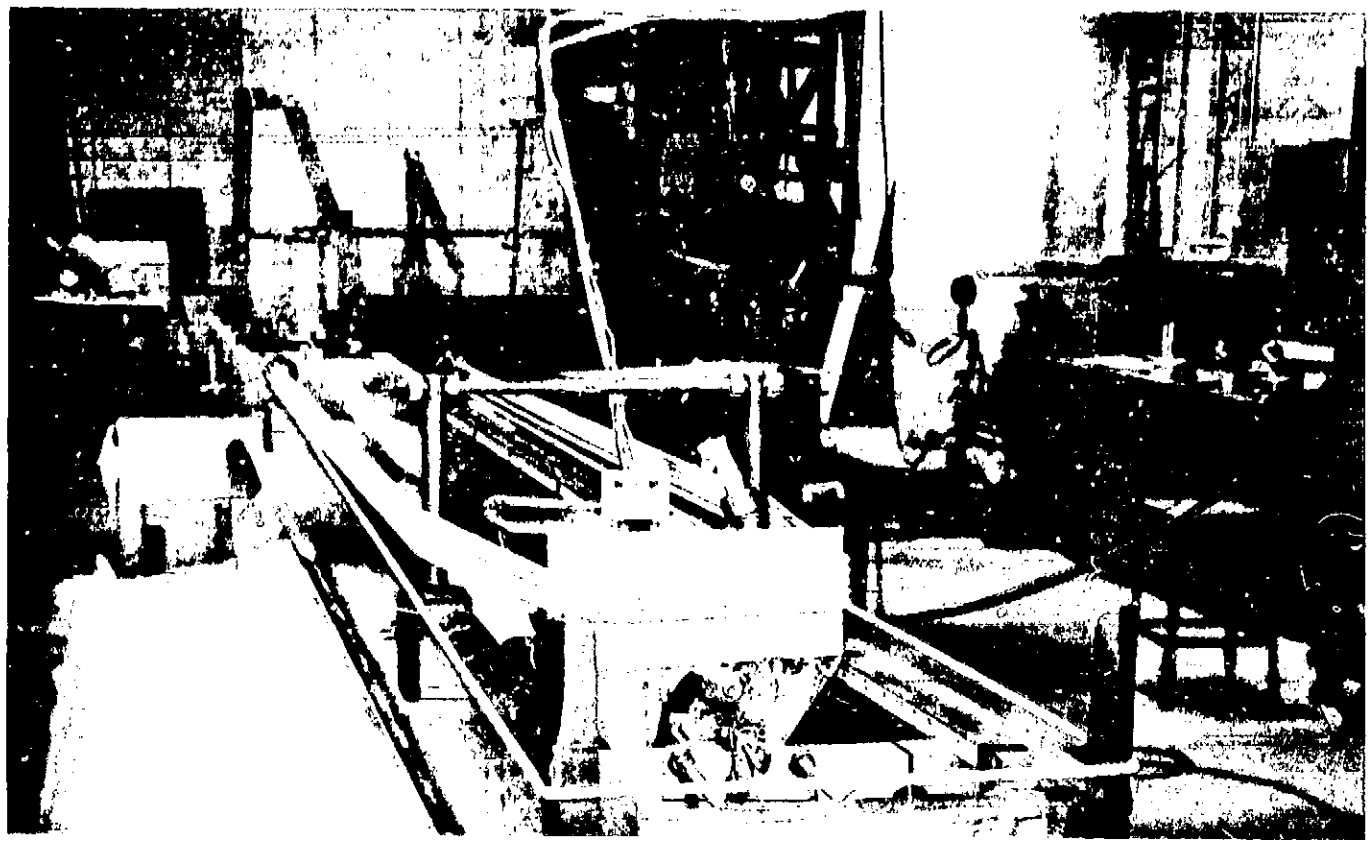

Figure 3-3. Rear View of Drag Test Equipment (Before Modification) Showing Acceleration Device

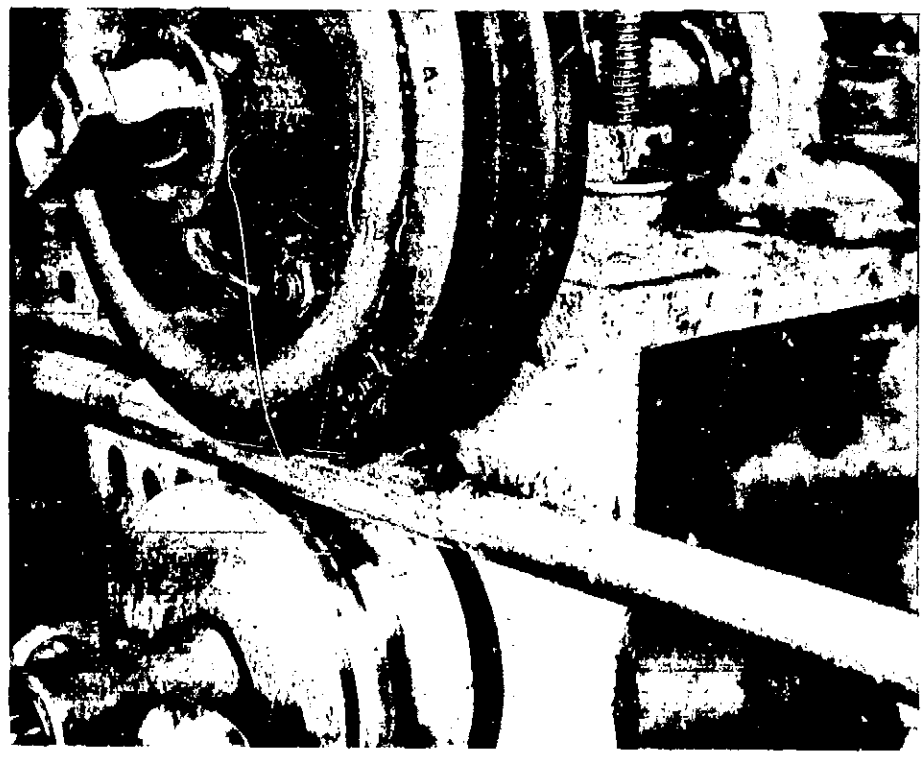

Figure 3-4. Close Up View of Constant Velocity Drive Mechanism

3.2.4 Instrumented Strut (Load Cell) Design

To establish a workable design for a three-axis load cell for measuring vertical, drag, and side forces acting on the footpad, an idealized sensor system was first conceived. This scheme was then reduced to a practical hardware arrangement that would meet requirements of sensitivity, accuracy, and small physical size in combination with the necessary strength and durability.

Figure 3-5 schematically illustrates an idealized system for measuring these forces. The central loading bar is suspended and restrained from motion by five ball-ended links. Strain gages (R_z) installed on the single link extending from the end of the loading bar measure the load in the z-axis (F_z).

Lateral load in the x-axis (F_x) is balanced by the sum of forces on the pair of links in the same plane. One end of each of these links is anchored to cantilever beams, and strain gages (R_{x1} and R_{x2}) attached near the bases of the cantilever beams measure the forces in each link and thus the force F_x. Forces in the y-axis are measured in a similar fashion by strain gages R_{y1} and R_{y2}.

Theoretically, if there is no clearance or friction in any of the ball joints and there is no large deflection in the links and cantilever beams, any force acting in one axis should not affect the force readings (strain gage output) in the other two axes. From a practical standpoint, however, this idealized system could not be packaged within the small envelope available, and is presented here only to illustrate the basic load sensing principle that was used.

Figure 3-6 presents a reasonably practical arrangement of the idealized load cell and illustrates its operating principle. The four-load sensing cantilever beams shown in Figure 3-5 are replaced by a single thin-wall sensor tube which is anchored to a solid structure by a flange at its mid-section. The sensor tube is, essentially, two cantilever beams, one extending above and the other below the anchor point. A strut to which the footpad would be attached (center rod in Figure 3-6) is located inside of the sensor tube, supported at the extremities of the two cantilever sections, and is restrained vertically by a ball-ended link. Strain gages on this link would measure the vertical force (F_z).

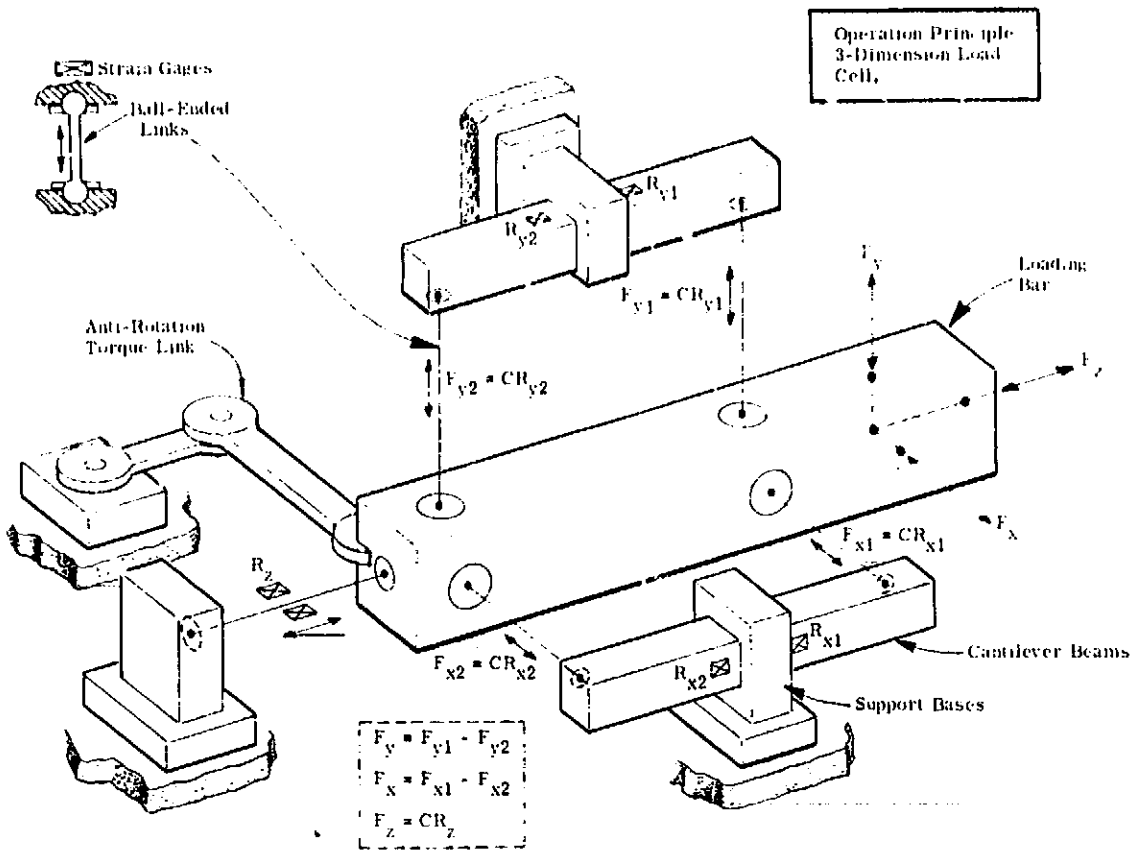

Figure 3-5. Idealized Three-Dimensional Load Cell

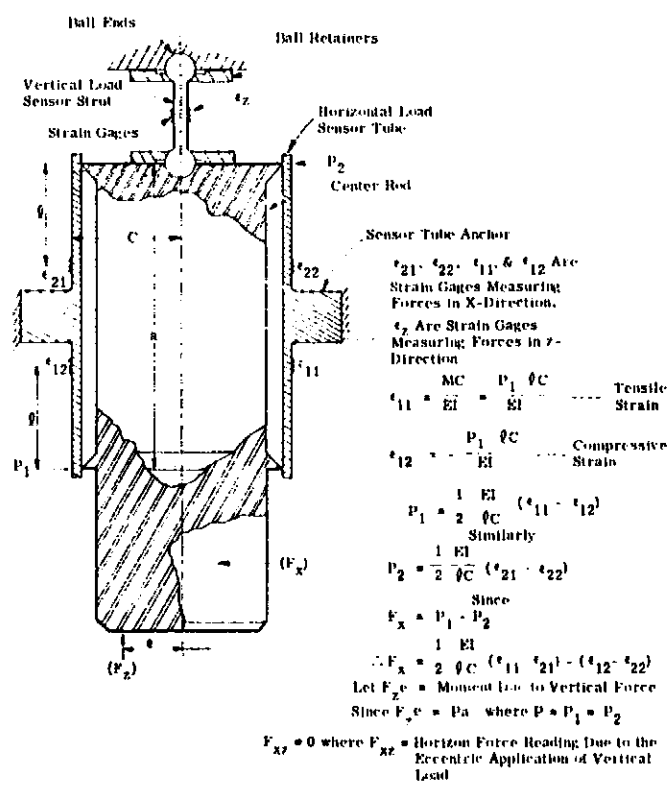

Figure 3-6. Operational Principle of the Three-Dimensional Load Cell

A lateral load (F_x) applied to the strut would cause bending of the upper and lower ends of the sensor tube and induce corresponding maximum tensile and compressive strains on the surface of the tube in the plane of the force vector (x-plane). By locating four appropriately interconnected strain gages (11, 12, 21, 22) on the sensor tube in the x-plane, as shown, the magnitude of force F_x could be obtained. A similar arrangement of gages located exactly 90° around the tube circumference would be used to measure forces in the opposite or y-plane.

The effects of combined F_x and F_y loading would be accommodated through precalibration of the system. However, accuracy and sensitivity of load measurement - particularly F_z - would be impaired by friction and clearance between the strut support points (P 1 and P 2) and the sensor tube ID.

These problems were resolved as shown in Figure 3-7, which is a schematic diagram of the instrumented strut in its final form. The hollow sensor tube was machined from aluminum with a uniform wall thickness of 0.031 inch between the three flanges. The middle flange is firmly anchored to the lower end of the piston by a threaded clamp-up nut. The upper and lower flanges at the free ends of the cantilever sections provide seats for mounting eight close-tolerance needle bearings.

Four of the needle bearings are positioned at exactly 90° to each other on each of the two flanges and secured to the flanges to provide zero clearance with the attachment strut OD. The upper and lower bearing sets are mounted precisely in line and hold the sensor tube concentric with the attachment strut. The strut is restrained in the vertical direction by the ball ended link which is anchored by ball sockets to the lower face of the piston and upper end of the strut.

Horizontal forces on the footpad react through the needle bearings to cause deflection of the sensor tube cantilever sections. Load measurement is accomplished, as described earlier, by eight strain gages mounted on the tube. Four gages are located in each of two perpendicular planes exactly in line with the centerlines of the frictionless bearings.

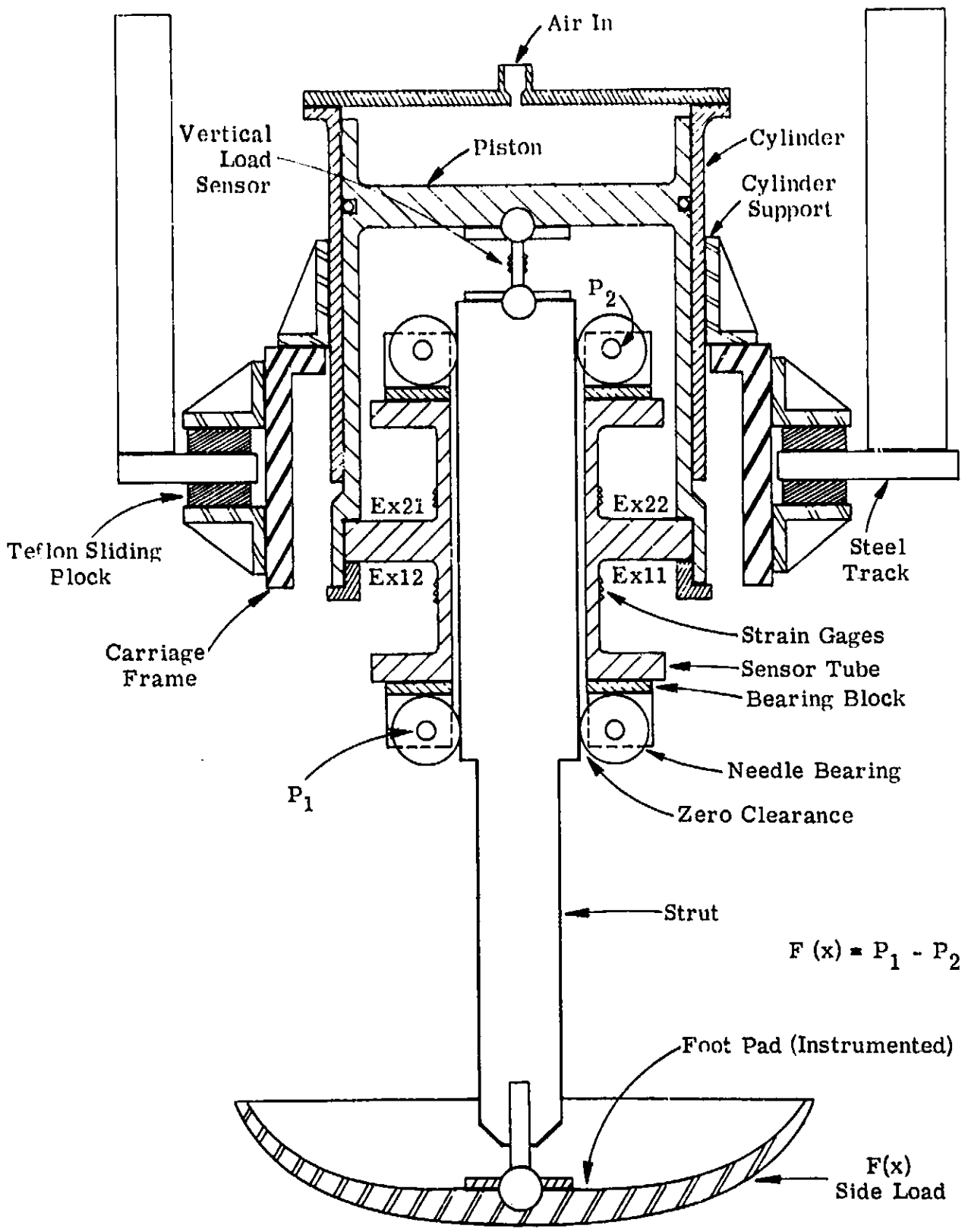

Figure 3-7. Schematic Diagram of Three-Dimensional Load Cell for Subscale Drag Test System

Vertical footpad loads are measured by strain gages mounted on the ball-ended sensor link above the strut. These gages measure tensile or compressive axial loads in the link, but they are relatively insensitive to lateral loading because of ball-socket lubrication and assembly adjustments to insure practically zero ball to socket clearance. This is illustrated in Figure 3-8, which plots the effect of applied drag load on the vertical load sensor gages. For similar reasons (e.g., lubrication, frictionless bearings, and zero-clearance features), the horizontal load measurement system is relatively insensitive to applied vertical load, as shown in Figure 3-9. These curves were plotted from cross sensitivity checks made during calibration of the drag test load capsule and are typical of the negligible interaction effects between drag and side load gages and between vertical and side load gages.

The three-axis load cell/piston assembly slides in a vertically mounted air cylinder which is part of the carriage that travels horizontally above the soil surface. For constant footpad load tests the cylinder is pressurized to obtain the desired vertical load, and the footpad/load cell components are allowed to displace vertically. For constant footpad penetration tests, the piston is mechanically locked to the air cylinder in the desired position.

3.2.5 Instrumented Footpad Design

Basic instrumentation requirements for the subscale footpad were to measure footpad angular position (e.g., pitch and/or roll angle) at all times during the test cycle. However, both footpad loads and pad position during the drag tests are influenced by shape differences between subscale and full-scale hardware systems because of soil flow into the pad and impingement against the attachment strut. Accordingly, a major design requirement for these elements of the drag test system was to maintain very close shape and silhouette similarity with the full-scale LM footpad/strut assembly. The design problems were compounded by the small physical space available.

Figure 3-10 illustrates the design which finally evolved from the various schemes studied. The 1/6-scale footpad is fabricated from steel with inside and outside contours simulating those of the full sized LM pad. The attachment strut simulates the lower end of the LM strut except for minor details at the ball socket attachment.

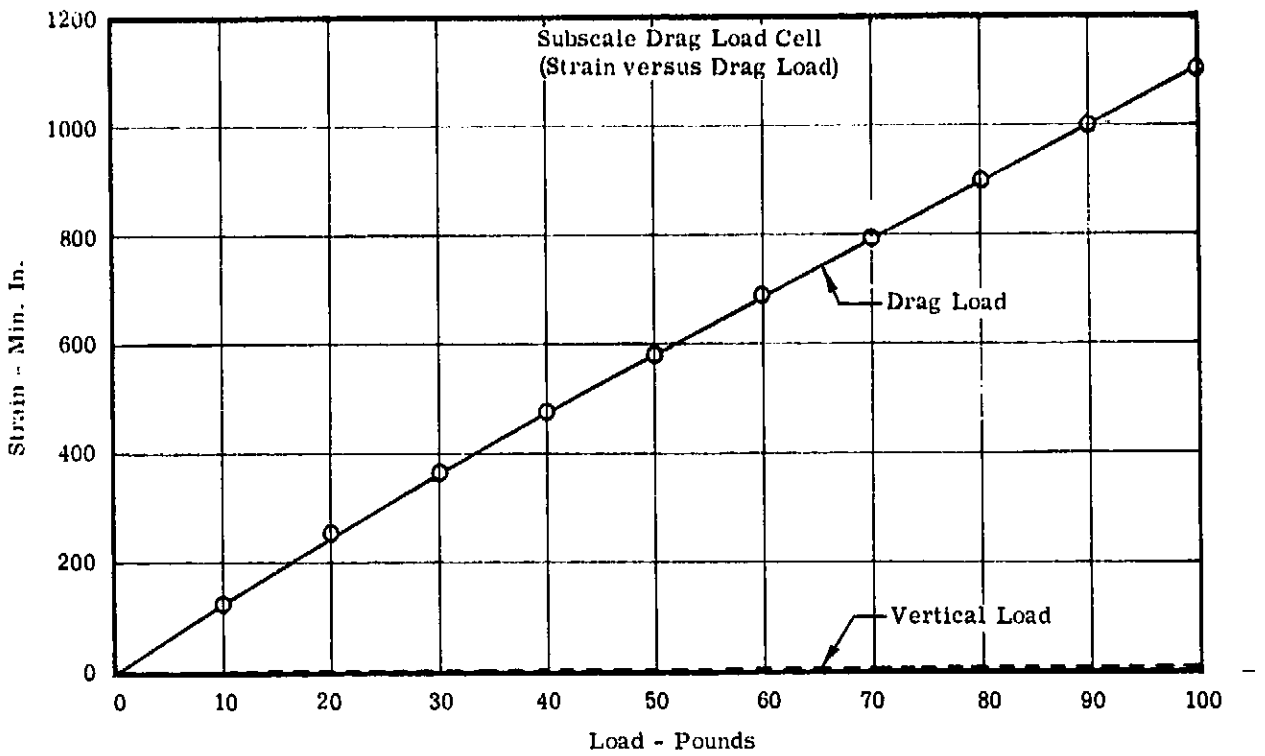

Figure 3-8. Effect of Drag Load on Vertical Load Sensor

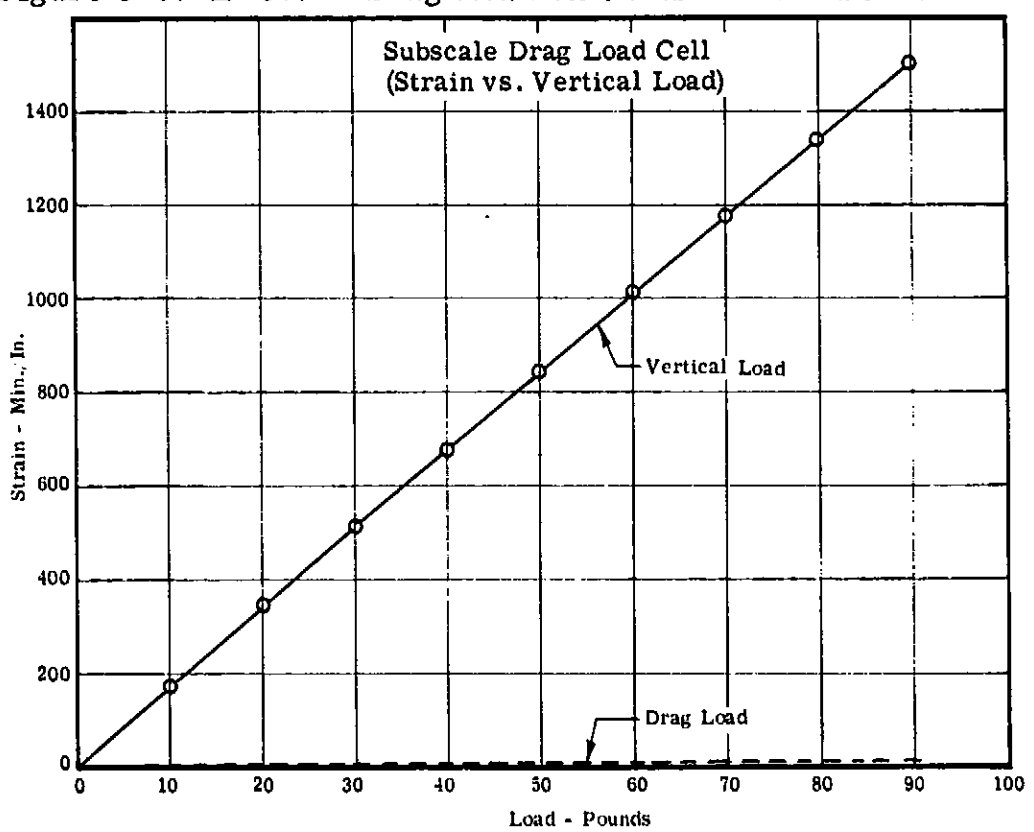

Figure 3-9. Effect of Vertical Load on Drag Load Sensors

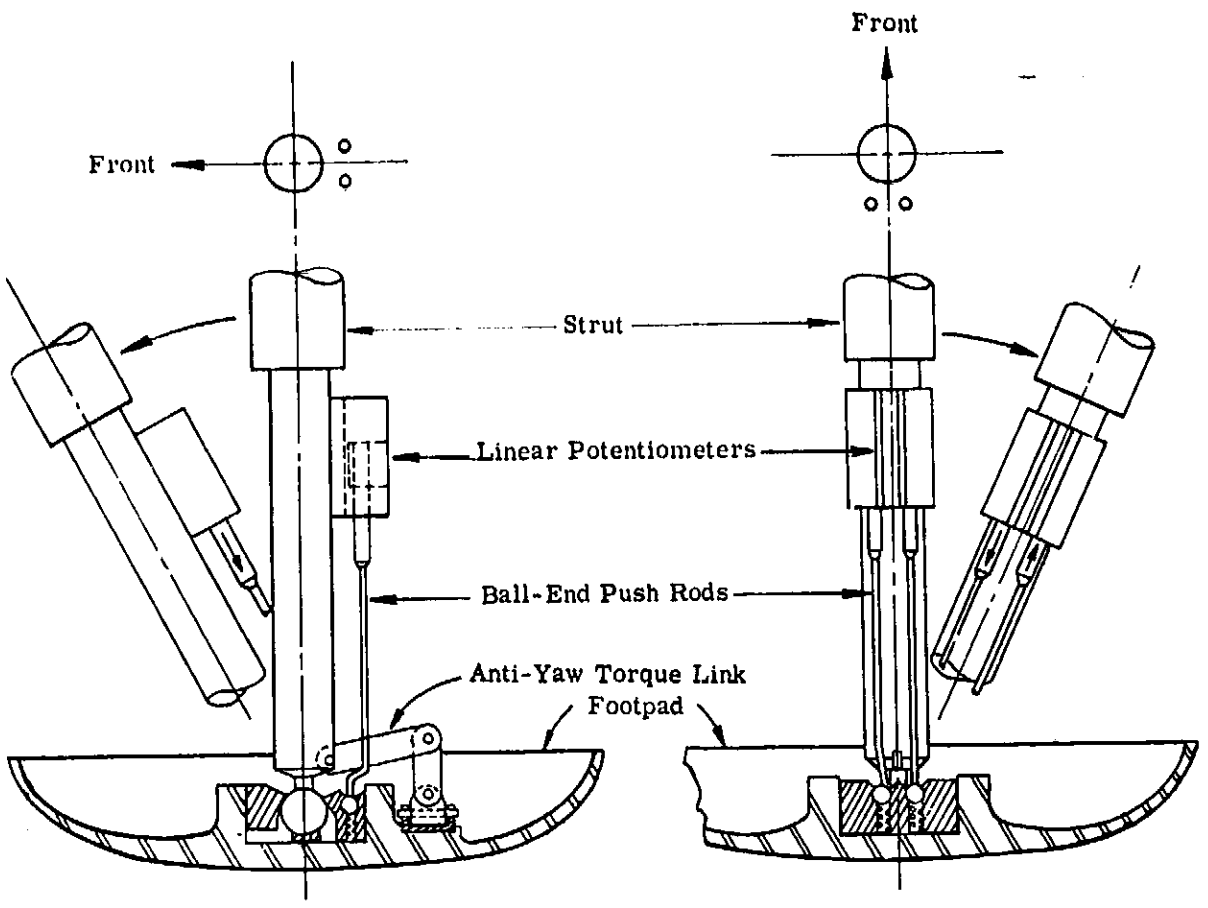

Figure 3-10. Subscale Instrumented Footpad for Drag Test

To measure footpad attitude, two small linear potentiometers are mounted on the rear side of the attachment strut approximately eight inches above the footpad. The potentiometers are actuated by thin ball-ended push rods which are attached to the footpad 45° each side of and behind the main pivot ball joint. Roll and pitch motions of the footpad, or combinations thereof, induce different outputs from each potentiometer from which the actual pad angular position can be calculated. The system is initially calibrated by moving the footpad to various known angles and recording the potentiometer outputs.

An antiyaw linkage prevents rotation of the footpad during tests. The footpad can be locked into a fixed attitude, when desired for certain tests, by replacing the main pivot ball retainer with a clamp-up fitting that is tightened firmly against the ball.

The potentiometers, push rod assemblies, and antirotation linkage are all located behind the attachment strut such that frontal area of the strut and footpad interior are not affected by the instrumentation. Protection of these parts from the soils and dust during tests is achieved by encasing the system in a plastic boot. The boot also extends over critical exposed portions of the instrumented load cell, described earlier.

3.2.6 Recording Instrumentation

Figure 3-11 presents a block diagram of the recording instrumentation used during the subscale drag test program. The oscillograph data records were manually reduced to provide the detailed information required from these tests.

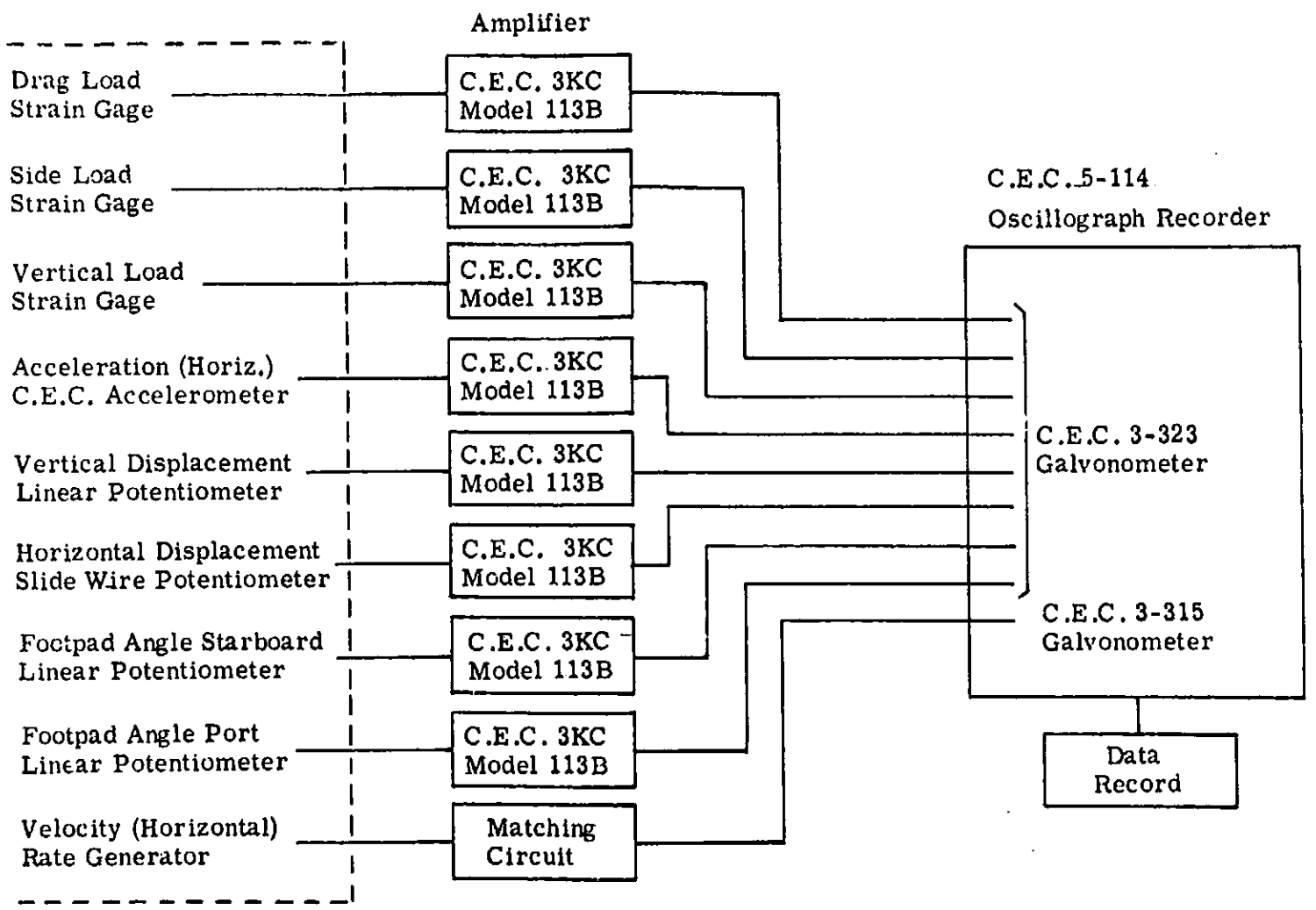

Figure 3-11. Diagram of Subscale Drag Test Data Recording Instrumentation

3.3 SUBSCALE OBLIQUE IMPACT TEST EQUIPMENT

3.3.1 Purpose and General Description

The oblique impact soil test equipment, shown in Figure 3-12, is designed to measure dynamic soil reactions on a footpad or other penetrating object which is impacting the soil at a controlled velocity, either vertically or at any desired angle with the soil surface between 0° (vertical) and about 80°. Equipment design is such that the impacting footpad moves as a free body before contacting the soil material, and the angle of impact can be maintained throughout the impact phase as well as during the penetration phase of a test.

This specialized test system facilitates individual control of the impacting mass, impact velocity, and angle of impact, with instrumentation devised to provide measurement of horizontal and vertical loads on the footpad, roll and/or pitch attitude of the footpad, and acceleration, impact velocity, and displacement of the footpad.

The oblique impact equipment was designed by Bendix during in-house studies and was used extensively during a subsequent program to develope a mathematical analysis for predicting earth landing behavior of the Apollo Command Module (ref. contract NAS 9-4511). The equipment was modified during the LM Soil Mechanics Study to accommodate testing of 1/6-scaled LM footpads. It is classified here as "subscale" equipment only to provide reference with the full-scale LM and other larger test equipment described in paragraph 3.4.

Figure 3-12 shows the equipment after modification and set up prior to a vertical footpad test over the three feet by eight feet by two feet deep soil bed. The system is essentially an air gun in which the impacting body is propelled by a combination of compressed air and gravity forces. The test footpad (A) is shown attached to the instrumented load cell (B) which is secured by a clevis (K) to the lower end of impact bar (J). The impact bar is fired by compressed air stored in pressure chamber (F) and manifold (G) acting on a small piston at the upper end of the impact bar.

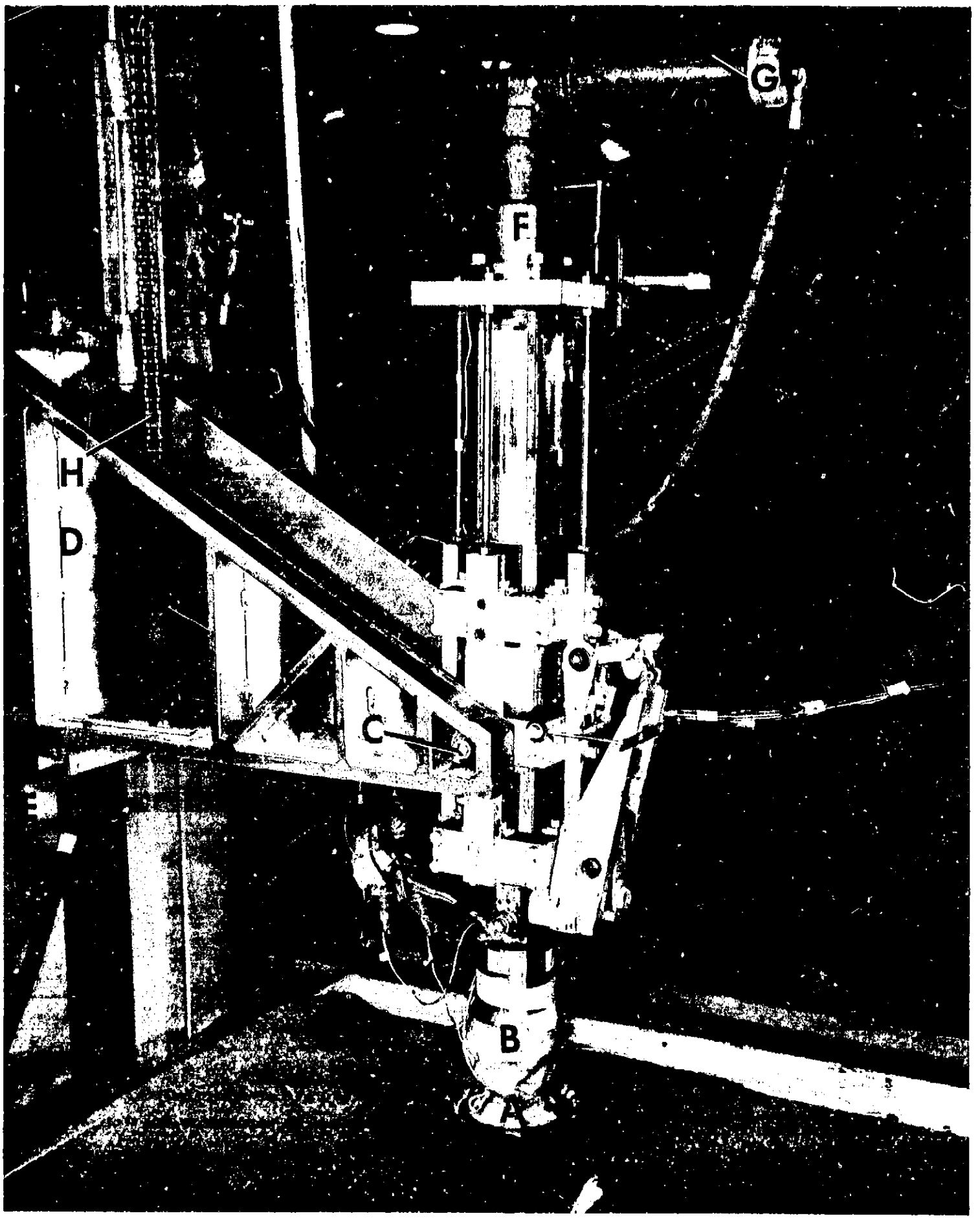

Figure 3-12. Subscale Oblique Impact Test Fixture

To vary the impact angle, the impact bar and firing mechanism rotates in support frame (D) around pivot point (C). The entire test system is mounted on a vertical I beam (E), and is raised or lowered by an air-operated chain hoist (H).

3.3.2 Equipment Modifications

Summarized below are the major changes that were incorporated in the originally developed impact test system to accommodate the 1/6-scaled LM footpad test and data requirements:

The impact bar was modified to allow both increasing and varying the impact mass by the addition of a number of small, circular lead blocks to the inside of the hollow bar. The lead weights are secured to the lower end of the impact bar by a special bolt added for this purpose. This cavity was previously part of the pressurized air storage system.

The above modification required redesign of the air pressure propelling system which included the addition of a small piston to upper end of the impact bar, replacement of the original adjustable stationary piston above the impact bar with an air cylinder, and the addition of an external manifold to provide sufficient compressed air volume.

Lateral rigidity of the equipment was increased by the addition of steel channel braces running diagonally to the outer end of the support frame.

A new instrumented load cell was required to measure footpad forces in three dimensions. This equipment is described in paragraph 3.3.4, and replaced a simpler and lighter weight unit previously used.

A 1/6-scale LM footpad, instrumented to measure footpad pitch and roll attitude, was added and is further described in paragraph 3.3.5.

In addition to the above, a new and larger soil bin was required, with suitable track and support for the soil bed preparation equipment.

3.3.3 Equipment Description and Operation

Figure 3-13 is a schematic layout of the oblique impact test equipment after modification. The main view shows the system set up for a vertical or 0° impact, and insert "A" illustrates orientation of the impact mechanism and footpad for a typical oblique angle test.

The 24-inch long, aluminum impact bar has a square cross section with all four faces surface ground to insure flatness and parallelism throughout their length. A 2-1/2-inch diameter hole, running lengthwise through the bar, is closed off at the lower end by a clevis fitting to which the instrumented load cell is attached. Lead weights, used to control impact mass, are installed in the 2-1/2-inch hole and anchored to the upper face of the clevis fitting by a retainer bolt.

The impact bar is supported by and slides on eight flat, Teflon-coated bearing plates mounted inside of a steel cage assembly. The bearing plates pivot to align with the surfaces of the bar and are adjusted at assembly to provide near zero clearance with the bar to restrain its motion to only one degree of freedom. Frequent cleaning and lubrication, in addition to the Teflon coating, minimize friction between the sliding surfaces.

An air cylinder is attached to the top of the bearing cage by four parallel steel rods, and its volume is extended by means of an externally attached manifold. A 2-1/2-inch diameter piston at the upper end of the impact bar extends approximately three inches into the discharge port of the air cylinder when the system is readied for test. A latching and release mechanism, mounted near the lower end of the bearing cage, locks the impact bar into its prefiring position. Operation is effected by introducing compressed air or gas into the manifold and air cylinder, and then triggering the release mechanism. The impact bar is accelerated by both air pressure and gravity forces until the piston clears the air cylinder discharge port, after which it travels as a free body except for the slight friction from the Teflon bearings.

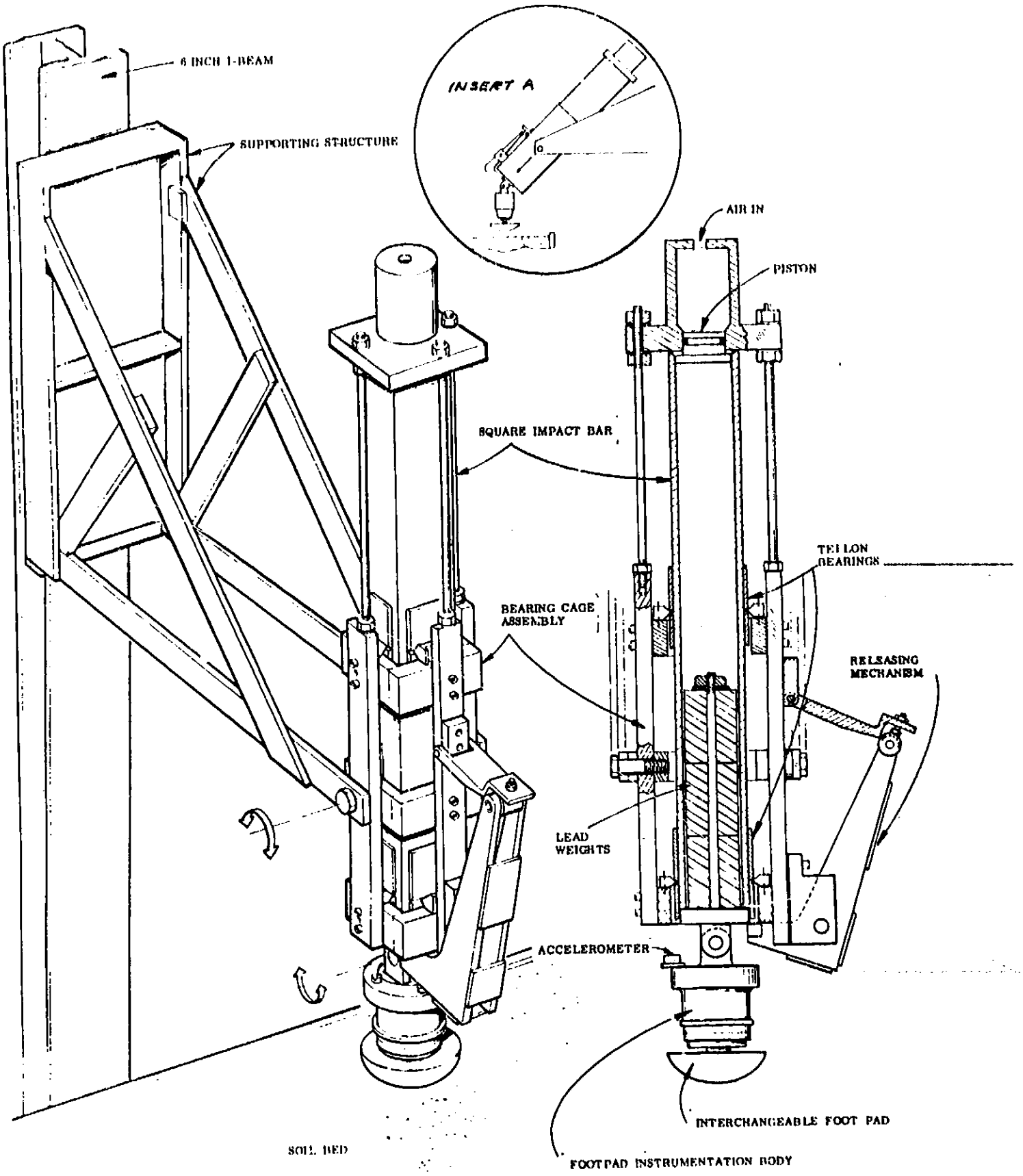

Figure 3-13. Subscale Oblique Impact Test Equipment

The bearing cage support structure is a welded steel frame, attached by bolts and clamps to a rigidly mounted vertical I beam, and is raised or lowered to the desired height above the soil bed by a powered hoist. The bearing cage can be tilted such that the footpad will impact the soil at any desired angle from vertical to near horizontal. The footpad/load cell unit is normally pivoted to compensate for angular adjustment of the impact bar (see insert, Figure 3-13), although the equipment design allows infinite variation of impact direction versus footpad orientation, if desired.

Impact mass of the system is determined by the combined weight of footpad, load cell, and impact bar, with mass variation accomplished by adding or deleting the number of lead weights installed inside of the bar. The minimum weight of the impact mass is about 32 pounds, and the maximum weight is about 50 pounds.

Impact velocity is controlled by varying the initial charging pressure in the manifold and the amount of travel or displacement of the bar before footpad impact. Velocities above 18 feet/second and impact forces up to 15,000 pounds vertical and 500 pounds horizontal can be obtained with the modified system.

Travel or stroke of the impact bar was measured by a slide wire potentiometer attached to one face of the bar. The instrumented load cell and footpad, discussed below, contained instrumentation to measure vertical, drag, and lateral forces acting on the footpad, as well as angular position of the pad. Acceleration of the impacting system was obtained from a high response accelerometer rigidly mounted on the top end of the load cell.

3.3.4 Instrumented Load Cell and Footpad

Figure 3-14 illustrates the three-axis load cell used to measure forces acting on the footpad during impact tests. Basic design of this unit and the sensing principles used to obtain both horizontal and vertical loads are identical to those developed for the subscale drag test equipment, and reference is made to paragraph 3.2.4 for a detailed description of the system. Since load magnitudes during impact tests are higher than those obtained from drag tests, all load measuring and/or load carrying elements of the impact test unit were designed proportionately stronger than for the drag test unit.

The load cell is attached to the lower end of the impact bar through the clevis fitting which permits angular adjustment of the cell and footpad assembly as desired.

The instrumented 1/6-scale footpad, shown in Figure 3-15, is fabricated from steel with outer contour duplicating the full scale LM footpad. The pad is attached to the lower end of the strut by a ball-socket joint designed to permit ±30° angular motion of the footpad in all directions.

Pitch and/or roll attitude of the footpad is measured by the two rotary potentiometers located at the intersection of links between the tilting footpad and the vertical strut as shown. The potentiometers, actuated by the upper links, are mounted on the lower links which are attached to swivel blocks in the footpad. Resulting linkage motion is such that each potentiometer measures footpad angular movement in only one plane. Initial calibration is achieved by moving the footpad to various known positions and recording the potentiometer outputs.

During calibration of the load cell sufficient checks were made to determine that cross-sensitivity effects between all three force measuring systems were negligible. The load cell calibration curves presented in Figures 3-16, 3-17, and 3-18 also illustrate the effects of drag-on-vertical, side-on-vertical, and vertical-on-drag load gages, respectively, and are typical of the interactions between drag and side load gages.

The footpad instrumentation components and exposed portions of the load cell are protected from dust and soil particles by encasing the system in a plastic boot.

3.3.5 Recording Instrumentation

A block diagram of the recording instrumentation used during the subscale oblique impact tests is shown in Figure 3-19. The oscillogram records were manually reduced to provide the necessary data.

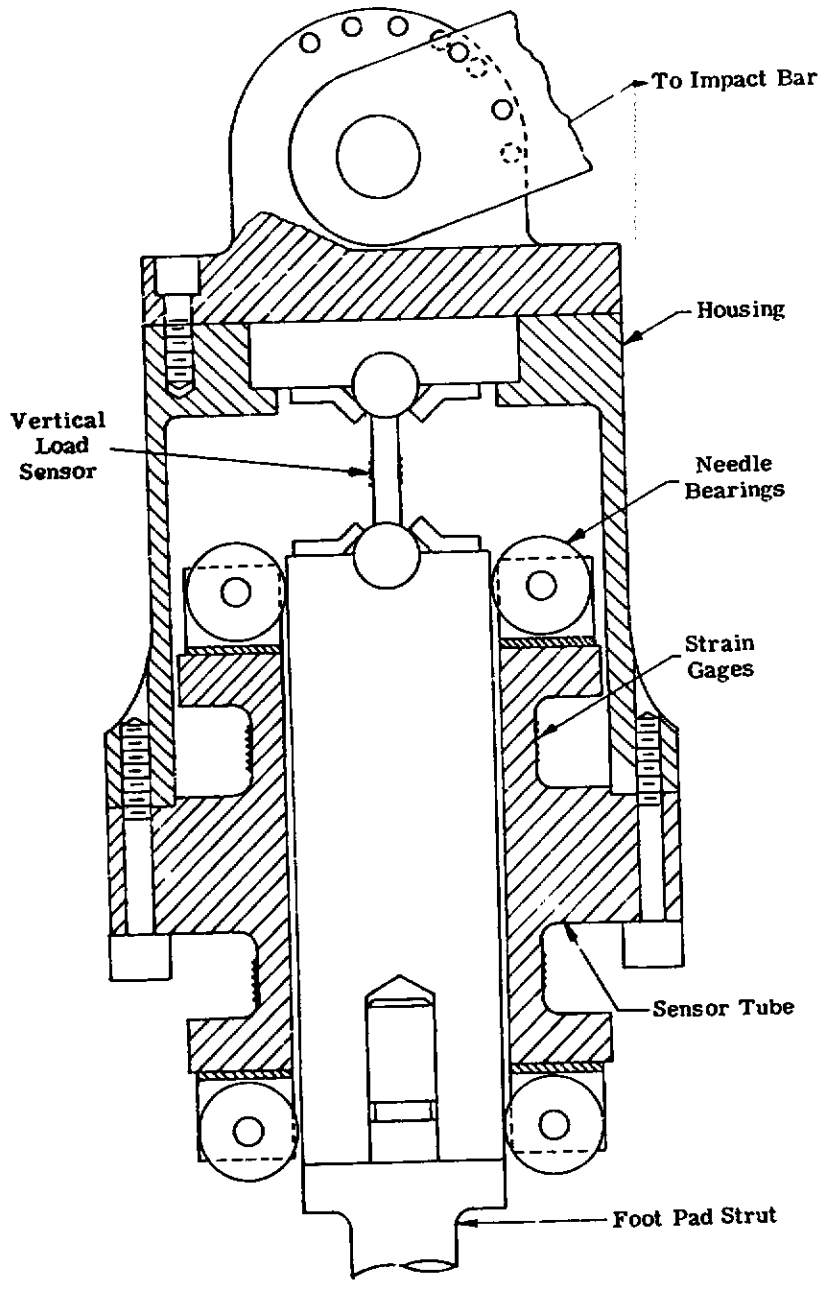

Figure 3-14. Three-Dimensional Load Cell for Subscale Oblique Impact Tests

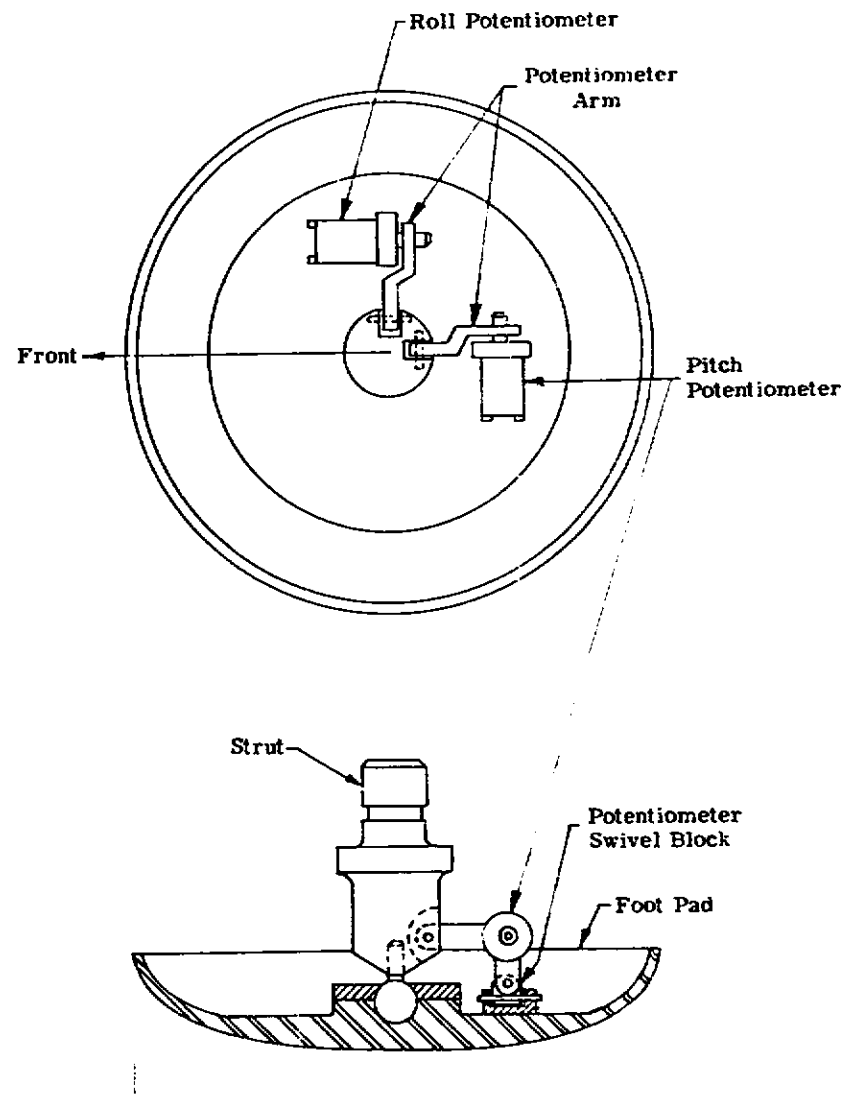

Figure 3-15. Subscale Instrumented Footpad for Oblique Impact Tests

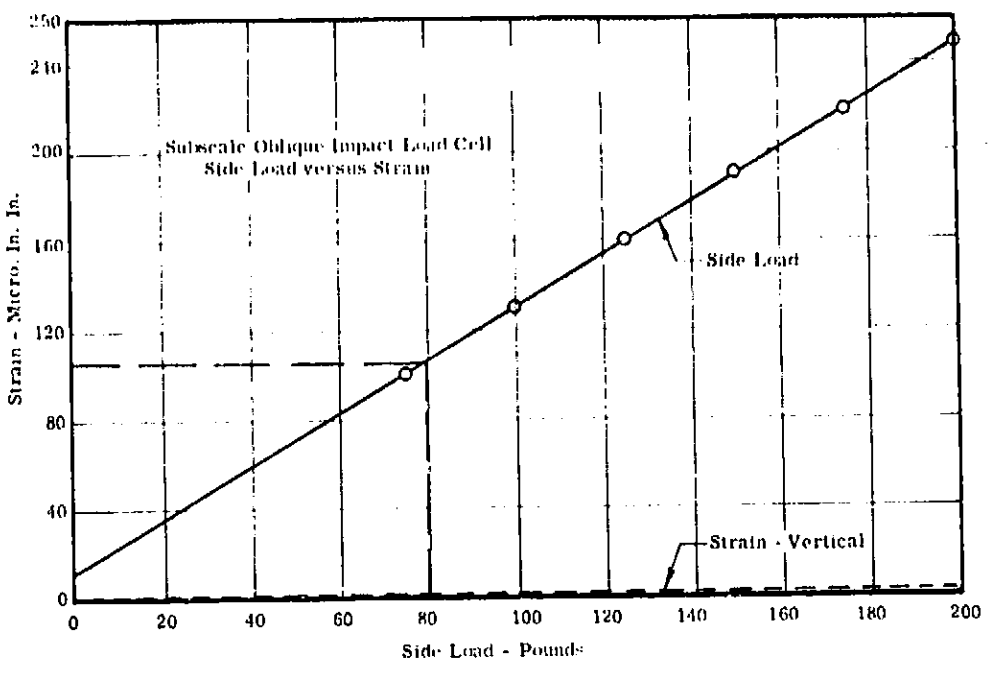

Figure 3-16. Effect of Drag Load on Vertical Load Sensor

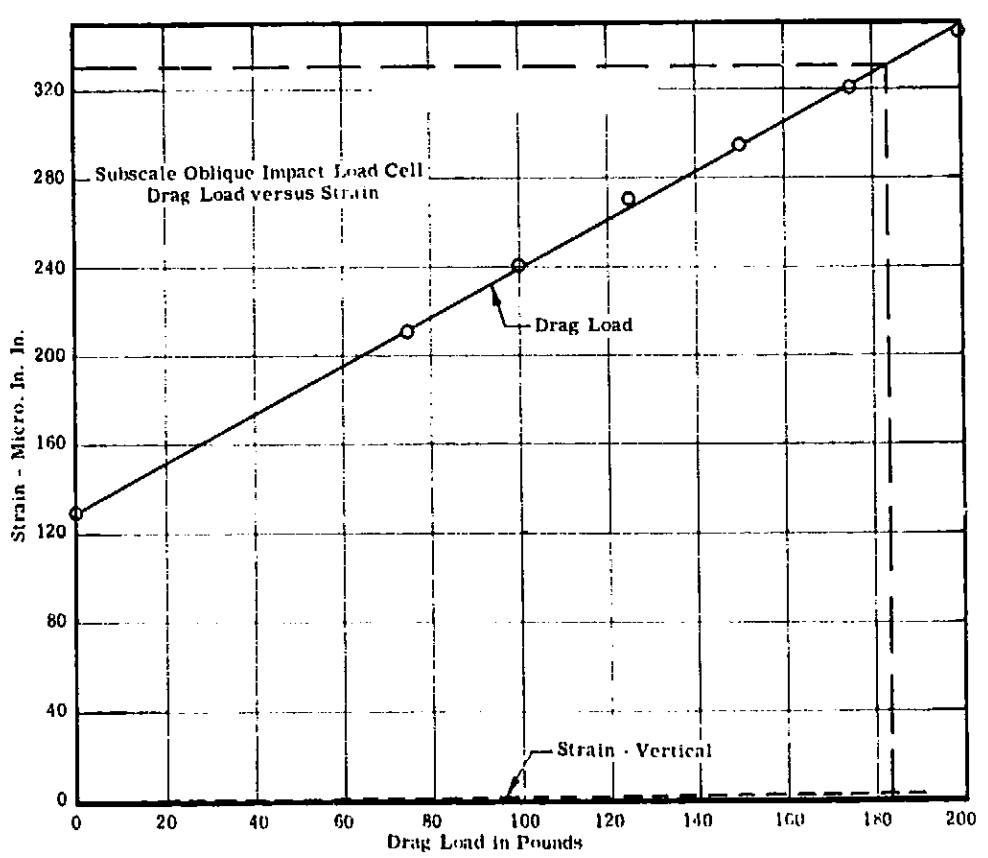

Figure 3-17. Effect of Side Load on Vertical Load Sensor

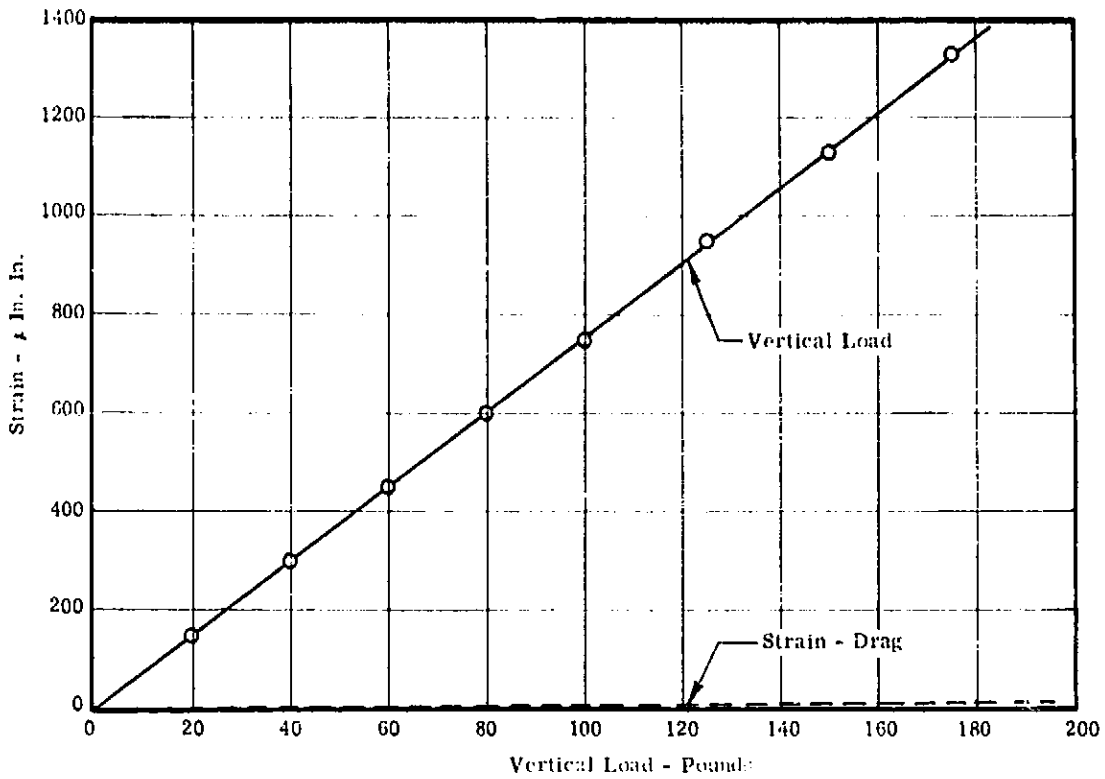

Figure 3-18. Effect of Vertical Load on Drag Load Strain

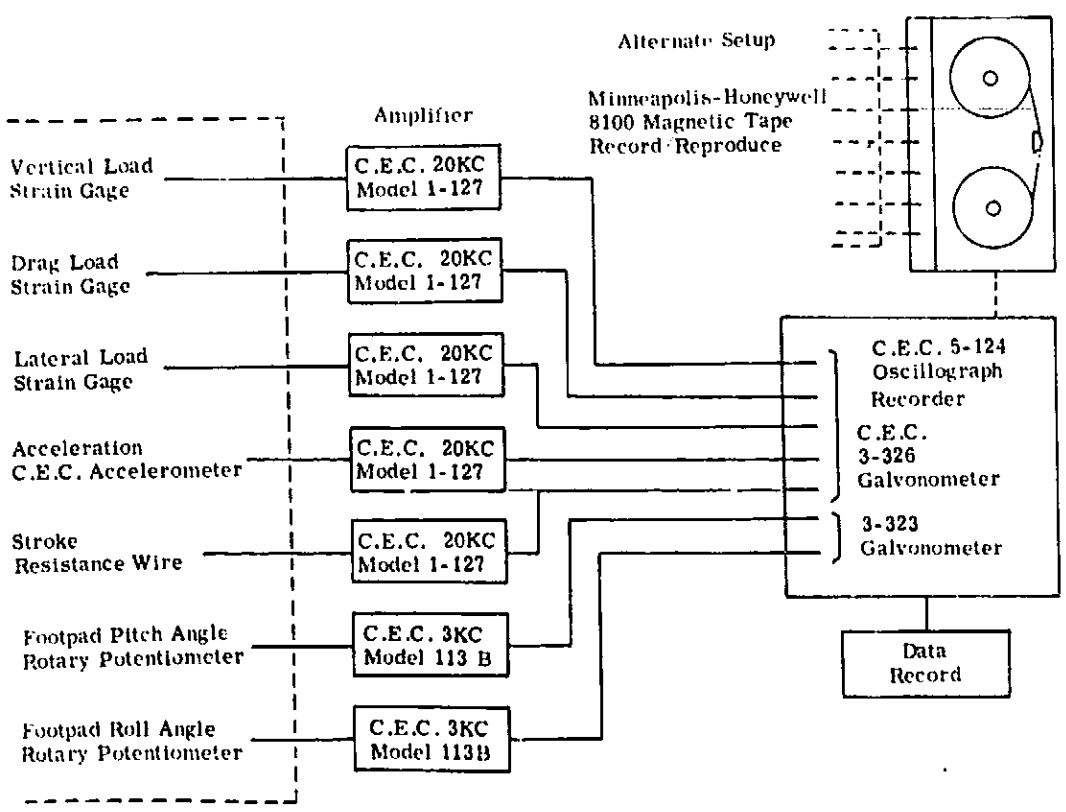

Figure 3-19. Diagram of Subscale Oblique Impact Test Recording Instrumentation

3.4 FULL-SCALE OBLIQUE IMPACT TEST EQUIPMENT

3.4.1 Purpose and General Description

The full-scale impact test equipment was designed to measure dynamic soil reactions on a full-scale simulated LM footpad impacting into the soil either vertically or at an oblique angle with the soil surface at a controlled impact velocity. The purpose of these tests was to provide a means to evaluate the scaling laws used in development of the LM soil interaction model by comparison of full and subscale experimental data having a common basis. Accordingly, basic design and implementation of the full-scale equipment is quite similar to the subscale equipment described in paragraph 3.3.

Figure 3-20 is a photograph of the full-scale system set up over one end of the 12-by 18-foot by 5-foot deep soil pit used for these tests. The equipment allows individual control of impact velocity, impact angle, and impact mass, with instrumentation to provide horizontal and vertical loads on the footpad and pitch attitude, acceleration, impact velocity, and displacement of the pad.

Similar to its subscale counterpart, the full-scale unit is essentially an air gun in which the impacting body is accelerated by a combination of compressed air and gravity forces. Figure 3-20 shows the full-scale footpad (A) attached to an instrumented load cell and support mechanism (B) which is secured to the bottom of the impact bar or ram. The ram is supported by a structure that pivots at (C) to vary the impact angle. A nitrogen charged cylinder (D) propels the ram and footpad mass to the desired velocity.

Support for the mechanism is provided by crossbeam (E) which is vertically adjustable on two support towers (H) by an electric powered chain drive arrangement. Counterweights (I) balance the weight of the impact mechanism and crossbeam and connect to the crossbeams by chains (F). The instrumentation wiring cable is shown as (G).

3.4.2 Equipment Design and Operation

Figure 3-21 is a schematic diagram of the full-scale equipment and Figure 3-22 presents some details of the design. Heavy-gauge structural steel was used to fabricate all members of the support structure and impact mechanism to minimize undesirable vibrations.

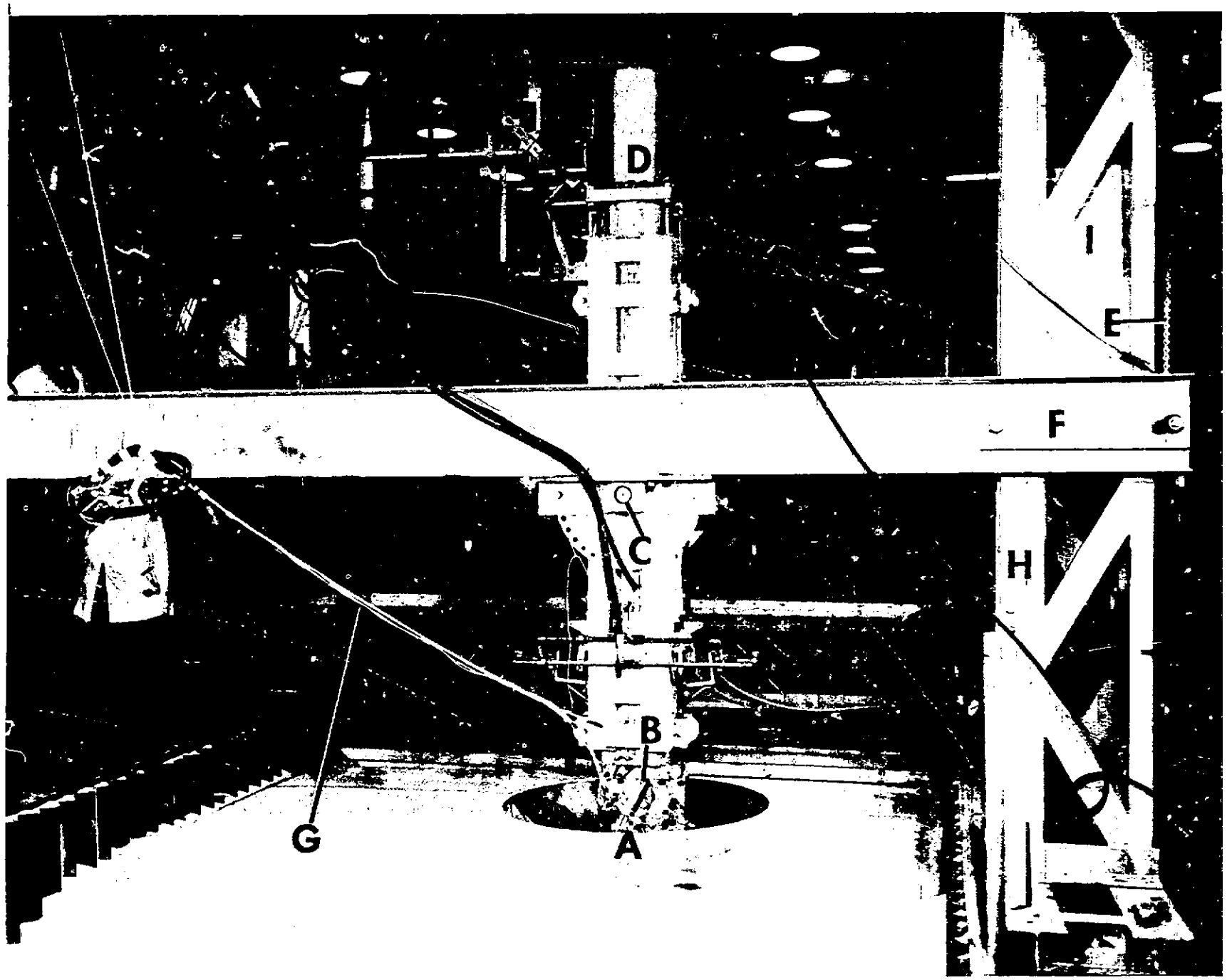

Figure 3-20. Full-scale Impact Test Fixture

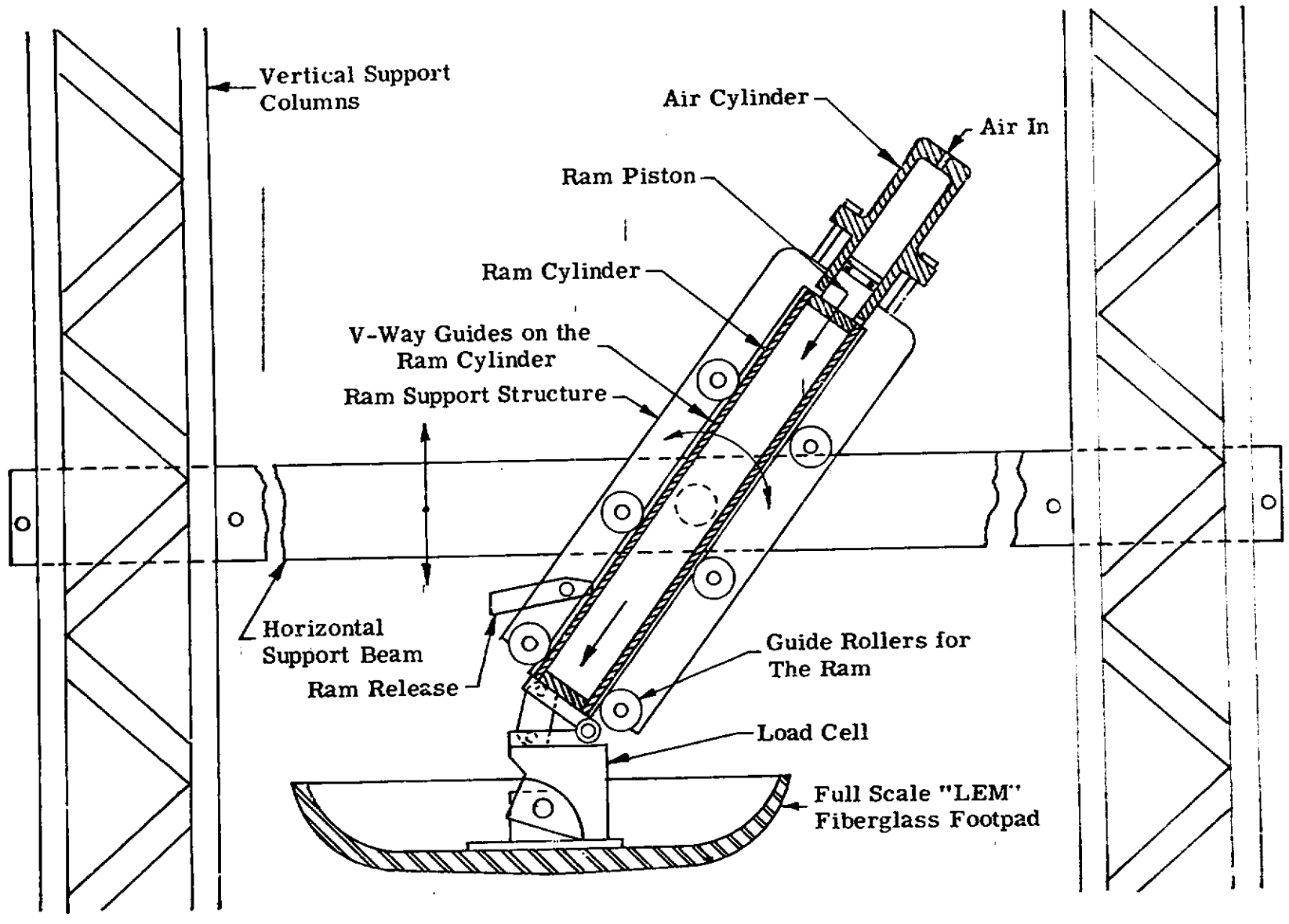

Figure 3-21. Full-scale Oblique Impact Test Rig

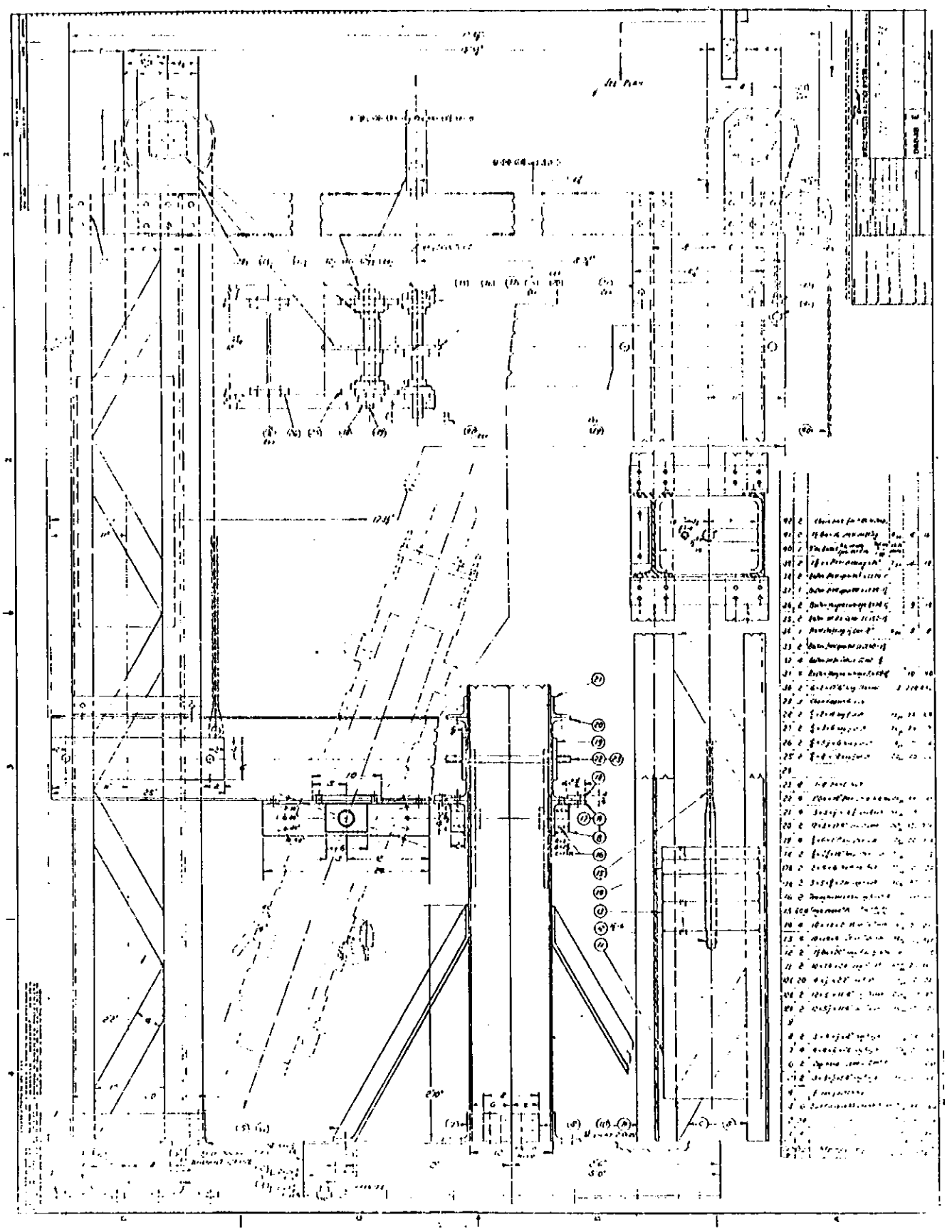

Figure 3-22. Oblique Impact Test Structure - Assembly

The support structure design permits positioning the impact mechanism horizontally along the beam to control the footpad impact zone in the soil bed. The crossbeam is fabricated from 12-inch deep steel channels, spaced to support and pivot the impact mechanism between them and suitably braced to form a rigid structure across the 12-foot wide soil bed. The ends of the beam are tightly secured to the support towers during test, and loosened for adjustment to the desired impact height.

The towers are box-section, fabricated from steel I beam, channel and plate stock, approximately 12 feet high, and firmly braced and anchored to the floor. The lead counterweights hang inside of the box-section and can be varied to compensate for changes in mass of the impact ram. The weights are attached to the crossbeam ends by heavy roller chains extended over large sprockets mounted at the top of each tower. An electrically powered drive sprocket, located near the top of one tower, engages one of the balancing chains to raise or lower the crossbeam. A separate set of sprockets and a roller chain between the towers synchronizes motion of the counterweights so that the crossbeam always remains horizontal.

The impact ram is made from hollow, eight-inch square steel tubing, about 5-1/2 feet long. Steel "V" ways are welded lengthwise to the centers of two opposing surfaces and machined to close tolerance for parallelism and straightness. The "V" ways engage — three pairs of "V"-grooved bronze guide wheels which are precision mounted on needle race and thrust bearings and attached to the ram support cage. The wheels are adjusted at assembly such that the impact ram has practically zero lateral clearance or "slop" and can move only in the axial direction. The free-rolling guide wheel design insures low friction which is further minimized by frequent cleaning of the "V" ways and lubrication of the bearings.

The lower end of the impact ram is capped with a heavy steel plate to which the instrumented load cell is attached through an adjustable hinged fitting. Lead blocks, used to vary the impact mass of the system, are mounted in the hollow interior of the ram and secured firmly together and to the bottom of the ram by a threaded steel rod which extends upward from the bottom plate.

A six-inch diameter piston is attached to the upper end of the ram and extends approximately six inches into the discharge port of the air cylinder chamber when the unit is positioned for test. The air cylinder is centered over and attached to the upper end of the ram support structure and provides the storage volume for compressed gas used to propel the impact ram. Locking and release of the ram is effected by two pneumatically-operated latches located on opposite sides of the cage structure near its lower end.

The impact bar is accelerated by the combined forces of gravity and air pressure until the piston clears the air cylinder port. It then travels as a free body except for very slight friction from the "V" wheels. The mechanism can be pivoted to provide an impact angle range between vertical and 40° from vertical. During angular impact tests, the load cell/footpad assembly is aligned vertically to compensate for the impacting angle, although the footpad can be varied (in the plane of the impact angle), if desired for special tests. A slide wire potentiometer - mounted lengthwise within the ram support cage - measures axial displacement of the ram.

The impacting mass is the combined weight of the footpad, load cell, impact ram, plus the lead weights installed in the ram. Minimum mass of the system is about 570 pounds, and with all lead blocks installed this can be increased to about 1300 pounds. By varying the mass, the height adjustment, and the charging pressure in the air cylinder, the system provides a range of impact velocities up to 15 feet/second with impact forces up to about 360,000 pounds vertical and 10,000 pounds horizontal.

3.4.3 Instrumented Load Cell and Footpad

Since the primary purpose of full-scale impact tests was to provide data for direct comparison with selected subscale test data, some reduction in the complexity of the load sensing system previously used was both desirable and practical. Accordingly, the footpad angular motion was limited to rotation in the pitch plane only, and forces were measured only in that plane. This permitted a two-axis rather than three-axis load measurement scheme.

Figure 3-23 is a schematic diagram of the load cell and footpad arrangement used. The load cell was designed with one ball-ended instrumented vertical link to measure forces in the vertical direction, and two pin-ended horizontal links to measure drag forces as a couple. One end of these sensors is attached to the rigid steel housing of the load cell which is maintained in vertical alignment at all times (regardless of impact angle) by the adjustable hinge fitting. The other end of each sensor is fastened to a steel strut which forms the footpad attachment fitting. The strut is kept in vertical alignment with the load cell housing by the load sensors and design arrangement.

During load cell calibration, cross-sensitivity of the vertical and drag load measurement system was checked, with the results shown in Figure 3-24 and Figure 3-25. Although the interactions for this load cell are slightly larger than for either of the subscale systems, the effects are still considered relatively insignificant. They are most probably a result of small variations between actual cell geometry under load and idealized (design) geometry, caused by clearances at the various sensor joints.

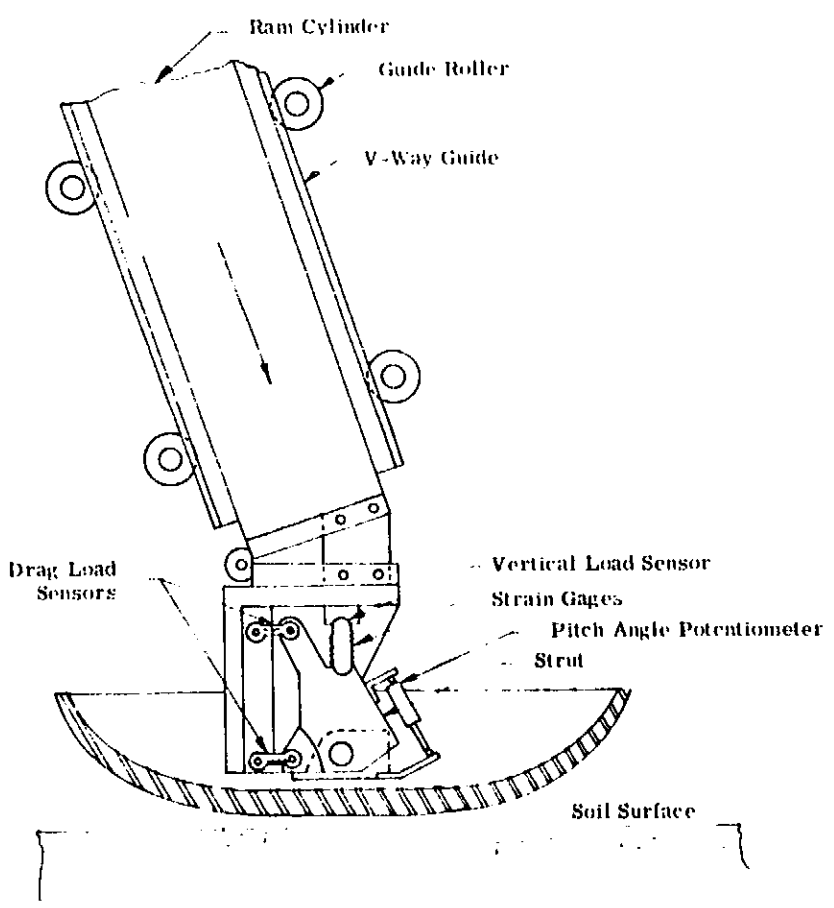

Figure 3-23. Full-scale Load Cell and Footpad

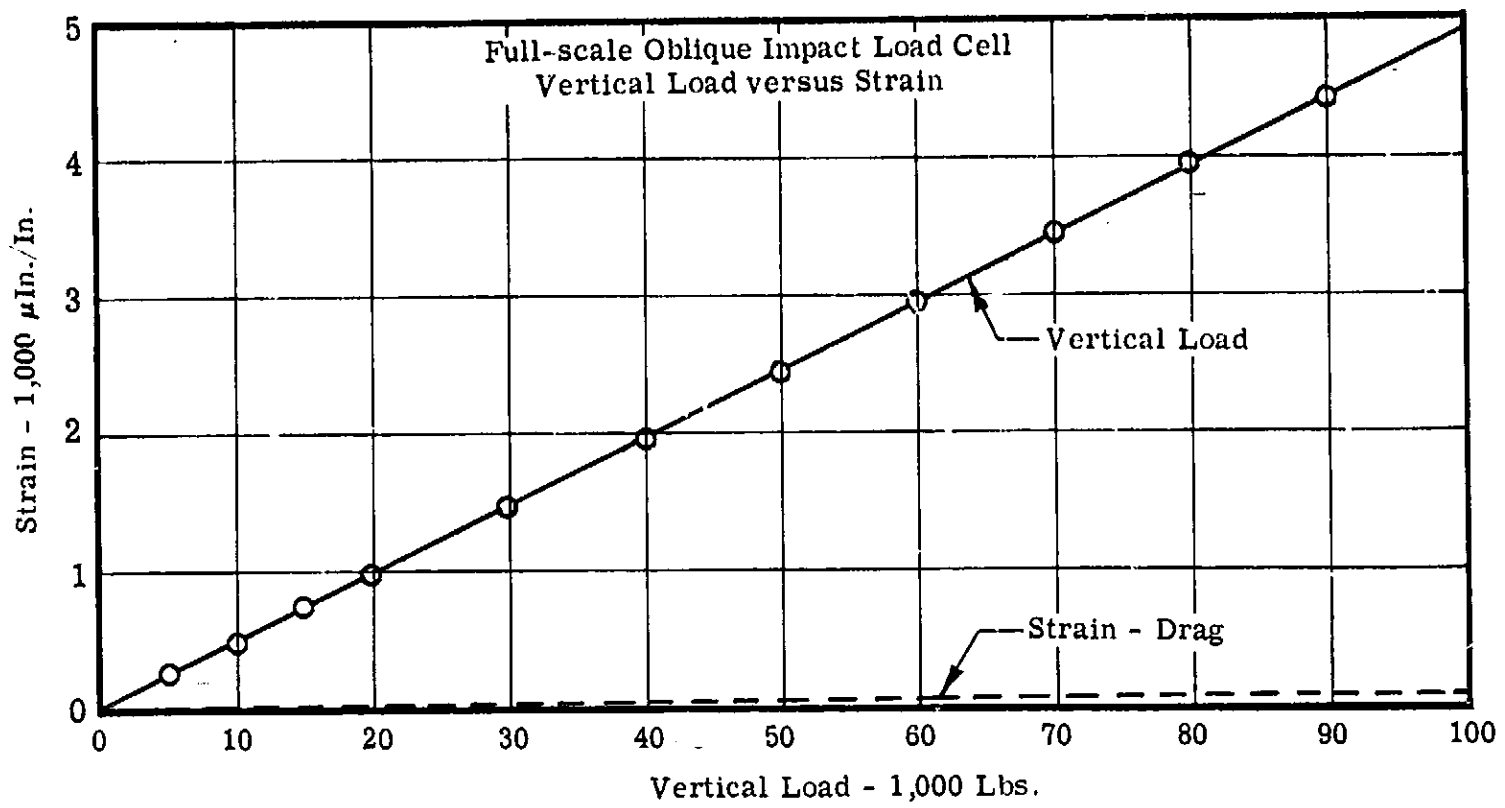

Figure 3-24. Effect of Vertical Load on Drag Load Sensors

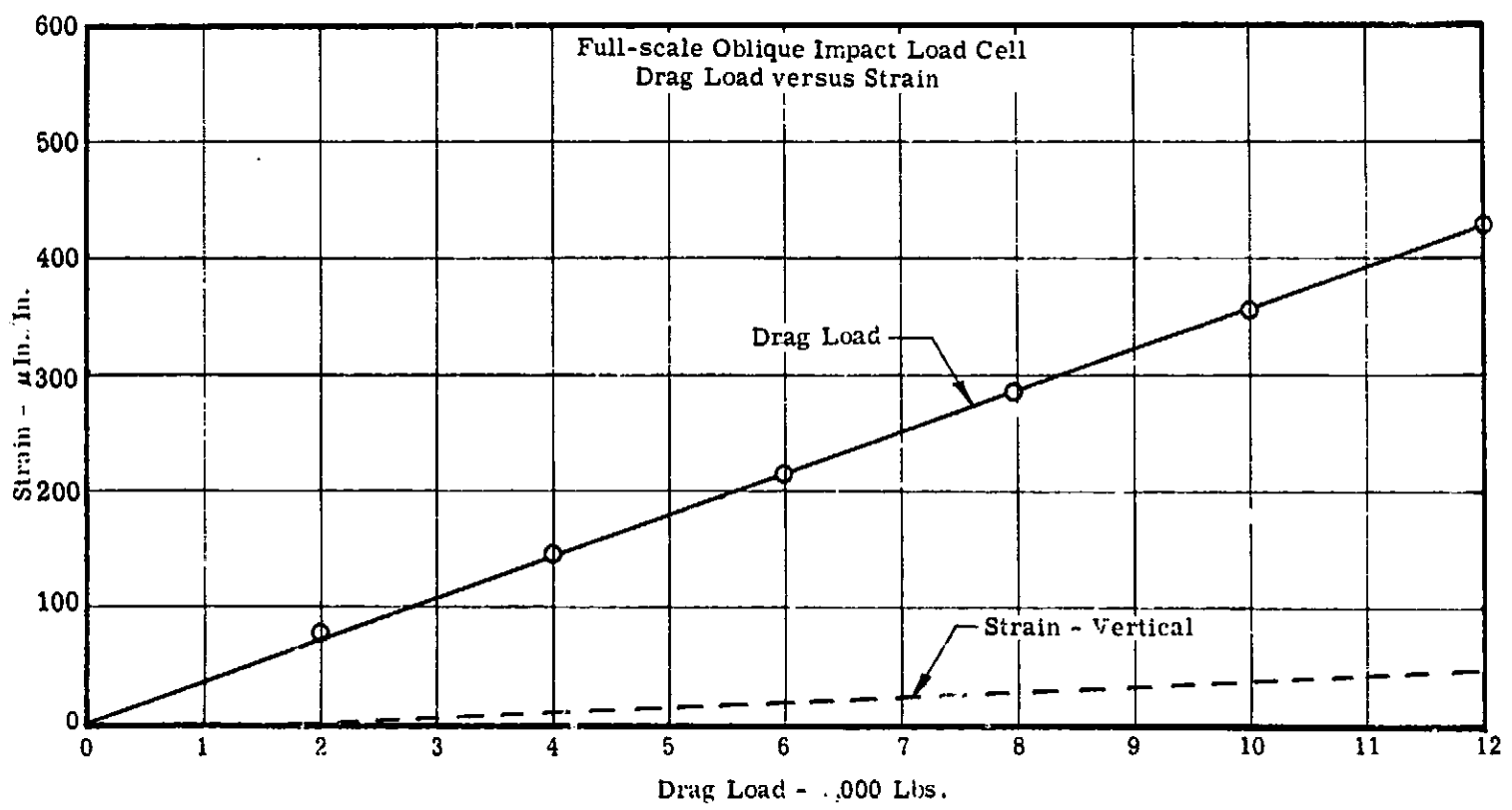

Figure 3-25. Effect of Drag Load on Vertical Load Sensor

The footpad is attached to the strut by a steel pin through the mating clevis lugs which restrict the footpad rotation to the pitch plane. Angular motion of the footpad is measured by a linear potentiometer mounted between the footpad clevis fitting and the strut. Two accelerometers are mounted on the strut (one each in the vertical and drag planes) to measure vertical and drag accelerations of the impacting mass.

The footpad used for full-scale impact tests is identical to the LM footpad in physical size and contour but differs radically in strength to accommodate the higher and repeated loading cycles to which it was subjected.

Figure 3-26 illustrates the design which is an epoxy/glass fiber composite generated over a disposable form and then cured and machined to final contour. Construction is simplified by simultaneously forming two identical pads, as shown, and then separating them at the intersecting plane.* The mounting clevis is securely embedded into the structure during fabrication. A spun-aluminum skin is bonded over the outer surface to simulate frictional characteristics of the actual LM pad.

Footpad and load cell exposed instrumentation components are protected from dust and soil particles by encasement in a plastic boot.

3.4.4 Recording Instrumentation

Figure 3-27 is a block diagram of the recording instrumentation arrangement used during the full-scale oblique impact tests. The oscillogram records were manually reduced to provide the necessary data.

3.5 FULL-SCALE DRAG TEST FACILITY DESIGN

3.5.1 Purpose and General Description

The original program technical plan required the design and construction of a footpad drag test facility of suitable size and power to enable testing a full-scale simulated LM

*The mating, unfinished footpad was originally planned for use with the full-scale drag test facility, described in paragraph 3.5.

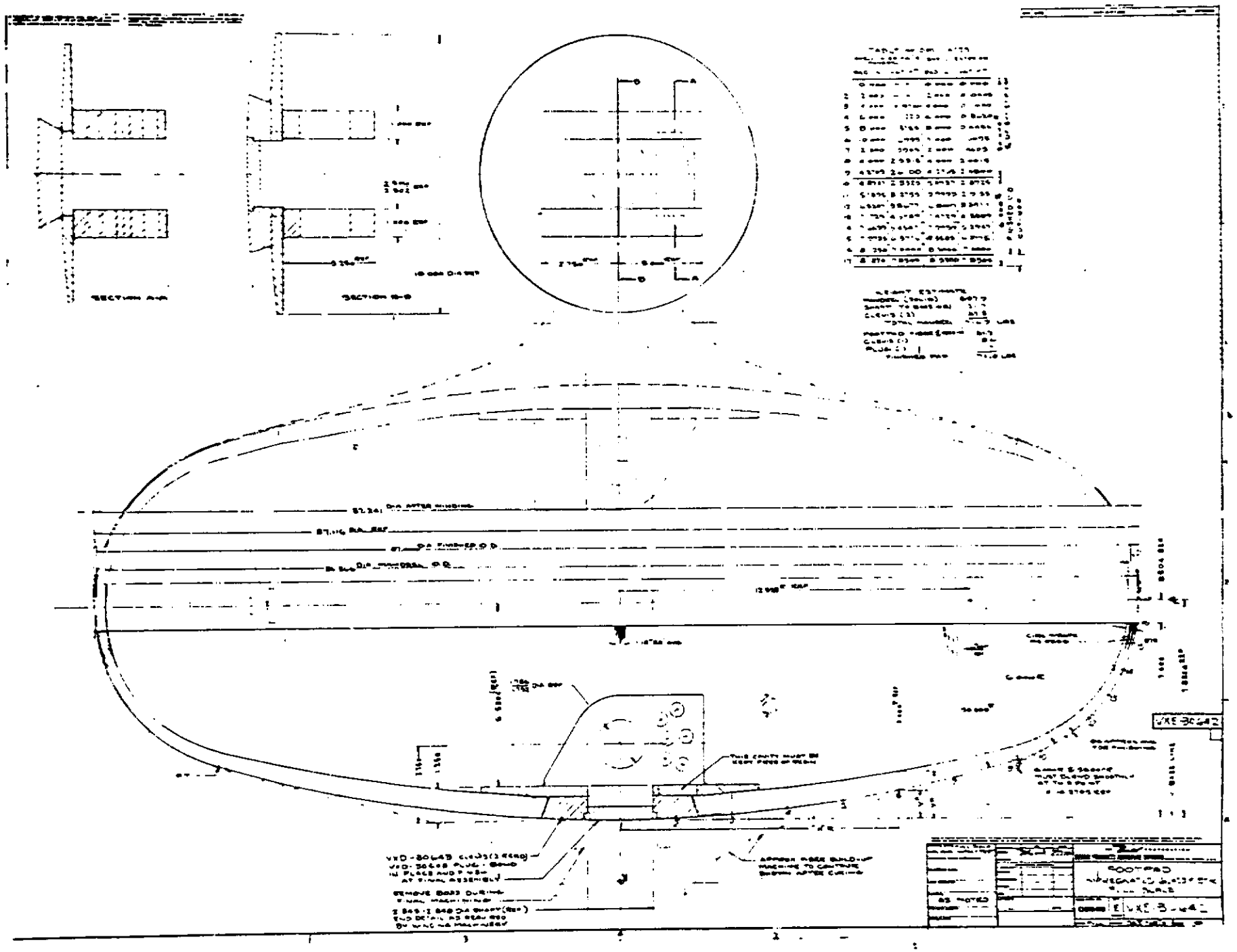

Figure 3-26. Simulated LM Footpad

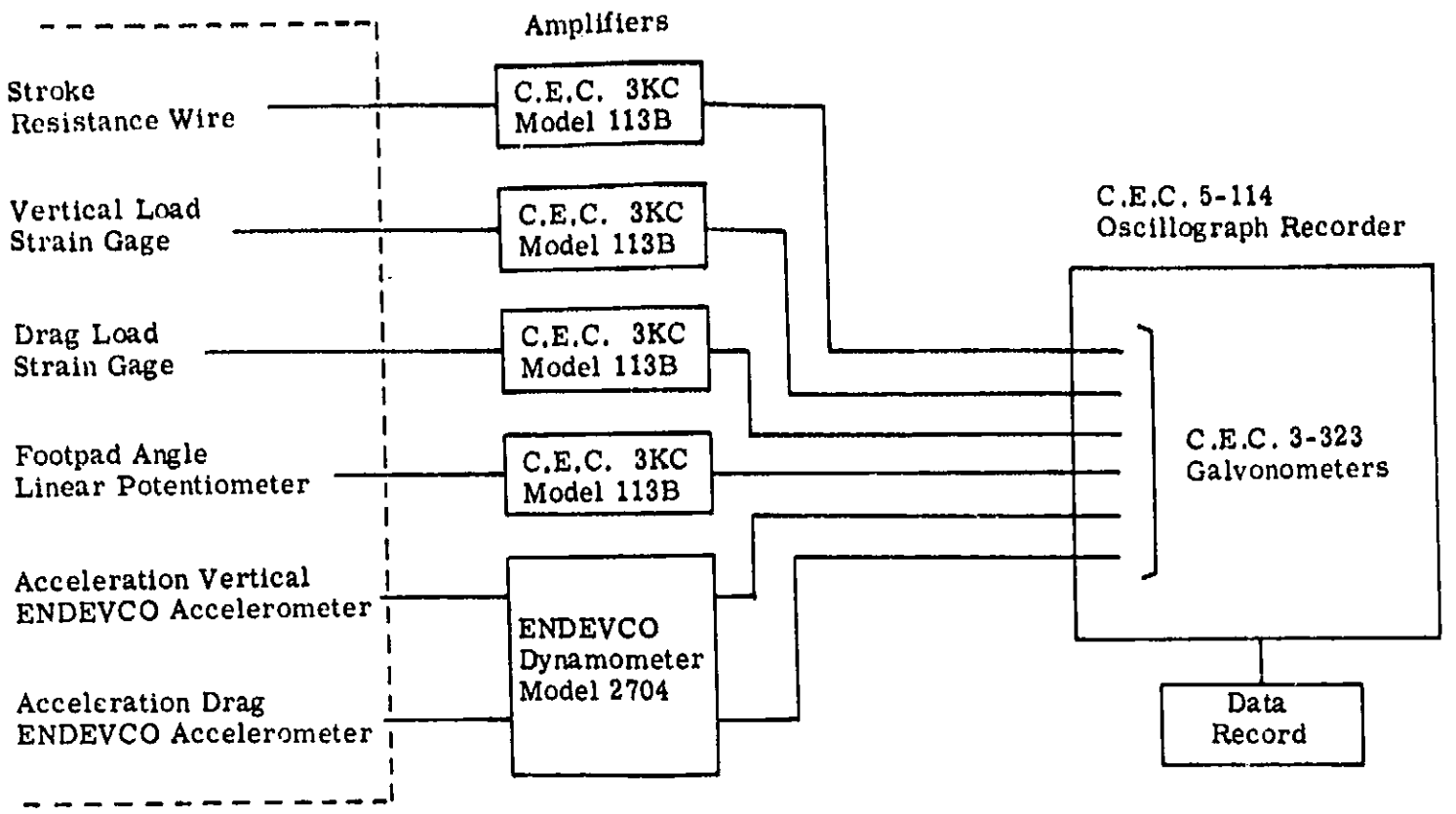

Figure 3-27. Full-scale Oblique Impact Test Recording Instrumentation

footpad in the various soil materials. This facility was intended to complement the subscale drag test equipment that was used during the program, described in paragraph 3.2.

For various reasons, actual construction of the full-scale system was deleted from the technical requirements shortly after program start. However, each of the three basic equipment components was carried through design to a stage that would permit hardware procurement and installation with a minimum of additional design costs and schedule. A summary description of the system that resulted from this effort is presented here, while a detailed discussion of each major component, operation of the system, and performance predictions are covered in Appendix D of this report.

The major equipment components of the full-scale facility are:

*1. The hydraulic power/control unit, including actuator and electrical controls.

2. The carriage and gantry structure to support and guide the instrumented strut and landing pad over the soil test beds.

3. The instrumented strut and full-scale simulated LM footpad.

Figure 3-28 is a sketch of this equipment installed over a soil bed. Floor space requirements are approximately 60 by 12 feet with maximum height less than 12 feet. The soil bed is a rectangular concrete pit 10 feet wide by 24 feet long and 5 feet deep with adjacent areas suitably reinforced to support the gantry and anchor the power/control system. Mobility of the gantry and power system facilitates a multiple soil bed arrangement with pits located adjacently.

The system was designed to accommodate either constant penetration or constant load drag tests of a full-scale LM simulated footpad at any constant velocity between two feet/second and fifteen feet/second with drag loads up to 7,000 pounds and footpad penetrations up to two feet. System capabilities predicted from analysis include achieving steady-state velocity within ±0.25 foot/second, and maintaining velocity variation within 0.1 foot/second during the test run with load fluctuations up to ten percent.

3.5.2 The Hydraulic Power/Control Unit

The hydraulic power/control unit, shown in Figure 3-29, provides and controls the draw-bar force required to move the footpad/strut and carriage assembly through acceleration, constant velocity, and deceleration phases of its transit across the soil bed. Choice of this type of system resulted from a feasibility study which also considered several electrical and mechanical drive arrangements.

---

*Design of the Power/Control Unit was accomplished by the Bendix Missile Systems Division, Mishawaka, Indiana, to meet technical requirements established by the Energy Controls Division. This work was performed between June and October 1966, under a working arrangement between the two Bendix Divisions.

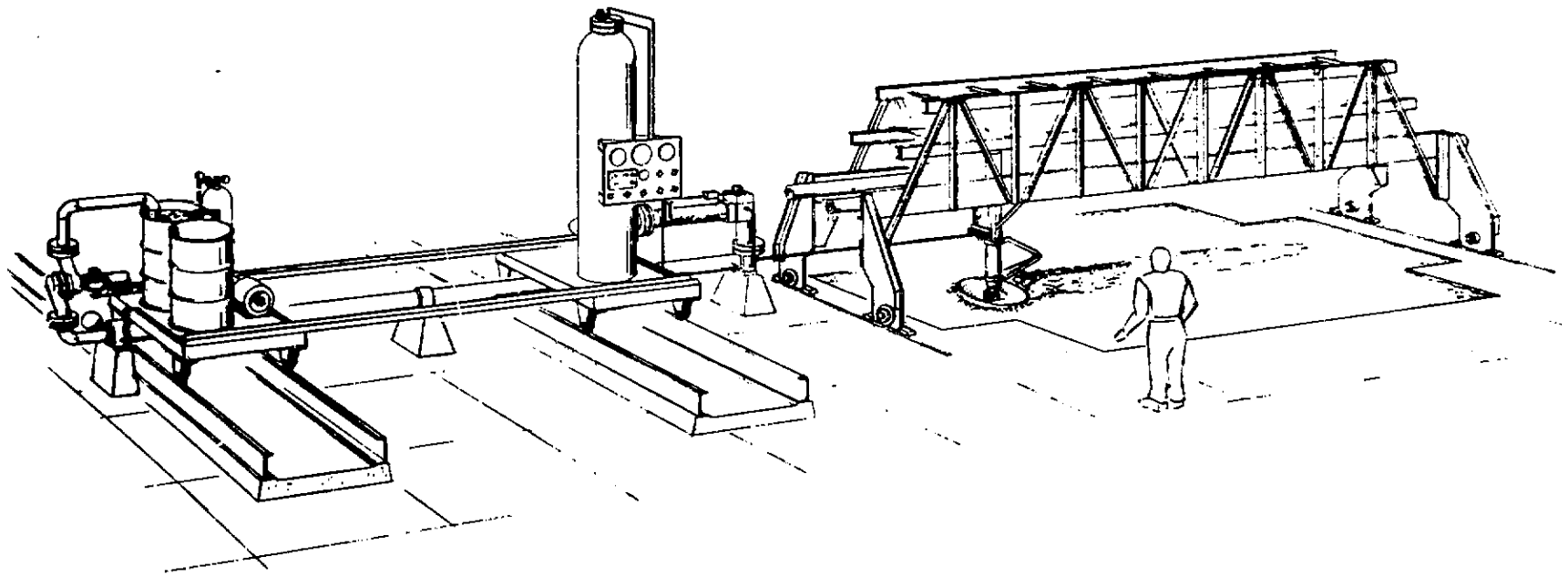

Figure 3-28. Perspective View of the Full-scale LM Footpad Drag Test Facility

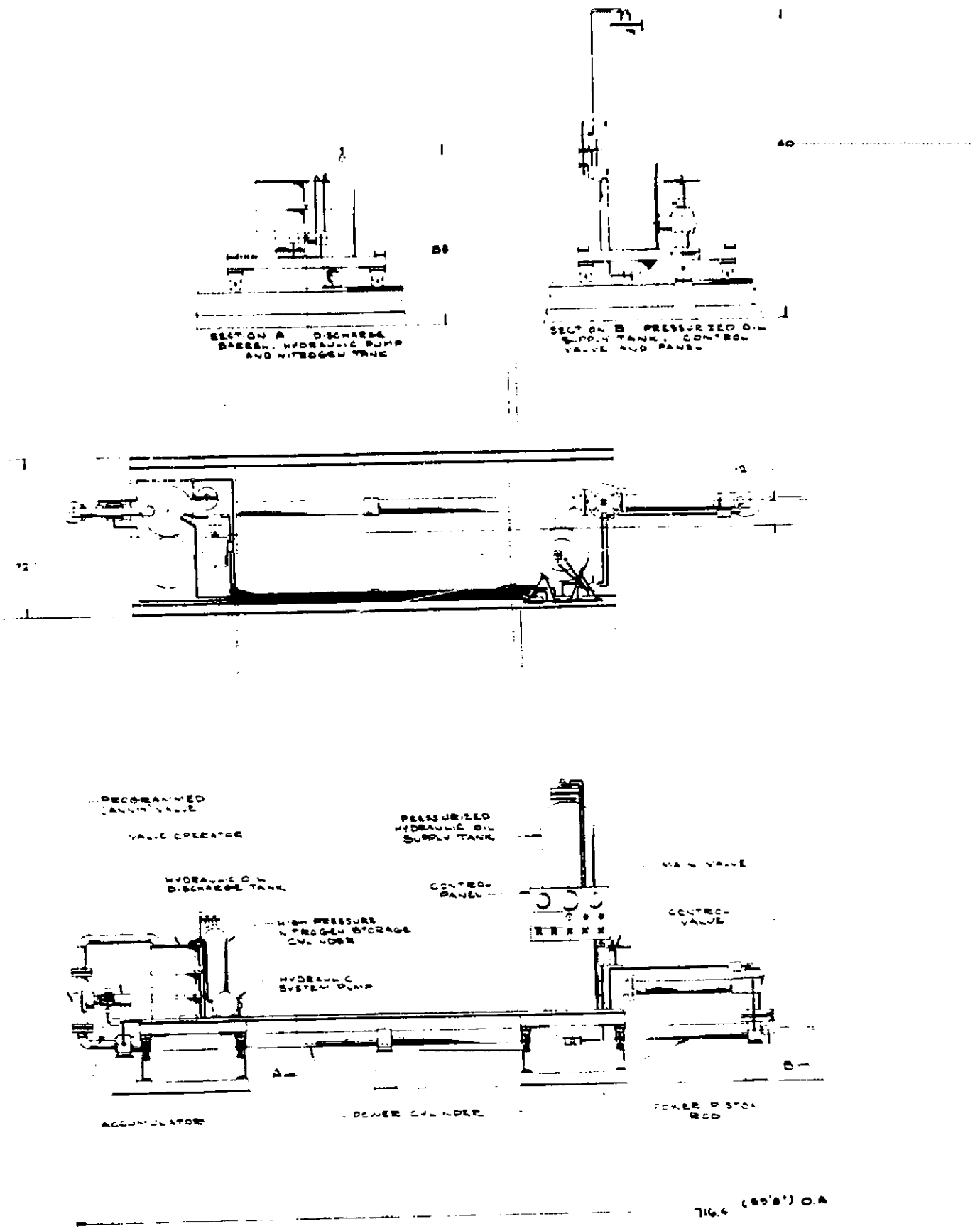

Figure 3-29. General Arrangement Hydraulic Power/Control Unit

The unit consists, essentially, of a five-inch diameter, 21-foot stroke hydraulic actuator and integrated hydraulic-electric control system. It is capable of accelerating a 7,000-pound load to scheduled velocity within three feet maximum travel and of maintaining an accurately programmed steady-state velocity for a minimum of 15 feet. Deceleration is accomplished within the final three feet of available piston travel.

The operating force is generated by compressed nitrogen gas at 2,000 psi acting upon the surface of hydraulic oil within a 20-cubic-foot pressure storage tank.

The required footpad velocity versus displacement profile is achieved by a high-response control valve which programs the rate of oil flow to the power piston during operation. The rate of travel is established by the control valve pneumatic setting and orifice selection. Both analog and digital computer analyses were used to evaluate the power/control system performance and to optimize critical sizes and arrangement of certain of the control valve components

The system is essentially open-loop in that there is no direct signal feedback to the valve from the moving carriage. However, it is a closed-loop system from the standpoint that flow to the power cylinder is sensed and regulates the control valve. Results of the analytical studies indicated good velocity control with only the flow feedback feature, although a carriage motion sensor could be incorporated - if found necessary - without major redesign of the system.

3.5.3 The Carriage and Gantry Structure

The instrumented strut and footpad is suspended from and guided across the soil test bed on a gantry supported carriage towed by the hydraulic piston drawbar. The carriage slides on circular bronze bushings engaging a pair of parallel tubular steel rail-like members within the gantry.

The carriage is approximately five feet long and two feet wide, excluding the two circular bearing housings located at each end. It is made of structural steel with suitable provisions for mounting of the instrumented strut and attachment of the drawbar.

The gantry is, essentially, a 31-foot long structural steel bridge that spans the length of the soil test bed and supports the carriage on the tubular rails. The design contains features for both vertical and lateral adjustment of the rails to enable leveling and to insure absolute parallelism and straightness throughout their length.

The gantry can be moved laterally for the selection of various test areas or for servicing or "parking" while test soil beds are under preparation. Relocation is accommodated by pairs of wheels on each end of the structure which can be lowered for the relocation operation or retracted to permit bolting the entire structure solidly against the floor during execution of the drag tests.

3.5.4 The Instrumented Strut and Footpad

The strut shown in Figure 3-30 is a variable-loading, extendable pneumatic cylinder rigidly mounted to the gantry carriage. The lower end terminates in a load cell equipped with a ball-clevis to which the footpad is attached. The load cell has the capability of sensing and transmitting data pertinent to footpad vertical, side, and drag loads, while a potentiometer at the junction of the strut torque arms senses strut length or depth of footpad penetration. Except for physical size of its components the basic design of the three-axis load cell and the sensing principles used are identical to those developed for the subscale drag test equipment, and reference is made to paragraph 3.2.4 for a detailed description.

Strut length has been optimized to provide a maximum footpad-soil penetration of 24 inches, while regulation of the strut cylinder pneumatic pressure permits a broad range of footpad loading conditions. A locking mechanism incorporated into the strut permits it to be manually fixed at any height increment between "park," at six inches above the soil surface, and maximum penetration. The main structural components of the strut would be fabricated from steel with lower end contours approximating those of the actual LM hardware.

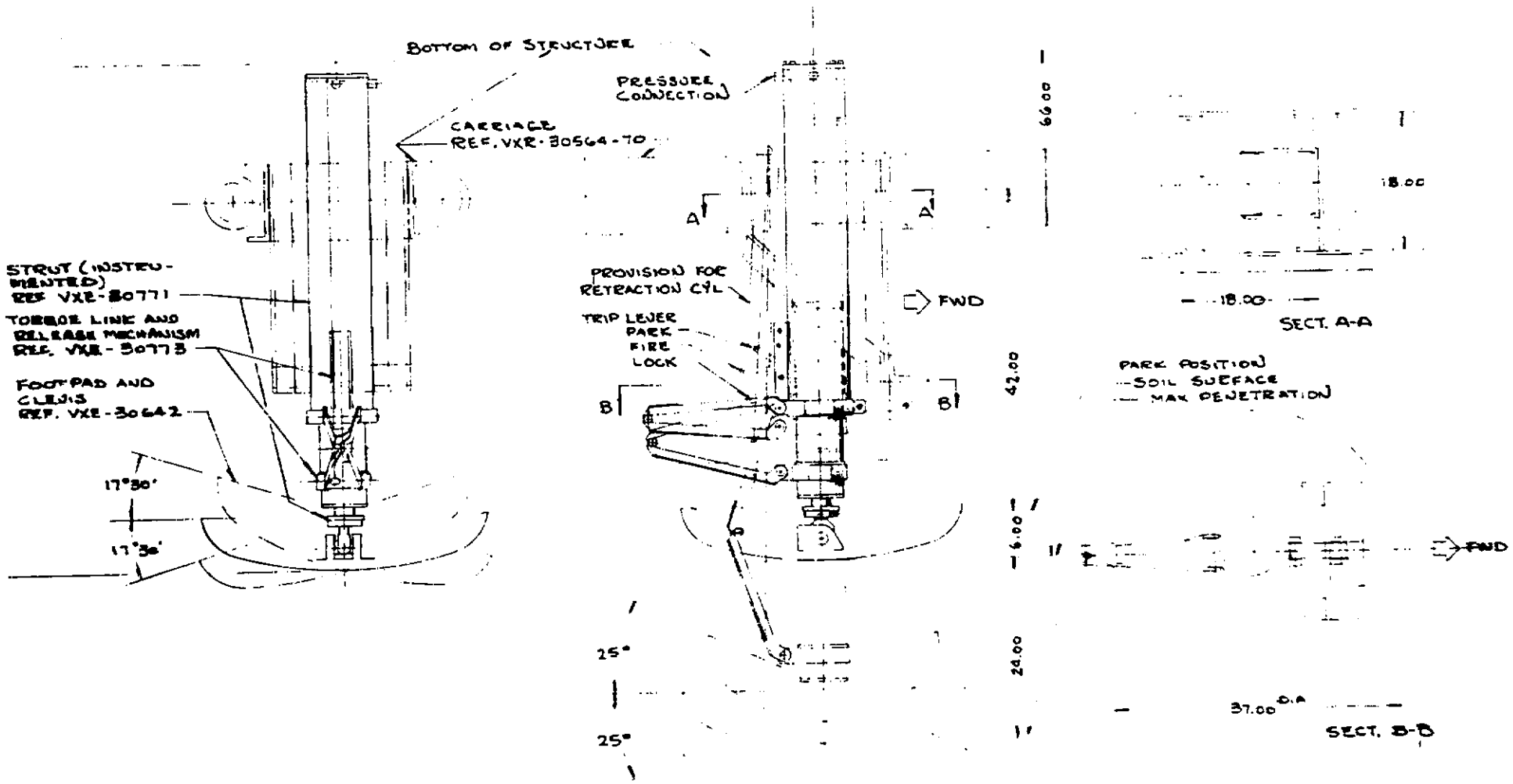

Figure 3-30. Strut and Footpad - Full-scale Drag Test System

The full-scale LM simulated footpad is the actual interface between the drag test equipment and the various test soils. It is a "saucer" contoured 37-inch diameter structure pivoted at the base of the instrumented strut on the ball-clevis universal joint. The design allows pitch and roll rotation to 25° and 17-1/2°, respectively, from axes normal to the strut. A pair of rotary potentiometers, mounted at 90° to each other on the centerline of the universal joint, sense and transmit angular deviations to the data recording equipment.

Although attachment and instrumentation requirements were different, the design of the full-scale drag test footpad is identical to the unit used for full-scale oblique impact tests, described in paragraph 3.4 and shown in Figure 3-26. The impact test pad has completed a series of full-scale tests without measurable deterioration. The pad is fabricated of an epoxy/glass-filament-generated structure with the attachment clevis solidly embedded during the winding process. Footpad profile and lip cross sections conform precisely to the actual LM pad, and the other surface is aluminum-skinned to simulate frictional characteristics of the LM footpad.

3.6 VACUUM/ATMOSPHERIC IMPACT TESTER AND SUBGRAVITY SIMULATOR

The atmospheric and vacuum footpad impact tests and the reduced gravity tests were conducted by the IIT Research Institute at Chicago, Illinois, under subcontract to Bendix. The subscale impact tester and the subgravity simulator were designed by IIT to meet technical requirements established by Bendix.

Detailed description of this test apparatus and the associated instrumentation systems are covered in Appendix E of this report.

SECTION IV

DEVELOPMENT OF SOIL/FOOTPAD INTERACTION MODEL

4.1 INTRODUCTION

The specific problem with which this study is concerned is the development of force laws which predict the forces acting on the Apollo Lunar Module footpads during landing on the lunar surface. The form of the force laws, to be utilized in existing digital computer simulation of the LM spacecraft dynamics, must relate instantaneous triaxial forces produced on the spacecraft footpads to the soil properties and the instantaneous triaxial positions, velocities and accelerations of the footpads. In addition, since each footpad is free pivoting on a spherical hinge, it is also necessary to predict the instantaneous angular position of the footpad as a function of the motion variables. Since the remaining dynamical equations are already established, knowing the above interrelationship makes it possible to compute the complete vehicle motion history from touchdown until the time that the vehicle comes to complete rest.

The general motion situation when a spacecraft footpad impacts and penetrates a soil surface is shown schematically in Figure 4-1. The sequence can be divided into three phases; initial impact, slideout and static equilibrium. The soil reactive forces during the impact phase are expected to be a result of:

(1) Soil mechanical strength,
(2) momentum transfer from the footpad to the soil particles,
(3) acceleration of the soil, and
(4) friction at the footpad-soil interface.

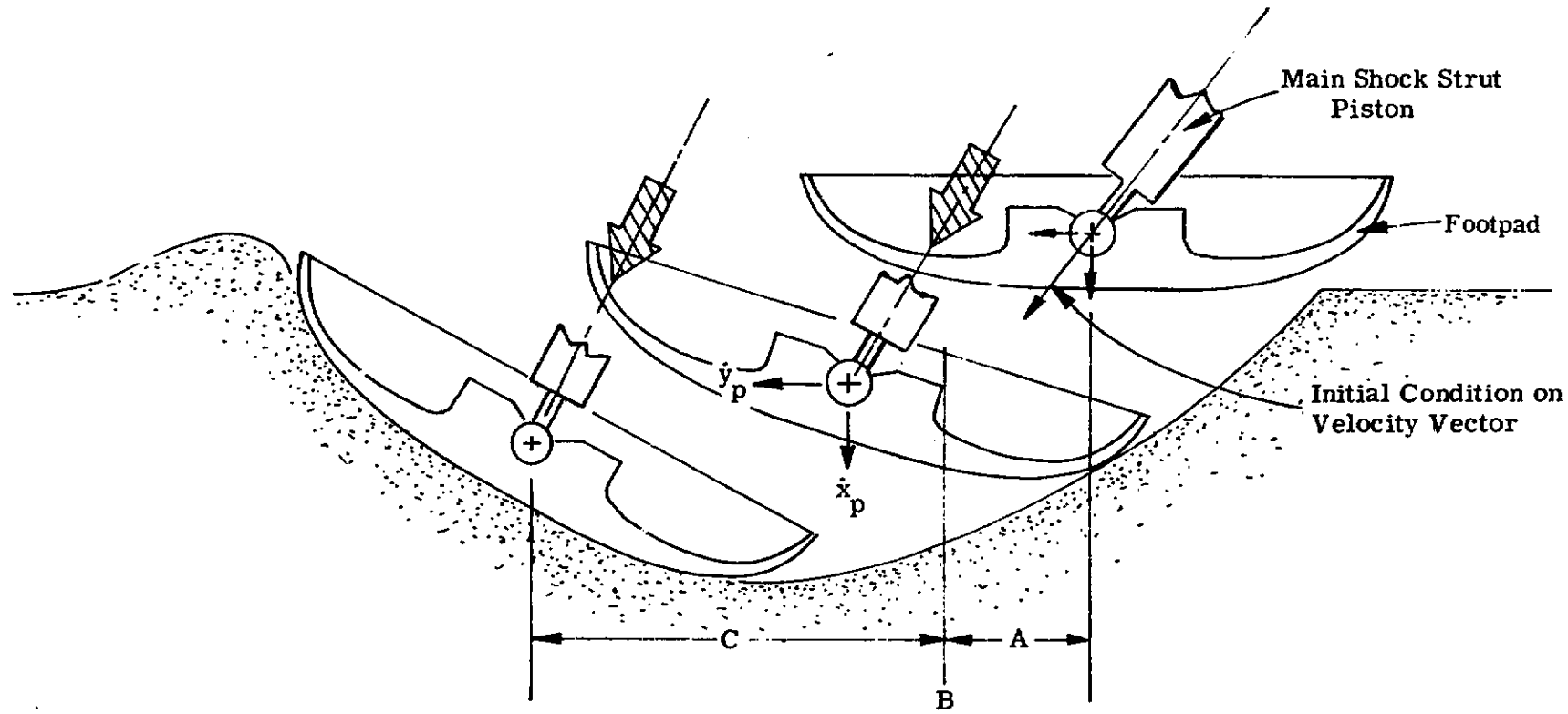

A	Impact Phase	Mechanical Strength Momentum Transfer Acceleration of Soil	Oblique Impact Tests	$F_V(t)$ $F_H(t)$
B	Transition			
C	Slide out Phase	Mechanical Strength Momentum Transfer	Drag Tests	$F_V(t)$ $F_H(t)$
D	Static Equilibrium			

Figure 4-1. Impact Phase Division

These mechanisms are not independent processes. The surface friction effect, for example, is the result of tangential stresses produced by normal stresses from all three of the other processes.

When the contribution of the acceleration of the soil becomes insignificant in comparison to the forces due to the other three mechanisms, the impact phase is considered complete and the slideout phase begins. This differentiates the two phases without a loss of continuity of forces, since the other mechanisms continue to act throughout the slideout phase. Likewise, when the forces due to the momentum transfer become insignificant and the transient motion of the soil within the "disturbed volume" surrounding the footpad dies away, the static equilibrium phase ensues.

Although it would be possible to devise a single test setup which would yield data for the three phases of footpad/soil interaction, the use of such a device in this program was deemed impractical due to the difficulty both in controlling footpad motion variables and in interpreting the resulting test data. Three separate types of tests were conducted, offering simpler control of the motion variables and more straightforward interpretation of the measured test parameters at some sacrifice in data for the transition from one phase to another. A series of oblique impact tests was employed in the development of the interaction laws for the primary impact phase and a series of drag tests provided the data for the development of equations describing the slideout phase. Slow penetration tests, using the oblique impact equipment, provided data for the static equilibrium phase.

4.2 DESCRIPTION OF DRAG TEST PROGRAM

The purpose of the subscale drag test program was to determine the effect of footpad motion variables and soil property parameters upon the forces acting on the footpad during the slideout phase of landing impact.

The footpad motion parameters felt to be of interest are footpad geometry, velocity, depth of penetration, and vertical loading. Soil properties included in the study were bulk density, relative density, internal friction angle, cohesive shear stress parameter, mean

grain size, uniformity coefficient, and sonic modulus. To facilitate the separation of the effects of this relatively large number of independent parameters, a test plan was derived which included a total of approximately 400 tests in the eleven soils selected for the study.

Figure 4-2 shows the range over which the motion and geometry parameters were varied for the subscale drag test program. All possible combinations of these parameters would give 96 tests for each of the eleven soils in the study, not including duplication of tests for the purpose of determining repeatability. The scope of the drag test program actually conducted was a compromise designed to obtain a statistically significant quantity of data with which to develop the general footpad/soil force laws in a reasonably short period of time. The drag test program in terms of the number of tests conducted on each soil is shown in Figure 4-3. The decrease in the number of tests per soil following the first soil is a result of obtaining the necessary relationships between force and the motion and geometry parameters, thus leaving only soil property effects to be studied in the remaining soils. The complete drag test program included 363 tests.

Figure 4-4 shows some of the nomenclature associated with the measurements taken during the drag tests. F_D and F_V are the drag and vertical forces acting on the footpad and α is the footpad pitch angle measured about an axis normal to the plane defined by F_D and F_V. V_H is the horizontal velocity and d is the depth of penetration into the soil defined as the distance from the soil surface to the bottom of the footpad at zero pitch angle. A_{ft} is defined as the total frontal area of the footpad and A_{pt} is the total vertical area of the footpad. Measurements were also made of the footpad roll angle β measured about an axis parallel to the horizontal velocity vector, and the side load on the footpad, F_s, measured perpendicular to the plane of F_D and F_V.

A typical oscillograph recording of a subscale drag test is shown in Figure 4-5. This test involved a six-inch diameter footpad traveling at a horizontal velocity of 14 feet per second and a constant soil penetration depth of four inches. The soil for this run was PS loose, having a relative density near zero. The initial portion of the recording corresponds to acceleration of the footpad to the desired velocity. This is followed by a period of constant velocity which covers approximately five feet of the soil bed. The footpad and load cell carriage assembly is then decelerated at the end of the run. The measured

Constant Penetration Tests

Horizontal Velocity - 1.5, 3, 6, 9, 12, 15 fps
Depth of Penetration - 0.5, 1, 1.5, 2, 3, 4 inch
Footpad Size - 6-and 4-inch diameter

Constant Pressure Tests

Horizontal Velocity - 3, 6, 9, 12 fps
Footpad Vertical Pressure - 1, 3, 5 psi
Footpad Size - 6-and 4-inch diameter

Figure 4-2. Subscale Drag Test Parameter Values

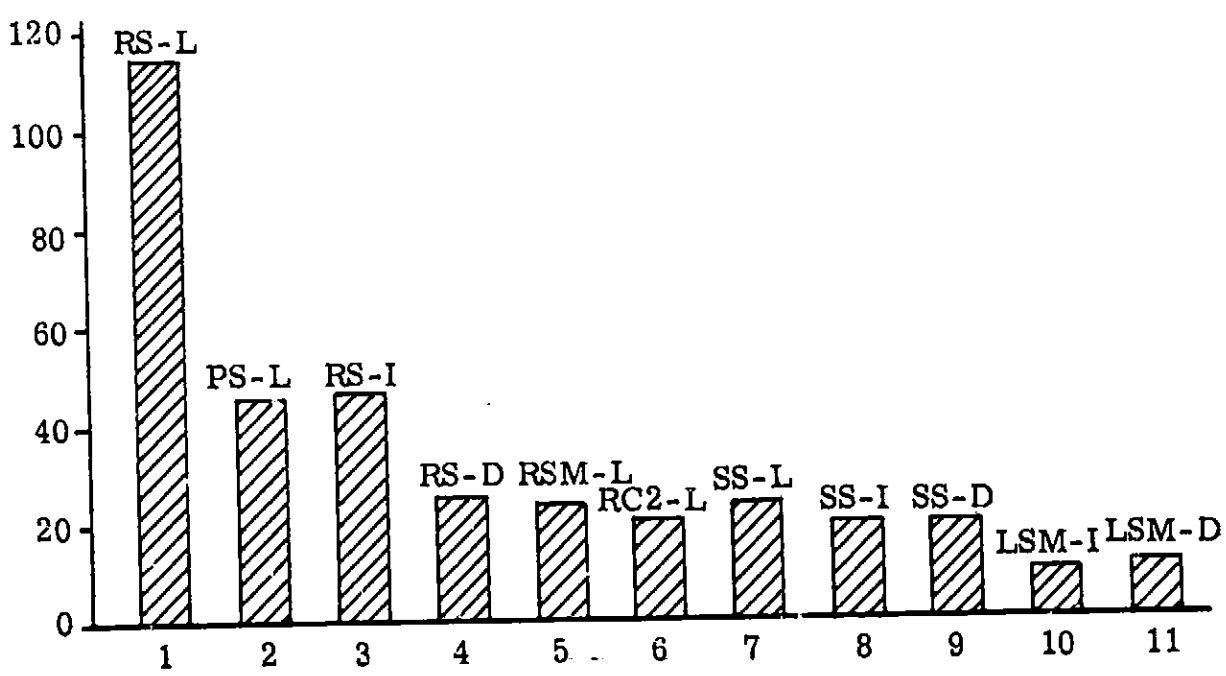

Figure 4-3. Number of Subscale Drag Tests for Each of the Soils Studied

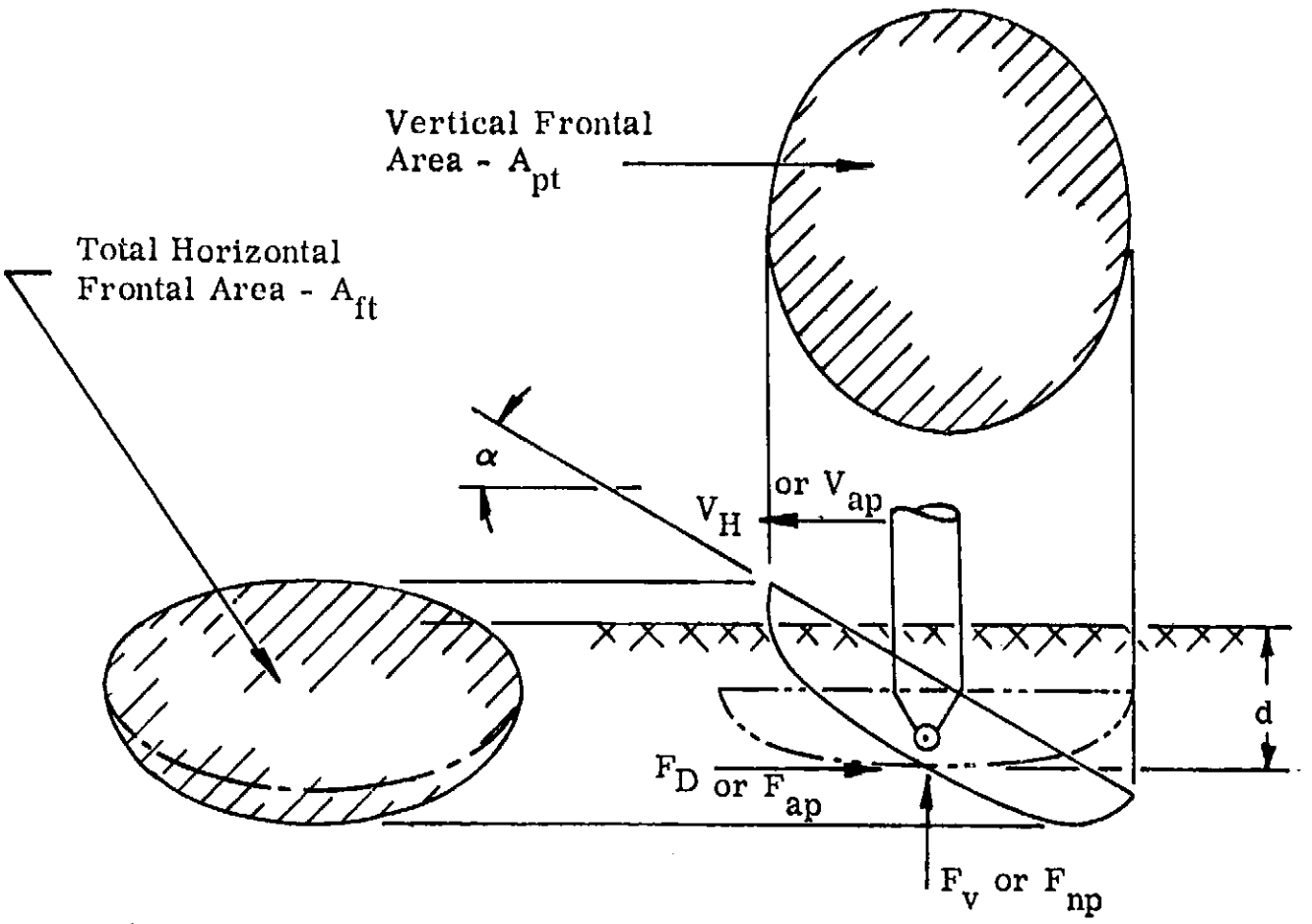

Figure 4-4. Nomenclature for Constant Penetration Drag Tests

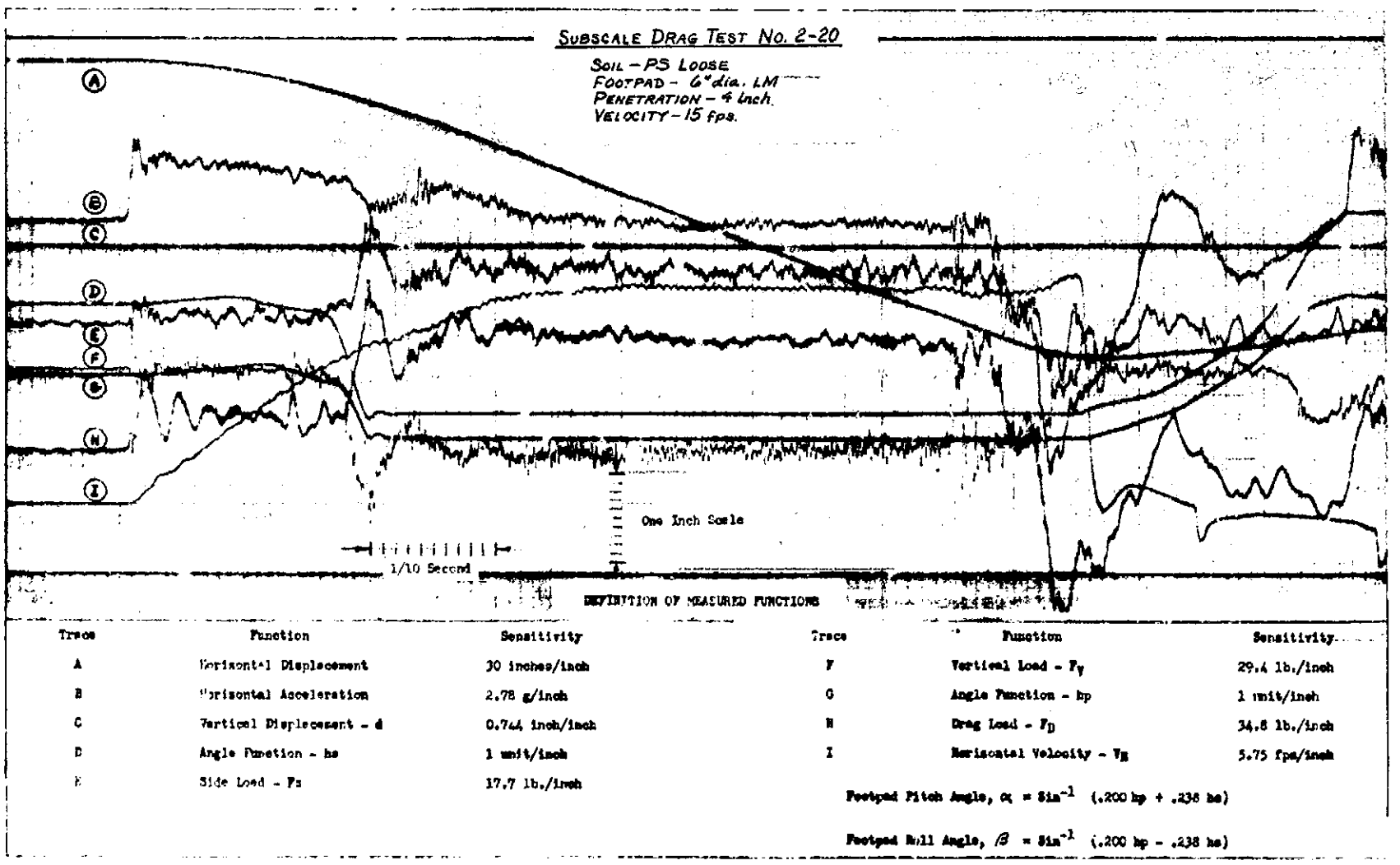

Figure 4-5. Drag Test Record Run No. 2-20

functions were generally read from the records at three positions of horizontal displacement covering a total displacement of 40 inches. The three readings were obtained to determine the degree to which steady-state conditions had been achieved during the run. In general, the readings did not vary significantly with horizontal position, and the midpoint reading was used in the development of the force equations.

Figures 4-6a through 4-16 are tables showing all of the pertinent readings obtained during constant penetration drag tests conducted in the test soils. The tables also include several combinations of measured variables which were found to be useful during the analysis of this data. Soil relative and bulk density data were determined from dynamic penetrometer tests ($\overline{g}_p$) of the soil bed.

4.3 DESCRIPTION OF IMPACT TEST PROGRAM

The purpose of the oblique impact test program was to determine the effect of footpad motion and geometry parameters and soil property parameters upon the forces acting on the footpad during the primary impact phase of vehicle landing. Soil property parameters considered were the same as those included in the drag test program. Footpad motion parameters of interest were footpad geometry, velocity, angle of impact, mass of impacting body, and depth of penetration into the soil. Figure 4-17 shows the range over which these parameters were varied in the impact test program. The number of tests performed on each soil in order to separate the effects of the numerous variables is shown in Figure 4-18. The impact test program included 362 tests using subscale footpads and 21 tests using the full-scale footpad.

Measurements made during impact tests were three components of force, displacement, footpad pitch and roll angle, and footpad acceleration. These functions were either recorded on tape and then played back into an oscillograph recorder or recorded directly on oscillograph, depending on the expected footpad load pulse frequency. The oscillograph recordings were read manually at time intervals sufficiently small to ensure that the important features of the load versus time and displacement versus time histories were obtained. Accurate displacement readings were of added importance since they provided the only measure of footpad velocity throughout the impact period.

Run Number	D Inch	d Inch	V_H fps	$-g_p$	D_r	γ Lb./Ft.^{3}	F_D Lb.	F_V Lb.	$\frac{F_D}{d\gamma A_{ft}}$	$\frac{V_H}{\sqrt{dg}}$	$\frac{F_D}{A_{ft}}$	$\frac{F_V}{A_{pt}}$	α Deg.
1-1	6	1/2	2.82	12.1	0	41.1	6.6	12.5	49.1	2.4	0.57	0.43	17.0
1-2	6	1/2	2.76	10.8	0	41.1	8.3	11.3	64.6	2.4	0.75	0.39	15.7
1-3	6	1/2	2.82	10.8	0	41.1	8.3	10.7	62.8	2.4	0.73	0.37	16.1
1-4	6	1	2.88	11.5	0	41.1	9.0	15.4	31.8	1.8	0.74	0.54	18.4
1-5	6	1 1/2	2.82	12.1	0	41.1	15.3	20.6	32.4	1.4	1.13	0.74	22.0
1-6	6	2	2.82	12.0	0	41.1	20.8	26.6	32.2	1.2	1.50	0.96	22.9
1-7	6	2 1/2	2.82	11.5	0	41.1	22.6	26.1	25.1	1.1	1.46	0.96	26.8
1-8	6	4	2.76	10.9	0	41.1	40.3	41.8	28.6	0.8	2.65	1.53	26.0
1-10	6	1	5.40	12.3	0	41.1	10.4	15.4	32.2	3.2	0.75	0.56	24.0
1-11	6	1/2	5.45	12.1	0	41.1	9.0	11.0	63.7	4.7	0.74	0.38	18.5
1-12	6	1 1/2	5.40	13.6	0	41.1	17.0	20.3	29.8	2.7	1.04	0.76	28.8
1-13	6	2	5.45	12.1	0	41.1	20.1	24.1	29.2	2.3	1.36	0.88	25.0
1-14	6	3	5.35	11.6	0	41.1	37.4	33.4	36.4	1.9	2.53	1.22	25.2
1-15	6	4	5.17	14.8	0	41.1	38.1	39.5	27.4	1.6	2.54	1.44	25.5
1-16	6	1	8.22	12.2	0	41.1	21.4	25.2	60.7	5.0	1.41	0.93	26.2
1-17	6	1/2	8.40	12.2	0	41.1	17.4	20.9	111.0	7.3	1.29	0.75	22.0
1-18	6	1 1/2	8.05	13.0	0	41.1	24.1	26.1	44.5	4.0	1.55	0.96	26.8
1-19	6	1 1/2	8.28	11.6	0	41.1	23.6	25.0	46.5	4.1	1.62	0.91	24.7
1-20	6	2	8.11	12.1	0	41.1	23.5	30.4	34.6	3.5	1.61	1.11	25.8
1-21	6	3	8.16	12.6	0	41.1	36.5	35.4	32.7	2.9	2.27	1.33	28.4
1-22	6	3 1/2	8.22	13.7	0	41.1	41.7	39.3	31.8	2.7	2.59	1.47	28.4
1-23	6	1/2	12.82	12.6	0	41.1	18.3	22.5	97.4	11.0	1.13	0.84	28.7
1-24	6	1	12.42	12.1	0	41.1	22.3	26.4	61.6	7.6	1.43	0.98	27.0
1-25	6	1 1/2	12.12	12.0	0	41.1	30.7	33.0	58.8	6.1	2.05	1.21	25.7
1-26	6	2	11.85	12.4	0	41.1	43.4	40.4	62.6	5.1	2.91	1.33	25.4
1-27	6	3	11.83	12.1	0	41.1	43.6	41.5	39.5	4.2	2.74	1.47	27.9
1-28	6	3 3/4	11.78	12.4	0	41.1	53.1	48.2	40.1	3.7	3.49	0.84	26.2
1-29	6	1/2	15.05	12.1	0	41.1	15.7	21.6	93.9	13.0	1.09	0.98	24.0
1-30	6	1	14.83	13.8	0	41.1	21.5	26.2	60.7	9.1	1.41	1.21	26.0
1-31	6	1 1/2	14.77	12.2	0	41.1	32.1	33.4	59.7	7.4	2.08	1.47	26.6
1-32	6	2	14.66	11.4	0	41.1	36.0	36.5	49.1	6.3	2.28	1.55	27.6
1-33	6	3	14.19	12.7	0	41.1	50.3	49.9	47.1	5.0	3.27	1.77	26.6

Figure 4-6a. Subscale Drag Test Results - Soil No. 1 - RS Loose

Run Number	D Inch	d Inch	V_H fps	$-g_p$	D_r	γ Lb./Ft.^{3}	F_D Lb.	F_V Lb.	$\frac{F_D}{d\gamma A_{ft}}$	$\frac{V_H}{\sqrt{dg}}$	$\frac{F_D}{A_{ft}}$	$\frac{F_V}{A_{pt}}$	α Deg.
1-34	6	4	13.90	11.4	0	41.1	62.1	51.7	41.9	4.2	3.88	0.78	28.0
1-35	6	2	11.60	11.3	0	41.1	33.1	35.9	44.9	5.0	2.09	0.96	27.6
1-36	6	1 1/2	11.78	11.4	0	41.1	17.3	21.7	31.0	5.9	1.08	1.23	28.2
1-37	6	1	8.68	11.5	0	41.1	15.6	19.1	44.7	5.3	1.04	1.36	25.5
1-38	6	3	5.75	12.0	0	41.1	30.7	32.1	29.2	2.0	2.03	1.84	25.8
1-39	6	3	3.12	11.9	0	41.1	27.8	32.0	25.2	1 1	1.74	1.93	28.0
1-40	6	1 1/2	11.61	11.7	0	41.1	26.5	29.3	47.9	5.8	1.67	1.09	27.9
1-41	6	1	1.61	11.4	0	41.1	9.4	14.9	34.4	1.0	0.80	0.52	17.5
1-42	6	2	1.61	11.3	0	41.1	16.0	20.2	24.1	0.7	1.12	0.73	23.8
1-43	6	3	1.61	12.1	0	41.1	24.3	28.6	22.9	0.6	1.59	1.05	26.3
1-44	6	4	1.50	11.6	0	41.1	36.0	40.8	25.3	0.4	2.34	1.51	26.7
1-66	6	1	5.98	12.3	0	41.1	11.9	15.9	39.6	3.7	0.92	0.56	20.4
1-67	6	1	6.27	11.3	0	41.1	10.1	14.0	33.2	3.8	0.77	0.50	21.0
1-68	6	1	6.15	11.0	0	41.1	11.2	15.0	37.4	3.8	0.87	0.53	20.1
1-69	6	1	6.21	11.3	0	41.1	11.5	14.2	37.0	3.8	0.86	0.50	20.8
1-70	6	1/4	6.04	11.0	0	41.1	3.5	5.0	61.0	7.4	0.35	0.17	12.5
1-71	6	1/4	6.33	11.4	0	41.1	4.5	9.7	78.4	7.7	0.45	0.33	12.8
1-84	4	1	1.72	10.9	0	42.2	4.3	3.0	30.6	1.1	0.73	0.26	23.4
1-85	4	2	1.67	12.1	0	46.6	8.5	5.7	30.4	0.7	1.45	0.49	23.1
1-86	4	1	2.93	11.7	0	45.2	6.4	3.6	46.7	1.8	1.11	0.31	22.4
1-87	4	2	2.93	11.9	0	44.3	7.8	5.1	28.5	1.3	1.35	0.43	23.6
1-88	4	1	6.21	12.4	0	44.9	5.0	4.5	34.9	3.8	0.83	0.39	23.8
1-89	4	2	6.27	12.2	0	42.8	11.7	7.8	41.2	2.7	1.96	0.67	23.7
1-90	4	1	9.20	12.0	0	44.3	8.8	7.2	60.3	5.6	1.43	0.62	24.5
1-91	4	2	8.68	12.6	0	45.0	15.3	10.5	54.7	3.7	2.60	0.89	23.2
1-92	4	1	11.90	12.9	0	44.9	11.0	9.0	76.9	7.3	1.83	0.95	23.8
1-93	4	3	11.55	12.1	0	46.4	19.6	11.4	44.5	4.1	3.17	0.99	24.8
1-94	4	2	11.90	12.2	0	46.4	17.5	11.6	58.5	5.1	2.78	1.01	25.6
1-95	4	1	14.43	12.1	0	45.1	15.3	10.6	103.4	8.8	2.46	0.92	25.2
1-96	4	2	14.60	12.8	0	46.9	21.5	14.3	76.9	6.3	3.66	1.23	24.2
1-110	6	1	11.93	14.6	0	54.1	23.8	31.7	69.5	7.3	1.65	0.86	24.0
1-111	6	1	14.78	12.7	0	58.3	29.0	36.3	83.4	9.0	1.98	1.32	24.5

Figure 4-6b. Subscale Drag Test Results - Soil No. 1 - RS Loose

Run Number	D Inch	d Inch	V_H fps	$-g_p$	D_r	γ Lb./Ft.^{3}	F_D Lb.	F_V Lb.	$\frac{F_D}{d\gamma A_{ft}}$	$\frac{V_H}{\sqrt{dg}}$	$\frac{F_D}{A_{ft}}$	$\frac{F_V}{A_{pt}}$	α Deg.
1-112	6	2	14.60	12.9	0	51.6	42.6	43.0	58.0	6.3	2.86	1.57	25.4
1-113	6	1	6.15	13.3	0	52.7	11.4	14.9	36.2	3.8	0.86	0.53	21.4
1-114	6	1	6.15	13.8	0	56.5	11.2	14.1	27.8	3.8	0.90	0.49	19.2

Figure 4-6c. Subscale Drag Test Results - Soil No. 1 - RS Loose

Run Number	D Inch	d Inch	V_H fps	$-g_p$	D_r	γ Lb./Ft.^{3}	F_D Lb.	F_V Lb.	$\frac{F_D}{d\gamma A_{ft}}$	$\frac{V_H}{\sqrt{dg}}$	$\frac{F_D}{A_{ft}}$	$\frac{F_V}{A_{pt}}$	α Deg.
2-1	6	1	3.05	7.8	0	24.4	5.9	7.9	31.6	1.9	0.46	0.28	20.4
2-2	6	2	3.13	7.3	0	24.4	9.1	10.8	24.5	1.4	0.71	0.38	20.1
2-3	6	3	2.99	7.7	0	24.4	19.0	19.0	33.1	1.0	1.44	0.67	21.0
2-4	6	4	2.99	8.4	0	24.4	21.6	19.8	30.4	1.0	1.76	0.69	18.9
2-5	6	1	5.92	7.7	0	24.4	8.0	9.1	46.4	3.6	0.67	0.32	17.8
2-6	6	2	5.98	8.0	0	24.4	10.1	12.0	25.8	2.5	0.75	0.43	21.8
2-7	6	3	5.92	7.4	0	24.4	14.0	15.7	24.1	2.1	1.05	0.56	21.4
2-8	6	4	5.81	7.4	0	24.4	27.9	22.0	36.8	1.8	2.13	0.78	21.0
2-9	6	1	8.74	8.0	0	24.4	9.4	10.0	43.9	5.3	0.64	0.36	25.2
2-10	6	2	8.74	7.9	0	24.4	16.2	17.1	37.8	3.8	1.09	0.62	25.1
2-11	6	3	8.92	7.5	0	24.4	22.0	19.4	33.2	3.1	1.45	0.71	26.0
2-12	6	4	8.74	7.5	0	24.4	28.3	23.1	32.2	2.6	1.86	0.85	26.1
2-13	6	1	11.32	7.8	0	24.4	12.1	12.1	55.8	6.9	0.81	0.44	25.7
2-14	6	2	11.67	7.7	0	24.4	18.2	17.9	41.3	5.1	1.20	0.66	26.1
2-15	6	3	11.56	8.0	0	24.4	27.7	25.3	42.2	4.0	1.84	0.93	25.8
2-16	6	4	11.44	7.8	0	24.4	31.9	25.2	36.3	3.4	2.10	0.93	26.1
2-17	6	1	14.82	7.8	0	24.4	21.5	19.2	96.4	9.1	1.40	0.71	26.5
2-18	6	2	14.20	8.3	0	24.4	19.9	21.6	44.6	6.1	1.29	0.76	26.6
2-19	6	3	14.28	9.4	0	24.4	35.2	26.9	53.3	5.0	2.31	0.99	26.2
2-20	6	4	14.20	8.1	0	24.4	44.3	27.6	49.4	4.4	2.86	1.02	26.9
2-21	6	1	6.15	8.8	0	24.4	8.1	7.1	36.1	3.8	0.52	0.26	26.9
2-23	6	1	1.61	9.0	0	24.4	6.3	7.4	36.6	1.0	0.53	0.22	17.8
2-24	6	2	1.67	8.0	0	24.4	10.8	10.6	25.9	0.7	0.75	0.38	24.1
2-25	6	3	1.67	8.0	0	24.4	15.9	13.1	24.4	0.6	0.73	0.58	25.5
2-26	6	4	1.61	8.3	0	24.4	22.4	19.0	25.0	0.5	1.06	0.70	26.8

Figure 4-7. Subscale Drag Test Results - Soil No. 2 - PS Loose

Run Number	D Inch	d Inch	V_H fps	$-g_p$	D_r	γ Lb./Ft.^{3}	F_D Lb.	F_V Lb.	$\frac{F_D}{d\gamma A_{ft}}$	$\frac{V_H}{\sqrt{dg}}$	$\frac{F_D}{A_{ft}}$	$\frac{F_V}{A_{pt}}$	α Deg.
3-9	6	2	5.81	34.3	0.45	45.9	37.0	41.2	42.0	2.5	2.72	1.47	22.0
3-10	6	3	5.75	31.0	0.45	45.9	72.5	88.4	55.6	2.0	5.41	3.14	21.6
3-11	6	4	5.35	34.1	0.45	45.9	95.8	113.0	56.0	1.6	7.26	4.01	21.2
3-12	6	1	3.05	28.1	0.45	45.9	10.6	32.6	28.4	1.9	0.92	1.13	16.9
3-13	6	2	2.70	29.0	0.45	45.9	40.8	64.8	53.9	1.2	3.49	2.25	17.3
3-14	6	3	2.70	34.2	0.45	45.9	70.0	102.0	59.0	1.0	5.74	3.57	18.6
3-15	6	4	2.53	34.4	0.45	45.9	74.8	122.0	49.0	0.8	6.45	4.23	17.0
3-16	6	1	1.67	33.0	0.45	45.9	19.2	47.2	68.2	1.0	2.21	1.21	9.4
3-17	6	2	1.61	35.7	0.45	45.9	38.7	77.6	53.8	0.7	3.49	2.67	15.8
3-18	6	3	1.61	36.1	0.45	45.9	43.8	73.7	46.6	0.6	4.52	2.51	12.2
3-19	6	4	1.49	31.1	0.45	45.9	58.4	126.6	34.8	0.5	4.53	4.47	20.4
3-20	6	1	8.74	35.8	0.45	45.9	38.5	51.4	87.8	5.3	2.85	1.83	21.9
3-21	6	2	8.45	35.6	0.45	45.9	60.0	67.0	66.5	3.6	4.32	2.40	22.9
3-22	6	3	8.16	33.9	0.45	45.9	82.1	93.2	61.5	2.9	5.98	3.33	22.4
3-23	6	4	8.16	33.5	0.45	45.9	103.5	100.9	54.5	2.5	7.08	3.66	24.6
3-24	6	1	11.26	33.7	0.45	45.9	43.1	49.0	94.0	6.9	3.05	1.76	23.4
3-25	6	2	10.80	32.2	0.45	45.9	66.6	69.3	73.4	4.7	4.76	2.48	23.0
3-26	6	3	10.57	37.2	0.45	45.9	92.5	89.9	64.2	3.7	6.24	3.27	25.2
3-27	6	4	9.95	29.4	0.45	45.9	122.6	106.0	69.0	3.0	8.96	3.79	22.4
3-28	6	1	13.80	31.2	0.45	45.9	51.1	51.4	108.3	8.4	3.52	1.86	24.4
3-29	6	2	13.16	28.1	0.45	45.9	86.2	71.0	93.6	5.7	6.07	2.55	23.5
3-30	6	3	11.83	40.5	0.45	45.9	117.4	128.8	79.6	4.2	7.73	4.73	26.2
3-31	6	4	11.49	31.8	0.45	45.9	141.2	127.0	77.0	3.5	10.00	4.58	23.7
3-32	4	1	2.99	30.0	0.45	45.9	10.2	9.7	42.5	1.8	1.38	0.83	23.6
3-33	4	2	2.93	34.8	0.45	45.9	20.0	19.6	51.9	1.3	3.37	1.67	22.8
3-34	4	1	5.86	28.3	0.45	45.9	10.4	10.2	55.1	3.6	1.79	0.87	22.7
3-35	4	2	5.98	31.8	0.45	45.9	22.6	22.4	60.1	2.6	3.90	1.91	22.5
3-36	4	1	8.80	33.1	0.45	45.9	13.1	13.3	70.0	5.4	2.27	1.24	22.4
3-37	4	2	8.80	33.2	0.45	45.9	26.6	23.0	71.1	3.8	4.62	1.95	22.3
3-38	4	1	11.50	30.5	0.45	45.9	18.5	18.9	97.5	7.0	3.17	1.61	22.8
3-39	4	2	11.15	30.9	0.45	45.9	38.0	27.8	98.2	4.8	6.37	2.38	23.5
3-40	4	3	2.93	30.8	0.45	45.9	27.4	23.6	48.1	1.0	4.68	2.01	22.8

Figure 4-8. Subscale Drag Test Results - Soil No. 3 - RS Intermediate

Run Number	D Inch	d Inch	V_H fps	$-g_p$	D_r	γ Lb./Ft.^{3}	F_D Lb.	F_V Lb.	$\frac{F_D}{d\gamma A_{ft}}$	$\frac{V_H}{\sqrt{dg}}$	$\frac{F_D}{A_{ft}}$	$\frac{F_V}{A_{pi}}$	α Deg.
4-3	6	1	10.46	72.9	0.80	50.6	69.4	98.6	180.0	6.4	5.30	3.49	21.0
4-4	6	2	10.17	79.2	0.80	50.6	95.6	131.0	119.6	4.3	7.03	4.68	22.6
4-5	6	3	8.97	74.3	0.80	50.6	135.0	145.0	104.8	3.2	9.25	5.27	24.6
4-6	6	1	8.28	78.7	0.80	50.6	34.0	52.0	88.0	5.1	2.59	1.84	20.8
4-7	6	1	5.75	64.9	0.80	50.6	43.1	56.2	113.6	3.5	3.34	1.99	20.4
4-8	6	1	1.61	67.2	0.80	50.6	32.1	32.4	113.9	1.0	3.35	1.10	11.7
4-9	6	1	11.90	67.0	0.80	50.6	102.8	116.1	238.0	7.3	7.00	4.22	24.8
4-10	6	1	2.93	74.4	0.80	50.6	20.6	25.1	64.3	1.8	1.89	0.86	15.2
4-11	4	1	2.88	73.7	0.80	50.6	15.3	19.4	115.7	1.8	3.40	1.59	14.8
4-12	4	1	5.85	70.1	0.80	50.6	23.0	26.0	139.6	3.6	4.11	2.20	21.6
4-13	4	1	8.56	71.7	0.80	50.6	43.1	45.9	232.4	5.2	6.84	3.72	25.5
4-14	4	1	11.38	73.9	0.80	50.6	20.7	20.8	115.4	6.9	3.39	1.80	24.0
4-15	4	1	13.73	75.5	0.80	50.6	50.4	46.5	285.8	8.4	8.41	3.98	23.5
4-16	4	1	1.67	62.7	0.80	50.6	10.4	15.1	75.2	1.0	2.21	1.24	16.1
4-17	4	2	1.55	72.0	0.80	50.6	37.0	43.5	112.3	0.7	6.61	3.66	21.1
4-18	4	2	2.82	62.9	0.80	50.6	31.0	33.0	85.0	1.2	5.00	2.86	24.8
4-19	4	2	5.64	71.0	0.80	50.6	35.0	33.2	97.6	2.4	5.74	2.86	24.3
4-20	4	2	8.51	64.8	0.80	50.6	46.6	45.8	125.8	3.7	7.40	3.98	25.6
4-21	4	2	9.43	58.5	0.80	50.6	57.7	59.8	148.6	4.0	8.75	5.28	27.4
4-22	4	2	12.88	77.5	0.80	50.6	31.4	32.4	84.8	5.6	4.98	2.82	25.6

Figure 4-9. Subscale Drag Test Results - Soil No. 4 - RS Dense

Run Number	D Inch	d Inch	V_H fps	$-g_p$	D_r	γ Lb./Ft.^{3}	F_D Lb.	F_V Lb.	$\frac{F_D}{d\gamma A_{ft}}$	$\frac{V_H}{\sqrt{dg}}$	$\frac{F_D}{A_{ft}}$	$\frac{F_V}{A_{pt}}$	α Deg.
5-1	6	1	2.99	14.9	0	58.2	13.3	10.9	25.2	1.8	0.88	0.40	26.0
5-2	6	2	2.98	15.4	0	58.2	21.0	14.7	19.9	1.3	1.38	0.54	26.0
5-3	6	3	2.88	15.0	0	58.2	29.6	20.8	19.9	1.0	2.07	0.75	23.8
5-4	6	3	5.87	14.8	0	58.2	26.8	34.0	18.8	2.1	1.96	1.21	22.3
5-5	6	2	5.64	15.6	0	58.2	20.5	30.5	21.2	2.4	1.46	1.09	23.2
5-6	6	1	5.98	14.1	0	58.2	13.7	14.7	29.2	3.6	1.01	0.52	21.9
5-7	6	1	8.23	15.3	0	58.2	18.5	20.2	38.9	5.0	1.35	0.72	22.4
5-8	6	2	8.28	15.5	0	58.2	21.2	22.0	23.3	3.6	1.62	0.78	21.0
5-9	6	3	8.11	14.9	0	58.2	45.2	40.5	32.0	2.9	3.32	1.44	22.2
5-10	6	1	11.26	15.8	0	58.2	32.6	31.2	67.2	6.9	2.33	1.12	23.1
5-11	6	2	11.09	17.3	0	58.2	50.3	43.8	51.1	4.8	3.54	1.57	23.7
5-12	6	3	10.81	14.9	0	58.2	53.3	44.8	35.4	3.8	3.68	1.62	24.2
5-13	6	1	13.45	16.9	0	58.2	33.2	29.4	73.0	8.2	2.53	1.05	22.0
5-14	4	1	2.99	15.6	0	58.2	5.8	3.7	28.8	1.8	1.00	0.31	22.3
5-15	4	2	3.05	16.5	0	58.2	12.0	7.4	28.4	1.3	1.97	0.64	24.1
5-16	4	1	5.81	16.0	0	58.2	8.0	8.6	37.8	3.5	1.31	0.74	24.0
5-17	4	2	5.92	16.6	0	58.2	14.8	11.0	34.9	2.5	2.43	0.95	24.7
5-18	4	1	8.63	16.6	0	58.2	11.0	9.1	45.3	5.3	1.57	0.82	29.8
5-19	4	2	8.40	17.9	0	58.2	18.1	13.4	38.3	3.6	2.66	1.20	28.6
5-20	4	1	11.20	16.7	0	58.2	14.2	11.5	59.3	6.8	2.06	1.03	29.4
5-21	4	2	11.38	16.8	0	58.2	26.4	17.5	63.5	4.9	4.40	1.50	23.9
5-22	6	1	2.99	16.2	0	58.2	14.2	20.4	32.6	1.8	1.13	0.72	19.7
5-23	6	2	2.99	16.0	0	58.2	24.2	27.0	23.7	1.3	1.65	0.98	24.6

Figure 4-10. Subscale Drag Test Results - Soil No. 5 - RSM_a Loose

Run Number	D Inch	d Inch	V_H fps	$-g_p$	D_r	γ Lb./Ft.^{3}	F_D Lb.	F_V Lb.	$\frac{F_D}{d\gamma A_{ft}}$	$\frac{V_H}{\sqrt{dg}}$	$\frac{F_D}{A_{ft}}$	$\frac{F_V}{A_{pt}}$	α Deg.
6-1	6	1	2.70	16.9	0	59.4	12.7	23.5	38.6	1.64	1.35	0.80	11.3
6-2	6	2	2.76	15.8	0	59.4	28.5	36.7	33.4	1.18	2.34	1.28	18.5
6-3	6	3	2.76	16.4	0	59.4	37.8	43.4	27.9	0.97	2.93	1.53	20.4
6-4	6	1	5.81	15.3	0	59.4	18.7	22.0	40.8	3.54	1.43	0.78	21.0
6-5	6	2	5.75	15.7	0	59.4	27.0	26.3	30.6	2.46	2.14	0.92	19.6
6-6	6	3	5.81	15.0	0	59.4	44.3	34.9	34.3	2.04	3.60	1.22	18.9
6-7	6	1	8.56	15.3	0	59.4	20.0	19.0	44.7	5.22	1.56	0.67	20.1
6-8	6	2	8.56	14.8	0	59.4	35.5	27.2	39.7	3.67	2.78	0.96	20.2
6-9	6	3	7.99	15.5	0	59.4	44.3	30.8	31.9	2.81	3.36	1.09	21.0
6-10	6	1	11.43	13.4	0	59.4	30.3	27.5	68.6	8.73	2.40	0.97	19.6
6-11	6	2	11.21	14.7	0	59.4	39.9	33.0	45.3	4.82	3.17	1.16	19.7
6-12	6	3	10.69	14.5	0	59.4	50.9	36.7	37.0	3.77	3.88	1.30	20.8
6-13	4	2	2.93	15.2	0	59.4	13.5	9.9	31.7	1.26	2.21	0.85	24.0
6-14	4	1	2.99	16.0	0	59.4	5.9	3.7	31.2	1.82	1.09	0.31	20.1
6-15	4	1	5.87	15.2	0	59.4	10.4	6.4	43.8	3.58	1.53	0.55	22.6
6-16	4	2	5.86	15.3	0	59.4	13.3	9.2	32.8	2.52	2.29	0.79	22.7
6-17	4	1	8.57	14.8	0	59.4	10.6	8.6	51.4	5.23	1.80	0.74	23.4
6-18	4	2	8.51	14.3	0	59.4	17.7	13.0	43.6	3.65	3.05	1.11	22.4
6-19	4	2	11.43	17.3	0	59.4	25.9	14.9	62.8	4.92	4.39	1.28	23.4
6-20	4	1	11.55	14.7	0	59.4	15.5	10.4	72.6	7.05	2.54	0.90	24.4

Figure 4-11. Subscale Drag Test Results - Soil No. 6 - RC2 Loose

Run Number	D Inch	d Inch	V_H fps	$-g_p$	D_r	γ Lb./Ft.^{3}	F_D Lb.	F_V Lb.	$\frac{F_D}{d\gamma A_{ft}}$	$\frac{V_H}{\sqrt{dg}}$	$\frac{F_D}{A_{ft}}$	$\frac{F_V}{A_{pt}}$	α Deg.
7-1	6	1	2.76	17.8	0	94.7	23.3	25.1	29.7	1.68	1.64	0.91	23.6
7-2	6	2	2.76	18.0	0	94.7	34.6	26.6	20.1	1.19	2.22	0.98	26.6
7-3	6	3	2.76	16.6	0	94.7	47.5	35.1	18.5	0.97	3.07	1.30	26.9
7-4	6	4	2.76	15.5	0	94.7	57.0	36.2	17.5	0.84	3.70	1.33	26.6
7-5	6	1	5.81	13.8	0	94.7	17.8	15.7	20.8	3.54	1.15	0.58	26.8
7-6	6	2	5.86	15.1	0	94.7	31.8	25.4	18.5	2.52	2.04	0.94	27.2
7-7	6	3	5.63	14.8	0	94.7	51.9	36.8	19.2	1.98	3.18	1.38	28.8
7-8	6	4	5.46	15.5	0	94.7	72.3	54.4	21.0	1.66	4.44	2.04	28.9
7-9	6	1	8.68	15.3	0	94.7	26.6	23.6	29.5	5.29	1.63	1.00	28.8
7-10	6	2	8.46	15.6	0	94.7	48.9	44.7	27.2	3.63	3.00	1.68	28.8
7-11	6	3	8.00	19.6	0	94.7	71.6	51.4	27.9	2.82	4.62	1.89	26.8
7-12	6	4	8.05	14.7	0	94.7	76.2	48.9	23.0	2.45	4.85	1.82	27.4
7-13	6	1	10.98	16.2	0	94.7	42.4	33.2	49.8	6.70	2.75	1.22	26.5
7-14	6	2	10.85	14.7	0	94.7	53.2	39.0	31.4	4.67	3.47	1.44	26.4
7-15	6	3	10.40	14.1	0	94.7	74.7	53.3	30.1	3.67	4.98	1.95	25.5
7-16	6	4	10.18	14.6	0	94.7	92.5	63.6	32.9	3.11	6.95	2.25	21.3
7-17	4	1	2.76	15.1	0	94.7	8.9	5.6	30.4	1.68	1.68	0.47	19.4
7-18	4	2	2.88	15.1	0	94.7	14.2	10.5	24.3	1.24	2.68	0.88	19.3
7-19	4	1	5.35	16.3	0	94.7	11.2	8.7	39.1	3.26	2.16	0.72	18.9
7-20	4	2	5.35	15.6	0	94.7	14.8	10.5	24.3	2.29	2.68	0.83	19.4
7-21	4	1	8.45	15.3	0	94.7	12.7	10.4	43.3	5.15	2.39	0.87	19.6
7-22	4	2	8.51	16.4	0	94.7	16.3	11.8	28.8	3.65	3.18	0.98	18.5
7-23	4	1	11.27	15.2	0	94.7	17.8	13.6	61.4	6.88	3.39	1.13	19.4
7-24	4	2	11.54	15.0	0	94.7	28.8	17.1	46.2	4.96	5.10	1.48	20.1

Figure 4-12. Subscale Drag Test Results - Soil No. 7 - SS Loose

Run Number	D Inch	d Inch	V_H fps	$-g_p$	D_r	γ Lb./Ft.^{3}	F_D Lb.	F_V Lb.	$\frac{F_D}{d\gamma A_{ft}}$	$\frac{V_H}{\sqrt{dg}}$	$\frac{F_D}{A_{ft}}$	$\frac{F_V}{A_{pt}}$	α Deg.
8-1	4	1	3.05	42.8	0.53	104.0	11.8	11.0	36.6	1.86	2.23	0.92	19.5
8-2	4	2	2.93	41.1	0.53	104.0	28.5	26.3	44.1	1.26	5.38	2.20	19.5
8-3	4	1	5.99	42.1	0.53	104.0	20.7	18.15	63.65	3.65	3.87	1.52	20.0
8-4	4	2	5.90	33.2	0.53	104.0	34.5	29.35	51.64	2.54	6.28	2.46	20.7
8-5	4	1	8.72	45.6	0.53	104.0	24.4	22.0	75.8	5.32	4.61	1.84	19.7
8-6	4	2	8.74	44.8	0.53	104.0	43.1	34.2	66.8	3.75	8.13	2.86	19.6
8-7	4	1	11.49	34.9	0.53	104.0	29.2	27.5	89.0	7.00	5.41	2.31	20.2
8-8	4	2	11.32	42.4	0.53	104.0	46.0	35.5	70.1	4.86	8.52	2.98	20.4
8-9	6	1	2.88	40.8	0.53	104.0	36.2	65.5	66.3	1.76	4.03	2.22	10.0
8-10	6	2	2.76	36.4	0.53	104.0	64.5	85.0	42.8	1.19	5.20	2.98	19.2
8-11	6	3	2.70	44.6	0.53	104.0	104.9	105.9	39.9	0.95	7.29	3.83	24.1
8-12	6	1	5.80	41.7	0.53	104.0	57.7	59.8	65.0	3.54	3.95	2.17	24.5
8-13	6	2	5.46	42.6	0.53	104.0	81.5	96.7	46.0	2.34	5.62	3.50	24.4
8-14	6	3	5.18	42.8	0.53	104.0	111.7	111.2	40.8	1.82	7.44	4.09	25.5
8-15	6	1	7.80	42.6	0.53	104.0	70.7	74.8	80.7	4.76	4.91	2.70	24.1
8-16	6	2	7.59	33.4	0.53	104.0	108.0	108.8	57.4	3.26	6.97	4.02	26.9
8-17	6	3	7.48	37.0	0.53	104.0	97.8	117.6	33.5	2.64	6.11	4.38	28.0
8-18	6	1	10.58	33.0	0.53	104.0	68.6	76.5	75.4	6.45	4.58	2.80	25.7
8-19	6	2	9.72	34.3	0.53	104.0	113.2	105.8	60.5	4.18	7.35	3.90	26.6
8-20	6	3	9.31	36.7	0.53	104.0	142.9	109.8	46.3	3.28	8.46	4.18	30.3

Figure 4-13. Subscale Drag Test Results - Soil No. 8 - SS Intermediate

Run Number	D Inch	d Inch	V_H fps	$-g_p$	D_r	γ Lb./Ft.^{3}	F_D Lb.	F_V Lb.	$\frac{F_D}{d\gamma A_{ft}}$	$\frac{V_H}{\sqrt{dg}}$	$\frac{F_D}{A_{ft}}$	$\frac{F_V}{A_{pt}}$	α Deg.
9-1	6	1	2.88	50.6	0.69	107.0	52.6	60.5	64.2	1.76	4.04	2.13	20.7
9-2	6	1	10.52	50.7	0.69	107.0	78.0	76.8	79.2	6.42	5.00	2.84	27.2
9-3	6	2	9.36	45.2	0.69	107.0	150.3	130.3	75.0	4.02	9.46	4.86	27.9
9-4	6	3	8.96	42.6	0.69	107.0	188.2	162.0	63.7	3.16	12.05	6.00	27.2
9-5	6	1	7.87	56.5	0.69	107.0	83.2	86.3	86.2	4.81	5.44	3.17	26.3
9-6	6	2	7.58	35.9	0.69	107.0	81.8	118.7	44.4	3.25	5.60	4.31	24.6
9-7	6	3	6.90	55.0	0.69	107.0	158.1	146.2	53.6	2.43	10.14	5.41	27.1
9-8	6	1	5.86	56.3	0.69	107.0	62.9	71.2	69.7	3.57	4.40	2.57	23.9
9-9	6	2	5.35	35.3	0.69	107.0	110.2	113.8	57.1	2.29	7.21	3.82	26.4
9-10	6	3	5.29	38.2	0.69	107.0	128.0	117.6	44.6	1.87	8.43	4.32	26.1
9-11	6	2	2.76	46.5	0.69	107.0	68.9	71.0	40.4	1.18	5.11	2.53	22.4
9-12	6	3	2.64	42.9	0.69	107.0	98.5	131.6	47.3	0.94	8.95	4.54	15.5
9-13	4	1	2.99	42.2	0.69	107.0	14.0	21.6	59.9	1.82	3.78	1.74	9.3
9-14	4	2	2.93	50.3	0.69	107.0	36.2	38.4	47.8	1.26	6.03	3.29	23.8
9-15	4	1	5.81	43.1	0.69	107.0	28.1	33.8	73.1	3.54	4.62	2.92	24.6
9-16	4	2	5.64	52.4	0.69	107.0	45.9	44.7	55.1	2.42	6.96	3.94	27.2
9-17	4	1	8.56	50.4	0.69	107.0	28.1	27.5	67.5	5.22	4.26	2.43	27.7
9-18	4	2	8.05	35.6	0.69	107.0	51.6	54.5	62.9	3.45	7.93	4.78	26.6
9-19	4	1	11.21	52.1	0.69	107.0	36.5	32.8	83.9	6.84	5.29	2.93	28.8
9-20	4	2	11.03	54.1	0.69	107.0	65.0	50.8	78.1	4.74	9.85	4.48	27.2

Figure 4-14. Subscale Drag Test Results - Soil No. 9 - SS Dense

Run Number	D Inch	d Inch	V_H fps	$-g_p$	D_r	γ Lb./Ft.^{3}	F_D Lb.	F_V Lb.	$\frac{F_D}{d\gamma A_{ft}}$	$\frac{V_H}{\sqrt{dg}}$	$\frac{F_D}{A_{ft}}$	$\frac{F_V}{A_{pt}}$	α Deg.
10-1	4	1	2.87	9.8	0.50	77.5	31.4	17.3	147.5	1.75	6.83	1.49	23.9
10-2	6	1	2.93	8.2	0.50	77.5	31.5	29.0	46.7	1.79	2.16	1.05	24.6
10-3	6	2	2.88	7.2	0.50	77.5	37.0	24.8	25.7	1.24	2.38	0.92	26.9
10-4	6	1	5.75	6.1	0.50	77.5	28.8	31.5	43.3	3.50	2.00	1.14	24.2
10-5	6	2	5.52	5.9	0.50	77.5	53.3	33.4	37.6	2.37	3.48	1.23	26.4
10-6	6	3	5.41	6.6	0.50	77.5	73.0	41.2	34.8	1.90	4.84	1.51	25.8
10-7	6	1	9.03	7.1	0.50	77.5	26.3	28.2	36.4	5.50	1.69	1.04	27.2
10-8	6	2	8.74	7.5	0.50	77.5	59.9	41.0	41.8	3.75	3.87	1.51	26.9
10-9	6	1	11.09	9.2	0.50	77.5	12.8	21.6	17.7	6.77	0.82	0.80	27.0
10-10	6	2	10.12	8.7	0.50	77.5	69.4	41.6	49.0	4.35	4.53	1.53	26.4

Figure 4-15. Subscale Drag Test Results - Soil No. 10 - LSM Intermediate

Run Number	D Inch	d Inch	V_H fps	$-g_p$	D_r	γ Lb./Ft.^{3}	F_D Lb.	F_V Lb.	$\frac{F_D}{d\gamma A_{ft}}$	$\frac{V_H}{\sqrt{dg}}$	$\frac{F_D}{A_{ft}}$	$\frac{F_V}{A_{pt}}$	α Deg.
11-1	6	1	2.01	24.2	0.81	82.0	190.0	161.3	224.0	1.22	13.20	5.84	24.2
11-2	6	2	0.63	27.1	0.81	82.0	223.0	140.1	144.8	0.27	14.50	5.16	26.6
11-3	6	1	5.41	10.3	0.70	82.0	69.0	52.0	91.9	3.30	4.60	1.90	25.5
11-4	6	2	4.89	10.1	0.70	82.0	131.2	83.5	84.6	2.10	8.48	3.08	26.9
11-5	6	1	7.08	12.3	0.70	82.0	118.4	76.8	156.6	4.32	7.85	2.81	25.9
11-6	6	2	8.73	9.6	0.70	82.0	165.9	113.1	104.1	3.75	10.43	4.21	27.8
11-7	6	1	10.29	11.9	0.70	82.0	97.5	73.0	121.5	6.28	6.09	2.72	28.0
11-8	6	2	10.05	8.9	0.70	82.0	111.0	68.1	73.8	4.32	7.40	2.50	26.5
11-9	6	1	10.64	10.9	0.70	82.0	69.4	54.5	86.8	6.49	4.34	2.03	28.0
11-10	6	1	2.70	11.0	0.70	82.0	87.6	20.8	103.9	1.65	5.21	0.79	30.0
11-11	6	2	2.01	11.3	0.70	82.0	78.9	47.1	49.8	0.86	4.99	1.75	27.7

Figure 4-16. Subscale Drag Test Results - Soil No. 11 - LSM Dense

Subscale Tests

Impact Velocity - 1, 3, 6, 9, 12, 15 fps
Angle of Impact - 0, 17.5, 35, 52.5, 70 degrees
Impacting Mass - 31, 41, and 51 pounds
Footpad Size - 6- and 4-inch diameter

Full-scale Tests

Impact Velocity - 3, 6, 9, 12, 15 fps
Angle of Impact - 0, 10, 15, 25, 35 degrees

Figure 4-17. Oblique Impact Test Parameter Values

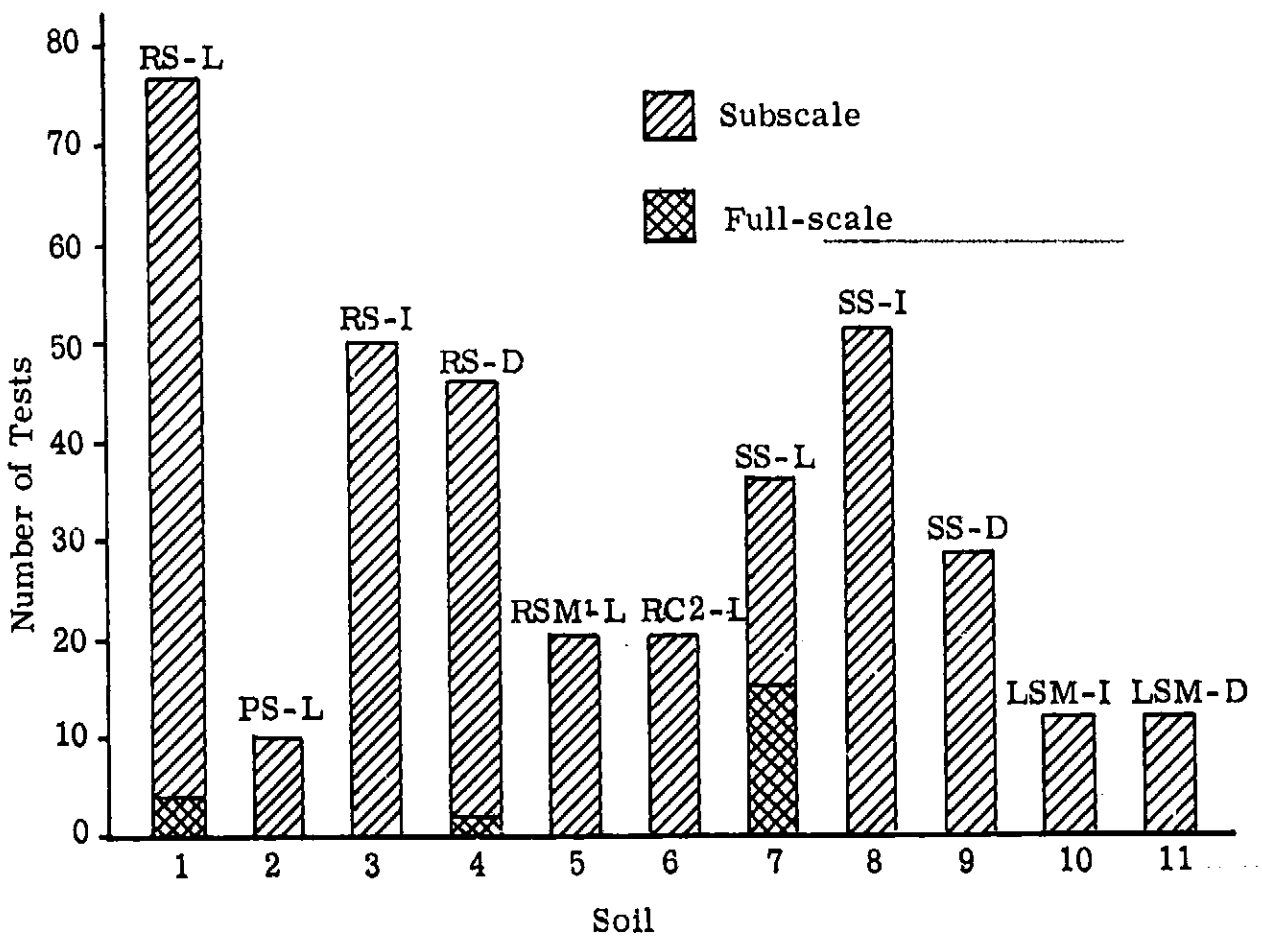

Figure 4-18. Number of Impact Tests for Each of the Soils Studied

The effect of soil strength on impact test results may be seen in Figure 4-19 which shows typical force and penetration versus time characteristics from subscale impact tests on RS loose, intermediate, and dense soil. These results are for vertical tests at an impact velocity of about six fps using a six-inch diameter footpad. These same results are shown as force versus penetration in Figure 4-20. The effect of mass of the impacting body is shown in terms of force versus penetration in Figure 4-21. Vertical impacts at about six fps in RS loose soil are shown for moving body weights of 31, 41, and 51 pounds.

Figure 4-22 depicts the force versus time results for tests at about six fps on RS loose soil using six and 37-inch diameter footpads. The ratio of impacting mass to footpad area is approximately the same for both the full-scale and subscale tests shown.

4.4 ANALYSIS OF SUBSCALE DRAG TEST DATA

The soil/footpad interaction force due to footpad motion through a soil medium is believed to be an extremely complex function of soil property and footpad motion parameters. The relationship between footpad motion and the resulting force is probably simplest for the case of a footpad moving at a constant horizontal velocity through a given soil volume, as in the constant penetration drag test conducted in this program.

For constant-velocity horizontal motion of a particular footpad the force opposing the velocity vector is assumed to be dependent upon footpad velocity, depth of penetration into the soil, and frontal area; in addition to the applicable soil descriptors. This relationship is expressed by the equation

$$F_{ap} = f(d, V_{ap}, A_{ft}, g, \rho, \phi, D_r) \qquad 4.1$$

To reduce the number of variables involved in the study of the drag test results, conventional methods of dimensional analysis were applied to obtain dimensionless parameters relating the significant variables. The parameters obtained were:

$$\text{Drag Force,} \qquad N_f = F_{ap}/d\rho g\, A_{ft} \qquad 4.2$$

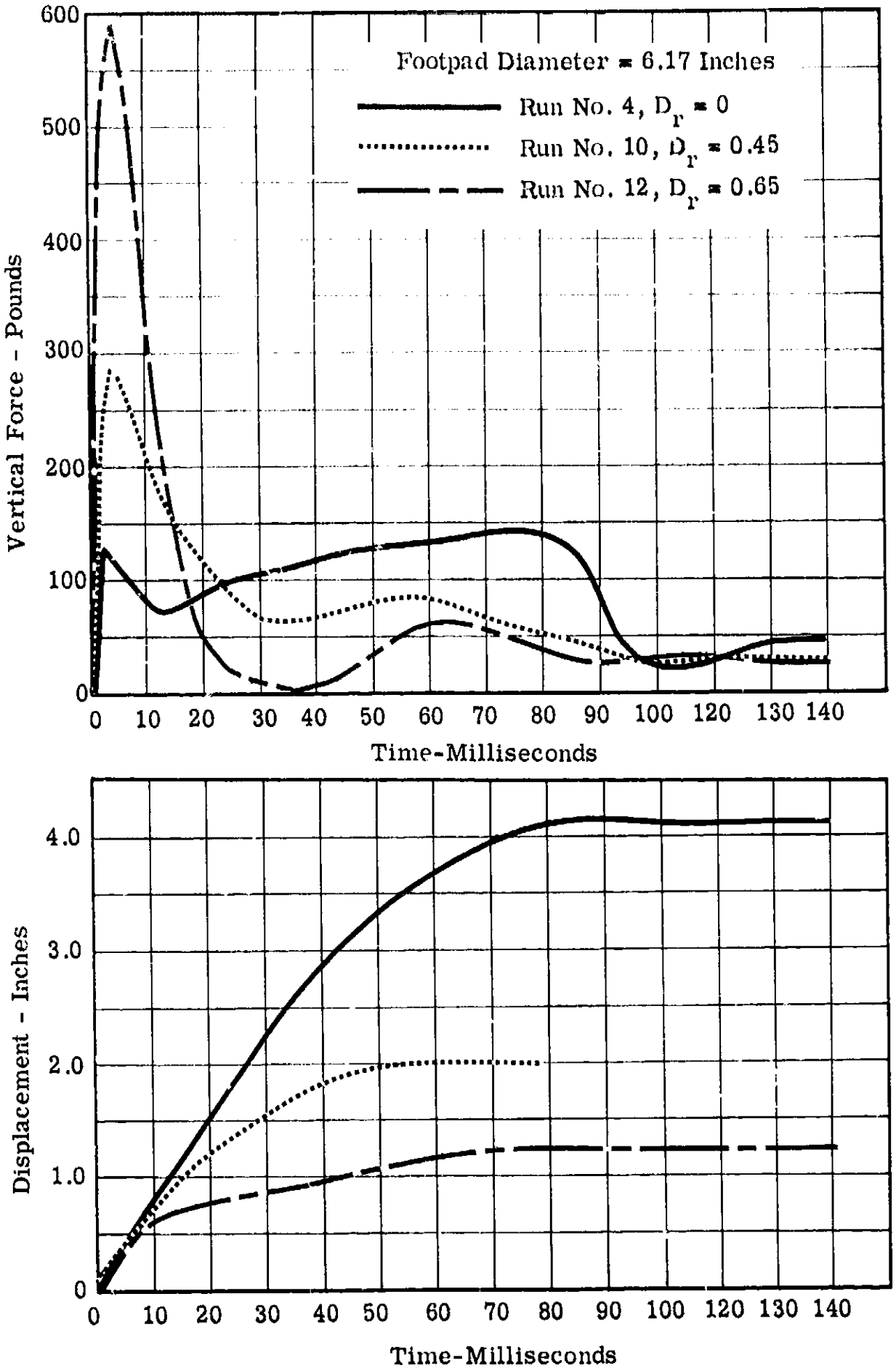

Figure 4-19. Force and Displacement versus Time for Vertical Impact Tests on Various RS Soils

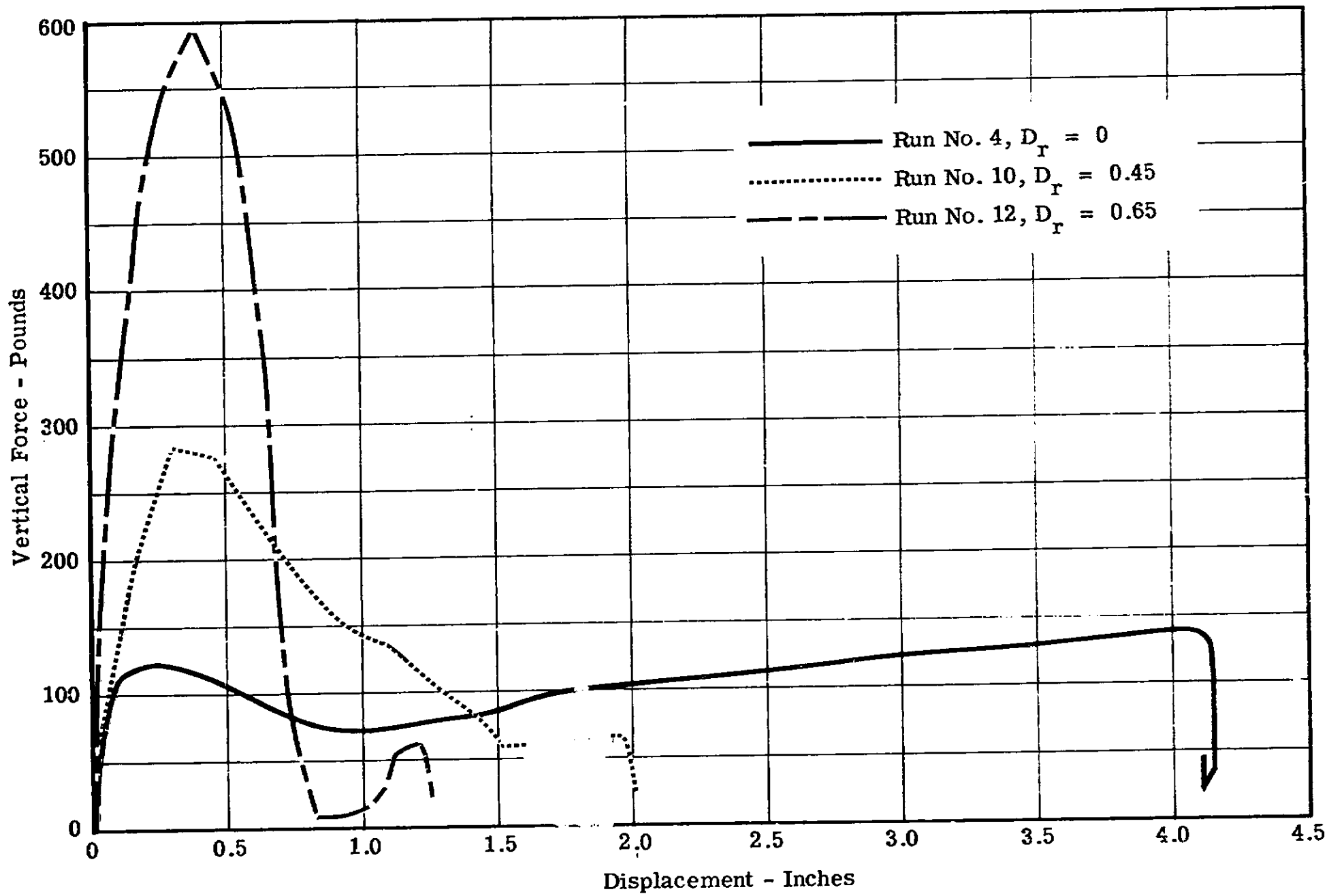

Figure 4-20. Force versus Displacement for Vertical Impact Tests on Various RS Soils
Footpad Diameter = 6.17 Inches

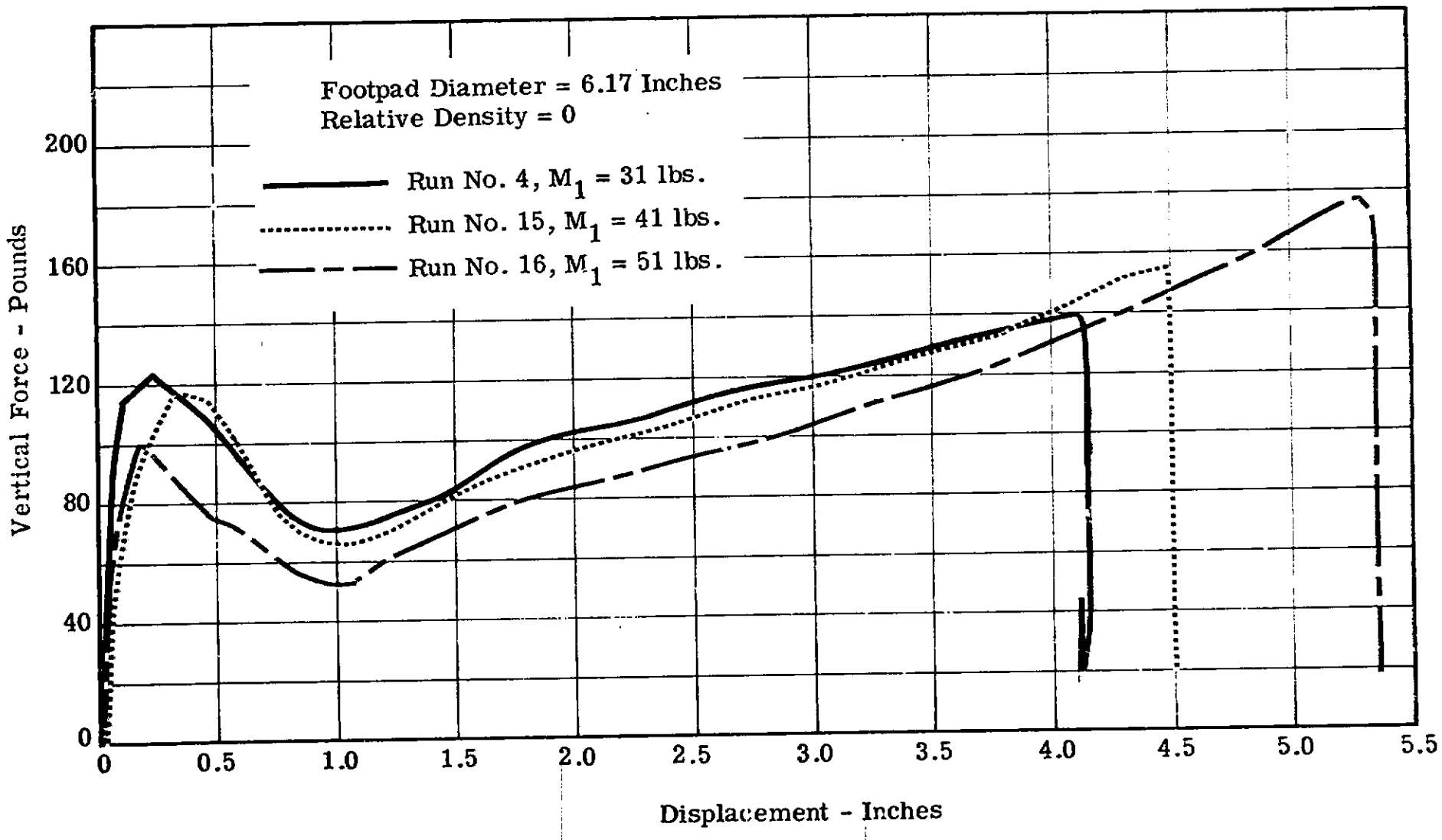

Figure 4-21. Force versus Displacement for Vertical Impact Tests on RS Loose Soil Using Various Weight Impacting Bodies (M_1)

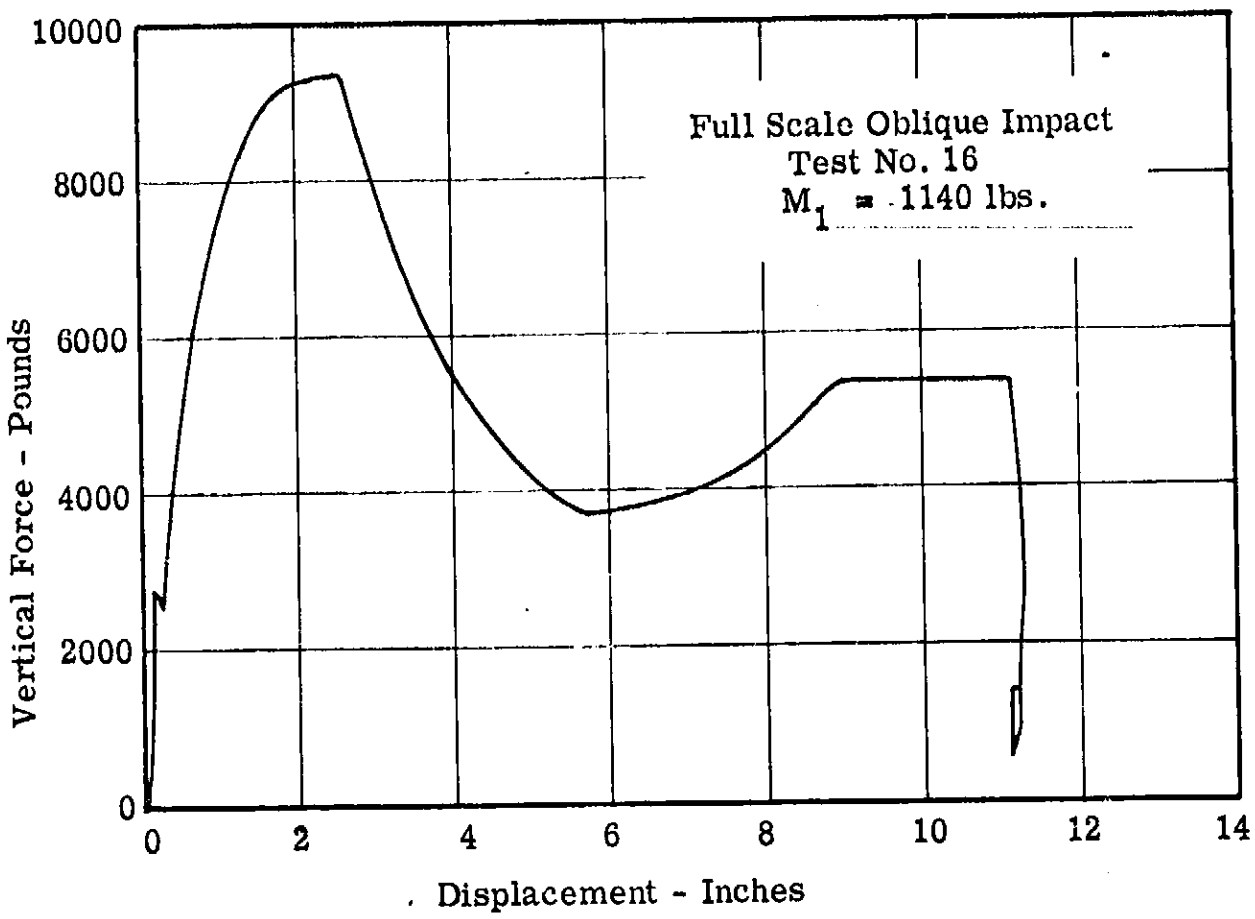

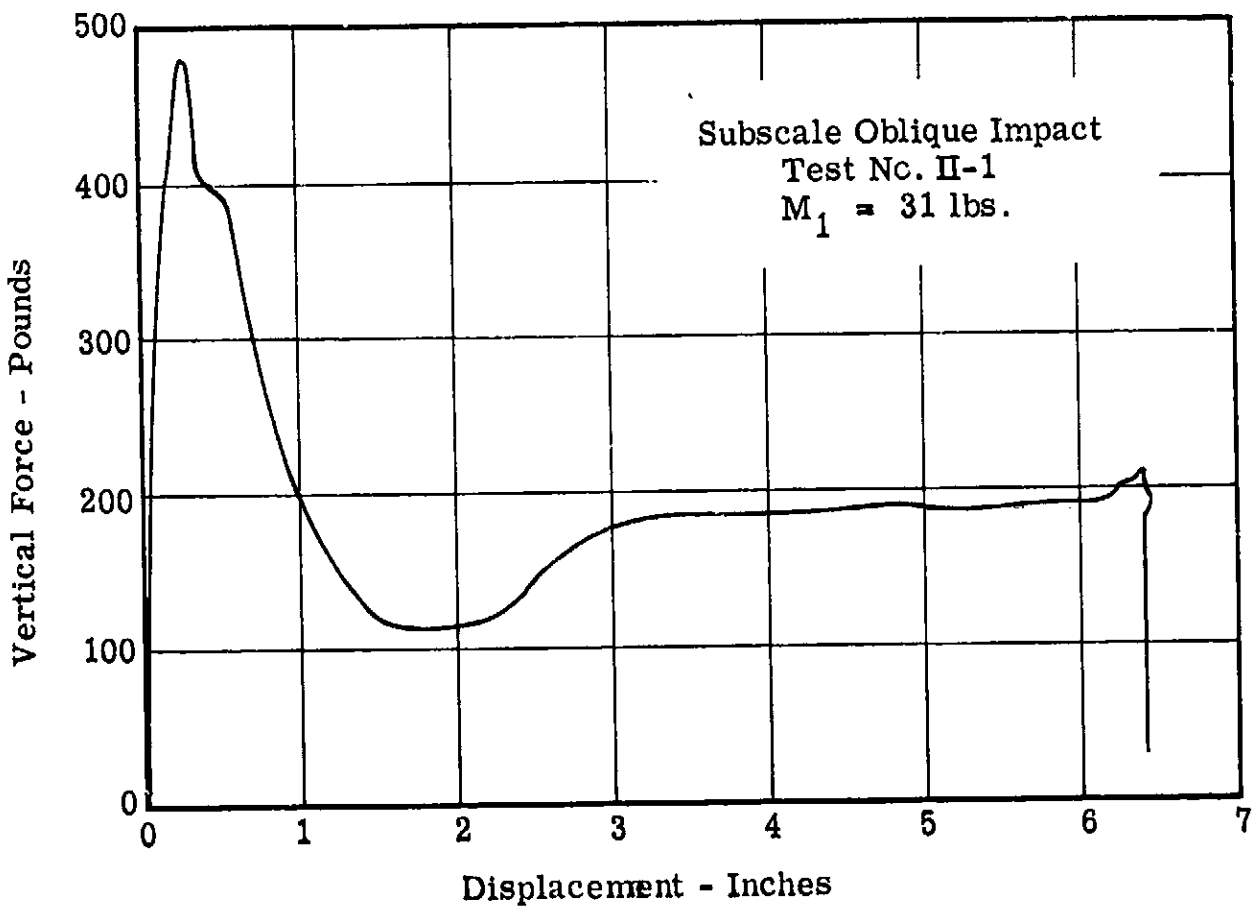

Figure 4-22. Force versus Displacement for Vertical Impact Tests Using 6.17-and 37-Inch Diameter Footpads

Velocity, $N_v = V_{ap}/\sqrt{dg}$ 4.3

Size, $N_s = d^2/A_{ft}$ 4.4

Friction Angle, $N_\phi = f(\phi)$ 4.5

Relative Density, $N_r = f(D_r)$ 4.6

which can be combined to form the dimensionless drag force relationship

$$N_f = f(N_v, N_s, N_\phi, N_r) \qquad 4.7$$

For a given soil, N_ϕ and N_r are constant and the drag force parameter is thus a function of only the velocity, depth, and size parameters. Figures 4-23 shows a plot of drag force parameter versus velocity parameter for all of the RS loose drag test data given in Figure 4-6. It would be expected that this plot would indicate a family of curves representing various values of the size parameter, which ranges in value from 0.004 to 3.2 for the plotted data. Since the data plotted in Figure 4-23 shows only the expected amount of scatter about some mean curve and the points appear to be randomly placed with respect to size parameter, it is concluded that N_s need not be considered in the drag force relationship.

The most general form of the drag force equation relating these parameters is assumed to be

$$N_f = C_o + C_1 N_v + C_2 N_v^2 + \cdots$$

or

$$N_f = \sum_{n=0}^{\infty} C_n N_v^n \qquad 4.8$$

where for a given shape footpad the coefficients C_n are unknown functions of the soil properties, as

$$C_n = f_n(N_\phi, N_r) \qquad 4.9$$

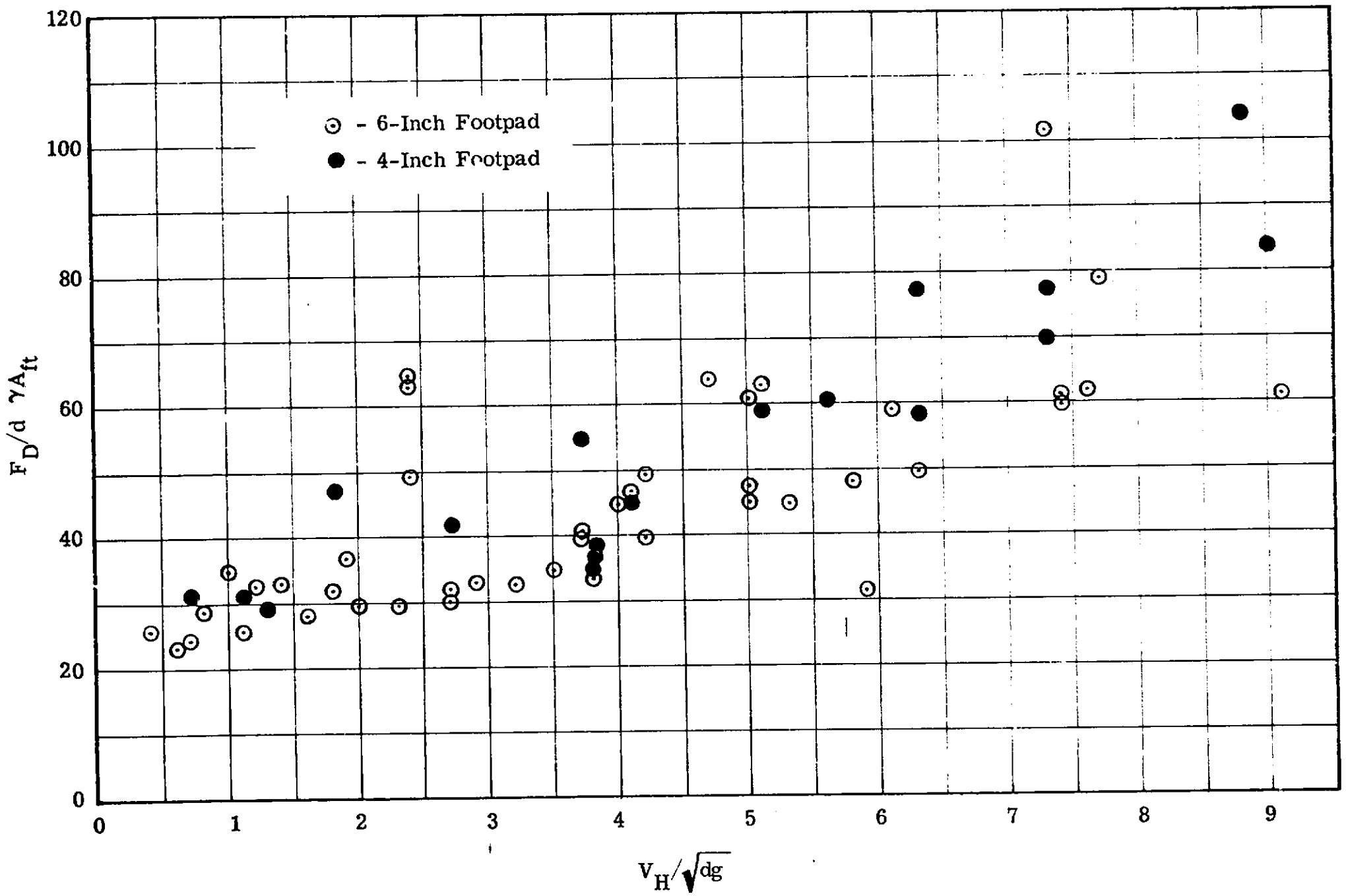

Figure 2-23. Drag Force Parameter versus Velocity Parameter
Soil No. 1 - RS Loose, Dr = 0

The information necessary to estimate the values of the C_n's will be provided by drag test data. The problem is obviously greatly simplified if a small number of terms in Equation 4.8 can yield a reasonably accurate drag force relationship. As was mentioned previously, the force during slideout phase of landing impact is expected to be governed by mechanical strength of the soil and momentum transfer from the footpad to the soil particles. Equation 4.8 may thus be reduced to

$$N_f = C_0 + C_2 N_v^2 \qquad 4.10$$

The elimination of the other terms in the general equation will be substantiated by a statistical analysis of the drag test data later in this report.

One method used in determining the constants C_o and C_2 for the RS loose data shown in Figure 4-6 was to plot the drag force parameter N_f versus velocity parameter N_v on logarithmic graph paper upon which lines having a slope of 2.0 had been drawn. A "best fit" line was drawn through the data and a constant was then subtracted from the curve until, by trial and error, a straight line having a slope of 2.0 was obtained. Once this was accomplished, the values of C_o and C_2 could be determined directly. C_o is the value subtracted to obtain a straight line and C_2 is the value of the drag force parameter at a velocity parameter of 1.0. For this data, values of C_o and C_2 of 26.5 and 0.8 were obtained.

A second, and more rigorous, estimate of the coefficients for this data was provided by the results of a statistical study based upon the maximum likelihood method. An equation of the form

$$N_f = C_o + C_1 N_v + C_2 N_v^2 + C_3 N_v^3 \qquad 4.11$$

or

$$F/d\gamma A = C_o + C_1 V/\sqrt{dg} + C_2 V^2/dg + C_3 V^3/(\sqrt{dg})^3 \qquad 4.12$$

was assumed. The analysis consisted of estimating the coefficients C_n in all physically realistic combinations of real and zero values in order to determine the optimum coefficient values. The results thus give an indication of the validity of eliminating the linear and

cubic terms as was done in Equation 4.10 as well as supplying another estimate of the value of the coefficients.

It is common practice in most applications of the maximum likelihood method to neglect the error in all variables except one, the dependent variable. In this case the dependent variable is, of course, the drag force F. During the course of the experiments it became apparent that the accuracy of the soil density measurements was difficult to establish. For this reason it was considered necessary to include the measurement errors of both F and γ in the analysis.

Let the measured values of these two quantities from the ith experiment be given by F_i and q_i respectively. Thus

$$f_i = F_i + e_i$$

and

$$q_i = \gamma_i + h_i \qquad i = 1, 2, \ldots, n \qquad 4.13$$

where F_i and γ_i are the "true" values and e_i and h_i are measurement errors. The latter are assumed to be statistically independent with zero means and constant variances, σ_f^2 and σ_q^2, respectively.

Before using the expressions in Equation 4.13 consider the form of 4.12 temporarily assuming that the density measurements are error free. For each data point the left-hand side of 4.12, using Equation 4.13, is $f_i(1/d_iA_i\gamma_i) = e_i(1/d_iA_i\gamma_i)$. Note that the coefficients $(1/d_iA_i\gamma_i)$ are essentially weighting factors. In statistical analyses of this type weighting factors are generally introduced to make the variance of the errors constant. Since we have already assumed that the variance of the e_i's is constant, the weighting factors must be removed. Fortunately, this can be done simply by multiplying Equation 4.12 by $d\gamma A$. These observations, of course, are equally true when γ is measured with error. This was pointed out principally because the form of Equation 4.12 is fairly standard and multiplication by $d\gamma A$ in this situation turns out to be not only convenient but necessary from a statistical point of view.

Returning to the case where error is present in γ, the substitution of F_i and γ_i from Equation 4.13 into Equation 4.12 gives (with multiplication first by $d_i \gamma_i A_i$)

$$f_i = C_o \mu_{oi}(q_i - h_i) + C_1 \mu_{1i}(q_i - h_i) + C_2 \mu_{2i}(q_i - h_i) + C_3 \mu_{3i}(q_i - h_i) + e_i$$

or

$$f_i = \sum_{j=0}^{3} C_j \mu_{ji}(q_i - h_i) + e_i \qquad 4.14$$

where

$$\left.\begin{aligned} \mu_{oi} &= d_i A_i \\ \mu_{1i} &= A_i V_i (d_i/g)^{1/2} \\ \mu_{2i} &= A_i V_i^2/g \\ \mu_{3i} &= A_i V_i^3/(d_i g^3)^{1/2} \end{aligned}\right\} \qquad 4.15$$

assume that the ratio of variances, $\lambda = \sigma_q^2/\sigma_f^2$ is a known quantity. This assumption is necessary to permit a straightforward evaluation of the coefficients (41, Chapter 9); further, it is not an unrealistic assumption.

To actually determine the estimates of the C_j's as well as estimates of σ_f^2 and the γ_i's, the method of maximum likelihood is used. (Since the values of the density γ_i are measured with error, the "true" values must be estimated.)

Based on the assumed normality of the errors e_i and h_i, the maximum likelihood estimator L is given by

$$L = \frac{1}{(2\pi \sigma_f \sigma_q)^n} \exp\left[-\frac{1}{2} \sum_{i=1}^{n} \left(\frac{e_i^2}{\sigma_f^2} + \frac{h_i^2}{\sigma_q^2}\right)\right]$$

or, with $\sigma_f^2 = \sigma^2$

$$L = \frac{1}{(\lambda\sigma^4)^{n/2}} \frac{1}{(2\pi)^n} \exp\left[-\frac{1}{2} \sum_{i=1}^{n} \frac{1}{\sigma^2} \left(e_i^2 + \frac{1}{\lambda} h_i^2\right)\right] \qquad 4.16$$

The maximum likelihood estimates are those which maximize L. The necessary condition for a maximum of L is that the partial derivative of L with respect to each estimate be zero. This gives a set of algebraic equations:

$\partial L/\partial C_m = 0$ gives

$$\sum_{i=1}^{n} \left[(f_i - \hat{q}_i \sum_{j=0}^{3} b_j \mu_{ji}) \hat{q}_i \mu_{mi}\right] = 0, \; m = 0, 1, 2, \text{ and } 3 \qquad 4.17$$

$\partial L/\partial \gamma_k = 0$ gives

$$(f_k - \hat{q}_k \sum_{j=0}^{3} b_j \mu_{jk}) \sum_{i=0}^{3} b_i \mu_{ik} + \frac{1}{\lambda} (q_k - \hat{q}_k) = 0, \; k = 1, 2, \ldots, n \qquad 4.18$$

and $\partial L/\partial \sigma^2 = 0$ gives

$$s^2 = \frac{1}{2n} \sum_{i=1}^{n} \left[(f_i - \hat{q}_i \sum_{j=0}^{3} b_j \mu_{ji})^2 + \frac{1}{\lambda}(q_i - \hat{q}_i)^2\right] \qquad 4.19$$

In these expressions, the b_j's are estimates of the C_j's, q_k's are estimates of the γ_k's and s^2 is an estimate of σ^2.

The equations indicated by Equations 4.17 and 4.18 form a set of n + p simultaneous, nonlinear algebraic equations in the n + p unknowns $\hat{q}_1, \hat{q}_2, \ldots \hat{q}_n$ and $b_o, \ldots b_{p-1}$. As will be seen later some sets of estimates will not involve all four of the C_i's, thus $p \leq 4$. Once these equations are solved Equation 4.19 gives the estimate of the variance, s^2.

However it is common practice (41, Chapter 9) to use a slightly different estimate for σ^2; that is

$$s^2 = \frac{1}{2n - (n+p)} \sum_{i=1}^{n} \left[(f_i - q_i \sum_{j}^{p} b_j \mu_{ji})^2 + \frac{1}{\lambda} (q_i - \hat{q}_i)^2 \right] \qquad 4.20$$

where $(n + p)$ is the total number of estimated quantities. Equation 4.20 with a denominator of $n - p$ rather than $2n$ gives a statistically consistent estimate of σ^2 by taking into account the loss in degrees of freedom due to the estimates of the p C_i's and n γ_i's.

Note that $(n - p)s^2$ is the sum of squares of deviations of the data from the estimated values, with a weighting factor of $1/\lambda$ associated with the γ_i's.

Since Equations 4.17 and 4.18 are nonlinear the solution is found numerically. Considerable simplification can be made by noting that each of the n unknowns, $\hat{q}_k$, can be obtained explicitly from Equation 4.18 and eliminated from Equation 4.17. Then, at most, four nonlinear equations need be solved simultaneously. The actual solution of these equations was carried out using the Newton-Raphson method on a digital computer. Since this is a rather common method no account of it is given here; only the results are given. For example, see Hildebrand (42).

A quantity λ was introduced earlier, where λ is the ratio of the error variances σ_q^2/σ_f^2. This ratio must be specified prior to the analyses, based upon the experimenter's judgement concerning the measurement techniques. As such, the value chosen here is unity, i.e., $\lambda = 1$. All of the results to follow are for this value. However, to determine the sensitivity of the results to changes in λ all calculations were repeated for $\lambda = 0$ and $\lambda = 2$. In general, the coefficients, C_i, were not significantly affected by changes in λ.

The analysis was conducted in three parts. First, the data in Figure 4-6 corresponding to a four-inch diameter footpad was analyzed and then the data from the six-inch diameter footpad. Finally, all of this data was combined and analyzed. For each group of data the analysis consisted of estimating the coefficients C_i, in the following combinations:

(1) C_o and C_1 estimated with $C_2 = C_3 = 0$

(2) C_o and C_2 estimated with $C_1 = C_3 = 0$

(3) C_o, C_1 and C_2 estimated with $C_3 = 0$

and finally

(4) all C_i's estimated, $i = 0, 1, 2, 3$

As a result, four corresponding forms of the equation were determined. Comparisons within each group of data were then made to determine the most efficient. By most efficient is meant that equation which fit the data well but has as few terms as possible. The results are shown in Figure 4-24. No attempt is made to compare groups; the results are simply presented. Unfortunately, the comparison of the different forms of the equation cannot be based upon an objective statistical test because the estimation used here is nonlinear. Even in the linear estimation situation, however, Draper and Smith (43), for example, present only subjective methods of comparison. The analyst determines the point of diminishing returns when adding additional terms to the equation. In linear multiple regression analysis one method, suggested by Draper and Smith, is to examine a statistic R. For the simple regression equation $y_i + C_o + C_1 x_i$, it is shown that

$$\frac{\sum_i (\hat{y}_i - y_i)^2}{\sum_i (y_i - \bar{y})^2} + \frac{\sum_i (\hat{y}_i - \bar{y})^2}{\sum (y_i - \bar{y})^2} = 1 = R' + R \qquad 4.21$$

where $\hat{y}_i = b_o + b_1 x_i$; b_o and b_1, are the unweighted estimates of C_o and C_1. Also the values of x_i are not subject to error. If the regression line passes through all of the experimental points $R' = 0$ and $R = 1$, where R is the variation "due to regression." Thus, $0 \leq R \leq 1$ and $0 \leq R' \leq 1$. If the addition of another term in the regression equation significantly increases R the term is retained, otherwise not. In the situation here it can be shown that if one defines a corresponding R such as

	Estimates of Coefficients				Variance Estimate	R' ($\times 10^2$)	R_ζ
	b_0	b_1	b_2	b_3			
Four-Inch Diameter Footpad	18.21	6.965	-	-	2.626	7.15	0.792
	28.65	-	0.8634	-	1.693	4.61	1.024
	26.33	1.393	0.7029	-	1.801	4.46	0.992
	23.26	5.130	-0.3288	0.0774	1.936	4.31	1.021
Six-Inch Diameter Footpad	20.14	4.885	-	-	7.901	4.67	0.778
	25.47	-	0.7413	-	8.213	4.71	1.029
	22.29	2.760	0.3355	-	7.521	4.31	0.901
	25.41	-1.956	1.948	-0.1488	7.231	4.01	0.871
Combined Data	19.83	5.127	-	-	7.188	3.69	0.591
	25.45	-	0.7710	-	6.842	3.43	0.885
	22.73	2.305	0.4389	-	6.472	3.24	0.760
	24.20	0.1234	1.164	-0.0649	6.527	3.20	0.719

Figure 4-24. Numerical Results of Statistical Estimation of Coefficients in the Drag Force Equation

$$R = \frac{\sum_i \left[(\hat{f}_i - \hat{\bar{f}})^2 + \frac{1}{\lambda}(\hat{q}_i - \bar{q})^2\right]}{\sum_i \left[(f_i - \bar{f})^2 + \frac{1}{\lambda}(q_i - \bar{q})^2\right]} \qquad 4.22$$

values of $R > 1$ can result. However it is still true that $0 \leq R'$ where R' is defined as

$$R' = \frac{\sum_i \left[(\hat{f}_i - f_i)^2 + \frac{1}{\lambda}(\hat{q}_i - q_i)^2\right]}{\sum_i \left[(f_i - \bar{f})^2 + \frac{1}{\lambda}(q_i - \bar{q})^2\right]} \qquad 4.23$$

Note that if the regression line passes through all of the experimental points, $R' = 0$. The table shows the values of R' for the various cases considered. The smaller the values of R', the better the fit.

For all groups of data, the values of R' are rather small indicating a reasonably good fit, in general. There is only one situation where the addition of another term makes a relatively significant change. In the first group (four-inch diameter footpad) going from the linear equation to the two-term quadratic has a change in R' from 0.0715 to 0.0461. Other than this case the changes in value of R', when more terms are added, are rather uninformative. Thus, the choice is arbitrary. As a further step to aid in the selection of the most efficient form of the equations consider the following. The data and the corresponding curves can be conveniently graphed when in the form of Equation 4.12 but not in the form of Equation 4.14. The latter would require five-dimensional plotting. Although, as mentioned earlier, Equation 4.12 is in a weighted form, the sum of squares of residuals can be calculated and compared since on the basis of changes in the R' any selection is almost as good as another. A choice based upon the weighted data would, at least, be the best appearing fit. Let ζ_i be defined as

$$\zeta_i = \frac{f_i}{d_i q_i A_i} \qquad 4.24$$

Using this a corresponding R_ζ can be defined where

$$R_\zeta = \frac{\sum_{i=1}^{n} (\hat{\zeta}_i - \bar{\zeta})^2}{\sum_{i=1}^{n} (\zeta_i - \bar{\zeta})^2} \qquad 4.25$$

In this case the larger the value of R_ζ the better the fit, since R_ζ corresponds to the amount of variation "due to the regression equation." These values are also shown in Figure 4-24.

For each of the three groups of data the largest value of R_ζ occurs for the equation containing only two terms and which has the form

$$\zeta_i = \frac{f_i}{d_i A_i q_i} = C_0 + C_2 \frac{V_i^2}{d_i g} \qquad 4.26$$

Consequently, this form was considered the most "efficient" in each case.

A linear plot of the drag force parameter for the RS loose drag test data is shown in Figure 4-25. The results of tests of both four- and six-inch diameter footpads are included. The equation derived for this data is shown as the solid line on the plot. It is seen that this curve represents a reasonable average for the data points, but there is a considerable amount of scatter in the data. The standard deviation of the departure of the data points from the derived equation was computed and is plotted as the dashed lines on the figure. A large degree of statistical significance cannot be given to the standard deviation because of the relatively small sample size available, but it does give some measure of the degree of scatter involved. Approximately sixty percent of the data falls within the plus and minus one sigma limits on this plot.

Figures 4-26 through 4-35 are plots of drag force parameter versus velocity parameter for the remainder of the soils included in this study. The equations obtained for each of the soils are shown on the plots. It is seen that the value of C_0 appears to be a dependent

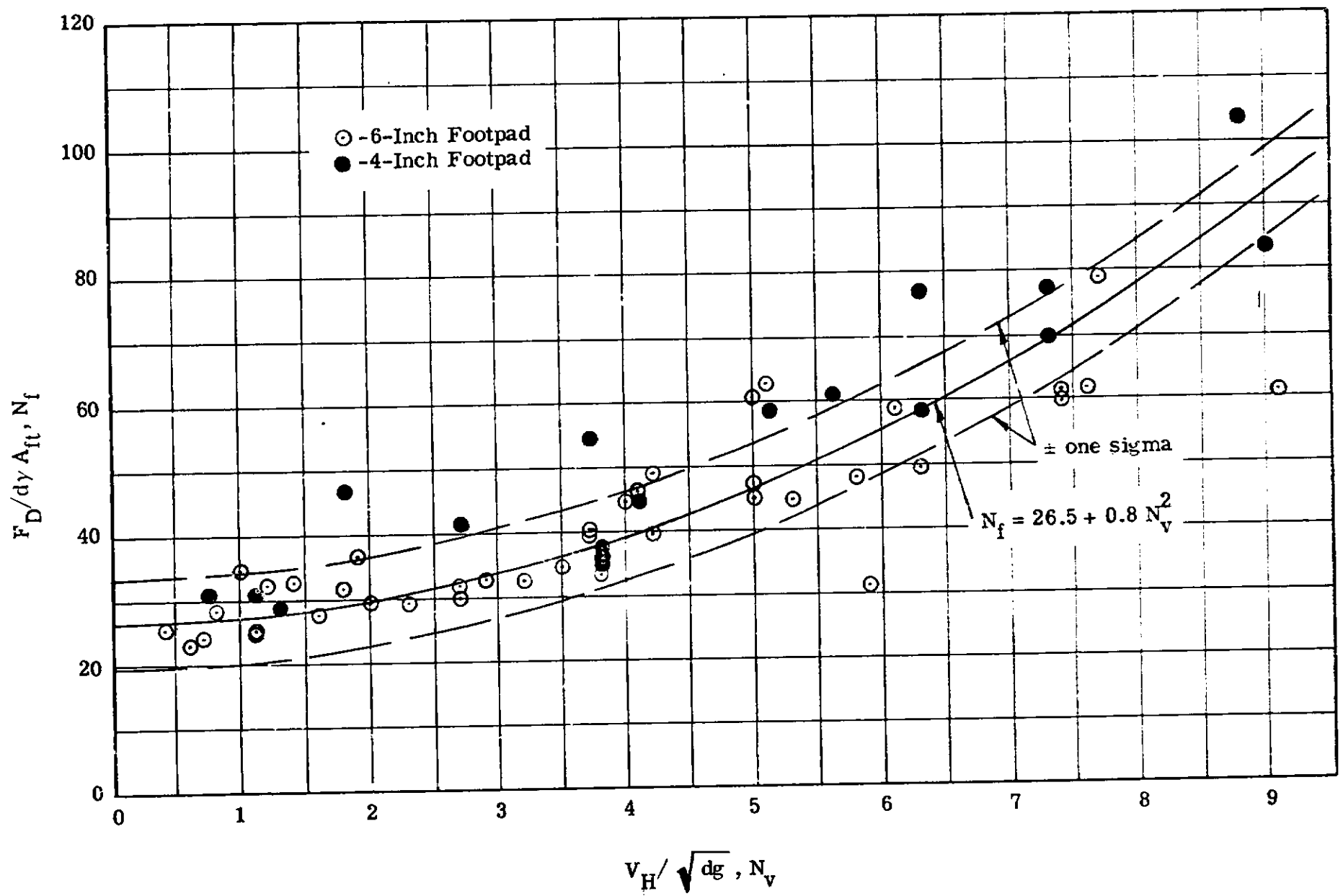

Figure 4-25. Drag Force Parameter versus Velocity Parameter
Soil No. 1 - RS Loose, $D_r = 0$

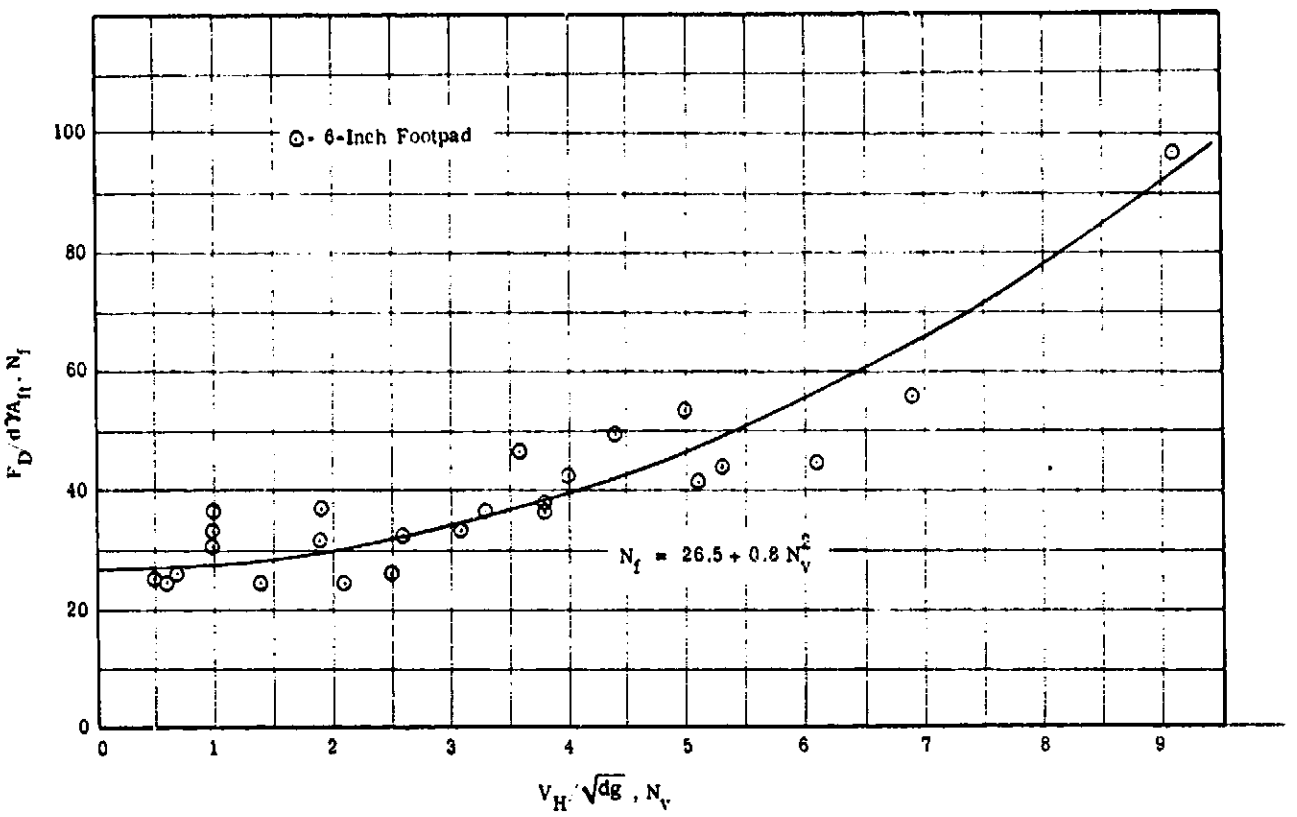

Figure 4-26. Drag Force Parameter versus Velocity Parameter
Soil No. 2 - PS Loose, $D_r = 0$

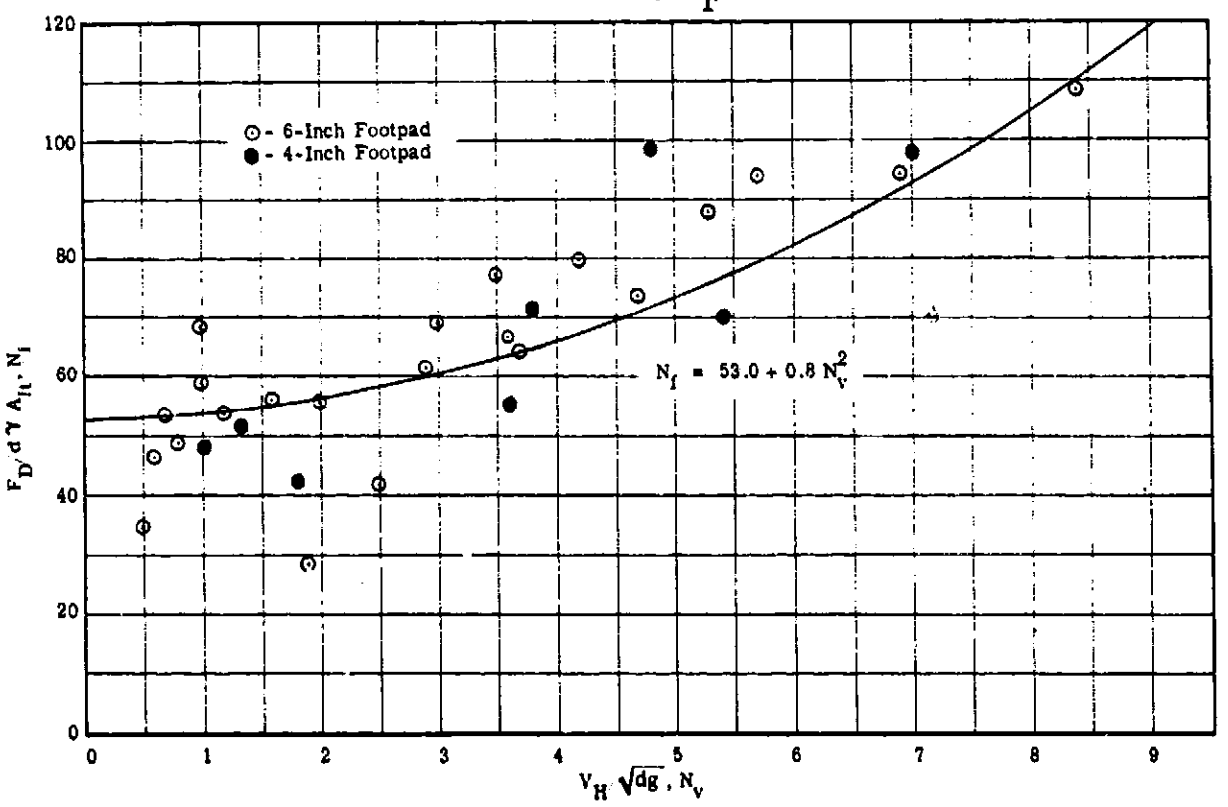

Figure 4-27. Drag Force Parameter versus Velocity Parameter
Soil No. 3 - RS Intermediate, $D_r = 0.45$

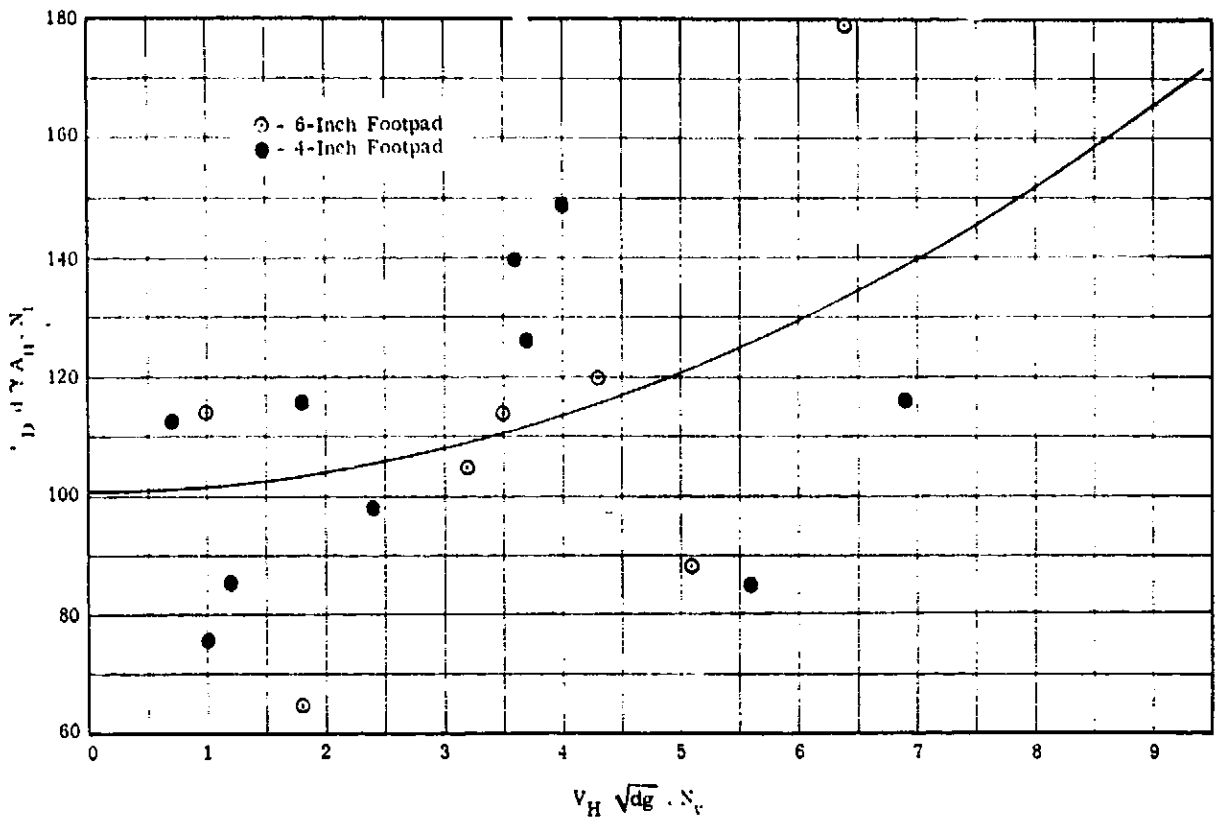

Figure 4-28. Drag Force Parameter versus Velocity Parameter
Soil No. 4 - RS Dense, $D_r = 0$

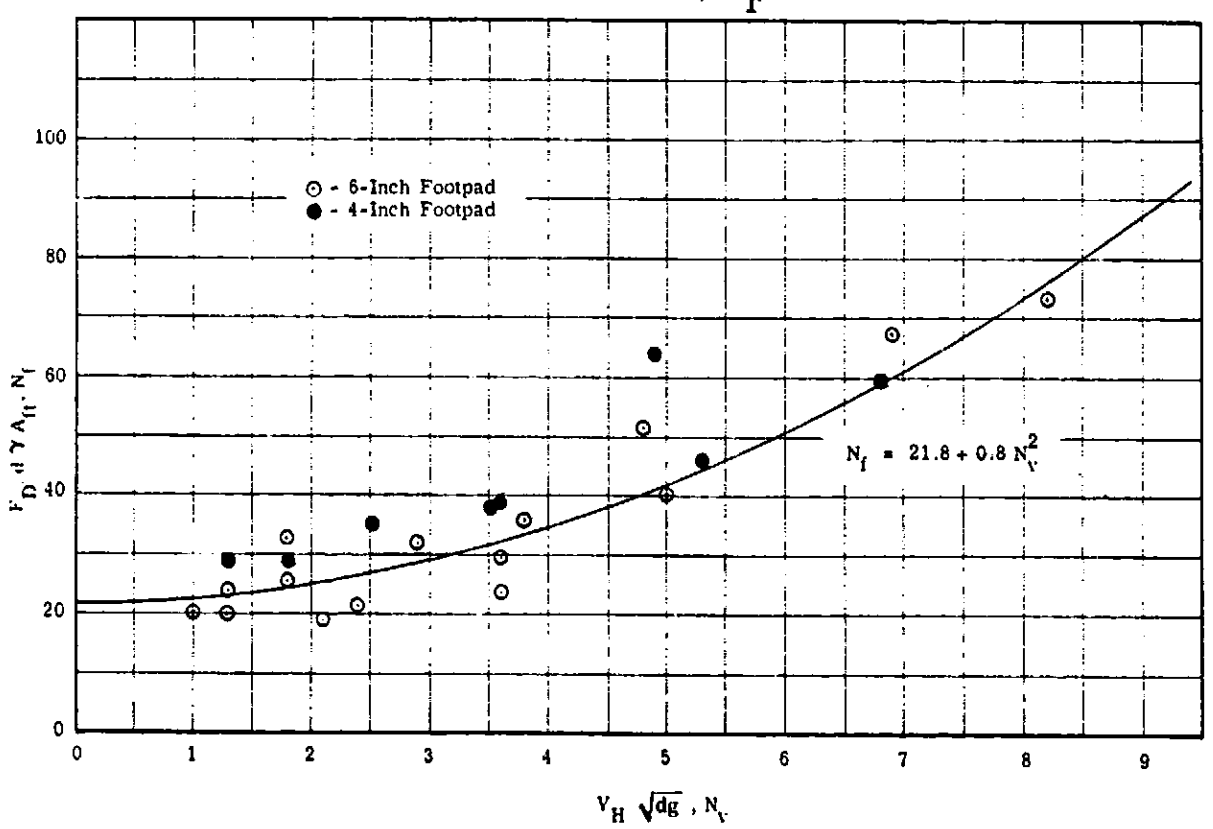

Figure 4-29. Drag Force Parameter versus Velocity Parameter
Soil No. 5 - RSMa Loose, $D_r = 0$

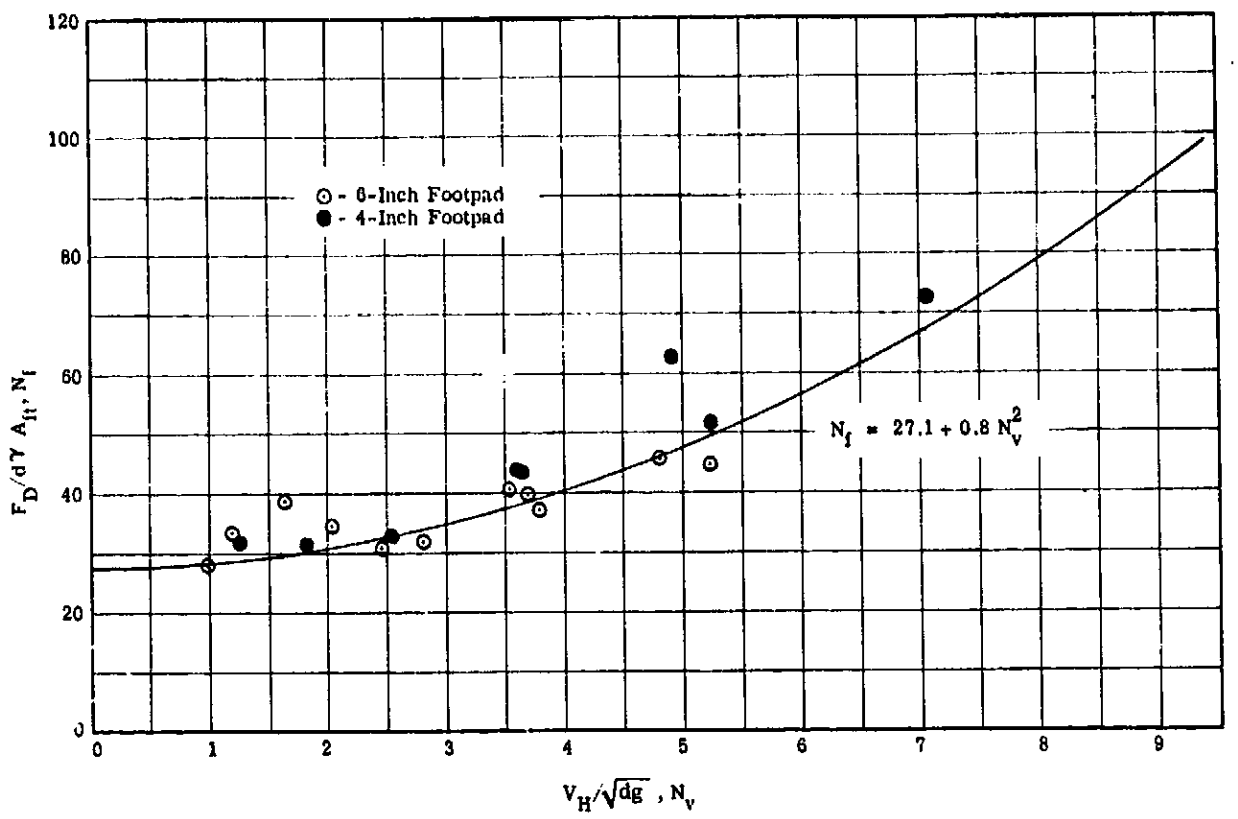

Figure 4-30. Drag Force Parameter versus Velocity Parameter
Soil No. 6 - RC2 Loose, $D_r = 0$

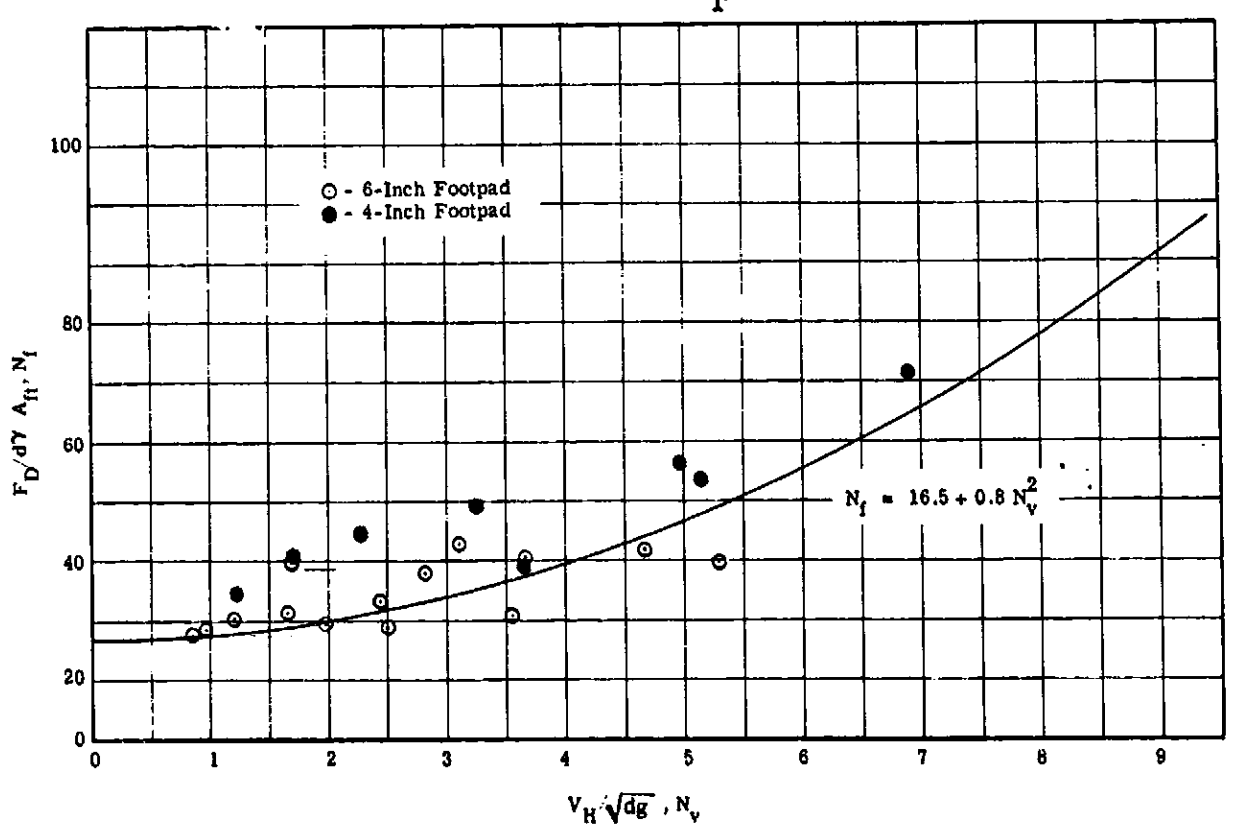

Figure 4-31. Drag Force Parameter versus Velocity Parameter
Soil No. 7 - SS Loose, $D_r = 0$

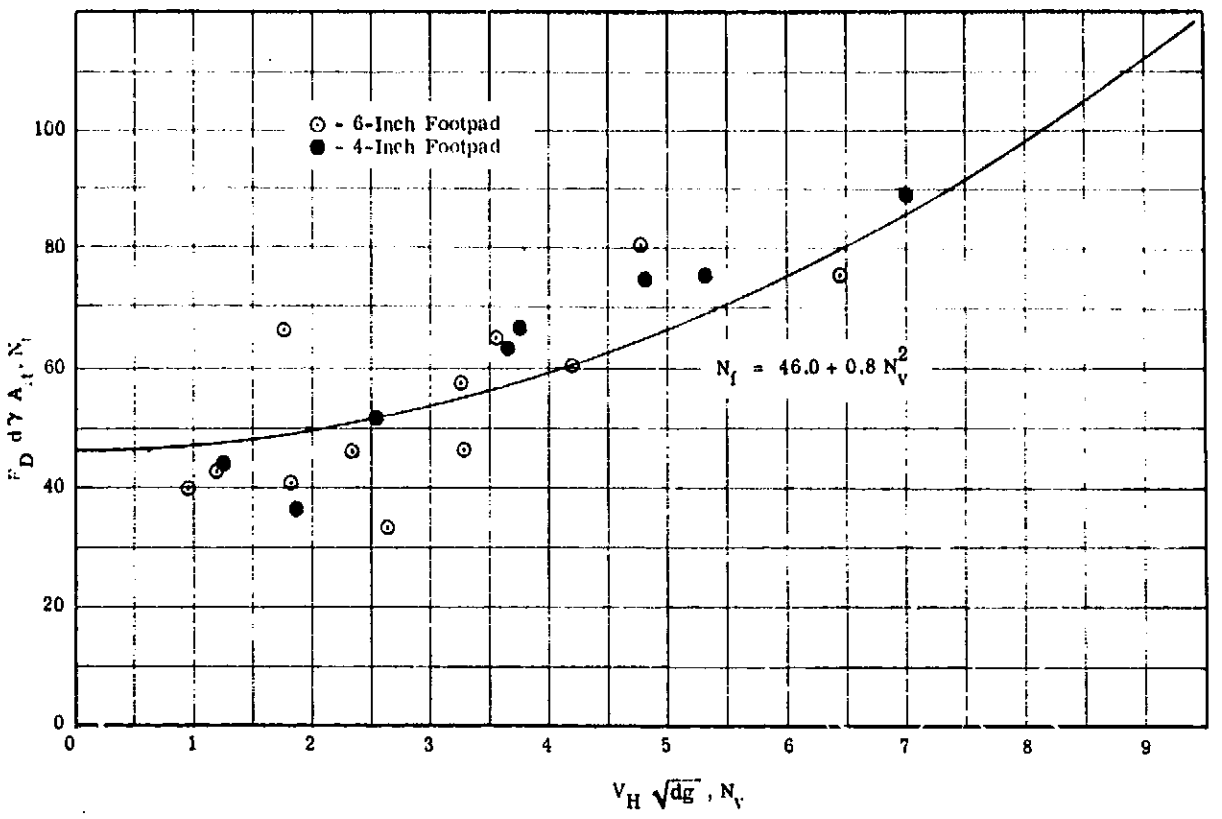

Figure 4-32. Drag Force Parameter versus Velocity Parameter
Soil No. 8 - SS Intermediate, $D_r = 0.53$

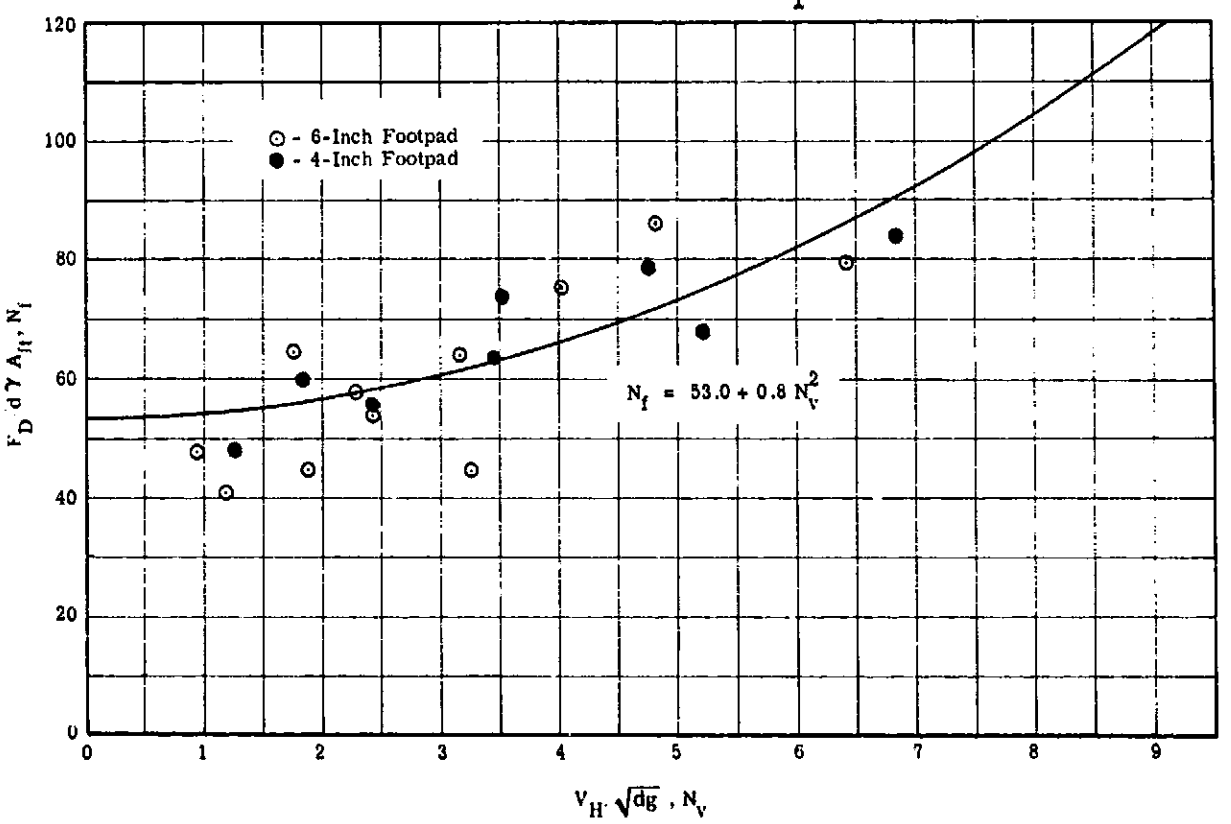

Figure 4-33. Drag Force Parameter versus Velocity Parameter
Soil No. 9 - SS Dense, $D_r = 0.69$

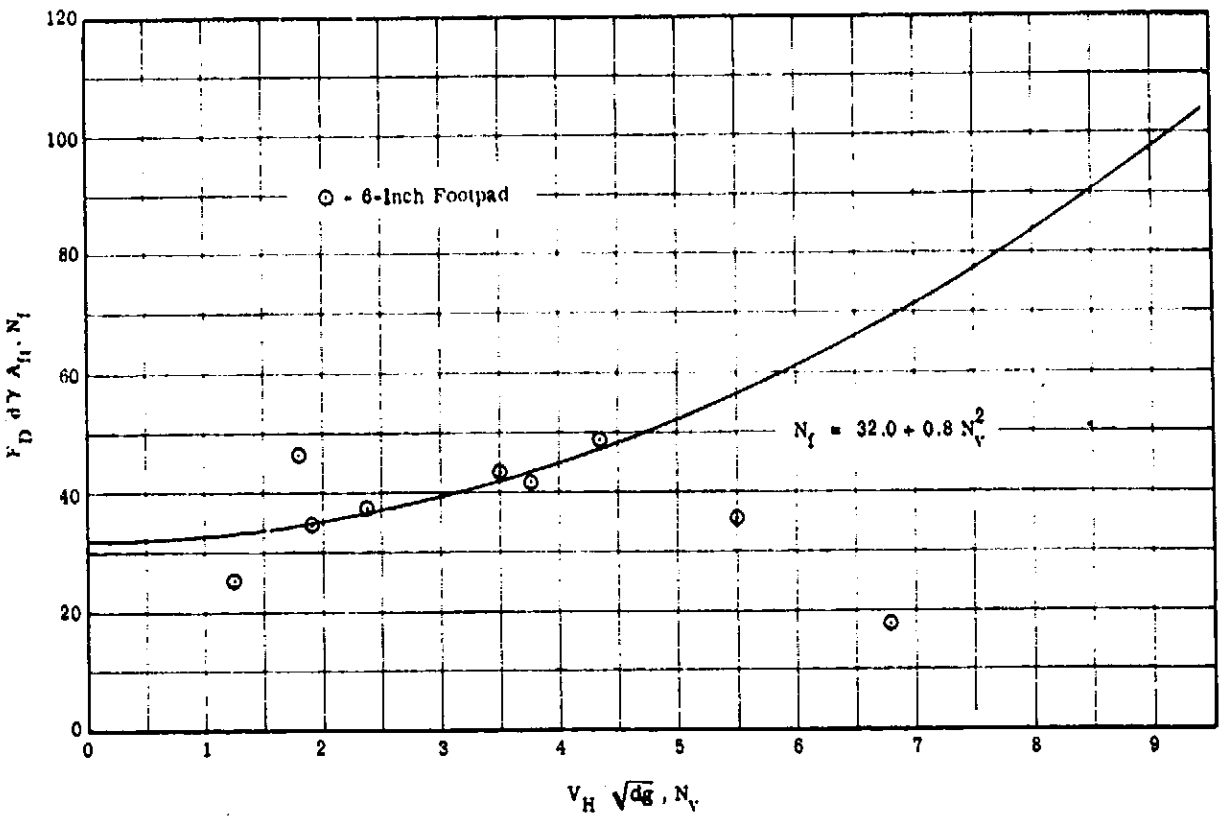

Figure 4-34. Drag Force Parameter versus Velocity Parameter
Soil No. 10 - LSM Intermediate, $D_r = 0.50$

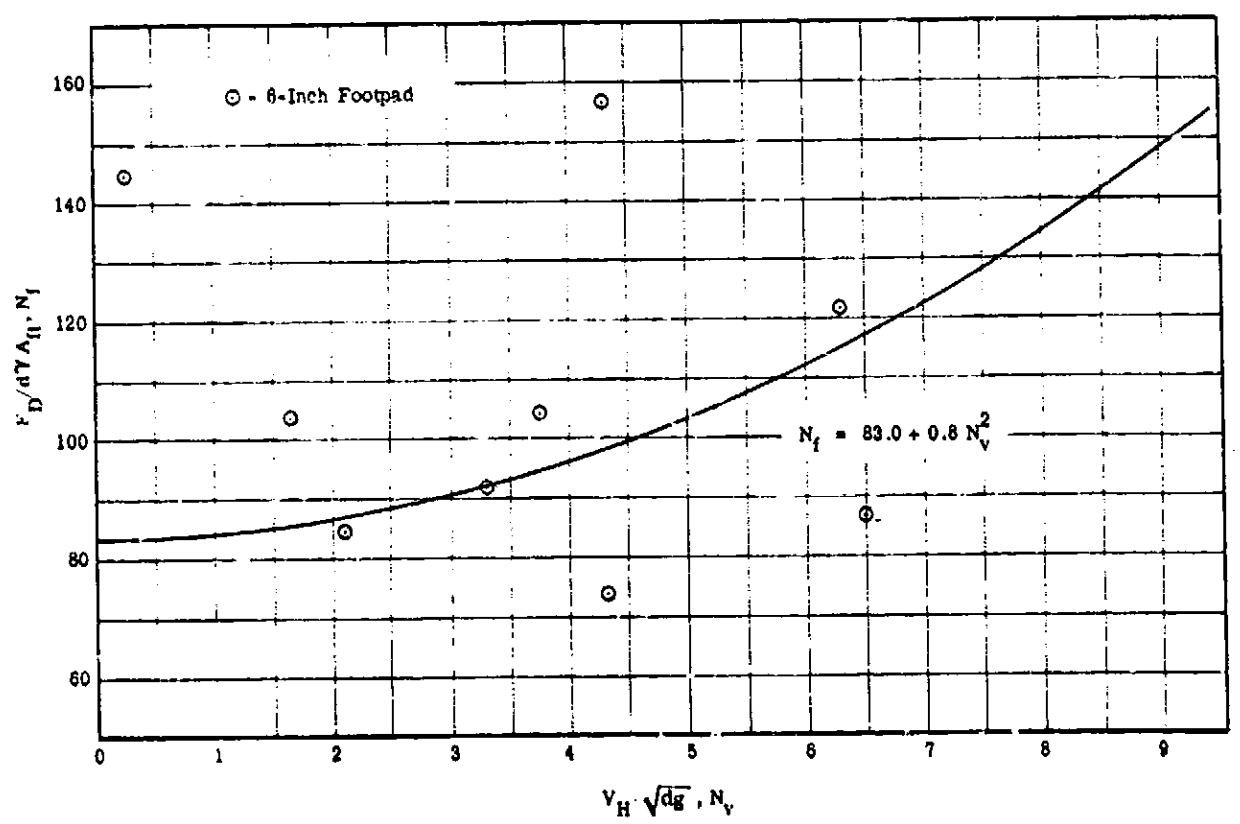

Figure 4-35. Drag Force Parameter versus Velocity Parameter
Soil No. 11 - LSM Dense, $D_r = 0.70$

upon soil type, but C_2 is the same value, 0.8, for all soils. It is reasonable that the term $C_2 N_v^2$ is not dependent upon soil strength, since it represents the force due to momentum transfer between the footpad and the soil and is therefore a function only of the mass flow rate of the soil past the footpad. C_2 is therefore considered to be a drag coefficient which is a function of only footpad geometry and will subsequently be referred to as C_D. The coefficient C_0 would be expected to vary from soil to soil because it represents the mechanical strength of the soil and is believed related to the static bearing strength of the soil. It is not surprising that the RS loose and PS loose test data yields the same value of C_0, since static tests of these soils showed that they have similar bearing strength properties.

At this point the equation relating drag force to footpad motion and soil properties has been defined in relatively general terms with the exception of the value of C_0. Since this coefficient is related to the mechanical strength of the soil, it will subsequently be referred to as the mechanical strength coefficient, C_{ms}.

Static bearing strength results presented in Section II of this report show that soil strength increases with both relative density and tangent of the internal friction angle. It is therefore expected that the mechanical strength coefficient would exhibit similar characteristics. Figure 4-36 is a plot of C_{ms} versus $\tan\phi$ for the five test soils having a relative density near zero.

These results show that the equation

$$(C_{ms})_{D_r=0} = 29 \tan\phi \qquad 4.27$$

is a reasonable representation of the mechanical strength relationship for these soils. The increase in strength with relative density is shown for all eleven test soils in Figure 4-37 which plots $C_{ms}/29 \tan\phi$ versus D_r. This data can be approximated by the equation

$$C_{ms}/29 \tan\phi = e^{1.4 D_r} \qquad 4.28$$

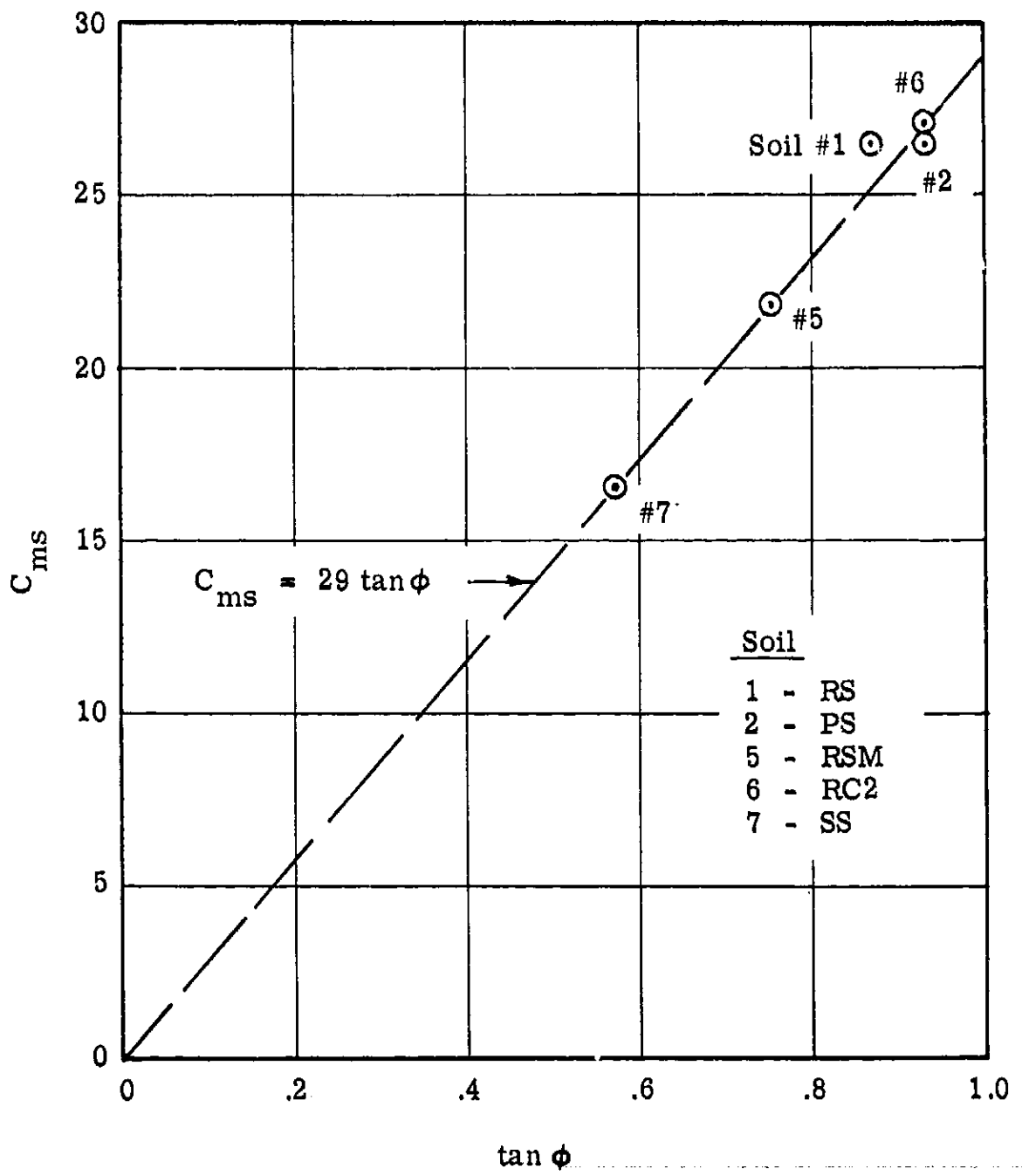

Figure 4-36. Mechanical Strength Coefficient versus tan ϕ for Zero Relative Density Test Soils

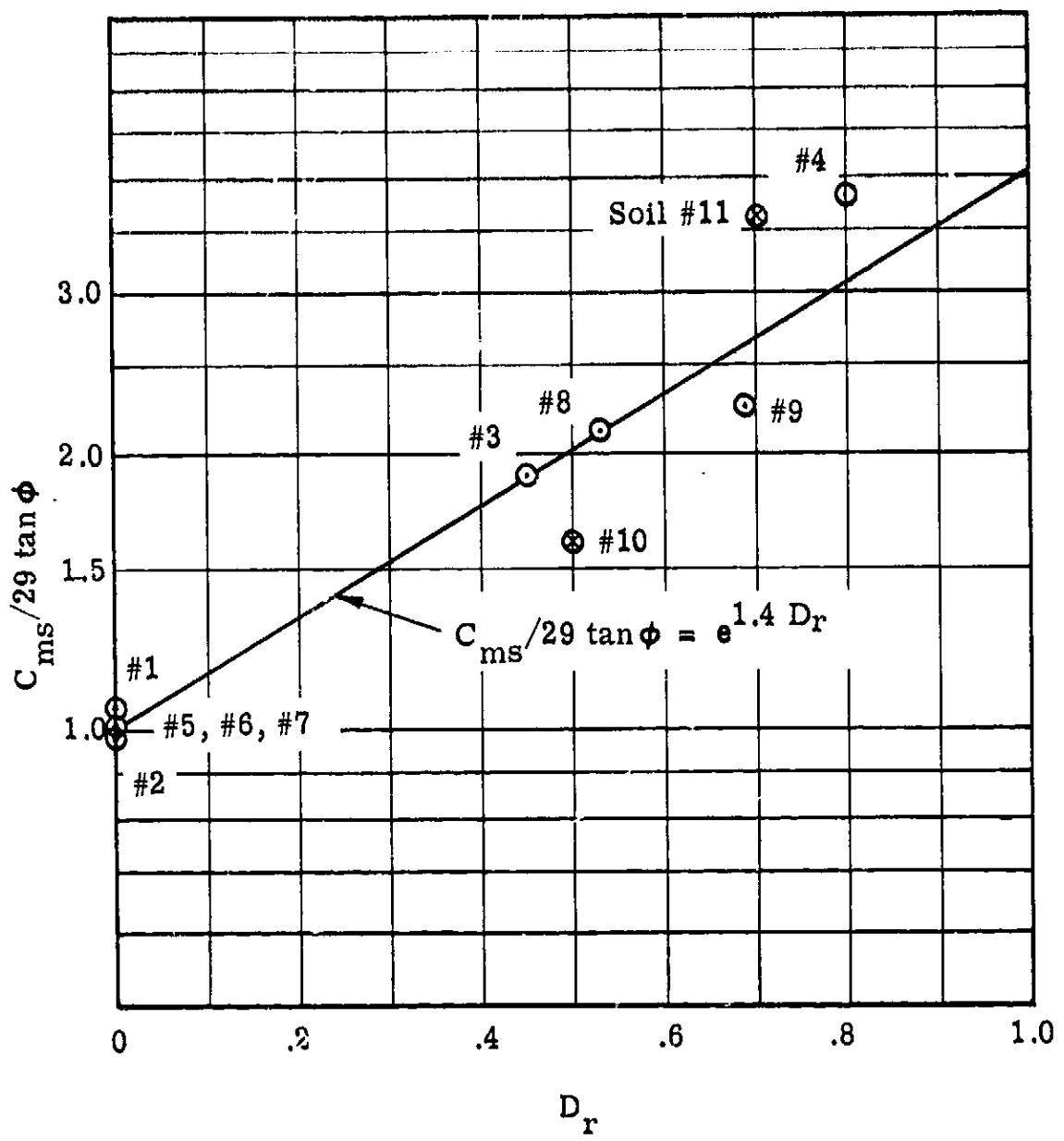

Figure 4-37. $C_{ms}/29 \tan\phi$ versus D_r for all Test Soils Based Upon Drag Test Results

4.5 ANALYSIS OF IMPACT PHENOMENA

Impact of a LM footpad in real soil was investigated using an approach combining analytical and experimental techniques. A two-degree-of-freedom mathematical model was derived in which the impact phase of the soil-footpad interaction was described by two nonlinear differential equations. The individual terms of the differential equation were associated with physical phenomena which are thought to be significant constituents of the soil-footpad interaction. The coefficients of these terms were determined by a semi-empirical method in which the forces recorded during impact tests were compared with the output of an analog computer simulation of the impact phenomenon. The results of these comparisons were ultimately generalized to describe the impact phenomenon as a function of impact conditions and soil descriptors.

Mathematical Model

The mathematical model which was derived is applicable either to vertical or oblique impact of a footpad at a specified velocity. This dynamic model is shown schematically in Figure 4-38 for vertical impact. Nomenclature for this discussion appears at the end of this section. The two differential equations comprising the dynamic model are the equation of motion of the impacting mass (including the footpad) and the "stagnation" mass which forms beneath the footpad. Equilibrium of forces on the impacting mass leads to

$$M_1 \ddot{\delta}_1 + \frac{r}{r_m} K_s (\delta_1 - \delta_2) - M_1 g = 0 \qquad 4.29$$

where M_1 is the impacting mass, K_s is the effective soil spring rate, g is the local acceleration of gravity, r is the radius of footpad contact area ($0 \leq r \leq r_m$), δ_1 is the axial penetration of the footpad and δ_2 is the axial displacement of the stagnation mass.

The first term is the inertial force on the impacting mass, the second term is due to elasticity of the soil and the third term is the weight of the impacting mass. The elastic force term is assumed to be of the same form as the elastic force developed in an elastic half-space loaded by a rigid circular disk; i.e., the force is proportional to radius and deflection (44).

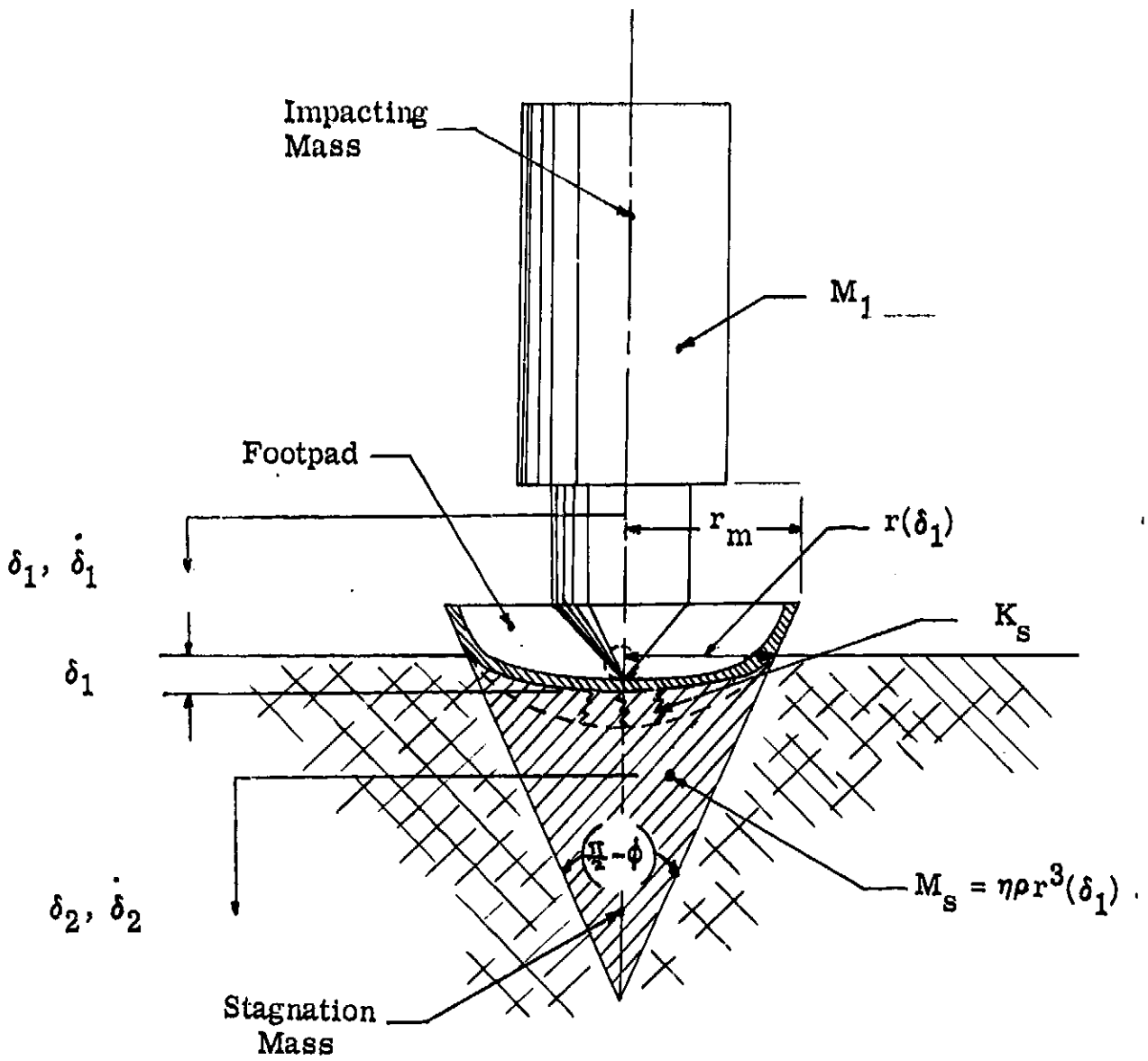

Figure 4-38. Schematic of Dynamic Model

The second differential equation is obtained from equilibrium of the stagnation mass. Since this mass is not constant, it is necessary to use the more general version of Newton's second law (force equals time rate of change of momentum). The equation obtained is

$$\frac{d}{dt}(\eta \rho r^3 \dot{\delta}_2) + C_{s2} r^2 \left|\dot{\delta}_2\right| \dot{\delta}_2 + a_1 \delta_2 - \frac{r}{r_m} K_s(\delta_1 - \delta_2) = 0 \qquad 4.30$$

where ρ is the soil bulk density. The expression in parentheses in the first term represents the momentum of the stagnation mass. The form of the expression is suggested by the mass of the soil cone which would form under a circular footing during a quasi-static loading:

$$M_s = \frac{\pi \rho r^3}{3 \tan(\pi/4 - \phi/2)} \qquad 4.31$$

The coefficient η in the momentum term of Equation 4.30 replaces the term $\pi/3 \tan(\pi/4 - \phi/2)$ and includes the correction necessary to account for the difference between the shape of the stagnation mass and the cone described in Equation 4.31.

Carrying out the indicated differentiation in Equation 4.30, the inertial and mass growth terms are defined:

$$\frac{d}{dt}(\eta \rho r^3 \dot{\delta}_2) = \eta \rho (r^3 \ddot{\delta}_2 + 3r^2 \dot{\delta}_2 \dot{r}) \qquad 4.32$$

but

$$\dot{r} = \frac{dr}{d\delta_1} \dot{\delta}_1 \qquad 4.33$$

so that Equation 4.30 becomes

$$\eta \rho (r^3 \ddot{\delta}_2 + 3r^2 \frac{dr}{d\delta_1} \dot{\delta}_1 \dot{\delta}_2) + C_{s2} r^2 \left|\dot{\delta}_2\right| \dot{\delta}_2 + a_1 \delta_2 - \frac{r}{r_m} K_s(\delta_1 - \delta_2) = 0 \qquad 4.34$$

The functions r and r^2 dr/d δ_1 are functions of footpad geometry and depth of penetration. Assuming that the footpad centerline is normal to the surface, r and r^2 dr/d δ_1 are as shown (in normalized form) in Figure 4-39. The C_{s2} term represents the momentum transfer phenomenon which occurs as the footpad-stagnation mass combination penetrates the surrounding soil. This force is proportional to the footpad cross section in the plane of the free surface, and to the square of the velocity of the stagnation mass. The a_1 term represents the soil strength and is proportional to the penetration of the stagnation mass into the surrounding soil.

A modification is required to describe oblique impacts. With the understanding that δ_1 and δ_2 are measured in the direction of the impact velocity, the differential Equation 4.29 becomes

$$M_1 \ddot{\delta}_1 + \frac{r}{r_m} K_s (\delta_1 - \delta_2) - M_1 g \cos \theta = 0 \qquad 4.35$$

where θ is the angle between the impact velocity vector and the surface normal. The form of Equation 4.34 remains unchanged.

Analog Computer Study

The equations of motion 4.34 and 4.35 were instrumented for analog computation to establish the values of coefficients C_{s2}, a_1, η and K_s for various subscale and full-scale vertical and oblique impact tests. The procedure followed was a two-step process. First, a group of tests was simulated to verify that the simulation was capable of providing a reasonable match with the experimental data and to obtain preliminary values of coefficients. Good correlation was obtained in the majority of the cases, and the values of a_1 obtained were used to formulate an empirical relationship between a_1 and the soil descriptors. A second group of tests, including some repeats from the first group, was simulated with the value of a_1 predetermined by the empirical relationship. The finalized coefficients η, K_s and C_{s2} were determined by matching the simulation with the data from the second group of tests. Empirical relationships were then constructed for η, K_s and C_{s2}.

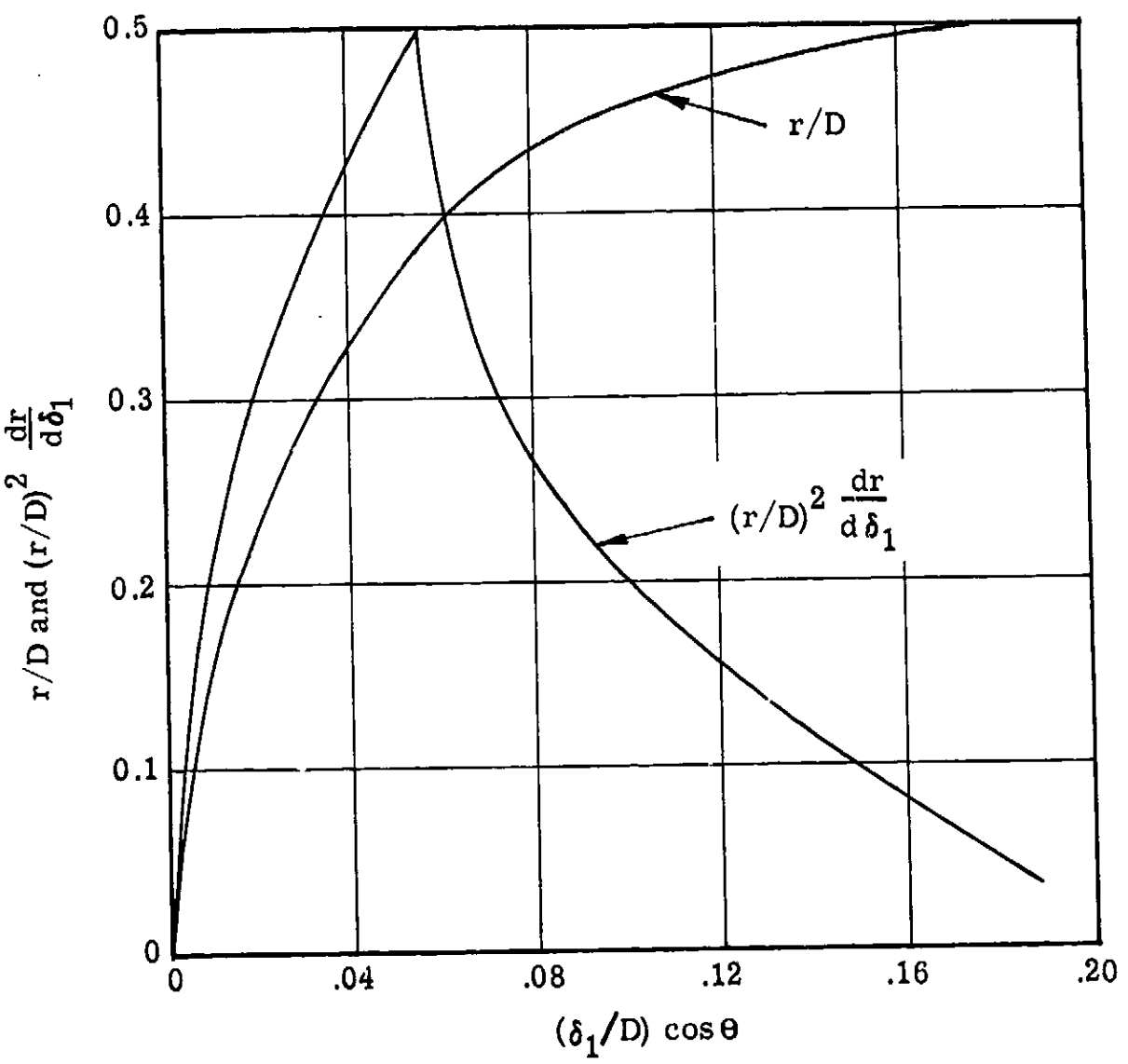

Figure 4-39. Normalized Footpad Geometry

Correlation was obtained for 26 full-scale and subscale impact tests. Preliminary values of the coefficients are presented in Figure 4-40. Two sets of coefficients are presented for some of the tests indicating that while the choice of coefficients is not unique for a given test, the variations are minor.

The results of this phase of the study were quite satisfactory. Figures 4-41 through 4-46 present selected examples of force versus time and force versus penetration comparisons between experimental and analog data. These are examples of good or fairly good correlation which constitute 90 percent of the cases studied. The black circles denote experimental data. Variations from nominal impact velocity (V_0) of ±10 inch/second are also shown as a conservative indication of the possible effect of uncertainty in the velocity data. Less satisfactory correlation was confined to oblique impacts at 52.5° and 70°. It is likely that increased bearing reactions due to the higher applied torque at these impact angles caused significant friction forces which are not accounted for in the simulation. Only one case was considered to correlate poorly. This case, an oblique impact at 70°, is shown in Figures 4-47 and 4-48.

The degree of correlation with experimental data indicates that the essential features of the impact phenomenon have been simulated adequately. Figure 4-49 is a reproduction of the analog computer output for the case shown in Figure 4-41. The various output functions are useful in providing an understanding of the interaction among the various types of forces affecting the footpad motion during impact.

The compressive force acting between the moving soil mass and the footpad is plotted as a function of time on Channel 5. This trace is characteristic of simulations of vertical impact in loose soil, and it shows a relatively high initial peak which blends into a region where the force is constant or changing slowly. The peak is due primarily to the momentum transfer force on the soil mass (Channel 6), but the mass growth term (Channel 14) is significant. The inertial force (Channel 1) is of less significance and tends to decrease the force on the footpad following initial acceleration of the soil mass. Subsequent to the initial peak, the momentum transfer force decreases at a rate approximately equal to the increase in the soil strength term. The soil strength term is proportional to δ_2 which

Soil	Scale	V_o (In./Sec.)	a_1 (Lb./In.)	C_{s2} (Lb.-Sec.^{2}/In.^{4})	η (Dimensionless)	K_s (Lb./In.)	θ (Degrees)
RS Dense (D_r = .65)	Full	95	3,000	.015	1.0	45,000	0
		95	4,000	.012	1.0	80,000	0
		175	2,500	.008	1.0	30,000	0
RS Loose (D_r = 0)	Full	115	625	.0005	1.6	15,000	0
		150	675	.0006	1.25	15,000	0
		177	600	.0007	1.25	15,000	0
RS Loose (D_r = 0)	1/6	52.7	35	.0007	2.5	1,750	0
		84	35	.0009	2.7	1,750	0
		108	33	.00085	2.5	1,350	0
		108	34	.0008	2.5	1,750	0
		128.4	32	.00075	2.1	1,750	0
		140	34	.0007	1.8	1,750	0
		140	34	.00075	1.7	1,750	0
		179	35	.0007	2.7	1,750	0
RS Intermediate/Loose (D_r = .25)	1/6	77.3	20	.0065	2.3	5,000	0
RS Intermediate (D_r = .45)	1/6	56.6	35	.0125	3.5	5,000	0
		76	35	.008	2.5	5,000	0
		70.6	17	.008	2.5	5,000	17.5
		77.4	19	.0047	2.5	5,000	35
		73.3	19	.0022	2.5	5,000	52.5
		70.2	8	.0009	.5	5,000	70
RS Dense (D_r = .65)	1/6	57.2	45	.033	3.5	10,000	0
		70.6	35	.035	1.75	12,500	0
		78	40	.025	1.75	12,500	0
		84.3	28	.0195	1.75	12,500	17.5
		76.6	19	.014	1.75	12,500	35
		77.4	14	.007	1.75	12,500	52.5
		71.3	13	.0017	1.75	12,500	70
RS Dense/Dense (D_r = .8)	1/6	68.6	55	.069	3.5	10,000	0

Figure 4-40. Preliminary Values of Coefficients

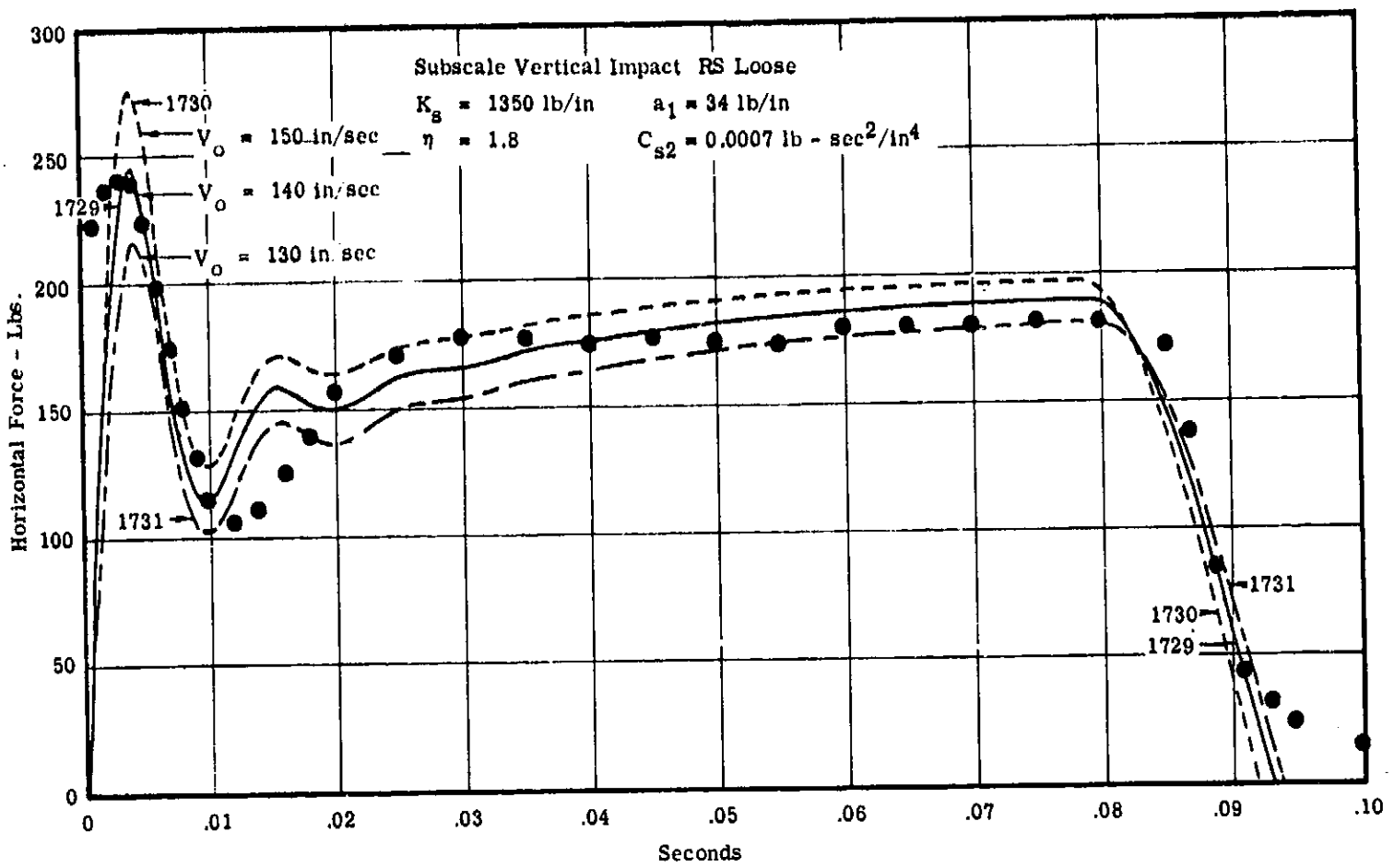

Figure 4-41. Comparison of Experimental and Computed Force versus Time Histories

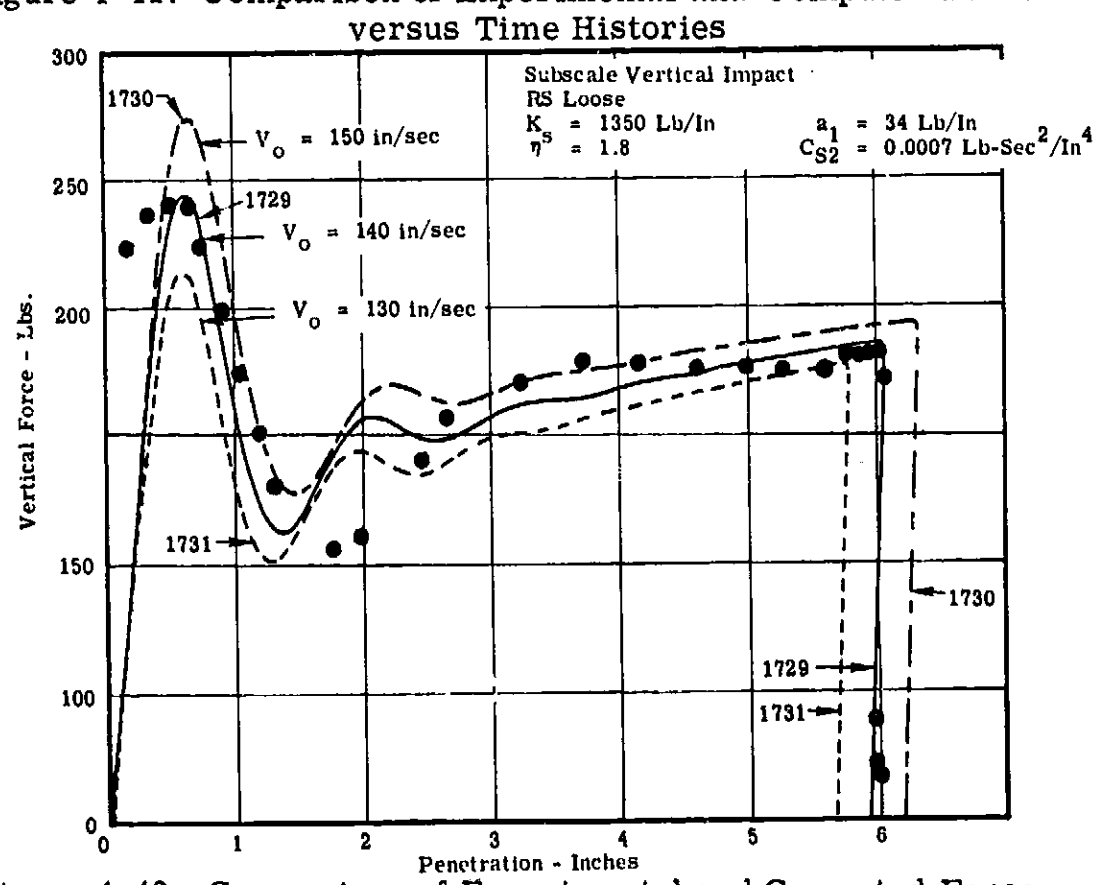

Figure 4-42. Comparison of Experimental and Computed Force versus Penetration Histories

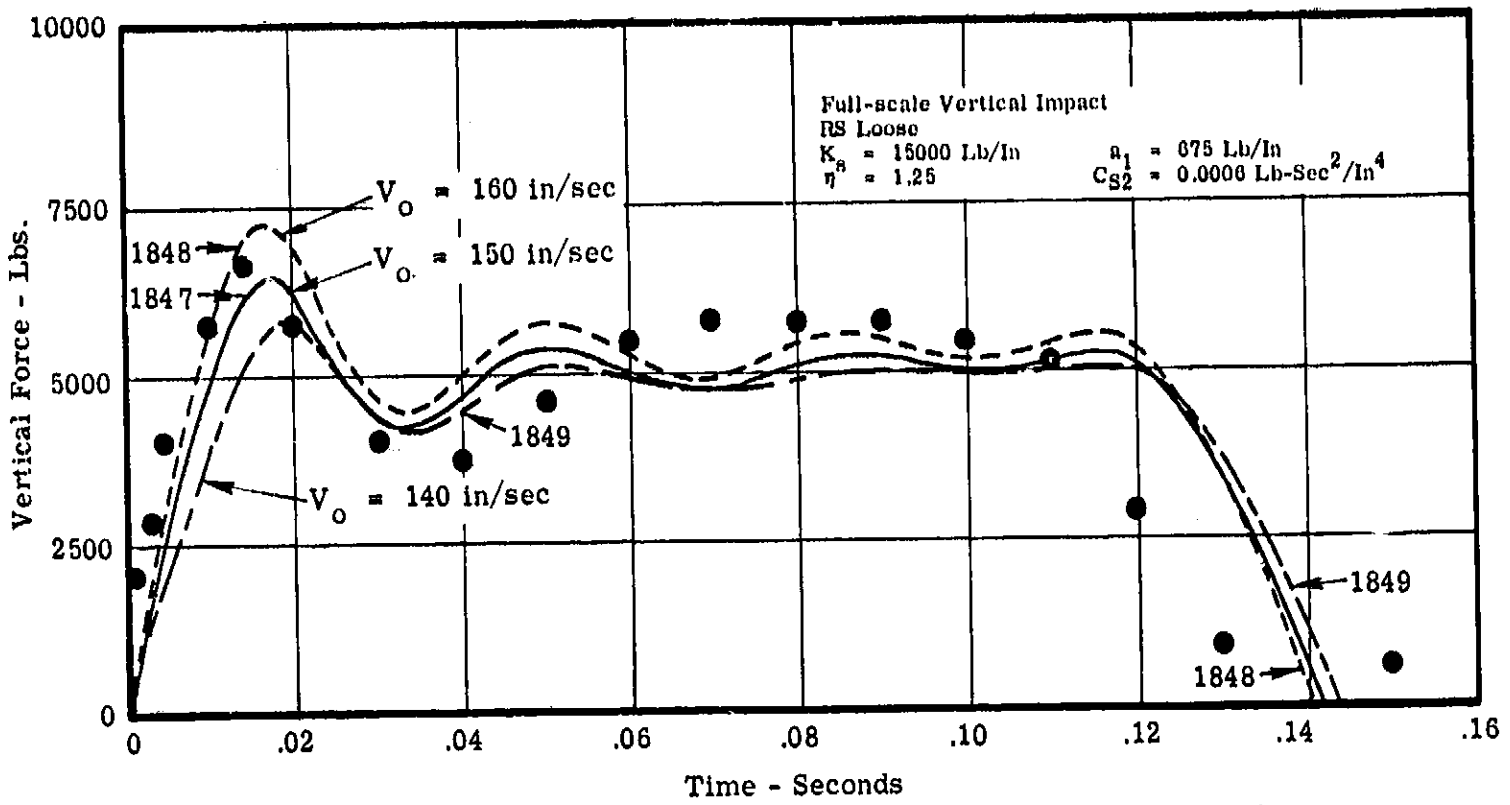

Figure 4-43. Comparison of Experimental and Computed Force versus Time Histories

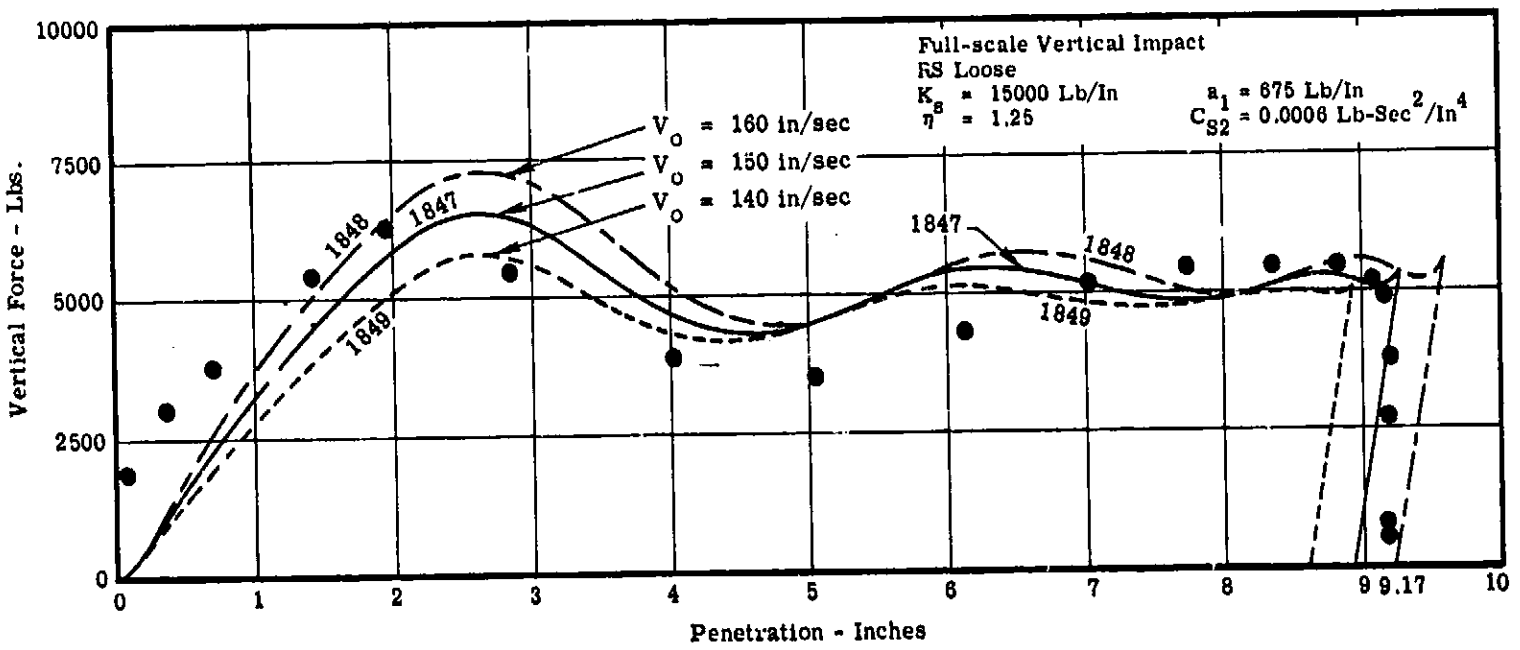

Figure 4-44. Comparison of Experimental and Computed Force versus Penetration Histories

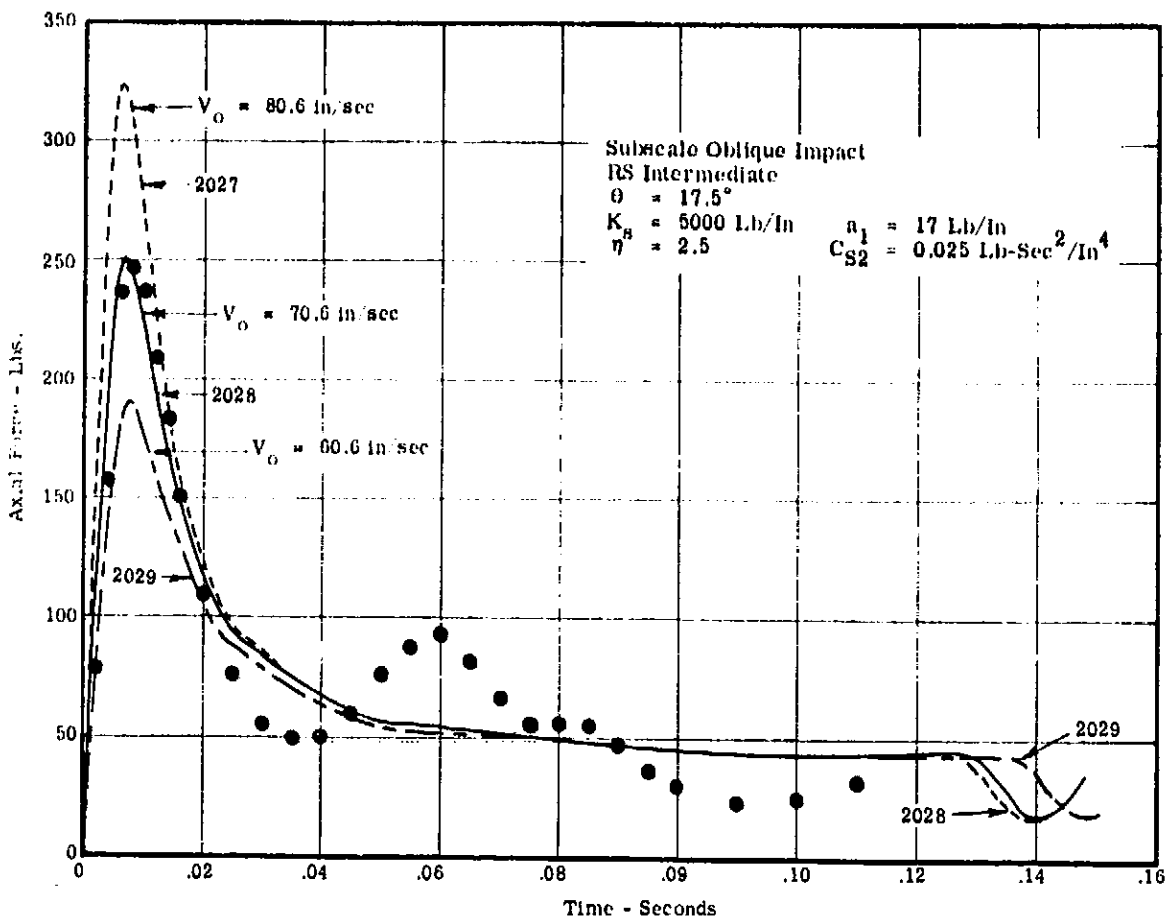

Figure 4-45. Comparison of Experimental and Computed Force versus Time Histories

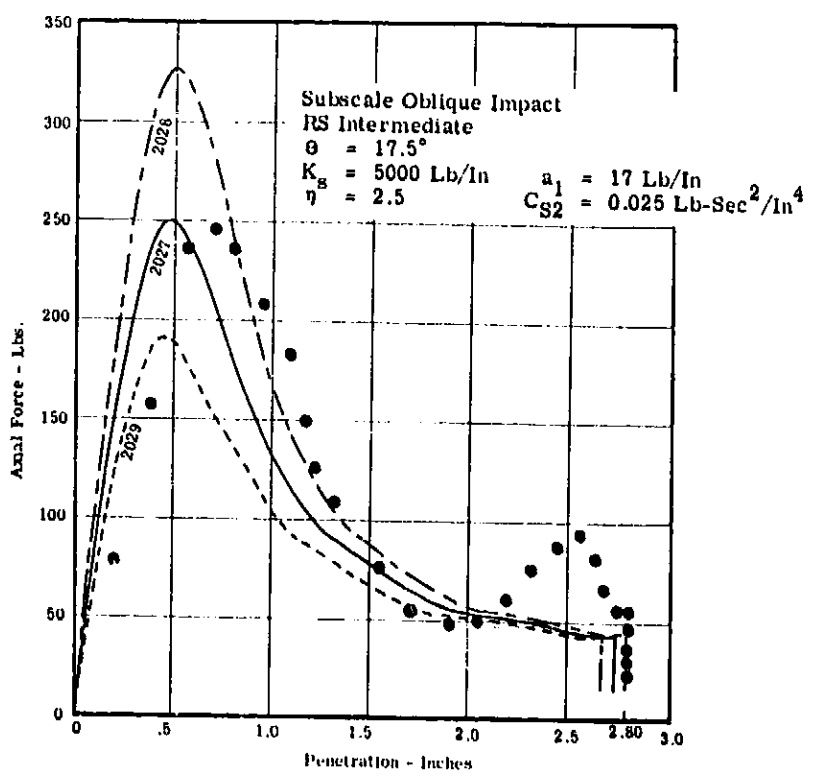

Figure 4-46. Comparison of Experimental and Computed Force versus Penetration Histories

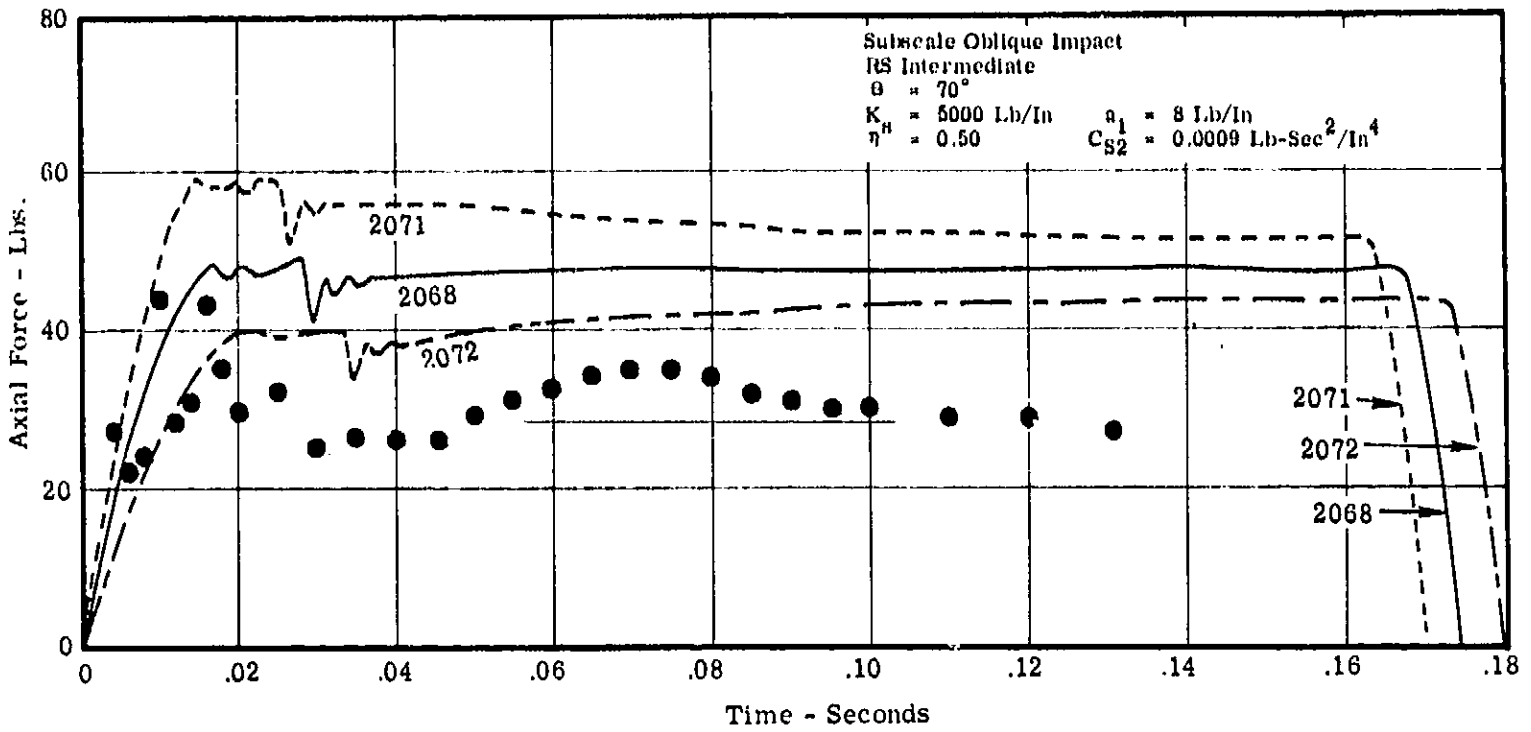

Figure 4-47. Comparison of Experimental and Computed Force versus Time Histories

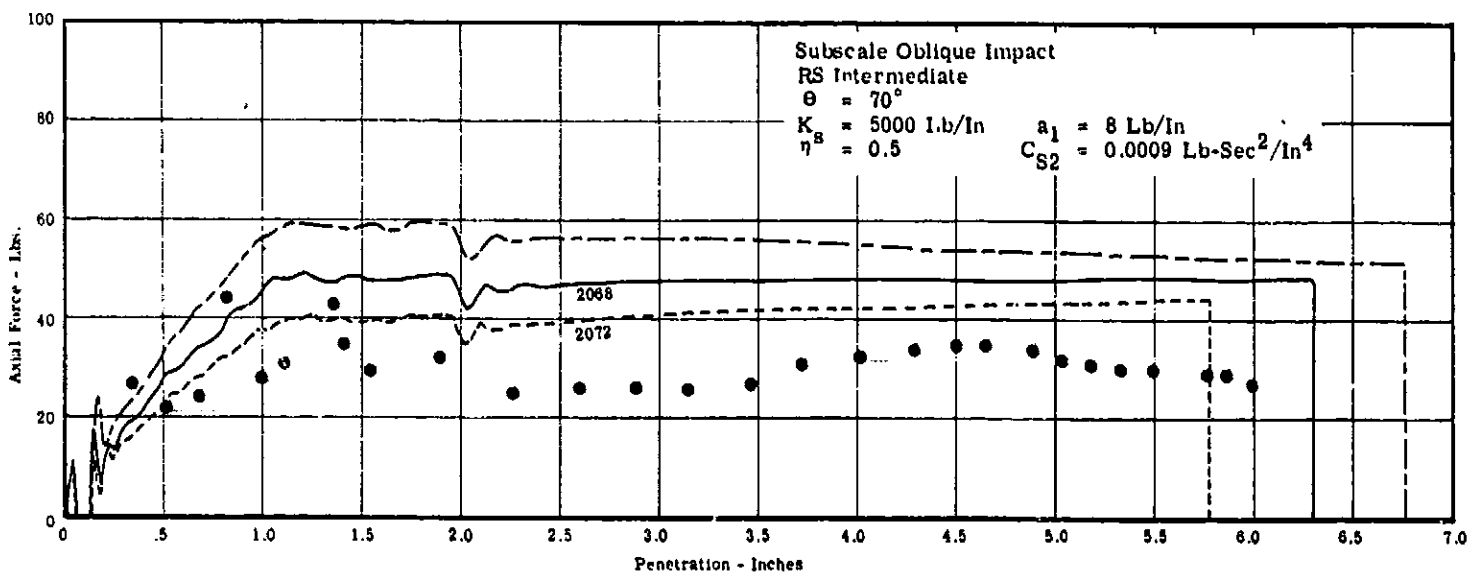

Figure 4-48. Comparison of Experimental and Computed Force versus Penetration Histories

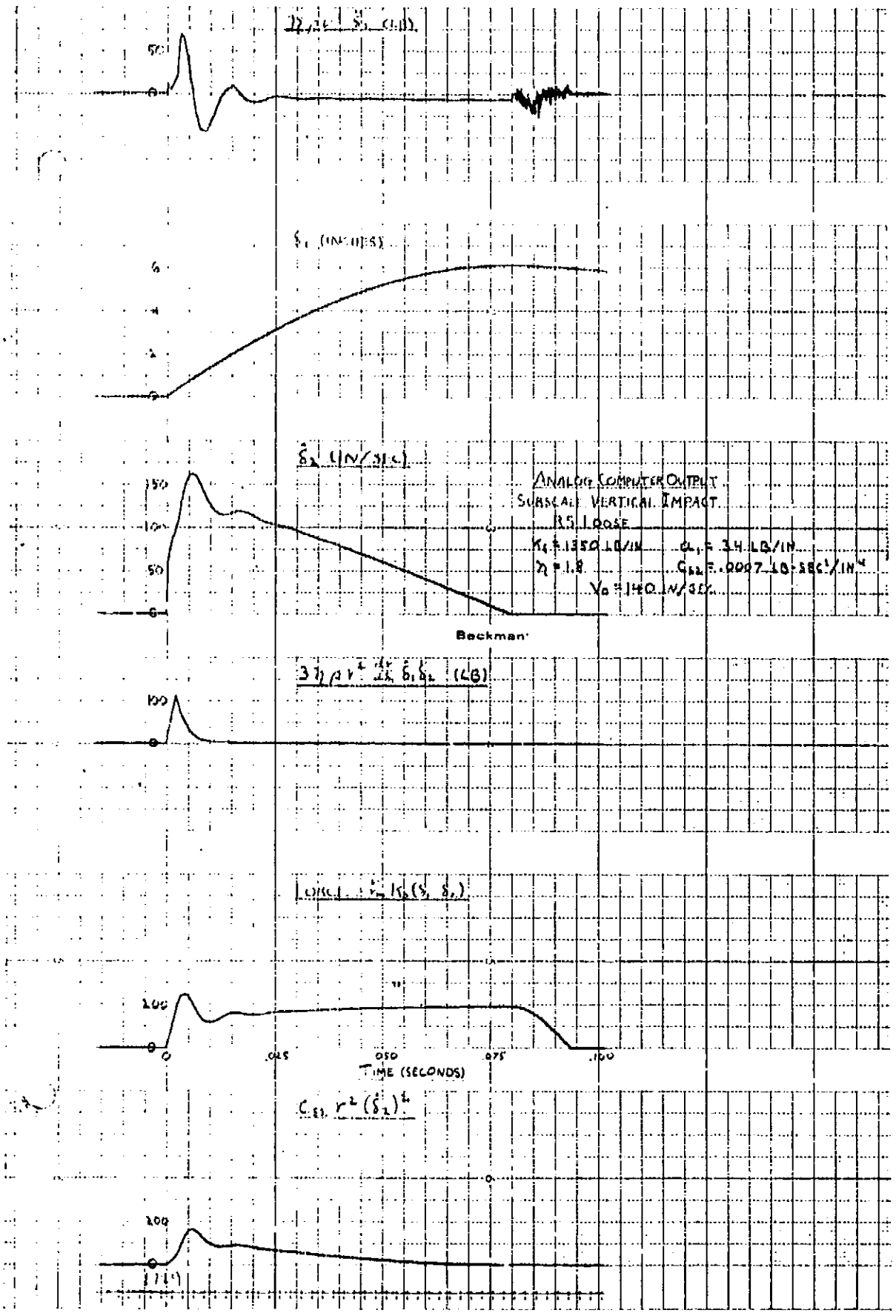

Figure 4-49. Sample Analog Computer Output

resembles δ_1 (Channel 2). For increased impact angles the peak footpad axial force tends to decrease. The magnitude of the peak force varies approximately as the square of the impact velocity due to the dominant momentum transfer term.

The values of a_1 found in Figure 4-40 were used in constructing Figure 4-50 which defines the variation of dynamic mechanical strength with relative density (this curve was subsequently approximated by $e^{1.4\ D_r}$ for digital computer simulation). The coefficient a_1 is related to the mechanical strength coefficient by the relation

$$a_1 = \rho g A_{ft}\ C_{ms} \qquad 4.36$$

The a_1 values were not applied directly to Equation 4.36 in all cases, however. One of the factors which had a strong effect on the choice of a_1 was the maximum penetration of the footpad. Every effort was made to obtain agreement between experimental data and the simulation in this respect.

But it was often observed that for other than loose soils a phenomenon occurred which is illustrated by Figure 4-46. Although maximum penetration correlates closely, there is a force discrepancy in the last 3/4 inch of penetration. This discrepancy probably results from the fact that the simulation does not account for changes in soil strength due to transition from dynamic to static conditions (this effect is discussed in more detail elsewhere in the report). It appears that the force level near the end of a test is more reliable than maximum penetration for selecting the proper value of a_1. Accordingly, most of the values of a_1 from the analog study were factored upward before applying them to Equation 4.36.

In the second phase of the study, 22 subscale vertical and oblique impact tests were simulated using values of a_1 consistent with Figure 4-50. The procedure of matching analog computer output with experimentally determined axial force data was repeated to finalize values of C_{s2}, K_s and η. Variations in a_1 of ± 15 percent were considered so that the sensitivity of these coefficients to variations in a_1 could be assessed. Tests chosen for simulation were selected to provide information on the effects of relative

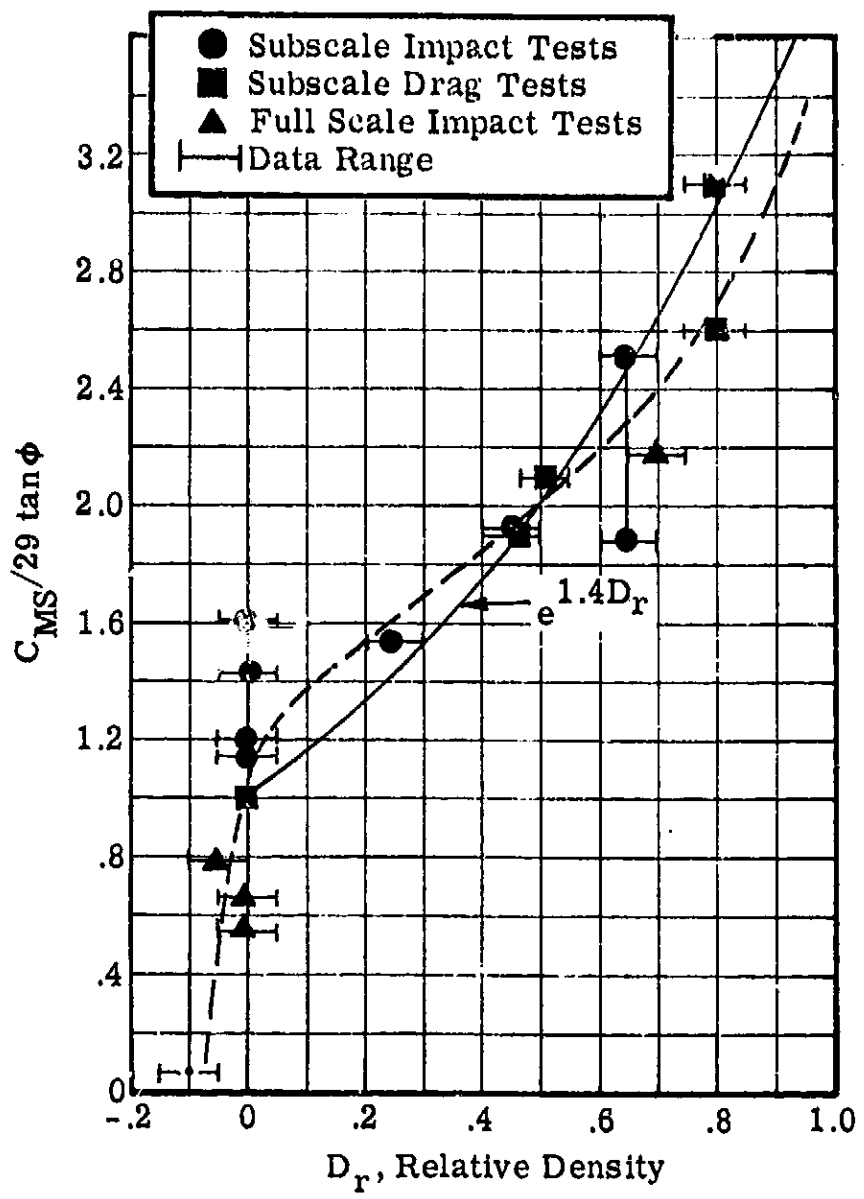

Figure 4-50. Variation of Normalized Dynamic Mechanical Strength with Relative Density - Drag and Impact Test Results

density, impact angle, and impact velocity. The finalized values of the coefficients are presented in Figure 4-51. The ± 15 percent variation in a_1 has little effect on the other coefficients.

Figures 4-52 through 4-55 are presented as examples of data comparison from which the finalized coefficients were obtained. Data from four subscale vertical impact tests on SS soil are presented covering a range of relative densities from 0 to 0.65. Correlation between the analog simulation and experimental data is good. Other correlation data (not shown) revealed that it was more difficult to obtain good correlation for higher impact angles. This difficulty was also experienced in the first phase of the analog study.

The analog simulation was also used to determine coefficients applicable to a short series of subscale impact tests performed in a reduced gravity environment. There tests were performed on an SS soil having a very high relative density (about 0.85). The coefficients determined from these tests are listed in Table 4. Correlation between the simulation and test data was adequate. The coefficient a_1 was selected from Figure 4-50 by using the reduced value of g in Equation 4.36. Figure 4-56 shows a tendency for C_{s2} to decrease as gravitational acceleration decreases.

4.6 DESCRIPTION OF SOIL MODEL

The results of analysis of the drag and impact test data are sufficient to define general relationships between LM footpad/soil interaction force law coefficients and pertinent soil and motion parameters. The following section describes the development of the general soil model for the LM footpad based upon the analysis of drag and impact test results covered in the previous discussions.

The basic concept of the dynamic soil model developed in this study is a representation of the soil/footpad system as a nonlinear two degree-of-freedom mechanical system as shown in Figure 4-57. The two masses of the system are the footpad and a moving stagnation volume of soil, M_s. The footpad, which is at an angle α with the soil surface, is moving along an arbitrary path with the velocity vector at an angle θ to the surface normal. The path is determined by an integration of the three translational equations of

Soil	V_o (In./Sec.)	a_1 (Lb./In.)	C_{s2} (Lb.-Sec.^{2}/In.^{4})	η (Dimensionless)	K_s (Lb./In.)	θ (Degrees)	Comments
RS Dense Dense (D_r = .8)	68.6	97.5*	.068	3.5	10,000	0	Relative Density Variation
	68.6	82.9	.067	3.5	10,000	0	Relative Density Variation
	68.6	68.2	.068	3.5	10,000	0	Relative Density Variation
RS Dense (D_r = .65)	78	68*	.025	3.5	10,000	0	Relative Density Variation
	78	78.2	.0245	3.5	10,000	0	Relative Density Variation
	78	57.8	.025	3.5	10,000	0	Relative Density Variation
RS Intermediate (D_r = .45)	76	49.9*	.008	3	8,500	0	Relative Density Variation
	76	57.4	.0077	3	8,500	0	Relative Density Variation
	76	42.4	.0079	3	8,500	0	Relative Density Variation
RS Intermediate Loose (D_r = .25)	77.3	38.4*	.0070	2	8,500	0	Relative Density Variation
	77.3	44.1	.0070	2	8,500	0	Relative Density Variation
	77.3	32.6	.0070	2	8,500	0	Relative Density Variation
RS Loose (D_r = 0)	84	23*	.0011	2.5	1,250	0	Relative Density Variation
	84	26.4	.00105	2.5	1,250	0	Relative Density Variation
	84	19.6	.0011	2.45	1,250	0	Relative Density Variation
SS Dense/Dense (D_r = .65)	80.7	97.2*	.025	3	40,000	0	Relative Density Variation
	80.7	111.8	.025	3	40,000	0	Relative Density Variation
	80.7	82.6	.025	3	40,000	0	Relative Density Variation
SS Dense (D_r = .6)	78.3	90.7*	.0285	3	40,000	0	Relative Density Variation
	78.3	104.2	.028	3	40,000	0	Relative Density Variation
	78.3	77.1	.028	3	40,000	0	Relative Density Variation
SS Intermediate (D_r = .3)	83.9	50.5*	.01	2	15,000	0	Relative Density Variation
	83.9	58.1	.01	2	15,000	0	Relative Density Variation
	83.9	43	.01	2	15,000	0	Relative Density Variation
SS Loose (D_r = 0)	83.3	28.8*	.00145	1.8	1,500	0	Relative Density Variation
	83.3	33.2	.00145	1.75	1,500	0	Relative Density Variation
	83.3	24.5	.00145	1.8	1,500	0	Relative Density Variation
SS Dense (D_r = .6)	71.3	64*	.0195	1	15,000	35	Impact Angle Variation
	71.3	54.4	.020	1	15,000	35	Impact Angle Variation
	71.3	73.6	.0195	1	15,000	35	Impact Angle Variation
	65.9	13.3*	.003	.25	2,500	70	Impact Angle Variation
	65.9	11.3	.003	.25	2,500	70	Impact Angle Variation
	65.9	15.3	.003	.25	2,500	70	Impact Angle Variation
SS Intermediate (D_r = .3)	69.3	35.6*	.0085	1	7,500	35	Impact Angle Variation
	69.3	30.3	.0087	1	7,500	35	Impact Angle Variation
	69.3	41	.0085	1	7,500	35	Impact Angle Variation
	68	7.4*	.0012	.15	1,500	70	Impact Angle Variation
	68	6.3	.0012	.15	1,500	70	Impact Angle Variation
	68	8.5	.0012	.15	1,500	70	Impact Angle Variation

Figure 4-51. Finalized Values of Coefficients - 1/6 Scale Footpad

Soil	V_o (In./Sec.)	a_1 (Lb./In.)	C_{s2} (Lb.-Sec.^{2}/In.^{4})	η (Dimensionless)	K_s (Lb./In.)	θ (Degrees)	Comments
SS Loose (D_r = 0)	80.7	20.3*	.0012	1.5	1,500	35	Impact Angle Variation
	80.7	17.2	.0012	1.5	1,500	35	Impact Angle Variation
	80.7	23.4	.0012	1.5	1,500	35	Impact Angle Variation
	76	6*	.000193	.1	1,000	30	Impact Angle Variation
	76	5.1	.000193	.1	1,000	30	Impact Angle Variation
	76	6.9	.000193	.1	1,000	30	Impact Angle Variation
RS Loose (D_r = 0)	84.6	21*	.0008	2.4	1,200	17.5	Impact Angle Variation
	84.6	24.2	.0008	2.4	1,200	17.5	Impact Angle Variation
	84.6	17.9	.00085	2.4	1,200	17.5	Impact Angle Variation
	80	16.2*	.00065	1.4	1,200	35	Impact Angle Variation
	80	18.6	.00065	1.4	1,200	35	Impact Angle Variation
	80	13.8	.00065	1.4	1,200	35	Impact Angle Variation
	79.3	9.15*	.0005	.9	1,000	52.5	Impact Angle Variation
	79.3	10.5	.0005	.9	1,000	52.5	Impact Angle Variation
	79.3	7.77	.0005	.9	1,000	52.5	Impact Angle Variation
SS Loose (D_r = 0)	127.9	28.8*	.0015	1.8	2,500	0	Impact Velocity Variation
	127.9	33.2	.0015	1.8	2,500	0	Impact Velocity Variation
	127.9	24.5	.0016	1.8	2,500	0	Impact Velocity Variation
	83.3	28.8*	.002	1.5	2,500	0	Impact Velocity Variation
	83.3	33.2	.00195	1.5	2,500	0	Impact Velocity Variation
	83.3	24.5	.002	1.5	2,500	0	Impact Velocity Variation
	61.9	28.8*	.0018	2.2	1,250	0	Impact Velocity Variation
	61.9	33.2	.0017	2.3	1,250	0	Impact Velocity Variation
	61.9	24.5	.0019	2.2	1,250	0	Impact Velocity Variation
	9.33	28.8*	.008	.5	1,000	0	Impact Velocity Variation
	9.33	33.2	.008	.5	1,000	0	Impact Velocity Variation
	9.33	24.5	.008	.5	1,000	0	Impact Velocity Variation

*Nominal Value

Figure 4-51. Finalized Values of Coefficients - 1/6 Scale Footpad (Concluded)

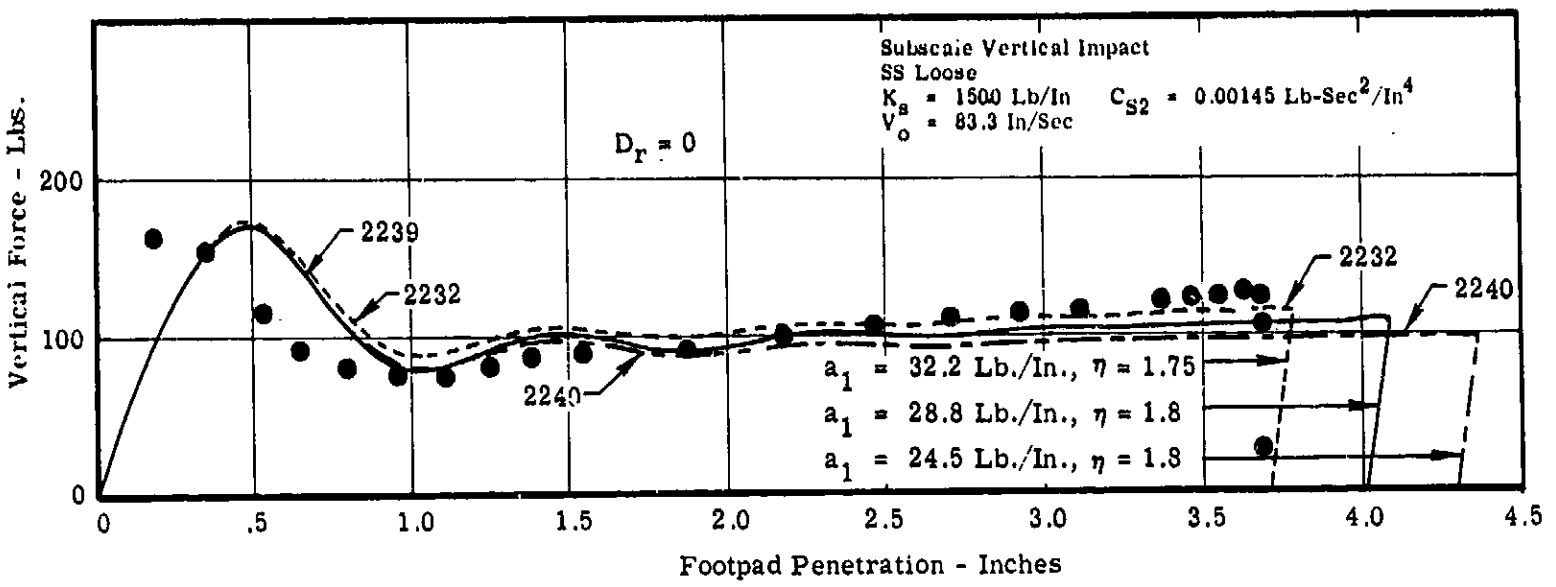

Figure 4-52. Comparison of Experimental and Computed Force versus Penetration Histories

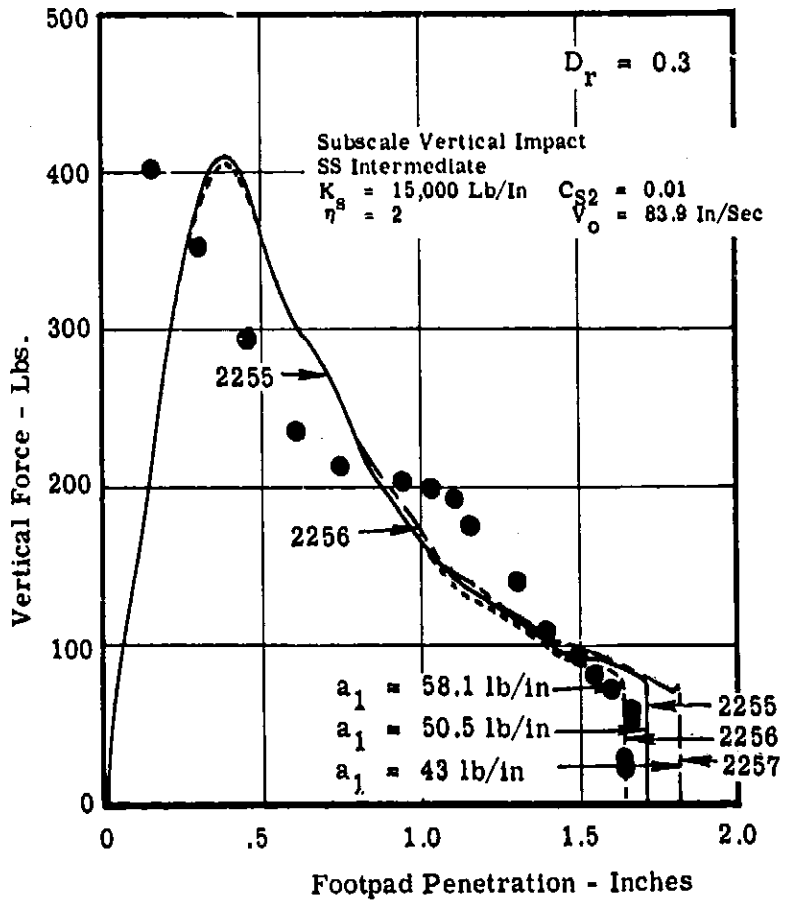

Figure 4-53. Comparison of Experimental and Computed Force versus Penetration Histories

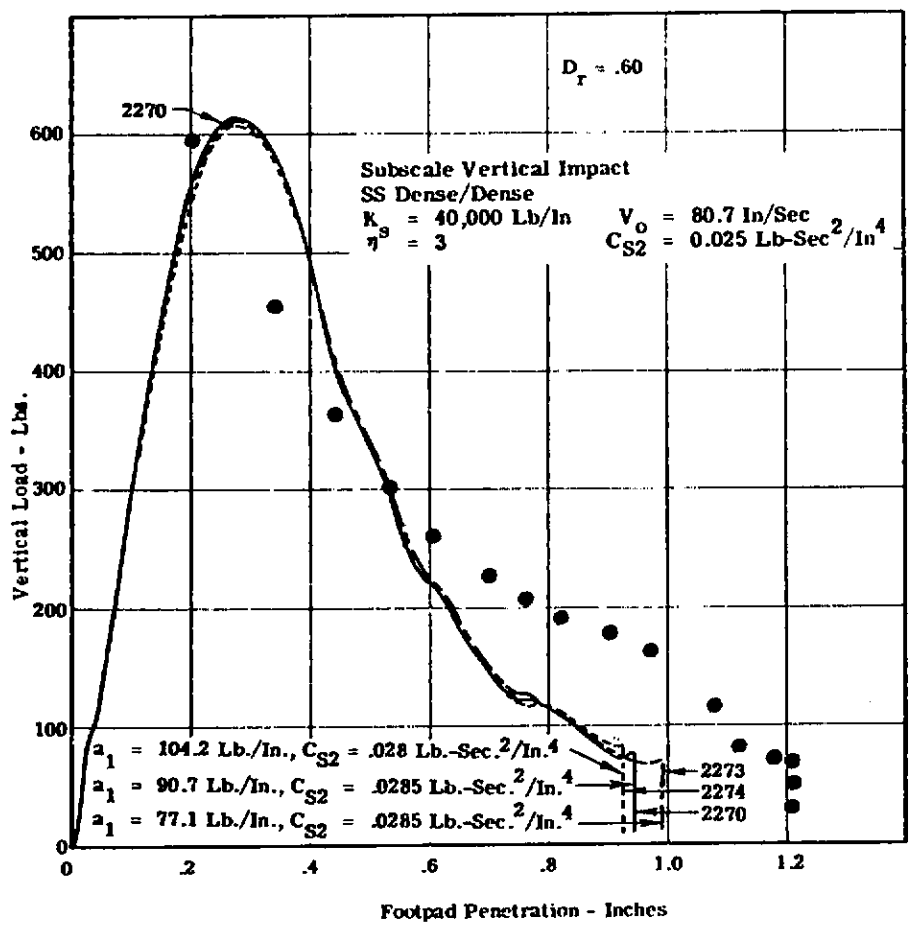

Figure 4-54. Comparison of Experimental and Computed Force versus Penetration Histories

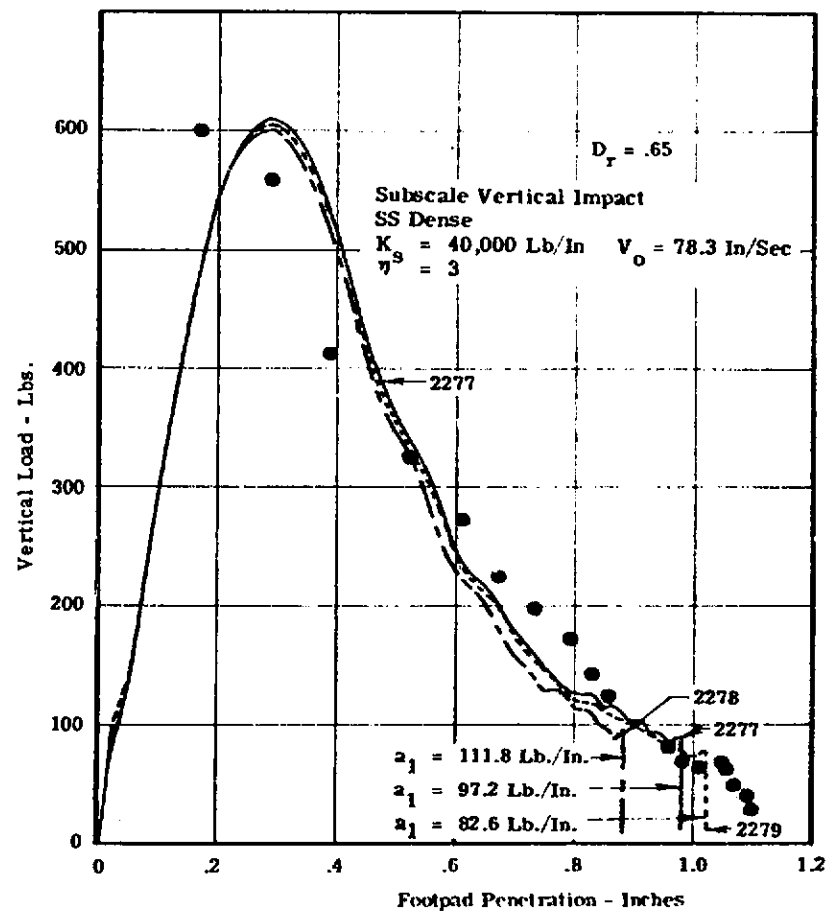

Figure 4-55. Comparison of Experimental and Computed Force versus Penetration Histories

Soil	V_o (In./Sec.)	a_1 (Lb./In.)	C_{s2} (Lb.-Sec.^{2}/In.^{4})	η (Dimensionless)	K_s (Lb./In.)	θ (Degrees)	g/g_e
SS (D_r = .85)	103.3	138.5	.068	3.5	16,000	0	1
	106.3	68.8*	.030	3.5	25,000	0	.49
	106.3	79.1	.030	3.5	25,000	0	.49
	106.3	58.5	.030	3.5	25,000	0	.49
	105.1	64.1*	.028	3.5	25,000	0	.46
	105.1	73.7	.028	3.5	25,000	0	.46
	105.1	54.5	.028	3.5	25,000	0	.46
	103	33.4*	.024	3.5	25,000	0	.24
	103	38.4	.024	3.5	25,000	0	.24
	103	28.4	.024	3.5	25,000	0	.24
	103.1	28.6*	.013	3.5	25,000	0	.21
	103.1	32.8	.013	3.5	25,000	0	.21
	103.1	24.3	.013	3.5	25,000	0	.21

* Nominal Value

Figure 4-56. Coefficients Applicable to Reduced Gravity Test - 1/6 Scale Footpad

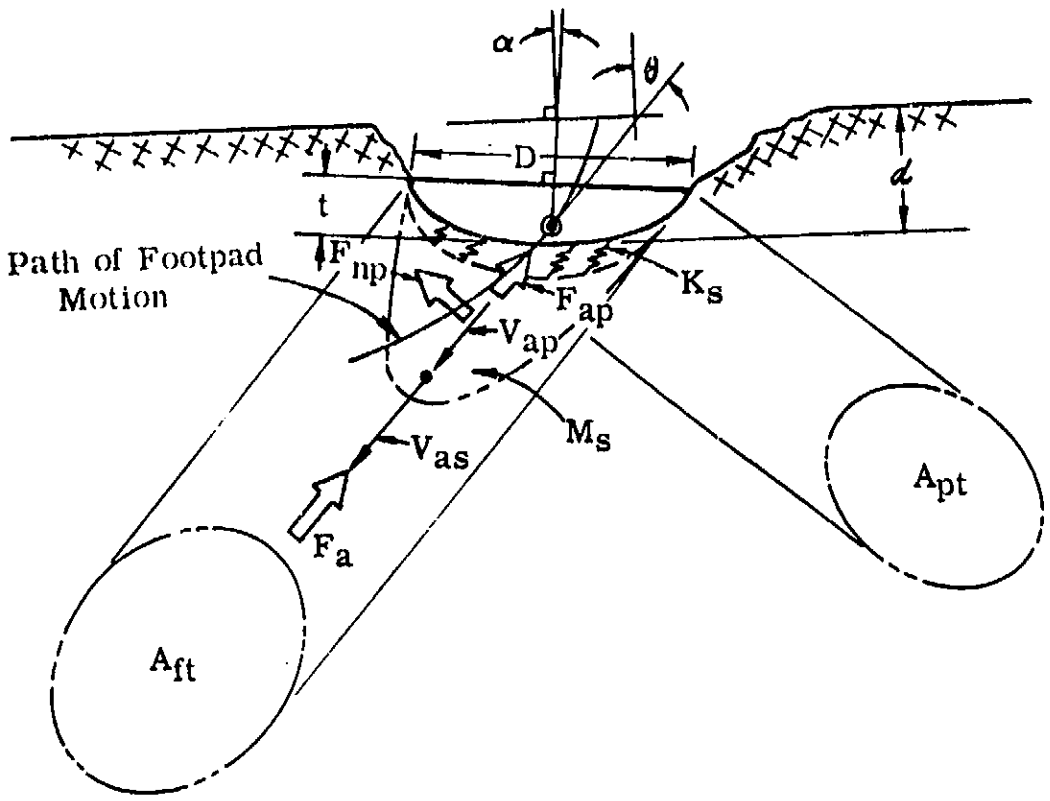

Figure 4-57. Schematic and Nomenclature for Dynamic Soil Model

motion of the footpad, taking into account two sets of forces - those acting from the landing gear shock struts and those acting from the soil to the footpad. The footpad/soil interaction forces consist of a tangential force F_{ap} and a normal force F_{np}, both defined relative to the footpad velocity vector V_{ap}. Immediately beneath the footpad, and separating it from the stagnation mass, is a compressive spring K_s which is a lumped-parameter representation of the distributed elasticity of the soil. The stagnation mass moves along the same path as the foopad, but it moves with a velocity V_{as} rather than V_{ap} due to the relative motion allowed by the spring K_s. The forces acting on the stagnation mass consist of the footpad reaction F_{ap} transmitted through the compressive spring and the soil reaction F_a. The equation of motion of the stagnation mass is thus given by

$$\frac{d}{dt}(M_s V_{as}) = F_{ap} - F_a \qquad 4.37$$

where the soil force acting on the footpad along the velocity vector is given by

$$F_{ap} = K_s S_w \qquad 4\text{-}38$$

the spring compression S_w is given by

$$S_w = \int_0^t (V_{ap} - V_{as})\, dt \qquad 4.39$$

The soil spring rate is not constant but varies as a function of the footpad contact area. Based on an extension of the deflection solution for a semi-infinite elastic continuum loaded by a rigid disc, the spring rate is give by

$$K_s = \frac{2E_e}{1-\mu^2}\, r(d) \left(\frac{A_{ft}}{A_{ftm}}\right)^{1/2} \qquad 4.40$$

The axial force acting on the stagnation mass was found to be,

$$F_a = C_{ms} \rho g\, A_{ft} d + C_D \rho A_{ft}\, V_{as}^{\ 2} \qquad 4.41$$

where C_{ms} and C_D are dimensionless coefficients determined from drag and impact test data.

The stagnation mass is given by

$$M_s = \eta \rho r^3(d) \left(\frac{A_{ft}}{A_{ftm}}\right)^{3/2} \qquad 4.42$$

where η is a dimensionless shape factor related to the soil angle of internal friction.

The force acting on the footpad normal to the velocity vector is given by

$$F_{np} = \psi F_{ap} \qquad 4.43$$

where ψ is a function of footpad motion parameters.

The dynamic soil model is now defined except for the determination of equation coefficients in terms of soil property and footpad motion parameters. These coefficients; the mechanical strength coefficient C_{ms}, the momentum transfer drag coefficient C_D, the soil wedge shape factor η, the effective elastic modulus of the soil E_e, the footpad pitch angle α relationship with motion variables, and the ψ function relating F_{np} and F_{ap}, are determined from the results of analyses of the drag and impact test data in the following sections.

Mechanical Strength Coefficient

The mechanical strength of the soil is that portion of the total penetration resistance which is functionally dependent upon the displacement of the footpad as opposed to velocity or acceleration effects. In the static or slow penetration situation the strength arises from the interaction of two factors - the stresses created by the gravitational body forces on the individual particles and the aggregate property of shear failure stress per given normal stress. For cohesionless soils of the type under consideration the static mechanical strength is proportional to the bulk-weight density of the soil and therefore the local gravitational field. The resistance increases linearly for increasing depth (following a failure point load) and also increases with the area of the penetrating body. The static strength of the soil is also affected by failure mode which is dependent upon the relative density. This leads to a preliminary dynamic mechanical strength model of the form

$$F_{ms} = f(\rho g, d, A_{ft}, \theta, \dot{V}_{as}, \phi, D_r) \qquad 4.44$$

The soil acceleration $\dot{V}_{as}$ is included to account for both gravitational and D'Alembert inertial effects acting on the individual particles under dynamic conditions.

Data from the drag tests provided the basis for a model applicable to the case of $\theta = 90°$. The results of this analysis, which were presented in Section 4.4, showed that a dimensionless force parameter ($F_{ap}/\rho g d A_{ft}$) could be equated to a constant times a dimensionless velocity parameter ($V_{ap}/\sqrt{dg}$) squared plus a term representing the mechanical strength portion of the overall resistance whose magnitude was some function of soil properties. The fact that the data for all eleven of the test soils could be organized via the dimensionless force parameter indicates a direct proportionality between the mechanical strength and the product of mass density, acceleration due to gravity, depth of penetration, and total footpad frontal area for the restrictions of $\dot{V}_{as} = 0$ and $\theta = 90°$. Several tests were conducted in which the velocity of the footpad was not constant. From these it was concluded that for $\dot{V}_{as} < 1.5$ g's the drag force mechanical strength was independent of the rate of change of the footpad (or soil mass) velocity. These results may be found in Reference 47.

Additional analysis in Paragraph 4.4 of the mechanical strength portion of the drag resistance indicated that it could be approximated by an equation of the type

$$(F_D)_1 = C_{ms} \rho g d A_{ft}, \quad \text{where}$$

$$C_{ms} = 29 \tan\phi \, e^{1.4 D_r}, \quad \theta = 90° \qquad 4.45$$

For values of θ less than ninety degrees the determination of the mechanical strength of the soil was based on results from subscale and full-scale oblique impact tests. The analysis of this data was complicated by the fact that acceleration and momentum transfer effects occur simultaneously with the mechanical strength effects. In the drag tests the acceleration could be held to zero or constant value, but in the oblique impact tests the footpad acceleration and velocity varied continuously. Analysis of the data was achieved by setting up an analog simulation of the equations of motion of the soil mass and the impacting mass and, by an iterative technique, selecting the best set of numerical values for all of the parameters of the problem. This analysis was covered in Paragraph 4.5.

The quantity $C_{ms}/29 \tan \phi$, as determined from the analog simulation of subscale and full-scale oblique impact tests, is shown plotted versus relative density in Figure 4-58. Results from subscale drag tests in the eleven test soils are also shown. It can be seen that, within the accuracy of the test bed relative density and the range of mechanical strength coefficients giving reasonable correlation with the test results, all of the data can be approximated by the relationship,

$$C_{ms}/29 \tan \phi = e^{1.4D_r} \qquad 4.46$$

The greatest amount of data scatter occurs in the vicinity of zero relative density. It is possible to achieve relative densities less than zero in the test beds since the standard test used for obtaining the theoretical minimum density is not the same as the placement procedure used in the test beds. Very low relative density soil beds are subject to a marked reduction in mechanical strength since the soil approaches an unstable point where it would collapse from its own weight if disturbed by even a small external force. Slight relative density increases from this point result in a stable soil configuration having a more uniform strength versus relative density relationship.

For the dynamic case the angular effects on the soil mechanical strength are accounted for by the variations of A_{ft} with angle and also with the definition of d as the vertical penetration rather than the penetration path distance.

The static mechanical strength of the soil is much greater than the dynamic mechanical strength due to the full mobilization of the gravitational body forces on the soil in the vicinity of the penetration path and also due to the differences in the subsurface shear planes. In addition, the static force versus penetration curve is nonlinear while the dynamic mechanical strength variation is linear. Figure 4-59 shows a typical static strength versus penetration curves for RS soils having relative densities ranging from 0 to 78 percent. Soil property data are noted on the curves. This RS soil is slightly degraded from handling and the bulk densities are higher than the "fresh" soil densities.

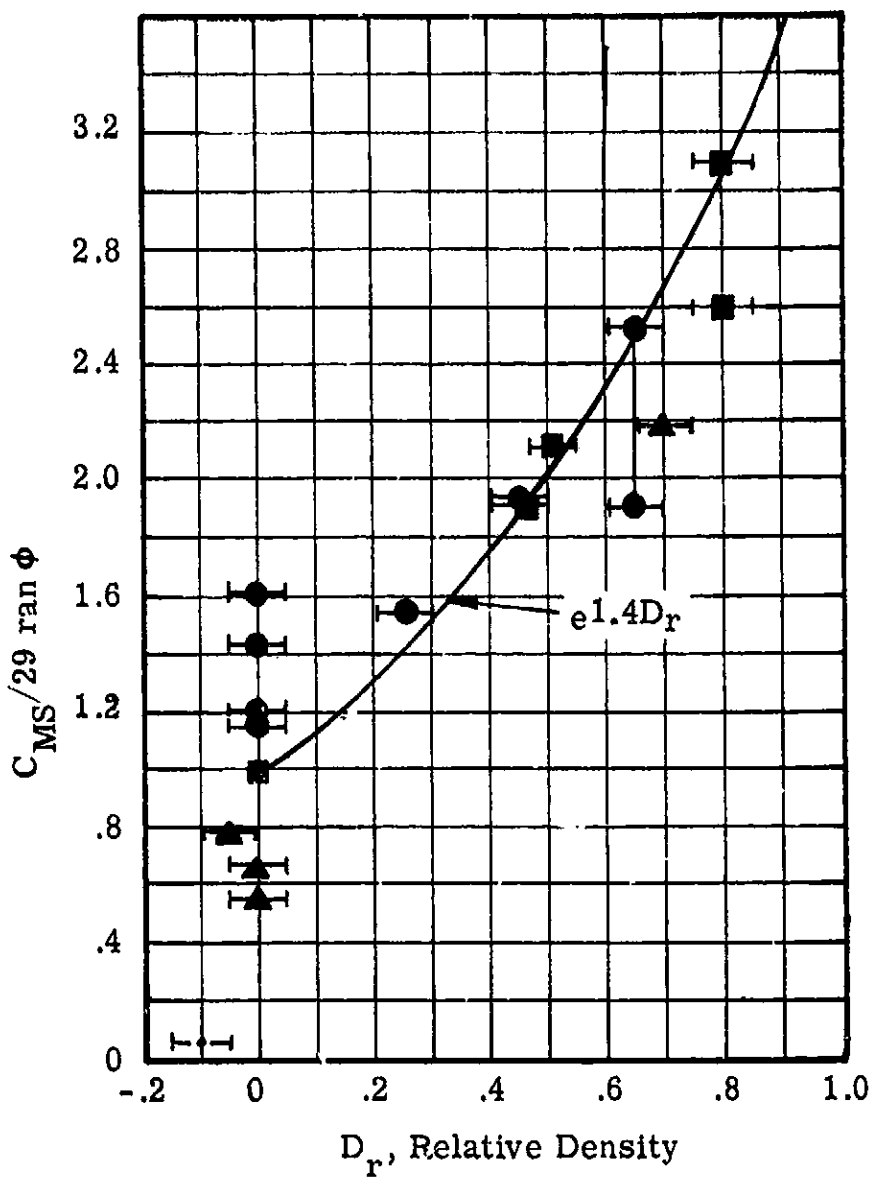

Figure 4-53. Variation of Normalized Dynamic Mechanical Strength with Relative Density - Drag and Impact Test Results

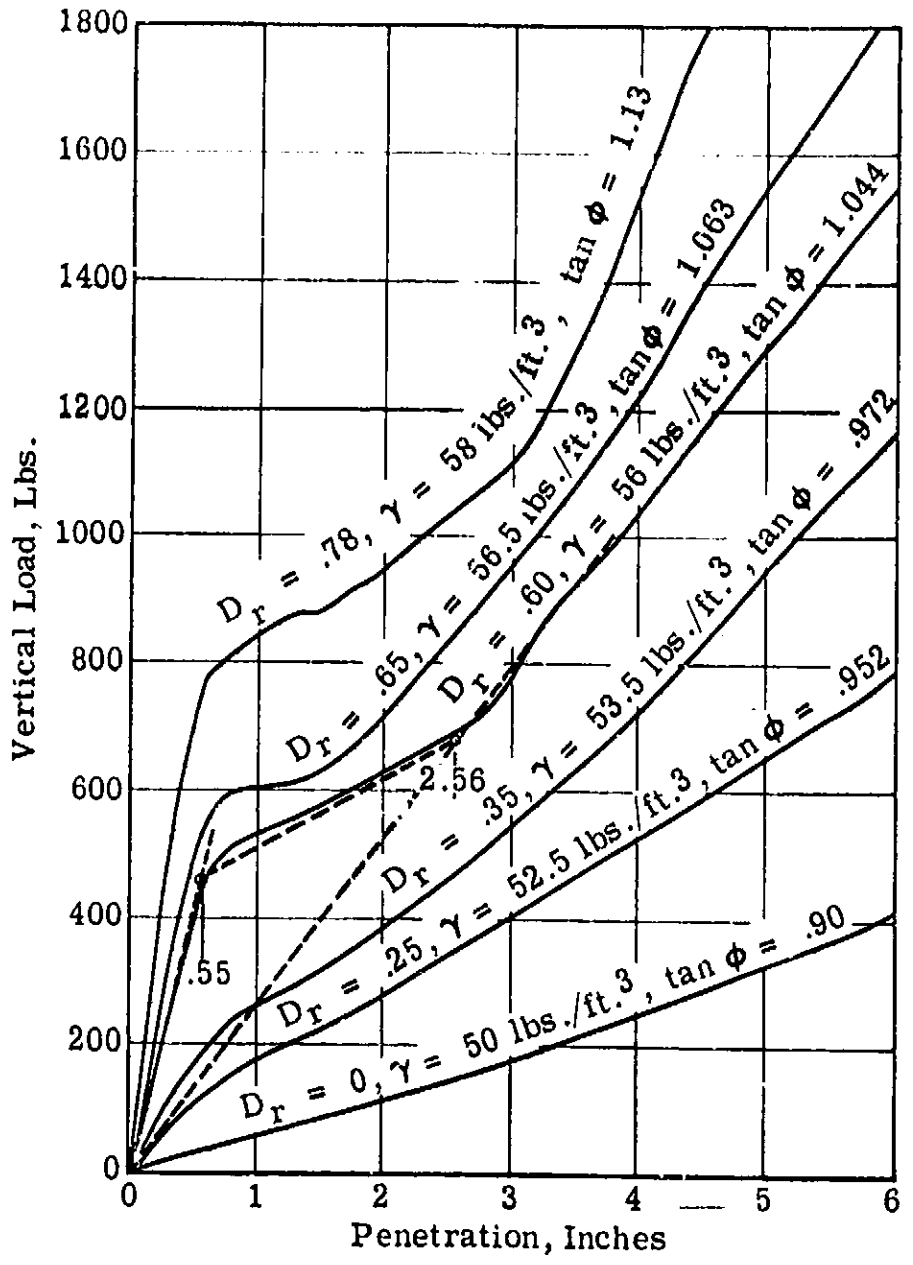

Figure 4-59. Static Load versus Penetration Curves for RS Type Soils with D_r from 0 to 78 Percent - 1/6 Scale Footpad

The static strength can be described by two slope coefficients and two breakpoints. For example, Figure 4-59 shows a piecewise linear approximation for $D_r = 0.60$ (dotted lines) in which the initial slope is maintained up to $d/D = 0.09$, ($D = 0.55$ inch). This is followed by a transition region which joins the initial portion to a second linear portion at $d/D = 0.40$, ($d = 2.56$ inch). The breakpoints are not sensitive to the soil parameters for a fixed shape of penetrator. The static vertical resistance of the soil is therefore given for $0 \leq d < 0.09D$ by

$$F_{vs} = C_{ms1} \rho g A_{ft} d$$

for $0.09\ D \leq d > 0.40D$ by

$$F_{vs} = \rho g A_{ft} \left[0.09\ C_{ms1}\ D + (1.29\ C_{ms2} - 0.29\ C_{ms1})(d - 0.09D)\right]$$

and for $0.40\ D \leq d \leq 1.5\ D$ by

$$F_{vs} = C_{ms2} \rho g A_{ft}\ d. \qquad 4.47$$

The parameters C_{ms1} and C_{ms2} are analogous to the dynamic mechanical strength coefficient C_{ms}, but they are greater in magnitude for a given relative density soil. Figure 4-60 shows plots of $C_{ms}/29 \tan \phi$, $C_{ms1}/29 \tan \phi$, and $C_{ms2}/29 \tan \phi$ versus relative density for RS and SS type soils. The static mechanical strength for the RS and SS soils are not normalized by the factor $29 \tan \phi$, but indicate a higher power dependency on $\tan \phi$. Figure 4-61 shows the static strength data normalized by the factor $29(\tan \phi)^{(1 + 2.5\ D_r)}$. The data is reasonably represented by the relationships

$$C_{ms1} = 29(3.0 + 25.0\ D_r + 18.75\ D_r^2) \tan \phi^{(1 + 2.5\ D_r)} \qquad 4.48$$

and

$$C_{ms2} = 29(3.0 + 9.25\ D_r) \tan \phi^{(1 + 2.5\ D_r)} \qquad 4.49$$

For the type of soils considered in this study the static mechanical strength varies approximately linearly with the penetration path angles. Thus the static resistance is given as a function of θ by

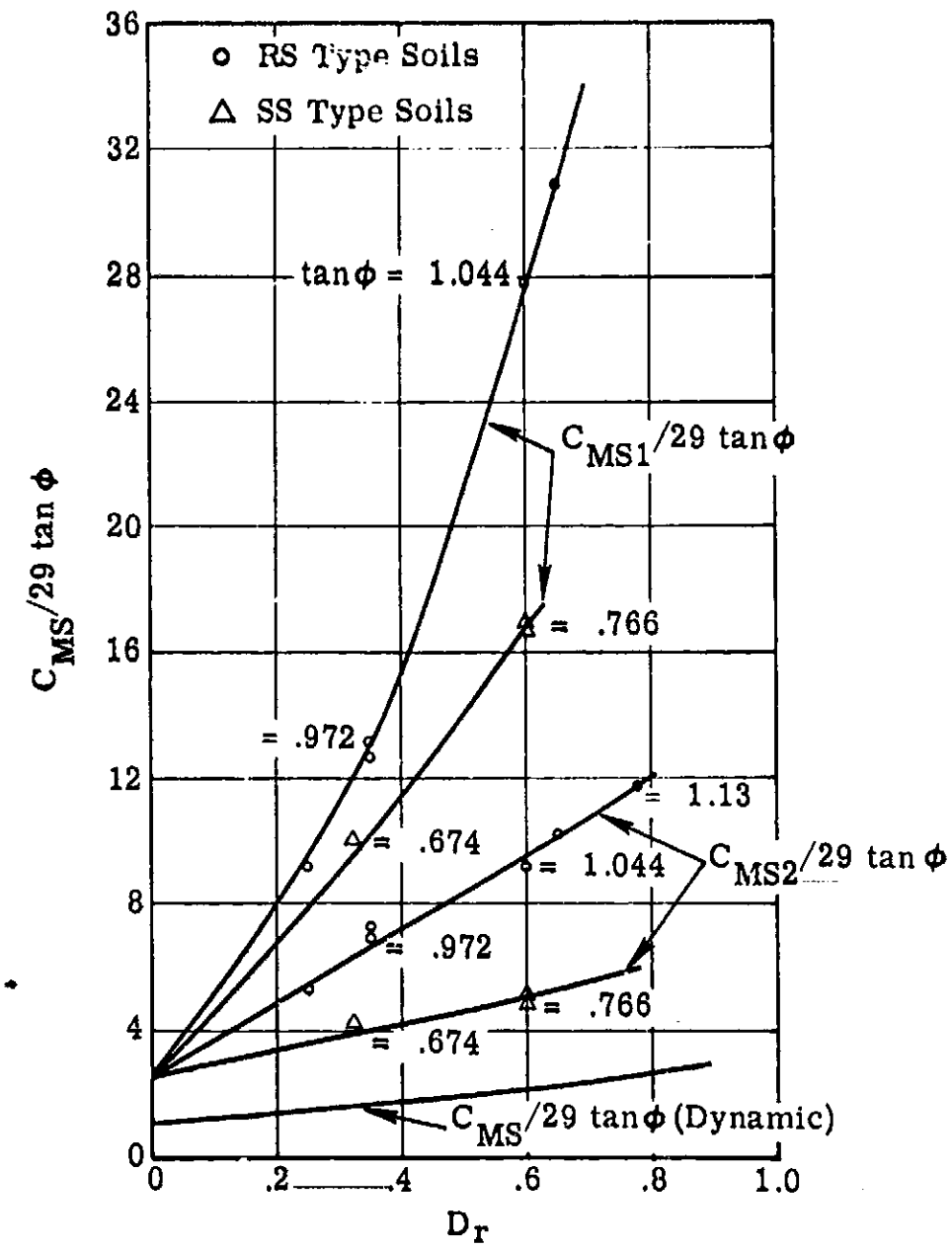

Figure 4-60. Dynamic and Static Mechanical Strength Coefficients versus D_r. (The dynamic normalizing factor of 29 tan ϕ does not organize the static data.)

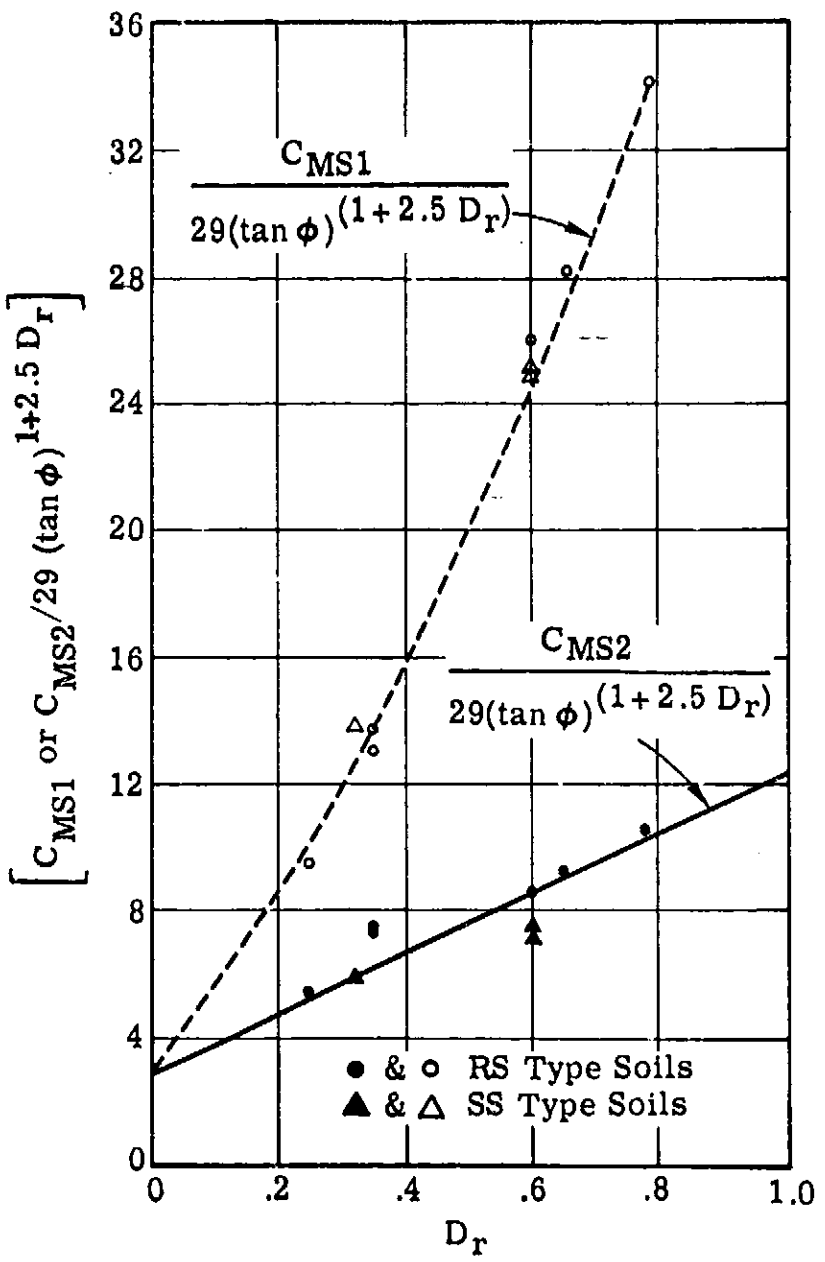

Figure 4-61. Normalized Static Mechanical Strength Coefficients versus D_r

$$F_{ms}(\theta) = F_{hs} + (F_{vs} - F_{hs})\left(1 - \frac{2\theta}{\pi}\right) \qquad 4.50$$

where F_{hs} is the static strength at $\theta = 90°$ and is equal to the dynamic strength at $\theta = 90°$.

The transition from dynamic to static strength is a function of the amount of time required for transient accelerations to decay in the disturbed soil region surrounding the footpad. Since this is a complex function of the point coordinates within the annular region and requires a detailed knowledge of the stress-strain law of the soil for its determination, it is not practical to obtain a rigorous prediction of these accelerations. As a first approximation the peak velocity of the penetrating soil wedge may be applied as an upper bound on the separation velocity of surface particles to calculate the time required for these particles to recontact the surface. It is then assumed that the full static strength will be recovered at this amount of time following the point at which the peak velocity occurs. The time required for recontact is given by

$$T_c = \frac{2(V_{as})\ \text{peak}}{g} \qquad 4.51$$

The time of the peak value of V_{as} is called t_1. For $t_1 < t < t_1 + T_c$ empirical evidence indicates that the dynamic mechanical strength applies up to time $t_1 + T_c/2$, following which the static resistance is recovered in a linear manner between $t_1 + T_c/2$ and $t_1 + T_c$.

Most of the phenomena associated with the mechanical strength of the soil are illustrated by the static and dynamic test results shown in Figure 4-62 for a six-inch diameter footpad. Curve A is the load versus penetration curve obtained for a vertical impact test at approximately four fps. Curve B is the dynamic mechanical resistance determined from this test. Curve C is the static mechanical resistance on an identically prepared test bed and is seen to be over twice as great as the dynamic resistance. Following the impact test the footpad was left in the soil, and, using it as a penetrator, a slow penetration test was conducted. The load versus penetration result for this test is given by

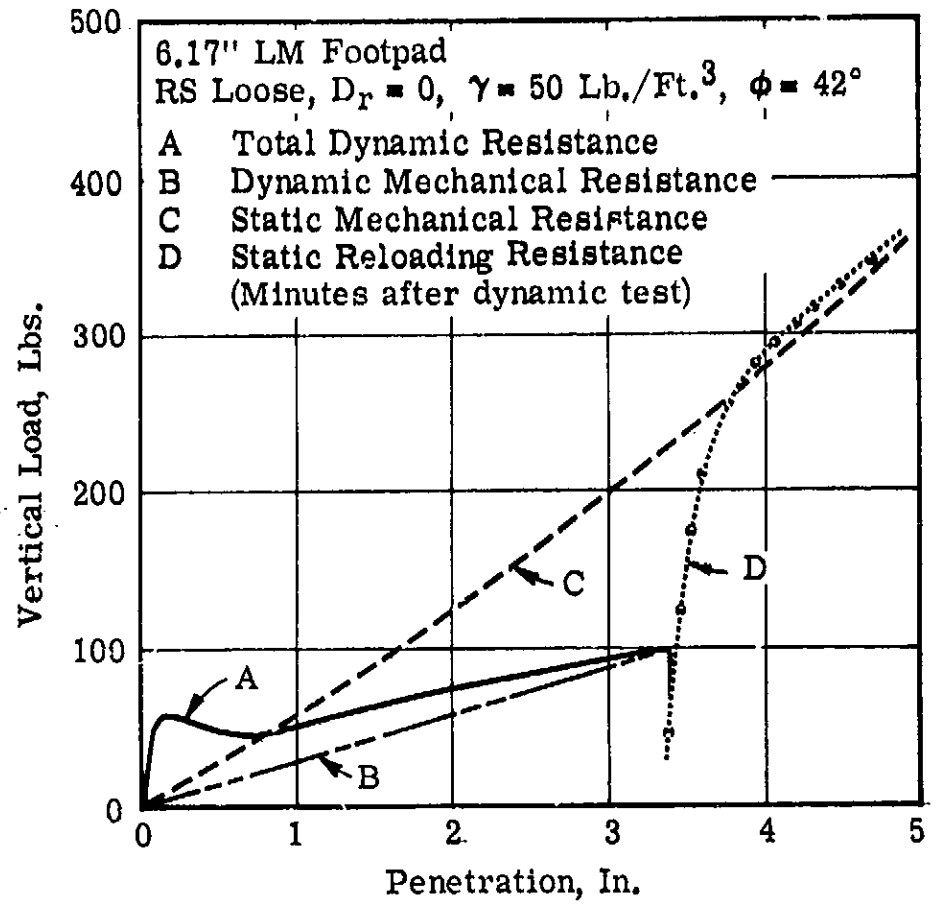

Figure 4-62. Dynamic Impact Test Results and Comparison of Pre and Post Impact Static Strength

curve D. It can clearly be seen that, following impact, the static mechanical strength again determines the soil resistance.

Momentum Transfer for Drag Coefficient

The portion of the axial force acting on the footpad due to momentum transfer is given by

$$F_{mt} = C_D \rho A_{ft} V_{as}^2 \qquad 4.52$$

where C_D is a dimensionless drag coefficient. In an ideal fluid medium C_D would be a function only of footpad geometry, but for footpad/soil interaction it would be expected that the drag coefficient might also depend upon soil and motion parameters. In the analysis of drag test data reported in Section 4.4 it was found that for $\theta = 90$ degrees a C_D value of 0.8 was applicable to all eleven soils for which drag tests were conducted.

Full-scale and subscale impact test results formed the basis for the determination of the drag coefficient for θ less than 90 degrees. The value of C_D for a particular impact test was determined from an analog simulation of the footpad/soil system as described in Paragraph 4.5. Using this method, the drag coefficient was developed for numerous soil types and relative densities, various impact velocities and path angles, and several footpad diameters. The results for vertical impact ($\theta = 0$) are shown in Figure 4-63 as $(C_D - 0.8)/\tan\phi$ versus relative density. These results are approximated by a drag coefficient defined for $D_r < 0.5$ as

$$C_D = 0.8 + (4 + 80\, D_r)\,(r/r_m)^2\, f(\theta)\tan\phi$$

and for $D_r \geq 0.5$ by

$$C_D = 0.8 + 4\,(r/r_m)^2 e^{4.83 D_r}\, f(\theta)\tan\phi \qquad 4.53$$

where $f(\theta) = 1$ for $\theta = 0$
$f(\theta) = 0$ for $\theta = 90°$

Values of $f(\theta)$ determined from oblique impact test data for θ between 0 and 90 degrees are shown in Figure 4-64. These results indicate that $f(\theta)$ is relatively independent of soil properties and is reasonably approximated by

$$f(\theta) = 1 - \frac{2}{\pi}\theta \qquad 4.54$$

In addition to tests at earth gravity a limited number of oblique impact tests were conducted on an accelerating soil test bed resulting in effective gravitational body forces as low as 0.21 g's. These tests are reported in Appendix E. The effect of gravitational

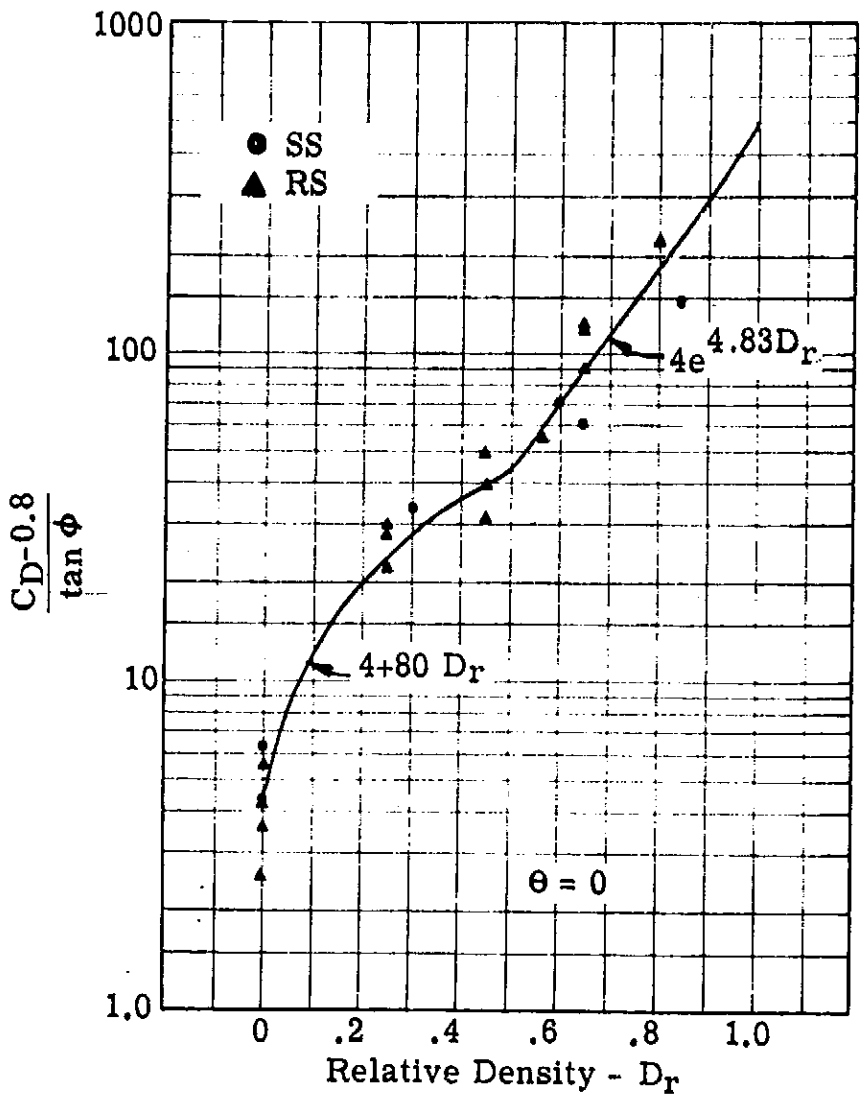

Figure 4-63. Normalized Momentum Transfer Drag Coefficient versus D_r

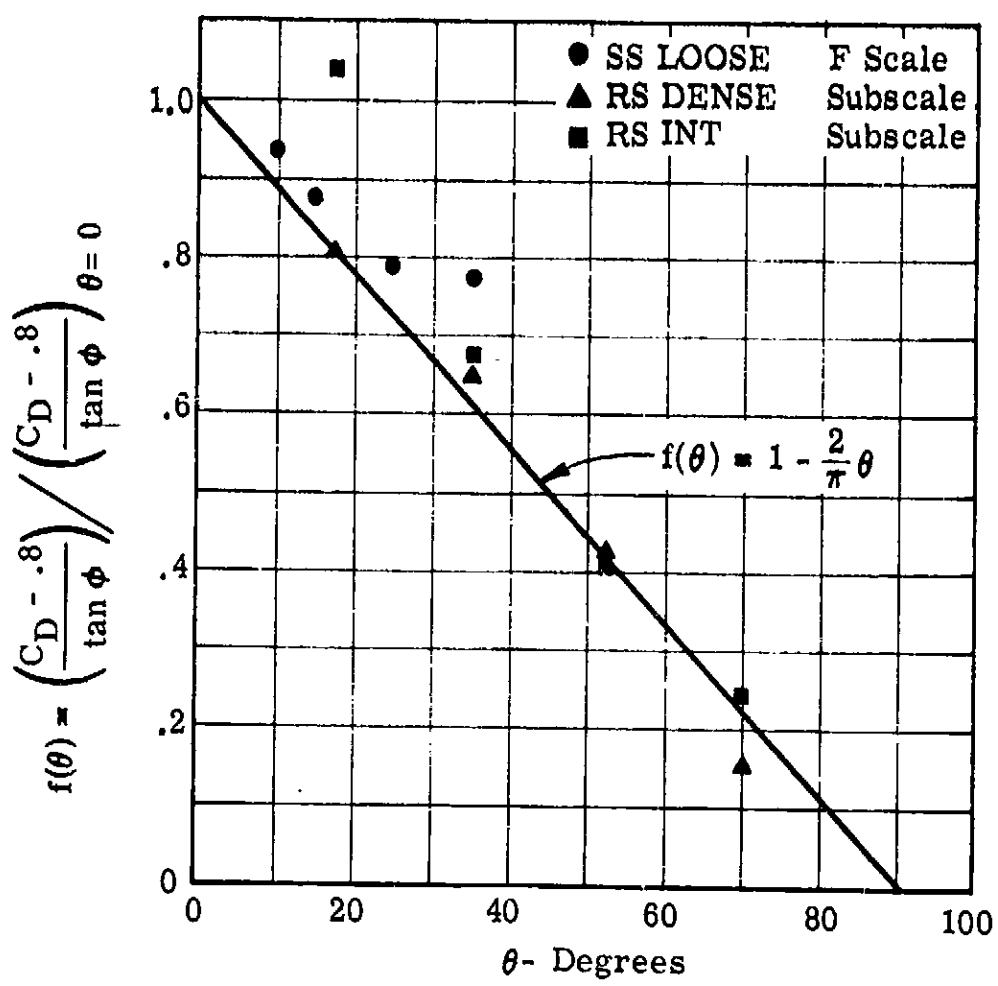

Figure 4-64. Effect of Path Angle, θ, on the Normalized Drag Coefficient

force on the drag coefficient is shown in Figure 4-65 which presents $(C_D - 0.8)/\tan\phi$ versus the fraction of earth gravity for a number of reduced gravity impact tests on SS dense soil. These results show the parameter $(C_D - 0.8)/\tan\phi$ to be proportional to g/g_e.

Combining these results leads to a complete definition of the drag coefficient as a function of soil properties, penetration path angle, and local gravitational force.

$$C_D = 0.8 + \frac{g}{g_e}(r/r_m)^2 \left(1 - \frac{2}{\pi}\theta\right)(4 + 80\, D_r) \tan\phi, \quad D_r < 0.5$$

and

$$C_D = 0.8 + \frac{g}{g_e}(r/r_m)^2 \left(1 - \frac{2}{\pi}\theta\right)(4e^{4.83D_r}) \tan\phi, \quad D_r \geq 0.5 \qquad 4.55$$

Soil Wedge Shape Factor

If it is assumed that the stagnation volume (wedge) beneath the footpad is represented by a conic soil mass of base radius r(d) and apex angle $(\pi/2 - \phi)$, the dimensionless wedge factor is given as a function of the soil angle of internal friction by

$$\eta_\phi = \frac{\pi}{3} \frac{(1 + \tan\frac{\phi}{2})}{(1 - \tan\frac{\phi}{2})} \qquad 4.56$$

Values of η for a variety of impact tests were determined from an analog computer simulation of the footpad/soil system and reported in Paragraph 4.5. These results are shown as the ratio of η to η_ϕ versus relative density in Figure 4-66. It is seen from these results that the simulation becomes less sensitive to the value of η as relative density is increased from 0 to 1. Also, η_ϕ is a reasonable approximation to the required value of η for all values of D_r.

The effects of footpad path and pitch angles on this wedge mass are adequately accounted for by the factor $(A_{ft}/A_{ftm})^{3/2}$ in the wedge mass relationship given in Equation 4.42. This results in a reduction in M_s with θ and α from $\eta\rho r^3$ at $(\theta - \alpha) = 0$ to $0.09\ \eta\rho r^3$ at $(\theta - \alpha) = 90$ degrees.

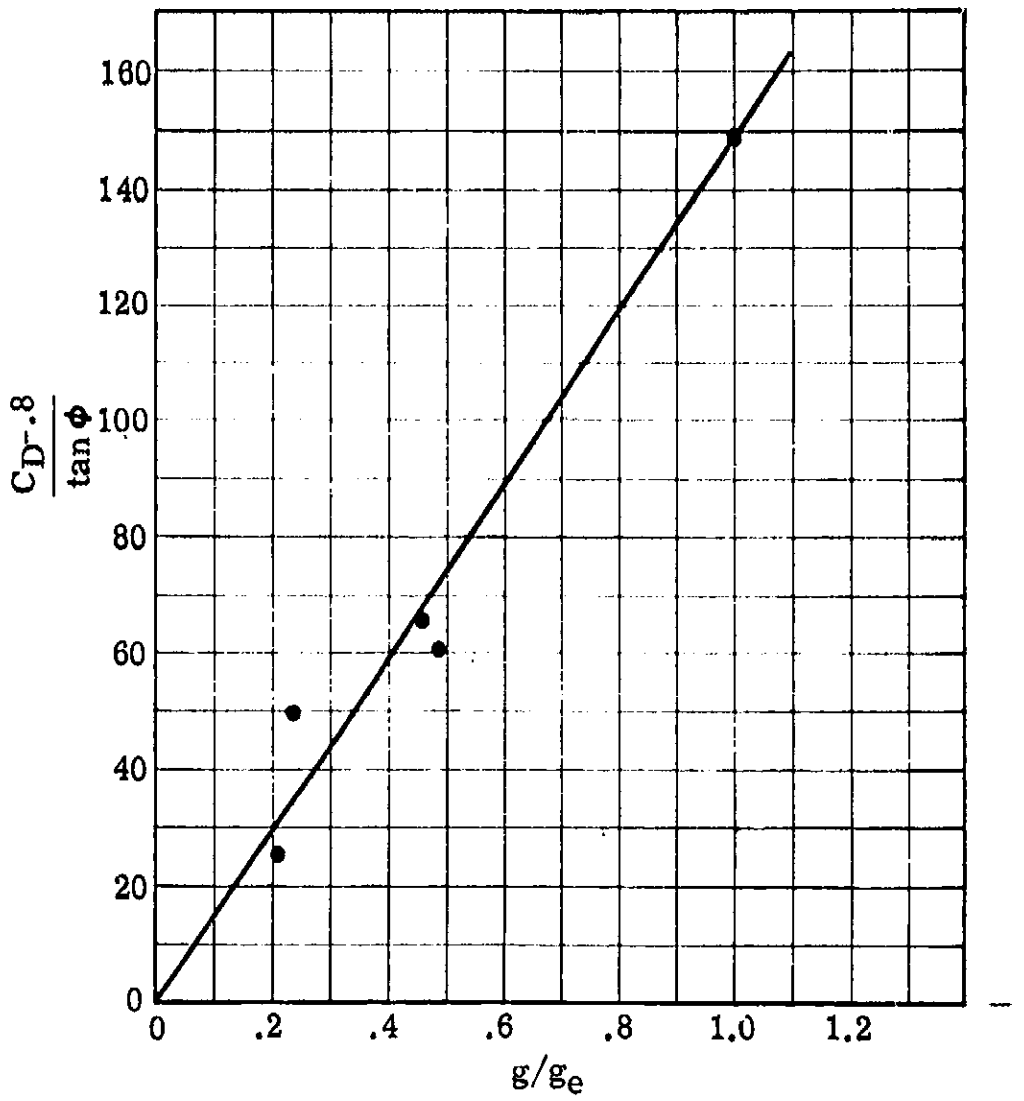

Figure 4-65. Effect of the Local Acceleration of Gravity on the Normalized Drag Coefficient - SS Dense Results with $D_r \simeq 0.75$ to 0.85

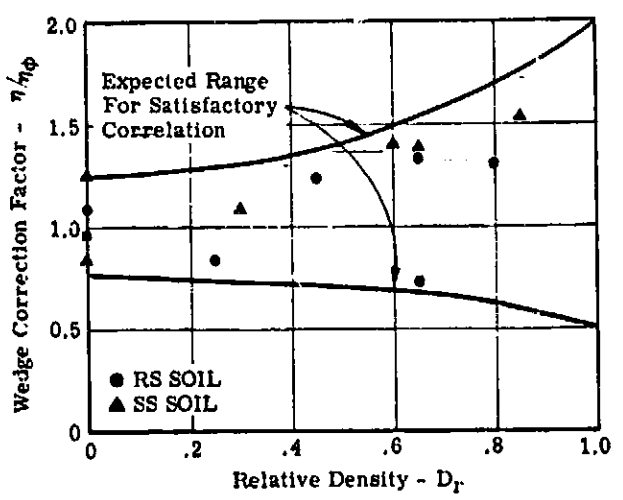

Figure 4-66. Ratio of Experimentally Determined η Values to Conical Soil Wedge Values versus Relative Density

Effective Elastic Modulus

If we consider the case of a semi-infinite elastic continuum, having an elastic modulus of E_e and Poisson's ratio μ, loaded via an infinitely rigid disc over a circular area of radius r with a net force of F, then the total deflection, δ, of the disc relative to the initial surface is given by (44, pp. 371 and 372).

$$\delta = \frac{F(1 - \mu^2)}{2rE_e} \qquad 4.57$$

Converting this to a spring rate, K_s

$$K_s = \frac{2rE_e}{1 - \mu^2} \qquad 4.58$$

This relationship is used for determining the compressive spring rate of the soil by using an effective elastic modulus E_e which is determined in an empirical manner.

The sonic modulii of the eleven test soils used in the study can, with the exception of the LSM soil, be approximated closely by the relationship

$$E_s = 2.73 \times 10^6 \rho_o^{.632} e^{1.1D_r} \qquad 4.59$$

where

ρ_o = mass density of soil at zero relative density (units of lb. sec.^{2}/in.)

The experimentally determined values of E_e are shown plotted in Figure 4-67 as a function of E_s. The values were determined by matching on an analog computer the rise time and initial peak of the axial load from oblique impact test results. The computer results were not overly sensitive to the exact value of K_s used so that a range is shown on the empirical values of E_e. Any value of E_e within the given range resulted in good correlation with the experimental results.

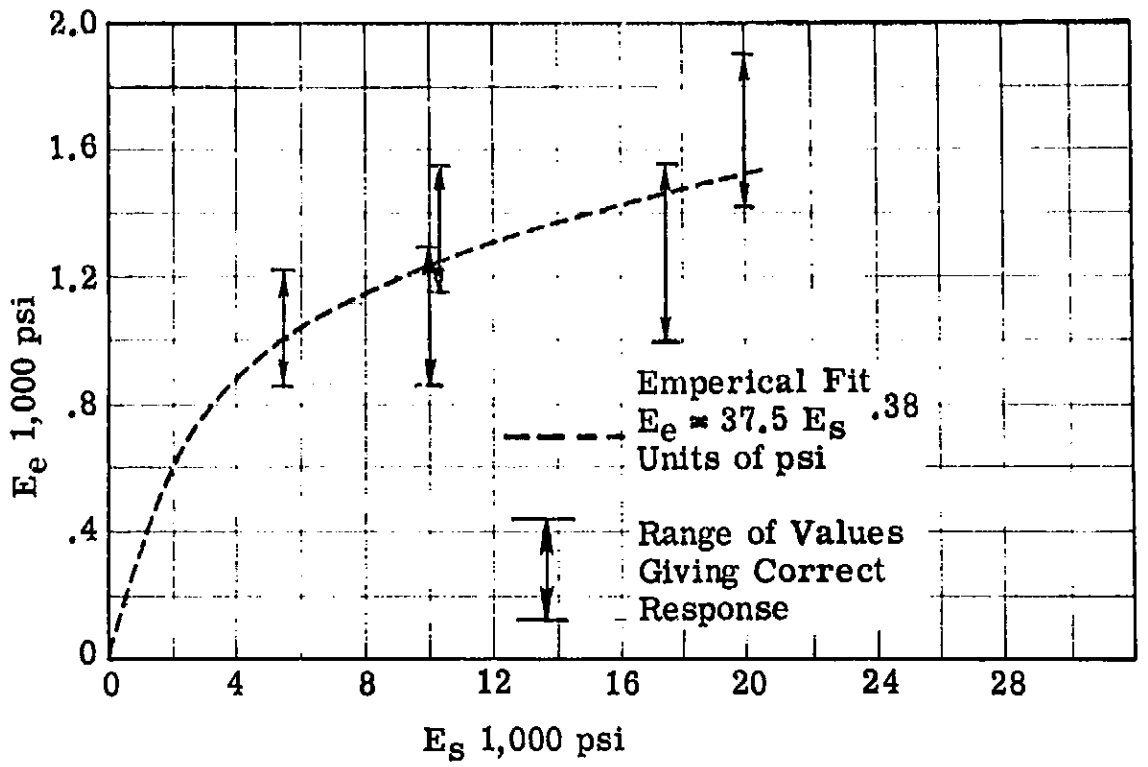

Figure 4-67. Effective Elastic Modulus versus Sonic Modulus at Four psi Confining Pressure

The mean curve through the experimental data is given by

$$E_e = 37.5\ E_s^{.38} \qquad 4.60$$

Substituting Equation 4.59 into Equation 4.60 yields

$$E_e = 10{,}470\ \rho_o^{.24} e^{.42 D_r} \qquad 4.61$$

Due to the smaller percentage variation in E_e for a given change in E_s the above relationship may be used for all eleven soils used in this study. In addition, since the force response of the soil is not overly sensitive to changes in E_e in the ±25 percent range of the nominal value, the above relationship is probably applicable to all but extreme variations from soil property values used in this study.

Footpad Pitch Angle

The footpad pitch angle relative to the soil surface is required so that the projected area functions can be evaluated. Constant penetration subscale drag test results have shown that the pitch angle stabilizes quite rapidly under conditions of pure horizontal motion. Figure 4-68 presents a plot of footpad steady-state pitch angle versus the dimensionless parameter $(V_{ap}/D)\sqrt{d/g}$ for constant penetration drag tests in RS loose, intermediate and dense soils. These results may be approximated by the equations

$$\alpha = 0.45\left(\frac{V_{ap}}{D}\sqrt{\frac{d}{g}}\right)^{1/2} \text{ radians}$$

$$\text{for} \quad 0.45\left(\frac{V_{ap}}{D}\sqrt{\frac{d}{g}}\right)^{1/2} \leq \alpha_{max} \text{ and} \qquad 4\text{-}62$$

$$\alpha = \alpha_{max}$$

$$\text{for} \quad 0.45\left(\frac{V_{ap}}{D}\sqrt{\frac{d}{g}}\right)^{1/2} > \alpha_{max} \text{ where}$$

the angle α_{max} is defined as the footpad stop angle in the plane of footpad motion.

Oblique impact test and constant pressure drag test results show that α is essentially zero when the vertical pressure on the footpad surface is high relative to the horizontal pressure. The footpad begins to pitch upward when the ratio of horizontal pressure to vertical pressure becomes greater than 0.6. The vertical pressure is given by

$$P_v = \frac{1}{A_v}(F_{ap}\cos\theta + F_{np}\sin\theta) \qquad 4.63$$

and the horizontal pressure is

$$P_h = \frac{1}{A_h}(F_{ap}\sin\theta - F_{np}\cos\theta) \qquad 4.64$$

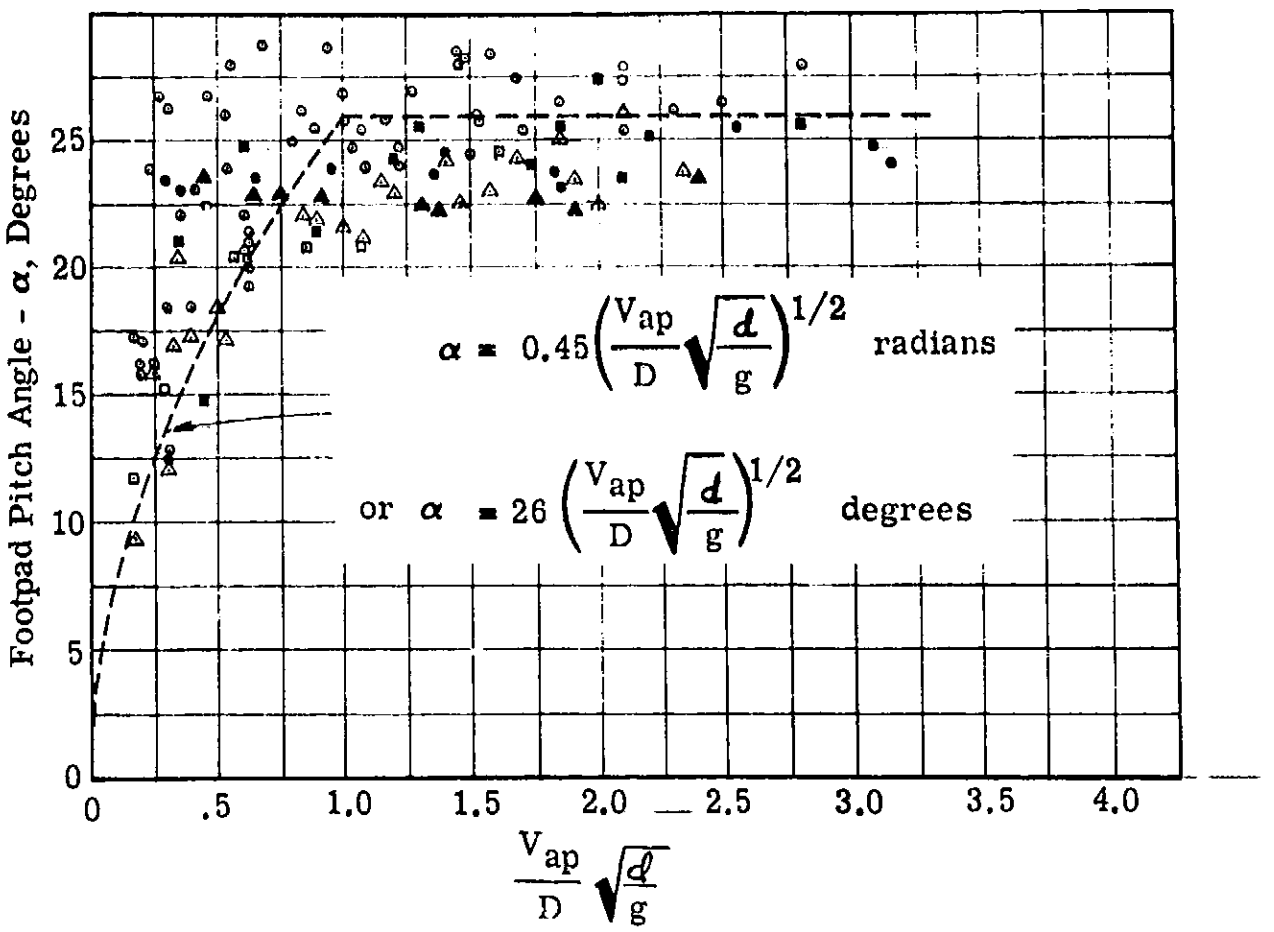

Figure 4-68. Footpad Pitch Angle versus Dimensionless Depth-Velocity Parameter

The footpad pitch angle is thus given by

$$\alpha = 0 \text{ for } P_h \leq 0.6\, P_v \qquad 4.65$$

and by Equations 4.62 for $P_h > 0.6\, P_v$.

Relationship Between Axial and Normal Forces

The relationship between F_{ap} and F_{np} for horizontal motion ($\theta = 90°$) was obtained from the results of drag tests using the one-sixth scale LM footpad. Figure 4-69 shows F_{np}/A_{pt} (vertical pressure) plotted versus F_{ap}/A_{ft} (drag pressure) for tests conducted in RS loose, intermediate, and dense soils. These tests covered a horizontal velocity range from 1.5 to 15 fps and penetration depths to four inches. These results may be approximated by the linear relationship

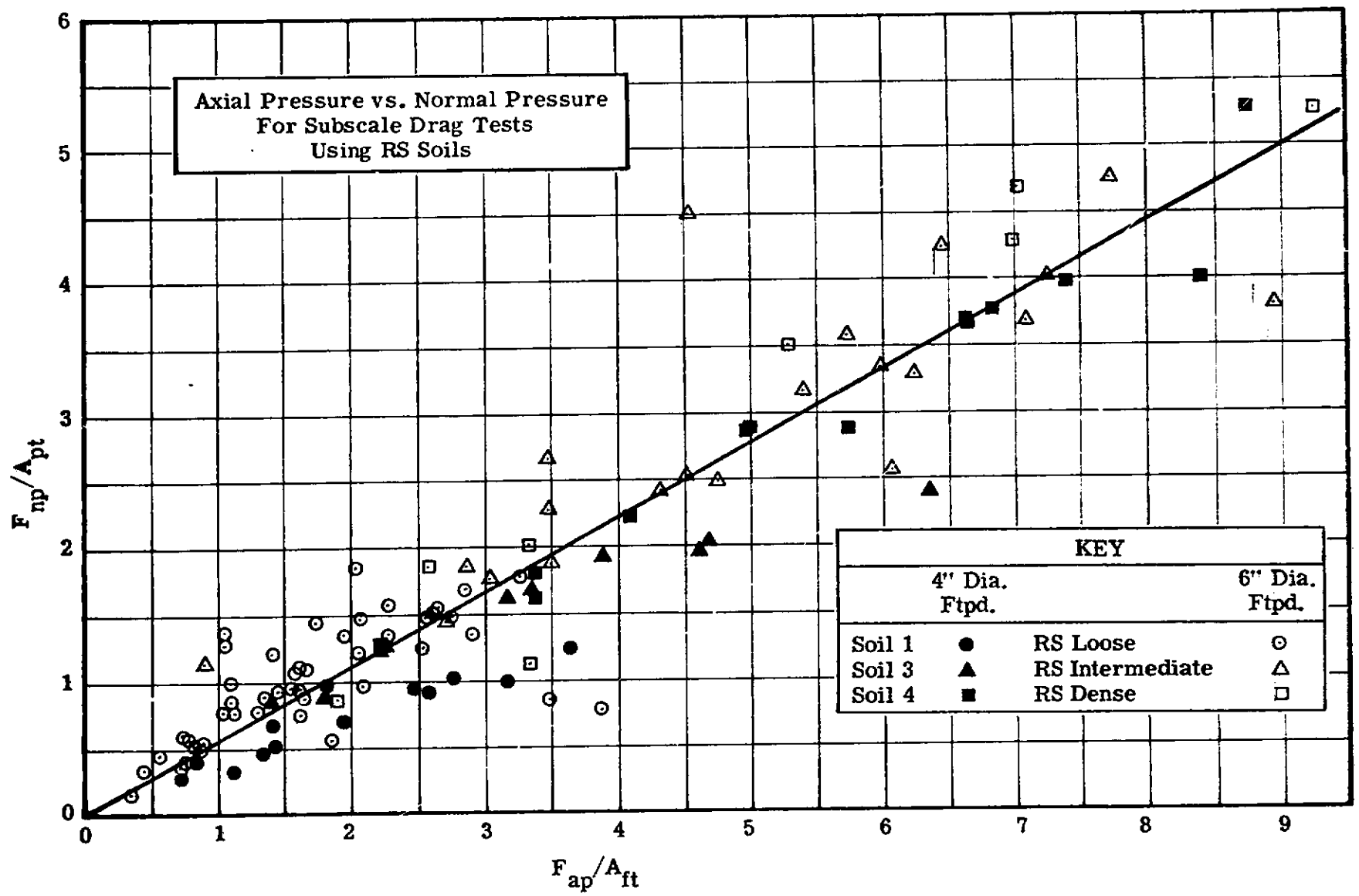

Figure 4-69. Axial Pressure versus Normal Pressure for Subscale Drag Tests Using RS Soils

$$\frac{F_{np}}{A_{pt}} = 0.55 \frac{F_{ap}}{A_{ft}} \qquad 4.66$$

which may be rewritten to give the ratio of normal to axial force as

$$\psi = \frac{F_{np}}{F_{ap}} = 0.55 \frac{A_{pt}}{A_{ft}} \qquad 4.67$$

This result is independent of soil properties and motion variables except as they enter into the drag and vertical pressures.

The ψ function for θ between 0 and 90 degrees was determined from the results of sub and full-scale oblique impact tests. Figure 4-70 shows ψ versus depth of penetration for full-scale impact tests at θ = 10, 15, 25, and 35 degrees in loose silica sand. This data indicates that the magnitude of ψ varies with θ, as would be expected, and also shows an approximately linear increase with depth of penetration.

Combining both the drag test and oblique impact test results and fitting the data empirically yields

$$\psi = .275\,(1 - e^{-50\theta}) \frac{A_{pt}}{A_{ft}} \left(1 + \sin\theta + \frac{11.2}{D}\,(d - \frac{t}{2}) \sin\theta \sin 2\theta\right) \qquad 4.68$$

for $0 \leq \theta \leq 90°$ where t is footpad thickness. Figure 4-71 shows the variation of ψ A_{ft}/A_{pt} with θ for various penetration depths.

The coefficient (.275) in the above ψ function does not show a detectable variation with coefficient of friction within the range of values obtained with the eleven test soils. The coefficient of friction between the soils and a smooth aluminum plate is 0.38 for the SS type soils and 0.45 to 0.49 for the volcanic cinder type soils. Lower coefficients may begin to show some effect but it would not be expected to be linear since the ψ function represents a combined effect of normal and tangential stresses on the footpad surface.

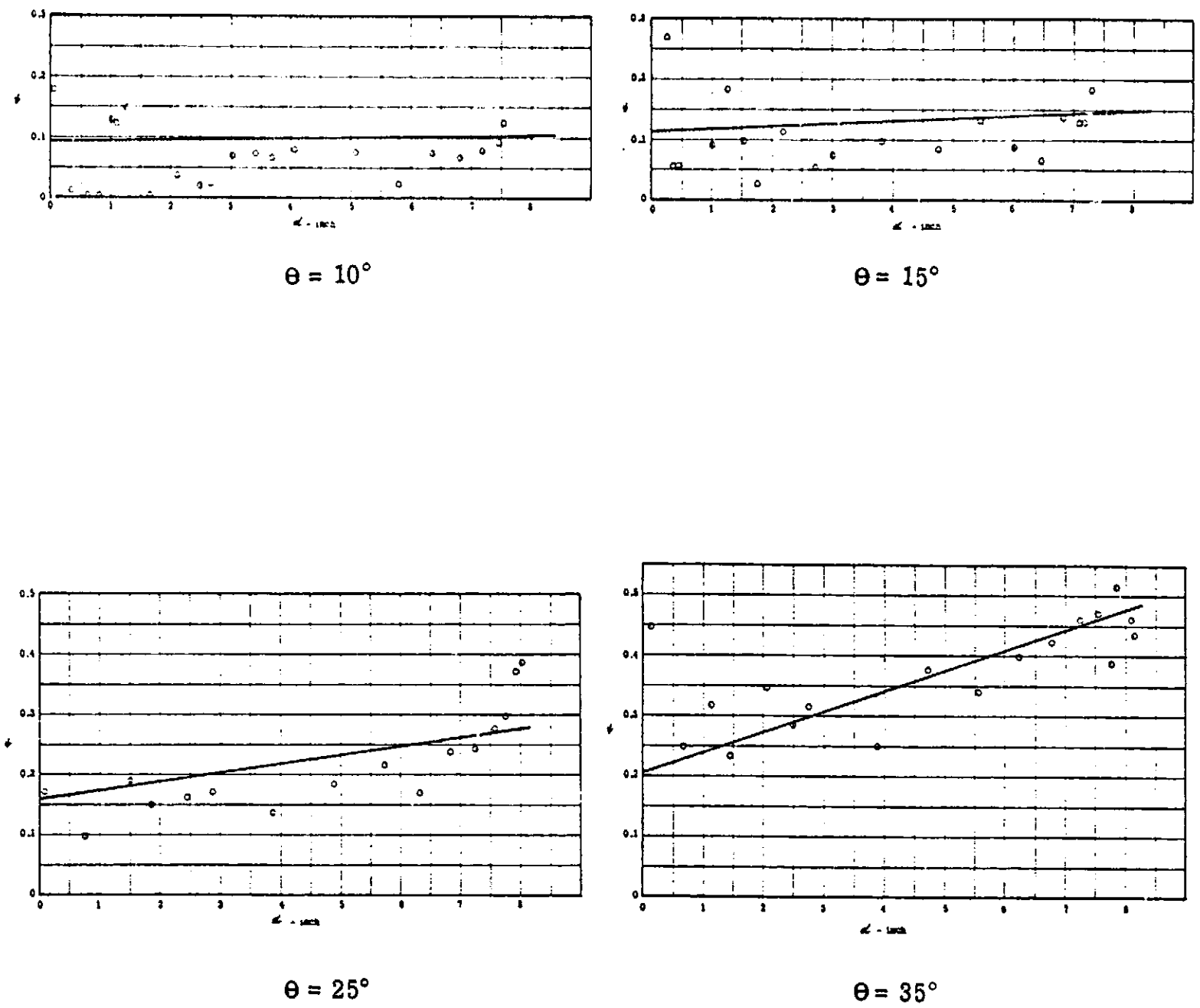

Figure 4-70. ψ versus Depth of Penetration for Full-scale Impact Tests at Various Values of θ in SS Loose Soil

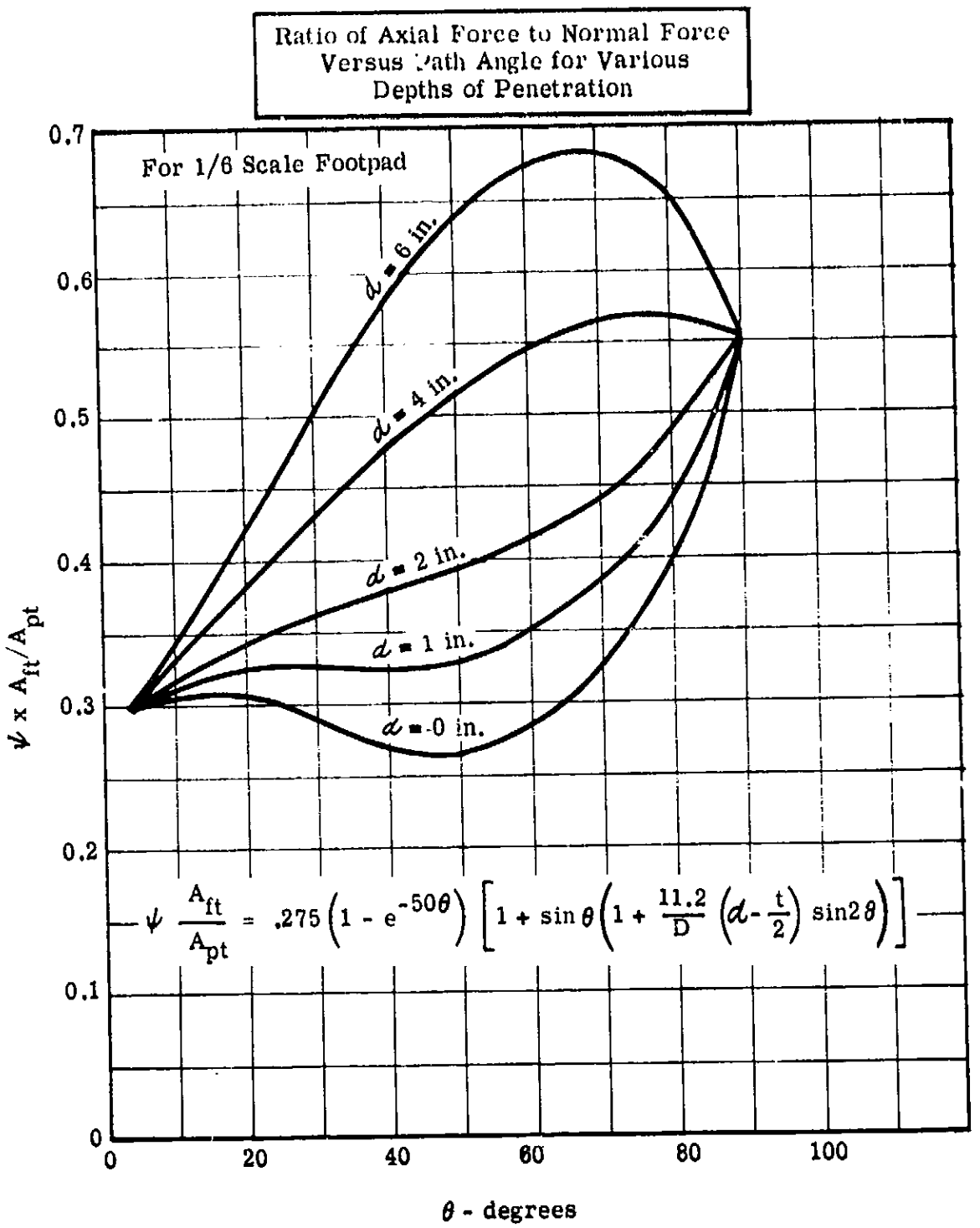

Figure 4-71. Ratio of Axial Force to Normal Force versus Path Angle for Various Depths of Penetration

A shortcoming in the ψ function given above is that it does not yield a valid relationship for values of θ greater than 90 degrees. A requirement for a realistic value of ψ for θ between 90 and 180 degrees is presented by a vehicle landing with a high horizontal velocity which tends to plane out of the soil after an initial period of footpad penetration. Since experimental data was not available for this situation it was decided to use the existing ψ function at 90 degrees for the stiutation where θ exceeds 90 degrees. Subsequent studies using a digital computer simulation of the vehicle/soil system showed that correlation was improved if the vertical force acting on the footpad were set equal to zero for θ greater than 90 degrees. Based upon these two sets of correlation results which bracketed the experimental data it appears that an intermediate value of ψ for θ greater than 90 degrees would yield satisfactory results. The value of ψ recommended is

$$\psi = .55 \frac{A_{pt}}{A_{ft}} \left(1 - \frac{\theta - \pi/2}{\theta_c - \pi/2}\right) \qquad 4.69$$

for $90 < \theta \leq \theta_c$ degrees, and for θ greater than θ_c

$$\psi = 0$$

where θ_c is an angle near 3 /4.

Although this relationship should yield satisfactory results from the standpoint of vehicle shock strut load history for a particular landing, some difficulty may be encountered in attempting to reproduce an experimentally determined stability profile. For this reason it is recommended that drag tests providing a θ value of greater than 90 degrees be conducted to obtain the data required to more accurately define the ψ function.

4.7 COMMENTS ON SOIL PROPERTIES APPEARING IN THE INTERACTION FORCE LAWS

In the initial stages of this study an analysis of the general vehicle lunar landing situation led to a number of soil properties which were believed to have possible first order effects on the footpad/soil interaction force laws. The soil descriptors chosen were:

(1) Bulk density, γ

(2) Relative density, D_r

(3) Elastic modulus, E_s

(4) Angle of internal friction, ϕ

(5) Cohesive strength parameter, C

(6) Mean grain size, μ_w

(7) Uniformity coefficient, C_u

Since the force laws were derived specifically for dry particulate, cohesionless soils, the cohesive strength parameter, C, does not enter as a term in the force law coefficients. Of the remaining parameters in the above list, all but mean grain size and uniformity coefficient were found to enter into the interaction equations presented earlier in this section of the report.

The value of mean grain size and uniformity coefficient for the test soils is given in the following table.

Soil Type	$\mu_{w,mm}$	C_u
RS	1.8	1.7
PS	1.8	1.7
RSM-a	1.8	1.7
RC2	0.7	17.0
SS	0.4	1.3
LSM	0.07	large

The absence of μ_w and C_u as parameters in the force laws was based upon a comparison of the drag and impact test results for SS, RC2, and LSM soils with those obtained for RS, PS, and RSMa soils. As may be seen in Figures 4-25 through 4-35, the empirically derived drag force equation yields good results for all but the LSM soils. The large amount of scatter in the LSM results shown in Figures 4-34 and 4-35 is not believed to be due to shortcomings in the drag force equation, but rather it is the result of difficulties encountered in preparing (and measuring the properties of) a consistent LSM soil bed from run to run. The drag force equation does yield a good average for the LSM test results, in spite of the extreme scatter involved.

Analysis of subscale impact test results for the RC2 soil yielded values of momentum transfer coefficient and mechanical strength coefficient which agreed favorably with the derived relationship shown in Figures 4-63 and 4-58. This result, in combination with the fact that RS and SS results could be correlated by the same set of equations, led to the conclusion that grain size and grain size distribution are of negligible importance in calculating interaction forces for the soils considered in this study. LSM impact test results did not agree with the empirical relationships describing the behavior of the other test soils, but this is believed to have been caused by pore air effects. Impact tests conducted in a vacuum for the LSM soils yielded results which were only slightly closer to the expected results. It has been assumed that the pore air is still present to a significant degree in the vacuum tests, probably because the soil bed was prepared under atmospheric conditions.

Based upon the good correlation obtained with the RC2 soil, it is felt that the derived equations are valid over a wide range of soil grain size and distribution. If it is deemed necessary or desirable to check the applicability of the empirical relationships derived in this study to very small grained and broadly-graded soils, additional tests under vacuum conditions will be required. For such tests it is recommen[illegible] soil bed be prepared and soil properties be measured in an evacuated chamb[illegible] minimize the possibility of pore air effects on the test results.

SECTION V

SUBSCALE MODEL LANDING PROGRAM

5.1 INTRODUCTION

The purpose of the model landing program was twofold. The primary reason for these tests was to provide experimental performance data on footpad/soil forces and motions and the effect of such reactions on overall vehicle motion. This data would then form a basis for determining the degree of correlation between the computer simulation of landings on a soil and the actual vehicle performance.

A secondary purpose of the model landing program was to study experimentally the amount of shock strut stroke (particularly the tensile stroke of the secondary shock struts) required for various "critical" landing conditions.

For the experimental/computer correlation study two types of drop tests were conducted. The first of these was termed "detailed correlation" drops and consisted of landings in which the instantaneous footpad positions, velocities and forces, and the instantaneous accelerations, velocities and positions of the vehicle were experimentally determined for later comparison to computer results. The second type of study was termed "gross correlation" and consisted of determining the transition from stable to unstable landings in the vertical velocity-horizontal velocity plane, for several landing conditions.

To form a baseline for the correlation studies of landings in soil, a hard surface stability profile was determined experimentally. The degree of correlation achieved between the computer and the experimental results for these landings then provided an upper limit of the precision to target for in the soil landing correlation studies.

The following sections describe the experimental equipment used in the scaled model landing program, and discuss each of the various groups of drop tests performed. A complete listing of all the drops made is provided in Section 5.3.

5.2 DESCRIPTION OF MODEL, INSTRUMENTATION AND DROP TEST FACILITY

The LM Model used in this drop test program was obtained from Langley Research Center at Hampton, Virginia. It was one of several identical 1/6-scale models built by Grumman for NASA to study experimentally LM landing performance. Figure 5-1 shows the model as received by Bendix and Table 5-T1 lists the basic scale factors for the model. The model, as received, was not instrumented and was not entirely compatible with the current LM configuration. The modifications carried out in this program resulted in an instrumented model which has the correct LM pad radius, center of gravity height, model weight, and footpad size, and is also very close to the present LM gear geometry. The energy absorbing media used on this model is crushable aluminum honeycomb capsules mounted inside the telescopic shock absorbers in an arrangement closely simulating the full scale LM.

TABLE 5-T1. BASIC MODEL SCALE FACTORS

Parameter	Scale Factor Ratio Full Scale/ Model Scale
Length, Displacement	6
Time, Vibration Period	6
Angular Velocity	1/6
Linear Velocity	1.0
Linear Acceleration	1/6
Mass	6^3
Mass Density	1.0
Mass Moment of Inertia	6^5
Force	6^2
Spring Rate	6.0
Coefficient of Friction	1.0

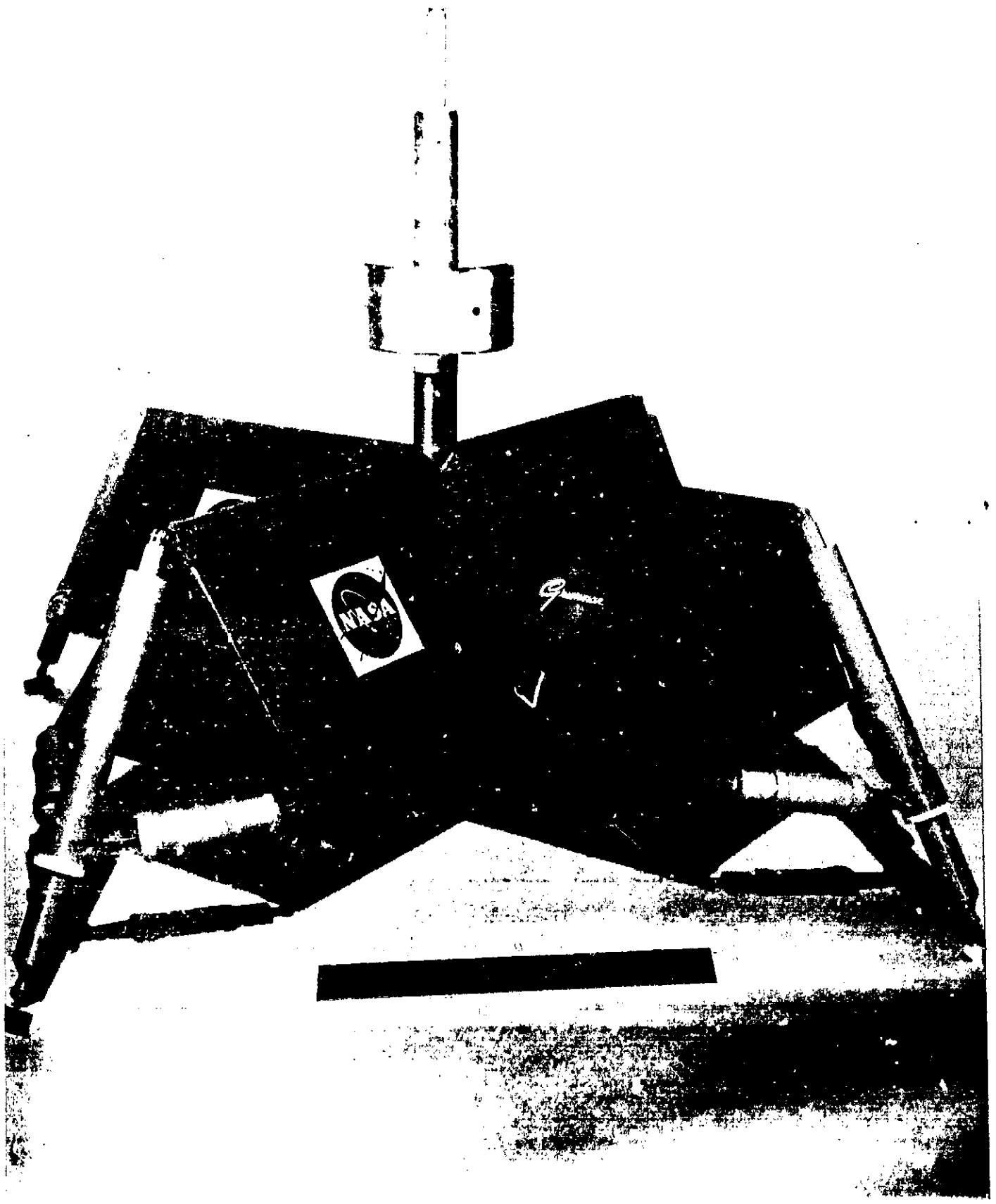

Figure 5-1. Langley-Grumman 1/6-Scale Dynamic Model of LM Before Modification

5.2.1 Modification - General Design and Instrumentation

In order to carry out the correlation studies with the analytical program it is necessary to determine the instantaneous vehicle linear and angular displacement, velocity, and acceleration during the model drop tests. It is also necessary to know the strokes and forces acting on all the struts, the footpad motion on at least one leg set, and the force and moment acting on the footpad. It was determined that a total of 37 differenct parameters must be obtained from the model during each drop test for the detailed correlation study and 30 parameters for the gross correlation study.

Three accelerometers (C.E.C. ± 50 g's) were installed at the CG of the model in the three principal axes, and three similar accelerometers were placed remotely and parallel to those at the CG. Load cells were installed at each strut to measure the stroking loads, and linear potentiometers were added internally or externally to each strut to measure the strokes. Scaled LM footpads were added to each leg and a special load cell was designed and constructed to measure the moments and forces acting on the principal footpad (the footpad on the No. 1 strut). Rotary potentiometers were also installed on the No. 1 footpad to measure the pad pitch and roll attitude during the drop tests. Figure 5-2 is a drawing of the model showing the modifications made to incorporate the instrumentation, and Figure 5-3 is a photo of the modified model. Many of the changes made are apparent when Figure 5-3 is compared to Figure 5-1.

5.2.1.1 Accelerometer Installation

To mount the three accelerometers at the center of gravity in a triaxial arrangement (1, Figure 5-3) and to make the model compatible with the model drop rig release mechanism, the original mast was cut off just above the model body and replaced with a filament wound fiberglass tube (2, Figure 5-3). This tube also provided space for the internally-mounted lead ballasting which was used to adjust the precise scale vehicle weight and the exact center of gravity location in the model. The fiberglass tube was attached to the model by bonding it into an adapter (3, Figure 5-3), which was, in turn, bolted to the portion of the original mast still remaining in the model. The adapter also served as a rigid platform for the triaxial accelerometer assembly. A fitting (4, Figure 5-3), on which two more accelerometers located 90 degrees to each other were mounted,

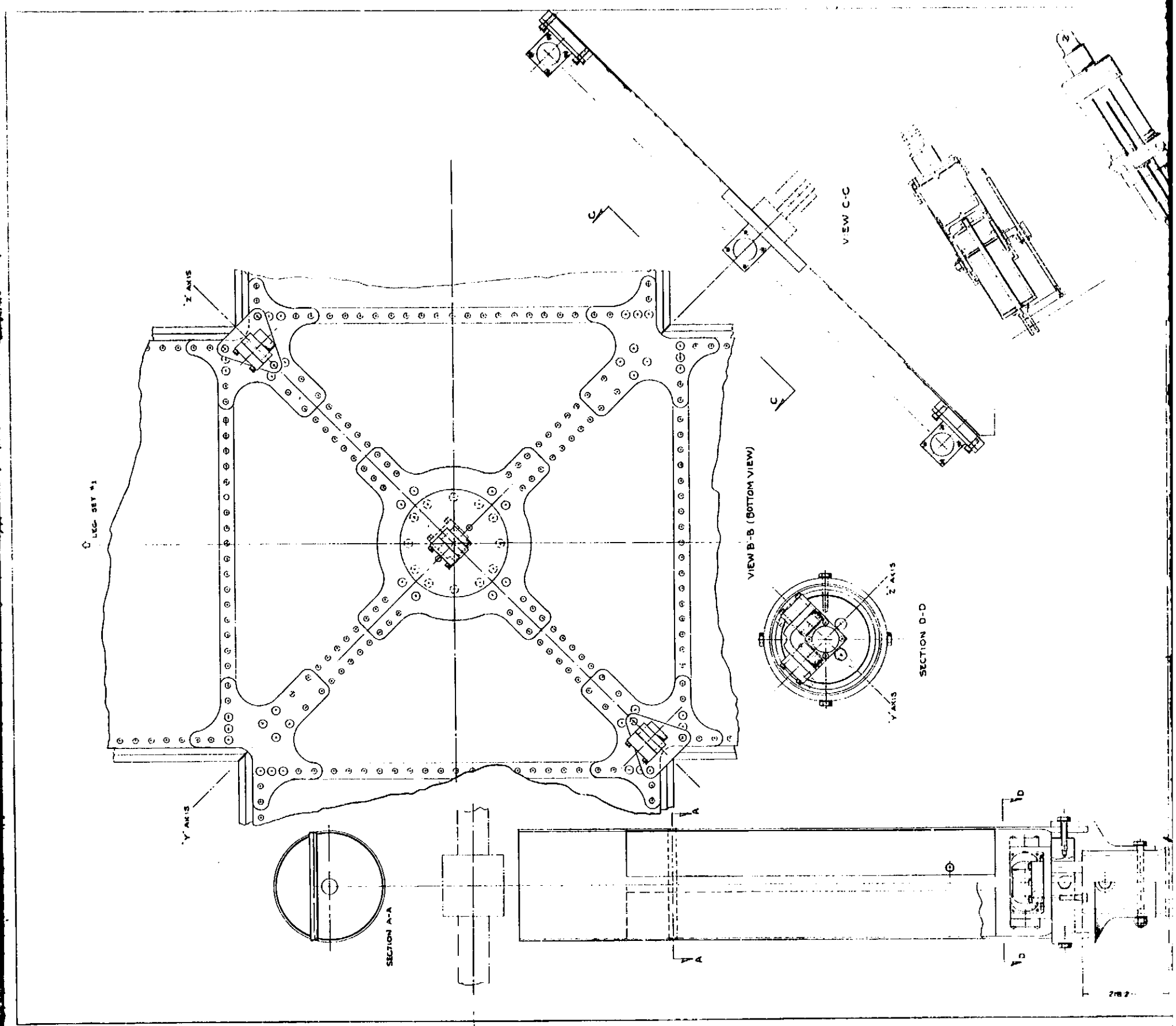

Figure 5-2. Modified LM Mod

FOLDOUT FRAME 1

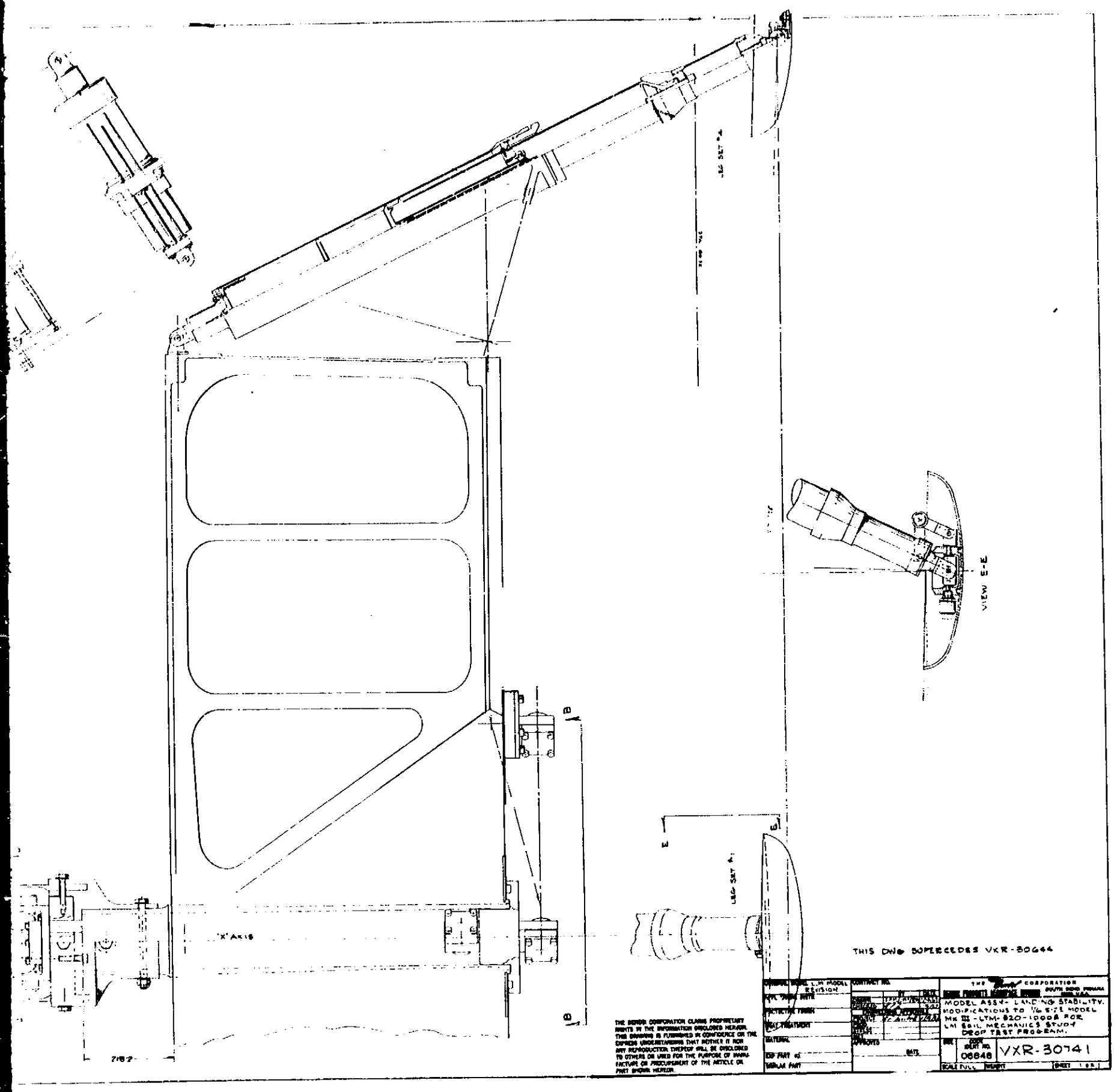

Modified LM Model

FOLDOUT FRAME 2

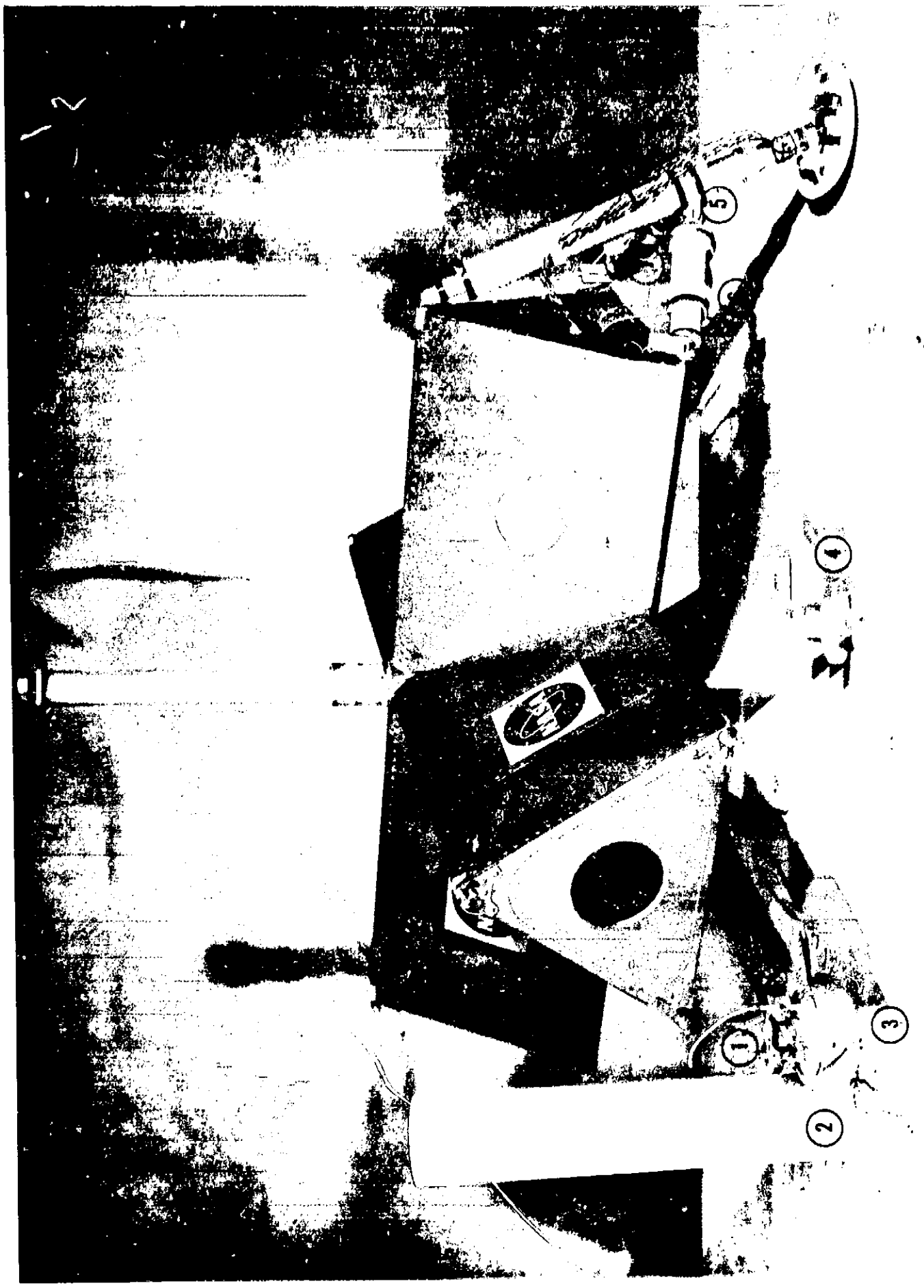

Figure 5-3. General View of Partly Assembled Modified Model

was itself attached to the bottom of the mast. The axes of the two accelerometers were oriented to parallel the y and z axes of those at the center of gravity location, Figure 5-2. These accelerometers, in conjunction with those at the center of gravity location, determined the pitch and roll motions of the vehicle. A sixth accelerometer was mounted below the body such that it is at the same distance below the center of gravity as the two accelerometers on the fitting, but oriented radially outward. This accelerometer, together with the one on the fitting, provided the data to determine the yaw motion of the model. A dummy accelerometer was mounted to the opposite side of the sixth accelerometer to balance the model.

5.2.1.2 Load and Stroke Measurement - Secondary Struts

Early studies indicated that the original model leg set components were not readily adaptable to the load and stroke instrumentation requirements of the program. Although original leg set hardware was used as much as possible, in several cases completely new components were required to avoid compromising load or stroke measurement. Figure 5-4 is an exploded view of a typical leg set after modification.

On all four leg sets, secondary strut axial loads were measured by instrumenting the secondary strut end fitting (5, Figures 5-3 and 5-4) which formed a part of the secondary to primary strut attachment. This end fitting replaced the original one suppliedwith the model and is of similar design to one used by Grumman on another version of the scaled model.

The secondary strut stroke was measured by linear potentiometers mounted externally on the strut (6, Figure 5-3). A resistor rod (1, Figure 5-4) was attached to a bracket (2, Figure 5-4) which in turn was fastened to the strut fitting. A spring wiper assembly (3, Figure 5-4) was attached to a nylon ring (4, Figure 5-4) which was seated in a split bearing. The split bearing was attached to the strut barrel (7, Figure 5-4). The nylon ring was held in place by two snap rings and rotates freely on the barrel. Two steel rods were used to align the resistor rod with the strut barrel (7, Figure 5-3). This arrangement provided free rotation of the barrel relative to the nylon ring to allow for the twisting motion of the strut during stroking. (It was found that the strut barrel rotated nearly 45 degrees from its initial position when the strut was fully compressed.)

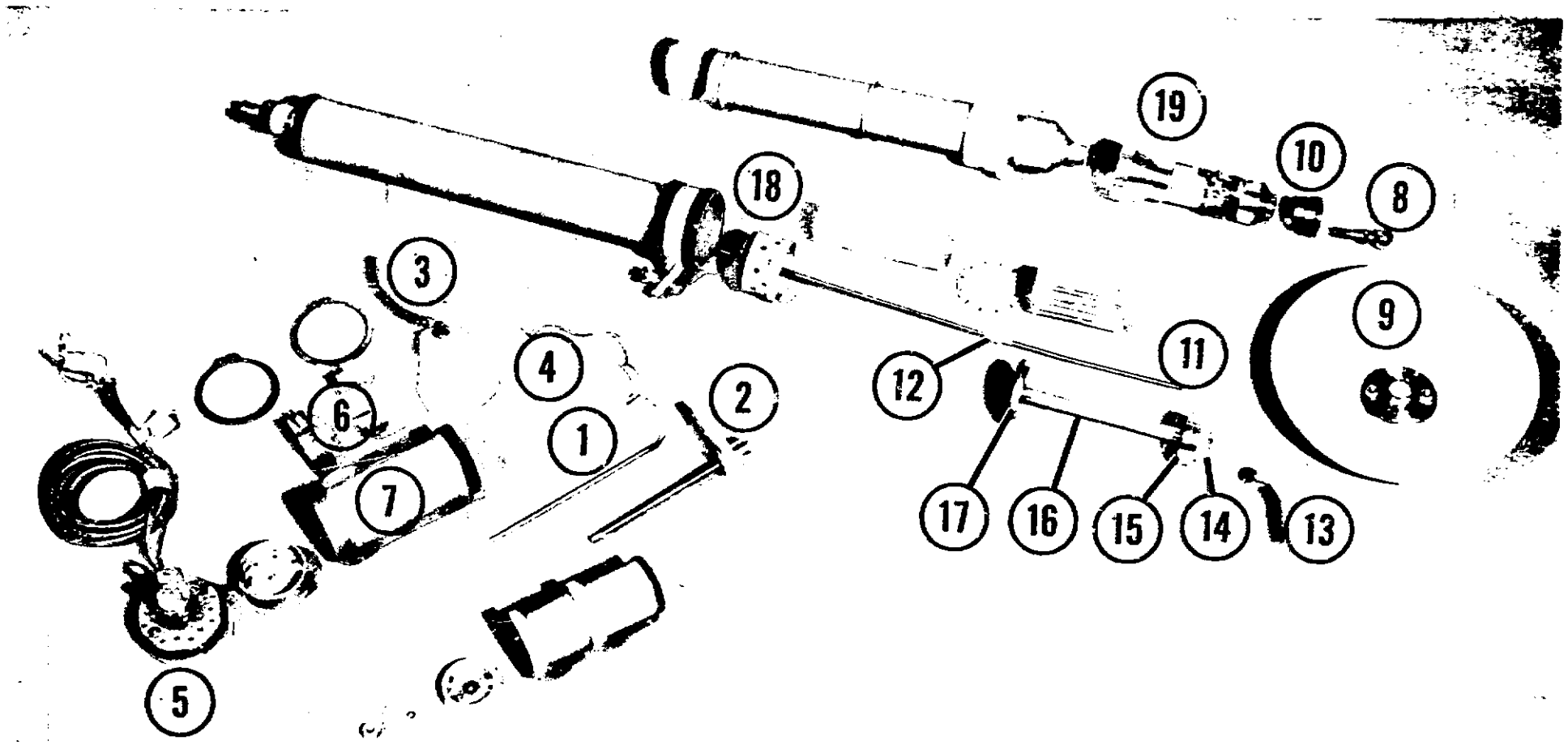

Figure 5-4. Exploded View of Leg Assemblies

5.2.1.3 Load Measurement - Primary Struts

Figure 5-5 indicates the identification assigned to each leg set and footpad, and to each of the shock struts. Leg set No. 1 contains the more heavily instrumented primary strut and instrumented footpad mentioned earlier.

On three of the primary struts (Nos. 4, 7, and 10), only the axial load was measured, using specially designed load cells (19, Figure 5-4) bolted to the end of the inner cylinders. These load cells formed integral extensions to the inner cylinders with their lengths designed so that the model footpad radius concurred with the current LM configuration. Four strain gages were located around the center of the load cell, forming a bridge to measure axial load.

The footpads for these three primary struts were attached to the lower ends of the load cells through ball joints which allowed the footpad to swivel freely. Mechanical stops in the design limited angular displacement of the footpads to 24 degrees in any direction from a position with the pad normal to the strut centerline. In a normal touchdown position, the footpads were set against the stop surfaces so they tilted up two degrees from a plane normal to the vehicle centerline.

The load cell on primary strut No. 1 is physically identical to the other three but was instrumented such that the footpad moments and forces could be resolved, in addition to axial load. A clevis fitting, instead of a ball socket, was assembled to the end of the load cell and was attached to the footpad through a swivel fitting forming a non-yawing universal joint. Figure 5-6 illustrates this assembly and the position of the twelve strain gages on the load cell. Figure 5-7 indicates the nomenclature for determining footpad moment. The four strain gages around the center of the cell (Figure 5-6) formed the bridge to measure axial load (as a separate parameter) similar to the other three primary struts.

A conical surface on the clevis fitting limited the footpad pitch and roll angles to 24 degrees, as on the other three pads. In the normal touchdown position the pad was set against the stop and tilted two degrees from the plane normal to the vehicle centerline (Figure 5-6).

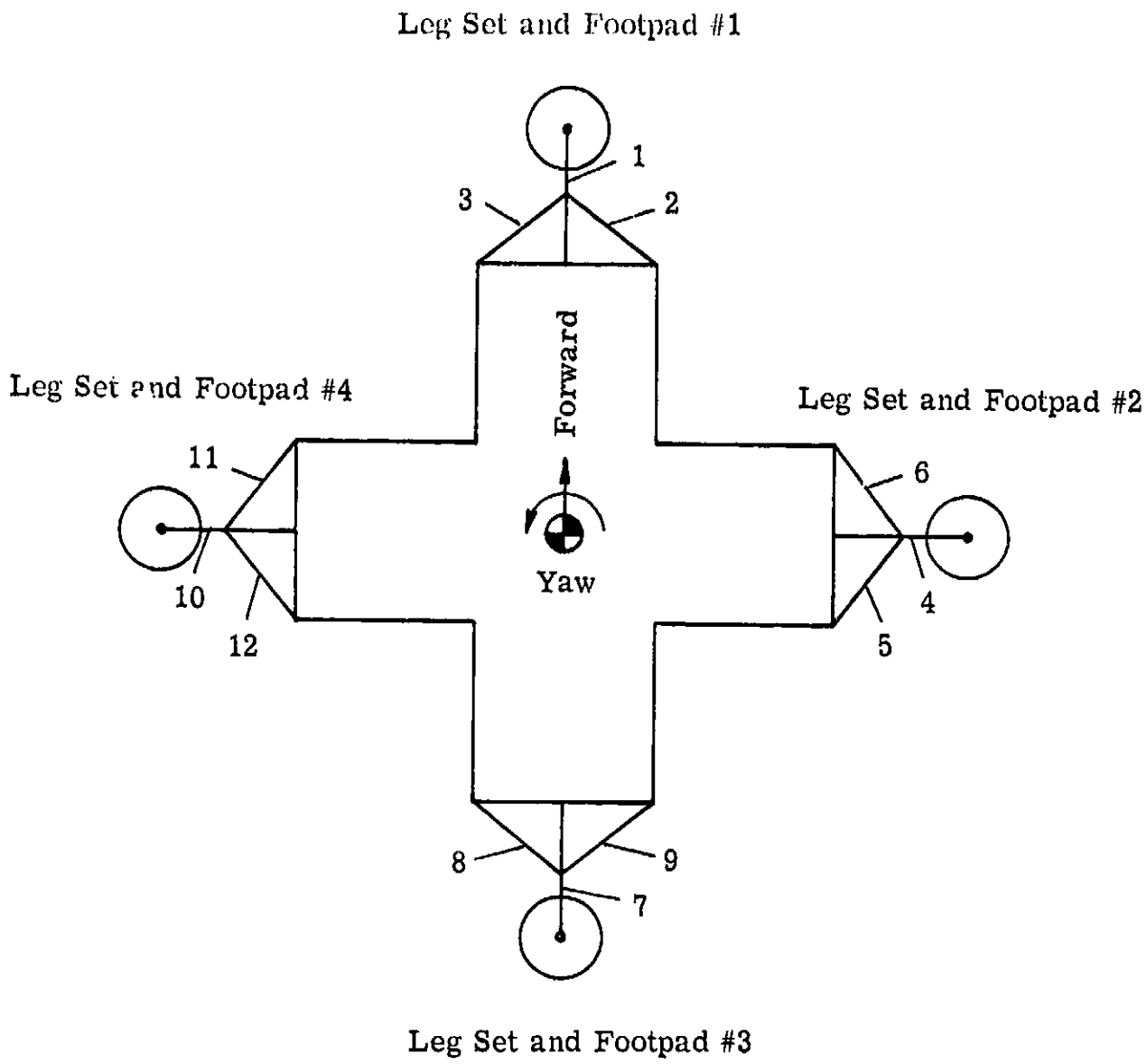

Figure 5-5. LM Model - Leg and Footpad Identification

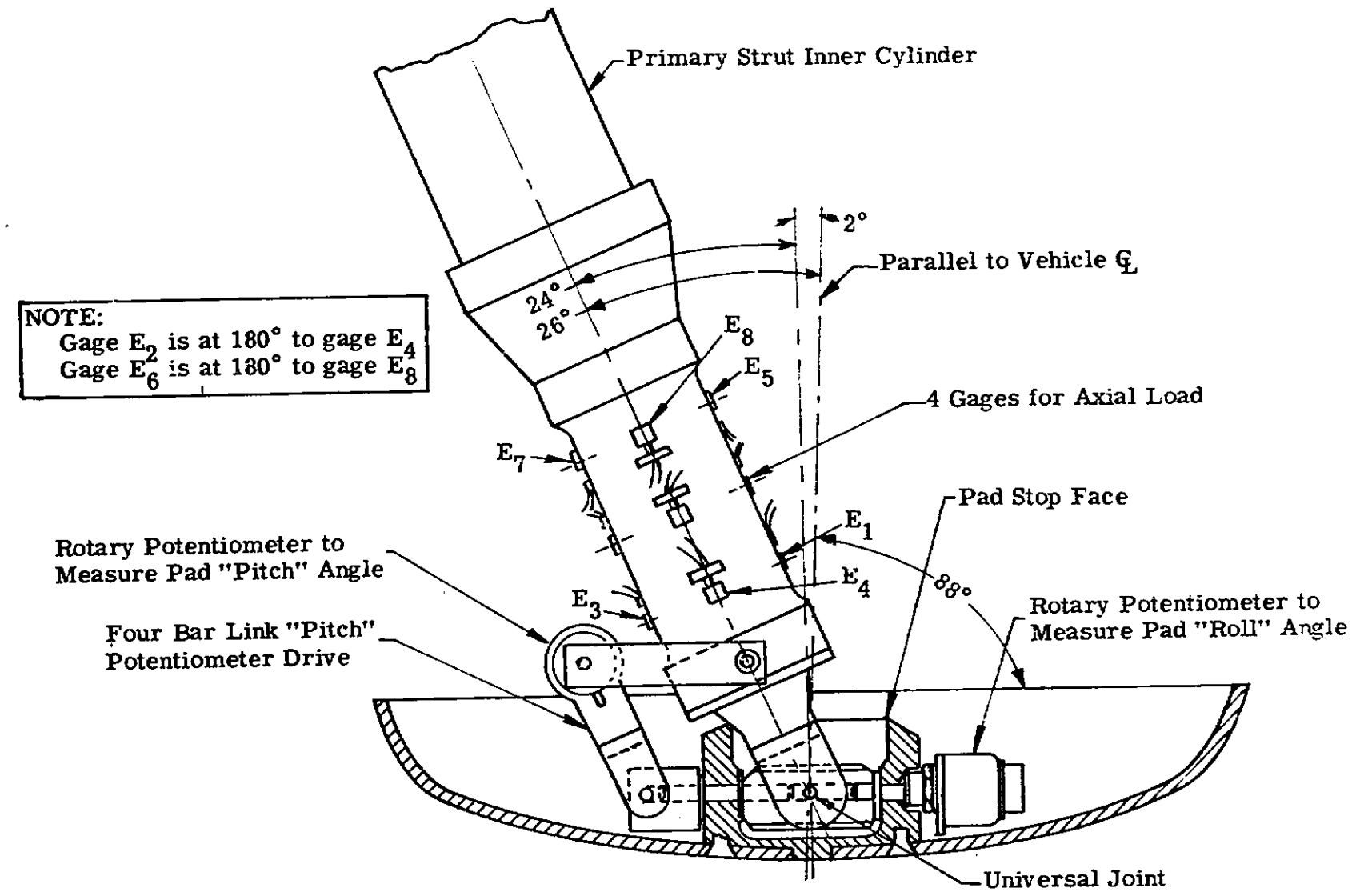

Figure 5-6. Instrumentation to Measure Pad Forces, Moments, and Angular Displacement on Dynamic Model (This Instrumentation on Leg Set No. 1 Only)

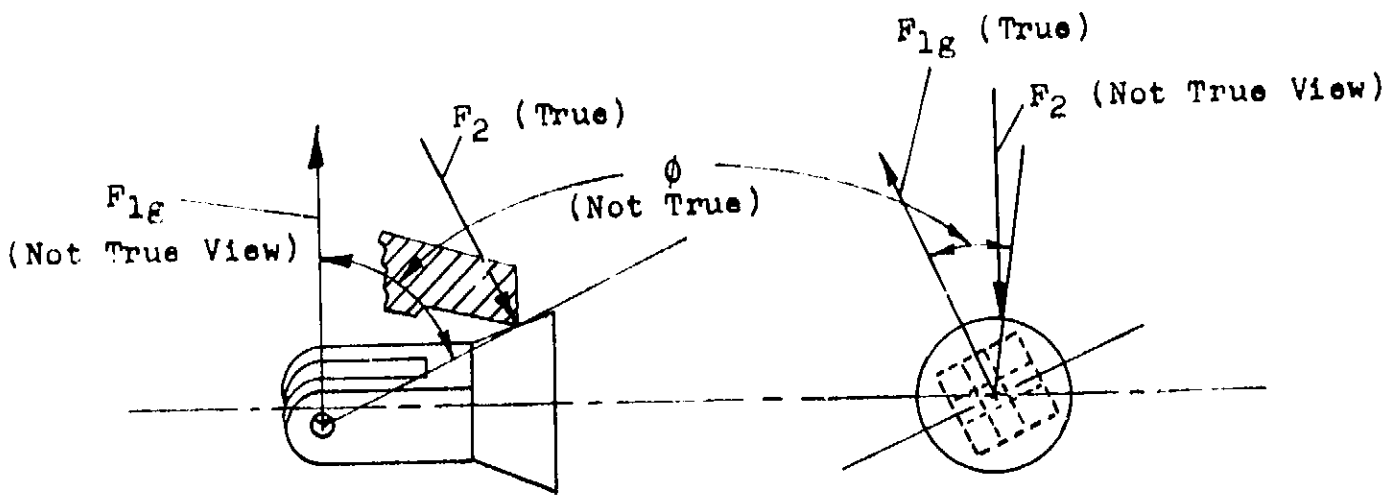

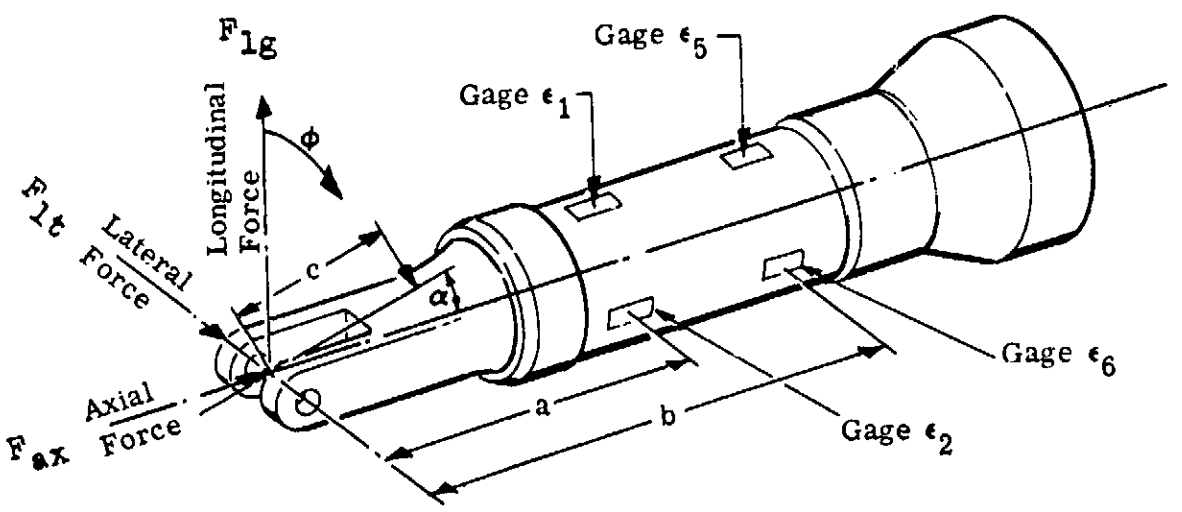

Figure 5-7. Nomenclature of Pad Moment and Force Resolution Equations

Footpad angular position was measured by rotary potentiometers mounted as shown in Figure 5-6. The "roll" potentiometer body was attached to the mounting block on the footpad and was drived by the swivel block with the potentiometer drive shaft acting as part of the swivel block pin. The pitch potentiometer was driven by a four-bar link mechanism. The body of the potentiometer was fixed to the upper end of the vertical link and its shaft fastened to the upper horizontal link. The lower end of the vertical link was pinned to a block which in turn was connected to the swivel block pin.

5.2.1.4 Stroke Measurement - Primary Struts

The stroke of each primary strut was measured with a linear potentiometer mounted inside the inner cylinder. A resistor rod (11, Figure 5-4) was screwed into an adapter (12, Figure 5-4) which was bonded to the honeycomb guide rod. A wiper assembly (13, Figure 5-4) was mounted on a nylon insulator (14, Figure 5-4) which was attached to a guide (15, Figure 5-4) and was bonded, through a tube (16, Figure 5-4) to the piston head (17, Figure 5-4). The resistor rod assembly passed through the center of the wiper mounting assembly which was installed inside the inner cylinder and secured by two screws as shown in Figure 5-4. The cup (18, Figure 5-4) was attached to the top of the primary strut outer cylinder by a screw to prevent the resistor wire assembly from moving out with the inner cylinder during the rebound stroke.

To prevent rotation of the No. 1 strut inner cylinder on which the instrumented footpad was attached, a square guide rod was used. This guide rod passed through a square hole in the piston head. The cup (18, Figure 5-4) for this strut had a mating hole for locating the guide rod and was attached to the outer cylinder by a screw, thus preventing rotation of the whole assembly. Figure 5-8 is a photo of the No. 1 strut after assembly and illustrates the primary strut load cell and footpad instrumentation.

5.2.2 Energy Absorbing Capsules

The configuration of the LM model after extensive modification and instrumentation appears to be fairly representative of the current full-scale LM vehicle. Figure 5-9 shows a comparison of the geometry of the model and the present LM, and Figure 5-10

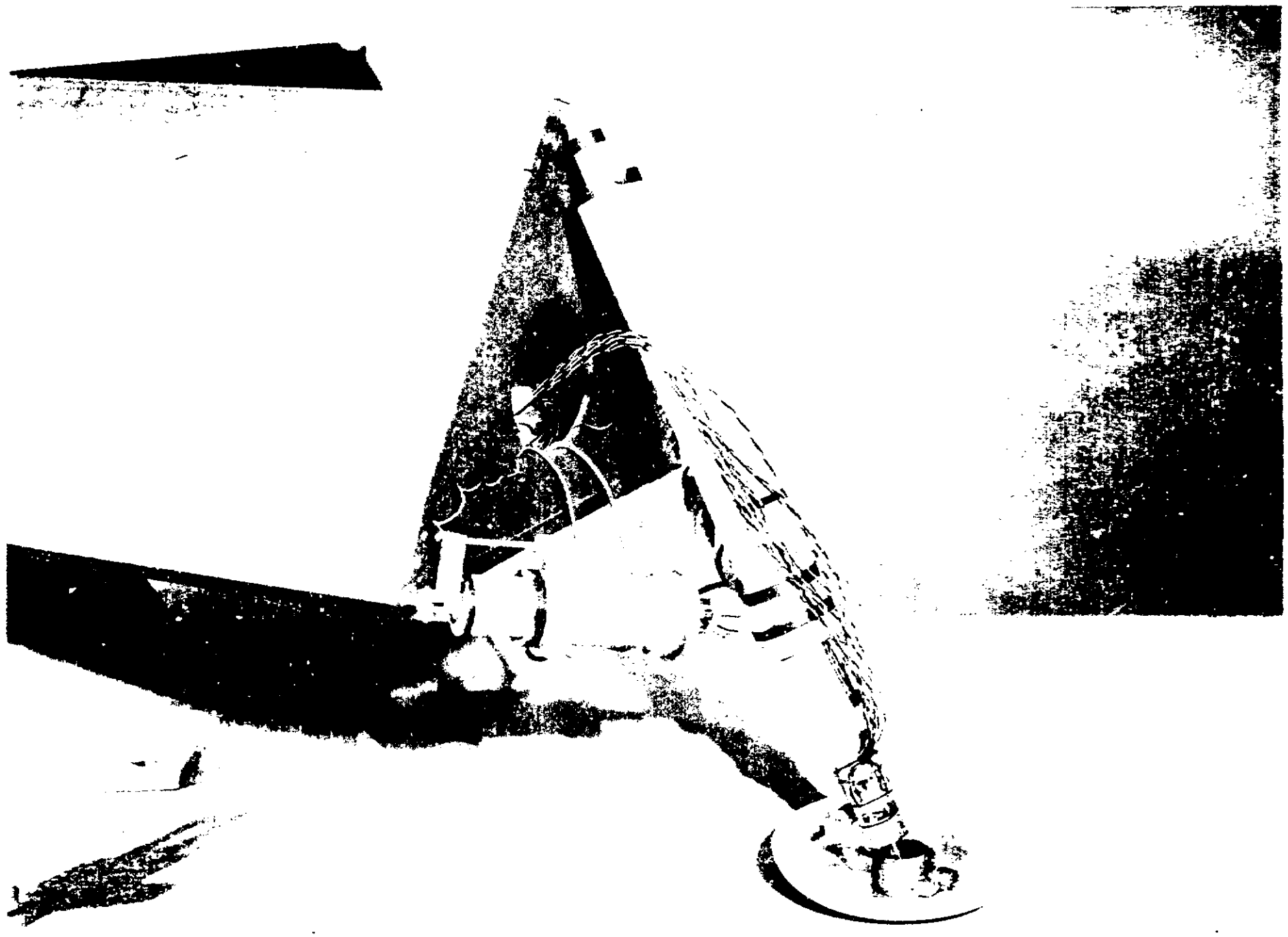

Figure 5-8. Pad Instrumented to Measure Forces, Moments, and Angles

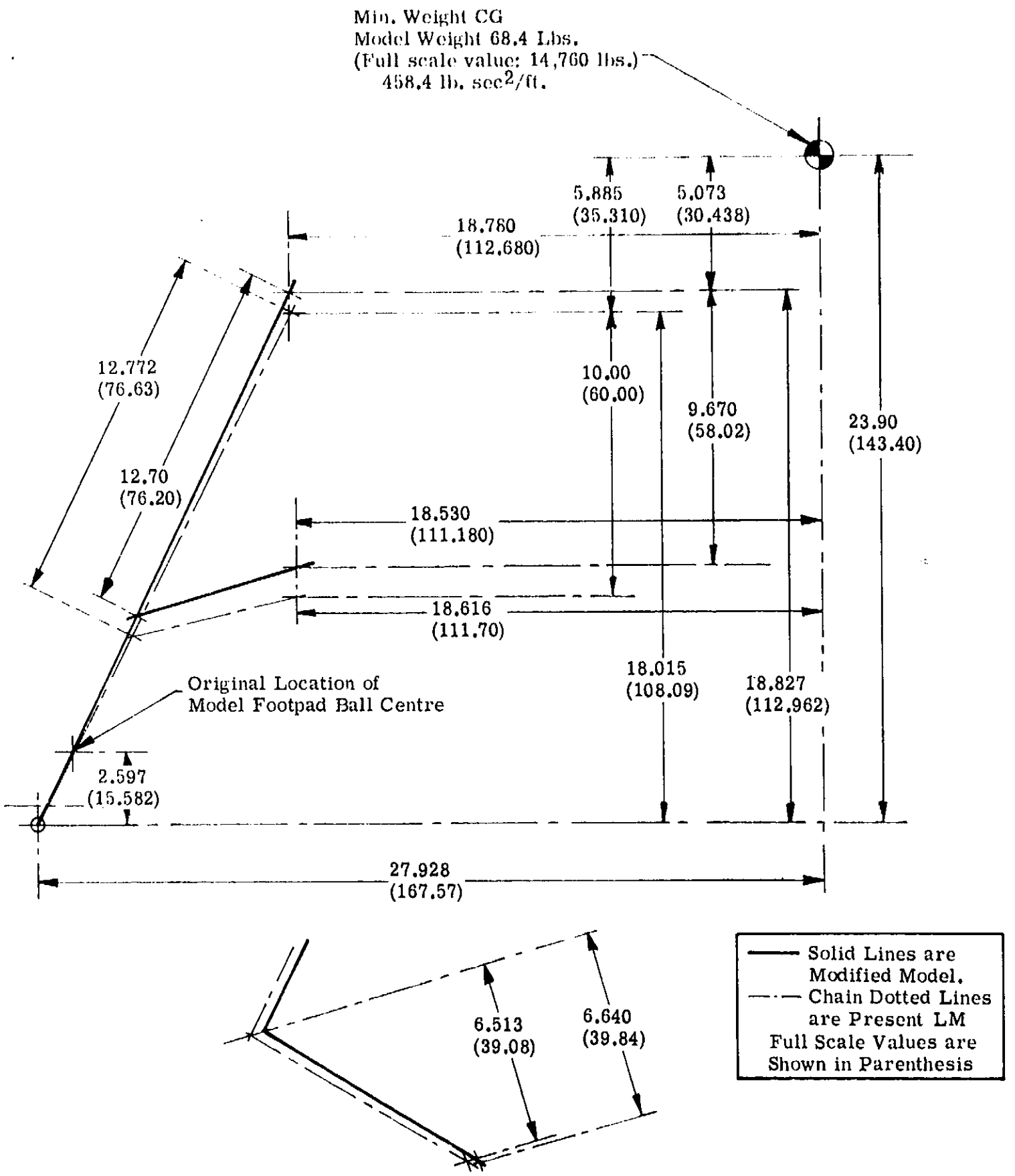

Figure 5-9. Comparison of Modified 1/6-Scale Model with Present LM Configuration

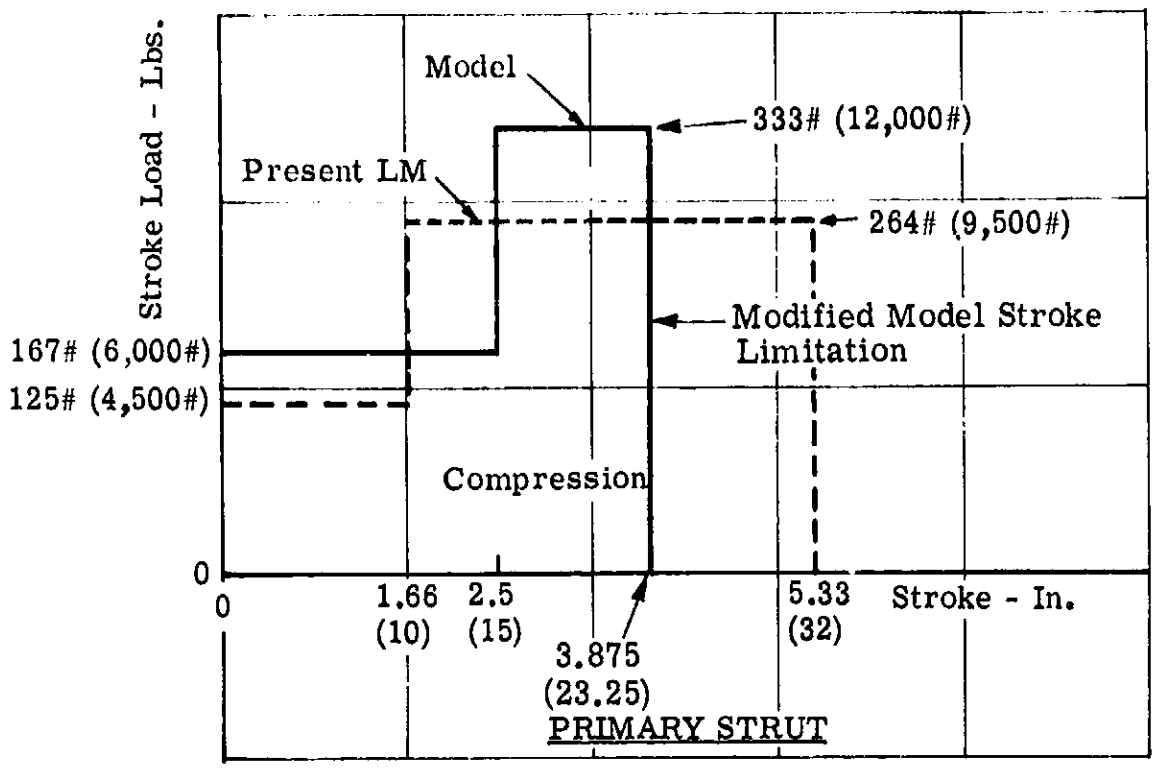

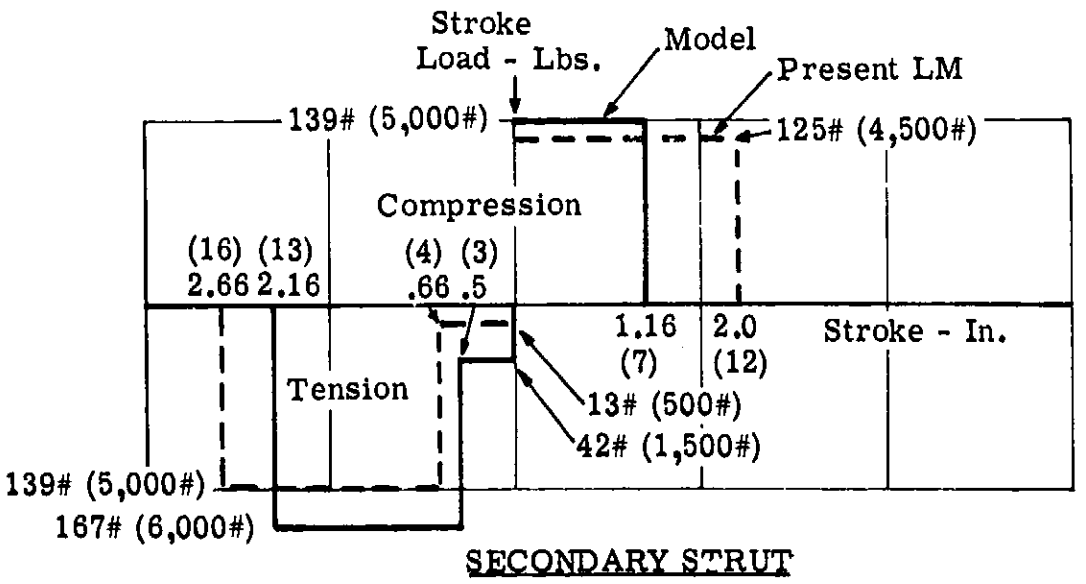

NOTE: Full Scale Values Shown in Parentheses.

Figure 5-10. Comparison of Modified 1/6-Scale Model and Present LM Loads versus Strokes

compares model and LM vehicle load-stroke characteristics. It is noted that the energy absorbing elements within each strut have load versus stroke characteristics which differ somewhat from those which would be obtained by scaling the corresponding characteristics of the current configuration full-scale LM. In certain situations this could cause the model to perform differently than the actual LM.

The energy absorbing material used was aluminum honeycomb with 1/8-inch cell size and foil thicknesses of 0.0007 inch and 0.001 inch. The stock was purchased from Hexcell Products, Inc., in sheets of different thicknesses. Each capsule was machined from the appropriate honeycomb stock and precrushed to smooth out the initial load peak. Controlled crush tests were performed on a number of randomly selected capsules of each of the five different sizes to determine their crush load/stroke characteristics. The tests utilized an Instron Model TTCM1-3 for load/deflection measurements, with the capsules mounted between two parallel flat plates with a guide pin running longitudinally through the center of the capsule.

These controlled crush tests showed a maximum crush load variation of ±10 percent between capsules of the same configuration. This amounts to a stroke load variation of 151 to 183 pounds for the primary strut low crush load compression stroke, and 300 to 366 pounds for the high crush load compression stroke. For the secondary struts, the variation was 125 to 153 pounds for the compression stroke, 38 to 46 pounds for the low tension stroke, and 151 to 183 pounds for the high tension stroke. The general trend of all the capsules tested during these controlled tests was towards the lower crush loads. The above ranges were obtained after a lengthy development program with the available honeycomb materials that were determined suitable for the scaled LM model.

In general, the strut axial (dynamic) loads measured during drop tests were slightly higher than the capsule crush loads indicated in Figure 5-10. This would be as expected because the load sensed by the load cell on each strut is actually the sum of the capsule crushing force (i.e., Figure 5-10) plus any other stroke resistive forces inherent to the shock strut's energy absorbing system. Although the actual observed load difference varied with model impact condition, it was most noticeable during the initial stroking of

the primary shock strut. This dynamic load was usually around 200 to 225 pounds, in contrast with the capsule crush load range of 151 to 183 pounds.

It is believed this difference is largely due to frictional forces between the piston and Teflon bearings which is further aggravated by the higher bending moment on the inner cylinder (due to footpad side or drag forces) during the initial stroking phase. Entrapped air in the honeycomb capsule cells could also contribute. Although the strut components were vented to minimize this effect, the strut stroking action occurs in just a few milliseconds and could conceivably cause some air pressure buildup in the cells.

5.2.3 Geometric and Physical Characteristics of the LM Model

A brief description of the coordinate system used in this project is necessary to enhance the understanding of the various physical quantities about to be given (refer to Figure 5-11).

A. Right-hand rule is used throughout.

B. Fixed coordinate system (ground):

X_f axis - Normal to the horizon, positive in the direction away from the ground surface.

Y_f axis - Normal to X_f, positive in the direction of the model horizontal velocity.

Z_f axis - as defined by the right-hand rule.

The origin of the fixed coordinate is a point on the ground, which is the vertical projection from the model center of gravity at the instant the first footpad touches the ground.

C. Body coordinate (vehicle) system:

X_b axis - upward (i.e., away from the legs) along the vehicle centerline, positive upward.

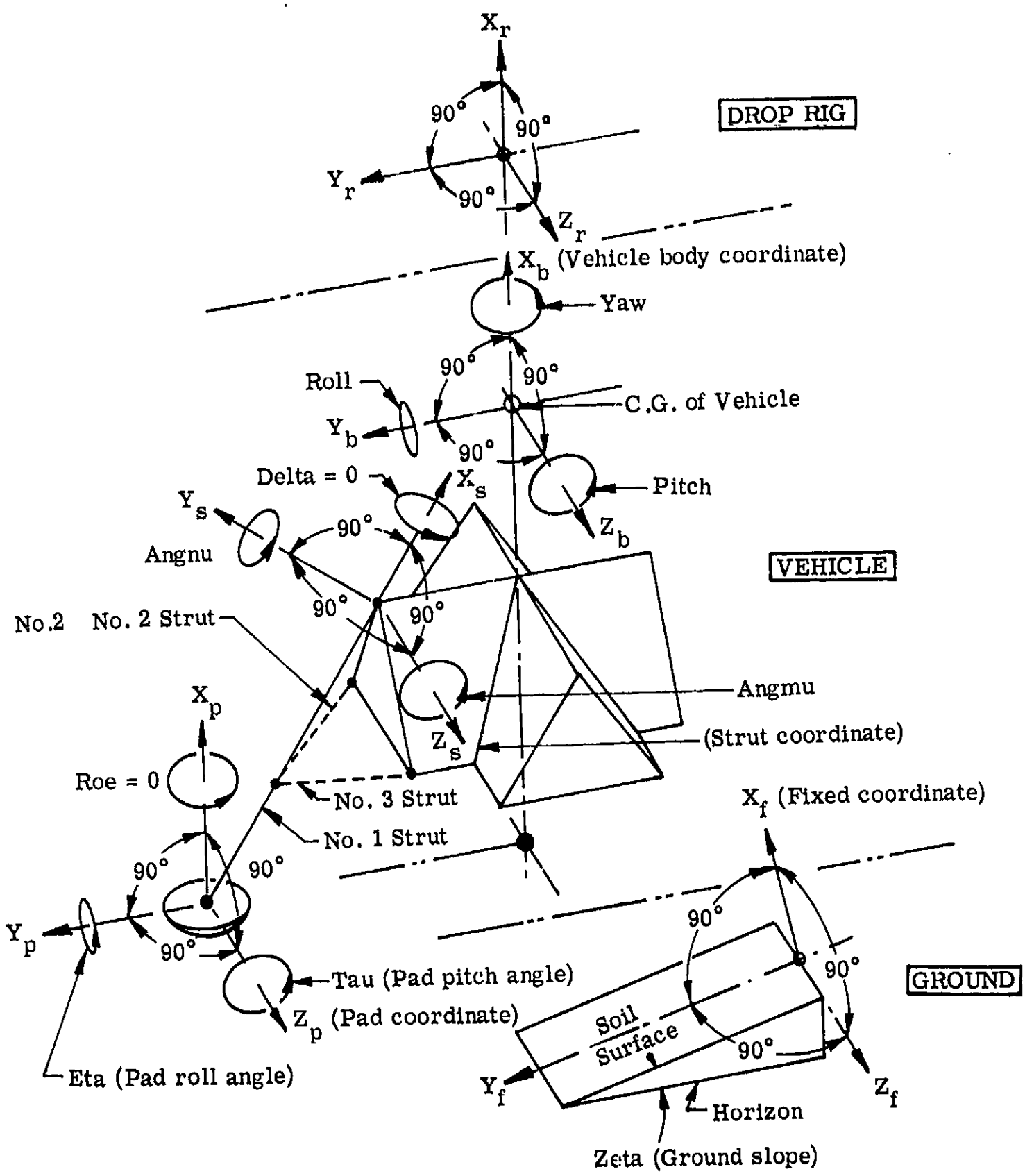

Figure 5-11. LM Model Coordinate System

Y_b axis - in the plane defined by the X_b axis and the No. 1 (primary) footpad.

Z_b axis - as defined by the right-hand rule.

The origin of the body coordinate is at the CG of the vehicle and moves with it.

Order of rotation of the vehicle:

1st - pitch
2nd - yaw
3rd - roll

where

Pitch angle = rotation about Z_b axis
Yaw angle = rotation about X_b axis
Roll angle = rotation about Y_b axis

D. Strut coordinate system:

X_s axis - along the centerline of the primary strut in the vertical position, positive upward.

Y_s axis - normal to X_s axis and positive outward from the body.

Z_s axis - along universal joint pin axis in the direction as defined by the right-hand rule.

The origin of the strut coordinate is the primary strut-to-vehicle attachment hard point, and the corrdinate system moves with the primary strut.

Order of rotation of the strut:

1st - Delta
2nd - Nu
3rd - Mu

where

Delta = rotation about X_s axis

Nu = rotation about Y_s axis

Mu = rotation about $_x$ axis

E. Pad coordinate system:

X_p axis - in the direction normal to the footpad disc plane and initially in the X_s-Y_s plane positive upward (i.e., away from the disc).

Y_p axis - normal to X_p and in the plane of the footpad disc and always lie in the X_s - Y_s plane.

Z_p axis - as defined by right-hand rule.

The origin of the pad coordinate is at the footpad pivot point. Order of rotation of the pad:

This coordinate system has only two angular degrees of freedom; namely, rotation about Z_p and Y_p axis.

1st - Tau

2nd - Eta

where

Tau = pad pitch angle - rotation about Z_p axis

Eta = pad roll angle - rotation about Y_p axis

Listed below in chart form is a summary of the important physical quantities of the LM model.

Symbol	Description	Value	Units
$I_o(X_b)$	Moment of Inertia about the X_b axis	1.6022	Slug ft.^{2}
$I_o(Y_b)$	Moment of Inertia about the Y_b axis	1.2880	Slug ft.^{2}
$I_o(Z_b)$	Moment of Inertia about the Z_b axis	1.3402	Slug ft.^{2}
$I_o(Y_s)$	Moment of Inertia about the Y_s axis	0.09917	Slug ft.^{2}
$I_o(Z_s)$	Moment of Inertia about the Z_s axis*	0.09914	Slug ft.^{2}
	Initial CG Height above a level ground	23.90	Inches
	Initial Primary Strut Assembly (include the footpad) CG distance from the upper hinge point	14.66	Inches
	Total Model Weight	68.4	Lbs.
	Primary Strut Assembly Weight (include footpad)	1.82	Lbs.
	Initial footpad to body centerline radius	27.928	Inches

*Footpad orientation does not affect the I_o readings in any coordinate.

5.2.4 Model Drop Test Facilities

The model drop tests were carried out at the Bendix spacecraft model dynamic drop test laboratory. The soil bed which forms the landing surface is 18 feet long and 12 feet wide, with a maximum below ground depth of five feet. The depth of soil used was adjusted to suit the varying test conditions. The LM model was launched by a six-degree-of-freedom drop test rig which is suspended above the soil bed. Figures 5-12 and 5-13 show the general arrangement of the test facility.

The launch mechanism is suspended by vertical and horizontal adjustable links that are supported from a cantilever frame which, in turn, is mounted on a vertical adjustable mechanism between upright H beams. For any given model drop initial conditions the required drop rig height, linkage angles, and linkage swing settings are obtained by a

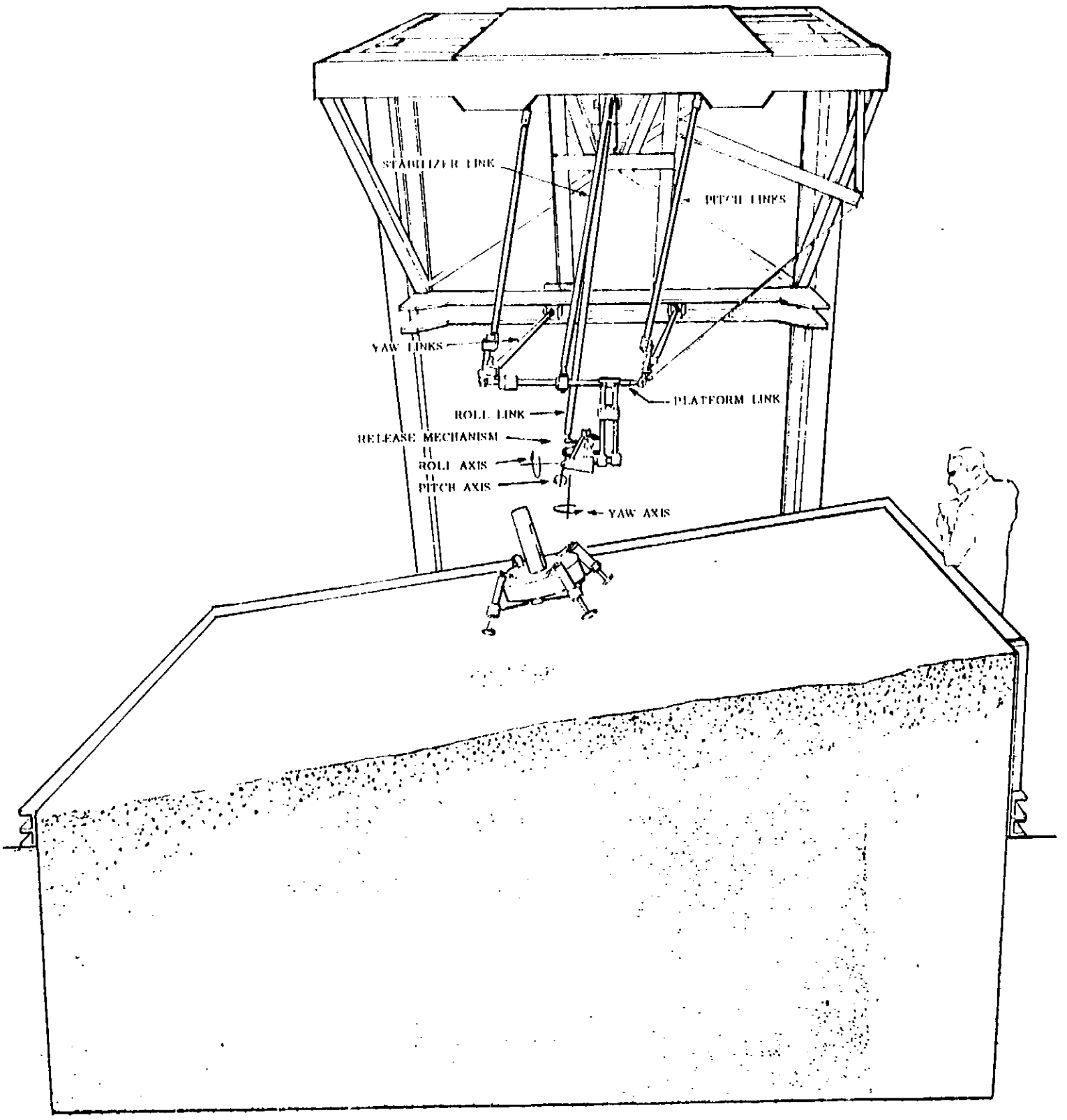

Figure 5-12. Sketch of Six Degree of Freedom Drop Test System and Soil Bed

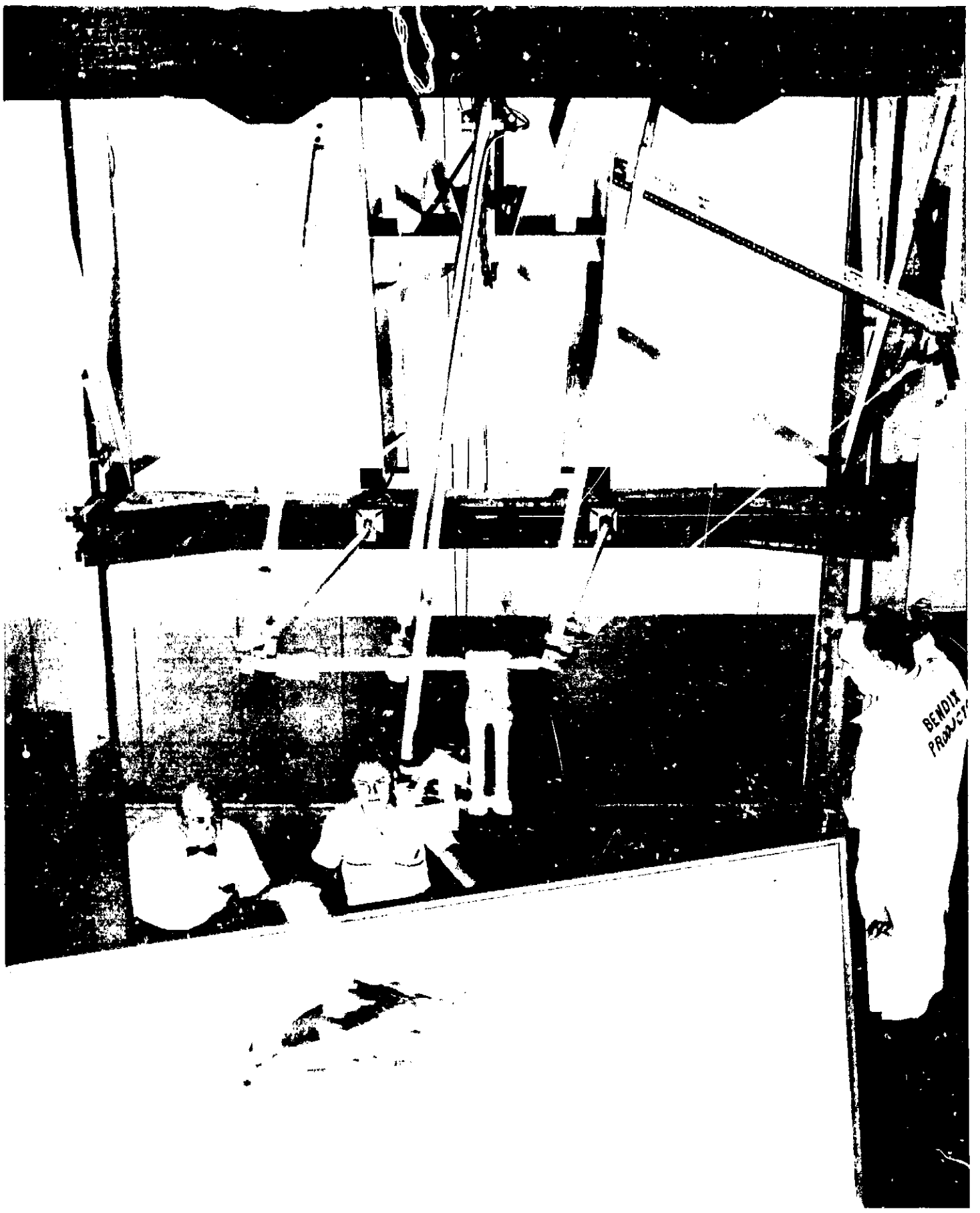

Figure 5-13. Six Degree of Freedom Drop Test Rig

digital computer program devised for this purpose. A complete description of this facility can be found in Section IV of Reference 1.

5.2.5 Instrumentation Recording System

Figure 5-14 is a block diagram of the data recording system used for detail correlation studies in which the output of all of the 37 model sensors was required. Figure 5-15 illustrates the magnetic tape-to-oscillograph reproduction system used. A detailed description of the instrumentation is covered in Paragraph 5.5.

Variations from Figure 5-14 used in the other groups of tests, depending upon the amount and type of data required, are discussed in the respective pages of Section V.

5.3 LISTING OF LM MODEL DROPS

Table 5-T2 lists all of the LM model drops made during the model test program, and provides details pertinent to the test conditions and test results in terms of stability.

A total of 77 drop tests were performed to satisfy the various test requirements, plus an additional four composite drops for instrumentation and computer program checkout purposes. A key at the end of the table identifies the particular types of tests, and reference is made to this listing, by test number, in the following sections.

It can be noted that a number of the drops were made only to confirm previous test results, while others were repeat drops that were necessary because of laboratory mishaps or equipment malfunctions.

5.4 RIGID SURFACE LANDING OF THE LM MODEL

Rigid surface drop tests of the LM model were made to form a baseline for the correlation studies of landings in soils.

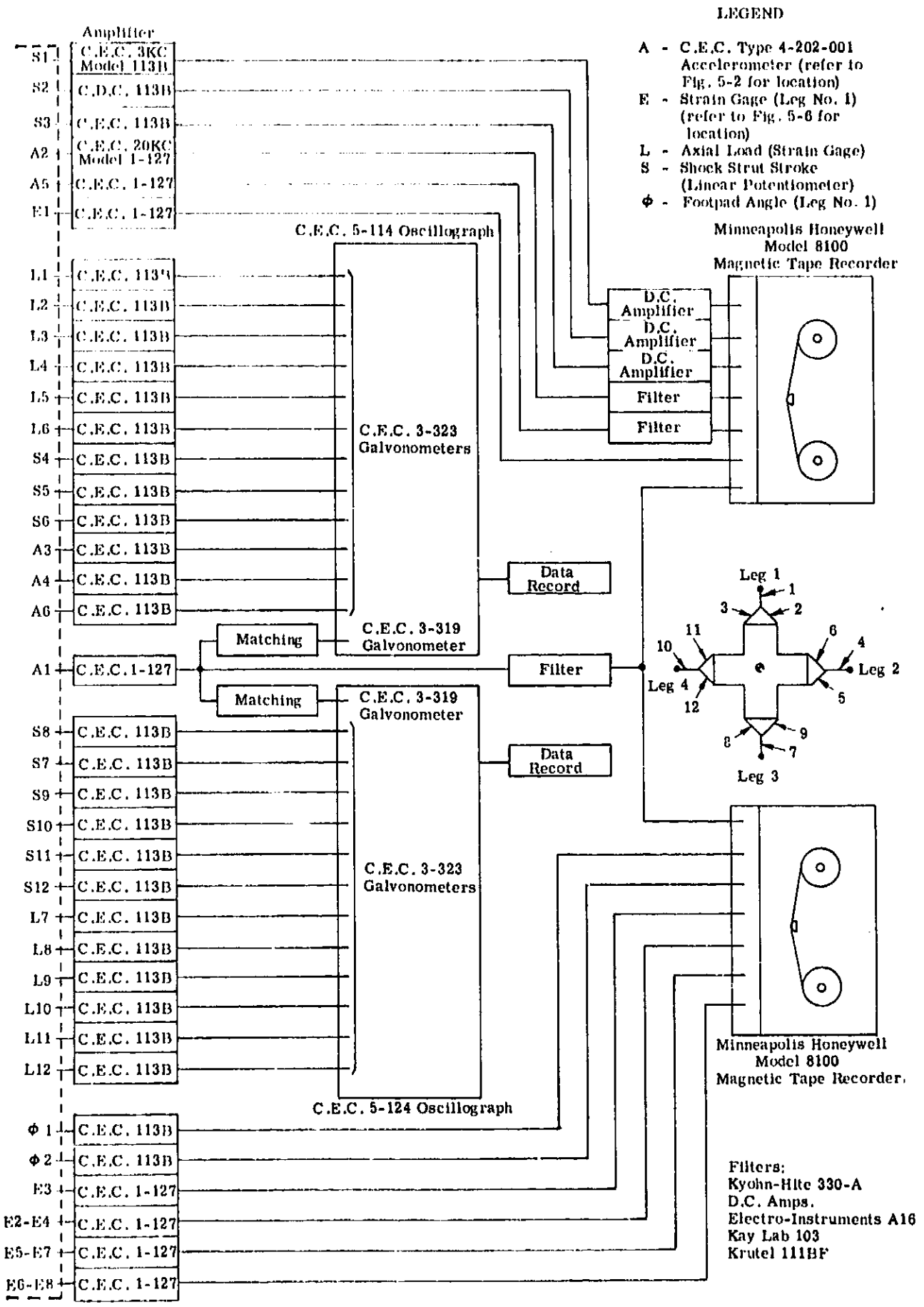

Figure 5-14. LM Model Drop Test Instrumentation

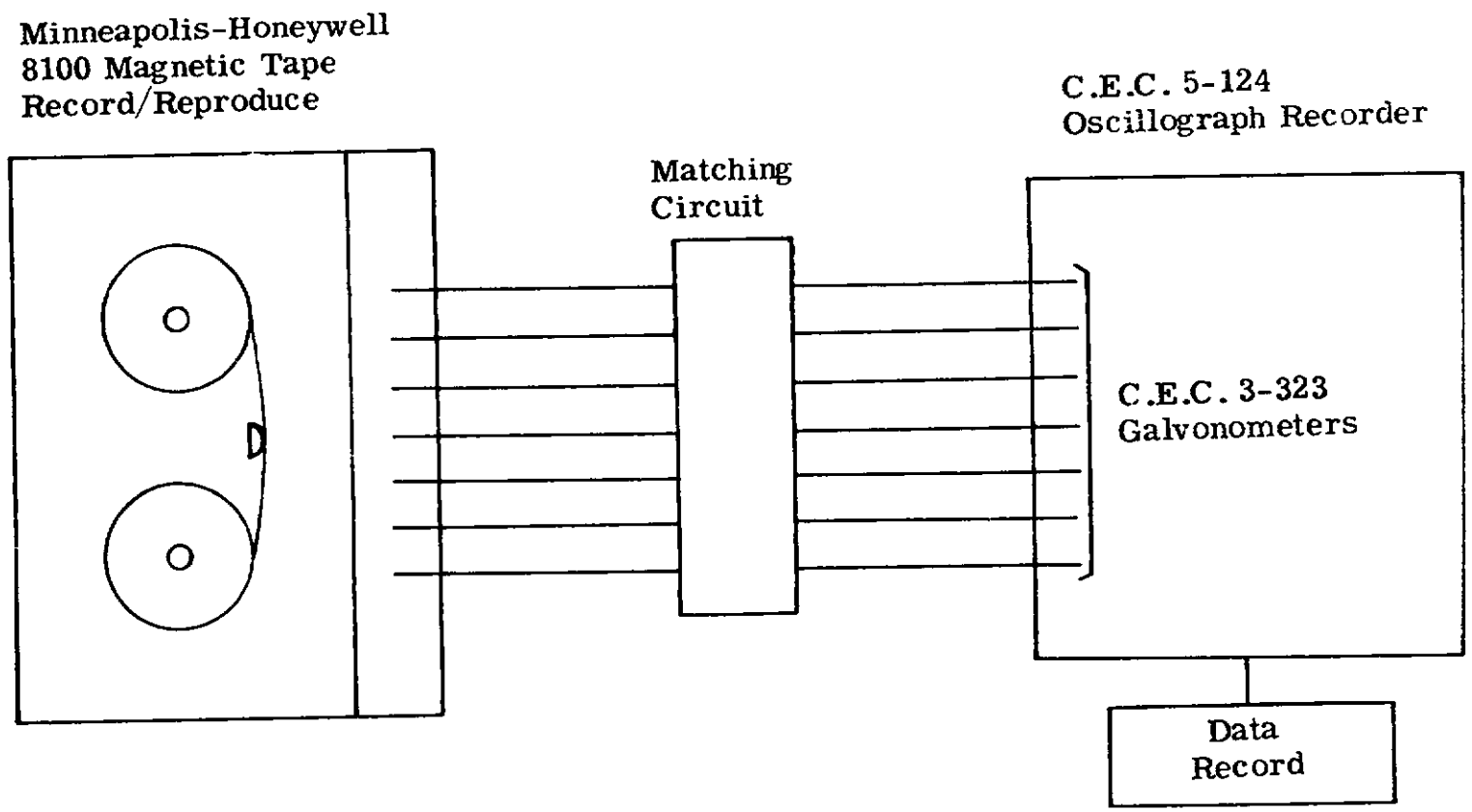

Figure 5-15. Magnetic Tape to Oscillograph Reproduction

TABLE 5-T2. LIST OF MODEL DROP TESTS

Series No. and Date	Test *Type	Soil	V_V	V_H	Ground Slope (Deg.) Zeta	Yaw Angle (Deg.)	Relative Density Dr	Density γ (Lbs. Ft.^{3})	Friction Angle Φ (Deg.)	Stable	Remarks
A 4-17-67	A	RS Dense	5	5	0	45 (2-2)	-	-	-	Yes	Drops A, B, C, and D were made to provide data for checking computer program. Only one 7-channel tape recorder was available so four drops of the same condition were made for composite set of input data.
B 4-18-67	A	RS Dense	5	5	0	45 (2-2)	-	-	-	Yes	
C 4-19-67	A	RS Dense	5	5	0	45 (2-2)	-	-	-	Yes	
D 4-20-67	A	RS Dense	5	5	0	45 (2-2)	-	-	-	Yes	
1 6-27-67	B	SS Dense	4.98	4.98	0	45 (2-2)	-	-	-	Yes	Trial drop 13 signals recorded on 2 tapes.
2 7-6-67	B	RS Dense	7	4	3 1/2	-160 (1-2-1)	-	-	-	Yes	Leg No. 1 touched ground first. Legs 2, 3, 4, in four-inch deep holes.
3 7-7-67	B	RS Dense	6	2.46	3 1/2	+160 (1-2-1)	-	-	-	Yes	Leg No. 1 touched ground first. Leg 2 in four-inch deep hole.
4 7-7-67	B	RS Dense	10	2.46	3 1/2	+160 (1-2-1)	-	-	-	Yes	Leg No. 1 touched ground first. Leg 2 in four-inch deep hole.
5 7-11-67	B	RS Dense	6	2.46	3 1/2	+70 (1-2-1)	-	-	-	Yes	Leg No. 4 touched ground first. Four and one-half inch deep hole under Leg No. 1. Waxed hard surface under Legs 2 and 4. Rough hard surface under Leg No. 3. Sand paper on Leg No. 3.
6 7-11-67	B	RS Dense	10	2.46	3 1/2	+70 (1-2-1)	-	-	-	Yes	
7 7-13-67	C	RS Loose	5	7	0	45	-	-	-	Yes	Model released too late. Specially prepared soil bed.
8 7-14-67	C	RS Loose	10	0	0	45	-	-	-	Yes	Bad instrumentation rerun.
9 7-17-67	C	RS Loose	5	7	0	45	-	-	-	Yes	Bad release timing. Release arm readjusted.
10 7-18-67	C	RS Loose	10	0	0	45	0	46.9	41	Yes	NASA Drop No. 1. Tests No. 1-8 McDonnell reduced.
11 7-19-67	C	RS Loose	5	7	0	45	0	46.9	41	Yes	NASA Drop No. 2.
12 7-20-67	C	RS Loose	5	7	0	45	0	47.1	41	Yes	NASA Drop No. 3
13 7-20-67	C	RS Loose	10	0	0	45	0	47.1	41	Yes	NASA Drop No. 4.
14 7-21-67	C	RS Inter-mediate	5	7	0	45	-	-	-	Yes	Bad tape recording.
15 7-21-67	C	RS Inter-mediate	10	0	0	45	-	-	-	Yes	Poor recording.

*See key at the end of this table.

TABLE 5-T2. LIST OF MODEL DROP TESTS (CONT.)

Bendix Drop No. and Date	Test *Type	Soil	V_V	V_H	Ground Slope (Deg.) Zeta	Yaw Angle (Deg.)	Relative Density Dr	Density γ (Lbs. Ft.^{3})	Friction Angle ϕ (Deg.)	Stable	Remarks
16 7-25-67	C	RS Inter-mediate	5	7	0	45	0.3	53.0	42.5	Yes	NASA Drop No. 5.
17 7-25-67	C	RS Inter-mediate	10	0	0	45	0.3	53.0	42.5	Yes	NASA Drop No. 6.
18 7-27-67	C	SS Loose	5	7	0	45	0	95.2	30	Yes	Bad recording.
19 7-27-67	C	SS Loose	10	0	0	45	0	95.2	30	Yes	Bad release.
20 7-28-67	C	SS Loose	5	7	0	45	0	96.0	30	Yes	NASA Drop No. 7.
21 7-28-67	C	SS Loose	10	0	0	45	0	96.0	30	Yes	NASA Drop No. 8.
22 8-3-67	D	RS Dense	10	5	15	45	0.72	56.9	47	Yes	RS Dense soil - 10 rolls per two-inch layer.
23 8-4-67	D	RS Dense	10	7	15	45	0.71	56.7	47	No	
24 8-7-67	D	RS Dense	12	5	15	45	0.81	59.3	48	Yes	
25 8-8-67	D	RS Dense	12	5	15	45	0.79	59.0	48	No	
26 8-8-67	D	RS Dense	14	4	15	45	0.81	59.3	48	Yes	
27 8-8-67	D	RS Dense	14	5	15	45	0.81	59.3	48	Yes	Borderline stability.
28 8-9-67	D	RS Dense	8.5	7.5	15	45	0.81	59.3	48	No	
29 8-9-67	D	RS Dense	8.5	6.5	15	45	0.73	58.2	47.5	No	
30 8-10-67	D	RS Dense	10	6	15	45	0.74	58.4	47.5	No	Borderline stability.
31 8-10-67	D	RS Dense	8.5	5.5	15	45	0.74	58.4	47.5	Yes	
32 8-10-67	D	RS Dense	7.5	6.5	15	45	0.74	58.4	47.5	No	
33 8-11-67	D	RS Dense	7.0	5.5	15	45	0.74	58.4	47.5	Yes	
34 8-11-67	D	RS Dense	10	6	15	45	0.73	58.2	47.5	No	
35 8-11-67	E	RS Dense	10	6	15	67.5	0.76	58.6	47.5	Yes	No. 4 leg touched ground first.

TABLE 5-T2. LIST OF MODEL DROP TESTS (CONT.)

Bendix Drop No. and Date	Test Type	Soil	V_V	V_H	Ground Slope (Deg.) Zeta	Yaw Angle (Deg.)	Relative Density Dr	Density γ (Lbs. Ft.^{3})	Friction Angle ϕ (Deg.)	Stable	Remarks
36 8-14-67	E	RS Dense	10	7	15	67.5	0.74	58.4	47.5	Yes	
37 8-14-67	E	RS Dense	14	7	15	67.5	0.75	58.5	47.5	Yes	
38 8-15-67	E	RS Dense	14	0	15	67.5	0.75	58.5	47.5	Yes	
39 8-15-67	E	RS Dense	16	4	15	67.5	0.80	59.1	48	Yes	
40 8-16-67	E	RS Dense	6.59	7.55	15	67.5	0.68	57.6	47	Yes	
41 8-17-67	E	RS Dense	16	6	15	67.5	0.72	58.1	47	Yes	
42 8-17-67	E	RS Dense	12	7.5	15	67.5	0.80	59.1	48	Yes	
43 8-18-67	E	RS Dense	8.7	7.5	15	67.5	0.76	58.9	48	Yes	
44 8-18-67	E	RS Dense	16	0	15	67.5	0.70	57.9	47	Yes	
45 9-27-67	F	Ply-wood Blocks	8	4.8	10	22.5	-	-	-	Yes	Borderline stability spiked footpad-10° board slope
46 10-2-67	F	Ply-wood Blocks	8	4.8	10	22.5	-	-	-	Yes	Borderline stability. Tests 45 and 46 to check rubber capsules.
47 10-3-67	F	Ply-wood Blocks	8	5.8	10	22.5	-	-	-	Yes	
48 10-4-67	F	Ply-wood Blocks	8	5.8	10	22.5	-	-	-	Yes	
49 10-4-67	F	Ply-wood Blocks	8	6.8	10	22.5	-	-	-	No	Very unstable.
50 10-5-67	F	Ply-wood Blocks	8	4.8	10	22.5	-	-	-	No	Borderline stability.
51 10-6-67°	F	Ply-wood Blocks	8	5.8	10	22.5	-	-	-	Yes	Repeat of drops 47 and 48.
52 10-6-67	F	Ply-wood Blocks	8	6.8	10	22.5	-	-	-	No	Very unstable.
53 10-9-67	F	Ply-wood Blocks	6	6	10	22.5	-	-	-	Yes	

TABLE 5-T2. LIST OF MODEL DROP TESTS (CONT.)

Bendix Drop No. and Date	Test *Type	Soil	V_V	V_H	Ground Slope (Deg.) Zeta	Yaw Angle (Deg.)	Relative Density Dr	Density γ (Lbs. Ft.^{3})	Friction Angle ϕ (Deg.)	Stable	Remarks
54 10-9-67	F	Ply-wood Blocks	6	7	10	22.5	-	-	-	No	
55 10-10-67	F	Ply-wood Blocks	10	4.5	10	22.5	-	-	-	Yes	
56 10-10-67	F	Ply-wood Blocks	10	5.5	10	22.5	-	-	-	Yes	
57 10-11-67	F	Ply-wood Blocks	10	6.5	10	22.5	-	-	-	No	
58 10-11-67	F	Ply-wood Blocks	12	6.5	10	22.5	-	-	-	No	
59 10-11-67	F	Ply-wood Blocks	12	5.5	10	22.5	-	-	-	Yes	
60 10-12-67	F	Ply-wood Blocks	8.5	5.5	10	22.5	-	-	-	No	
61 10-12-67	F	Ply-wood Blocks	9	5	10	22.5	-	-	-	No	
62 10-13-67	F	Ply-wood Blocks	9	4.5	10	22.5	-	-	-	Yes	
63 10-18-67	G	RSM 10 Rolls	12	7.5	15	22.5	0.80	86.0	48	Yes	
64 10-19-67	G	RSM 10 Rolls	10	6	15	45	0.78	85.6	48	No	
65 10-19-67	G	RSM 10 Rolls	10	5	15	45	0.65	83.6	47	Yes	
66 10-20-67	G	RSM 10 Rolls	10	5	15	45	0.77	85.5	48	Yes	Rerun of Test 65.
67 10-20-67	G	RSM 10 Rolls	12	5	15	45	0.75	85.2	48	Yes	
68 10-23-67	G	RSM	14	5	15	45	0.10	75.7	39	Yes	Soil not rolled.
69 10-23-67	G	RSM	14	5	15	45	0.79	85.7	48	No	Repeat of Test 68 on hard dense soil.
70 10-23-67	G	RSM Rolled	14	4	15	45	0.78	85.6	48	Yes	
71 10-24-67	G	RSM Rolled	12	0	15	45	0.86	87.2	48	No	

TABLE 5-T2. LIST OF MODEL DROP TESTS (CONC.)

Bendix Drop No. and Date	Test *Type	Soil	V_V	V_H	Ground Slope (Deg.) Zeta	Yaw Angle (Deg.)	Relative Density Dr	Density γ (Lbs./Ft.^{3})	Friction Angle ϕ (Deg.)	Stable	Remarks
72 10-25-67	G	RSM Rolled	8	5.5	15	45	0.73	84.8	48	Yes	
73 10-25-67	G	RSM Rolled	8	6.5	15	45	0.74	84.9	48	Yes	Borderline stability.
74 10-26-67	G	RSM Rolled	8	7	15	45	0.77	85.5	48	No	
75 10-26-67	G	RSM Rolled	7	7.5	15	45	0.8[illegible]	86.3	48	No	
76 10-26-67	G	RSM Rolled	7	6.8	15	45	0.78	85.6	48	No	
77 10-26-67	G	RSM Rolled	8	6.5	15	45	0.76	85.4	48	No	Borderline stability. Rerun of Test 73.
											KEY TO TEST TYPES A = Composite Drop Tests B = Exploratory Tests C = Detail Correlation Tests D = Gross Correlation Tests-RS Dense Soil - 45° Yaw E = Gross Correlation Tests-RS Dense Soil - 22 1/2° Yaw F = Rigid Surface Landings G = Gross Correlation Tests - RSM Soil - 45° Yaw

The degree of correlation between the two stability profiles, one of which is obtained experimentally on rigid surface model drops and the other obtained analytically from computer study of the same drop conditions, can form an upper limit on the precision that can be expected in the soil landing correlation studies.

5.4.1 Model Setup

For the rigid surface model drop tests the round simulated LM footpads were replaced with specially designed spiked footpads. The sharp spikes were used to simulate the condition of ground contact with infinite coefficient of friction. It was found through stress analysis that the primary strut extensions (load cells) of the model might fail from the bending load incurred during rigid surface landings or could cause failure of the primary strut piston. To protect these parts from the initial high peak load at impact, the spikes were cushioned with rubber elements.

Figure 5-16 shows the assembly drawing of the spiked footpad and cushioning device. The spike was positioned within the housing so that it could rotate in any direction with its pivot point at the center of a pivot bearing. The shaft of the spike could also slide within the bore of the pivot bearing. The rotation and sliding of the spike was restrained by rubber bushings and a rubber washer respectively. These rubber elements acted as shock absorbers which reduced the peak impact load on the main strut and the load cells to a safe level. The section and hardness of the rubber elements were so chosen that the axial spring rate at the spike was 4380 pounds/inch and the lateral spring rate was 1725 pounds/inch. The whole assembly was made of steel and is approximately equal in weight to the regular footpad it replaced. Figure 5-17 is a photograph of the spiked footpad assembly showing the various components.

5.4.2 Rigid Surface Landing Test Site

The rigid surface drop tests were performed on a surface tilted to a slope of 10 degrees. Sturdy wooden tables made of heavy lumber and topped by 3/4-inch thick fir plywood were fastened to the bottom of the soil box. The bottom of the soil box was made of four-inch thick laminated plywood sheets, and the soil box itself was seated on compacted

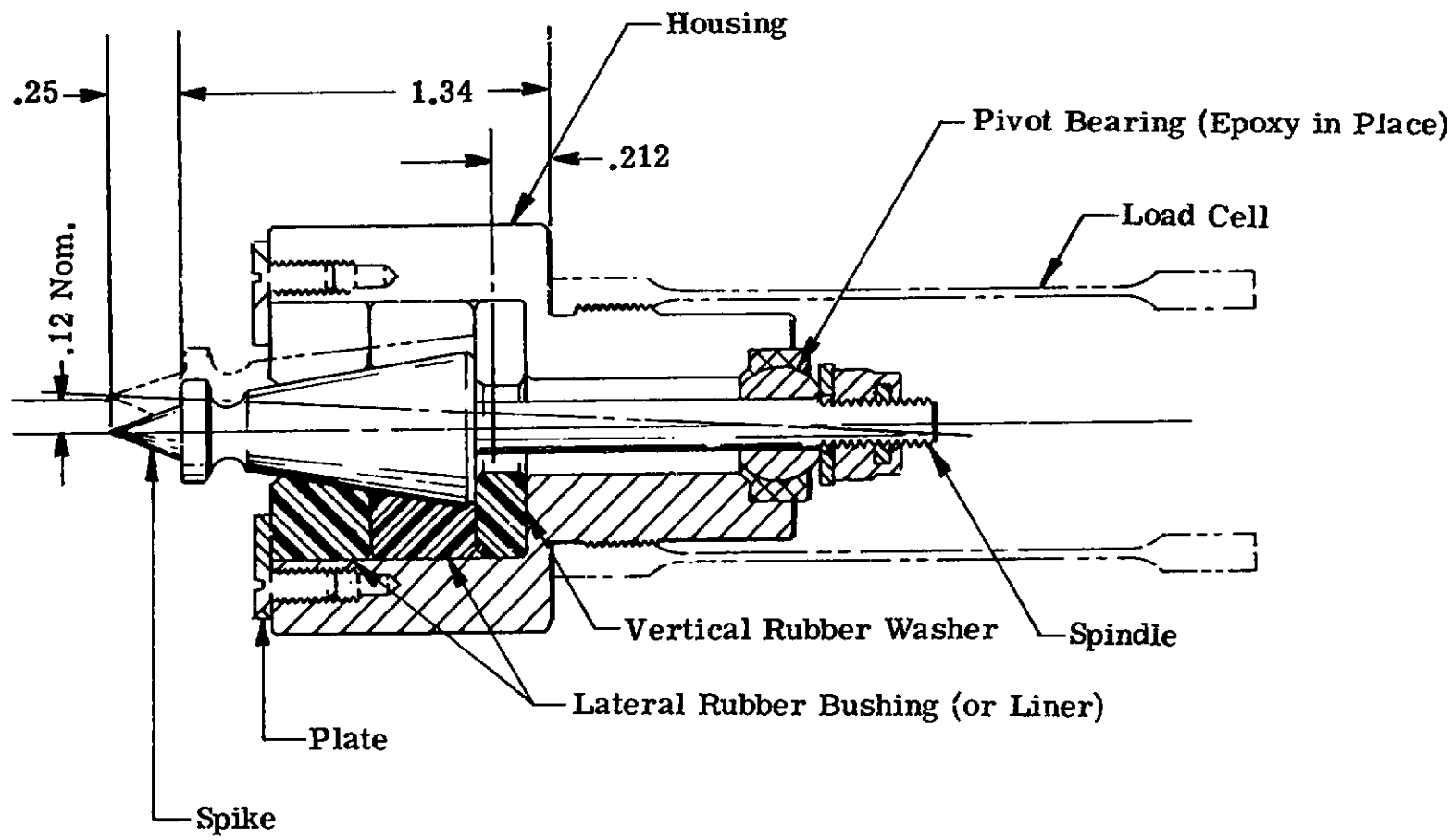

Figure 5-16. Spiked Footpad Assembly - Rigid Surface Tests

silica sand. The space between and below the wooden tables was filled with compacted RS soil (Figure 5-18). The surface for the model drop tests was thus made very rigid to reduce its influence on the dynamics of the LM model.

5.4.3 Rigid Surface Model Drop Tests

The initial model drop attitude for all the rigid surface tests was zero pitch and roll angles, and -22 1/2-degrees yaw angle (i.e., the rear right leg touched the landing surface first). There was no initial angular rate for any of these drops, and only the vertical and horizontal velocities were varied from drop to drop.

Figure 5-19 is a stroboscopic photograph of drop No. 53 on the rigid surface. The initial velocity conditions of this particular test were six feet/second vertical and six feet/second horizontal.

The photograph was taken with open shutter in a darkened room and the strobe light flashed at six cycles per second. These pictures were taken to help judge how close the model approached an unstable condition so that the initial velocities of the next test could be determined. It can be seen from the photograph that drop No. 53 was stable.

Since the primary interest of the rigid surface model drop tests is to establish a stability profile and to measure the load versus stroke characteristics of each of the 12 struts, only 30 of the 37 sensor signals were recorded using two oscillographs. The recorded signals include 12 loads and 12 strokes from the 12 struts, and the six accelerometers in the vehicle body. These signals were plotted against time and the graphs for all the 18 rigid surface drop tests (drop Nos. 45 to 62 inclusive) can be found in a separate data package. The details of each of these drop tests are listed in Paragraph 5.3 of this report.

Figure 5-20 shows a plot of the stability profile for the rigid surface model drop tests. The number near each of the test points is the laboratory drop sequence number which can be referred to the listing in Paragraph 5.3. Note that quite a few drops were concentrated around V_v = 8 feet/second in order to explore the rather abrupt profile changes that occurred in this region.

Figure 5-17. Spiked Footpad Assembly

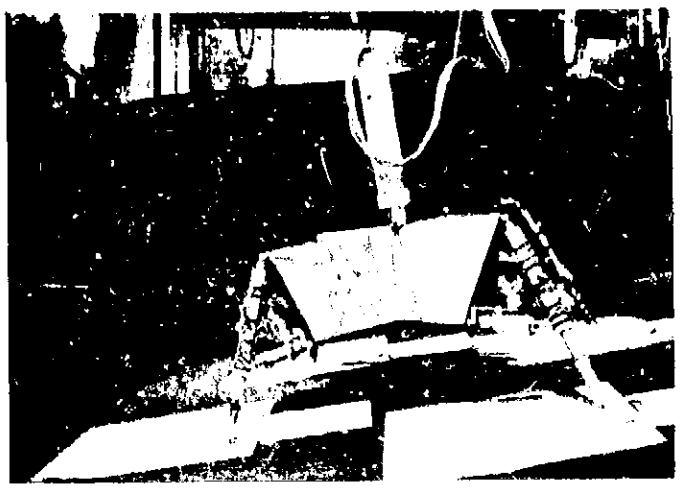

Figure 5-18. Rigid Surface Test Bed

Figure 5-19. Rigid Surface Landing Stroboscopic Photo Drop No. 53

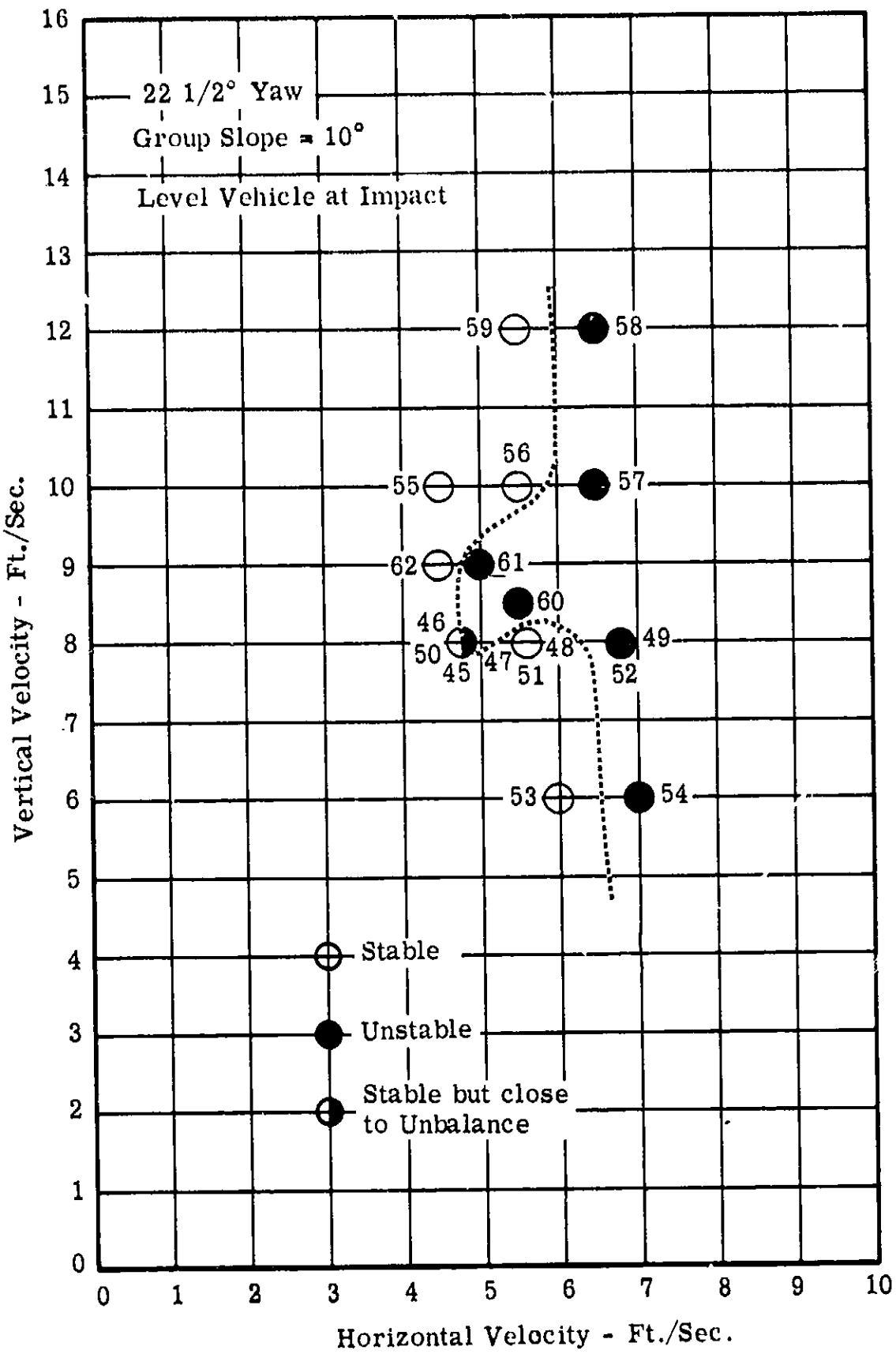

Figure 5-20. Stability Profile - Rigid Surface Tests

Paragraph 6.3 discusses correlation of the hard surface experimental results obtained at Bendix with the analytical results of the similar model drop conditions obtained at NASA.

5.5 DETAILED CORRELATION TESTS AND RESULTS

The main purpose of the detailed correlation study is to substantiate the semi-empirical soil/footpad interaction model which was developed through the analysis of data resulting from many controlled-motion footpad experiments, as described in Section IV. These experiments include the subscale footpad drag tests, the subscale footpad oblique impact tests, the full-scale footpad oblique impact tests, and various static tests.

In all of the above experimental studies the motion of the footpad was guided such that its direction was always a known factor. However, in a free-body LM landing, the direction of the footpad motion continually changes with time during the impacting period. The validity of the semi-empirical soil-footpad model can best be evaluated by measuring the motion and forces of the LM model footpad during actual soil landings and then comparing these measured values with the equivalent values obtained analytically, using the mathematical soil/footpad model. The LM model drops made for this purpose are classified as detailed correlation drop tests.

5.5.1 Instrumentation and Footpad Load Resolution

As noted in Paragraph 5.2.1, there was a total of 37 sensors installed on the LM model. For the detailed correlation studies the output of all 37 sensors was recorded during the drop tests. The wires used for transmitting the signals from the instrumented model were very fine and were suspended above the model such that their presence would not greatly influence the free-body motion of the model. Figure 5-14 presented a block diagram of the instrumentation and recording scheme that was used.

Of the 37 output signals, 13 were amplified and recorded on two 7-channel tape recorders, and the remaining 24 signals were recorded on two oscillographs. The thirteen signals recorded on magnetic tape were from the two accelerometers at the CG in the x and y directions, the single accelerometer at the lower level in y direction, the three linear

potentiometers on the three struts of the No. 1 leg group, the two rotary potentiometers on the No. 1 footpad, and the five strain gages from the No. 1 strut load cells. The two oscillographs accommodated the signals from the remaining three accelerometers, the linear (stroke) potentiometers on the nine struts comprising leg sets Nos. 2, 3, and 4, plus the axial load sensors on all 12 shock struts.

At the instant of model release, a short pulse signal was injected into the output of the accelerometer at the CG in the X direction. The signal from this accelerometer was recorded simultaneously on all the four recording devices (2 tape recorders and 2 oscillographs) to provide a common time base for data reduction.

Among the thirteen tape-recorded signals, the three accelerometers provided data from which the CG displacement, velocity, and acceleration in the x-y plane, and the pitch displacement, velocity and acceleration of the model could be calculated at any instant. The three linear potentiometers on the three struts of the No. 1 leg set measured the change in length of each strut at any instant. With the instantaneous length of each strut known, the position of the pivot point at which the footpad joins the main strut is established at all times with respect to the CG of the model.

The two rotary potentiometers on the No. 1 strut footpad measured the instantaneous footpad pitch and roll angles with respect to the main strut. Therefore, the motion of any point on this footpad could be described with respect to the main strut. Furthermore, the motion of any point on the model could be determined in relation to a fixed coordinate by performing the proper transformation between the various coordinates used in this study.

The eight strain gages on the primary strut load cell were placed such that forces acting on the footpad pivot point could be resolved in the three principal axes of the strut coordinates (see Figure 5-6 and Figure 5-7). These strain gages were so connected that only five output signals were recorded on magnetic tape. These signals were ϵ_1, ϵ_3, $(\epsilon_2 - \epsilon_4)$, $(\epsilon_5 - \epsilon_7)$, and $(\epsilon_6 - \epsilon_8)$, where ϵ indicates strain signal.

The following equations were used to calculate the forces at the primary strut footpad pivot point in the three principal axes of the strut coordinate system. Refer to Figure 5-7.

Pad stop force, F_2, normal to clevis cone face:

$$F_2 = \sqrt{\left[\frac{1}{(b-a)^2 c^2}\right]\left\{\left(\frac{AE}{2K}\right)^2 \left[b(\epsilon_2 - \epsilon_4) - a(\epsilon_6 - \epsilon_8)\right]^2 + \left(\frac{AE}{2K}\right)^2 \left[b(\epsilon_1 - \epsilon_3) - a(\epsilon_5 - \epsilon_7)\right]^2\right\}}$$

Angle, ϕ, between longitudinal force axis and point of stop contact:

$$\phi = \sin^{-1}\left(\frac{\frac{AE}{2K}\left[b(\epsilon_2 - \epsilon_4) - a(\epsilon_6 - \epsilon_8)\right]}{F_2\,(b - a)\,c}\right)$$

Axial force, F_{ax}, along strut axis:

$$F_{ax} = F_2 \sin\alpha - \frac{AE}{2}\,(\epsilon_1 + \epsilon_3)$$

Lateral force, F_{lt}, normal to strut centerline and parallel to clevis pin:

$$F_{lt} = -\frac{AE}{2K_a}\,(\epsilon_2 - \epsilon_4) - F_2\left(\frac{c}{a} - \cos\alpha\right)\sin\phi$$

Longitudinal force, F_{lg}, normal to strut centerline and normal to clevis pin:

$$F_{lg} = -\frac{AE}{2K_a}\,(\epsilon_1 - \epsilon_3) + F_2\left(\cos\alpha - \frac{c}{a}\right)\cos\phi$$

Where:

A = load cell cross sectional area

E = Young's Modulus for load cell

I = moment of inertia of load cell

C' = distance from neutral axis of load cell to extreme fiber.

$Z = \frac{I}{C'}$

$K = \frac{A}{Z}$

a = distance from pad pivot to the plane of gages ϵ_1, ϵ_2, ϵ_3, and ϵ_4 measured along the strut centerline.

b = distance from pad pivot point to the plane of gages ϵ_5, ϵ_6, ϵ_7, and ϵ_8 measured along the strut centerline.

c = distance from pad pivot to the pad stop contact point measured along the clevis cone face.

α = half cone angle of clevis cone face.

5.5.2 Data Handling for Detailed Correlation Studies

For detail correlation purposes, the thirteen tape recorded signals from the LM model must be reduced and read at very close intervals (every 1/1000 second) to achieve a reasonable degree of accuracy in the numerical integration used in the computation of the footpad and CG motions. The computation of these motions is very complicated because the free-body motion also involves the body itself changing shape due to stroking of the 12 struts. Thus, manual data reduction and computation for this problem is both difficult and expensive.

Accordingly, a computer program was written for calculating the motions and forces of the LM model with respect to some specified coordinates. For given model drop test initial conditions the computer program calls for the input of the 13 (tape recorded) signals every 1/1000 second, then calculates the instantaneous CG motion, the model attitude, the footpad velocity, the depth of footpad penetration into the soil, the forces acting on the footpad and other pertinent information required for detailed correlation study. A total of 17 output parameters result. Figure 5-21 shows the flow chart of the computer program.

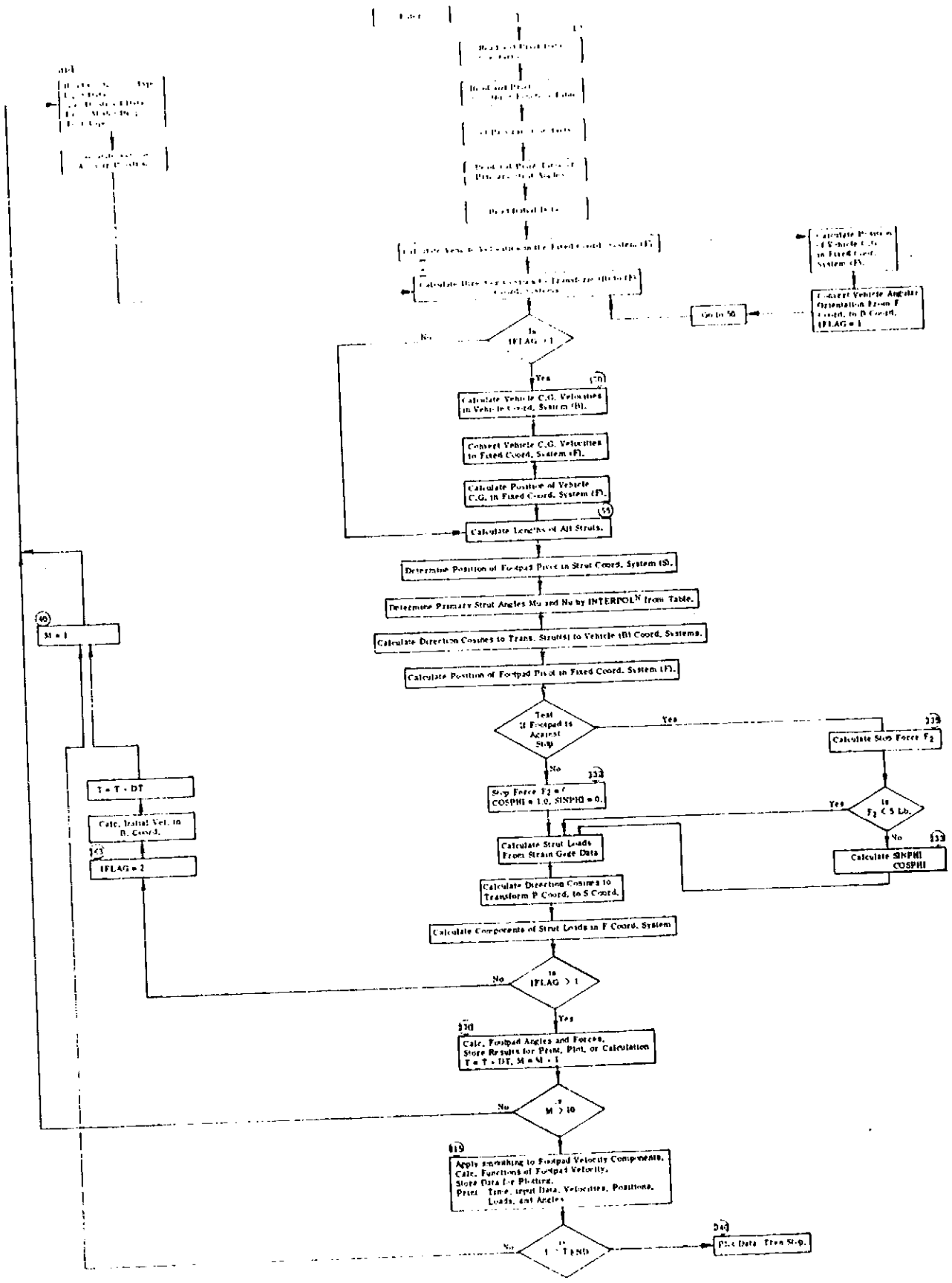

Figure 5-21. Flow Chart - Data Reduction Program

The thirteen signals which form the input for the computer program were machine reduced from the two reels of magnetic tape on which they were recorded. The tapes for each test were first processed through a filter to remove extraneous and undesired noise. The filtered signals were then fed into an analog-to-digital hybrid machine which yielded thirteen digital signals every 1/1000 second of model drop time as the input for the computer program. The processes of machine data reduction and computation of required output for each of the eight drops were accomplished by the McDonnell Automation Center of The McDonnell Douglas Corporation under subcontract to Bendix.

The digital computer output from McDonnell was submitted to Bendix in printed form and the seventeen output parameters were recorded on magnetic tape for transmittal to NASA, MSC for machine plotting. These seventeen parameters were then compared with the similar terms yielded from analytical study at MSC, using the LM landing dynamics program in which the footpad interaction model was incorporated.

5.5.3 Soil Preparation for Detailed Correlation Studies

For detail correlation tests, the LM model was landed on RS and SS loose and RS intermediate soils, using a level landing surface (e.g., zero slope). Soil emplacement was accomplished by means of a large, specially designed hopper (or spreader) which is described in Section II (reference Figure 2-63).

The spreader rolls horizontally on steel tracks along the edges of the soil pit, uniformly depositing the soil material in approximately four-inch layers across the surface of the bed with each pass. The soil is allowed to flow only when the spreader is moved in one direction. At the end of each pass, flow is stopped by a shutoff gate, the hopper is raised clear of the bed, returned to its starting position, and the process continued until the desired soil depth is reached.

For the RS and SS loose soil beds, no further handling was required once the soil was placed by successive passes of the spreader. It was found that the soil beds thus prepared had very uniform and consistent soil properties.

Preparation of the RS intermediate soil beds required compacting the soil after each pass of the spreader. This was accomplished using a 63-pound lawn roller which is 18 inches in diameter and 24 inches wide. The procedure for rolling the soil consisted of making eight straight back and forth passes of the roller (i.e., four cycles) for every 24-inch width of soil bed until the whole area had been traversed. The entire process of depositing and rolling one layer at a time was repeated until the desired soil depth (18 inches thick) was achieved.

Dynamic penetrometer readings were taken across the soil bed (but away from the area disturbed by the model footpads) after each model drop was made. The soil was then completely removed from the bed before a new soil bed was prepared.

Soil bed properties obtained for each of the detail correlation drop tests are given in Table 5-T3, and details of the methods of establishing the soil properties are described in Section II. In particular, the correlation between the relative density and the dynamic penetrometer readings is covered in Paragraph 2.7.1.

5.5.4 Detailed Correlation Drop Tests

Table 5-T3 specifies the eight model drop conditions for the detailed correlation study and cross-references the corresponding drop number in the listing given in Paragraph 5.3. It can be seen that among the eight drops only two different sets of initial conditions were used. The first condition (used for NASA Tests No. 1, 4, 6, and 8) was a pure vertical drop which had a nominal vertical velocity of teen feet per second. The second condition (used for the remaining tests) had a nominal vertical velocity of five feet per second and a nominal horizontal velocity of seven feet per second. The velocities shown in Table 5-T3 were calculated based on the exact time interval between the instant of model release to the instant of ground contact. This time interval could be measured very precisely from the readings of the accelerometer in the x direction. The initial drop conditions had zero angular rates, zero pitch and roll attitude, and all of the drops were released with 45-degree yaw angle (i.e., 2-2 landings).

TABLE 5-T3. DETAIL CORRELATION DROPS

NASA Test No.	Bendix Drop No.	V_v (In./Sec.)	V_h (In./Sec.)	τ (Sec.)	Soil	D_r	γ (Lb./Ft.^{3})	ϕ (Deg.)
1	10	-114.9	0	.298	RS Loose	0	46.9	41
2	11	-60.5	83.5	.177	RS Loose	0	46.9	41
3	12	-60.0	84.0	.156	RS Loose	0	47.1	41
4	13	-117.3	0	.304	RS Loose	0	47.1	41
5	16	-60.8	83.4	.146	RS Intermediate	.3	53.0	42.5
6	17	-117.1	0	.303	RS Intermediate	.3	53.0	42.5
7	20	-60.0	84.0	.154	SS Loose	0	96.0	30
8	21	-118.0	0	.306	SS Loose	0	96.0	30

V_v = Vertical velocity

V_h = Horizontal velocity

τ = Time interval between model release to touchdown

D_r = Soil relative density

γ = Soil density

ϕ = Internal angle of friction

As noted earlier, three different kinds of soil beds were used for the eight detailed correlation tests. Of the four drops made in RS loose soil test No. 4 was a duplicate of test No. 1, and test No. 3 was a duplicate of test No. 2. These duplicate drops were made to check the repeatability of the test equipment and procedure with due allowance for the slight variation of individual RS loose soil beds. Tests Nos. 5 and 6 repeated the two test conditions on RS intermediate soil, and tests Nos. 7 and 8 on SS loose soil. The detailed test conditions for all the drops can be found in Paragraph 5.3 (Table 5-T2) in which Bendix drops Nos. 10 to 21, inclusive, applied to the detailed correlation study. It can be seen that some trouble was encountered in the laboratory so that four of the drops had to be repeated.

5.5.5 Detailed Correlation Test Results

Figures 5-22 to 5-39, inclusive, show the typical results of tests Nos. 1 and 2. All of the parameters in these figures were plotted against time. For the pure vertical drop (test No. 1) seven parameters are presented. These are:

A. Absolute footpad velocity (VAP).
B. The angle (θ), between (VAP) and the fixed vertical coordinate X(f).
C. The depth of the footpad penetration into the soil (d).
D. The axial loads on struts Nos. 1, 2, and 3.
E. The vertical acceleration of model C.G.
F. The vertical velocity of model C.G.
G. The vertical displacement of model C.G.

For the drops with both vertical and horizontal velocities (test No. 2), in addition to the seven parameters described above, four more are listed.

They are:

H. Horizontal velocity of the C.G.
I. Horizontal displacement of the C.G.
K. Vehicle pitch velocity.
L. Vehicle pitch displacement.

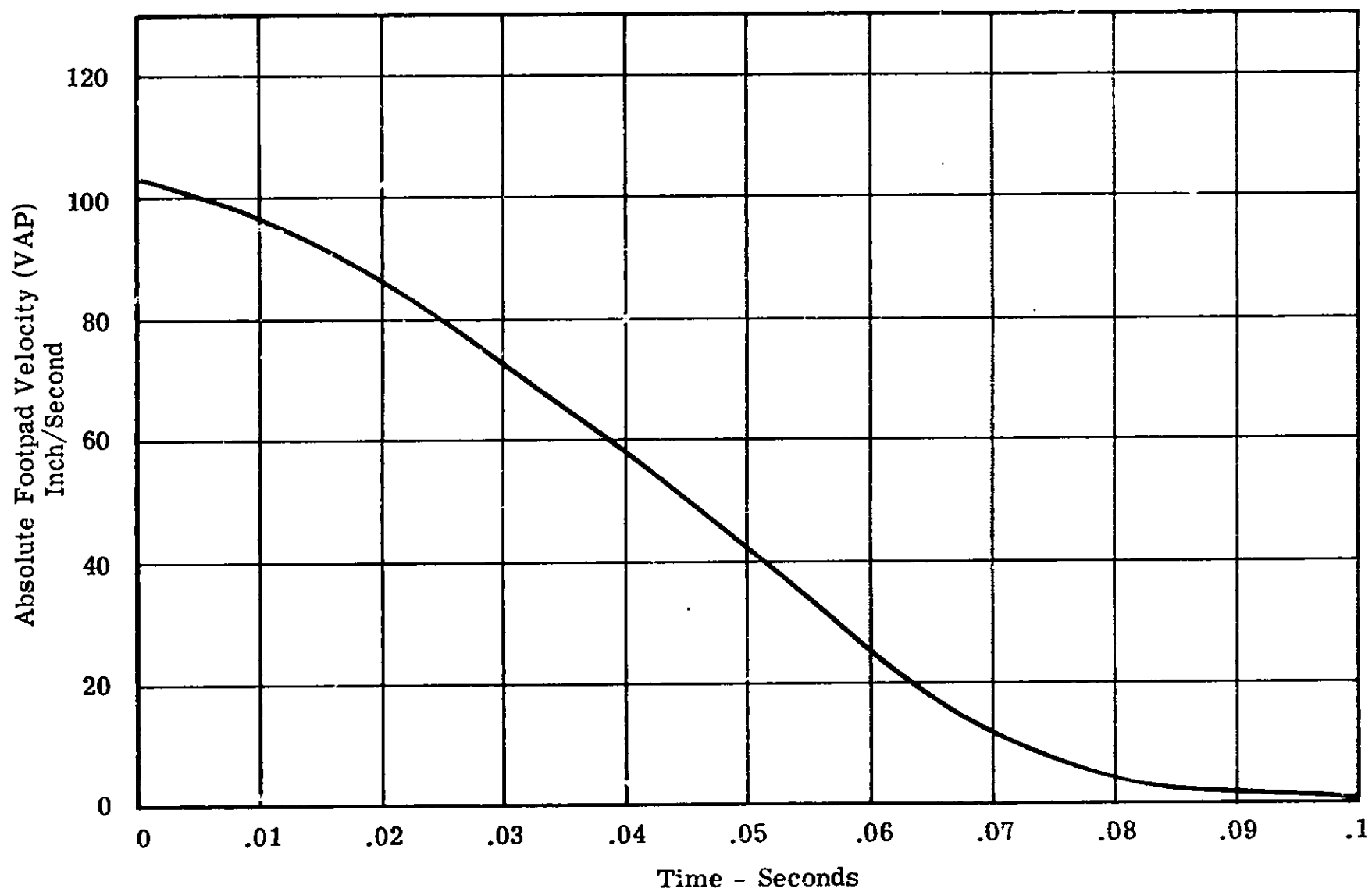

Figure 5-22. Absolute Footpad Velocity vs. Time (NASA Test No. 1)

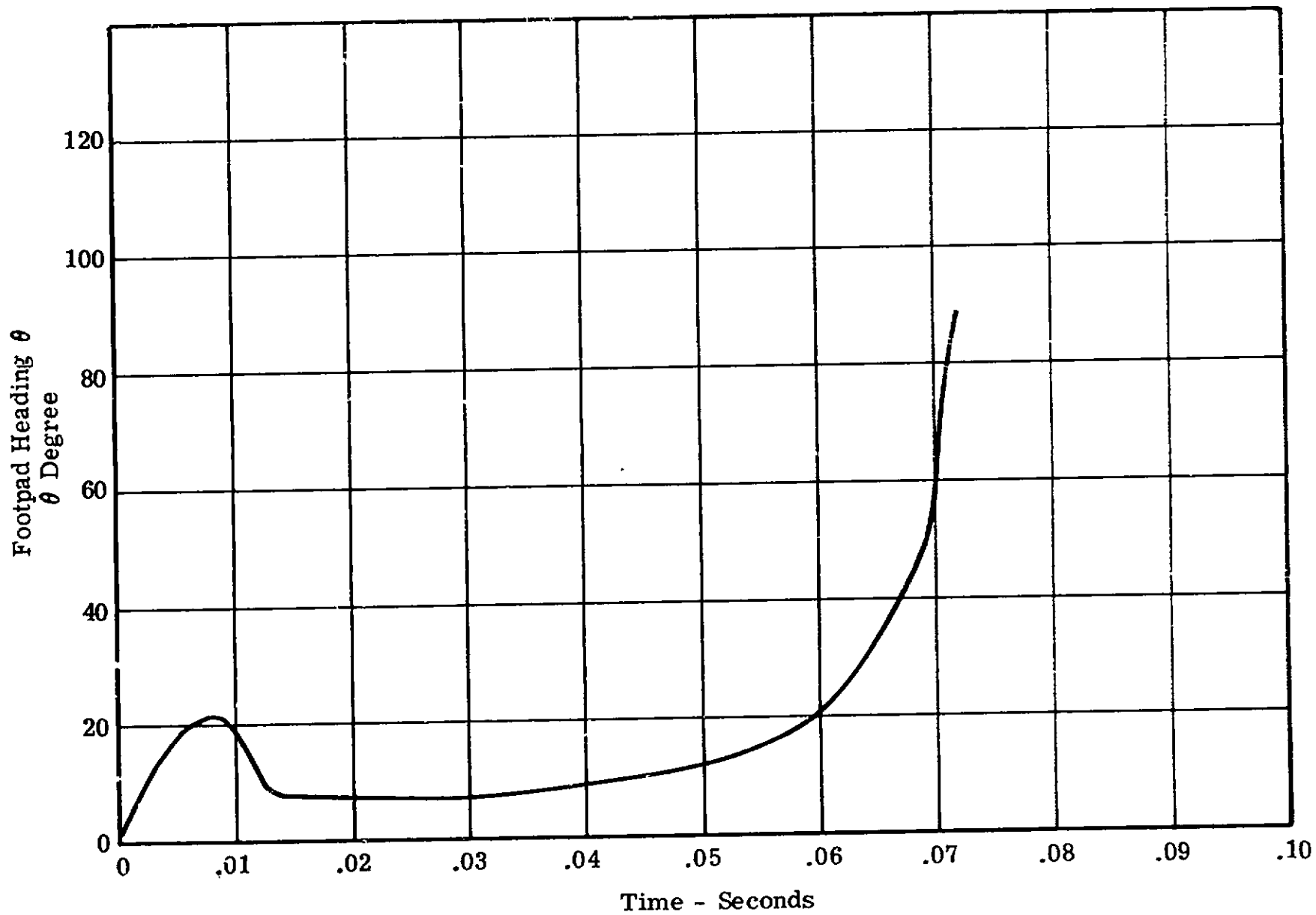

Figure 5-23. Footpad Heading With Respect to Vertical (θ) versus Time
(NASA Test No. 1)

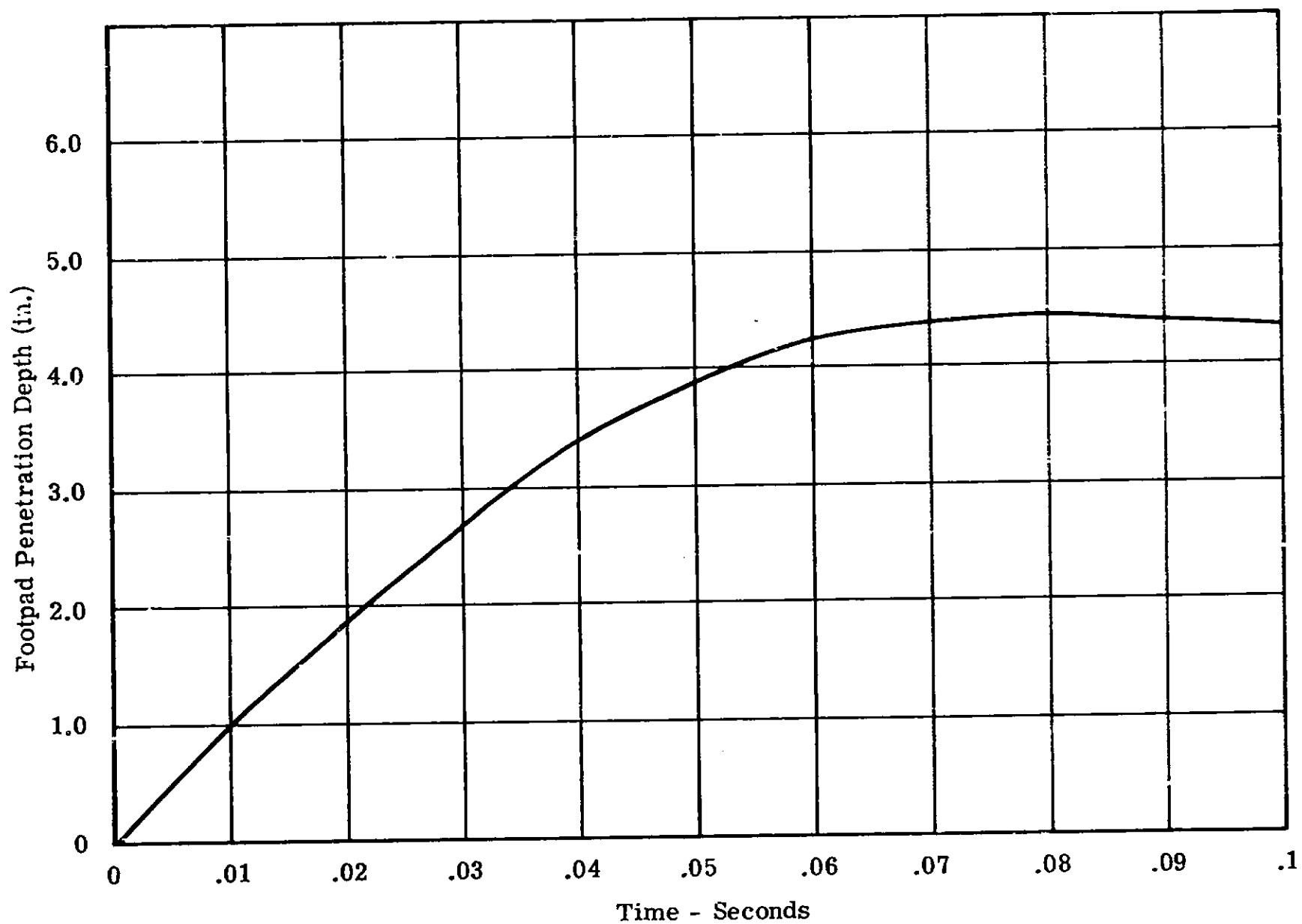

Figure 5-24. Footpad Penetration Depth versus Time (NASA Test No. 1)

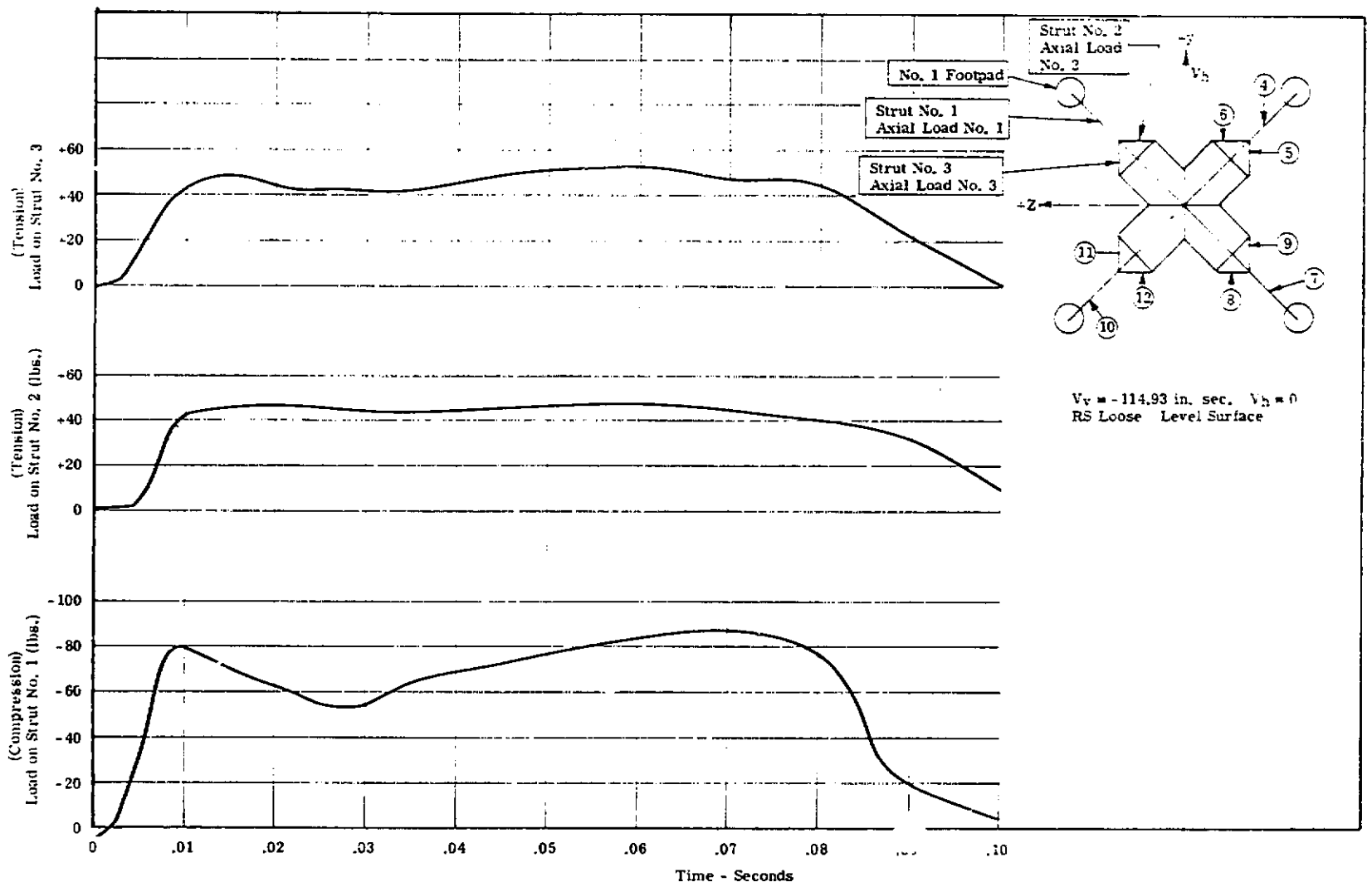

Figure 5-25. Strut Axial Load versus Time (NASA Test No. 1)

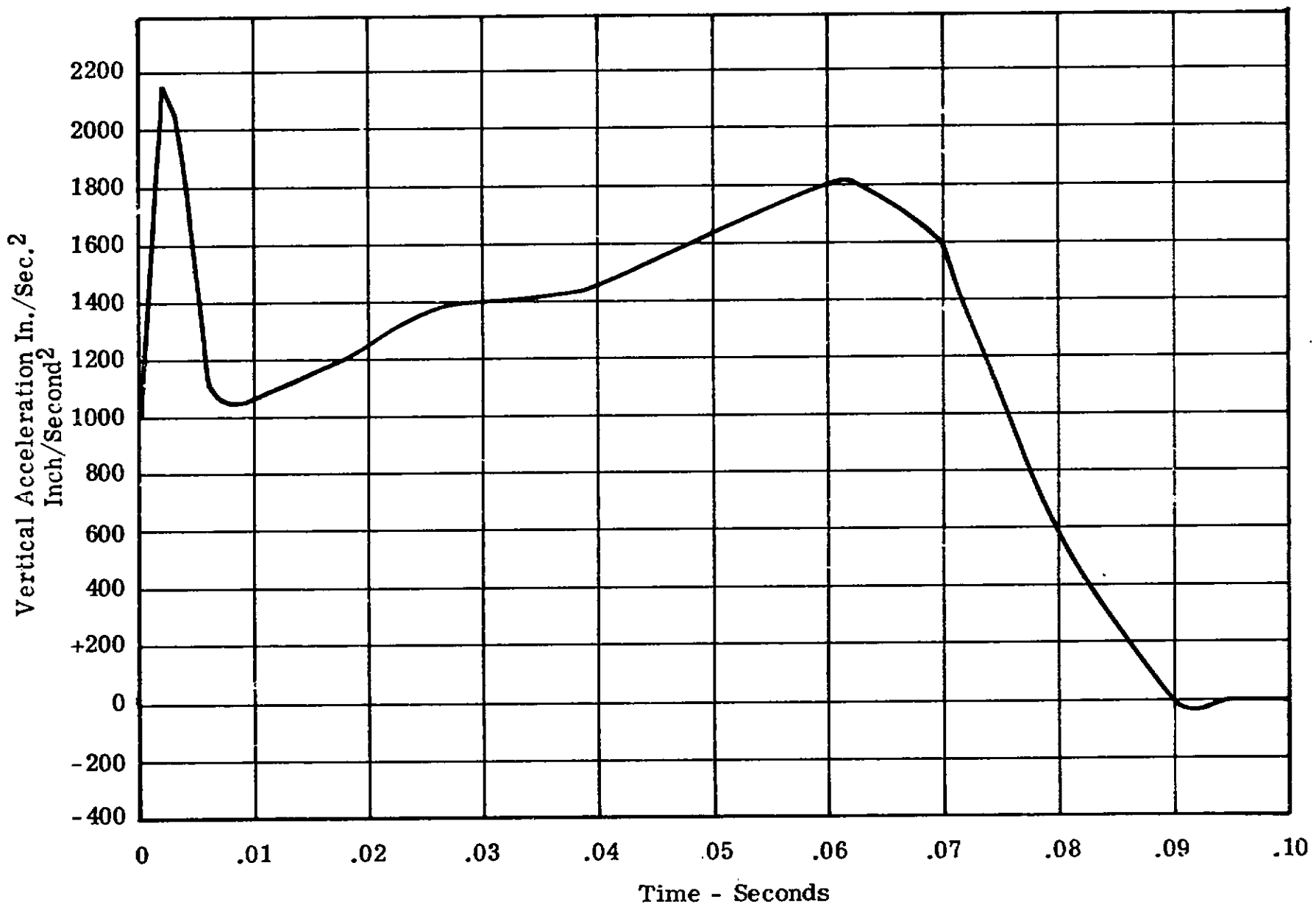

Figure 5-26. CG Vertical Acceleration versus Time (NASA Test No. 1)

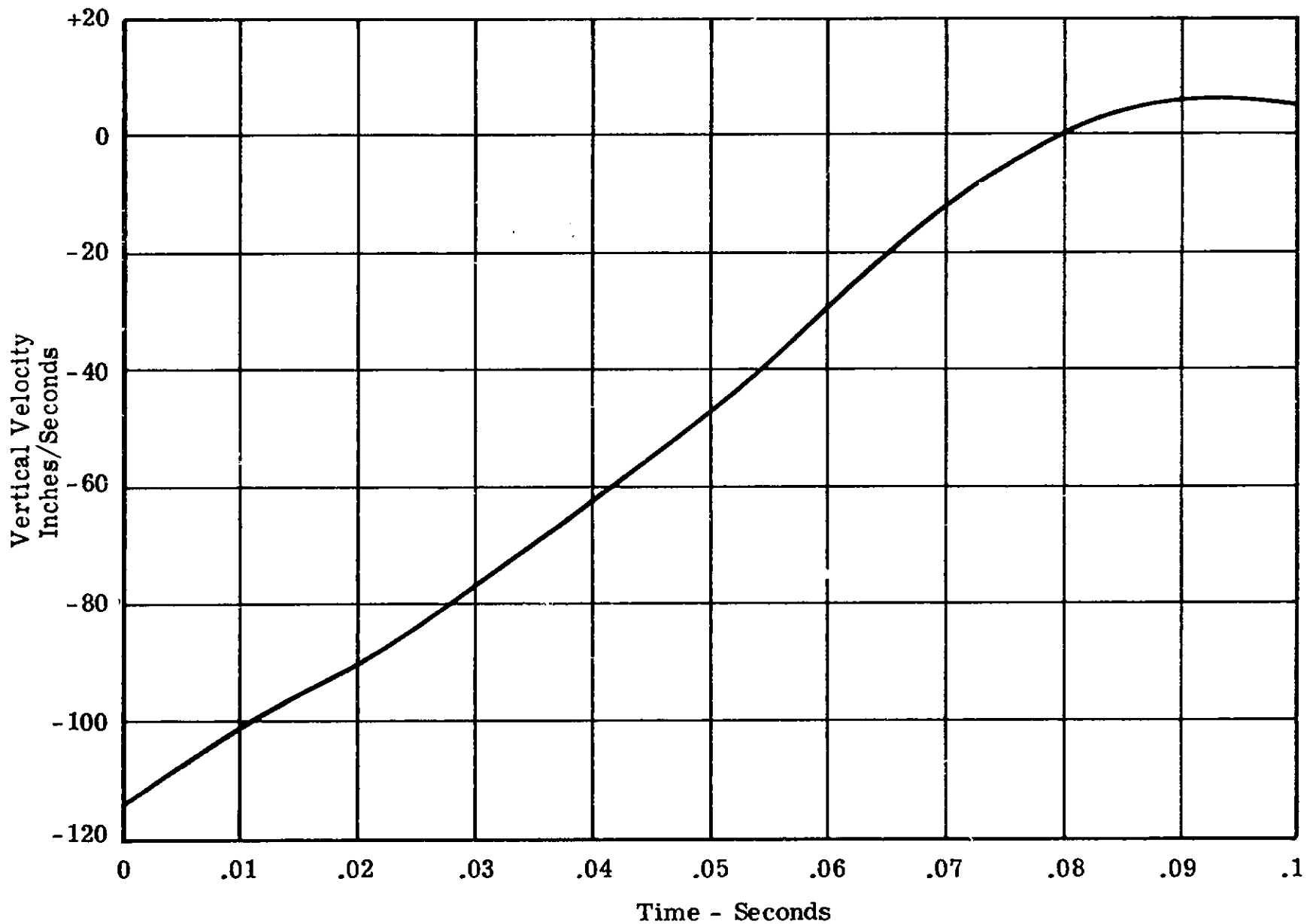

Figure 5-27. CG Vertical Velocity versus Time (NASA Test No. 1)

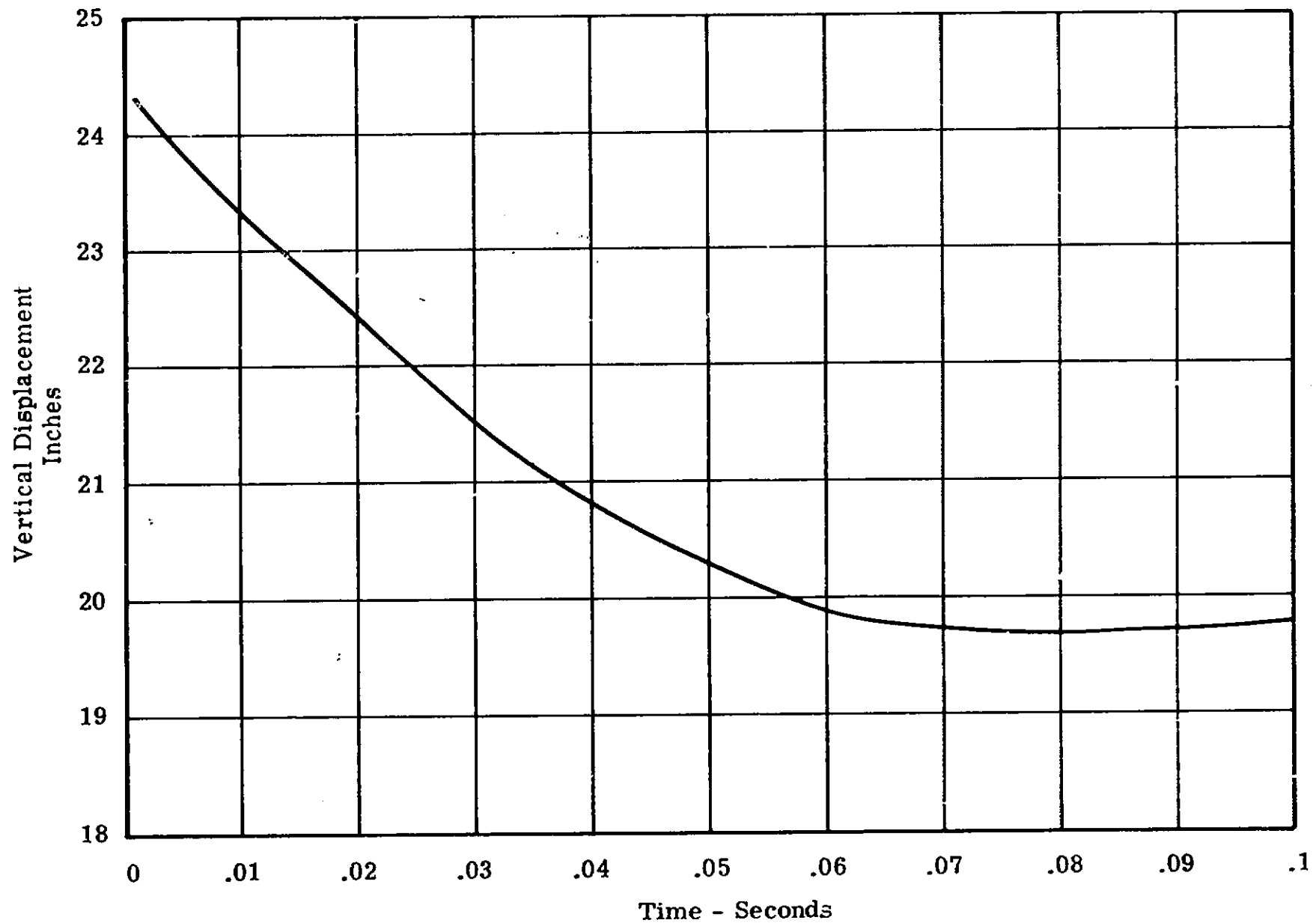

Figure 5-28. CG Vertical Displacement versus Time (NASA Test No. 1)

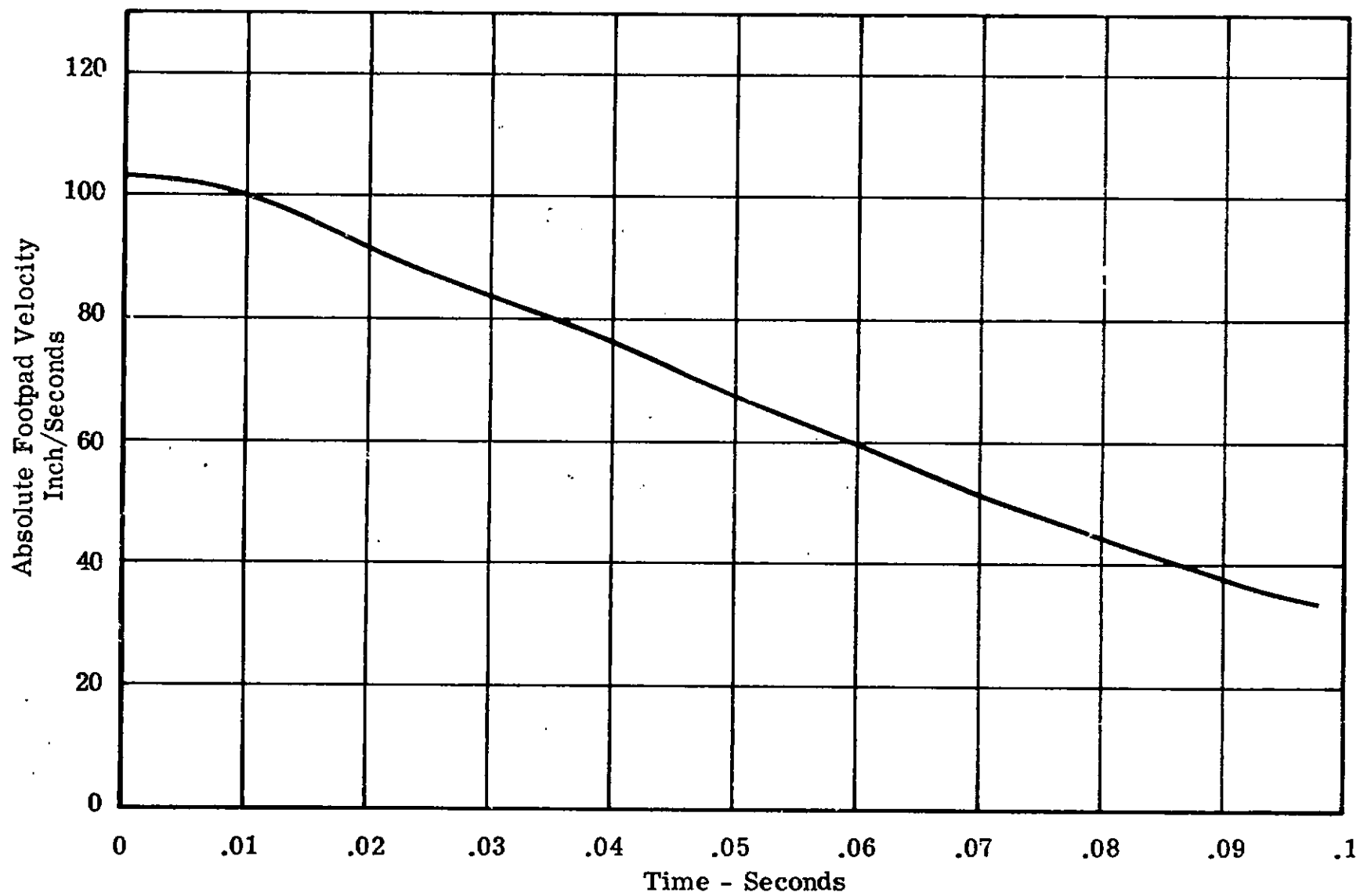

Figure 5-29. Absolute Footpad Velocity versus Time (NASA Test No. 2)

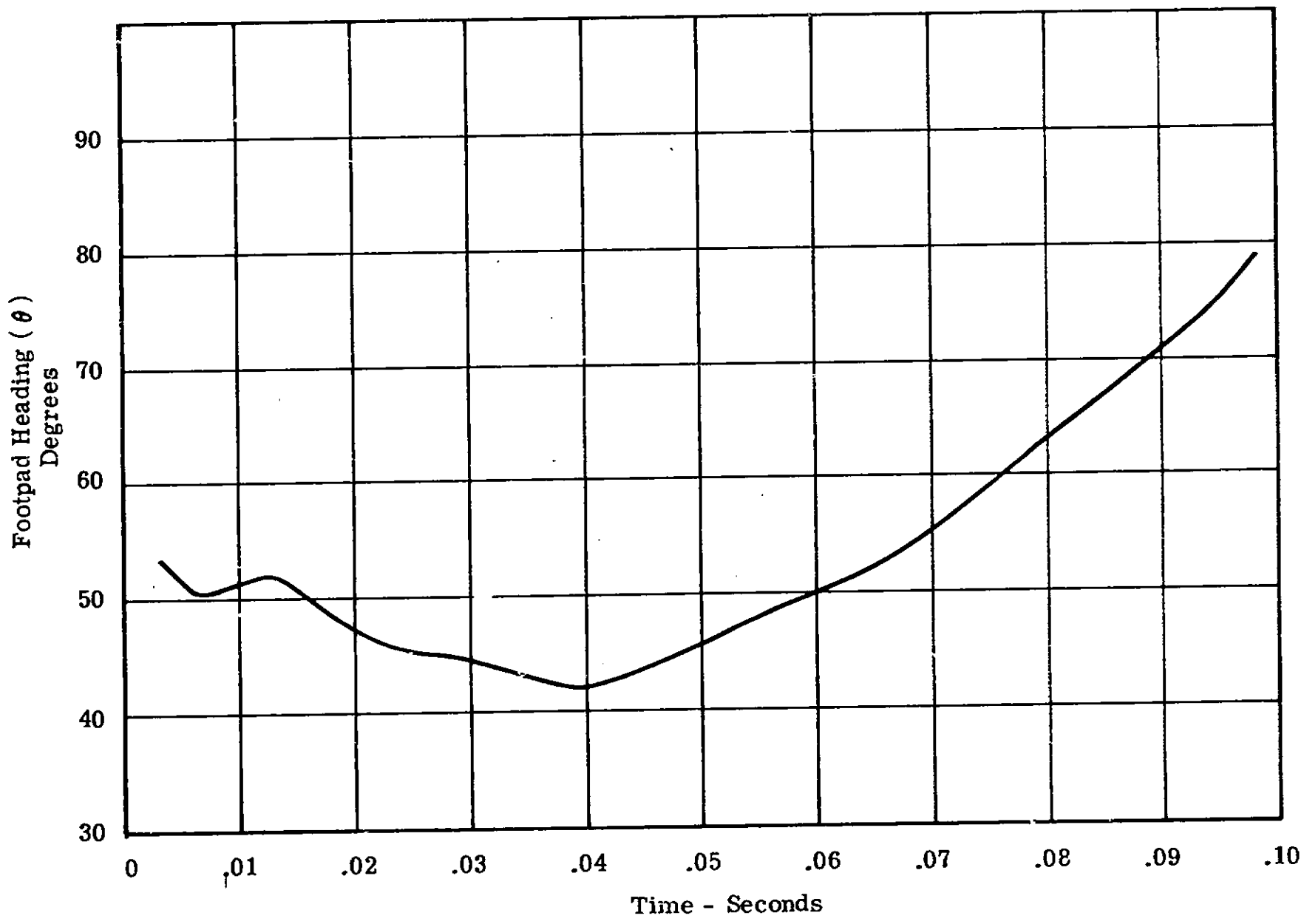

Figure 5-30. Footpad Heading With Respect to Vertical (θ) versus Time
(NASA Test No. 2)

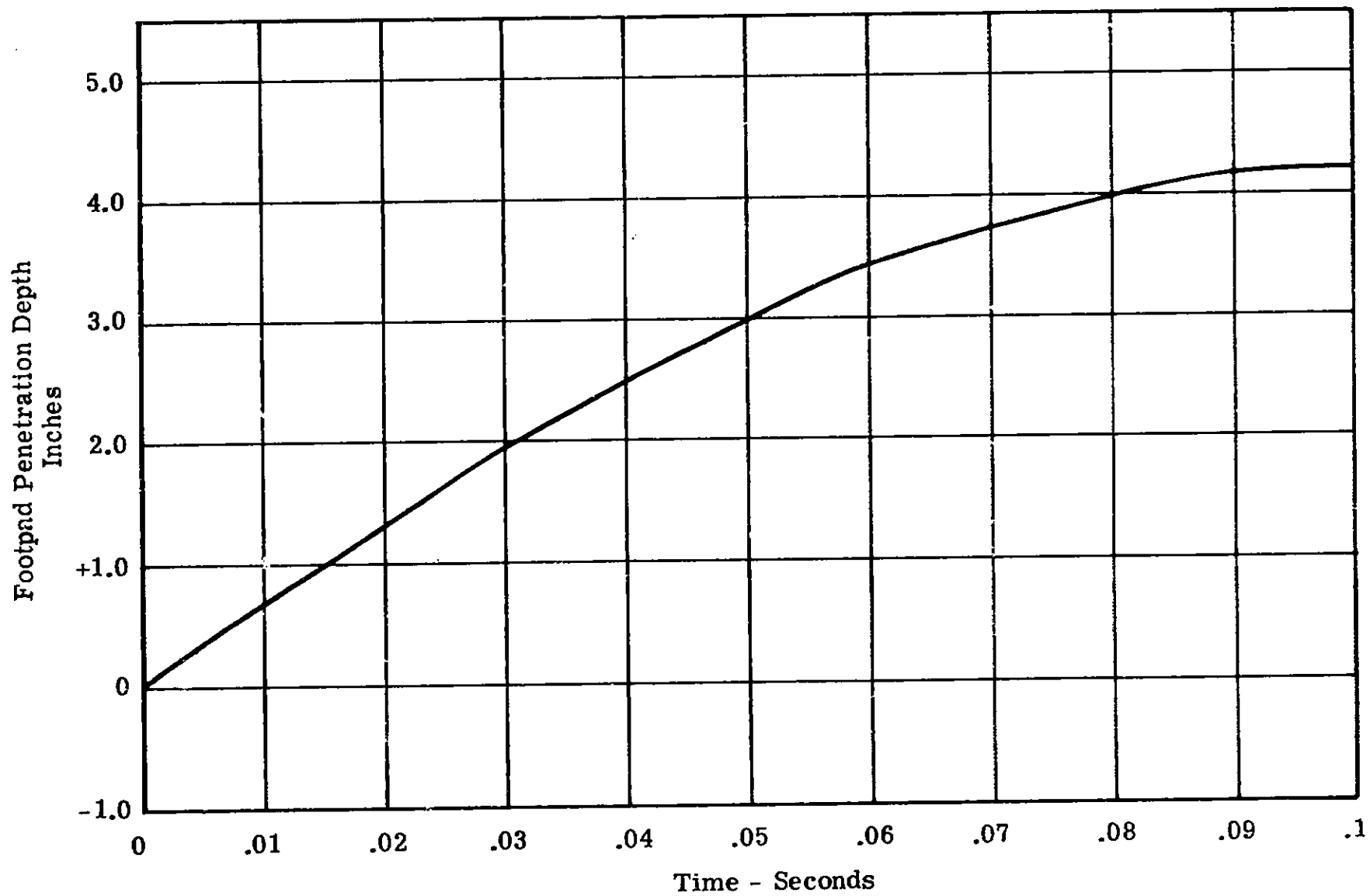

Figure 5-31. Footpad Penetration Depth versus Time
(NASA Test No. 2)

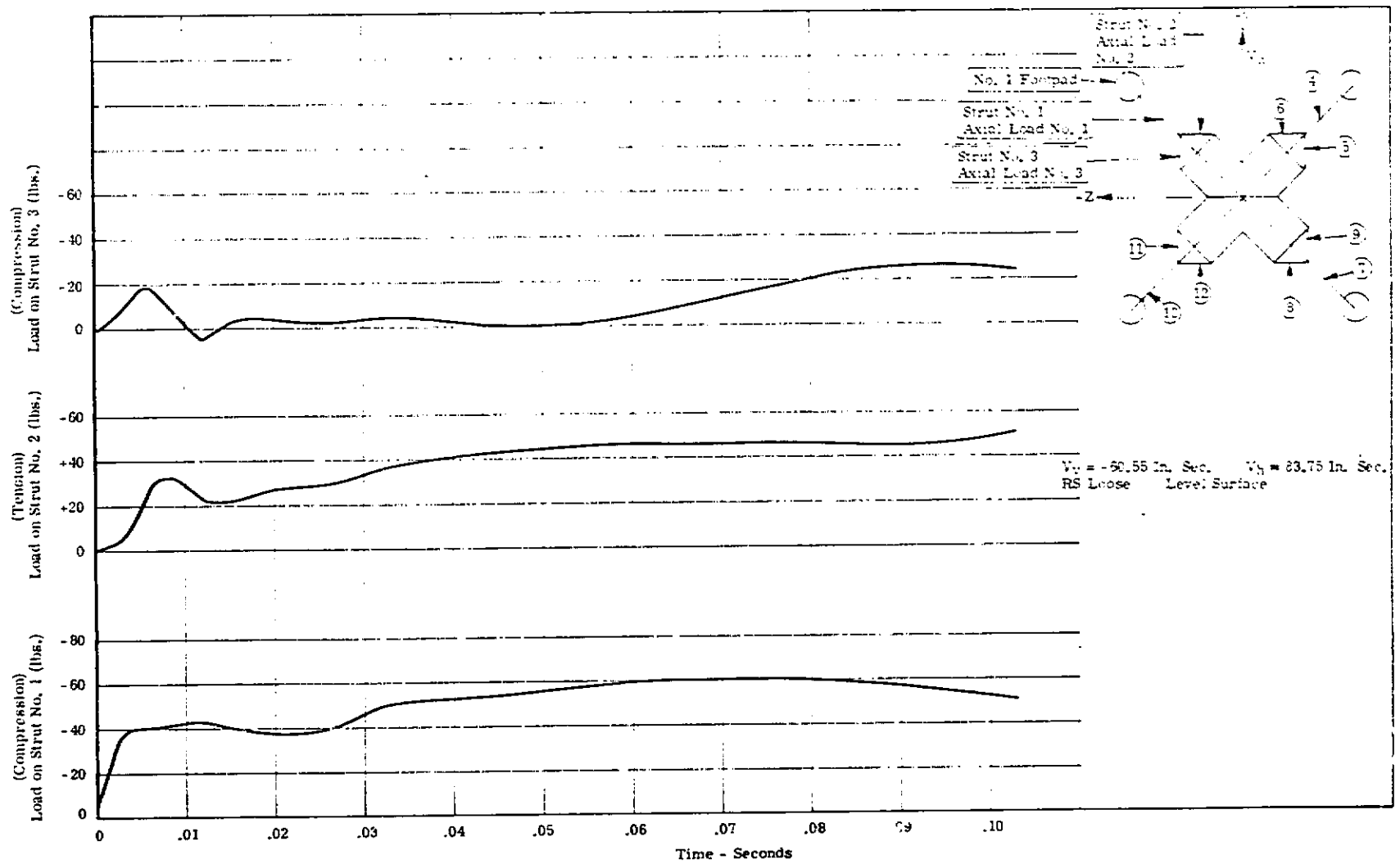

Figure 5-32. Strut Axial Load versus Time (NASA Test No. 2)

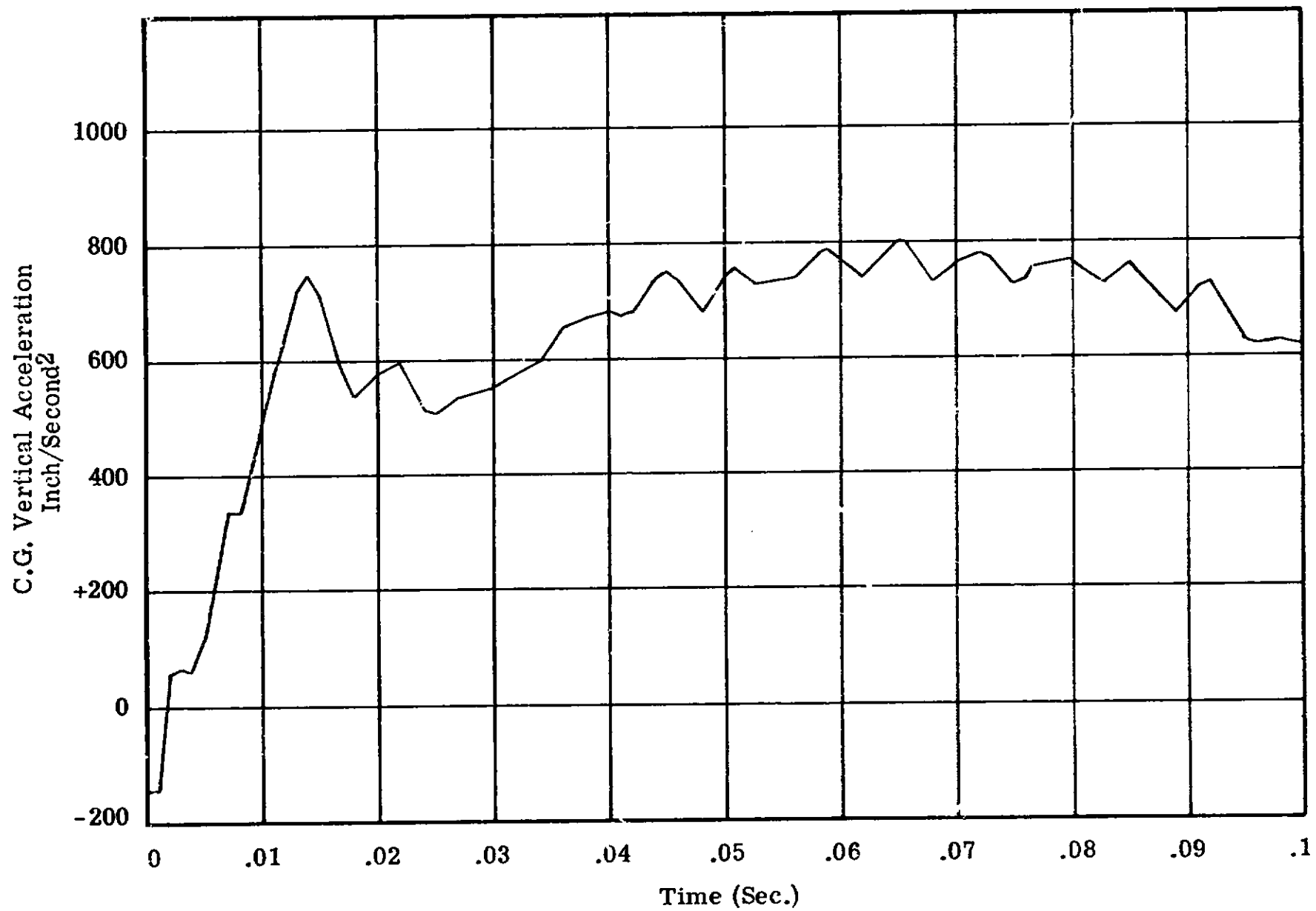

Figure 5-33. CG Vertical Acceleration versus Time (NASA Test No. 2)

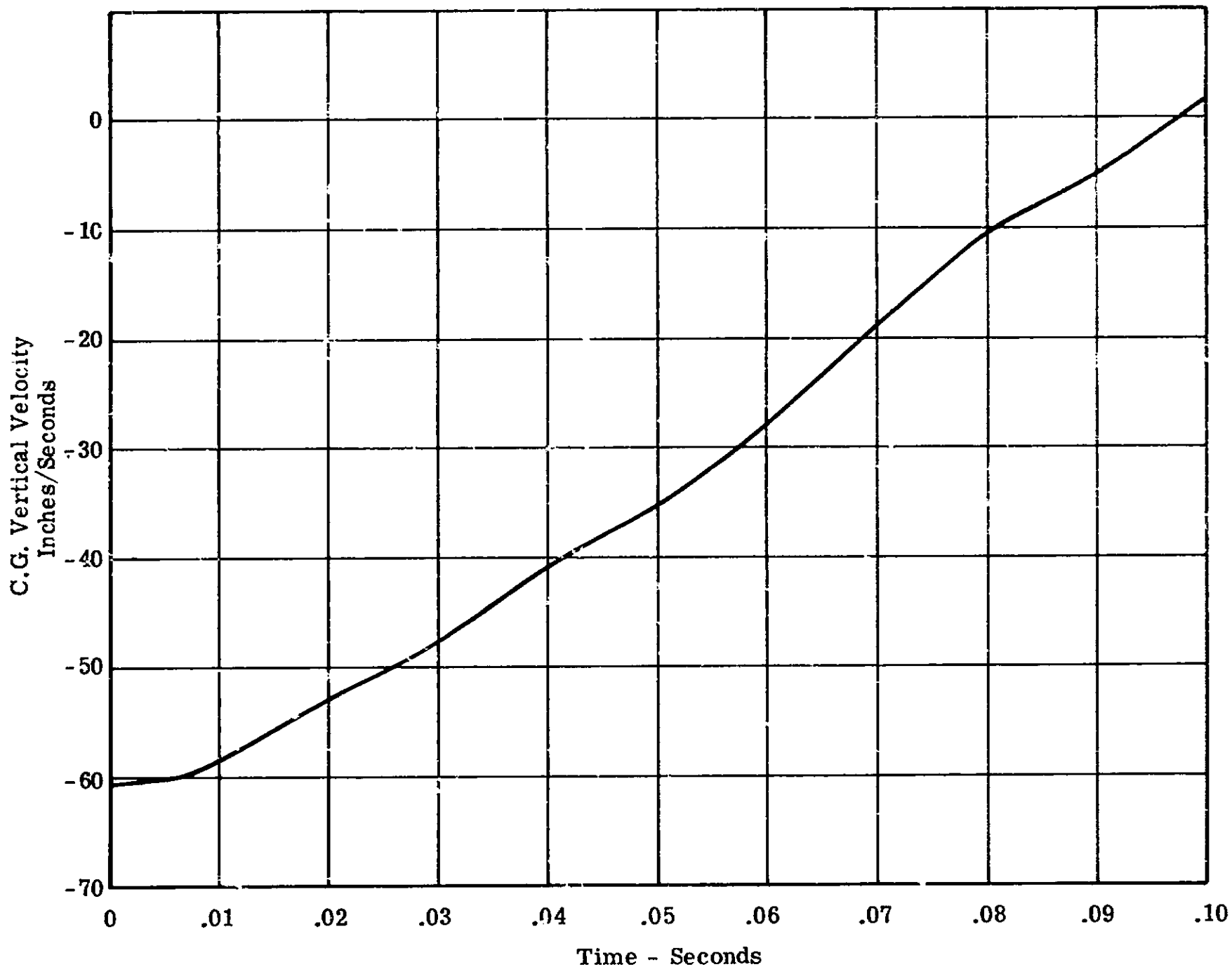

Figure 5-34. CG Vertical Velocity vs. Time (NASA Test No. 2)

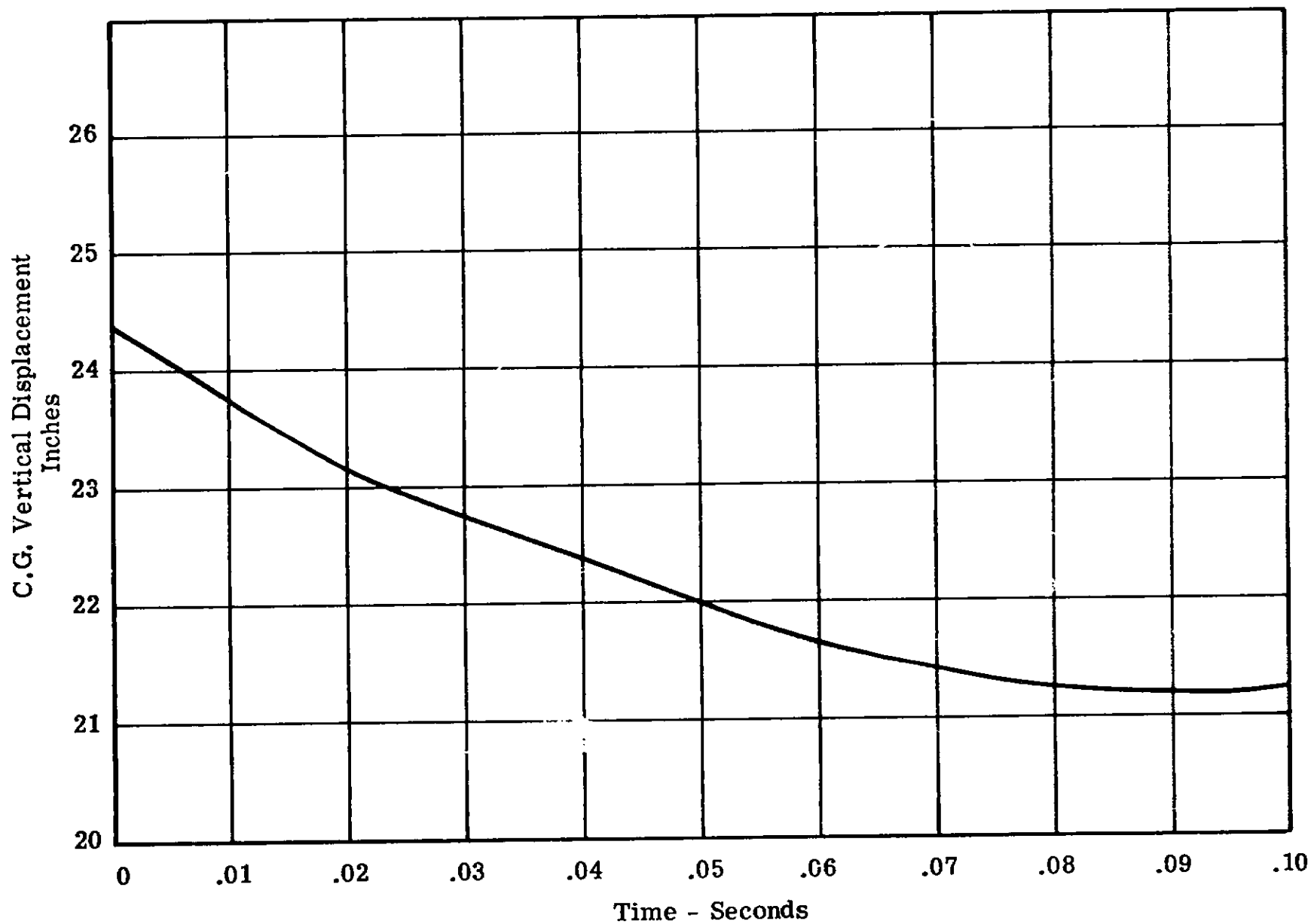

Figure 5-35. CG Vertical Displacement versus Time (NASA Test No. 2)

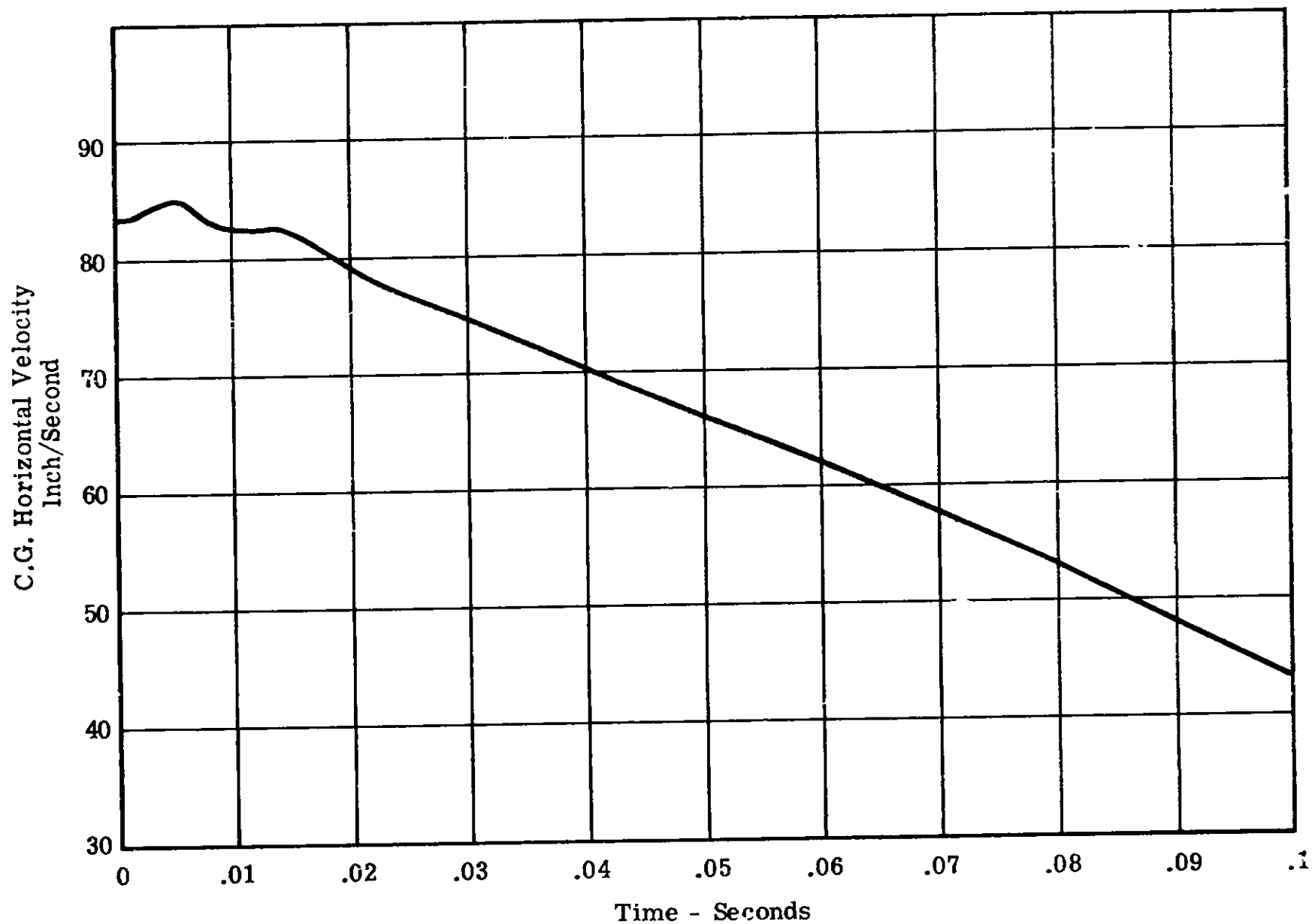

Figure 5-36. CG Horizontal Velocity versus Time (NASA Test No. 2)

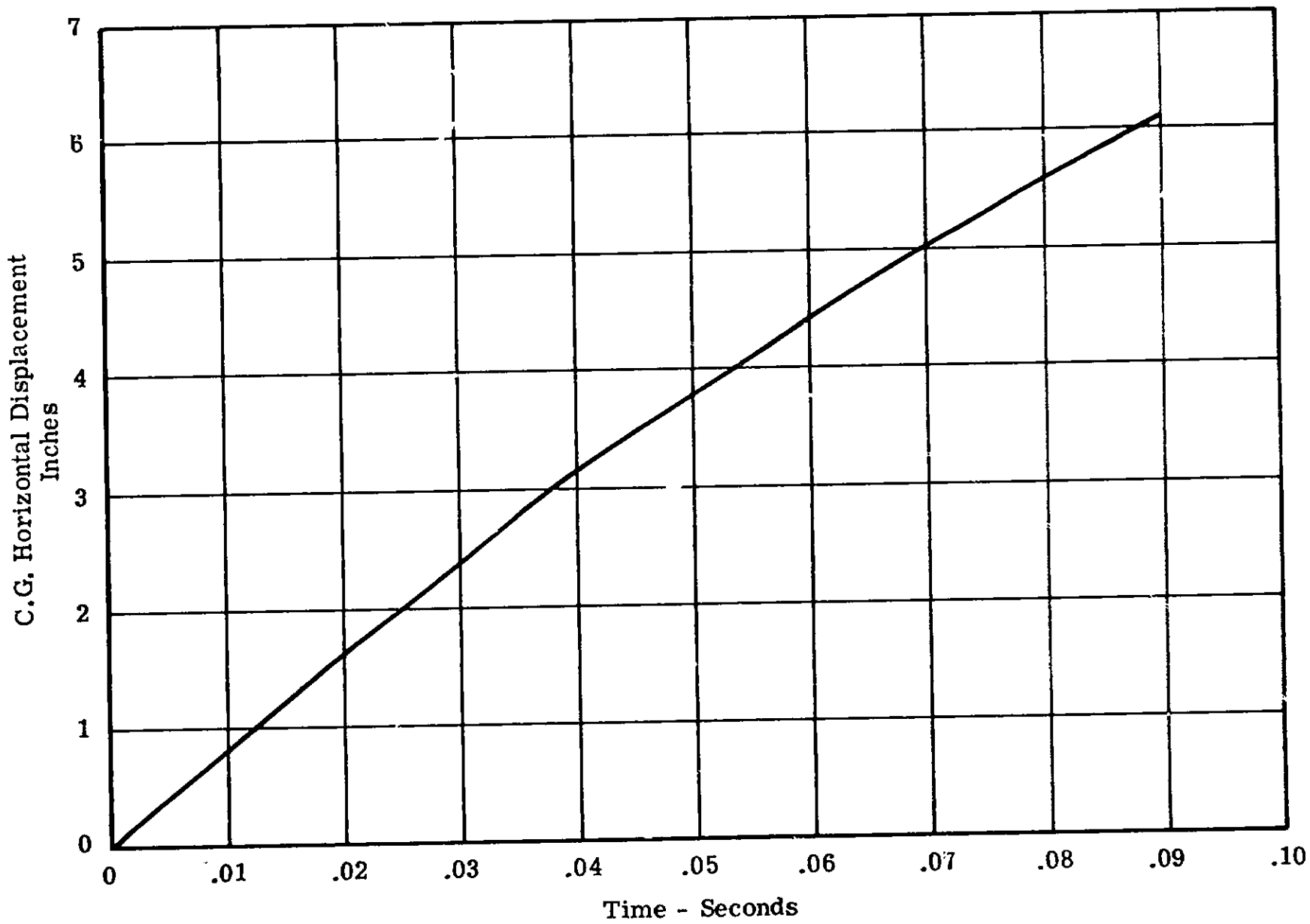

Figure 5-37. CG Horizontal Displacement versus Time (NASA Test No. 2)

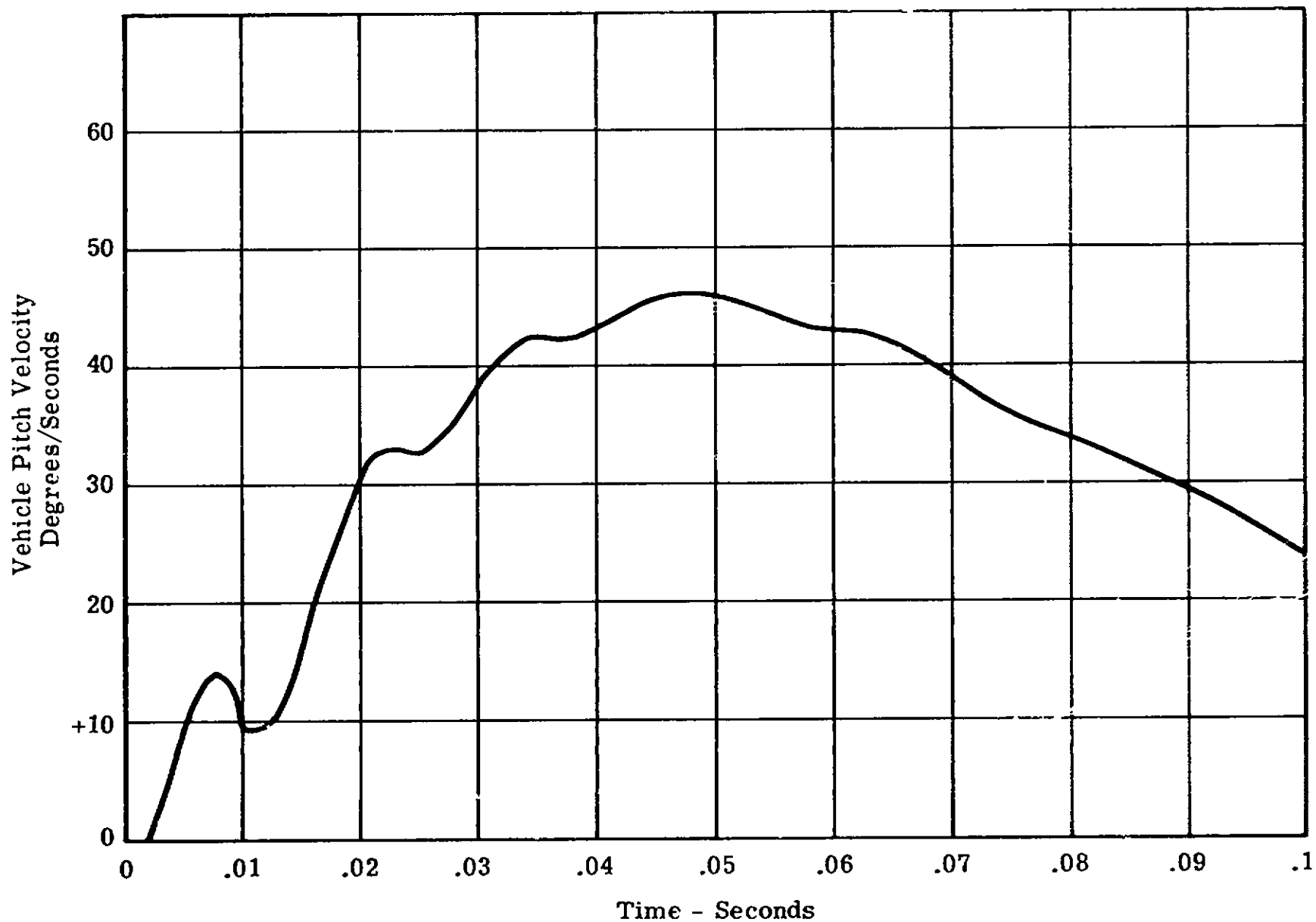

Figure 5-38. Vehicle Pitch Velocity versus Time (NASA Test No. 2)

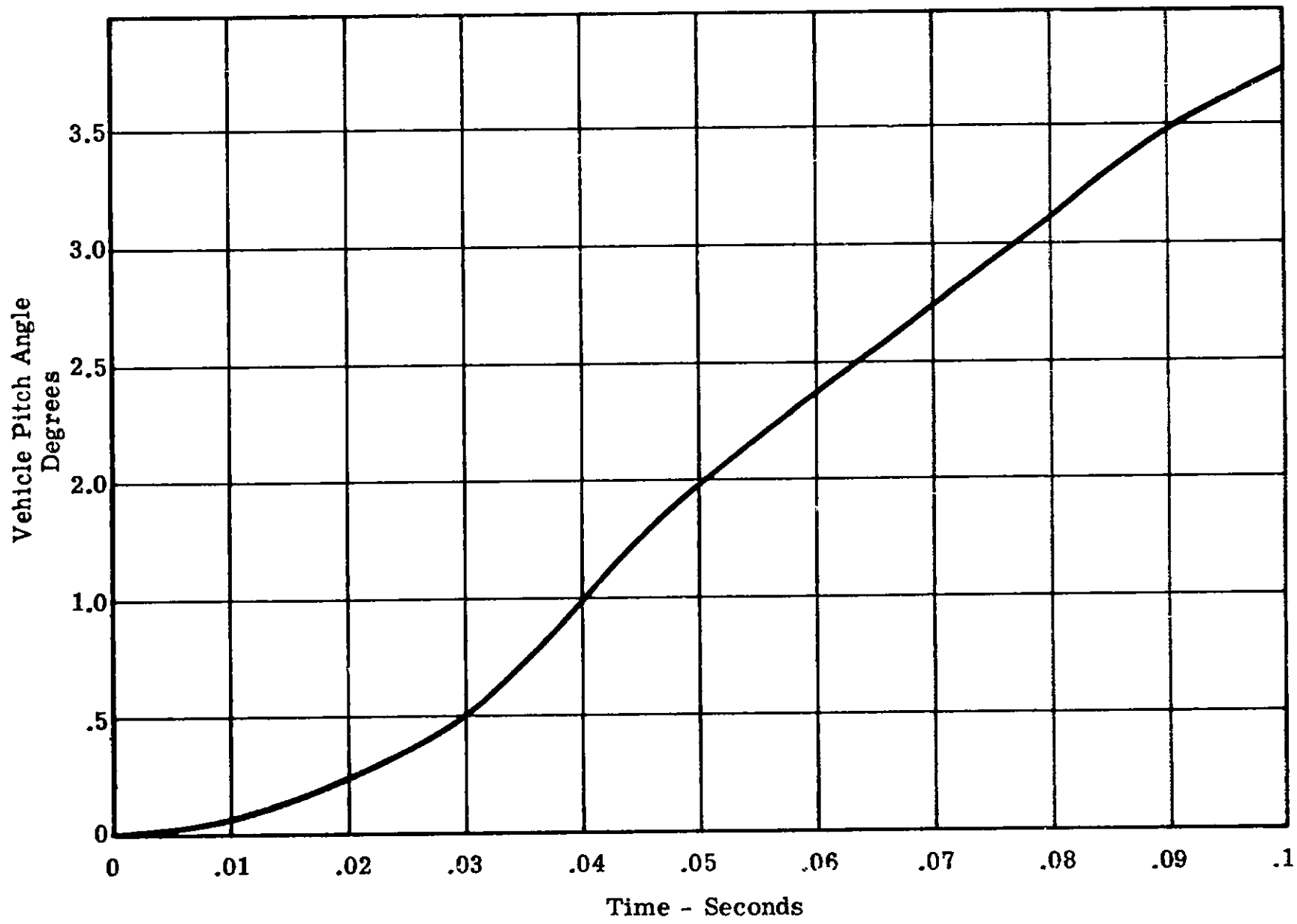

Figure 5-39. Vehicle Pitch Angle versus Time (NASA Test No. 2)

A detailed discussion of all of the eight drop tests and their comparison with the NASA, MSC analytical results can be found in Section VI of this report.

Although the automated procedures for test data reduction and computation (discussed earlier) served the purpose for which they were developed, various difficulties were encountered before the end results were actually achieved. As a result, some changes from the originally planned application and use of the data were required. A brief discussion of the problems is warranted, and it might be of interest to others attempting to follow a similar scheme.

One rather recurrent source of trouble in the laboratory that resulted in delay and sometimes rerun of tests was instrumentation noise. These noises could be generated in the amplifiers and recording equipment used but also, at times, came from the power line and the room itself (due to the presence of other electronic equipment). The thin sheet-metal covering of the model proved to be a good "sounding board" for undesirable signals, although this problem was considerably reduced by application of vibration damping tape.

The procedure for data handling involved three separate organizations (i.e., Bendix, McDonnell Douglas, and NASA, MSC) as described in Paragraph 5.5.2. When some inconsistency was discovered at Bendix on a final parameter plot received from MSC, the time lag between the actual drop tests (at Bendix) to the completion of final plotting (at MSC), and the remoteness of three organizations, made trouble-shooting extremely difficult.

The computational difficulties encountered are probably inherent to a complex program of this nature. It has been stated before that the 13 signals from the sensors in the LM model were merely inputs of a computer program from which calculations and transformation of coordinates must be made to obtain the desired parameters in the appropriate coordinates. The motions of LM model were calculated from the output of the three accelerometers in the vehicle. Any errors that might originate from the accelerometers, from the noise of the amplifiers and recorders, or from the numerical procedure used

in the computer program would be accumulated. The accumulated errors became significant when computer time was prolonged.

It was observed from the play-back of the oscillographs and magnetic tape recordings of the model drops that the main events that were worthy of attention and thorough study all happened within the first 100 milliseconds after impact. Yet from the digital output of the analog-to-digital hybrid machine the reduced data indicated that the motion and other signals never really reached zero even after 750 milliseconds. Obviously, some noise or tiny, but accumulative, errors were introduced along the line which made prolonged integration meaningless. It was therefore decided to limit the parameter versus time plots (Figures 5-22 through 5-39) to 100 millisecond-duration for detailed correlation purposes.

It was originally planned that one of the computer/experimental comparisons in the detail correlation study would deal with the forces acting from the ground to the footpad. However, footpad forces in the direction of the footpad velocity and those normal to footpad velocity were generally inconsistent with the accelerations recorded for the model. Analyses of the reduced data of the five strain gage readings showed excessive noise which was found to cause the calculated forces to be unreliable. (These five strain gage readings, in terms of actual strain, were used together with the load cell dimensions and material properties to calculate the footpad forces. Random noise on each of the five strain signals appeared to be the source of the problem). It was therefore decided not to include these footpad forces in the computer/experimental comparisons of the detailed correlation study. Instead, the three axial loads on each of the three struts in the No. 1 leg group were used for load comparisons.

The strain gages on each of these struts were wired to measure pure axial loads. They were calibrated and recorded so that the output was read directly as force, not strain, and no further calculation was required. These axial loads were recorded on this oscillographs, were read manually, and are known to be accurate.

Examples of the strut axial loads versus time are given in Figure 5-25, which applies to drop No. 10, and Figure 5-32 which applies to drop No. 11.

5.6 GROSS CORRELATION TESTS AND RESULTS

The gross correlation model drop tests provide a means for checking the soil-footpad interaction model on the basis of overall vehicle landing performance. In contrast to the detailed correlation study (where the ground was level, vehicle motion was relatively simple, and the main interest was on the forces and motions of only one footpad), the gross correlation study was concerned with nonlevel ground, more complex vehicle motions (particularly after first footpad input) and with the effect of footpad-ground reactions on the stability characteristics of the vehicle. For correlation purposes, the stability of the vehicle becomes a criterion which should be predictable from appropriate analytical study using the correct soil-footpad interaction model.

5.6.1 Test Setup and Instrumentation

The general setup for gross correlation tests was similar to that used for detail correlation except that all drops were made on a 15° sloped surface. This required creation of a special soil test surface and new soil handling and bed preparation procedures, described below. A 15° slope was selected to enhance possibilities of reaching a stability transition range before exceeding the horizontal velocity capabilities of the model drop test equipment.

The LM model instrumentation was the same as that used for detailed correlation study with the exception that the outputs of the five strain gages on the No. 1 strut and the two potentiometers on the No. 1 footpad were not recorded. The remaining 30 signals (see Paragraph 5.2) were recorded on two oscillographs. Data reduction of these 30 signals was done manually and the results are included in the separate data package.

5.6.2 Test Soils and Soil Bed Preparation

The large hopper/spreader, previously used during the preparation of the drop test soil beds, considerably speeds the otherwise laborious, time consuming process of test bed preparation, particularly where large volumes of materials are involved. However, the spreader runs on level tracks along the edge of the soil pit and could not be conveniently

adapted to preparation of soils on the 15° sloped surface. The development of other mechanized techniques was not practical at this time, which left manual test bed preparation as the alternative.

This factor, plus the relatively large number of tests anticipated, led to several decisions concerning the soil test surface and its preparation. One of these was to reduce the volume of material used for each test by utilizing as small and shallow a soil bed as practical (without developing excessive "edge" effects), to minimize material handling and preparation problems.

The other decision was to conduct the gross correlation tests on soils of high relative density that could more easily be uniformly prepared by hand on the sloped surface.

A flat wooden box or tray 12 feet long by 8 feet wide by 1 foot deep was constructed to contain the soils during tests. The box had a four-inch thick laminated plywood bottom, and rested on highly compacted silica sand which filled the remainder of the soil pit. The surface of the silica sand was graded to the 15° slope angle, and with the test soil placed inside the box and level with the sides, provided the correct ground slope for the tests.

Two types of soils were used in the gross correlation tests: RS dense and RSM-b dense. The RS soil was one of several acceptable materials that was selected, primarily, because of its availability and ease of handling.

The RSM-b material is a mixture of marble chips and RS soil that met specified requirements for a "reasonably different" and "unknown" material (i.e., had not been subjected to prior dynamic tests nor used in the development of the soil interaction model). It, therefore, served as a relatively independent medium with which the adequacy of the soil interaction model could be gaged.

The following soil preparation procedure was used for the gross correlation study. The soil was hand-placed in the box in layers about four inches thick, followed by rolling 20 times (10 back and forth cycles) for every 24-inch width of the soil bed, until the whole

area was rolled. The process of adding an approximately four-inch thick layer of soil, followed by rolling, was repeated until the total soil depth was slightly more than 12 inches. A final scraping of the soil surface using the two sides of the box as guides produced a uniform flat surface for the drop tests. After a drop test had been made, the disturbed soil surface was raked to a depth of four inches and was then rolled again. A slight amount of new soil was added each time before the final rolling to make up for that lost during the drop test and raking. The final scraping was again performed just before the drop tests.

Test bed characteristics were monitored by conducting approximately six dynamic penetrometer tests on the finished test bed and correlating the peak "g" readings of the dynamic penetrometer with the particular soil properties.

5.6.3 Gross Correlation Drop Tests and Results

As noted earlier, the gross correlation model drop tests were all made on soil beds with a 15° downhill ground slope. A total of 38 drop tests were conducted for the three groups of tests, and these are listed in Paragraph 5.3. The first group of tests (drop numbers 22 through 34) were made on RS dense soil with the initial mode[illegible] 45-degree yaw (2-2 landing) and zero initial angular rates. The second group [illegible] t (drop numbers 35 through 44) were also made on RS dense soil but at 22 1/2-degree initial yaw angle. The third group of tests (numbers 63 through 77) were made on RSM-b dense soil with the same initial conditions as that of the first group.

The final results of the gross correlation tests are presented in terms of vertical velocity-horizontal velocity stability profiles. Figures 5-40 and 5-41 are the profiles resulting from the first and third groups of tests. Since the test conditions of these two groups are identical, the minor differences in stability profiles are believed due to the differences in soil properties between the RS and RSM-b materials. Several duplicate drops were made to check repeatability of the results.

Figure 5-42 presents results from the second group of tests in which the model was landed at an initial yaw angle of 22 1/2 degrees. Although the extreme horizontal velocity

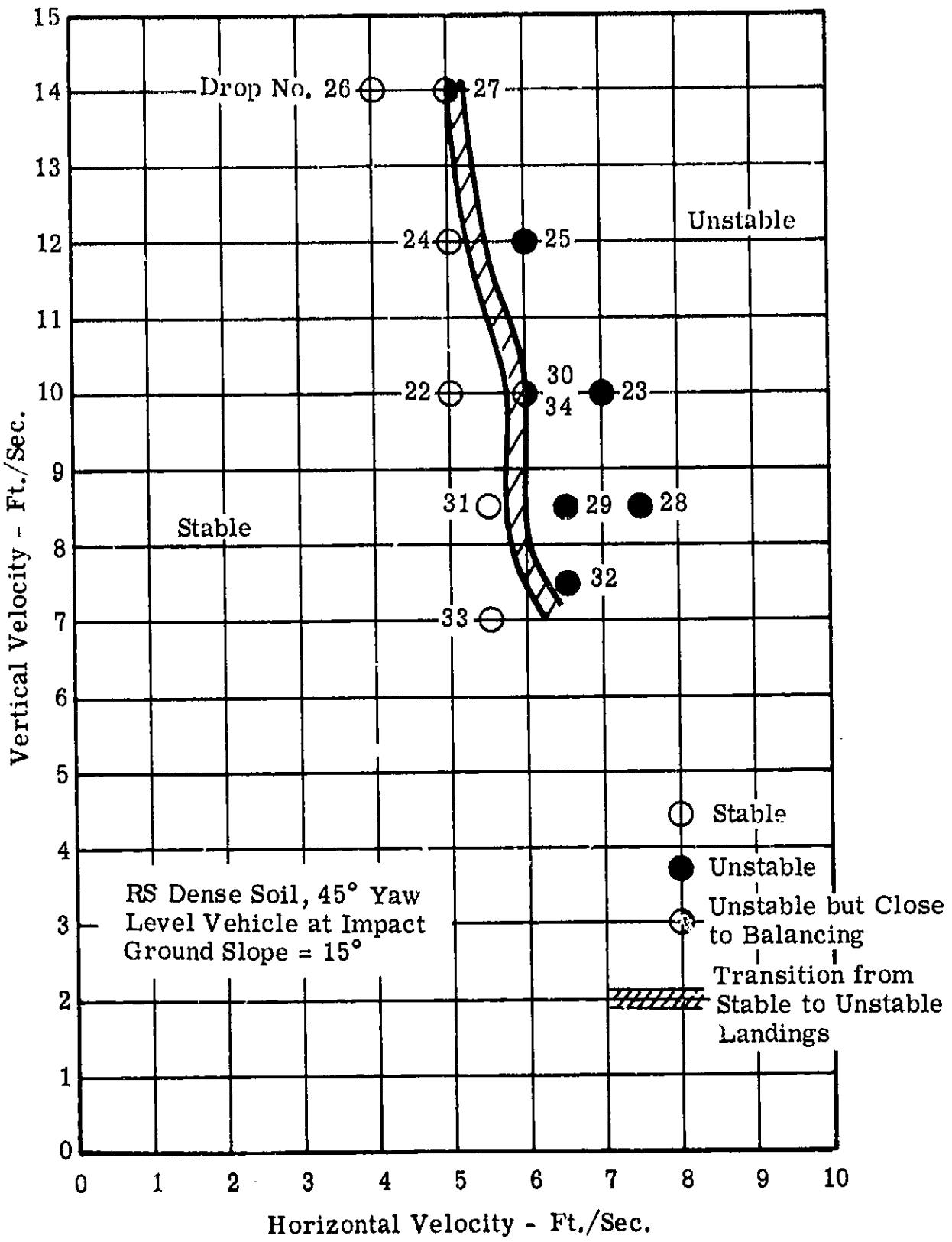

Figure 5-40. Stability Profile for Model Landings in RS Dense Soil, 2-2 Downhill

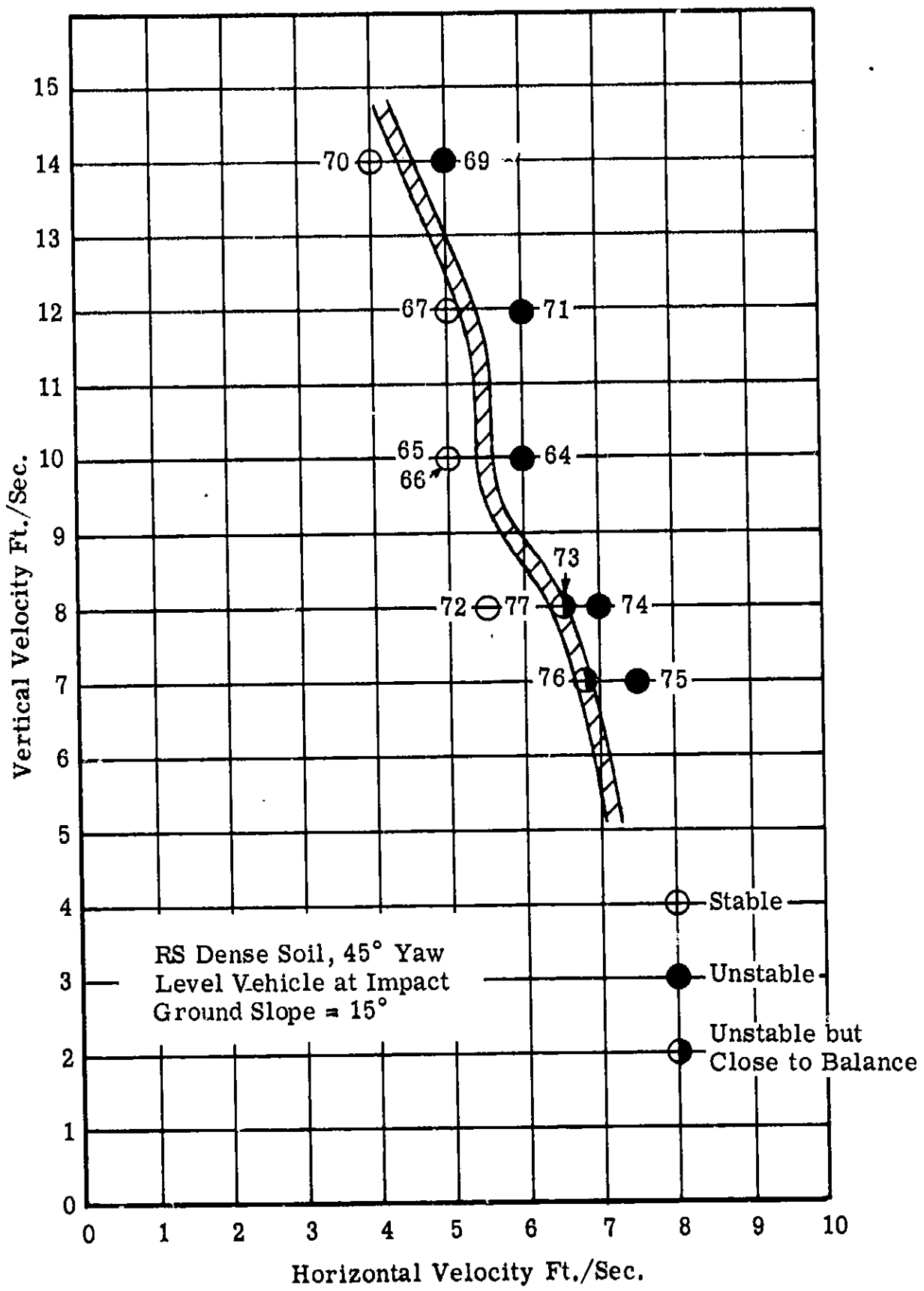

Figure 5-41. Stability Profile for Model Landing in RSM-b Soil, 2-2 Downhill

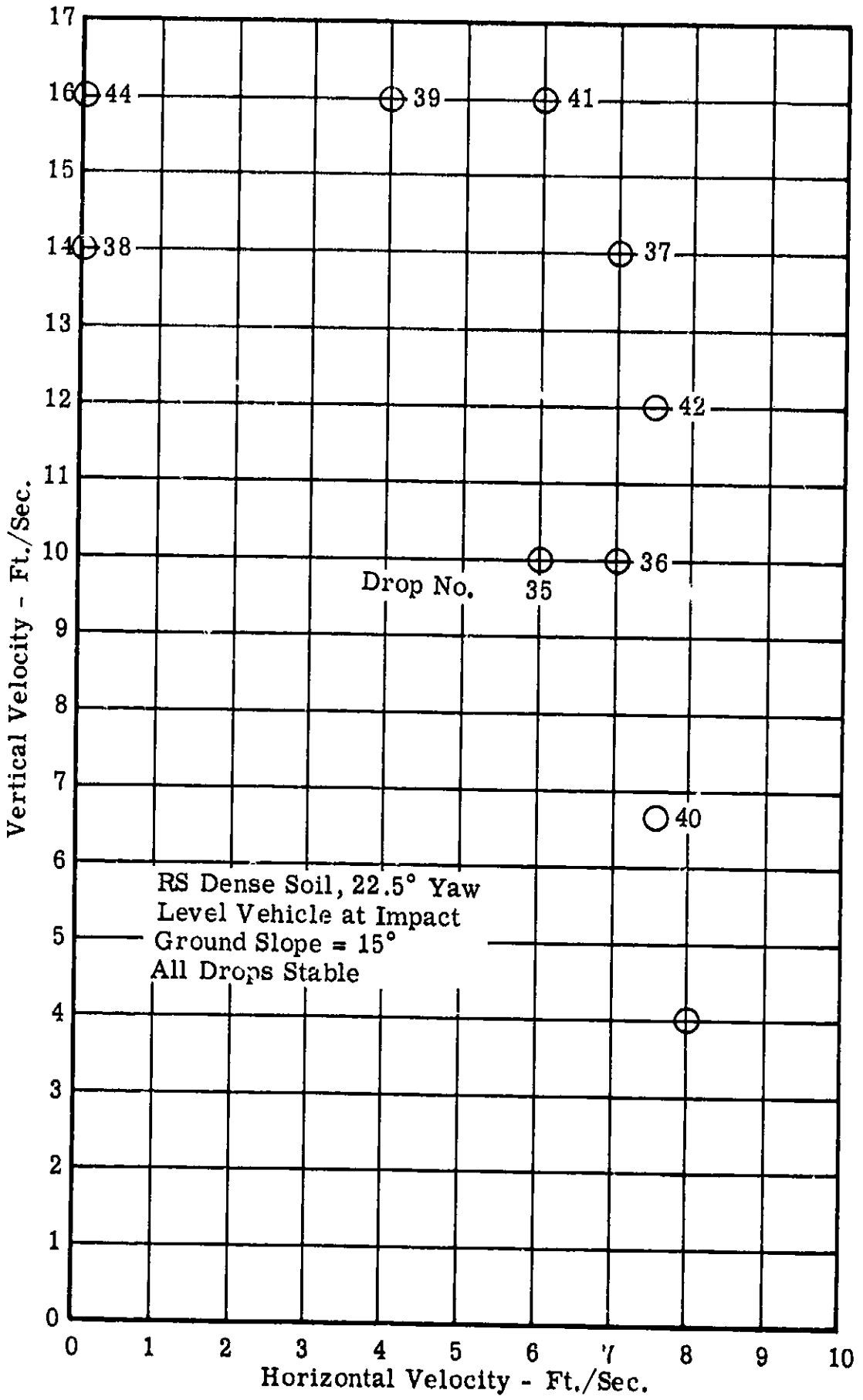

Figure 5-42. Stability Profile for Model Landing in RS Dense Soil, 22 1/2° Yaw Downhill

limits of the drop test equipment were reached, the stability transition range was not evident from these tests. Based on the degree of stability noted during the tests at the highest horizontal velocities tested, the stability boundary is felt to be well beyond a V_H of eight feet/second.

5.7 EXPLORATORY TESTS - INVESTIGATION OF SECONDARY TENSION

The purpose of the "exploratory" drop tests was to investigate the problem of possible bottoming (over extension) of the secondary shock struts. The drop conditions for this series of tests were based on selected initial conditions from an analytical study of the problem carried out by NASA, MSC using the LM landing dynamics computer program with a rigid lunar surface model. In the MSC studies the initial conditions of the vehicle's motion (orientation and translational velocities), the ground slope, surface protuberances, and surface depressions were randomly selected from assumed distribution functions for computer input data. The vehicle's performance was then computed and the results interpreted, via a Monte Carlo technique, as the statistical probability of a successful landing. Out of the approximately 1000 drop conditions investigated a few showed secondary tension strokes which equaled or exceeded the allowable stroke of the shock struts. The initial conditions of selected landings in this category were duplicated at Bendix in the exploratory drop test program to determine, experimentally, if landings on a soil produced similar, large tension stroke, results.

5.7.1 Test Setup for Exploratory Drops

For this series of tests, the LM model and instrumentation setup was the same as used for the gross correlation tests, previously described. RS dense soil was used and the ground slope was set at 3 1/2 degrees for all tests.

Five exploratory drop tests were made, listed as drops Nos. 2 through 6 in Paragraph 5.3. Each test had its own landing surface arrangement, drop attitude and velocities, as described below.

The first test (drop No. 2) was made at -160-degree yaw angle with strut No. 7 leading and strut No. 1 (the heavily instrumented strut) trailing. Three depressions, each four inches deep, were dug in the soil so that upon landing, the No. 1 footpad impacted the soil while the other three footpads penetrated into the depressions. The initial velocities were seven feet/second vertical and four feet/second horizontal. Figure 5-43 shows the test setup prior to the model drop.

The second test (drop No. 3) was made at +140-degree yaw angle so that the No. 1 strut touched ground first. A single four-inch deep depression was dug in the soil so that upon landing, the No. 2 footpad penetrated into it (see Figure 5-44). The vertical velocity for this test was six feet/second and the horizontal velocity was 2.46 feet/second.

In the third test (drop No. 4), the ground condition and model attitude were the same as for the second test; however, the initial vertical velocity was 10 feet/second and horizontal velocity was 2.45 feet/second. Figure 5-45 shows the model after the drop.

The fourth test (drop No. 5) was made with the same ground slope and the same RS soils as that of the previous tests except that thick wooden blocks were buried in the soil so that some of the footpads impacted on a hard surface as specified below. Figure 5-46 shows the test site arrangement before the drop tests. The model was set at +50 degrees yaw so that during drop test the No. 4 footpad impacted on a waxed, hard surface first. The No. 3 footpad also impacted a hard surface, but the surface was rough and sandpaper was bonded to the bottom of the No. 3 footpad to simulate very high coefficient of friction. The No. 2 footpad impacted on a waxed, hard surface, which, like the one under the No. 4 footpad, gave very low friction. The No. 1 footpad penetrated into a 4 1/2-inch deep depression in the soil. This ground condition was specified to impose unusually high tensile load on the secondary struts. The initial velocities for this test were five feet/second vertical and 2.46 feet/second horizontal.

The fifth, and last, exploratory drop test (drop No. 6) had the same ground setup as that in the fourth test. The initial velocities for this test were 10 feet/second vertical and 2.46 feet/second horizontal. Figure 5-47 shows the model after the fifth test.

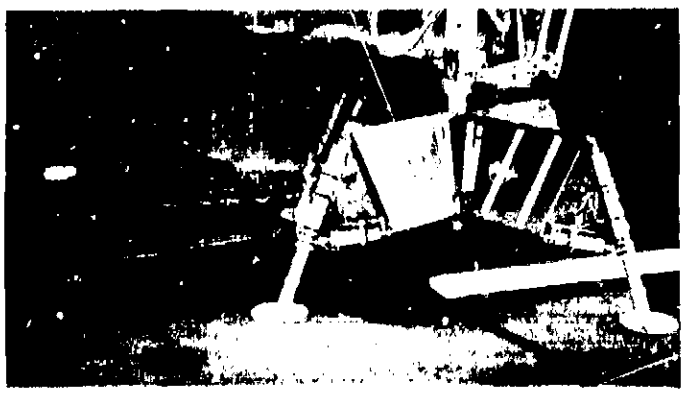

Figure 5-43. Exploratory Model
Drop No. 2

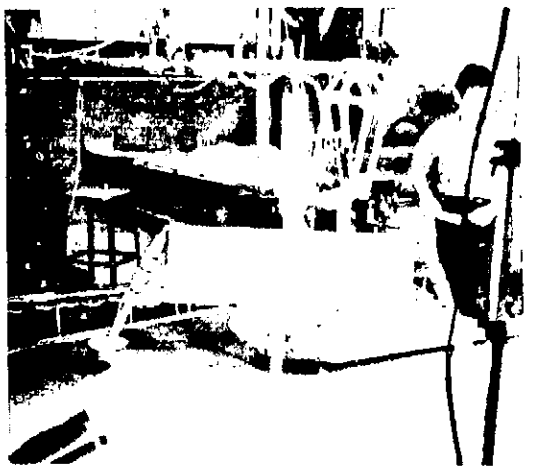

Figure 5-44. Exploratory Model
Drop No. 3

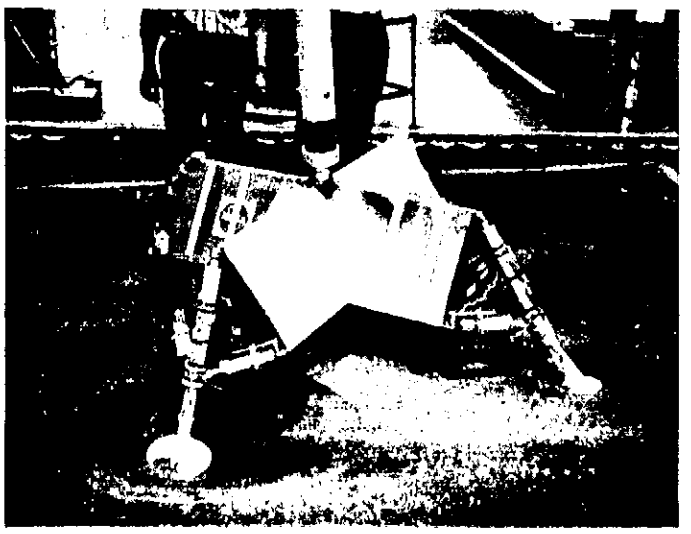

Figure 5-45. Exploratory Model
Drop No. 4

Figure 5-46. Exploratory Model Drop No. 5

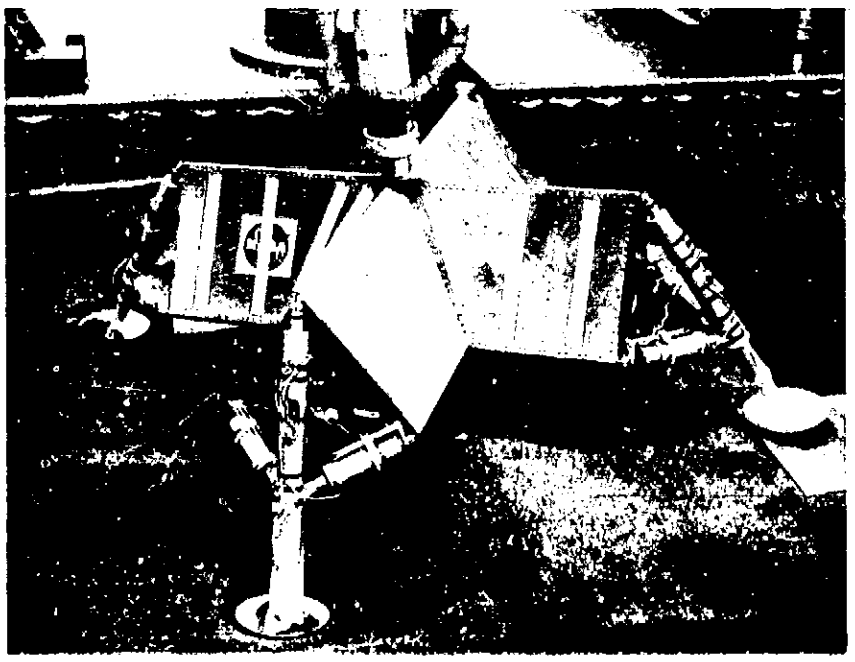

Figure 5-47. Exploratory Model Drop No. 6

5.7 Exploratory Drop Test Results and Discussion

The test results of the five exploratory drops showed that none of the secondary struts over-extended or "bottomed." Measurement of the crushable capsules in all the secondary struts showed that only one of the high tension capsules (167 pounds crush load) was deformed. This was in strut No. 12, and showed a deformation of only 0.021 inch beyond initial 1 2 inch stroke of the "soft" capsule, after the fifth drop. The high tension capsule has an initial length of 2 1/4 inches and a stroke capability of more than 1 1/2 inches.

The most plausible explanation for the qualitative difference between NASA's analytical findings and Bendix' experimental results can be found by examining Figure 5-10. It can be seen that for the LM model, the secondary strut low tension capsule has a crush load of 42 pounds while the equivalent (scaled-down) load for the full-size LM is only 13 pounds for the same capsule. The secondary strut high tension capsule has a 167-pound crush load for the LM model, and only 139 pounds equivalent crush load for the full-size LM. Therefore, it is much easier to initiate tension stroke in the secondary struts of the full-scale LM than in the secondary struts of the model.

The geometry of the three struts in any leg group is such that if the force acting on the footpad and the vehicle X_b axis (body coordinate, reference Figure 5-11) both remain vertical, then the larger the angle between X_b axis and X_s axis (strut coordinate), and the harder it is for the vertical force on the footpad to cause stroking of the main strut. When this angle becomes too large it is almost impossible to stroke the main strut because only the component of the vertical force along the axis of the main strut can cause it to stroke. The component of vertical force perpendicular to the main strut creates a moment on the inner cylinder of this strut. This moment increases the friction force at the sliding joint and further aggravates the stroking problem. If the main strut becomes horizontal, the vertical force can only bend the strut and no stroking will result.

Since the angle between X_b and X_s can increase only if one or both secondary struts lengthen (i.e., stroke in tension), very low crushing load for the tension capsules in the secondary struts, as those used in the LM, can easily cause these struts to lengthen and

therefore increases the main strut angle. This condition reduces the change of stroking the main strut and in doing so, channels more energy into the secondary struts and thus further lengthens them. The above condition can conceivably continue until the secondary struts bottom, if the vehicle motion continues.

The slight geometric difference between the full-scale LM and the LM scale model (Figure 5-8) may also influence the condition of secondary strut "bottoming." Analysis indicates, however, that since this geometric difference is relatively slight, the main reason for the qualitative difference observed was the difference in the shock strut loads between the LM and the full-scale equivalent of the model. This was verified by conducting an analytical drop test with the NASA LM landing dynamic computer program using inputs to correspond to the fourth exploratory drop test of the present program. When the analytical load versus stroke characteristics were set equal to those of the model, the resulting stroke correlated closely with that obtained in the drop test.

SECTION VI

CORRELATION STUDIES

6.1 INTRODUCTION

The purpose of the LM model correlation studies is to provide verification of the derived semi-empirical footpad/soil force laws. The study consists of comparisons of computer simulated landing performance with the performance of a one-sixth scale model of the LM which was drop tested onto a prepared soil bed. Two types of comparison are carried out, computed and experimental toppling stability profiles, and computed and experimental footpad motion histories and ground reactions (detail correlation).

6.2 LM LANDING DYNAMICS COMPUTER PROGRAM

The LM Landing Dynamics Computer Program was originally developed by NASA-MSC to study LM rigid surface landing performance. For its use in the LM Soil Mechanics Study, the landing dynamics program was modified by NASA-MSC with some assistance from Bendix to incorporate the semi-empirical force laws into the footpad dynamical equations. The resulting computer simulation of the LM accounts for six degrees of freedom of the vehicle c.g. and three degrees of freedom (X, Y, and Z translation) of each of the four footpads. Footpad pitch attitude in the plane of motion is also obtained, but this is not considered an additional degree of freedom since the angle is computed directly from footpad position and velocity information.

A block diagram for a "real soil" landing dynamics program is shown in Figure 6-1. This is similar to the flow diagram for a rigid surface analysis except that the soil/footpad interactions have replaced the interaction of a footpad with a rigid surface. Input information (initial conditions, spacecraft descriptors, and surface descriptors) is read into the computer and is used to define the vehicle configuration at touchdown. The vehicle c.g. and footpad configurations (positions and velocities) enable the shock strut

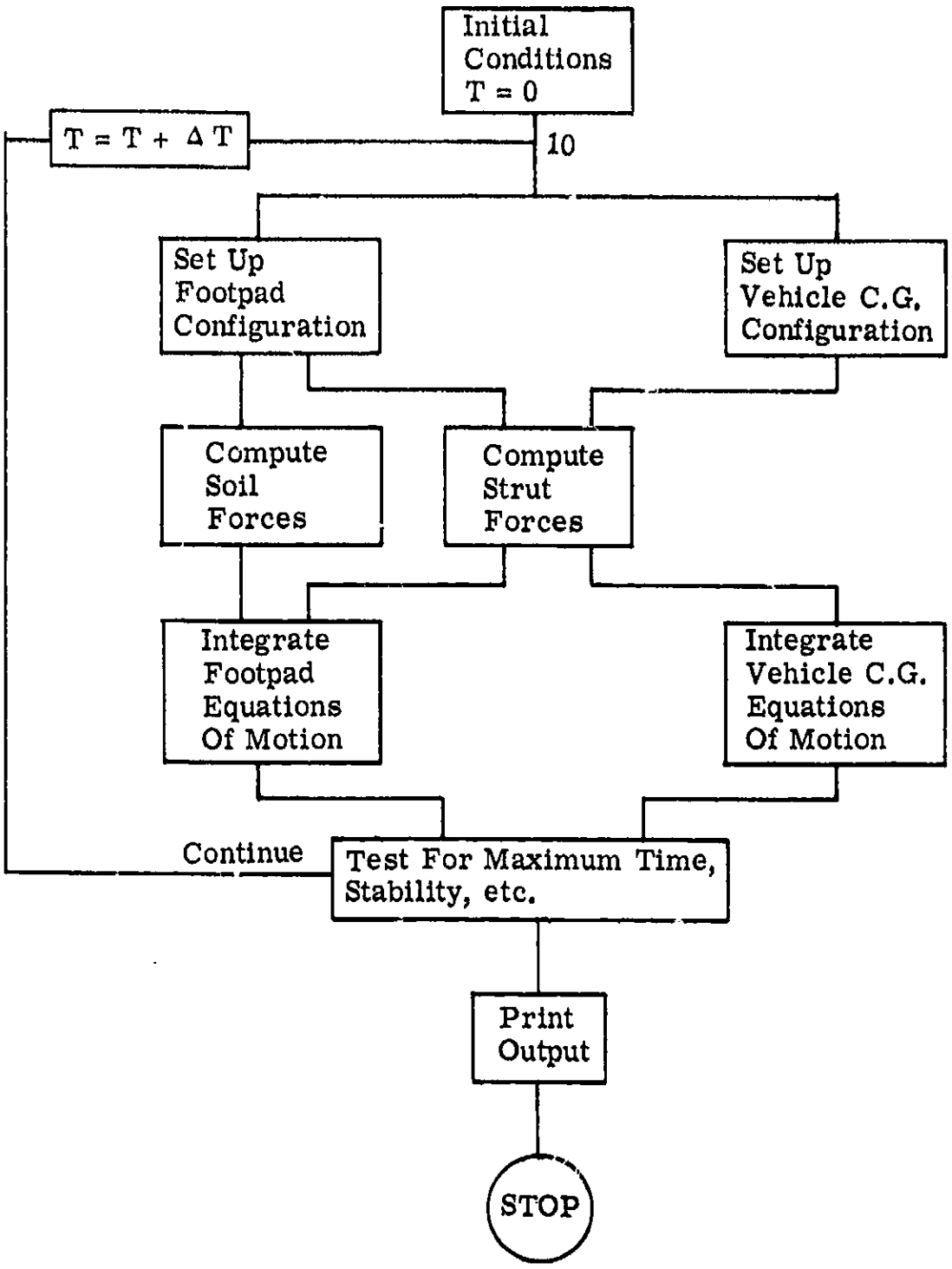

Figure 6-1. Block Diagram for Typical Landing Dynamics Computer Program

and footpad/soil interaction forces to be computed. The equations of motion are then formed and integrated, yielding the vehicle configuration at the next point in time. Following integration, a check is made for run completion (desired time reached, vehicle stability established, etc.) and the run is either stopped and the stored output information printed, or the above process is repeated until the run is completed.

In the LM Landing Dynamics Computer Program used in this study, the calculation of footpad/soil interaction forces was performed in subroutines SOIL and BEN, using the equations which were presented in Section IV, paragraph 4.6 of this report. Block diagrams of these subroutines are shown in Figures 6-2 and 6-3. The logic dealing with the conditions existing at the footpad/soil interface was checked out in a similar but far less complicated digital computer program written by NASA-MSC for the primary purpose of analyzing penetrometer response data. Full-scale LM footpad vertical impact test data, which had previously been used for analog computer correlation studies, as described in Section IV, paragraph 4.5, was used to "debug" the interaction equations and associated logic in the penetrometer program. The resulting equations and logic were then incorporated into the landing dynamics program with modifications being made to include two-dimensional motion and the capability of computing the footpad pitch attitude.

The interaction equations employed in these subroutines are quite simple as may be seen in Section IV, paragraph 4.6. The complications in the subroutines arise from seemingly elementary decisions which must be made for the purpose of determining if the footpad is moving into or out of the soil surface, or whether static or dynamic force conditions exist at the footpad/soil interface. Even a relationship as basic and pure as Newton's Second Law frequently becomes unrecognizable when entangled in the bowels of a complex landing dynamics computer program.

6.3 LM TOPPLING STABILITY COMPARISON

This analysis provides a comparison between the vehicle toppling stability determined experimentally with the one-sixth scale LM model and the stability profile computed using the NASA-MSC Lunar Module Landing Dynamics Computer Program with the

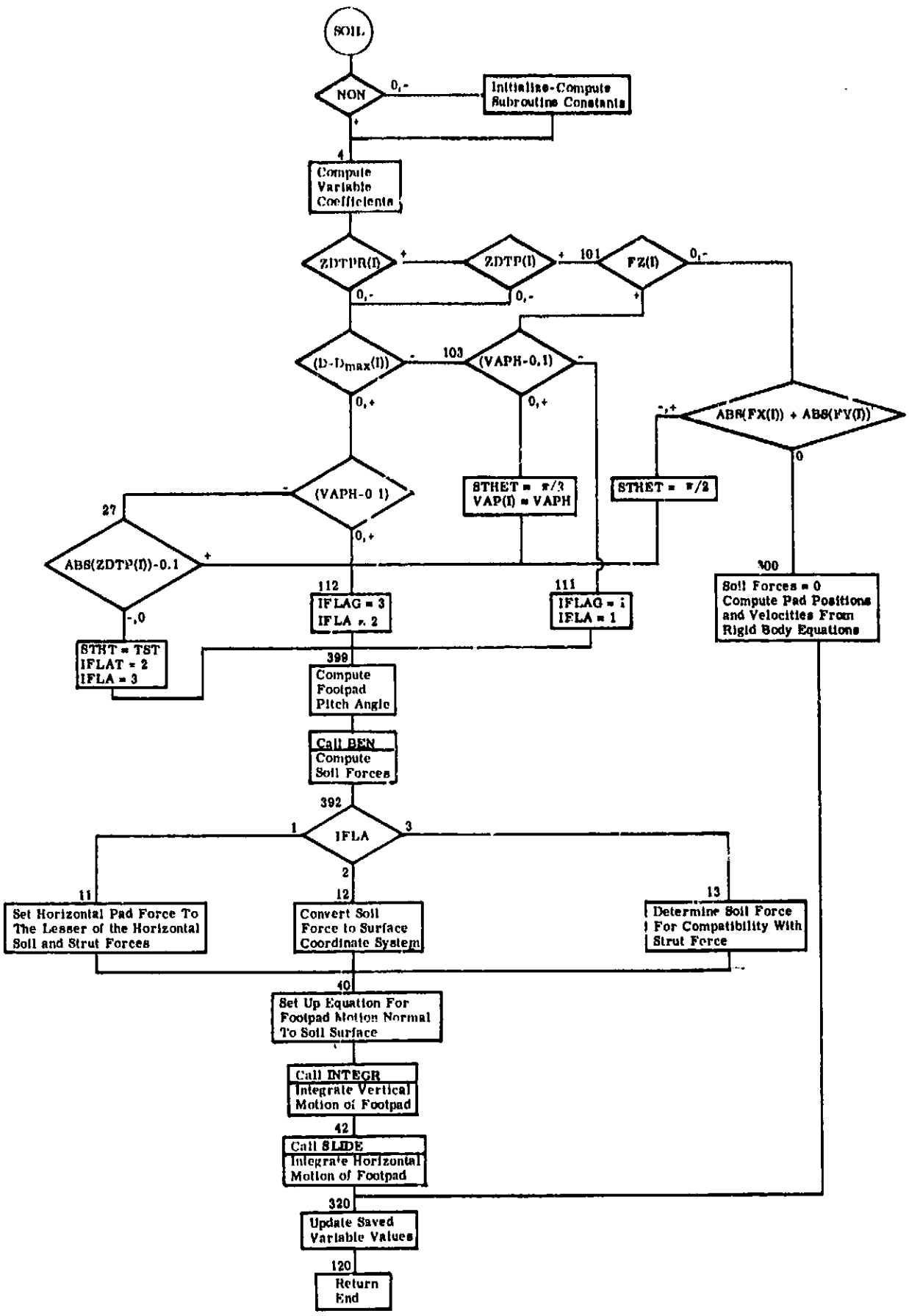

Figure 6-2. Flow Diagram for Subroutine SOIL

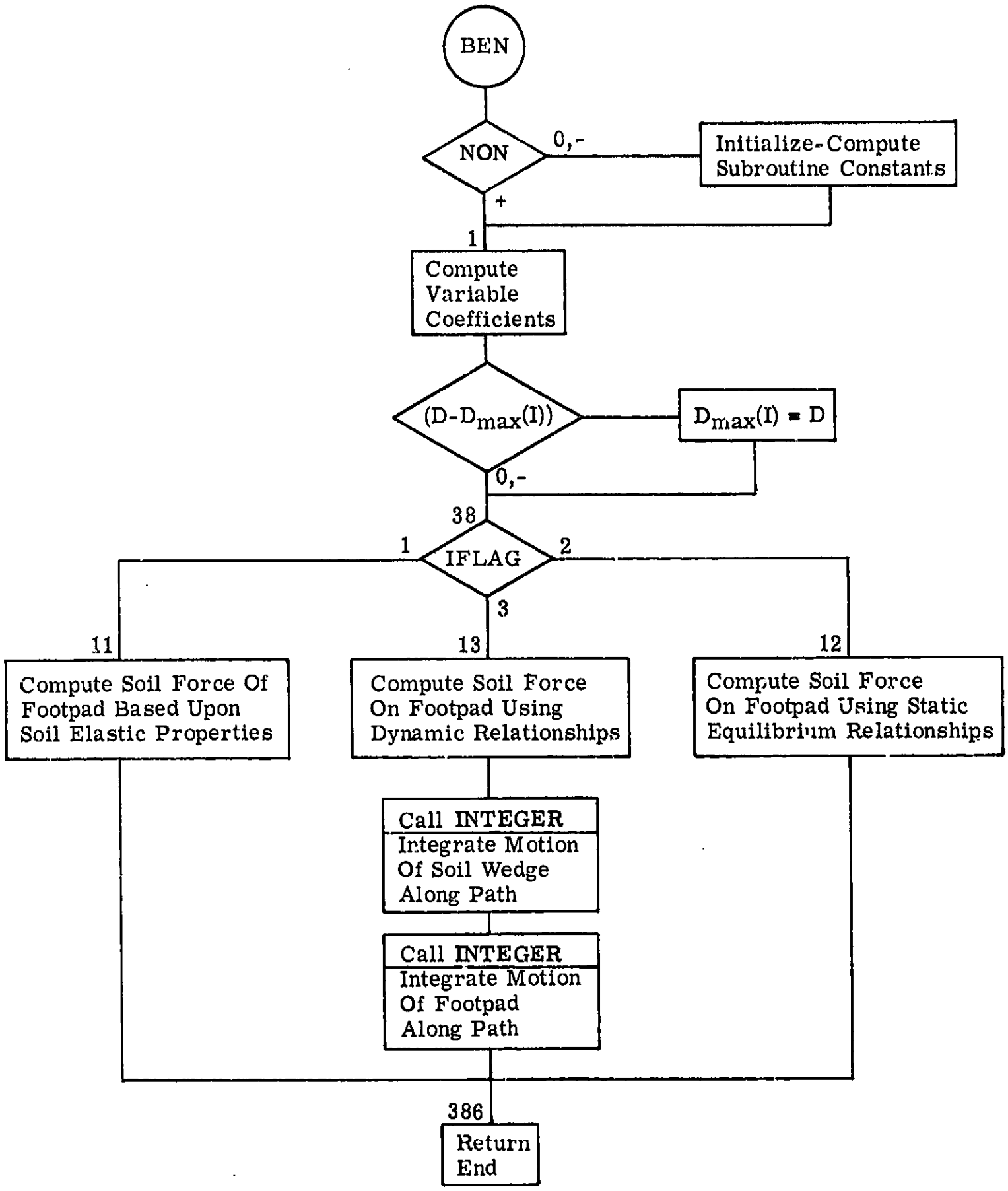

Figure 6-3. Flow Diagram for Subroutine BEN

semi-empirical force laws incorporated into its footpad dynamical equations. Stability profiles were obtained for two soils, RS Dense and RSM-b Dense, both having relative densities of approximately seventy-five percent. Good correlation between the experimental and computed stability profiles is required to demonstrate the accuracy with which full-scale LM landing performance can be predicted using the computer program.

To obtain rational basis for comparing the experimental and computed results for landings on soils, a comparison was made for a series of landings on a rigid surface. The surface used in this phase of the study had a slope of ten degrees and consisted of heavy plywood blocks embedded in a dense soil. The vehicle was level at impact and had a yaw angle of 22.5 degrees. All angular rates were zero. A table of the model drops made for these conditions is shown in Figure 6-4. Vehicle vertical velocity at impact was varied from 6 to 12 feet per second, and horizontal velocity was increased at each step in vertical velocity until an unstable landing condition was achieved. The resulting stability profile is shown in Figure 6-5 along with the calculated stability profile using the rigid surface version of the LM Landing Dynamics Computer Program. It may be seen that the computer results compare favorably with the experimental results even to the extent of matching the "nose" in the profile which occurs at a vertical velocity of about 9 feet per second. Based upon this result, it would be expected that the real soil version of the program would yield a similar degree of correlation if the footpad/soil interaction equations are realistic.

A table of model drops made on the RS Dense soil is shown in Figure 6-6. The soil slope was 15 degrees for this series of drops and the vehicle was level in a 2-2 configuration (45° yaw angle) at impact. These results are plotted in Figure 6-7. Also shown are stability profiles computed using several variations of the LM Landing Dynamics Computer Program. The calculated rigid surface results serve to point out the marked difference between the vehicle stability boundaries on rigid and real soil surfaces. The stability profile calculated using the original soil equations tended to predict excessive vehicle stability at low values of vertical velocity, although correlation was good at vertical impact velocities over 12 feet per second. The nonconservatism at the lower vertical velocities was attributed to excessive vertical force on the footpad during periods of predominantly horizontal motion, thus causing the footpad to plane out of the soil and increase

Bendix Drop No. and Date	Soil	V_V	V_H	Ground Slope (Deg.) Zeta	Yaw Angle (Deg.)	Relative Density Dr	Density γ (Lbs. Ft.^{3})	Friction Angle Φ (Deg.)	Stable	Remarks
45 9-27-67	Ply-wood Blocks	8	4.8	10	22.5	--	--	--	Yes	Borderline stability spiked footpad-10° board slope.
46 10-2-67	Ply-wood Blocks	8	4.8	10	22.5	--	--	--	Yes	Borderline stability. Tests 45 and 46 to check rubber capsules.
47 10-3-67	Ply-Wood Blocks	8	5.8	10	22.5	--	--	--	Yes	
48 10-4-67	Ply-wood Blocks	8	5.8	10	22.5	--	--	--	Yes	
49 10-4-67	Ply-wood Blocks	8	6.8	10	22.5	--	--	--	No	Very unstable.
50 10-5-67	Ply-wood Blocks	8	4.8	10	22.5	--	--	--	No	Borderline stability.
51 10-6-67	Ply-wood Blocks	8	5.8	10	22.5	--	--	--	Yes	Repeat of drops 47 and 48.
52 10-6-67	Ply-wood Blocks	8	6.8	10	22.5	--	--	--	No	Very unstable.
53 10-9-67	Ply-wood Blocks	6	6	10	22.5	--	--	--	Yes	
54 10-9-67	Ply-wood Blocks	6	7	10	22.5	--	--	--	No	
55 10-10-67	Ply-wood Blocks	10	4.5	10	22.5	--	--	--	Yes	
56 10-10-67	Ply-wood Blocks	10	5.5	10	22.5	--	--	--	Yes	
57 10-11-67	Ply-wood Blocks	10	6.5	10	22.5	--	--	--	No	
58 10-11-67	Ply-wood Blocks	12	6.5	10	22.5	--	--	--	No	
59 10-11-67	Ply-wood Blocks	12	5.5	10	22.5	--	--	--	Yes	
60 10-12-67	Ply-wood Blocks	8.5	5.5	10	22.5	--	--	--	No	
61 10-12-67	Ply-wood Blocks	9	5	10	22.5	--	--	--	No	
62 10-13-67	Ply-wood Blocks	9	4.5	10	22.5	--	--	--	Yes	

Figure 6-4. Rigid Surface LM Model Drops

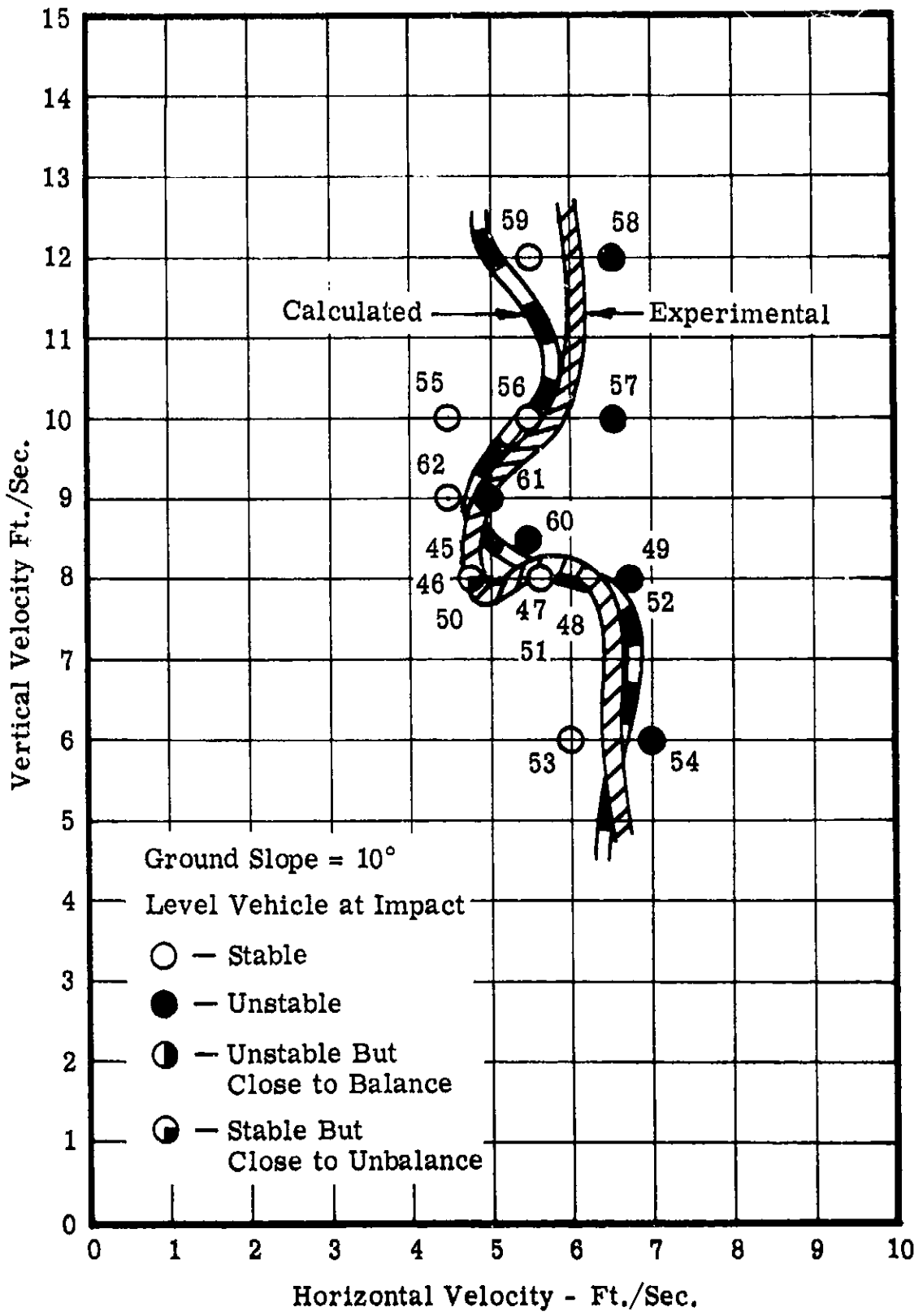

Figure 6-5. Stability Profile for Model Landing on Wooden Surface (Fir Wood) with Spiked Feet - 22 1/2° Yaw

Bendix Drop No. and Date	Soil	V_V	V_H	Ground Slope (Deg.) Zeta	Yaw Angle (Deg.)	Relative Density Dr	Density γ (Lbs./Ft.^{3})	Friction Angle ϕ (Deg.)	Stable	Remarks
22 8-3-67	RS Dense	10	5	15	45	0.72	56.9	47	Yes	RS Dense soil-10 rolls per two-inch layer.
23 8-4-67	RS Dense	10	7	15	45	0.71	56.7	47	No	
24 8-7-67	RS Dense	12	5	15	45	0.81	59.3	48	Yes	
25 8-8-67	RS Dense	12	5	15	45	0.79	59.0	48	No	
26 8-8-67	RS Dense	14	4	15	45	0.81	59.3	48	Yes	
27 8-8-67	RS Dense	14	5	15	45	0.81	59.3	48	Yes	Borderline stability.
28 8-9-67	RS Dense	8.5	7.5	15	45	0.81	59.3	48	No	
29 8-9-67	RS Dense	8.5	6.5	15	45	0.73	58.2	47.5	No	
30 8-10-67	RS Dense	10	6	15	45	0.74	58.4	47.5	No	Borderline stability.
31 8-10-67	RS Dense	8.5	5.5	15	45	0.74	58.4	47.5	Yes	
3[illegible] 8-1[illegible]-67	RS Dense	7.5	6.5	15	45	0.74	58.4	47.5	No	
33 8-11-67	RS Dense	7.0	5.5	15	45	0.74	58.4	47.5	Yes	
34 8-11-67	RS Dense	10	6	15	45	0.73	58.2	47.5	No	

Figure 6-6. LM Model Drops on RS Dense Soil

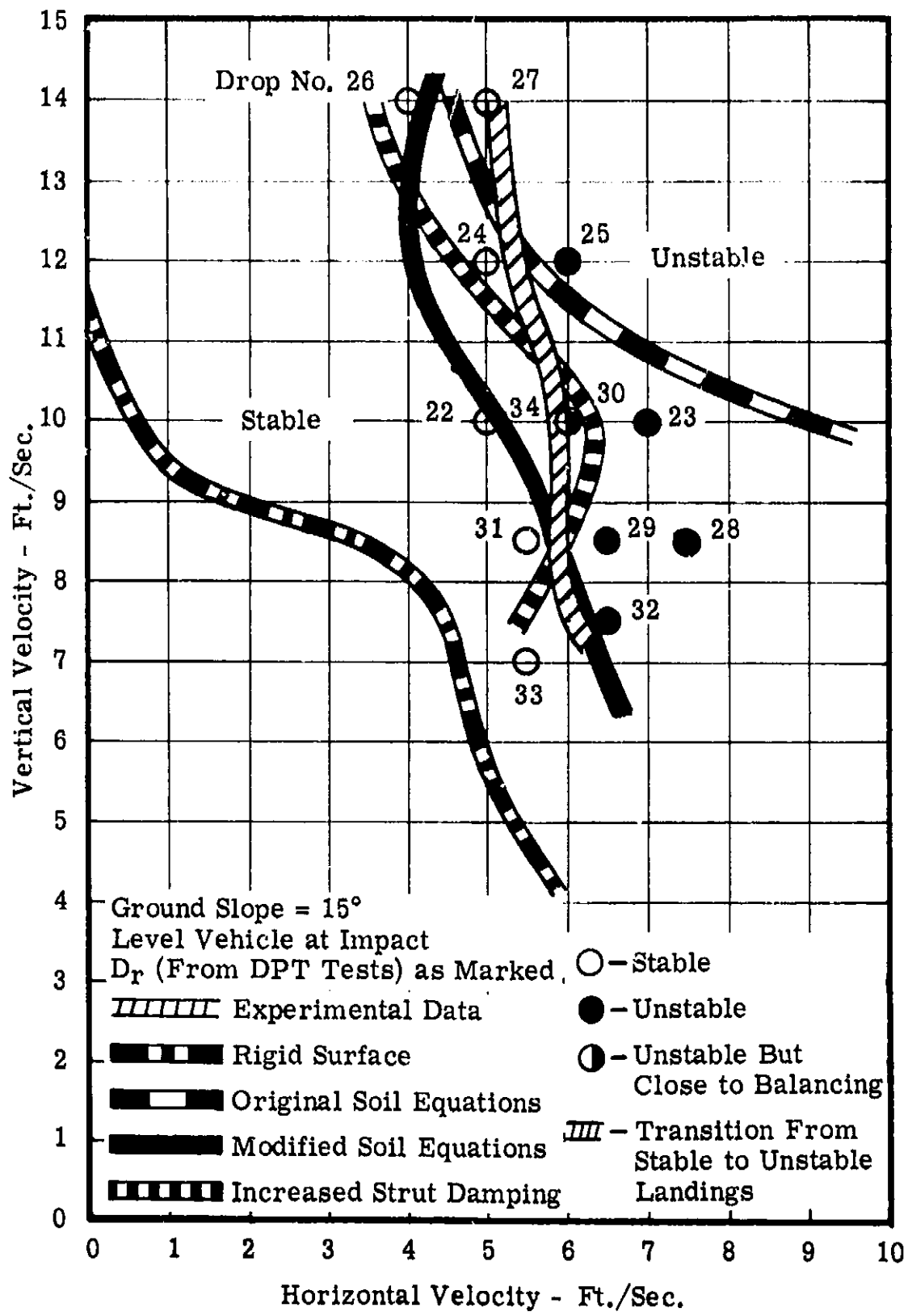

Figure 6-7. Stability Profile for Model Landings on RS Dense Soil, 2-2 Downhill

vehicle stability. In an attempt to remedy this problem the footpad vertical forces were set to zero when the vertical component of footpad velocity became positive (upward), yielding the stability profile labeled "modified soil equations" in Figure 6-7. The remaining profile was a result of increasing the shock strut damping in an effort to smooth the footpad force and motion histories. The strut damping forces for this series of runs was given by

$$F_{dp} = 10 \ \dot{S}^{1/2}$$

for the primary struts and

$$F_{ds} = 30 \ \dot{S}^{1/2}$$

for the secondary struts, where $\dot{S}$ is the strut stroking velocity in feet per second. Strut damping forces for all previous calculations were given by

$$F_{dp} = F_{ds} = 10 \ \dot{S} \ .$$

A similar comparison between experimental and calculated stability boundaries was conducted for RSM-b soil which had a relative density similar to the RS Dense soil but differed significantly in bulk density. A table showing the model drops conducted appears in Figure 6-8 and the resulting stability profiles are shown in Figure 6-9. The various analytically determined stability profiles show trends similar to those noted for the RS Dense soil except that the variation in the profiles for the various types of calculation is magnified. This increased sensitivity is probably due to the higher soil density which causes a higher force to be developed for a given footpad penetration and velocity. The unusual shape of the profile obtained using the modified soil equations (zero lift force) is believed to be due to a large amount of footpad "chatter." This condition was eliminated when the strut damping was increased for low stroking velocities.

Based on the results presented for 2-2 downhill landings on RS and RSM-b dense soils, the LM Landing Dynamics Computer Program using the semi-empirical footpad/soil

Bendix Drop No. and Date	Soil	V_V	V_H	Ground Slope (Deg.) Zeta	Yaw Angle (Deg.)	Relative Density Dr	Density γ (Lbs./Ft.^{3})	Friction Angle ϕ (Deg.)	Stable	Remarks
63 10-18-67	RSM 10 Rolls	12	7.5	15	22.5	0.80	86.0	48	Yes	
64 10-19-67	RSM 10 Rolls	10	6	15	45	0.78	85.6	48	No	
65 10-19-67	RSM 10 Rolls	10	5	15	45	0.65	83.6	47	Yes	
66 10-20-67	RSM 10 Rolls	10	5	15	45	0.77	85.5	48	Yes	Rerun of Test 65.
67 10-20-67	RSM 10 Rolls	12	5	15	45	0.75	85.2	48	Yes	
68 10-23-67	RSM	14	5	15	45	0.10	75.7	39	Yes	Soil not rolled.
69 10-23-67	RSM	14	5	15	45	0.79	85.7	48	No	Repeat of Test 68 on hard dense soil.
70 10-23-67	RSM Rolled	14	4	15	45	0.78	85.6	48	Yes	
71 10-24-67	RSM Rolled	12	6	15	45	0.86	87.2	48	No	
72 10-25-67	RSM Rolled	8	5.5	15	45	0.73	84.8	48	Yes	
73 10-25-67	RSM Rolled	8	6.5	15	45	0.74	84.9	48	Yes	Borderline stability.
74 10-26-67	RSM Rolled	8	7	15	45	0.77	85.5	48	No	
75 10-26-67	RSM Rolled	7	7.5	15	45	0.84	86.3	48	No	
76 10-26-67	RSM Rolled	7	6.8	15	45	0.78	85.6	48	No	
77 10-26-67	RSM Rolled	8	6.5	15	45	0.76	85.4	48	No	Borderline stability. Rerun of Test 73.

Figure 6-8. LM Model Drops for RSM-b Soil

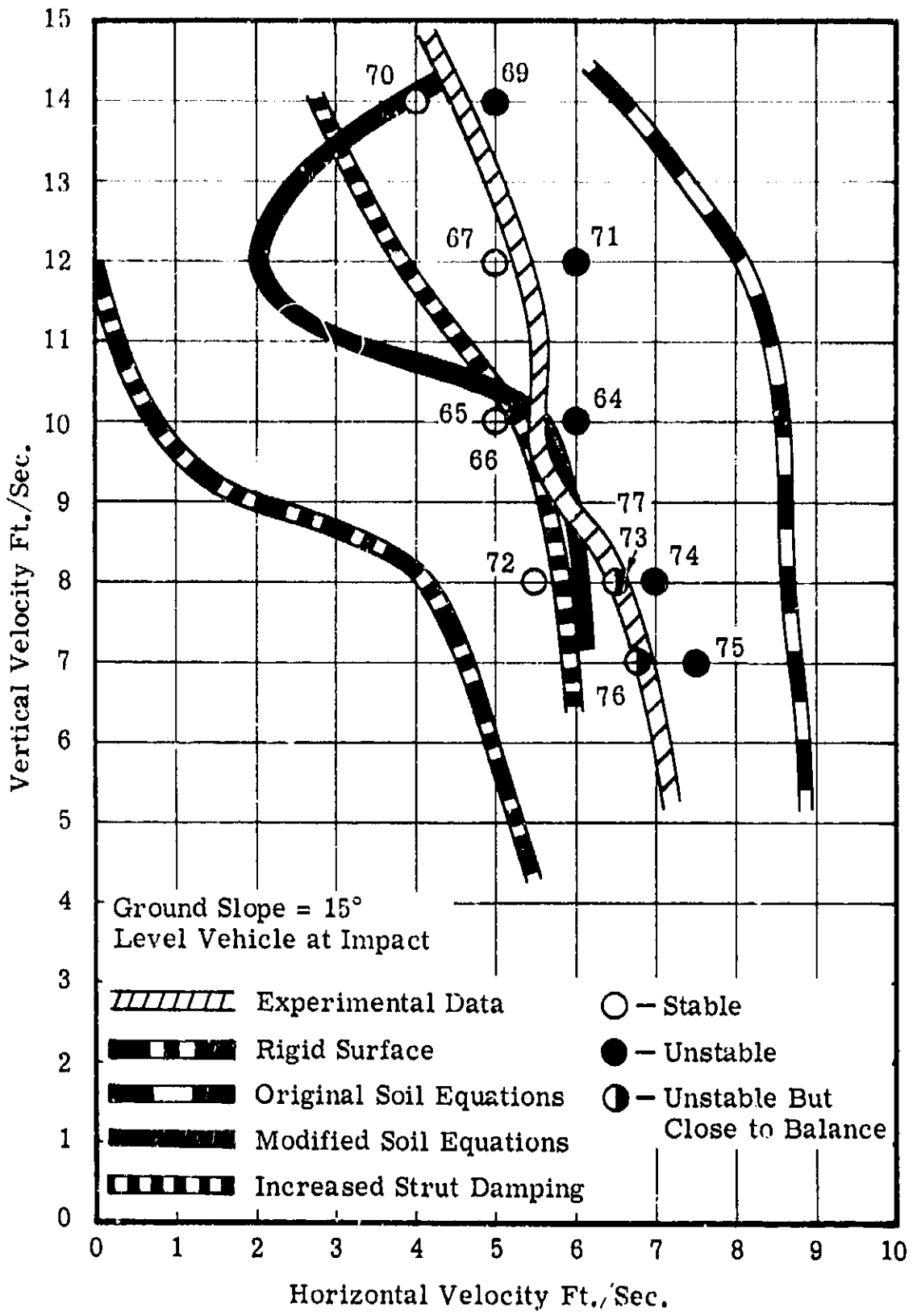

Figure 6-9. Stability Profile for Model Landing in RSM-b Soil, 2-2 Downhill

force laws provides a satisfactory means of predicting LM model stability profiles for landings on a real soil surface. In general, the profiles obtained using the original and modified soil equations bracket the experimental stability results, indicating that a compromise between the two methods of calculating vertical force on the footpad during sliding would yield even better results.

6.4 DETAIL CORRELATION STUDY

This study presents a comparison of computed and experimental footpad penetrations, velocities, velocity angles, and ground reactions, to demonstrate the degree to which the semi-empirical footpad force/motion model represents the actual footpad/soil interaction. For purposes of this study a series of eight model drop tests were conducted on several level soil surfaces. Sufficient vehicle acceleration and shock strut stroking measurements were made and recorded on tape to enable the position, velocity, and acceleration histories of the vehicle c.g. and footpads to be calculated. A table showing the drop tests conducted, as well as pertinent soil parameters, appears as Figure 6-10.

Due to the large number of detail correlation results to be presented, and since the results from the eight drop tests show similar trends, only one set of results will be discussed in detail. Drop number 2 has been chosen for this discussion since it was the first test having both horizontal and vertical components of velocity. The experimental and computed variables compared for this and other model drops in the series are as follows:

V_{ap} - footpad velocity - in./sec.

θ - footpad velocity angle relative to soil normal - degrees

d - depth of footpad penetration - inch

$\ddot{\Xi}$ - vehicle pitch acceleration - deg./sec.^{2}

$\dot{\Xi}$ - vehicle pitch rate - deg./sec.

Ξ - vehicle pitch angle - degrees

Z - vehicle c.g. vertical position - inch

NASA Drop No.	Bendix Drop No. and Date	Soil	V_V fps	V_H fps	Ground Slope (Deg.)	Yaw Angle (Deg.)	Relative Density Dr	Absolute Density Lb./Ft.^{3}	Friction Angle Φ	Stable
1	10 7-18-67	RS Loose	10	0	0	45	0	46.9	41	Yes
2	11 7-19-67	RS Loose	5	7	0	45	0	46.9	41	Yes
3	12 7-20-67	RS Loose	5	7	0	45	0	47.1	41	Yes
4	13 7-20-67	RS Loose	10	0	0	45	0	47.1	41	Yes
5	16 7-25-67	RS Inter-mediate	5	7	0	45	3	53.0	42.5	Yes
6	17 7-25-67	RS Inter-mediate	10	0	0	45	0.3	53.0	42.5	Yes
7	20 7-28-67	SS Loose	5	7	0	45	0	96.0	30	Yes
8	21 7-28-67	SS Loose	10	0	0	45	0	96.0	30	Yes

Figure 6-10. LM Model Drop Tests for Detail Correlation Studies

Y - vehicle c.g. horizontal position - inch

$\dot{Z}$ - vehicle c.g. vertical velocity - in./sec.

$\dot{Y}$ - vehicle c.g. horizontal velocity - in./sec.

$\ddot{Z}$ - vehicle c.g. vertical acceleration - in./sec.^{2}

$\ddot{Y}$ - vehicle c.g. horizontal acceleration - in./sec.^{2}

α - footpad pitch angle - degrees

β - footpad roll angle - degrees

The experimental and computed versions of these variables for LM model drop No. 2 are plotted in Figures 6-11(a) through 6-11(n). The primary and secondary strut damping forces for the computer results shown were given by 10 $\dot{S}$, where $\dot{S}$ is the strut stroking velocity in feet per second. From the standpoint of proving the adequacy of the soil force equations, the most important variables are footpad velocity and depth of penetration into the soil. As is shown in Figures 6-11(a, b and c), the experimental and calculated values of footpad velocity, velocity angle, and penetration correlate quite favorably, indicating that the computed soil forces were realistic. The correlation is less impressive toward the end of the run. This is attributed, in part, to slight errors in measuring soil properties which could be verified by making runs in which the soil properties are varied over some range (say ± 10 percent) about the nominal values given in Figure 6-10. Another, and perhaps more important reason for the divergence of the experimental and computed results was "drift" of the experimental results. This problem was discussed in paragraph 5.5.5 of this report. It should be noted that the footpad roll angle shown in Figure 6-11(n) is not calculated by the computer program but is, instead, assumed to remain at zero throughout the landing period. The experimental results shown here indicate that this assumption was valid since the footpad roll angle is less than eight degrees throughout the run.

It may be seen in Figures 6-11(a) through 6-11(n), and in particular those figures showing footpad motions, that the computed results are much more oscillatory than the experimental results. For this reason computer runs were made which employed higher strut damping at low stroking velocities in an attempt to smooth the footpad motion

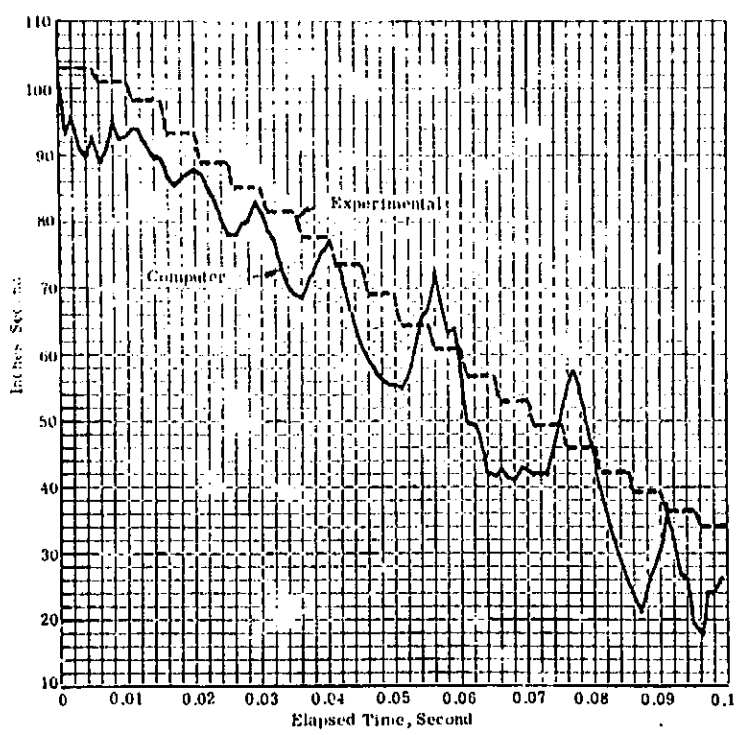

a) Footpad Velocity - V_{ap}

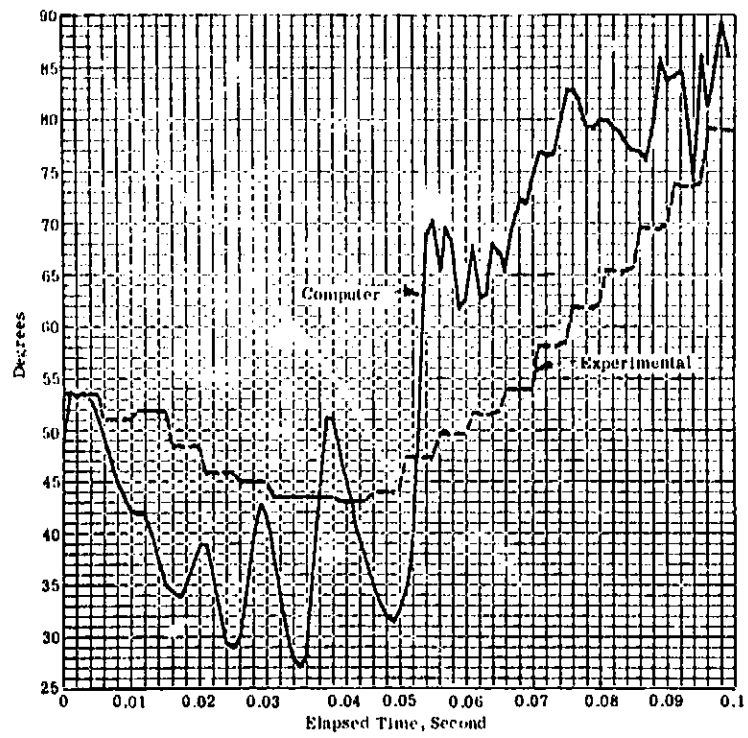

b) Footpad Velocity Angle - θ

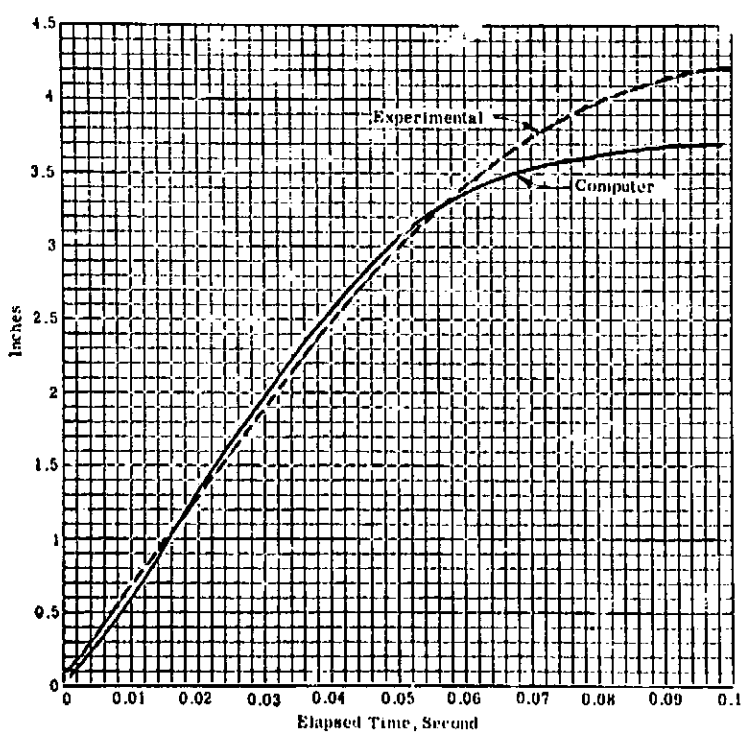

c) Footpad Penetration - d

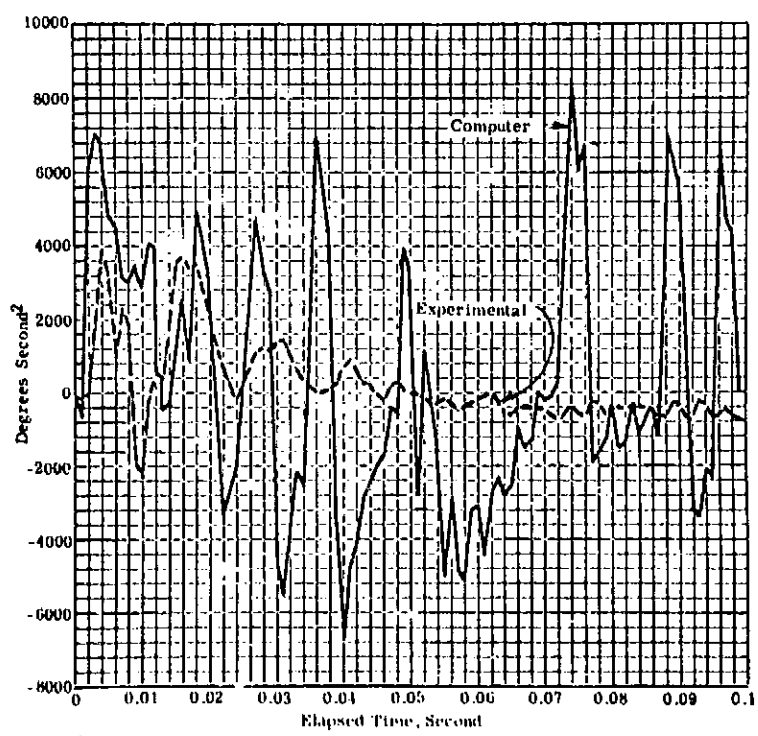

d) Vehicle Pitch Acceleration - $\ddot{\Xi}$

Figure 6-11. Detail Correlation Results for LM Model Drop No. 2 Using Low Strut Damping in Computer Simulation (See Figure 6-10 for drop conditions) (Sheet 1 of 4)

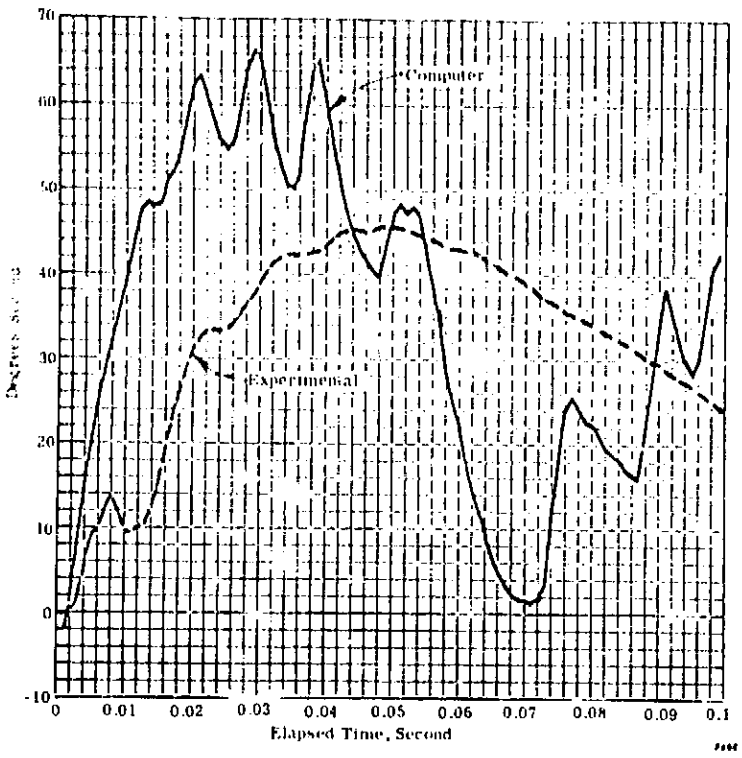

e) Vehicle Pitch Rate - $\dot{\Xi}$

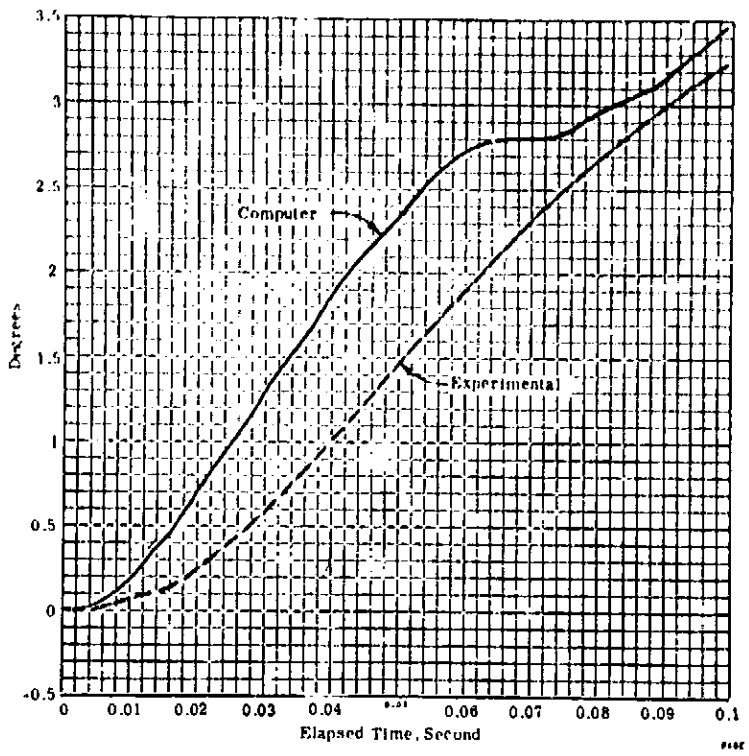

f) Vehicle Pitch Angle - Ξ

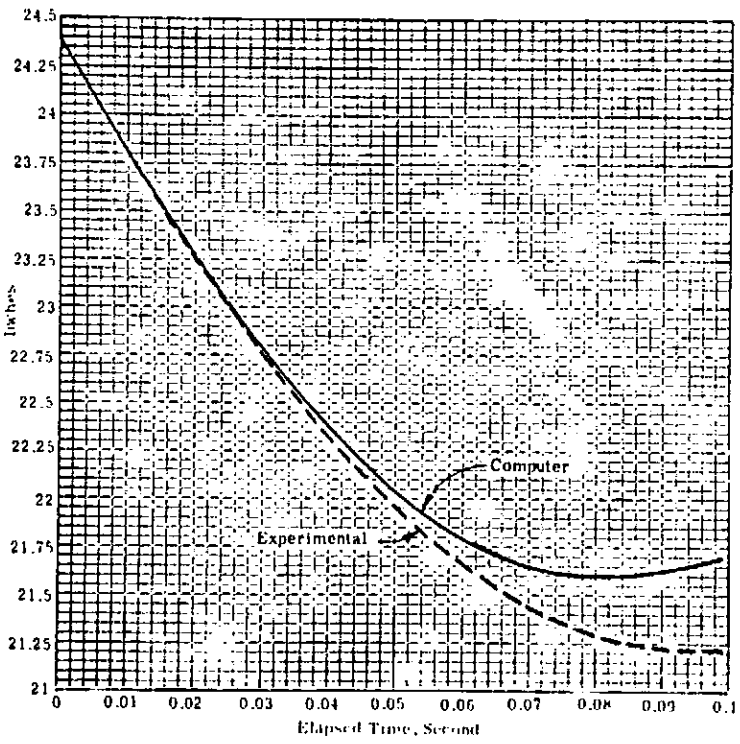

g) Vehicle c.g. Vertical Position - X

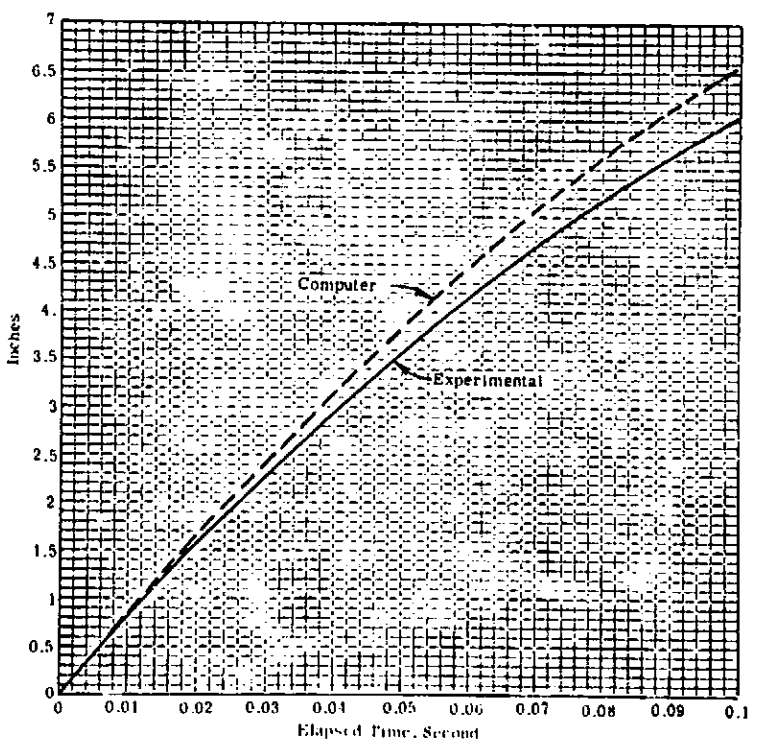

h) Vehicle c.g. Horizontal Position - Y

Figure 6-11. Detail Correlation Results for LM Model Drop No. 2 Using Low Strut Damping in Computer Simulation (See Figure 6-10 for drop conditions) (Sheet 2 of 4)

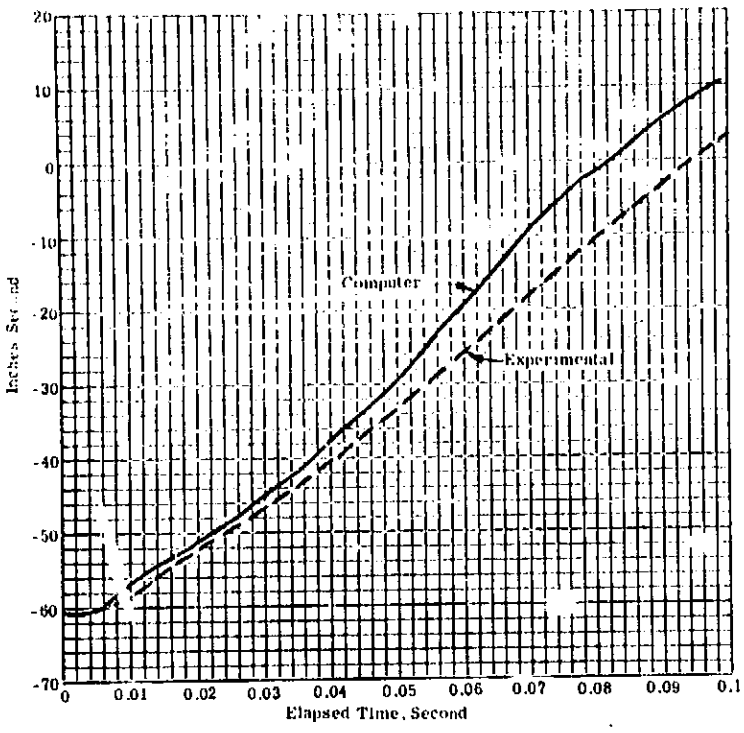

i) Vehicle c.g. Vertical Velocity - $\dot{X}$

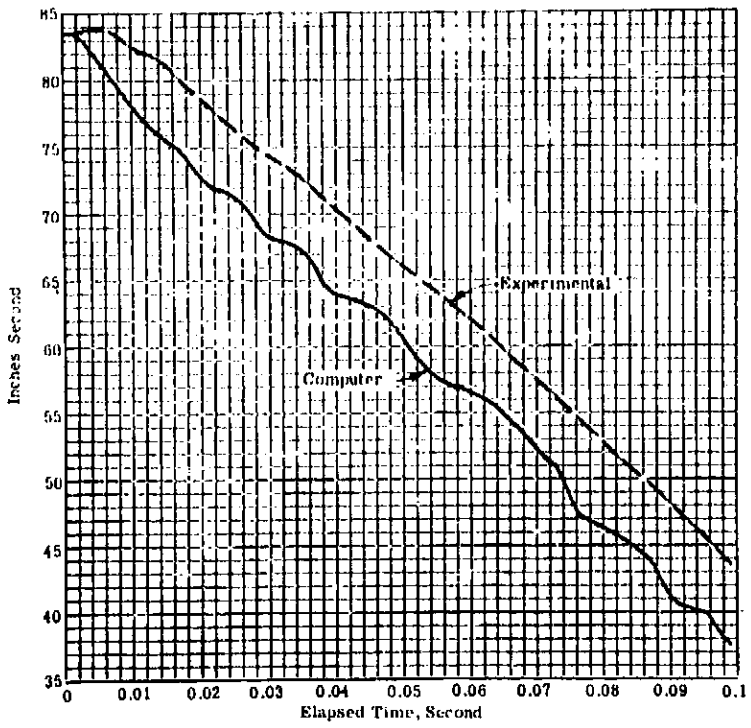

j) Vehicle c.g. Horizontal Velocity - $\dot{Y}$

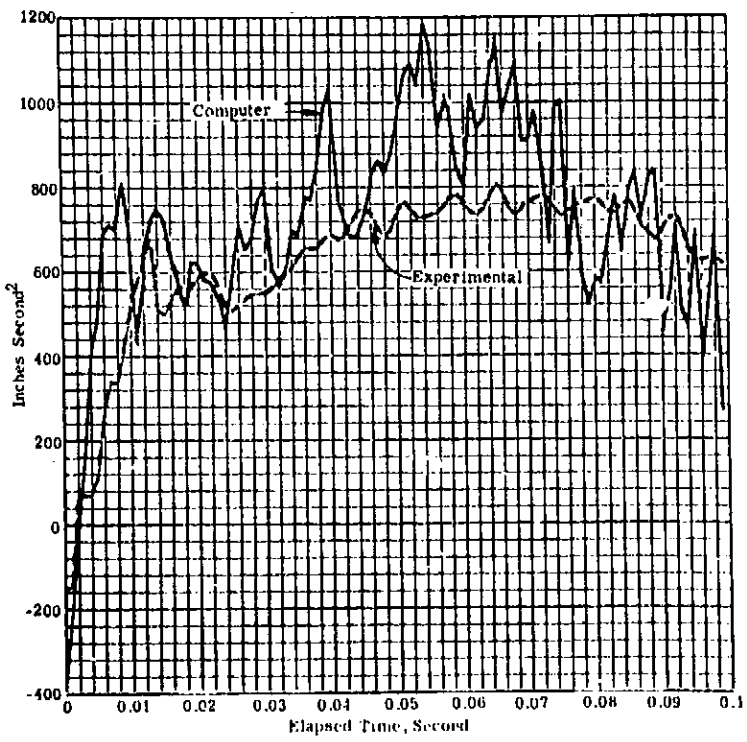

k) Vehicle c.g. Vertical Acceleration - $\ddot{X}$

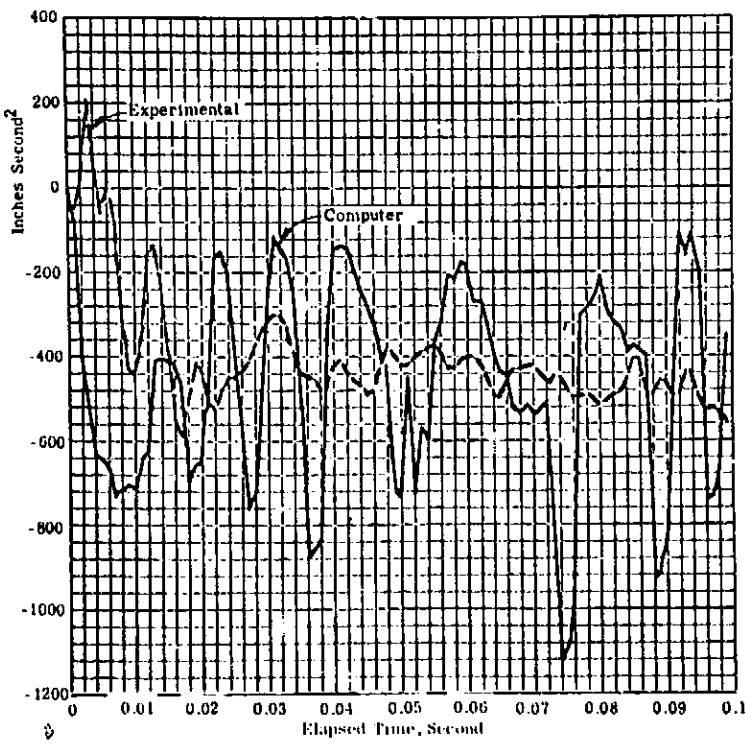

l) Vehicle c.g. Horizontal Acceleration - $\ddot{Y}$

Figure 6-11. Detail Correlation Results for LM Model Drop No. 2 Using Low Strut Damping in Computer Simulation (See Figure 6-10 for drop conditions) (Sheet 3 of 4)

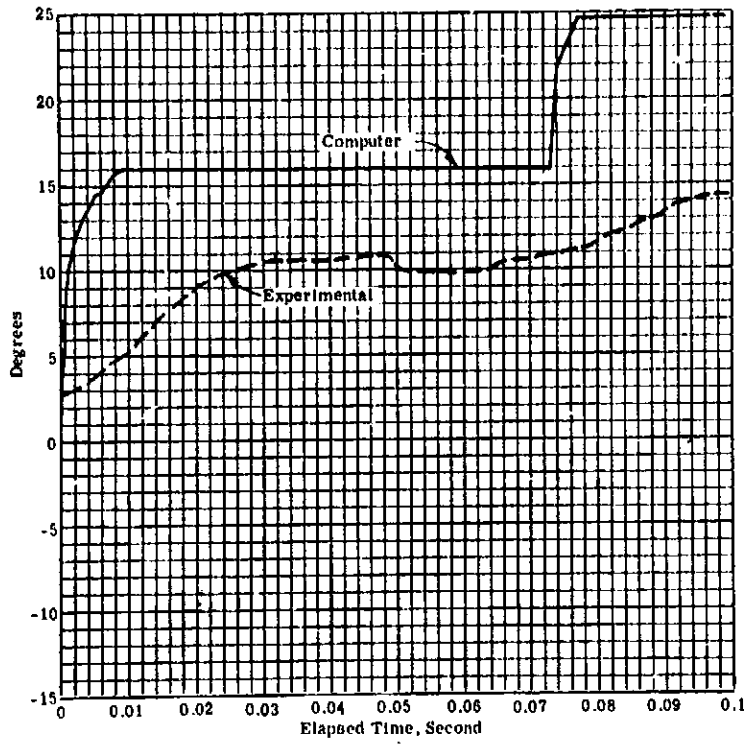

m) Footpad Pitch Angle - α

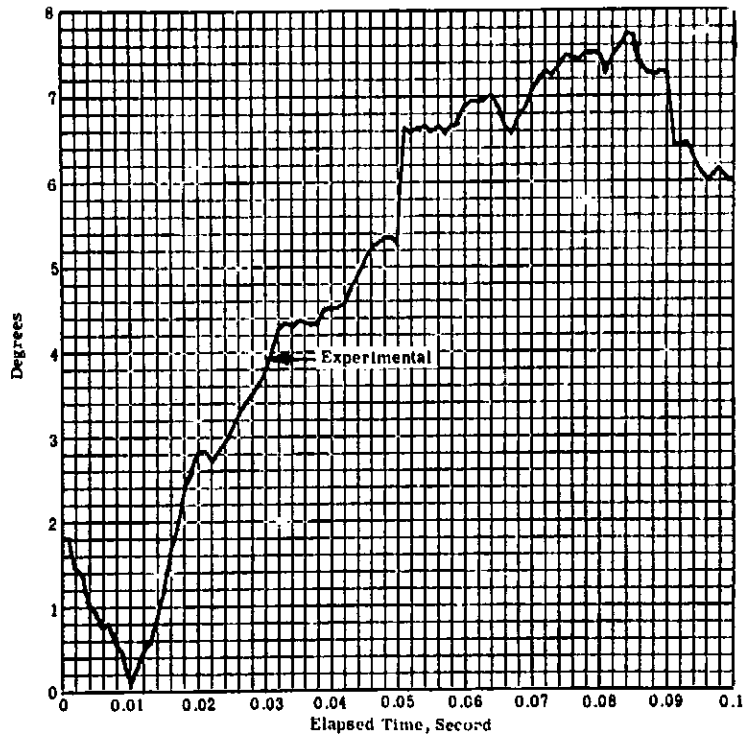

n) Footpad Roll Angle - β

Figure 6-11. Detail Correlation Results for LM Model Drop No. 2 Using Low Strut Damping in Computer Simulation (See Figure 6-10 for drop conditions) (Sheet 4 of 4)

variables. The increased damping took the form 10 $\dot{S}^{1/2}$ in the primary struts and 30 $\dot{S}^{1/2}$ in the secondary struts. These results are shown in Figures 6-12(a) through 6-12(m). The results show a marked smoothing of the variables with very little effect on the degree of correlation obtained. It is concluded from these results that the increased strut damping is desirable since the resulting computed variables more nearly resemble the experimental results and also since the smoother functions could lead to smaller integration errors and decreased computer times.

The results for the remainder of the LM model detail correlation drops, using the original strut damping (10 $\dot{S}$) in the computer model, are shown in Figures 6-13 through 6-19. The corresponding results for the higher strut damping at low stroking velocities are shown in Figures 6-20 through 6-26. These results are similar to those shown for Drop No. 2 and indicate a similar degree of correlation. In addition, these results show the degree of repeatability obtained (Drop No. 3 same as No. 1, No. 4 same as No. 2) and the correlation obtained on the more rigid soils (Drops No.'s 5 and 6).

In an attempt to provide a means of obtaining some insight into the general degree of correlation achieved in all of the detail correlation model drop tests, Figure 6-27 is presented. This figure shows the difference between calculated and experimental values for footpad penetration into the soil versus time for each of the eight tests. Although these plots do not provide a "quick look" evaluation of the correlation obtained, they do enable some sort of comparison between runs to be made and indicate the time characteristics of the correlation. It should be noted that this measure of correlation is influenced by errors in both the experimental and calculated versions of the penetration. For instance, some of the increase in the errors with time as shown in Figure 6-27 could be due to a small bias-type error in reading the model accelerometers.

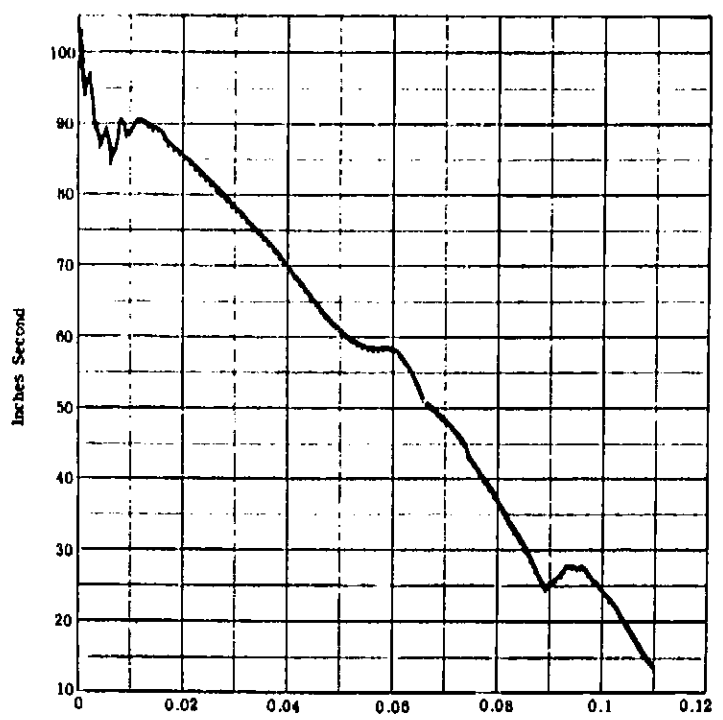

a) Footpad Velocity - V_{ap}

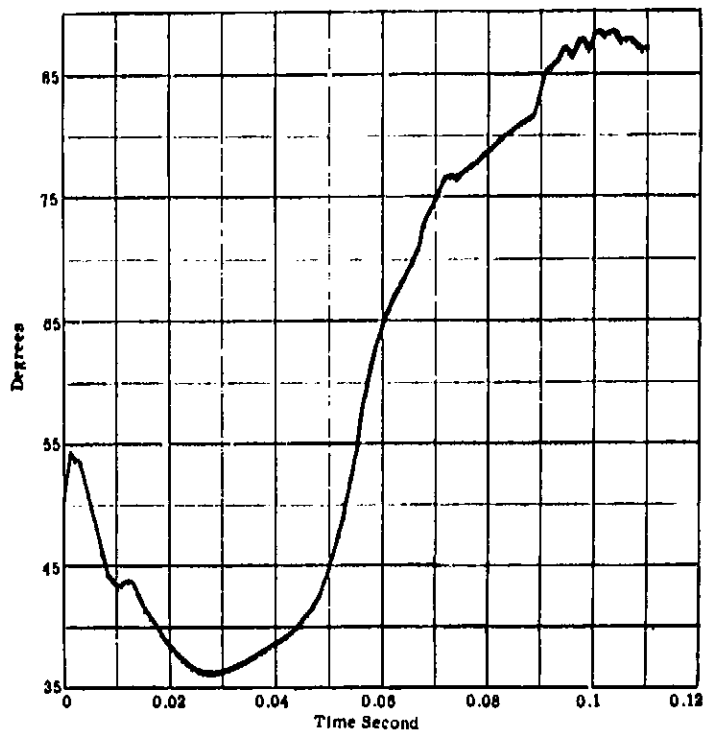

b) Footpad Velocity Angle - θ

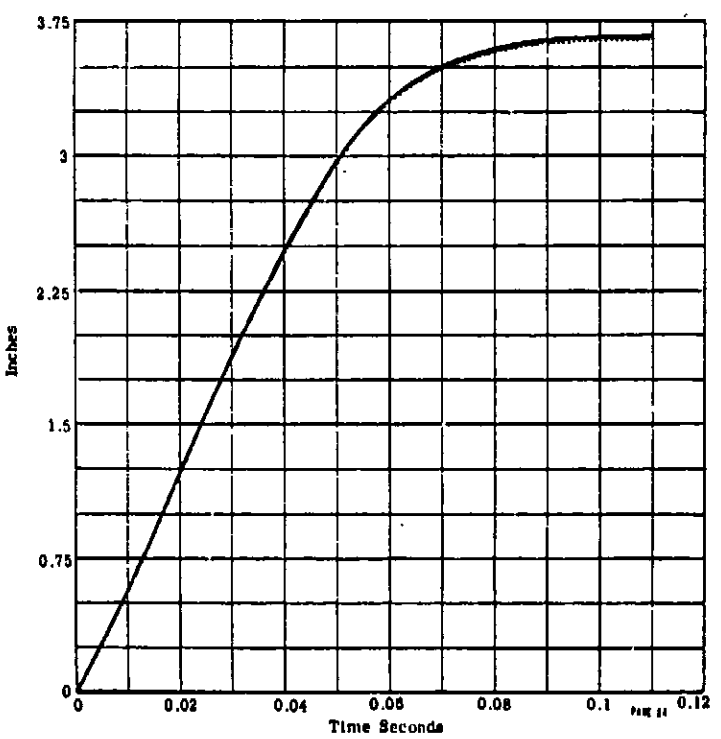

c) Footpad Penetration - d

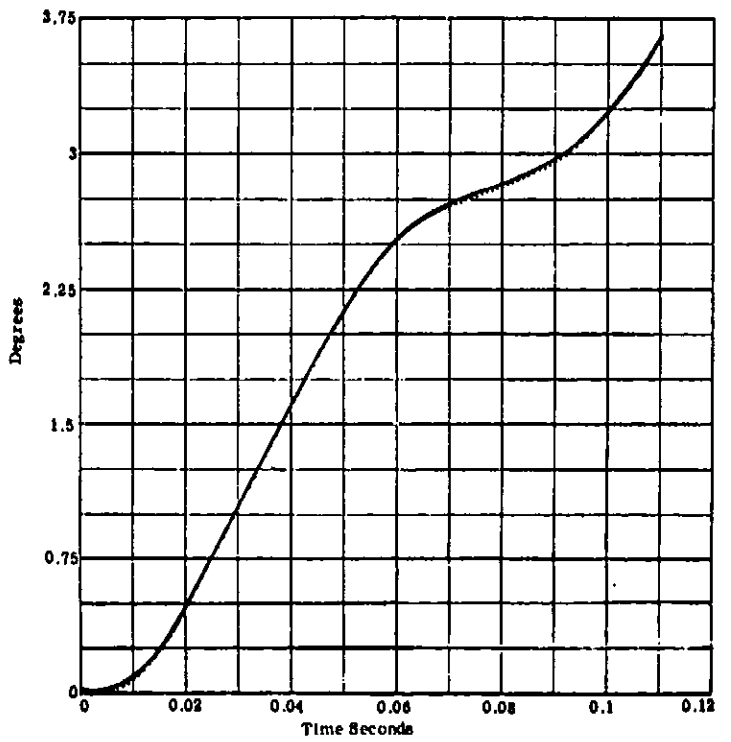

d) Vehicle Pitch Acceleration - Ξ

Figure 6-12. Computer Results for LM Model Drop No. 2 Using High Strut Damping In Simulation (See Figure 6-10 for drop conditions) (Sheet 1 of 4)

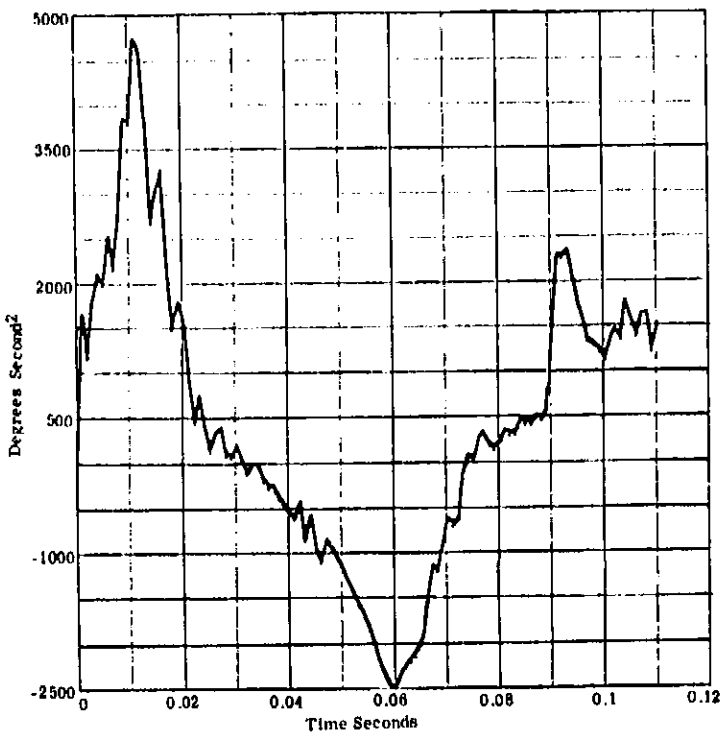

e) Vehicle Pitch Acceleration - $\ddot{\Xi}$

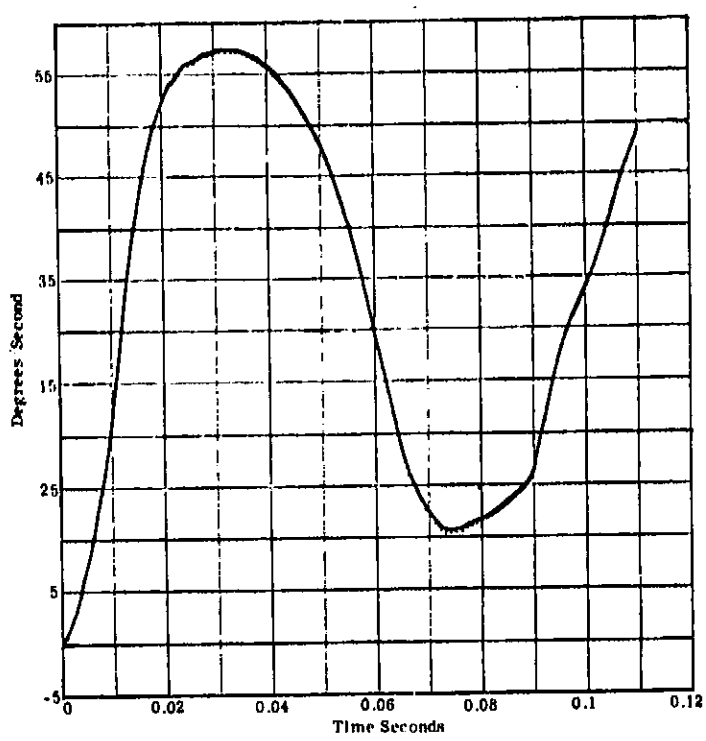

f) Vehicle Pitch Rate - $\dot{\Xi}$

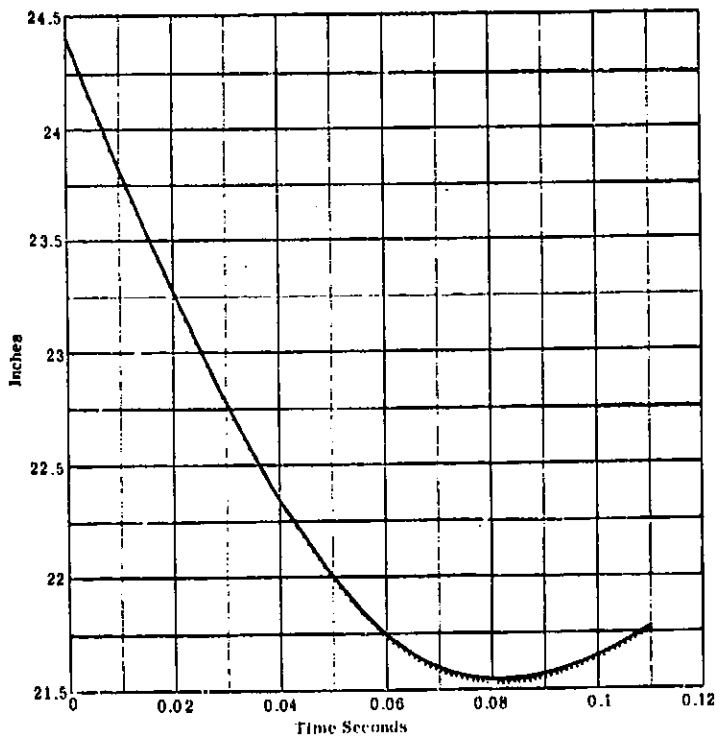

g) Vehicle c.g. Vertical Position - X

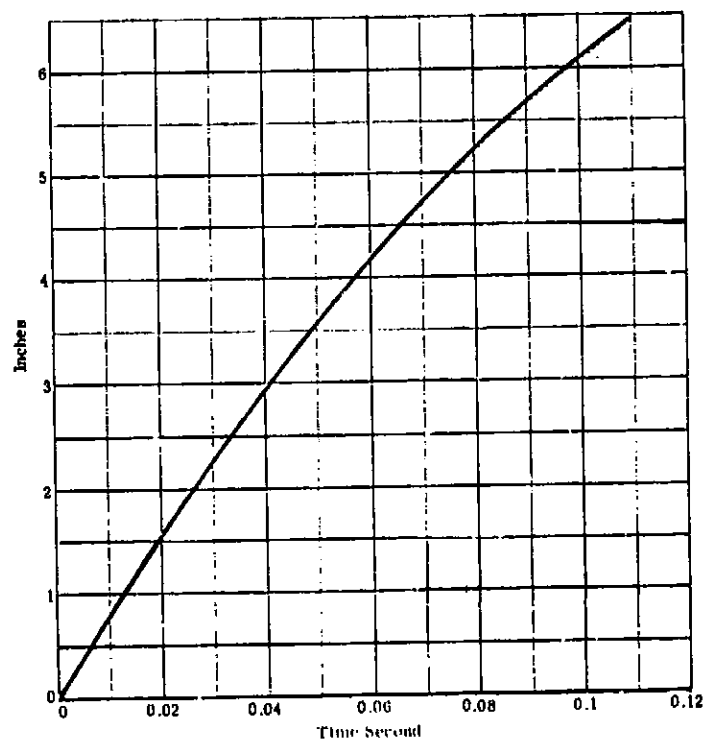

h) Vehicle c.g. Horizontal Position - Y

Figure 6-12. Computer Results for LM Model Drop No. 2 Using High Strut Damping In Simulation (See Figure 6-10 for drop conditions) (Sheet 2 of 4)

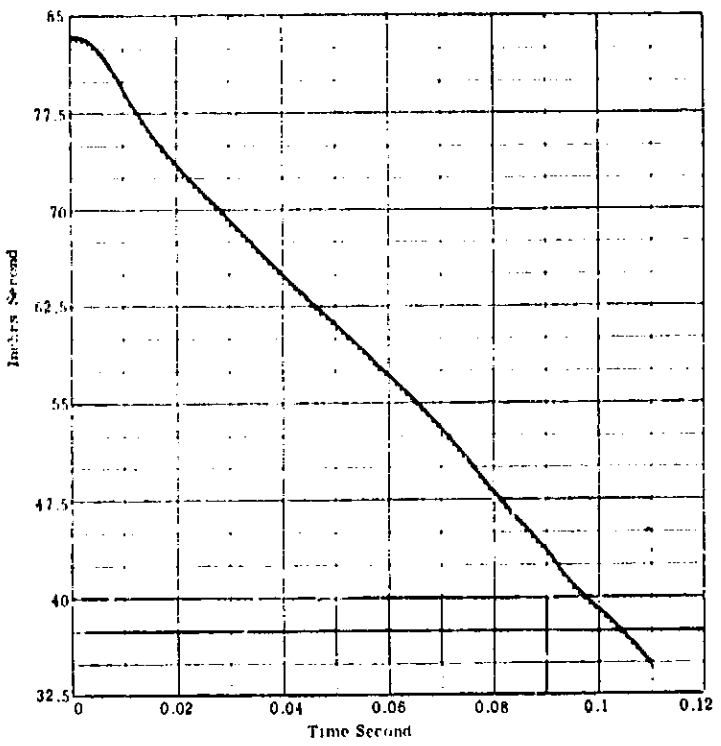

i) Vehicle c.g. Horizontal Velocity - $\dot{Y}$

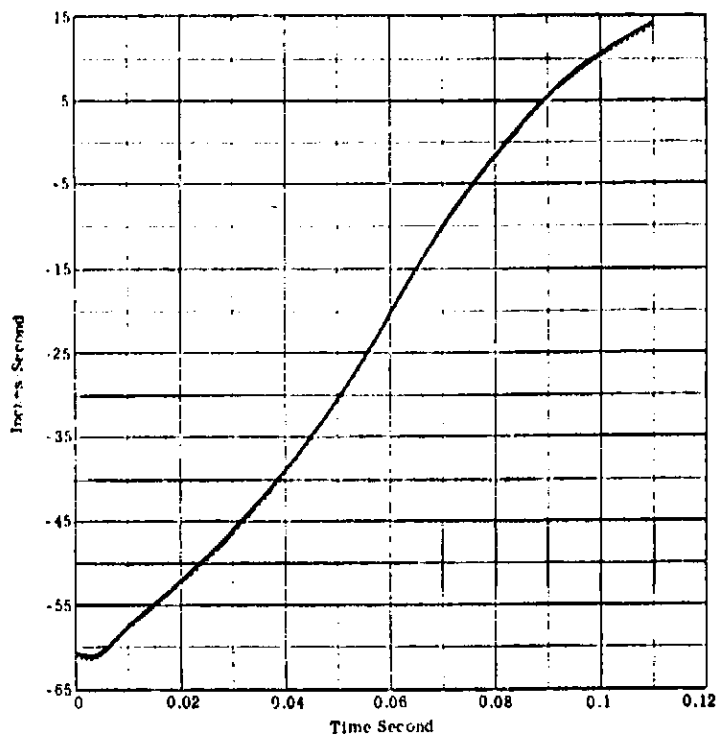

j) Vehicle c.g. Vertical Velocity - $\dot{X}$

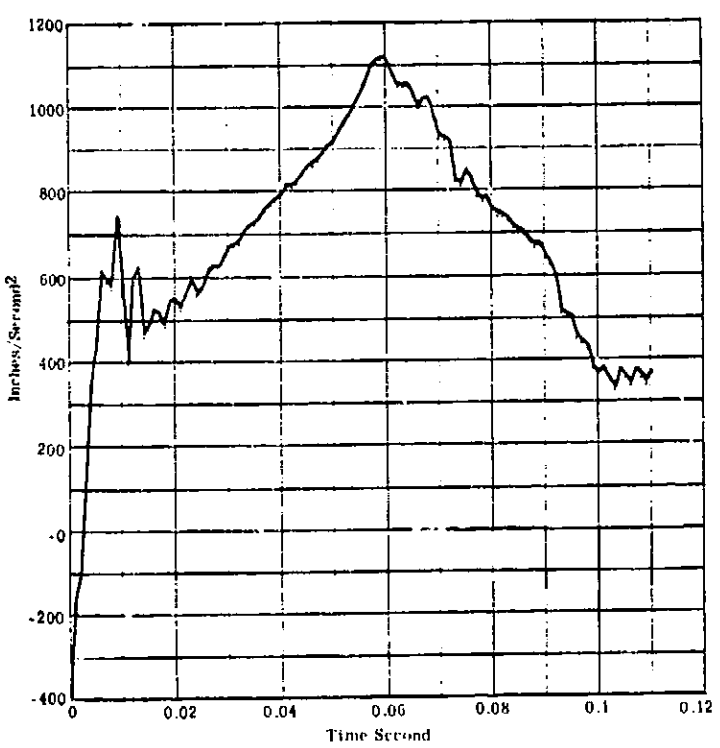

k) Vehicle c.g. Vertical Acceleration - $\ddot{X}$

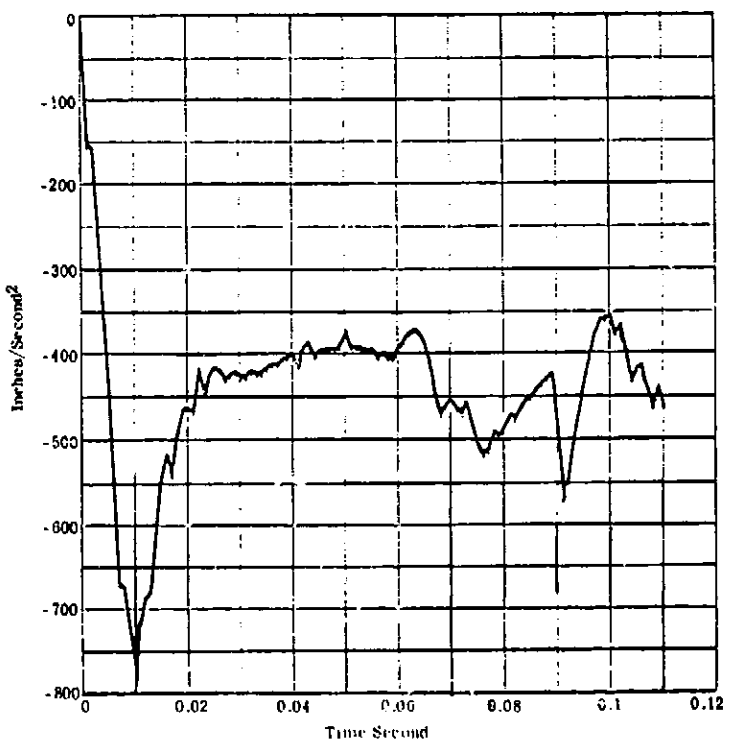

l) Vehicle c.g. Horizontal Acceleration - $\ddot{Y}$

Figure 6-12. Computer Results for LM Model Drop No. 2 Using High Strut Damping In Simulation (See Figure 6-10 for drop conditions) (Sheet 3 of 4)

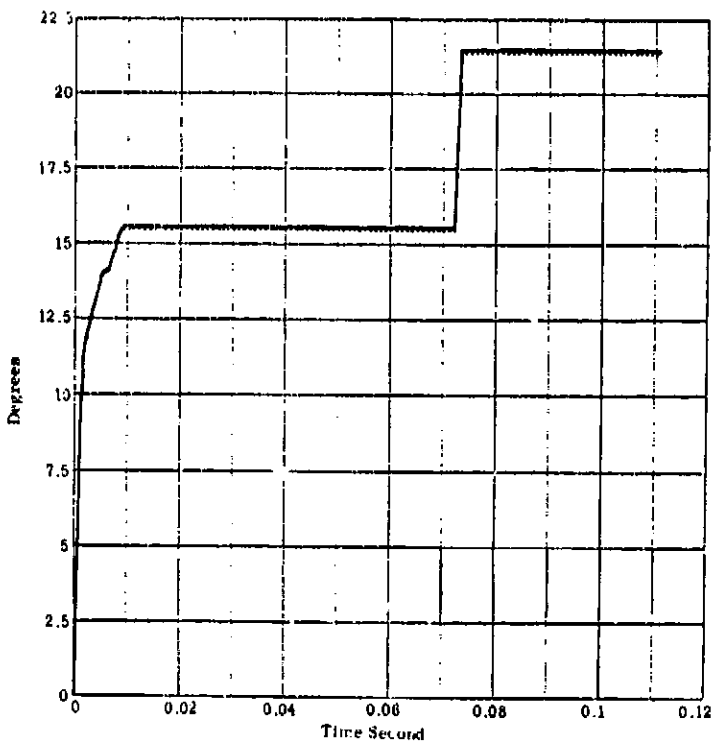

m) Footpad Pitch Angle - α

Figure 6-12. Computer Results for LM Model Drop No. 2 Using High Strut Damping In Simulation (See Figure 6-10 for drop conditions) (Sheet 4 of 4)

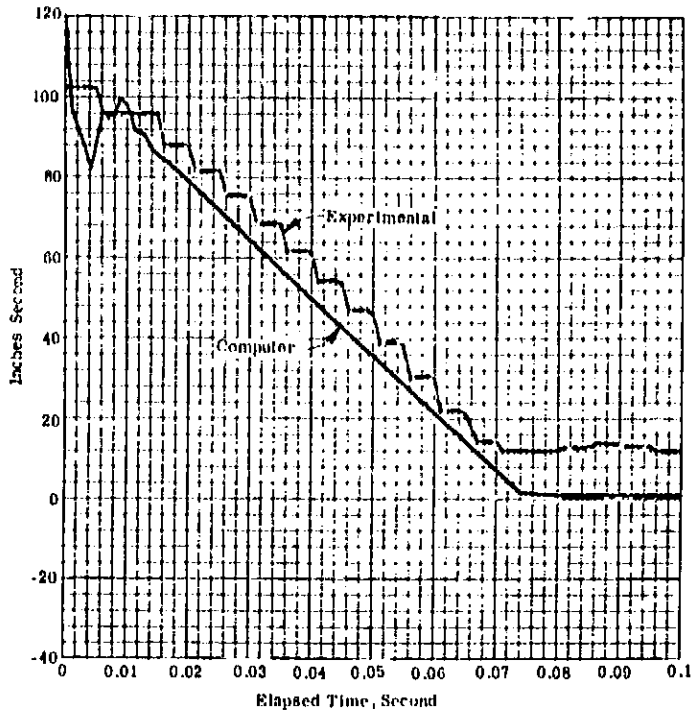

a) Footpad Velocity - V_{ap}

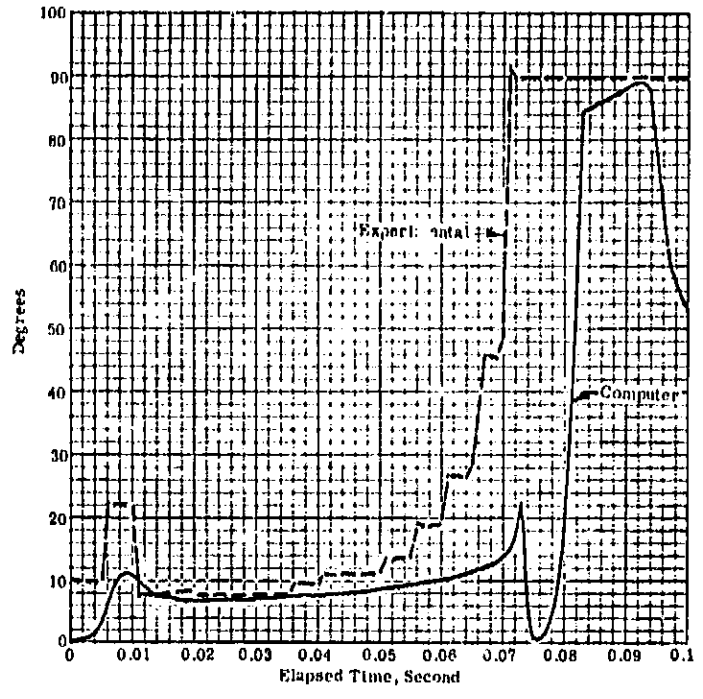

b) Footpad Velocity Angle - θ

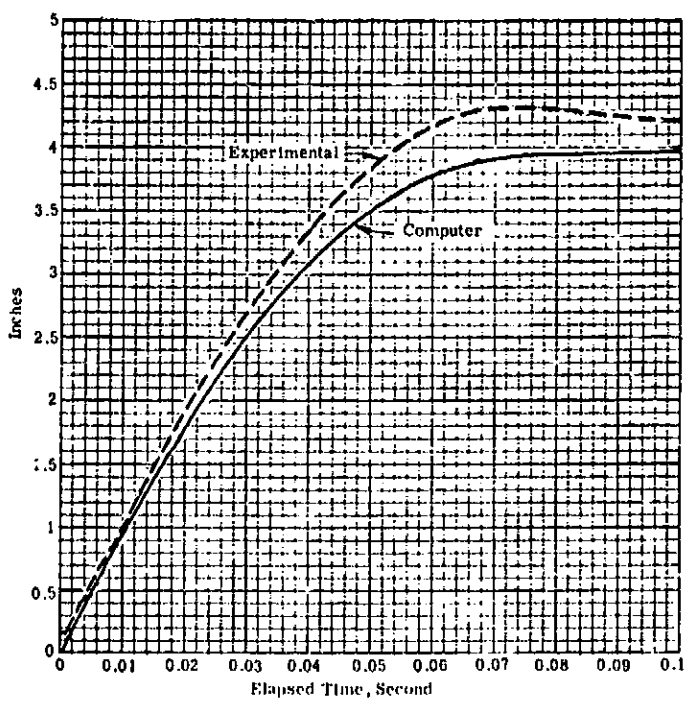

c) Footpad Penetration - d

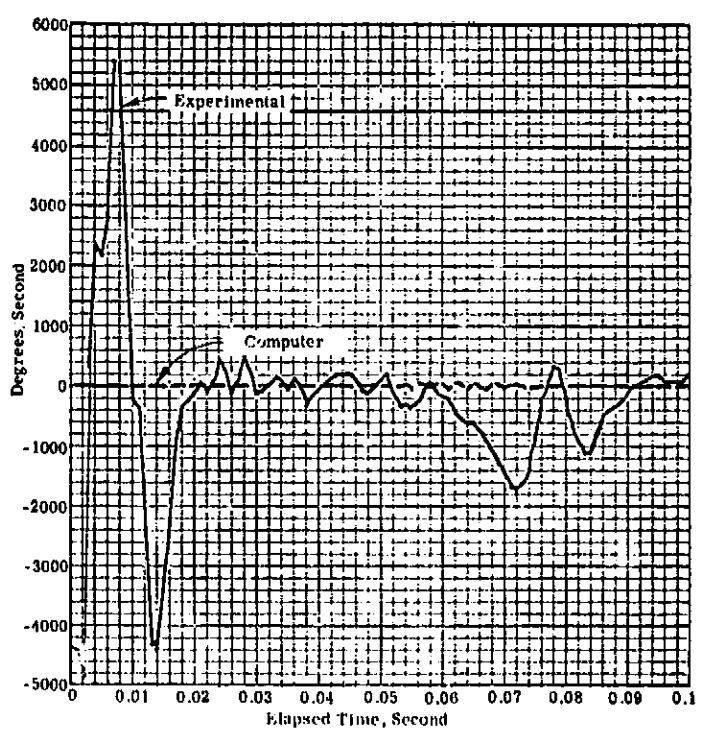

d) Vehicle Pitch Acceleration - $\ddot{\Xi}$

Figure 6-13. Detail Correlation Results For LM Model Drop No. 1 Using Low Strut Damping in Computer Simulation (See Figure 6-10 for drop conditions) (Sheet 1 of 4)

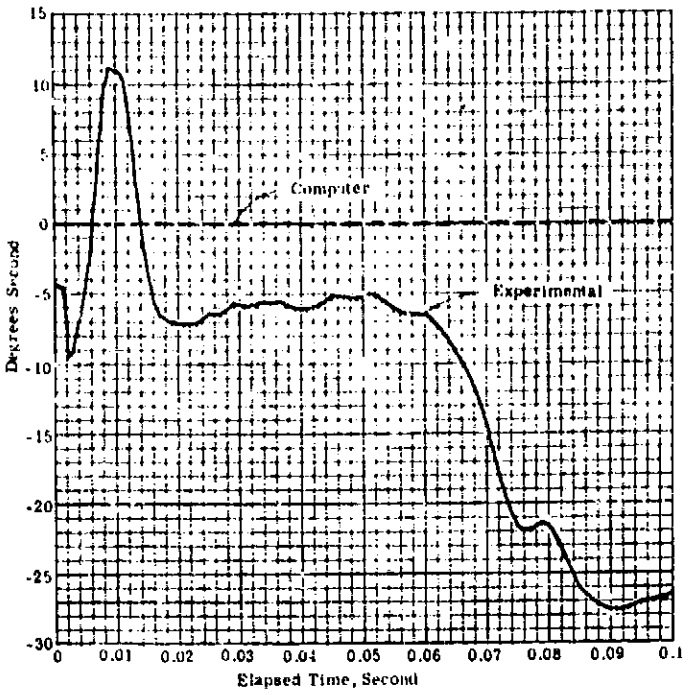

e) Vehicle Pitch Rate - $\dot{\Xi}$

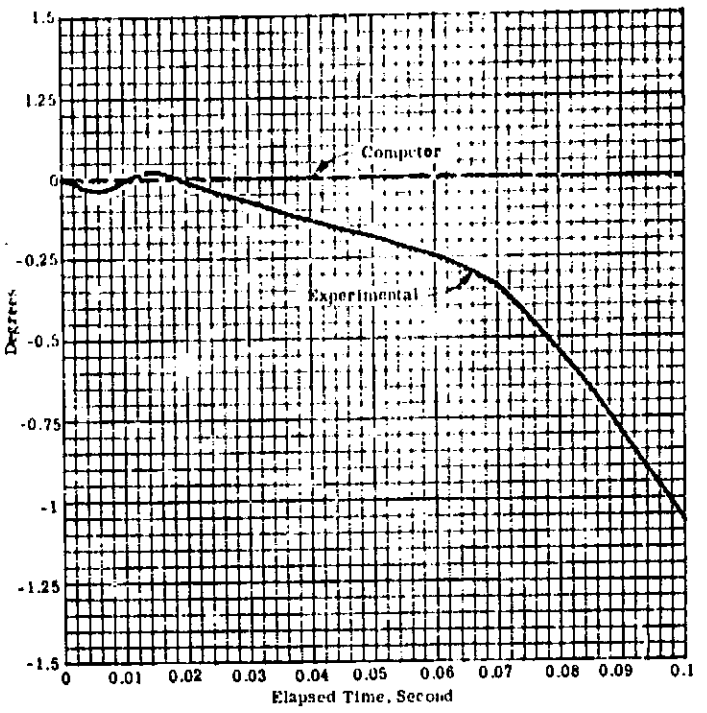

f) Vehicle Pitch Angle - Ξ

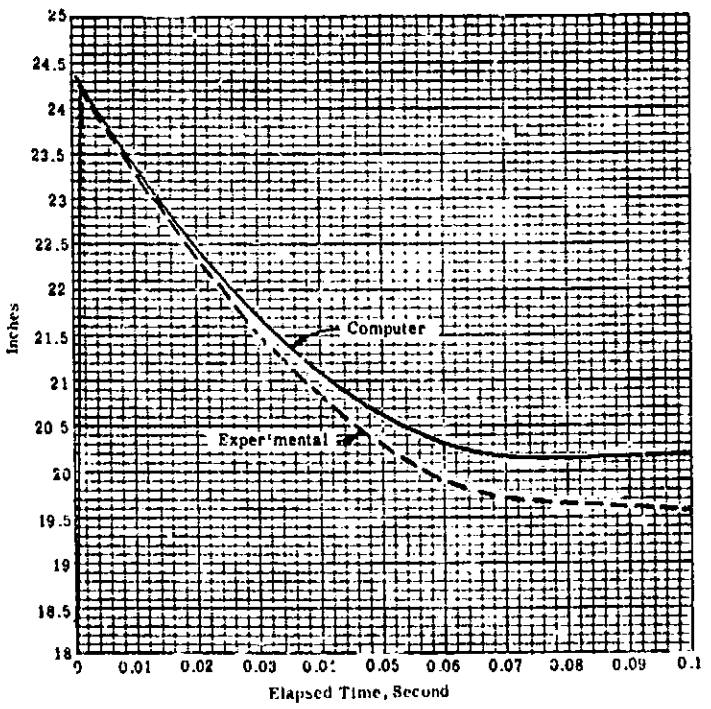

g) Vehicle c.g. Vertical Position - X

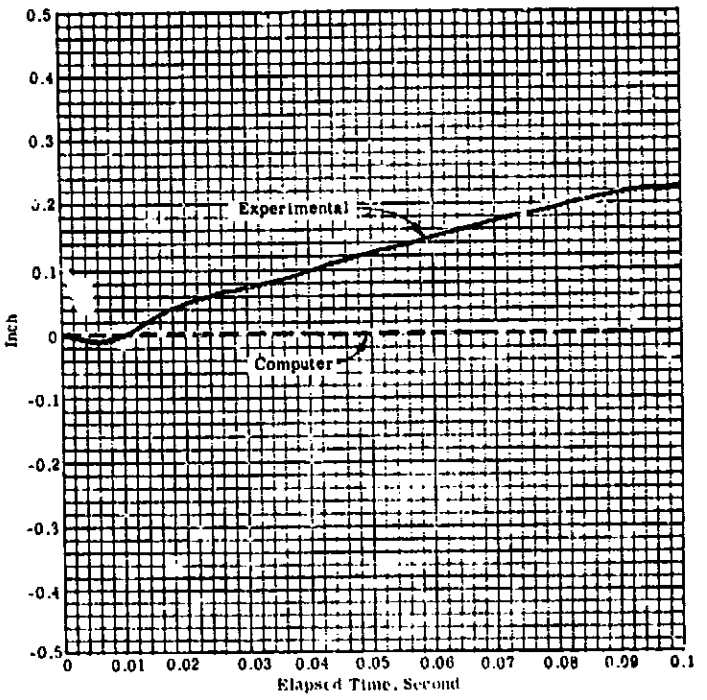

h) Vehicle c.g. Horizontal Position - Y

Figure 6-13. Detail Correlation Results For LM Model Drop No. 1 Using Low Strut Damping in Computer Simulation (See Figure 6-10 for drop conditions) (Sheet 2 of 4)

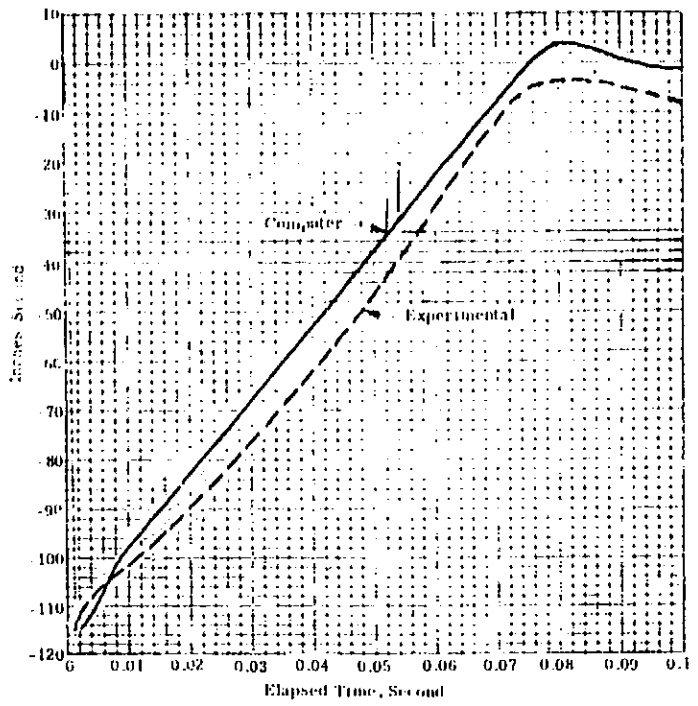

i) Vehicle c.g. Vertical Velocity - $\dot{X}$

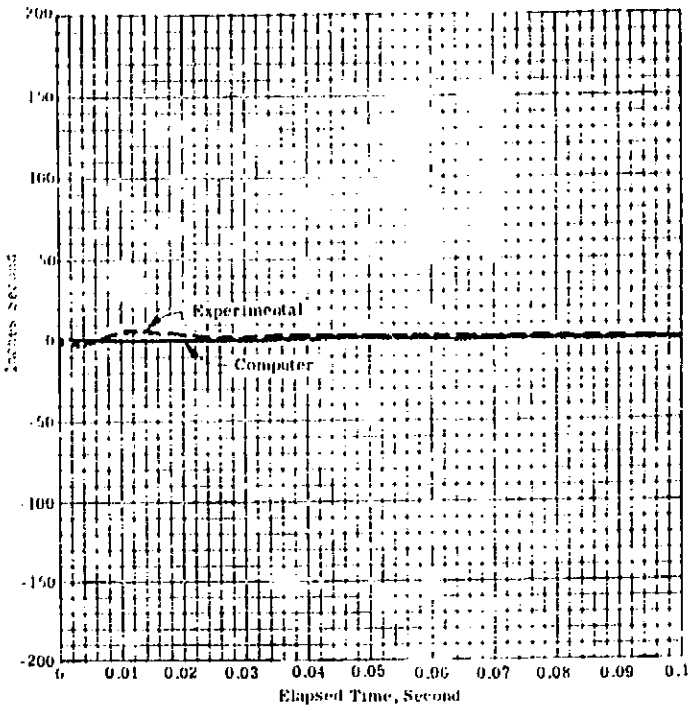

j) Vehicle c.g. Horizontal Velocity - $\dot{Y}$

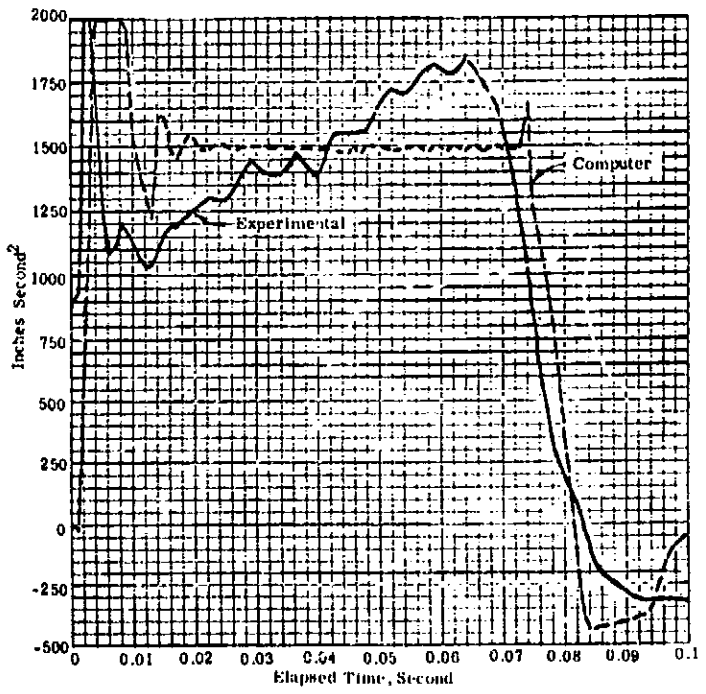

k) Vehicle c.g. Vertical Acceleration - $\ddot{X}$

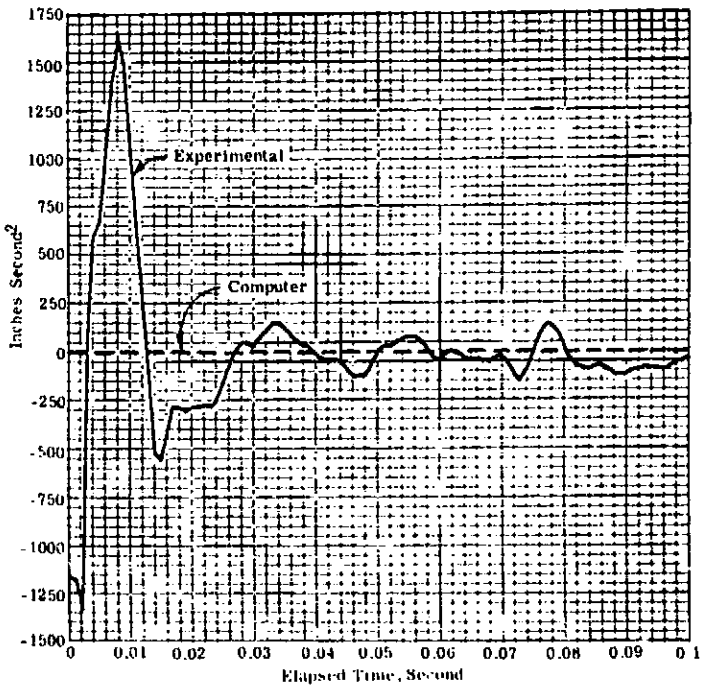

l) Vehicle c.g. Horizontal Acceleration - $\ddot{Y}$

Figure 6-13. Detail Correlation Results For LM Model Drop No. 1 Using Low Strut Damping in Computer Simulation (See Figure 6-10 for drop conditions) (Sheet 3 of 4)

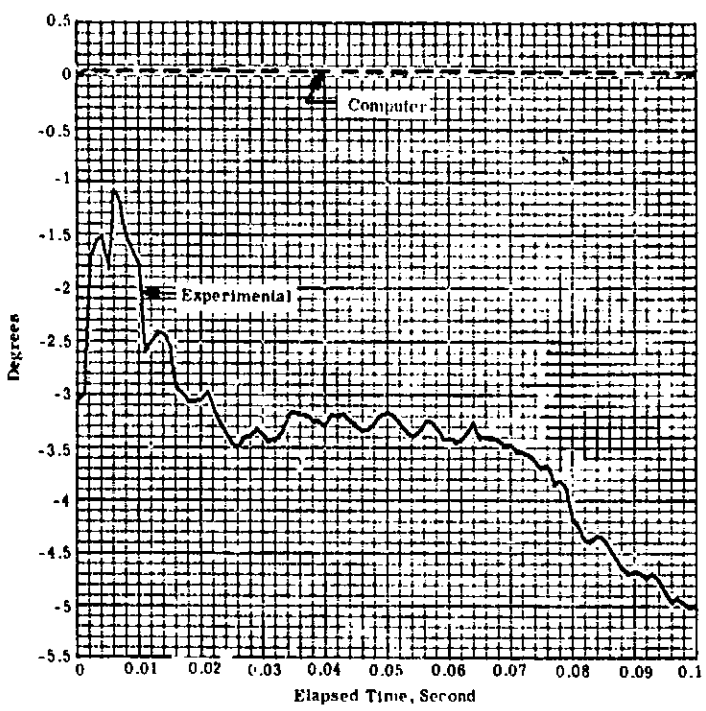

m) Footpad Pitch Angle - α

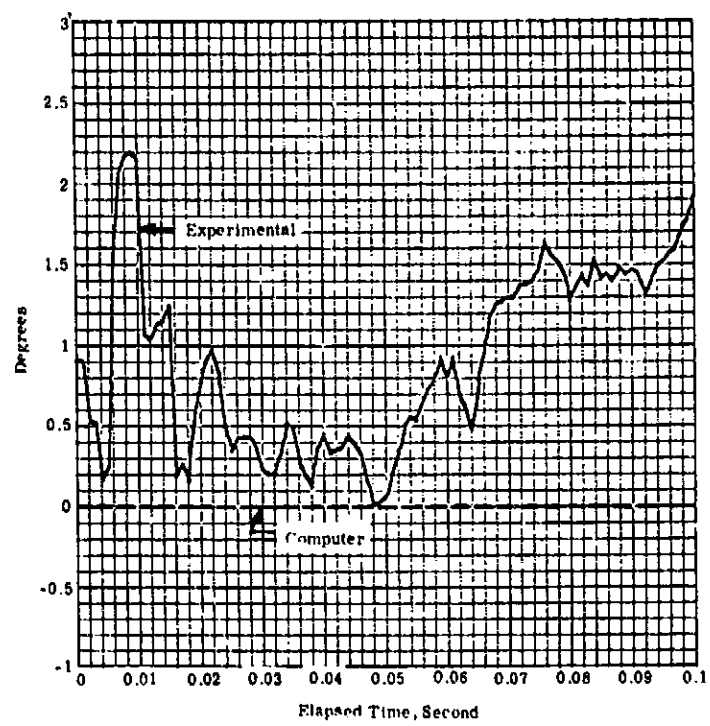

n) Footpad Roll Angle - β

Figure 6-13. Detail Correlation Results For LM Model Drop No. 1 Using Low Strut Damping in Computer Simulation (See Figure 6-10 for drop conditions) (Sheet 4 of 4)

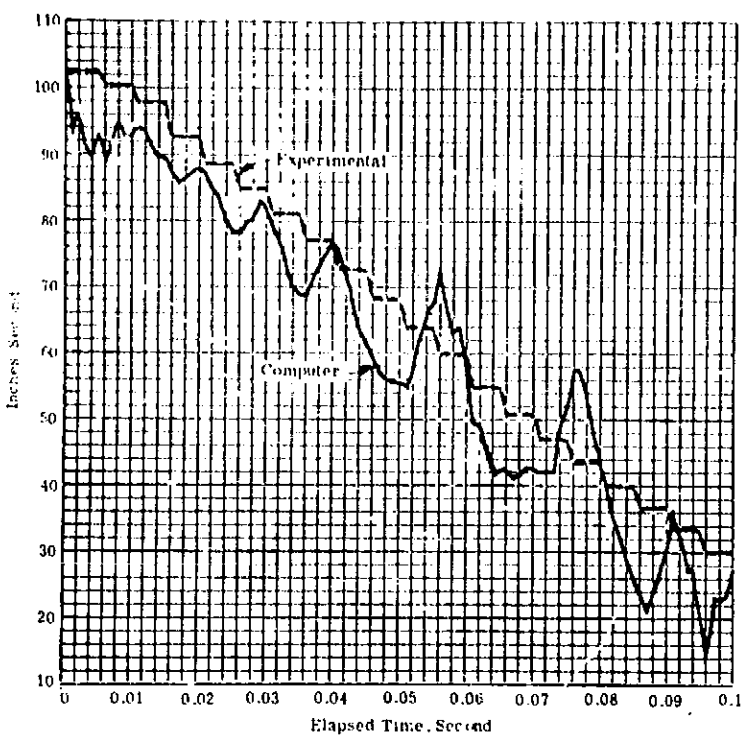

a) Footpad Velocity - V_{ap}

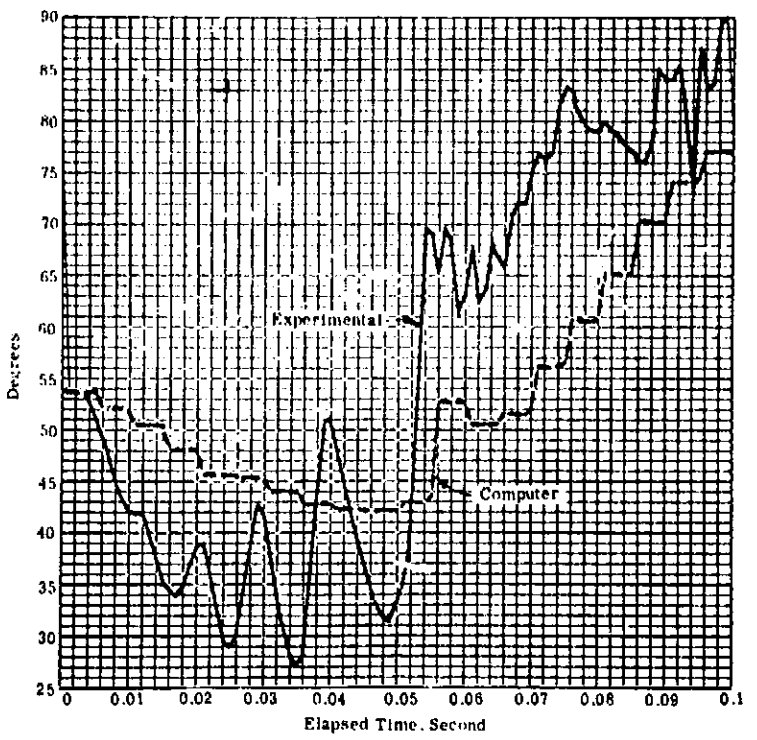

b) Footpad Velocity Angle - θ

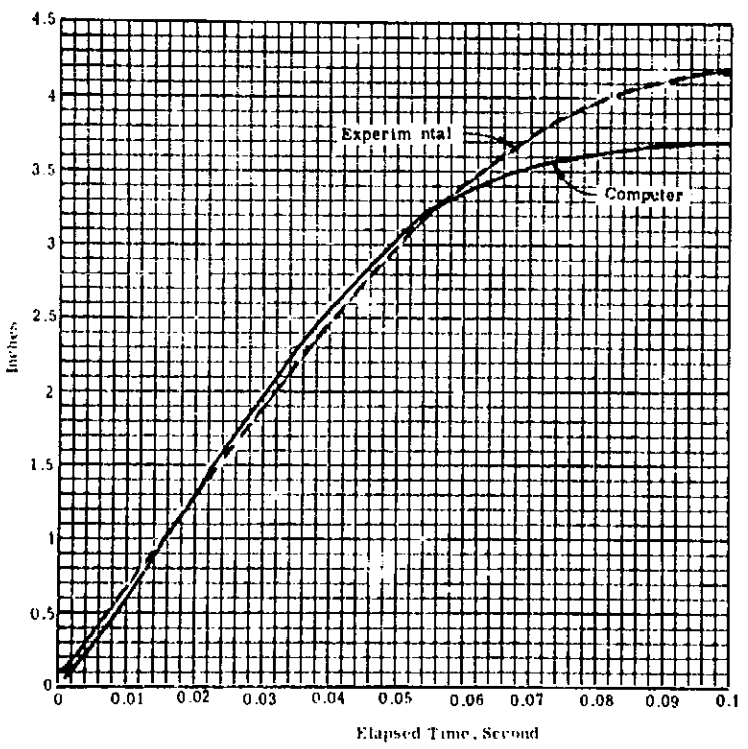

c) Footpad Penetration - d

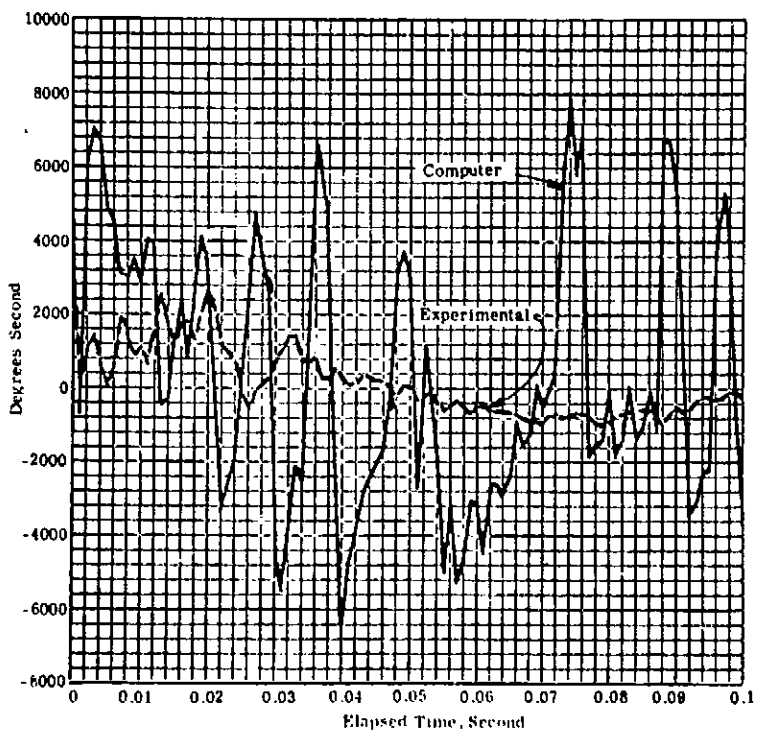

d) Vehicle Pitch Acceleration - $\ddot{\Xi}$

Figure 6-14. Detail Correlation Results For LM Model Drop No. 3 Using Low Strut Damping in Computer Simulation (See Figure 6-10 for drop conditions) (Sheet 1 of 4)

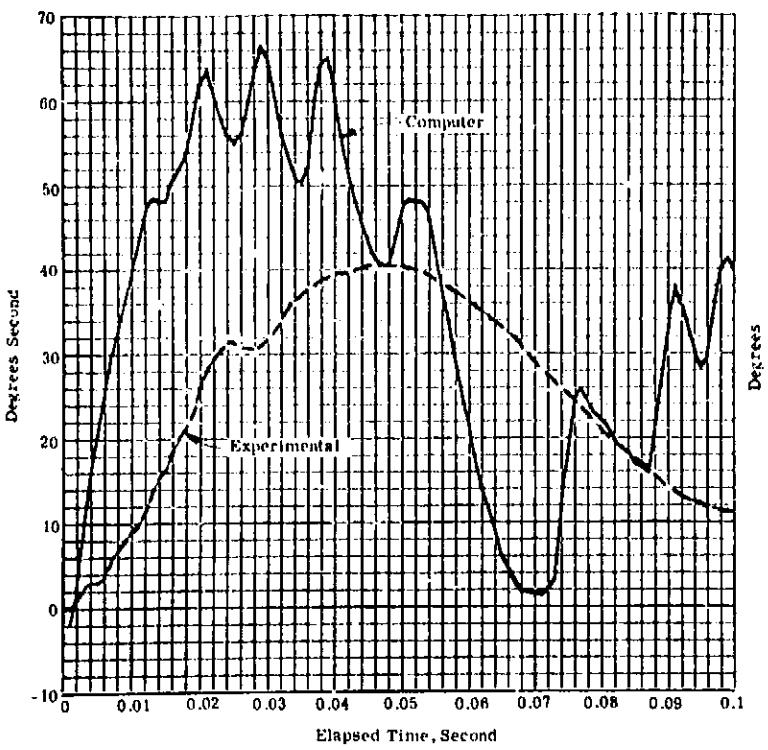

e) Vehicle Pitch Rate - $\dot{\Xi}$

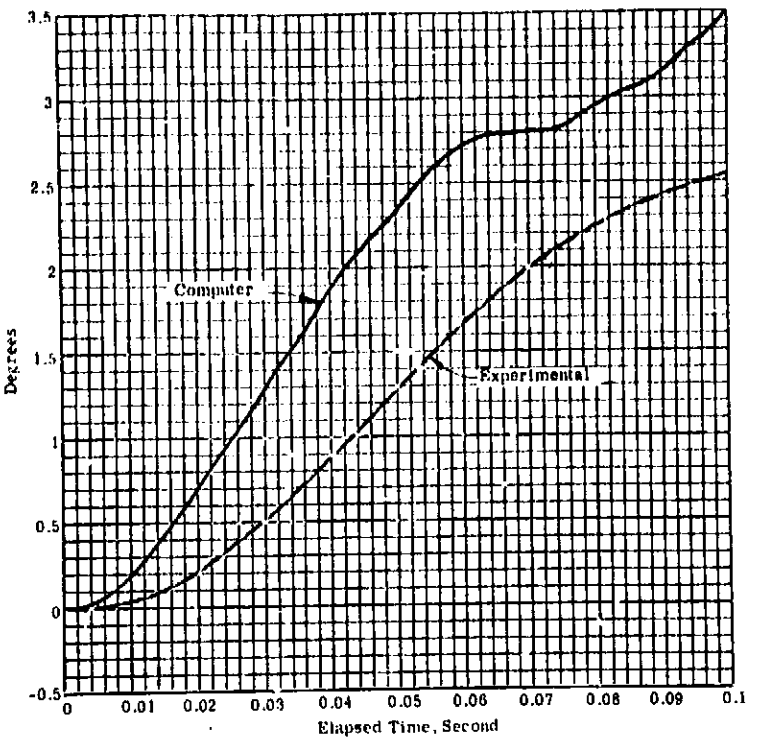

f) Vehicle Pitch Angle - Ξ

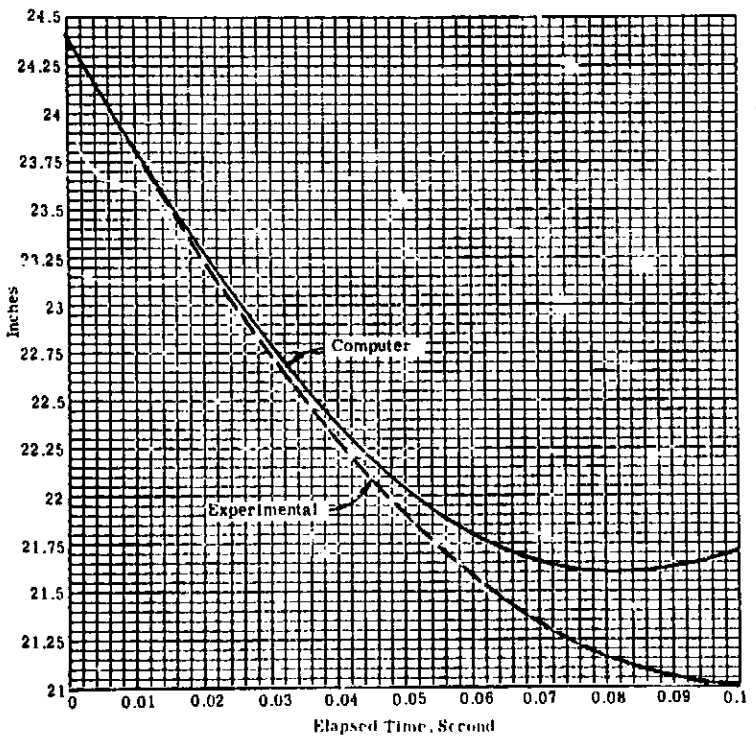

g) Vehicle c.g. Vertical Position - X

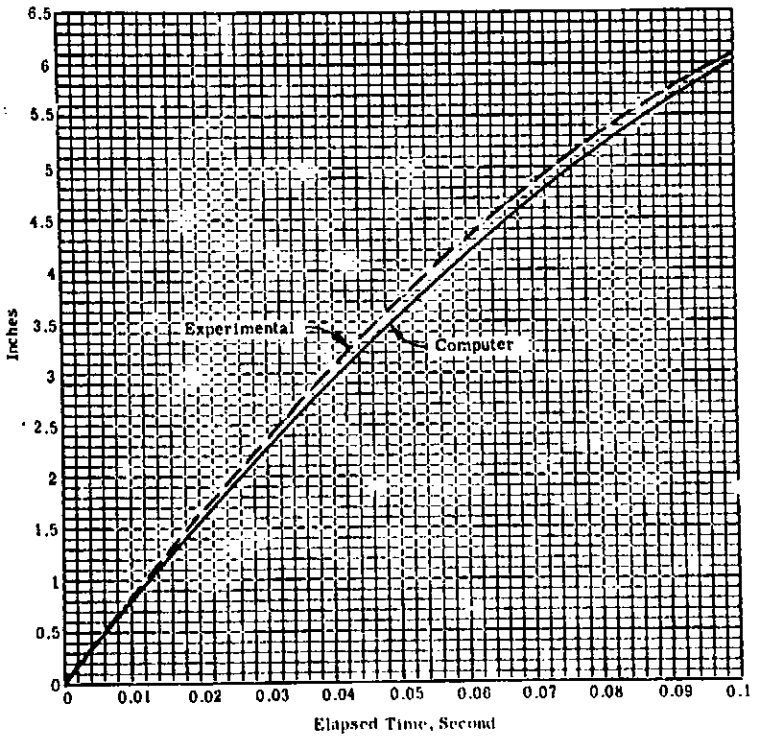

h) Vehicle c.g. Horizontal Position - Y

Figure 6-14. Detail Correlation Results For LM Model Drop No. 3 Using Low Strut Damping in Computer Simulation (See Figure 6-10 for drop conditions) (Sheet 2 of 4)

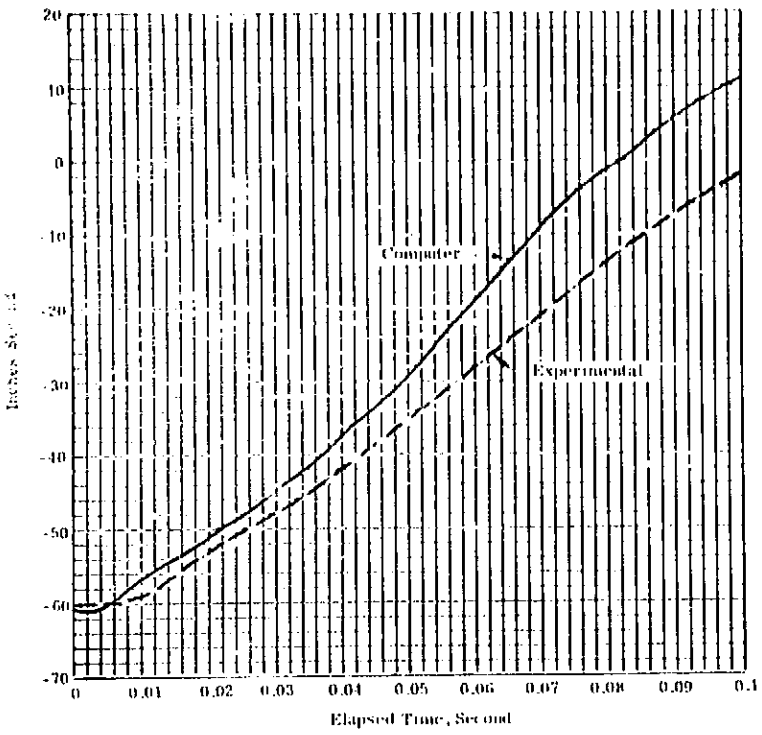

i) Vehicle c.g. Vertical Velocity - $\dot{X}$

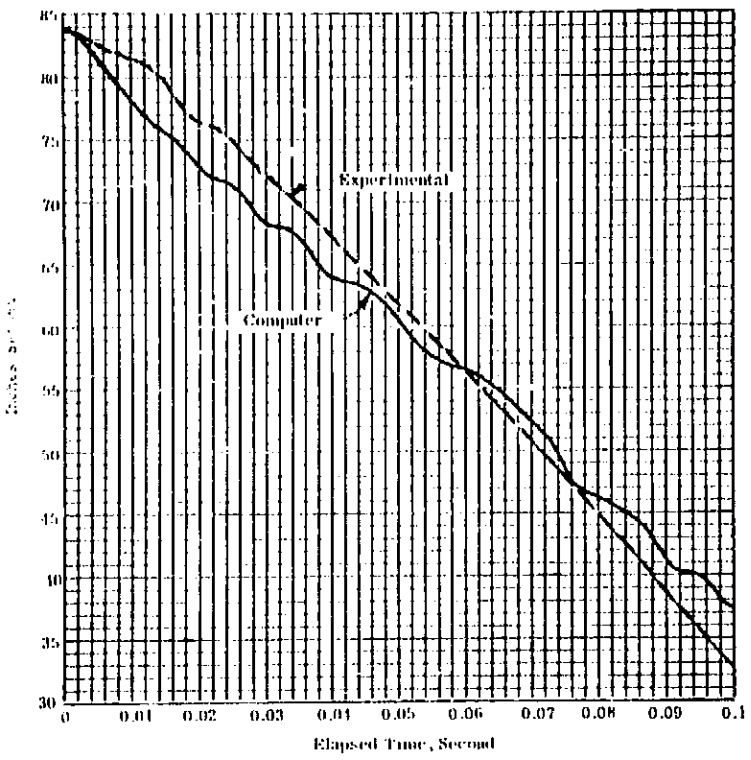

j) Vehicle c.g. Horizontal Velocity - $\dot{Y}$

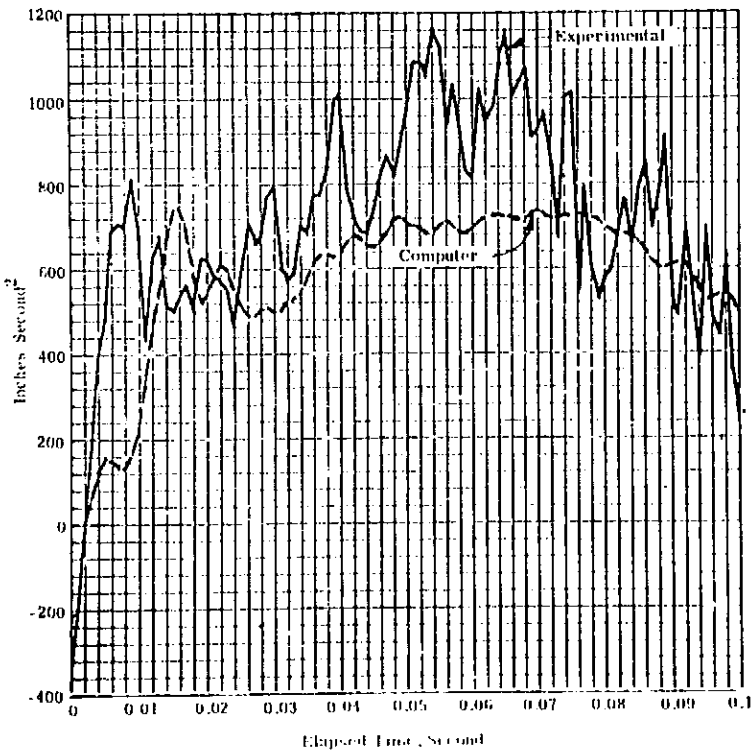

k) Vehicle c.g. Vertical Acceleration - $\ddot{X}$

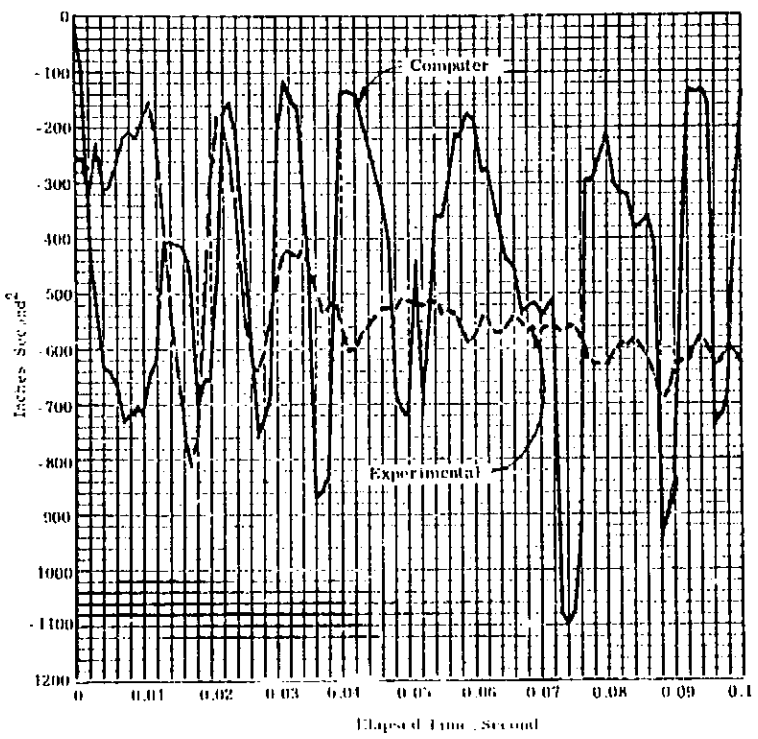

l) Vehicle c.g. Horizontal Acceleration - $\ddot{Y}$

Figure 6-14. Detail Correlation Results For LM Model Drop No. 3 Using Low Strut Damping in Computer Simulation (See Figure 6-10 for drop conditions) (Sheet 3 of 4)

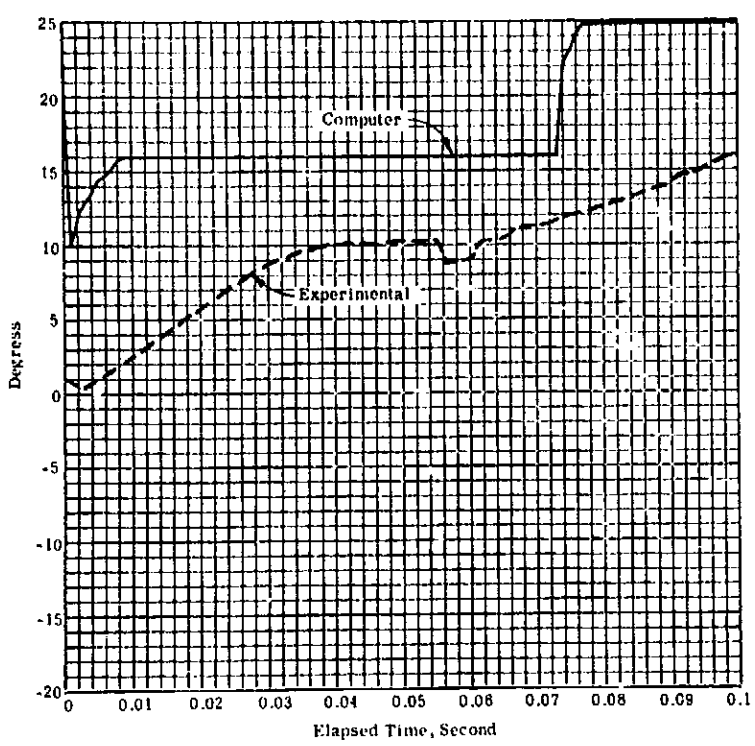

m) Footpad Pitch Angle - α

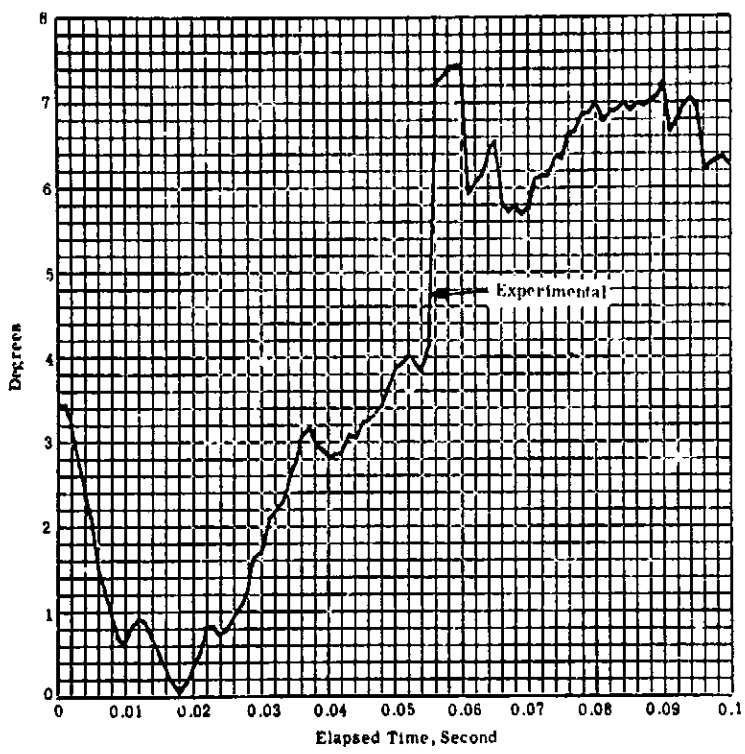

n) Footpad Roll Angle - β

Figure 6-14. Detail Correlation Results For LM Model Drop No. 3 Using Low Strut Damping in Computer Simulation (See Figure 6-10 for drop conditions) (Sheet 4 of 4)

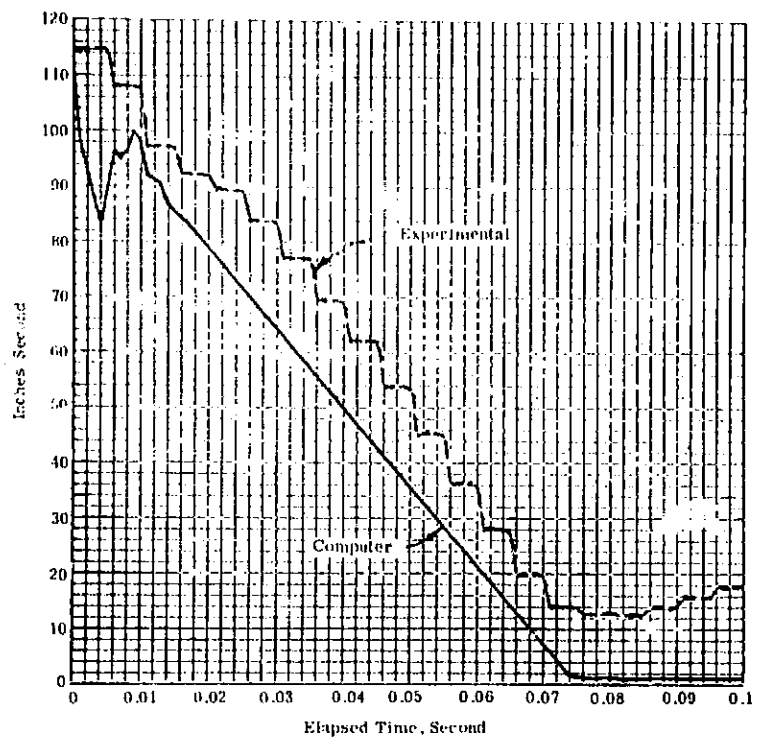

a) Footpad Velocity - V_{ap}

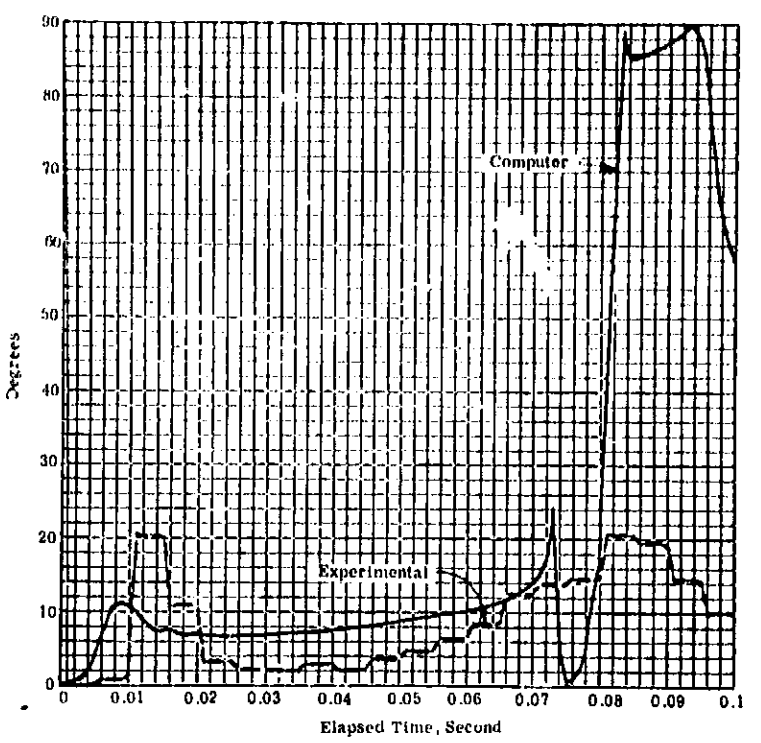

b) Footpad Velocity Angle - θ

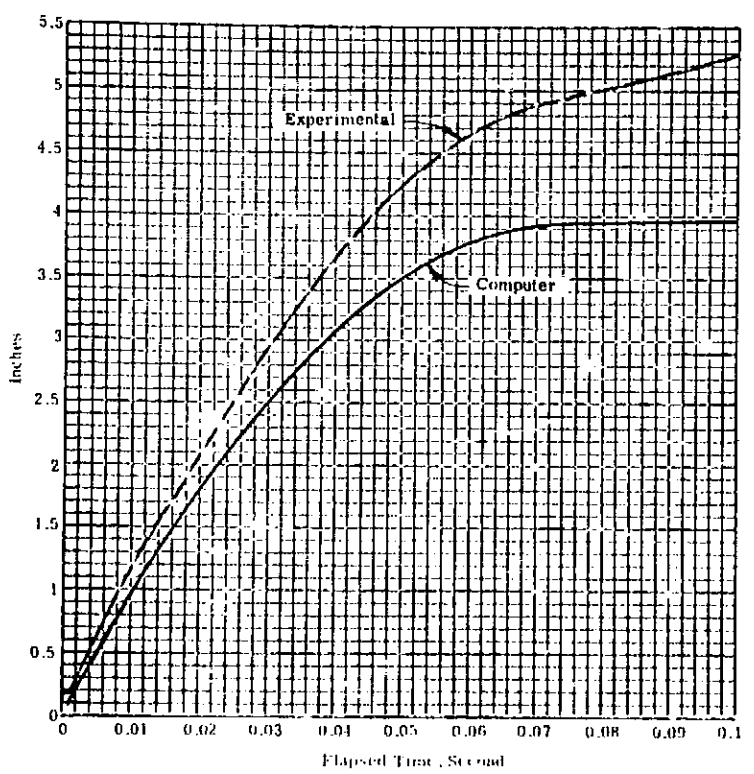

c) Footpad Penetration - d

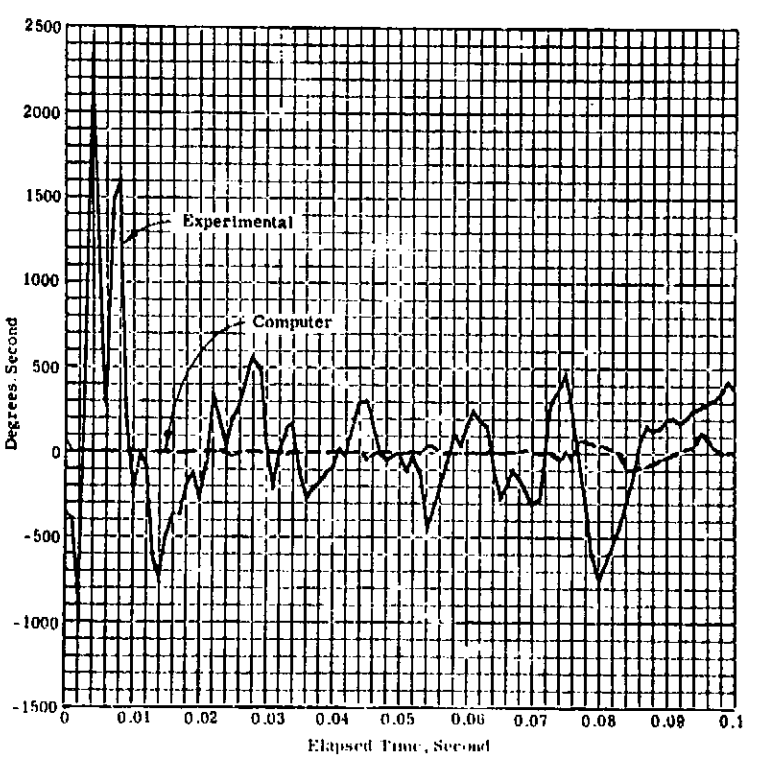

d) Vehicle Pitch Acceleration - $\ddot{\theta}$

Figure 6-15. Detail Correlation Results For LM Model Drop No. 4 Using Low Strut Damping in Computer Simulation (See Figure 6-10 for drop conditions) (Sheet 1 of 4)

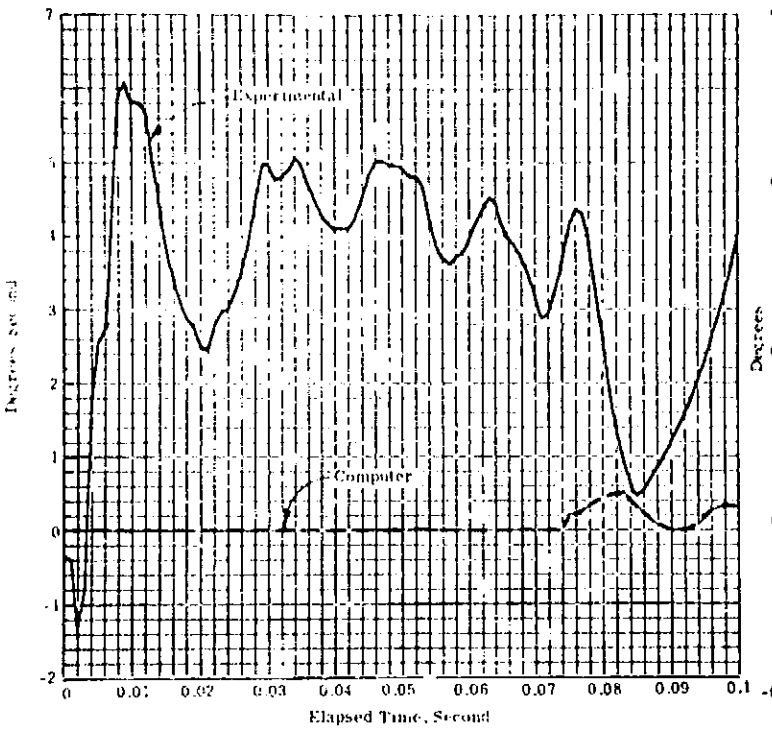

e) Vehicle Pitch Rate - $\dot{\Xi}$

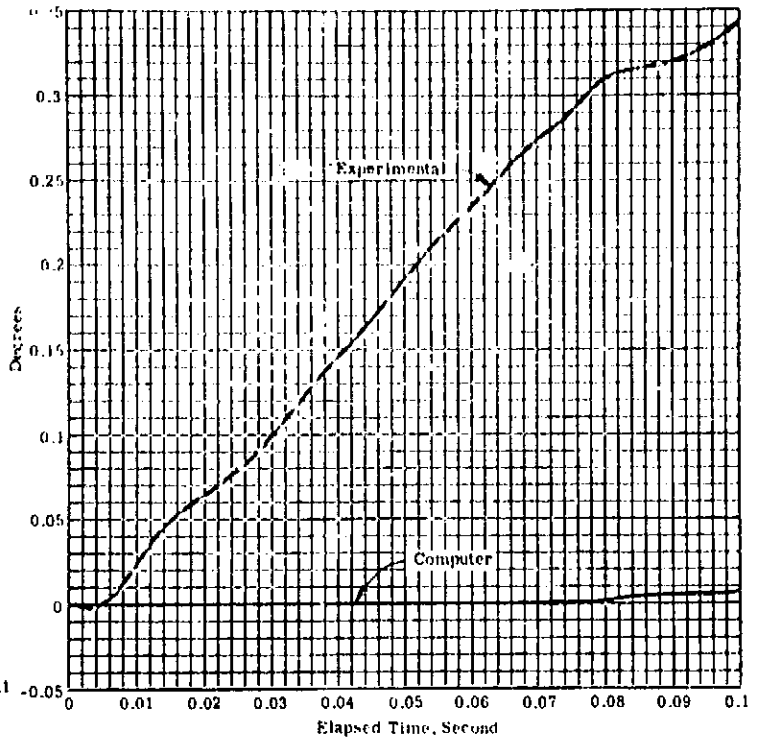

f) Vehicle Pitch Angle - Ξ

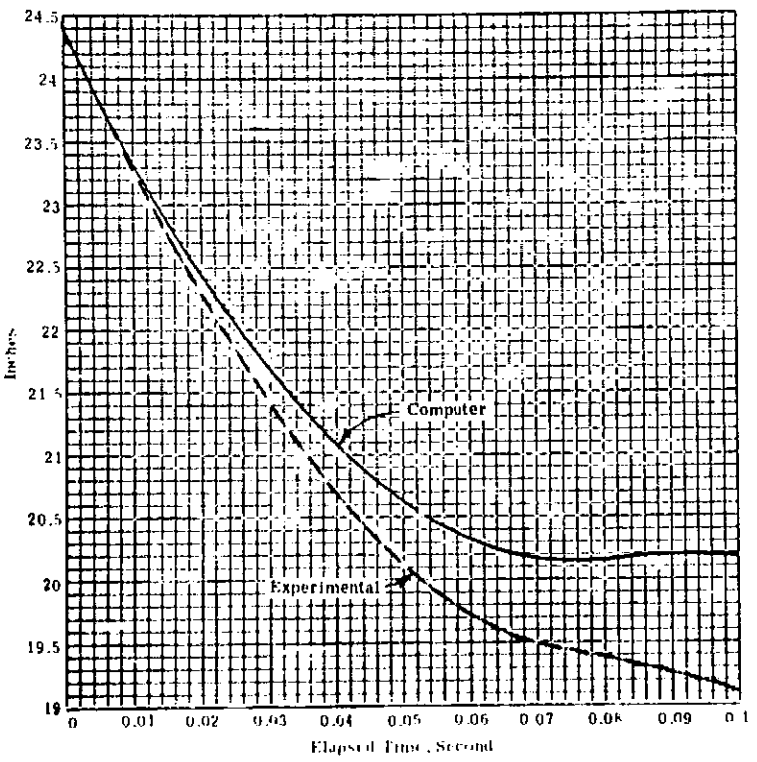

g) Vehicle c.g. Vertical Position - X

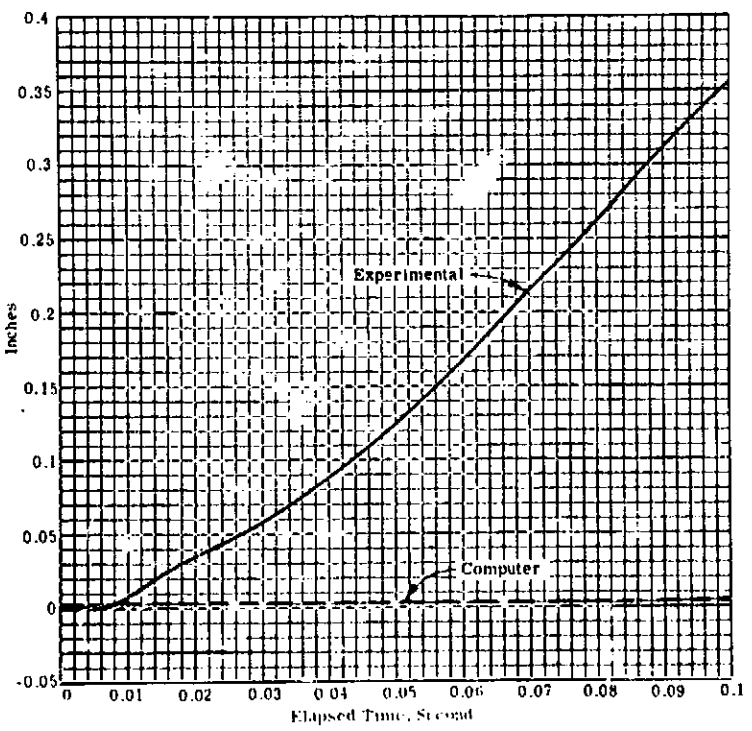

h) Vehicle c.g. Horizontal Position - Y

Figure 6-15. Detail Correlation Results For LM Model Drop No. 4 Using Low Strut Damping in Computer Simulation (See Figure 6-10 for drop conditions) (Sheet 2 of 4)

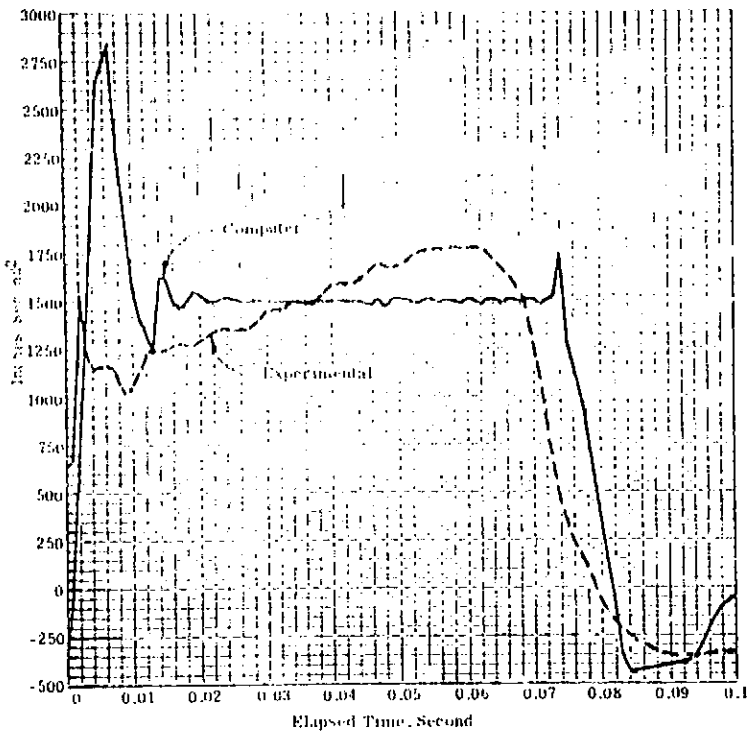

i) Vehicle c.g. Vertical Velocity - $\dot{X}$

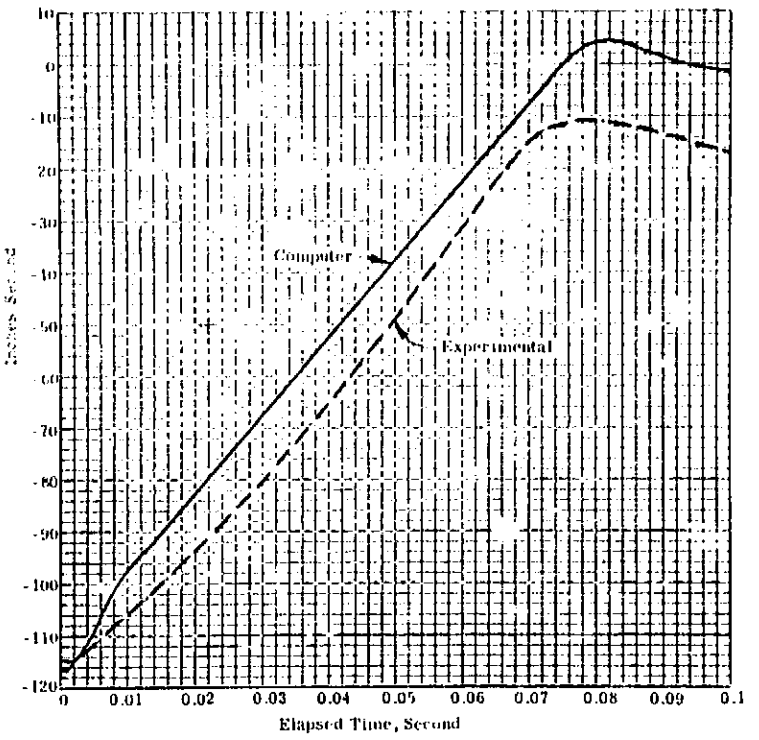

j) Vehicle c.g. Horizontal Velocity - $\dot{Y}$

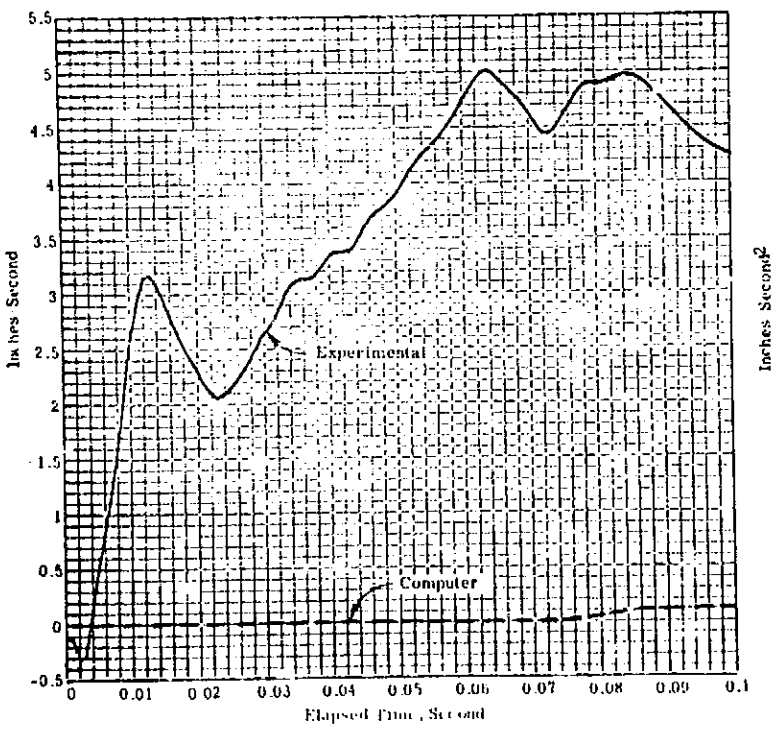

k) Vehicle c.g. Vertical Acceleration - $\ddot{X}$

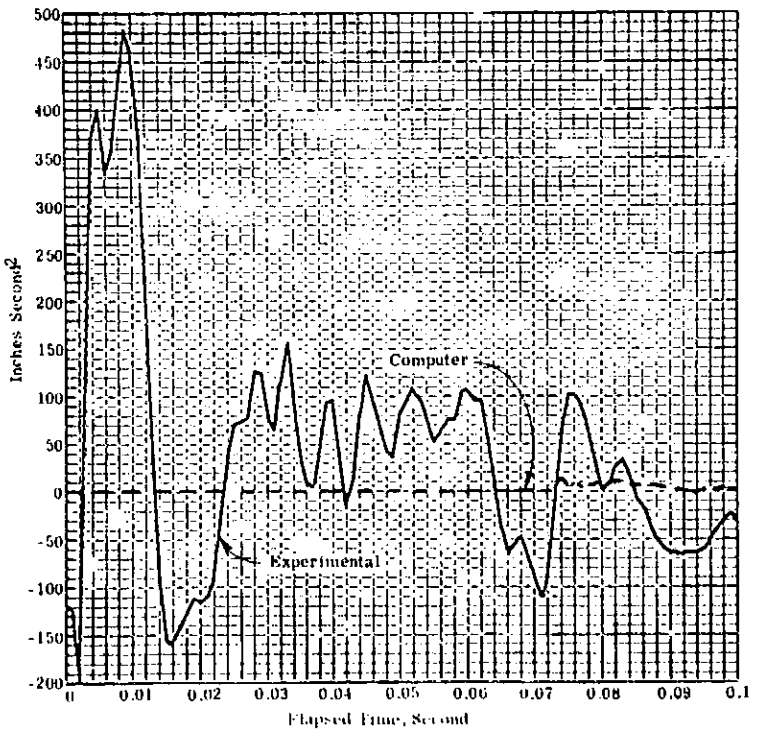

l) Vehicle c.g. Horizontal Acceleration - $\ddot{Y}$

Figure 6-15. Detail Correlation Results For LM Model Drop No. 4 Using Low Strut Damping in Computer Simulation (See Figure 6-10 for drop conditions) (Sheet 3 of 4)

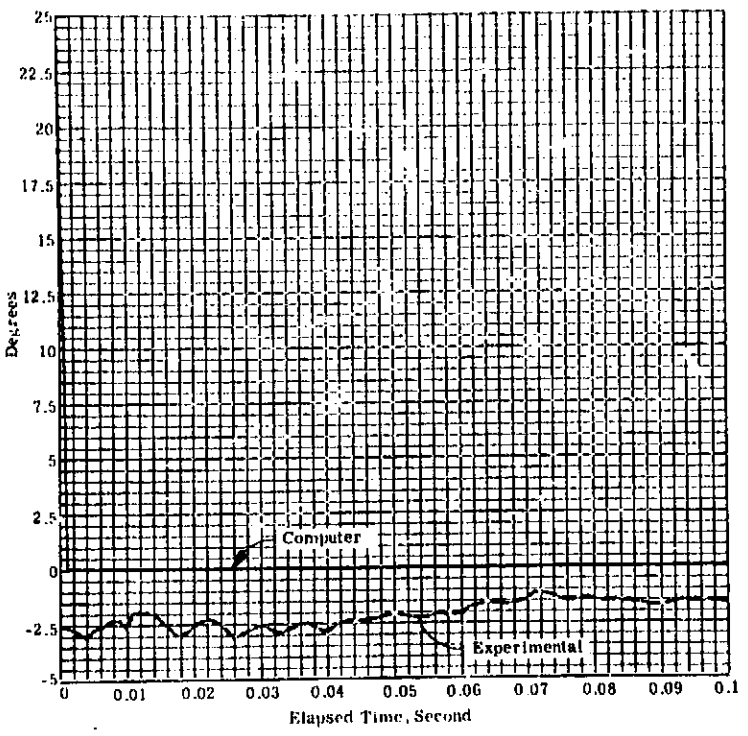

m) Footpad Pitch Angle - α

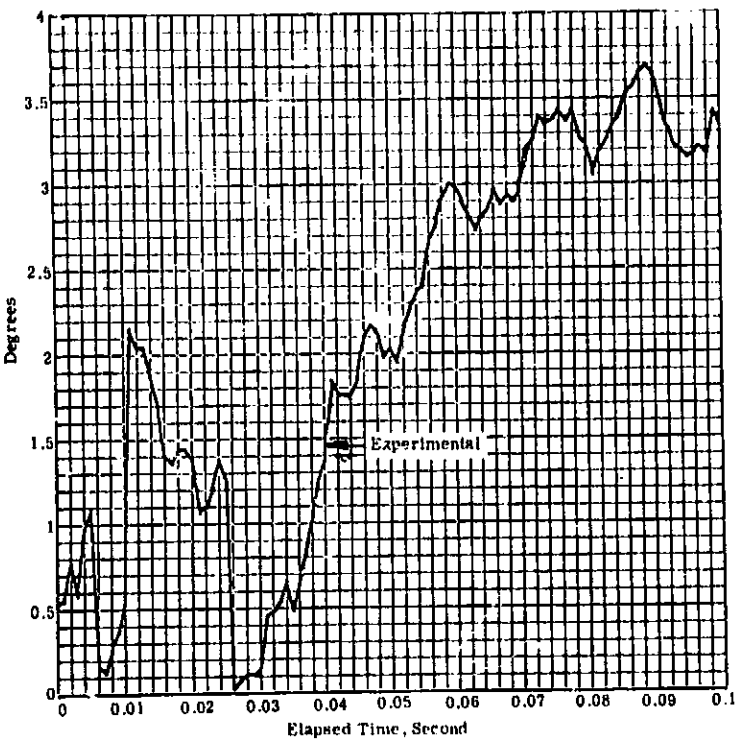

n) Footpad Roll Angle - β

Figure 6-15. Detail Correlation Results For LM Model Drop No. 4 Using Low Strut Damping in Computer Simulation (See Figure 6-10 for drop conditions) (Sheet 4 of 4)

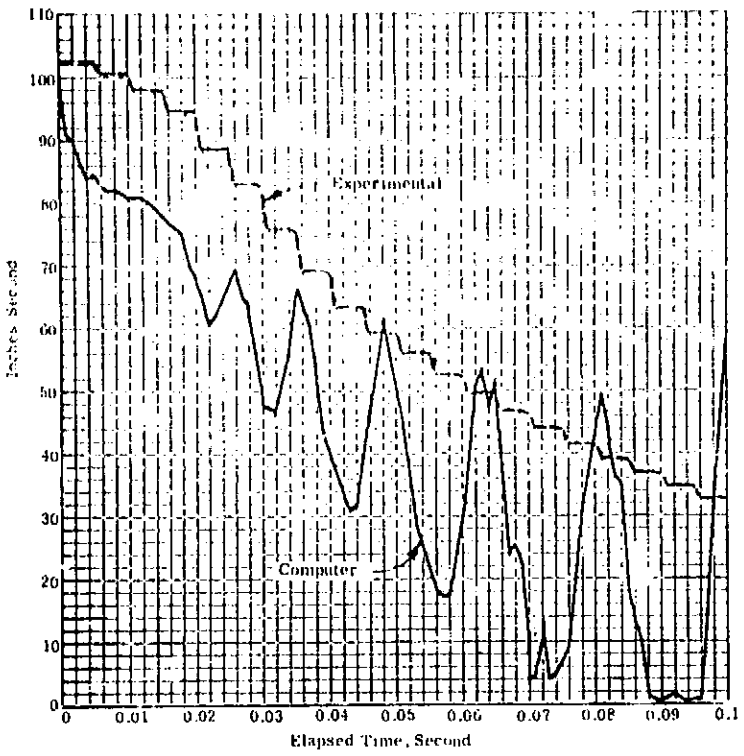

a) Footpad Velocity - V_{ap}

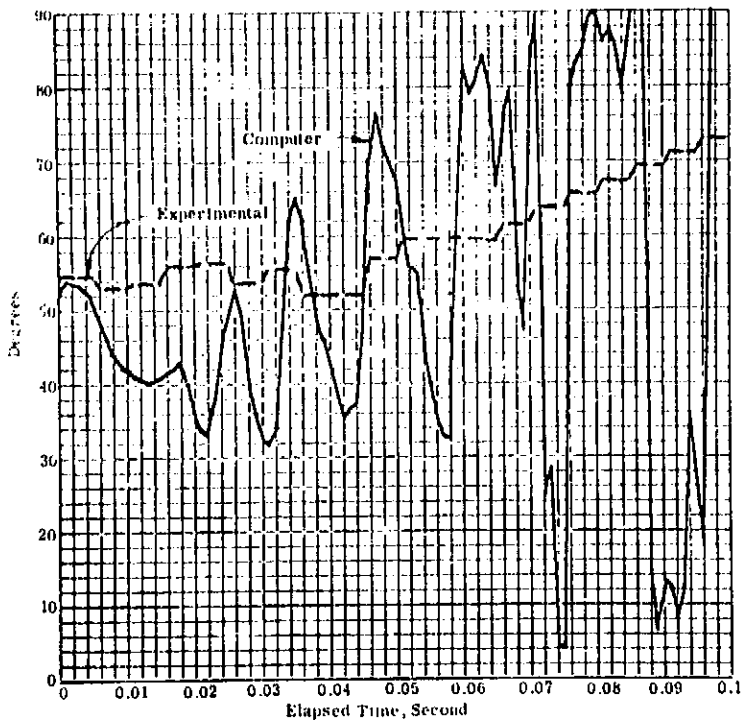

b) Footpad Velocity Angle - θ

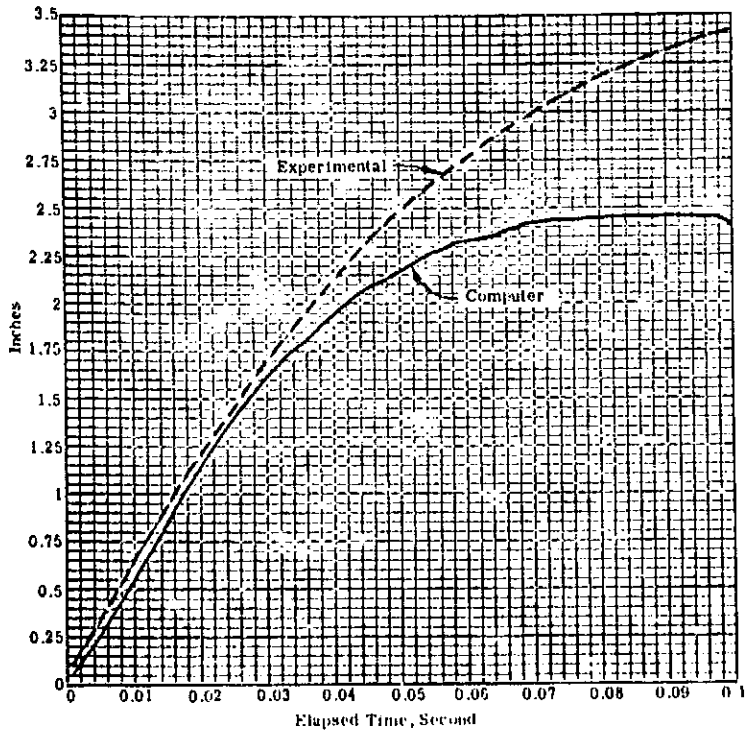

c) Footpad Penetration - d

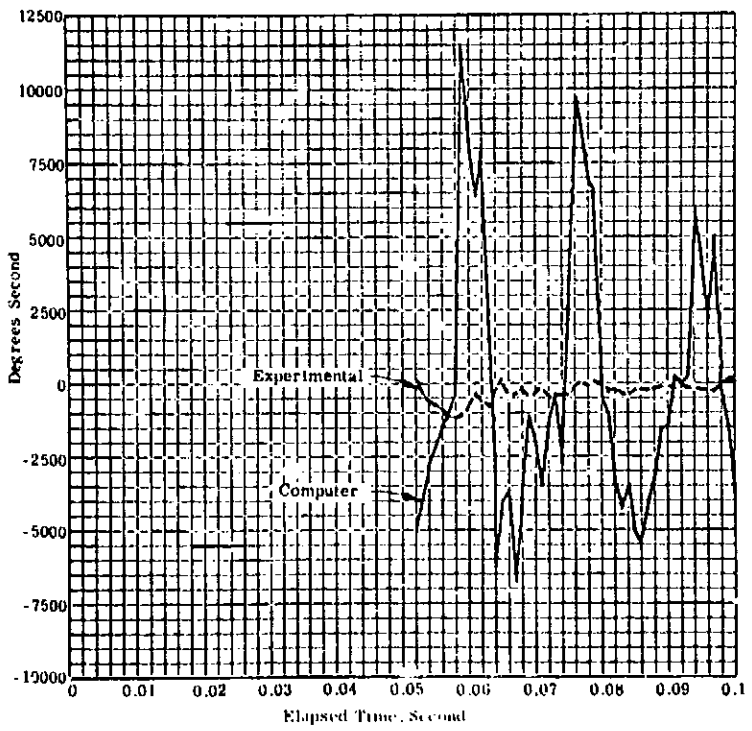

d) Vehicle Pitch Acceleration - $\ddot{\Xi}$

Figure 6-16. Detail Correlation Results For LM Model Drop No. 5 Using Low Strut Damping in Computer Simulation (See Figure 6-10 for drop conditions) (Sheet 1 of 4)

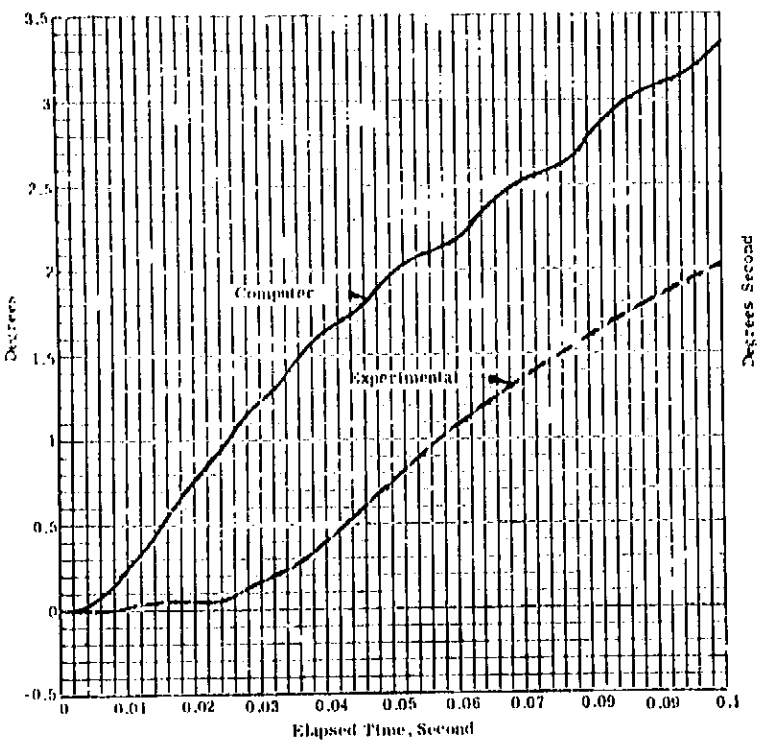

e) Vehicle Pitch Rate - $\dot{\Xi}$

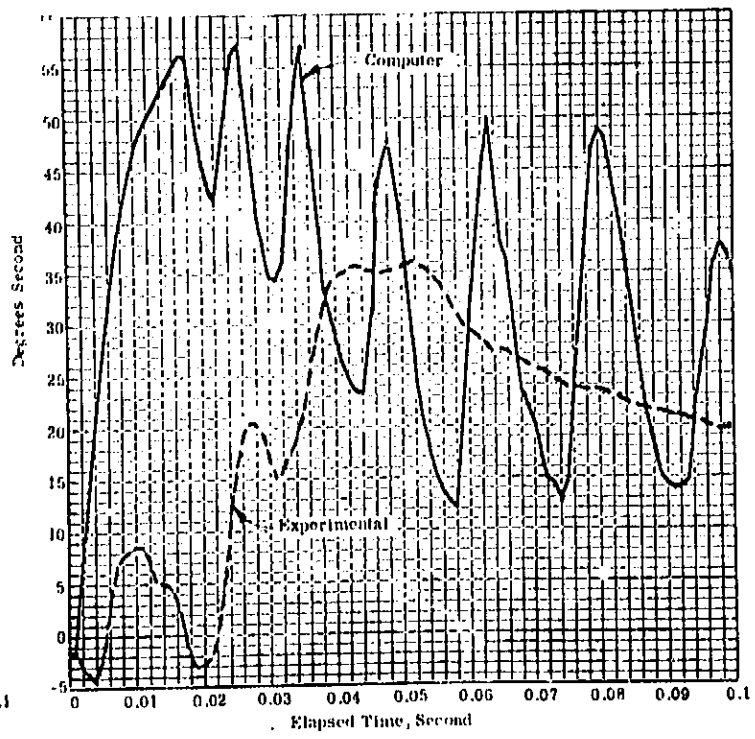

f) Vehicle Pitch Angle - Ξ

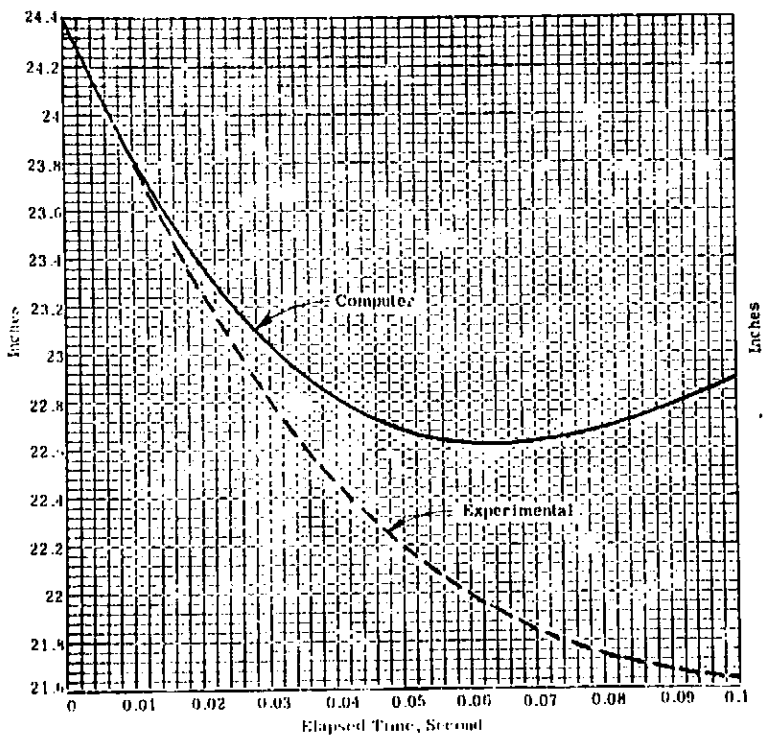

g) Vehicle c.g. Vertical Position - X

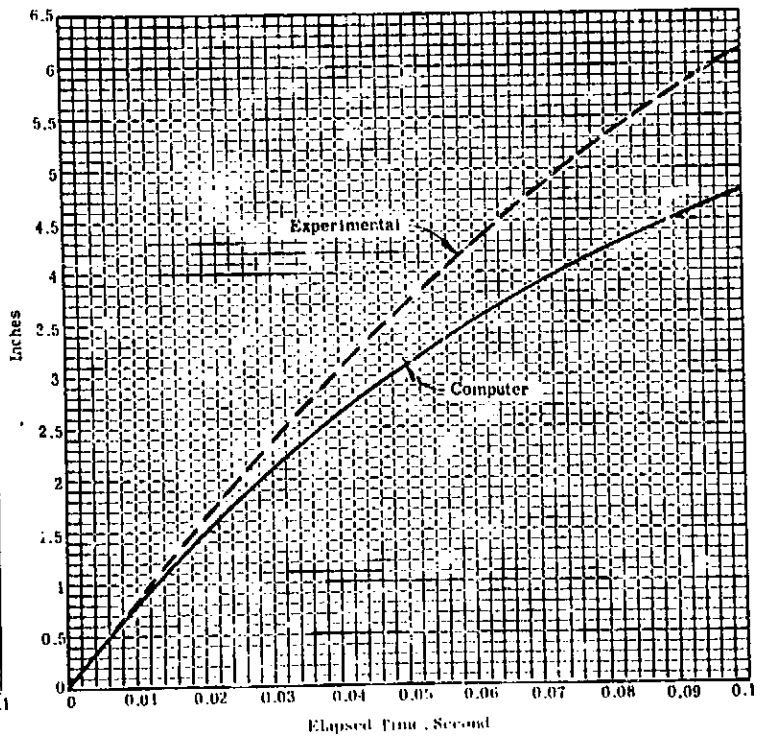

h) Vehicle c.g. Horizontal Position - Y

Figure 6-16. Detail Correlation Results For LM Model Drop No. 5 Using Low Strut Damping in Computer Simulation (See Figure 6-10 for drop conditions) (Sheet 2 of 4)

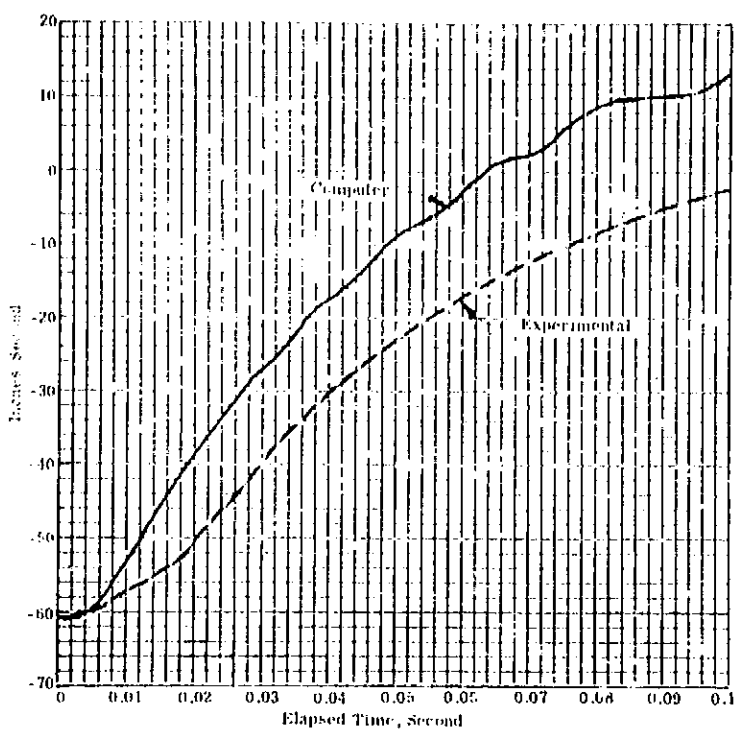

i) Vehicle c.g. Vertical Velocity - $\dot{X}$

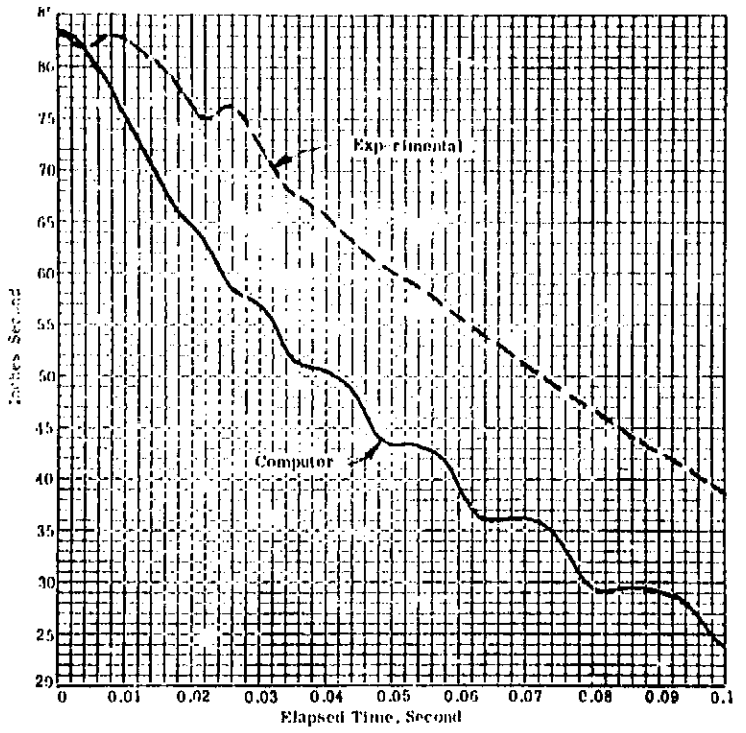

j) Vehicle c.g. Horizontal Velocity - $\dot{Y}$

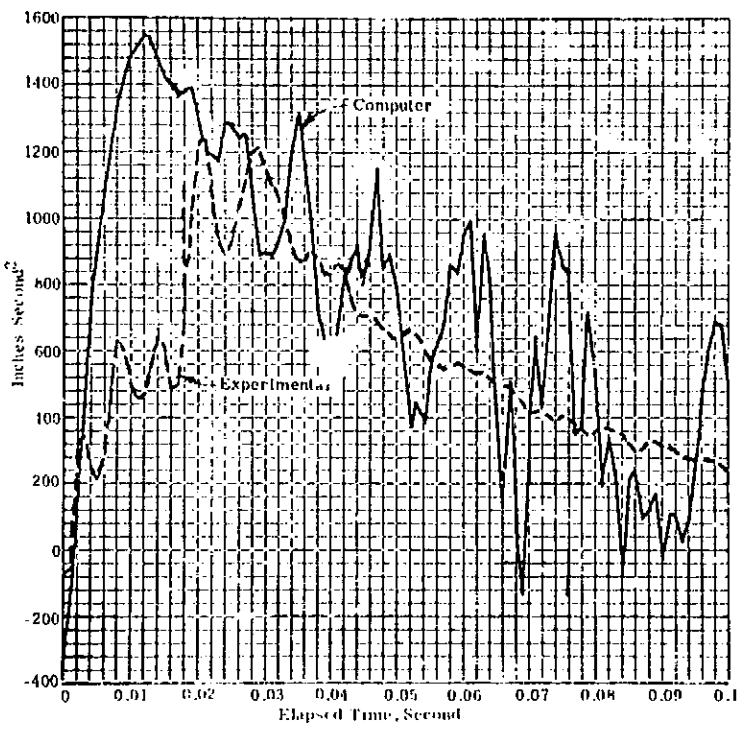

k) Vehicle c.g. Vertical Acceleration - $\ddot{X}$

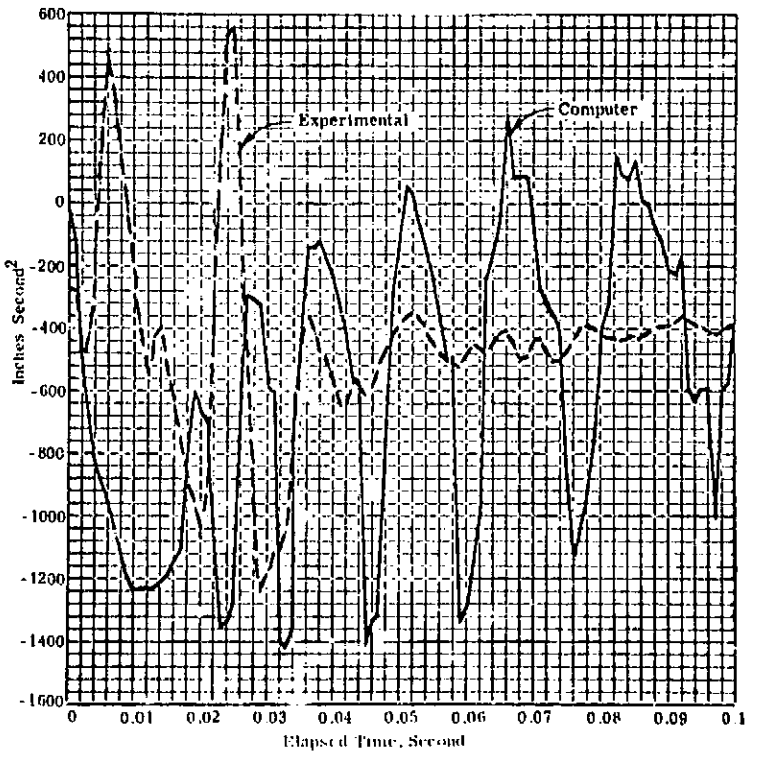

l) Vehicle c.g. Horizontal Acceleration - $\ddot{Y}$

Figure 6-16. Detail Correlation Results For LM Model Drop No. 5 Using Low Strut Damping in Computer Simulation (See Figure 6-10 for drop conditions) (Sheet 3 of 4)

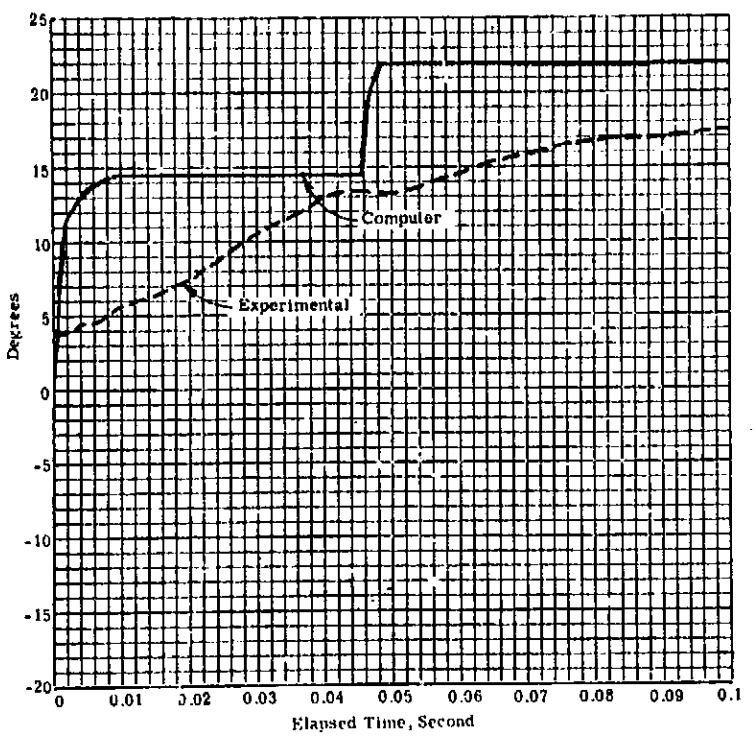

m) Footpad Pitch Angle - α

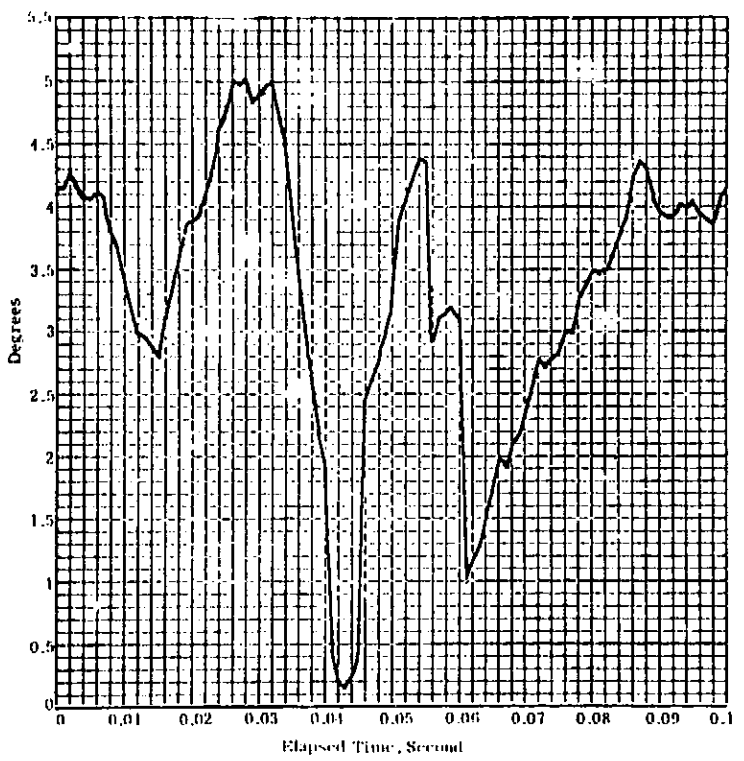

n) Footpad Roll Angle - β

Figure 6-16. Detail Correlation Results For LM Model Drop No. 5 Using Low Strut Damping in Computer Simulation (See Figure 6-10 for drop conditions) (Sheet 4 of 4)

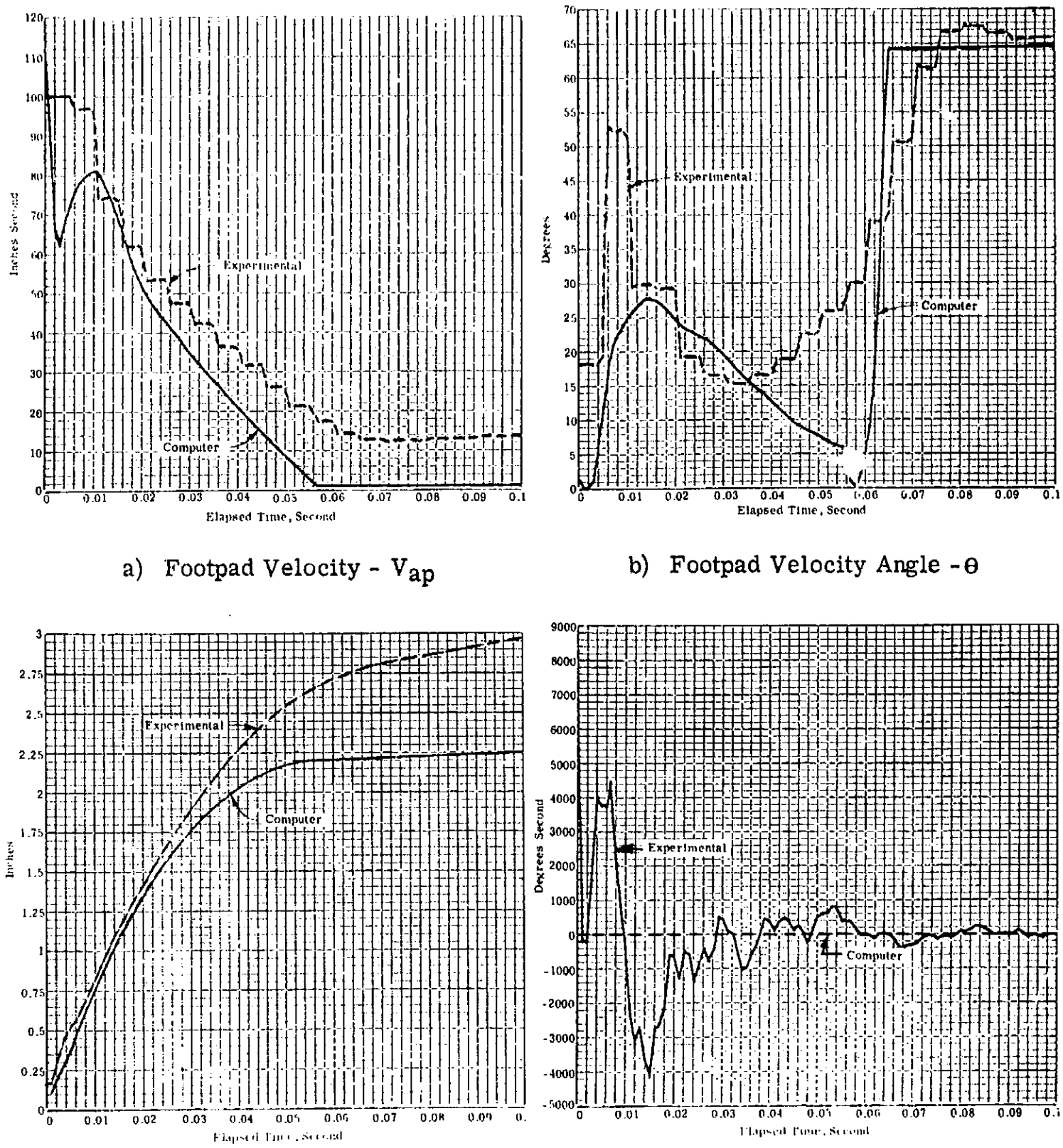

a) Footpad Velocity - V_{ap}

b) Footpad Velocity Angle - θ

c) Footpad Penetration - d

d) Vehicle Pitch Acceleration - $\ddot{\Xi}$

Figure 6-17. Detail Correlation Results For LM Model Drop No. 6 Using Low Strut Damping in Computer Simulation (See Figure 6-10 for drop conditions) (Sheet 1 of 4)

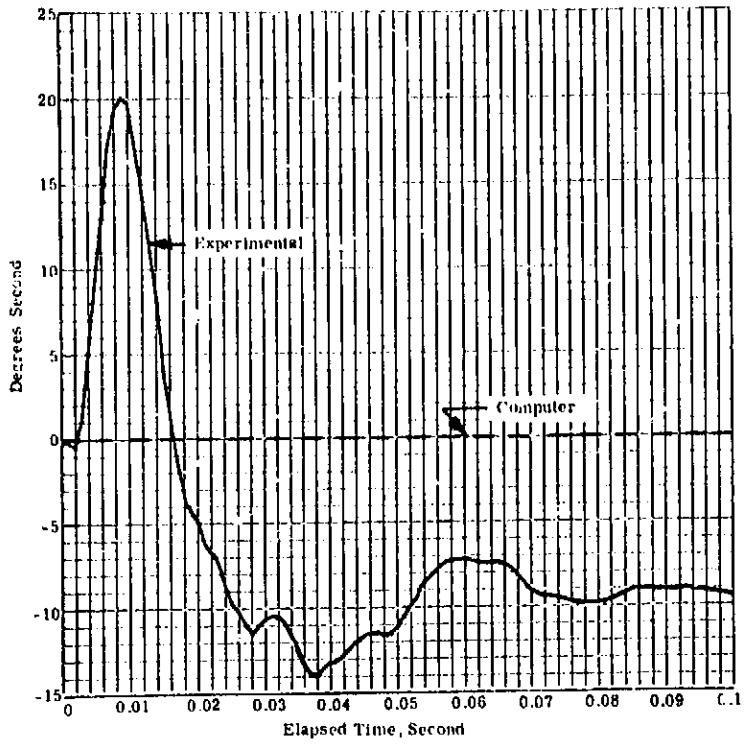

e) Vehicle Pitch Rate - $\dot{\Xi}$

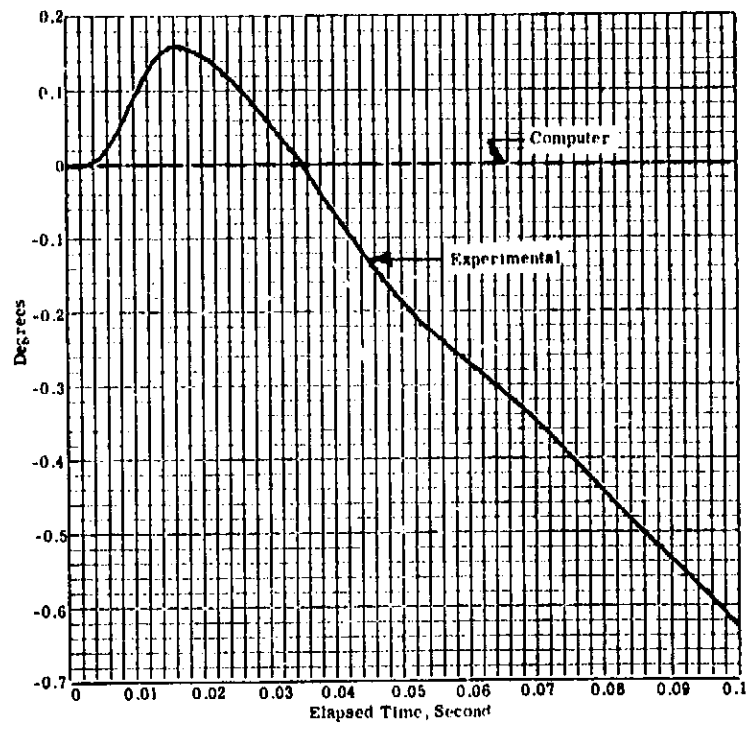

f) Vehicle Pitch Angle - Ξ

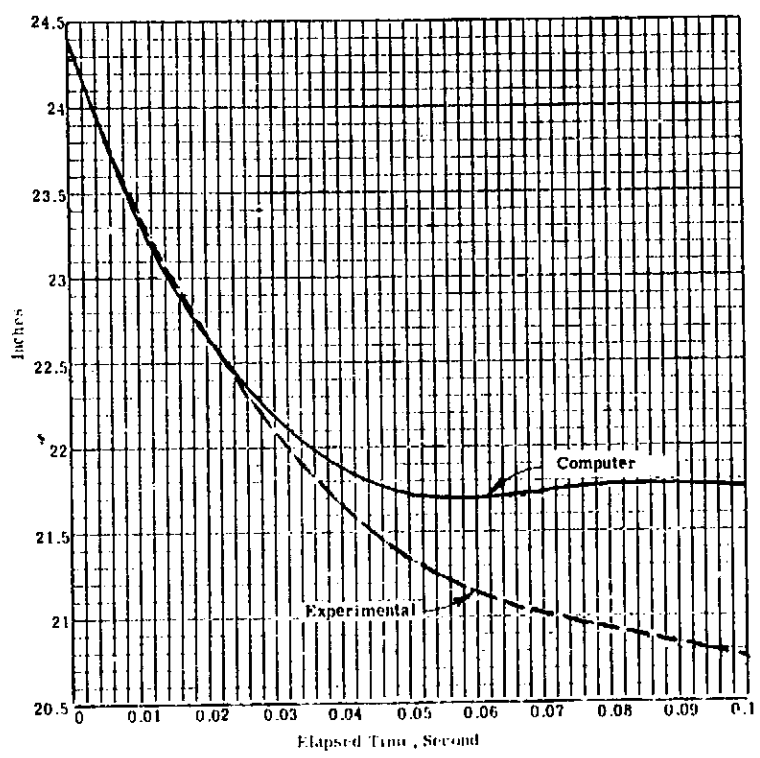

g) Vehicle c.g. Vertical Position - X

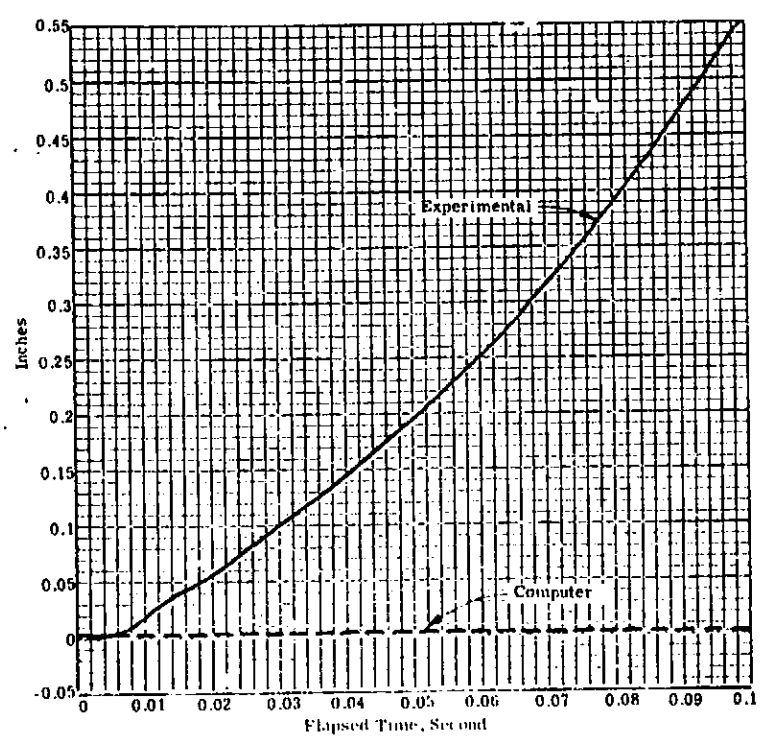

h) Vehicle c.g. Horizontal Position - Y

Figure 6-17. Detail Correlation Results For LM Model Drop No. 6 Using Low Strut Damping in Computer Simulation (See Figure 6-10 for drop conditions) (Sheet 2 of 4)

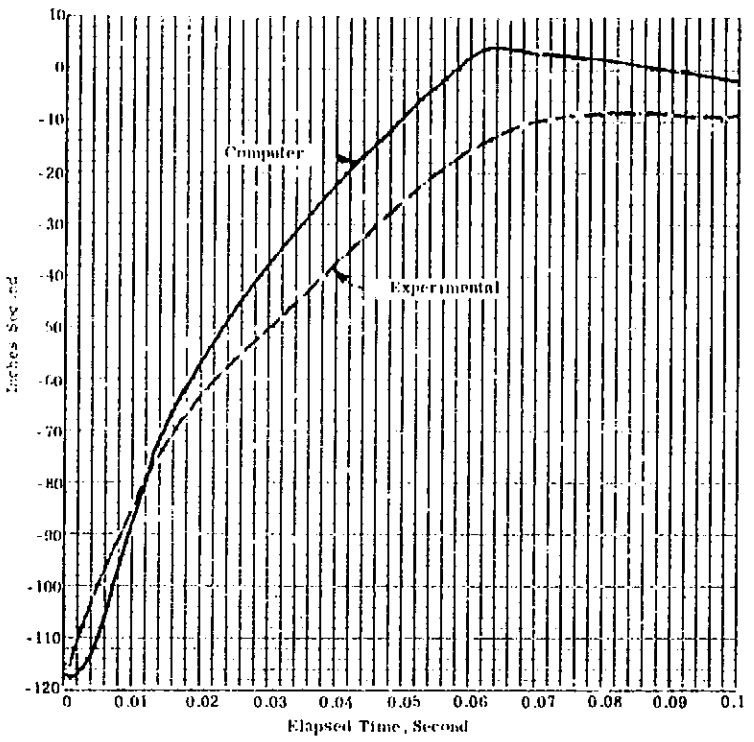

i) Vehicle c.g. Vertical Velocity - $\dot{X}$

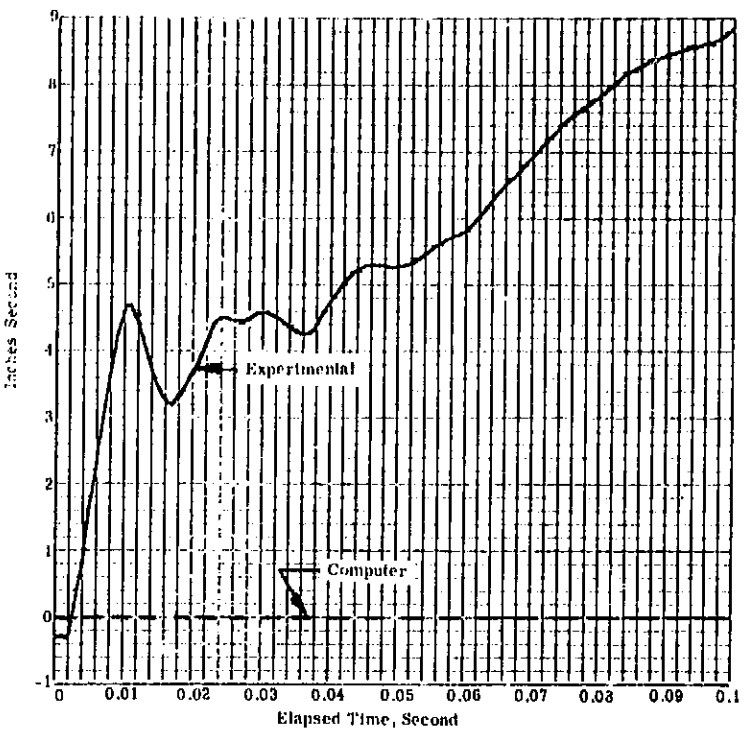

j) Vehicle c.g. Horizontal Velocity - $\dot{Y}$

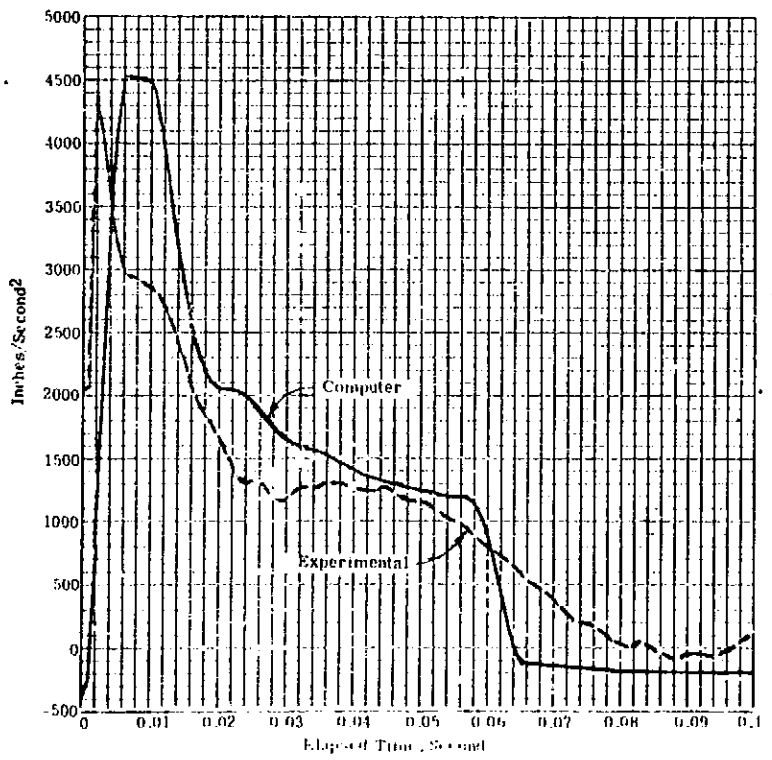

k) Vehicle c.g. Vertical Acceleration - $\ddot{X}$

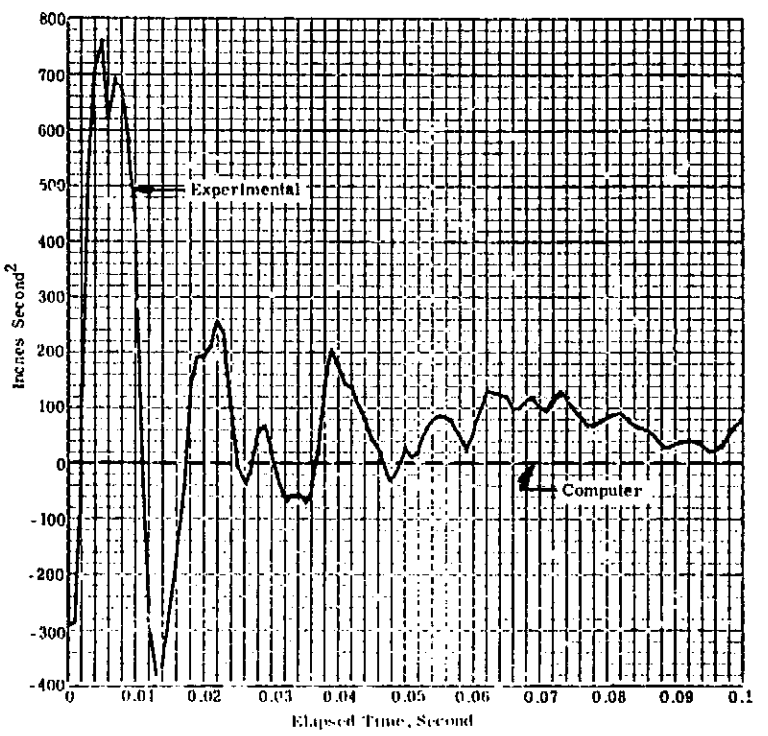

l) Vehicle c.g. Horizontal Acceleration - $\ddot{Y}$

Figure 6-17. Detail Correlation Results For LM Model Drop No. 6 Using Low Strut Damping in Computer Simulation (See Figure 6-10 for drop conditions) (Sheet 3 of 4)

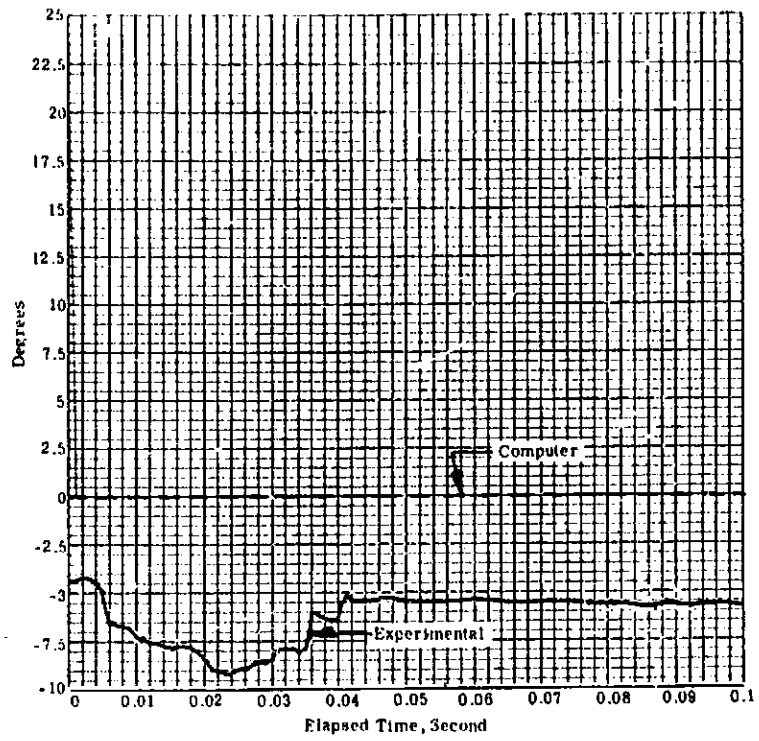

m) Footpad Pitch Angle - α

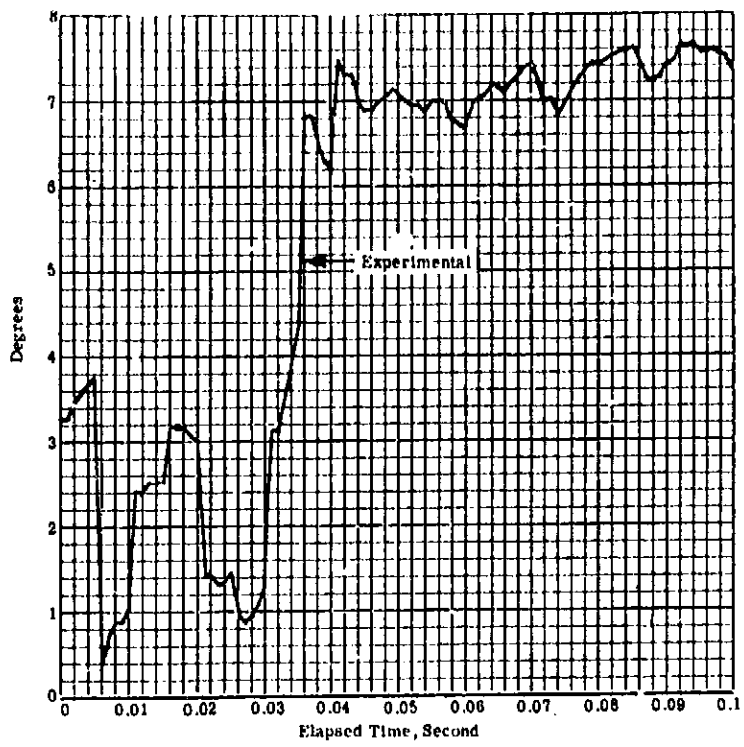

n) Footpad Roll Angle - β

Figure 6-17. Detail Correlation Results For LM Model Drop No. 6 Using Low Strut Damping in Computer Simulation (See Figure 6-10 for drop conditions) (Sheet 4 of 4)

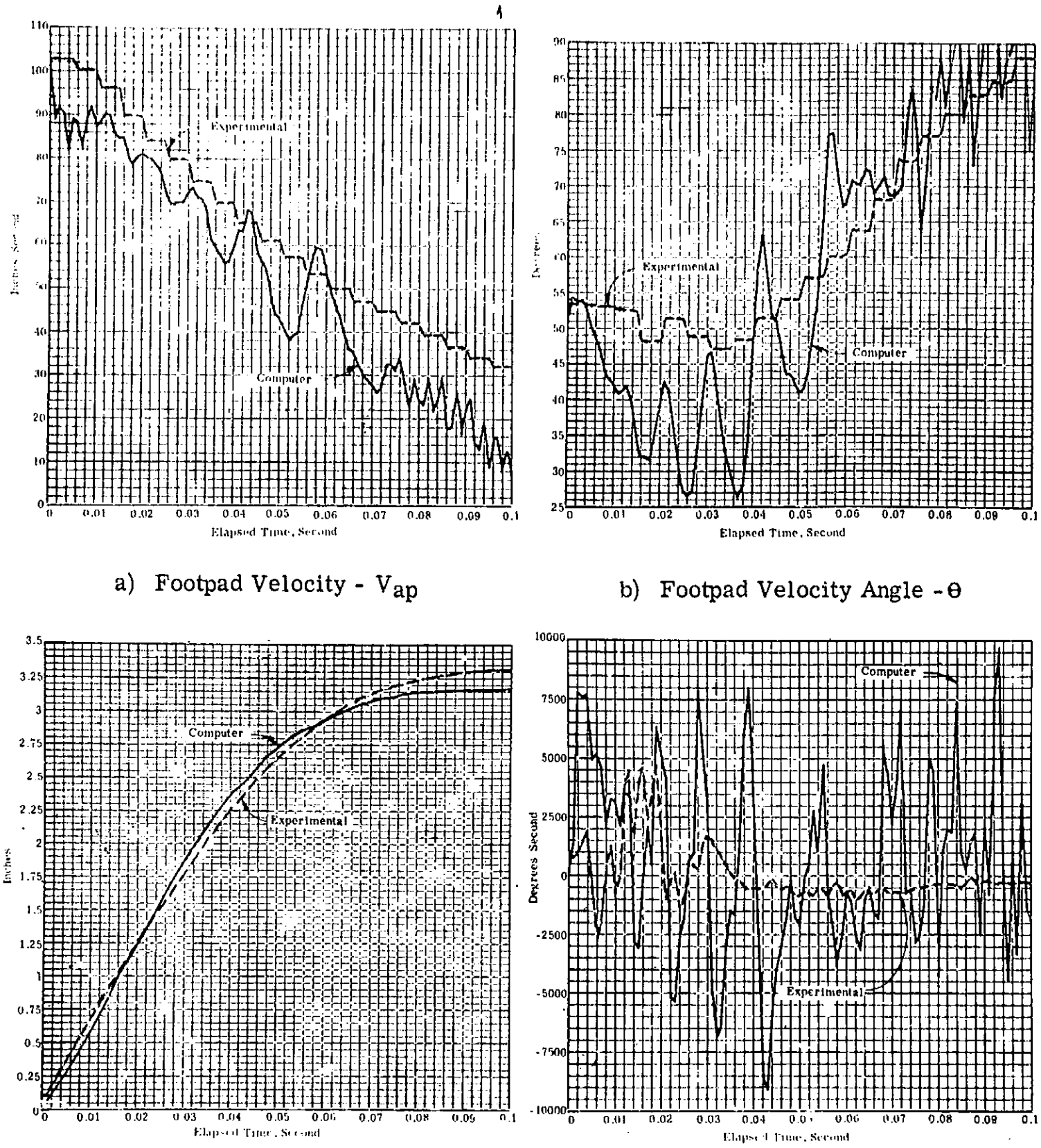

a) Footpad Velocity - V_{ap}

b) Footpad Velocity Angle - θ

c) Footpad Penetration - d

d) Vehicle Pitch Acceleration - $\ddot{\theta}$

Figure 6-18. Detail Correlation Results For LM Model Drop No. 7 Using Low Strut Damping in Computer Simulation (See Figure 6-10 for drop conditions) (Sheet 1 of 4)

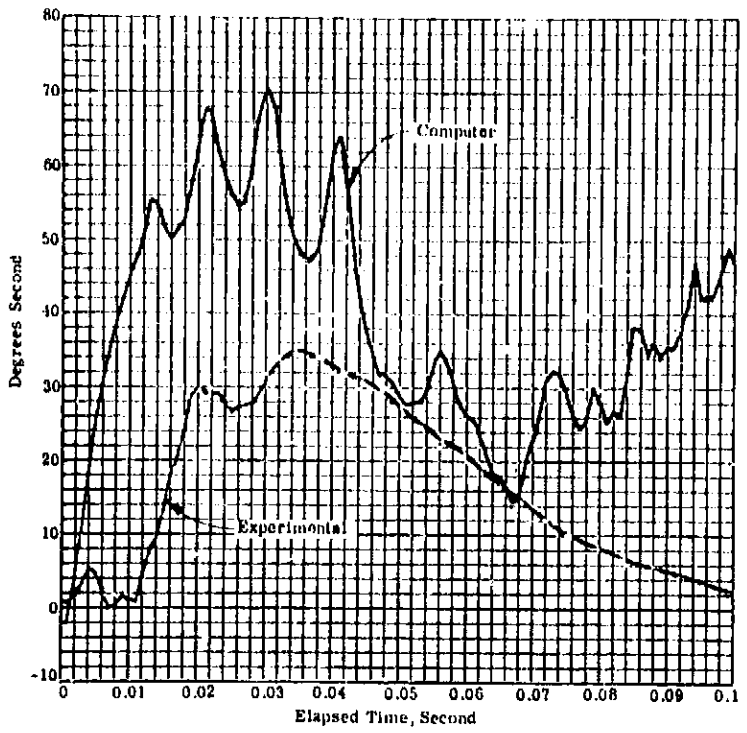

e) Vehicle Pitch Rate - $\dot{\Xi}$

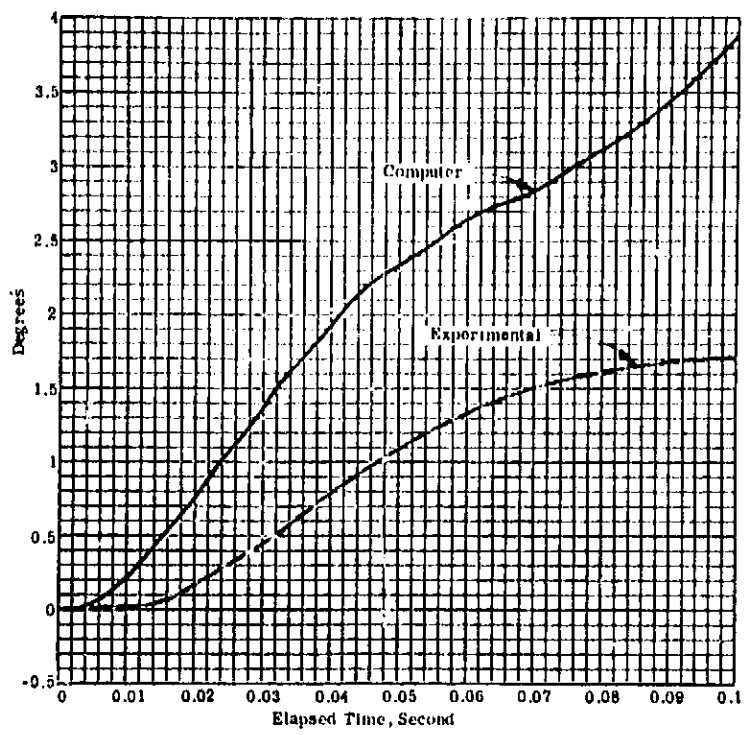

f) Vehicle Pitch Angle - Ξ

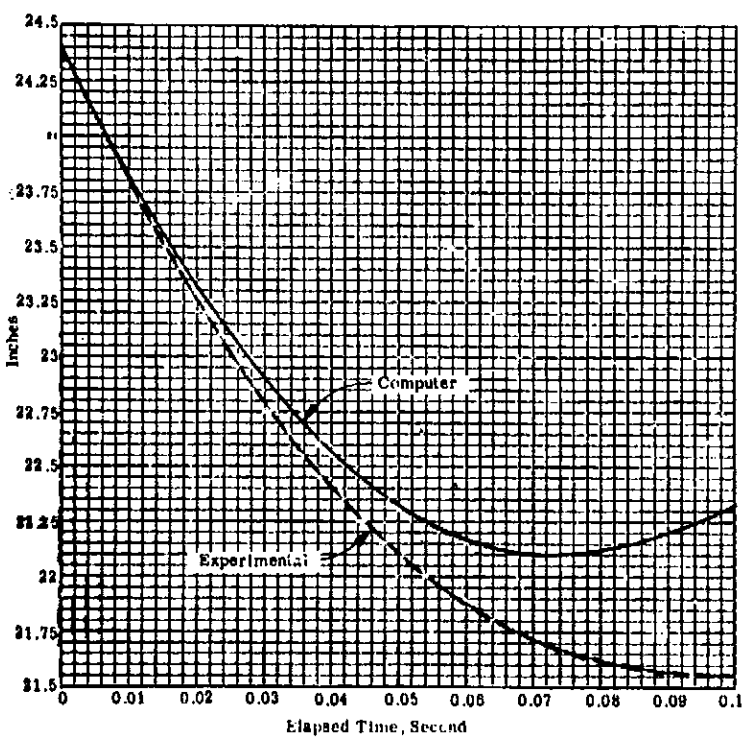

g) Vehicle c.g. Vertical Position - X

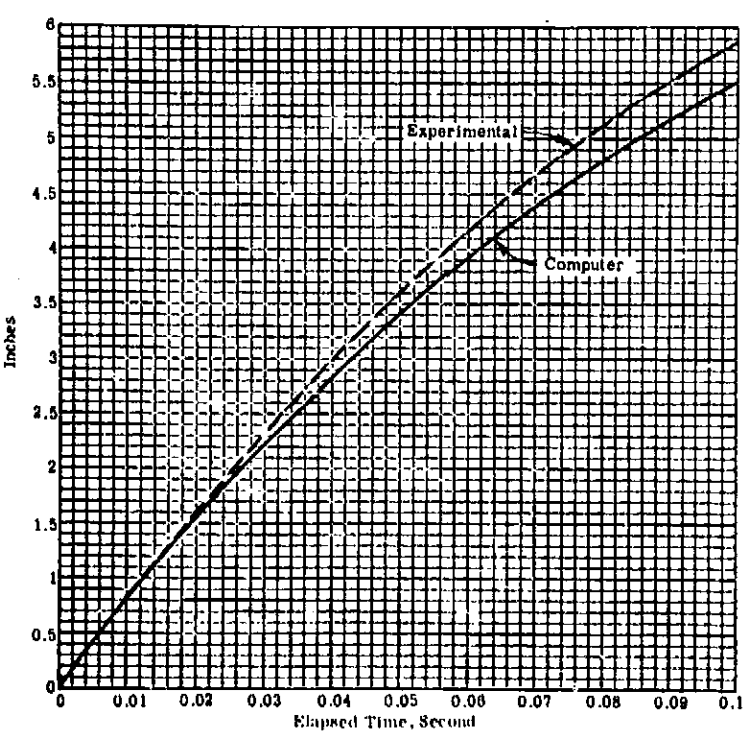

h) Vehicle c.g. Horizontal Position - Y

Figure 6-18. Detail Correlation Results For LM Model Drop No. 7 Using Low Strut Damping in Computer Simulation (See Figure 6-10 for drop conditions) (Sheet 2 of 4)

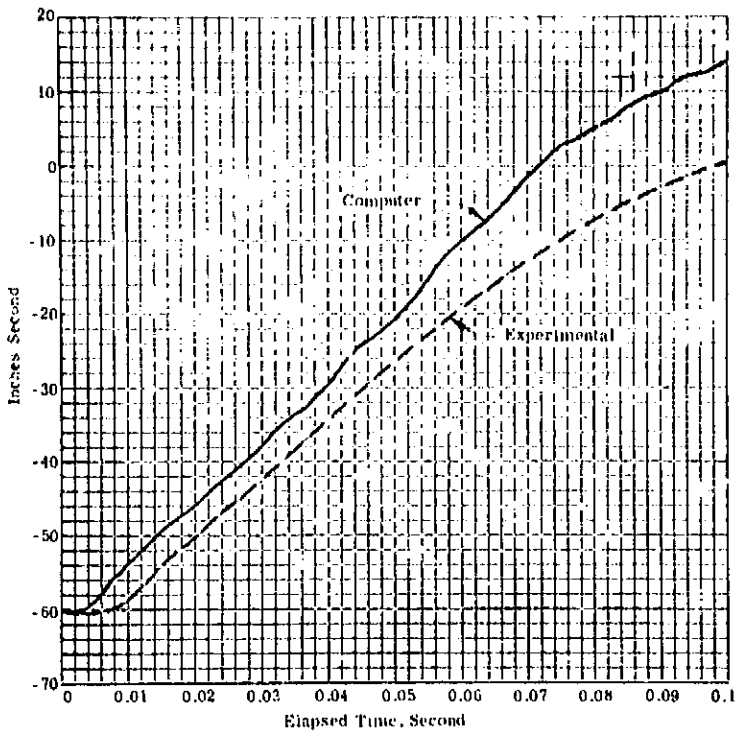

i) Vehicle c.g. Vertical Velocity - $\dot{X}$

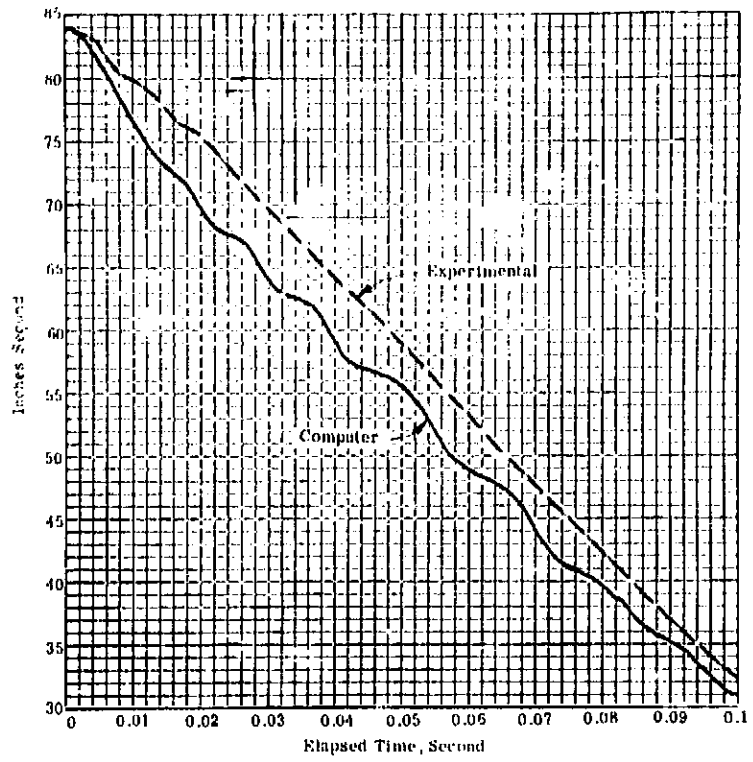

j) Vehicle c.g. Horizontal Velocity - $\dot{Y}$

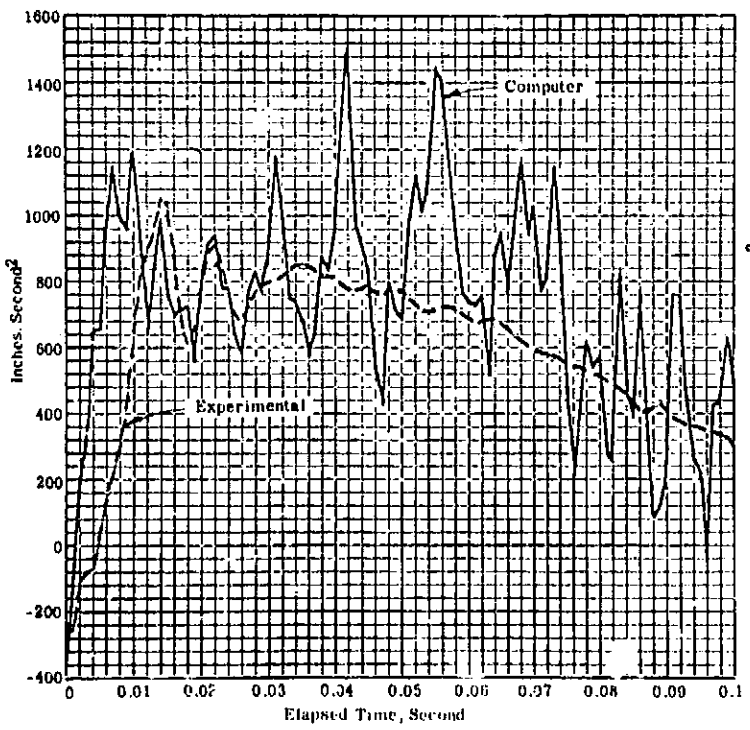

k) Vehicle c.g. Vertical Acceleration - $\ddot{X}$

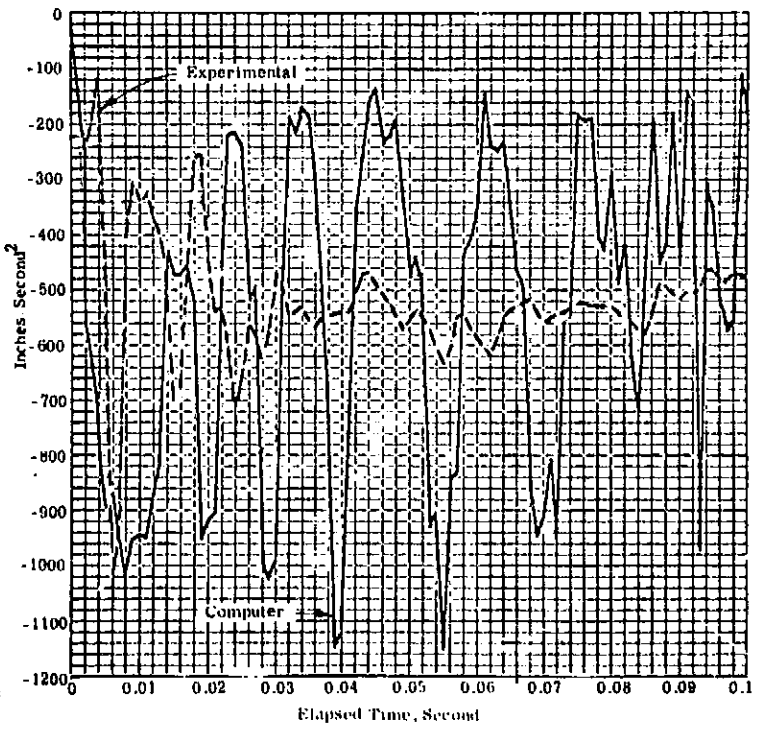

l) Vehicle c.g. Horizontal Acceleration - $\ddot{Y}$

Figure 6-18. Detail Correlation Results For LM Model Drop No. 7 Using Low Strut Damping in Computer Simulation (See Figure 6-10 for drop conditions) (Sheet 3 of 4)

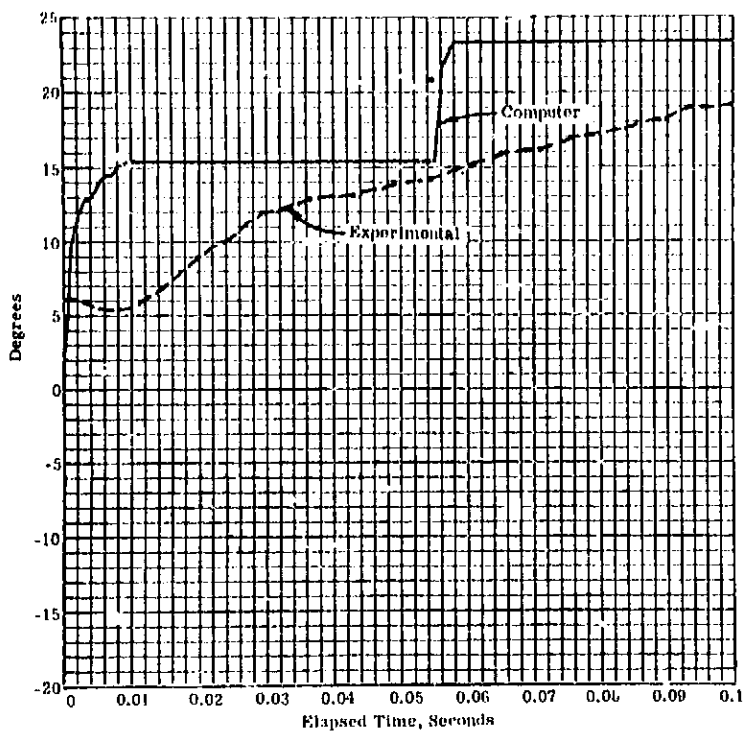

m) Footpad Pitch Angle - α

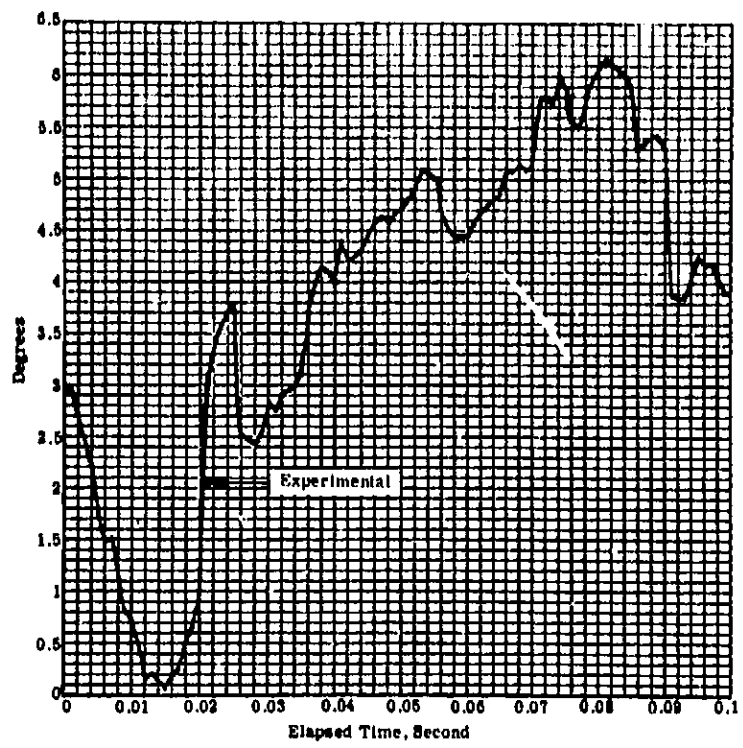

n) Footpad Roll Angle - β

Figure 6-18. Detail Correlation Results For LM Model Drop No. 7 Using Low Strut Damping in Computer Simulation (See Figure 6-10 for drop conditions) (Sheet 4 of 4)

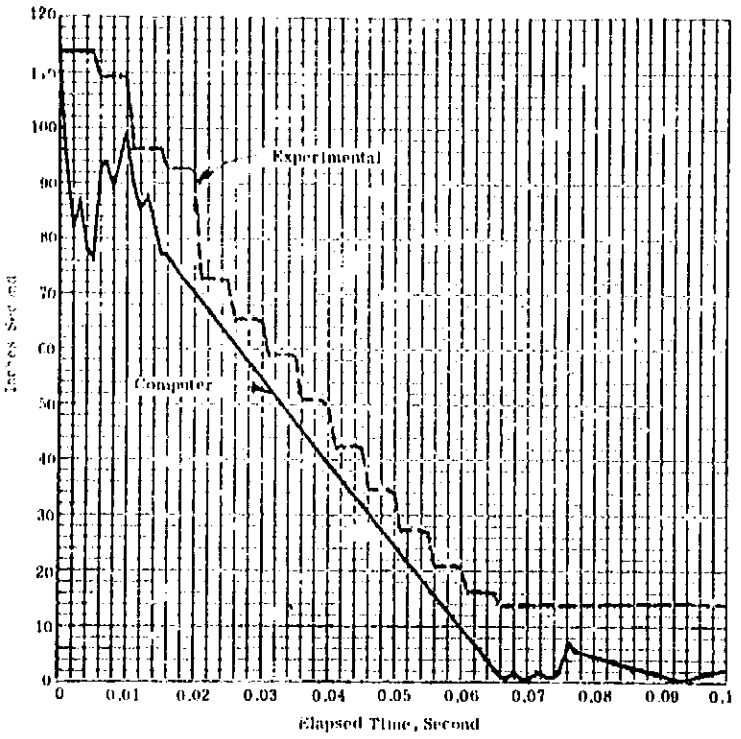

a) Footpad Velocity - V_{ap}

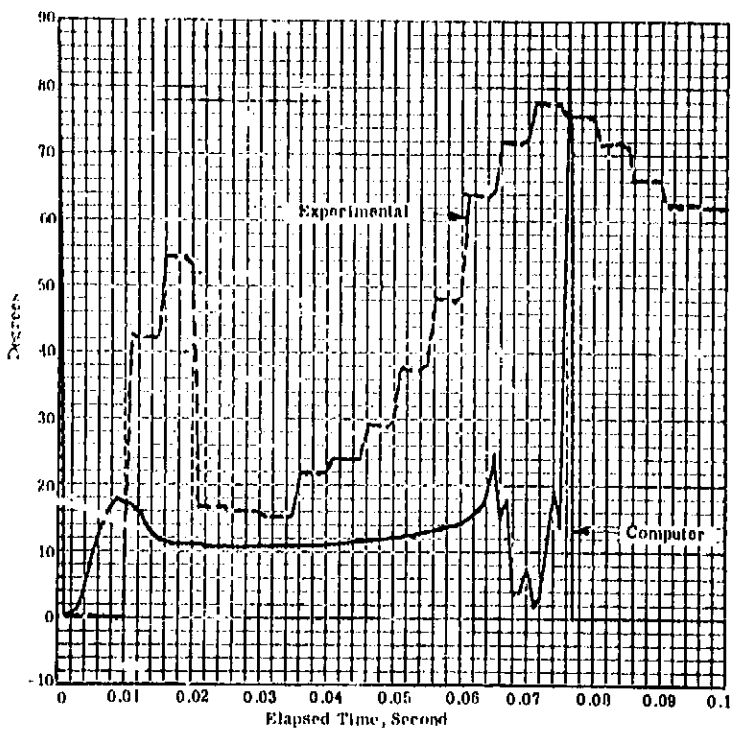

b) Footpad Velocity Angle - θ

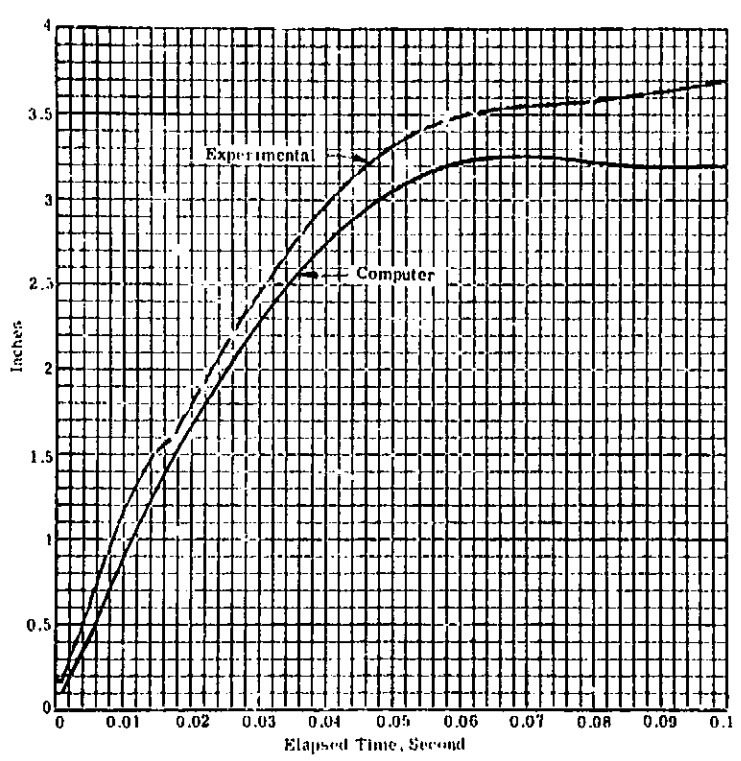

c) Footpad Penetration - d

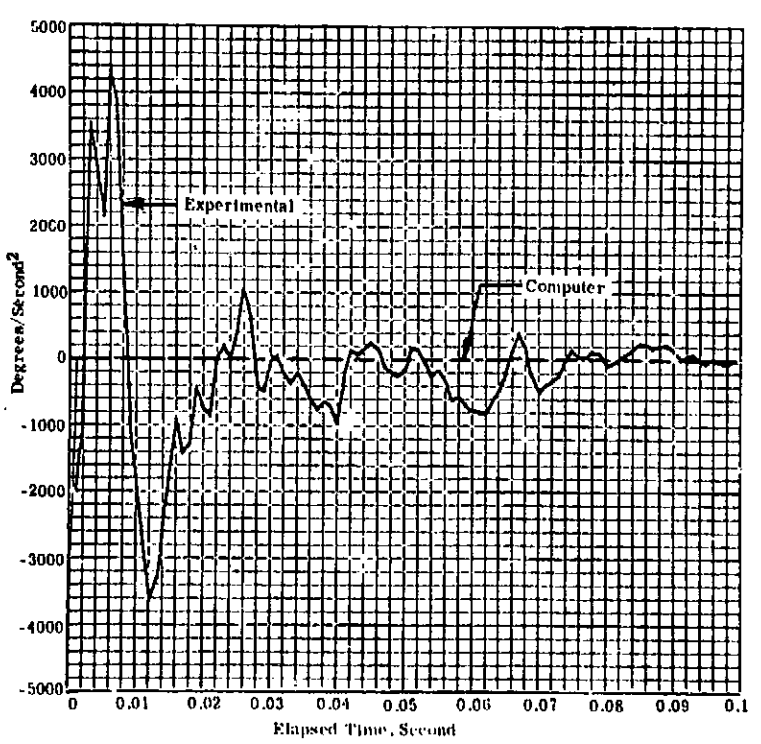

d) Vehicle Pitch Angle - Ξ

Figure 6-19. Detail Correlation Results For LM Model Drop No. 8 Using Low Strut Damping in Computer Simulation (See Figure 6-10 for drop conditions) (Sheet 1 of 4)

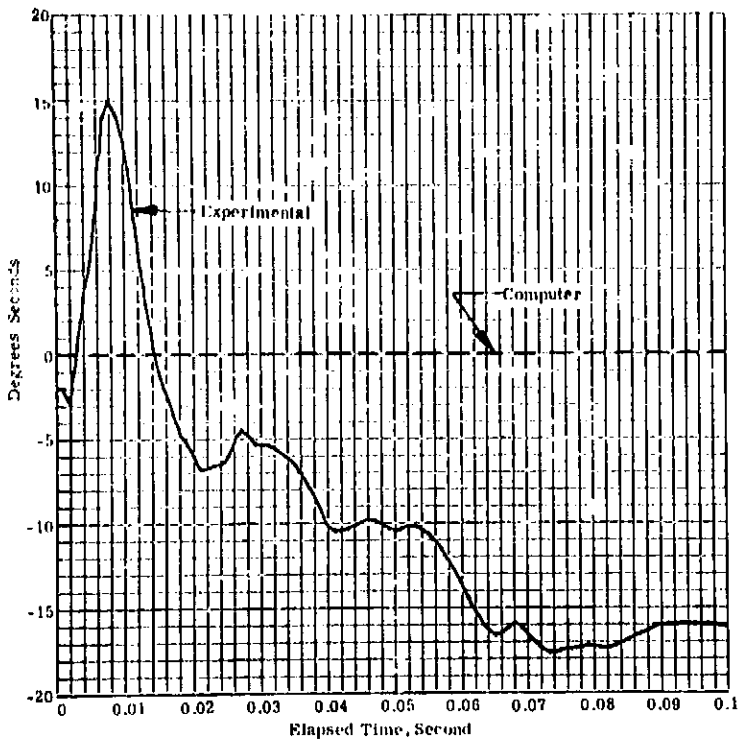

e) Vehicle Pitch Rate - $\dot{\Xi}$

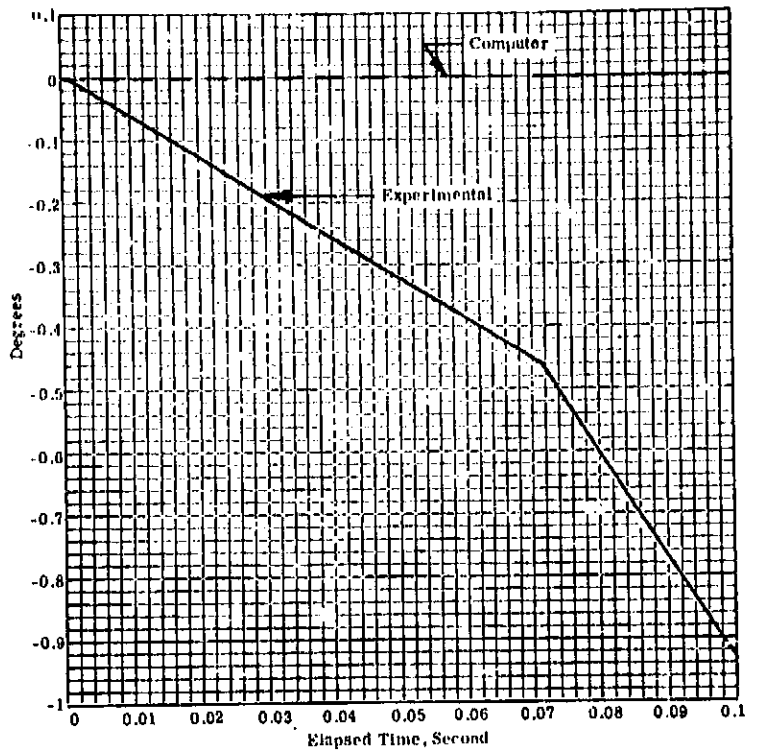

f) Vehicle Pitch Angle - Ξ

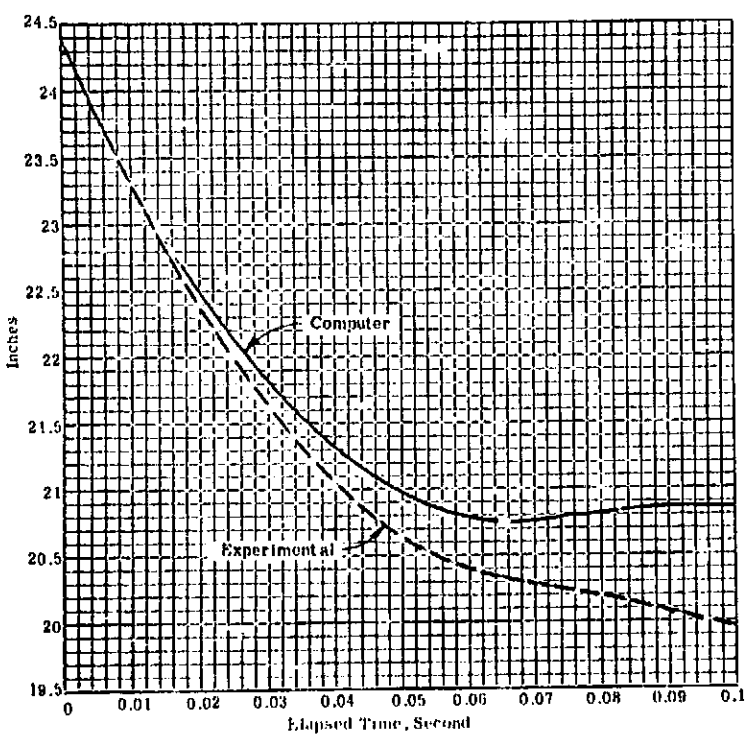

g) Vehicle c.g. Vertical Position - X

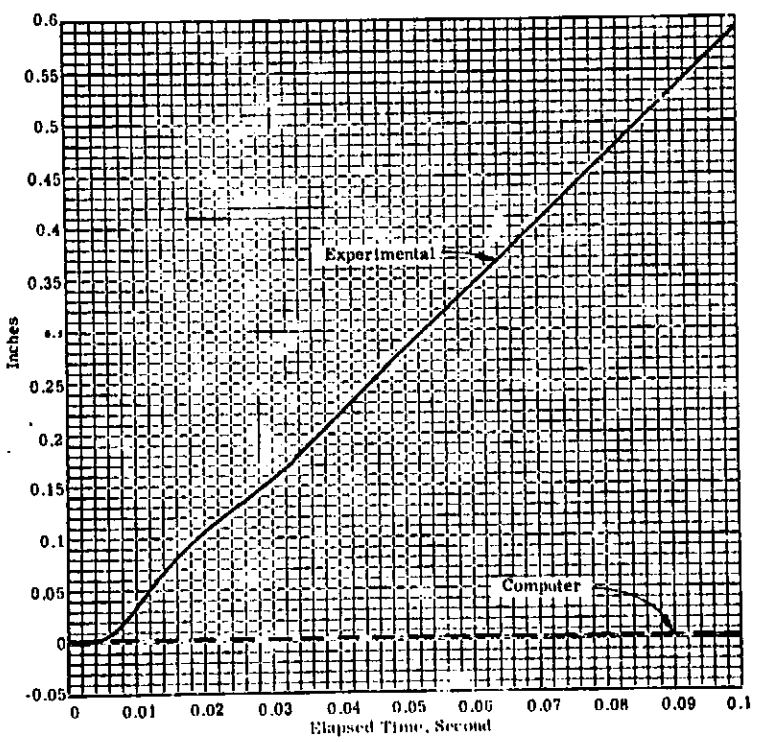

h) Vehicle c.g. Horizontal Position - Y

Figure 6-19. Detail Correlation Results For LM Model Drop No. 8 Using Low Strut Damping in Computer Simulation (See Figure 6-10 for drop conditions) (Sheet 2 of 4)

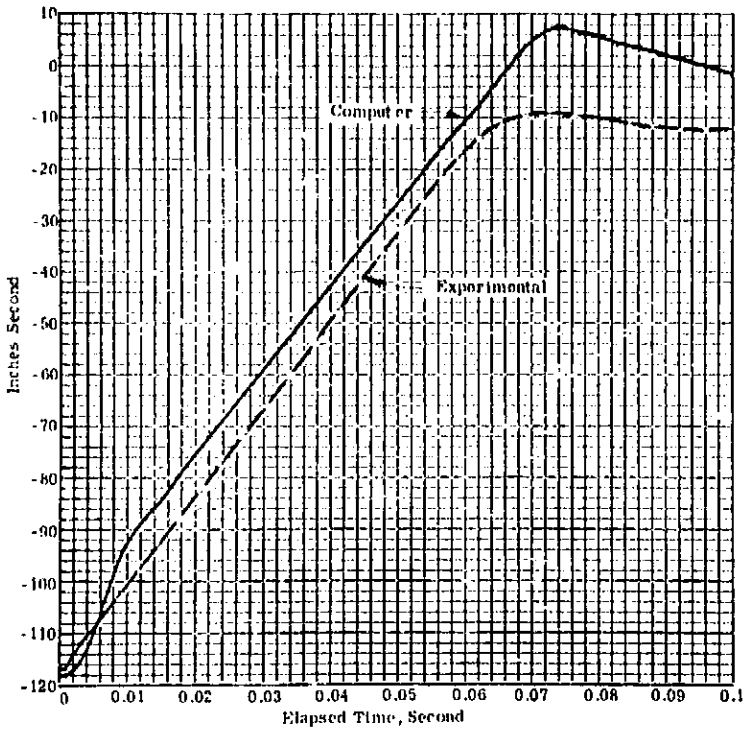

i) Vehicle c.g. Vertical Velocity - $\dot{X}$

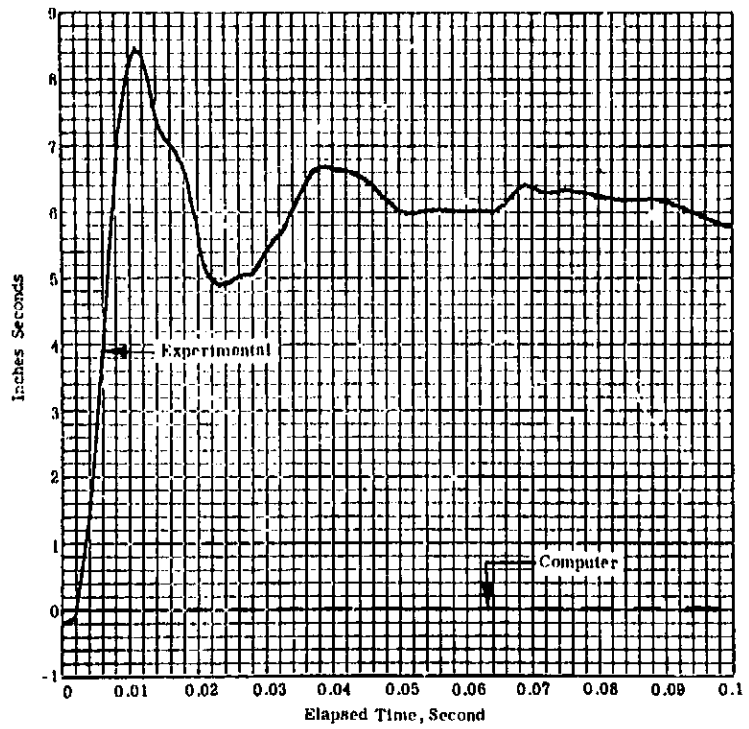

j) Vehicle c.g. Horizontal Velocity - $\dot{Y}$

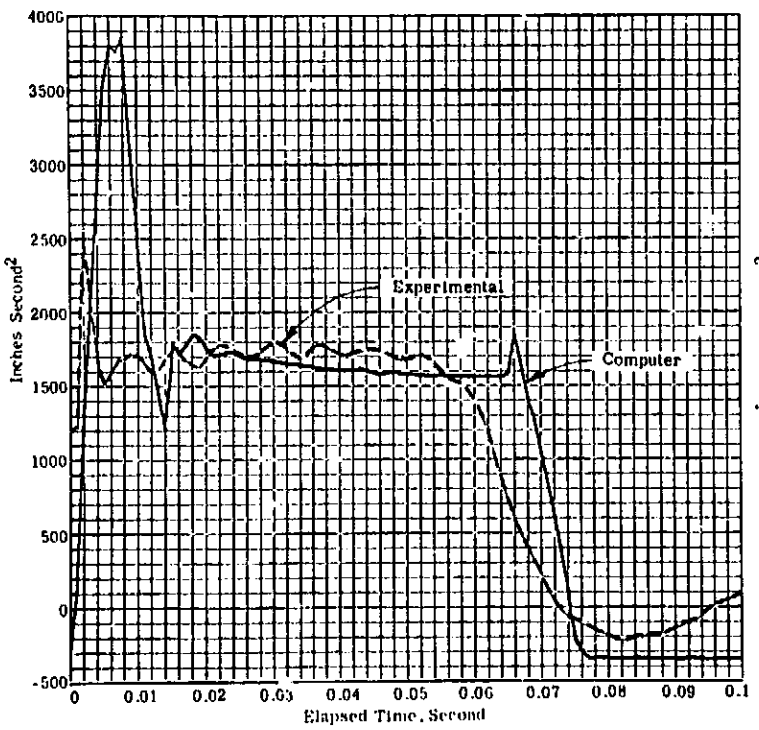

k) Vehicle c.g. Vertical Acceleration - $\ddot{X}$

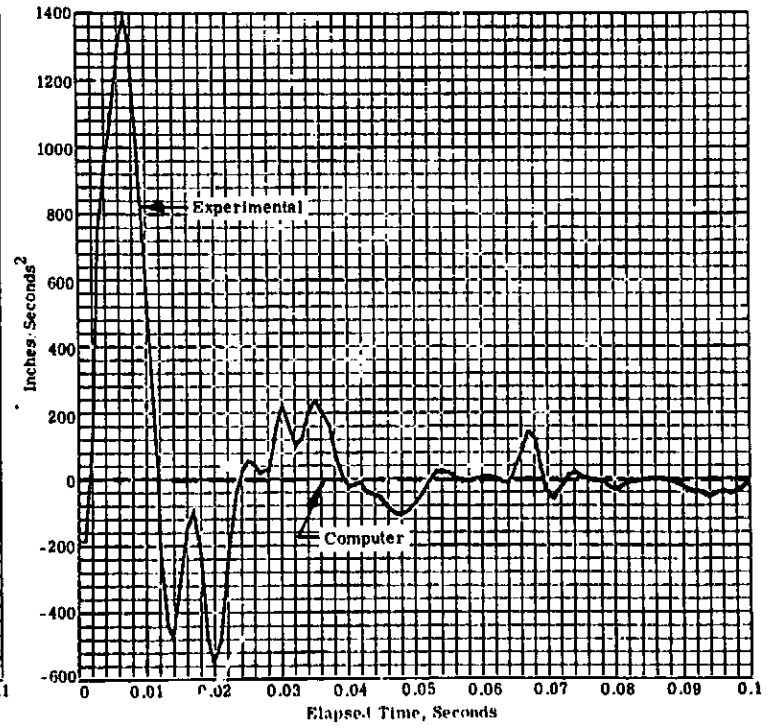

l) Vehicle c.g. Horizontal Acceleration - $\ddot{Y}$

Figure 6-19. Detail Correlation Results For LM Model Drop No. 8 Using Low Strut Damping in Computer Simulation (See Figure 6-10 for drop conditions) (Sheet 3 of 4)

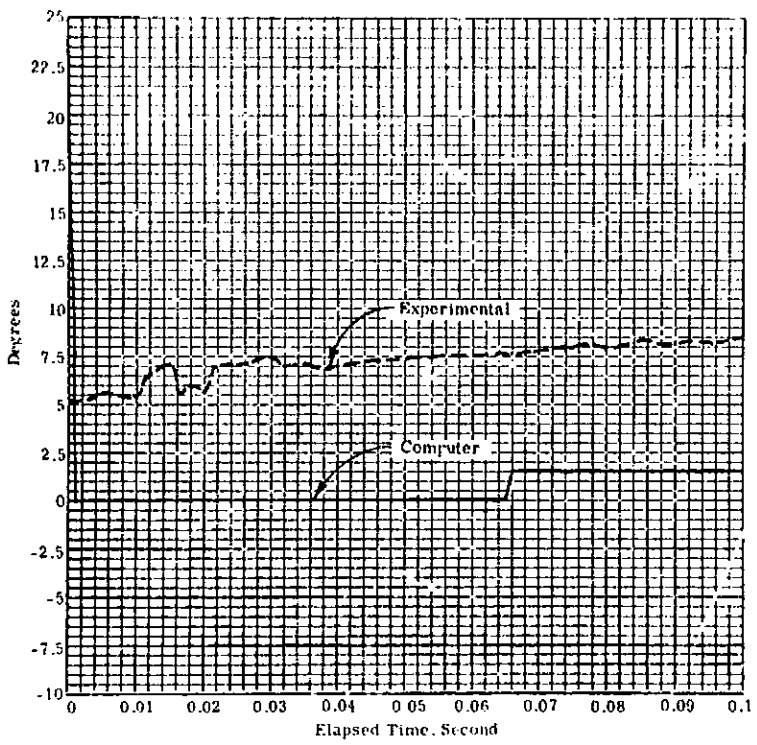

m) Footpad Pitch Angle - α

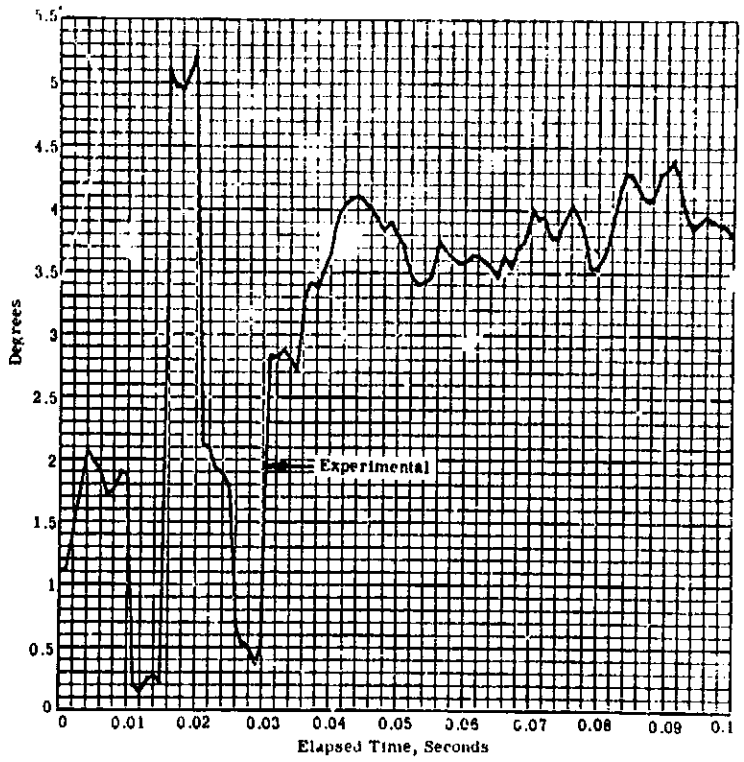

n) Footpad Roll Angle - β

Figure 6-19. Detail Correlation Results For LM Model Drop No. 8 Using Low Strut Damping in Computer Simulation (See Figure 6-10 for drop conditions) (Sheet 4 of 4)

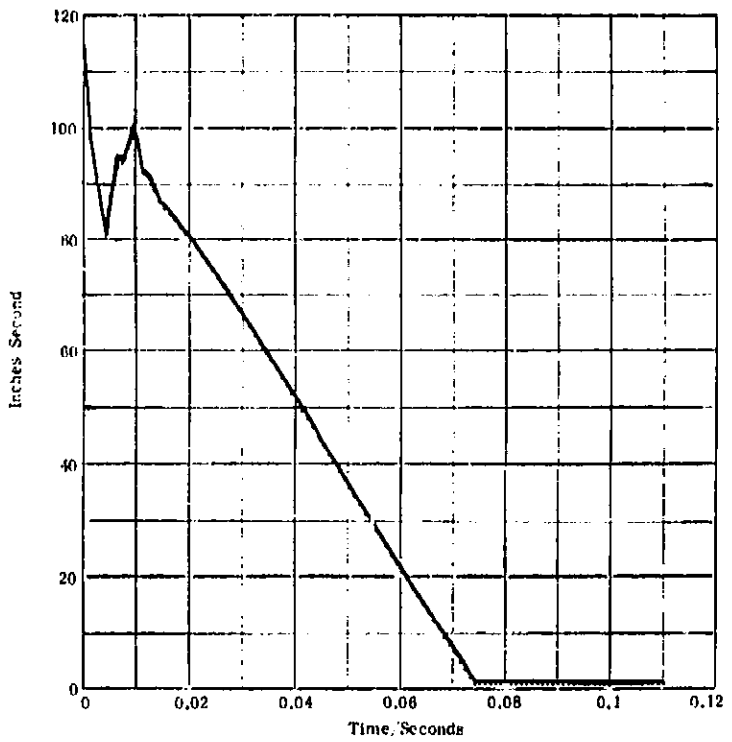

a) Footpad Velocity - V_{ap}

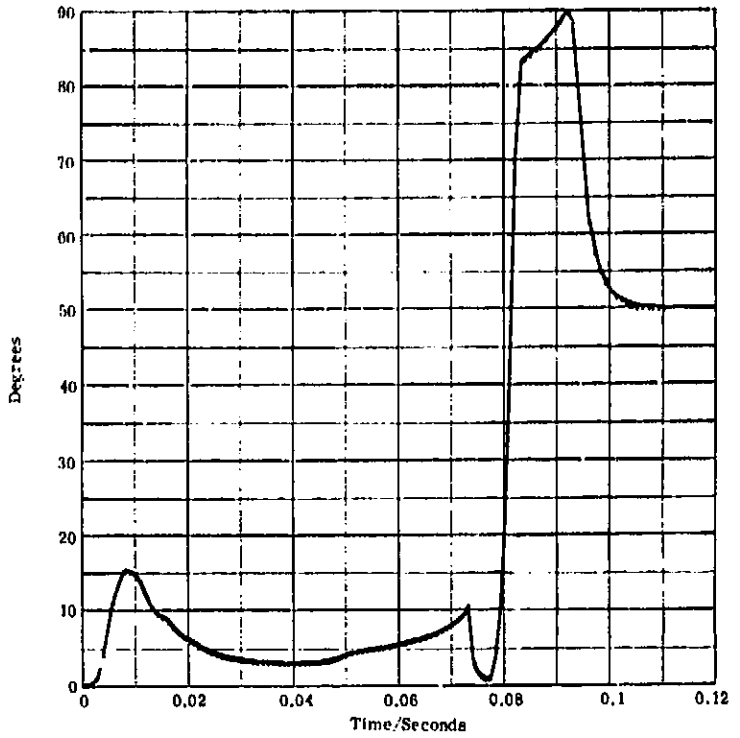

b) Footpad Velocity Angle - θ

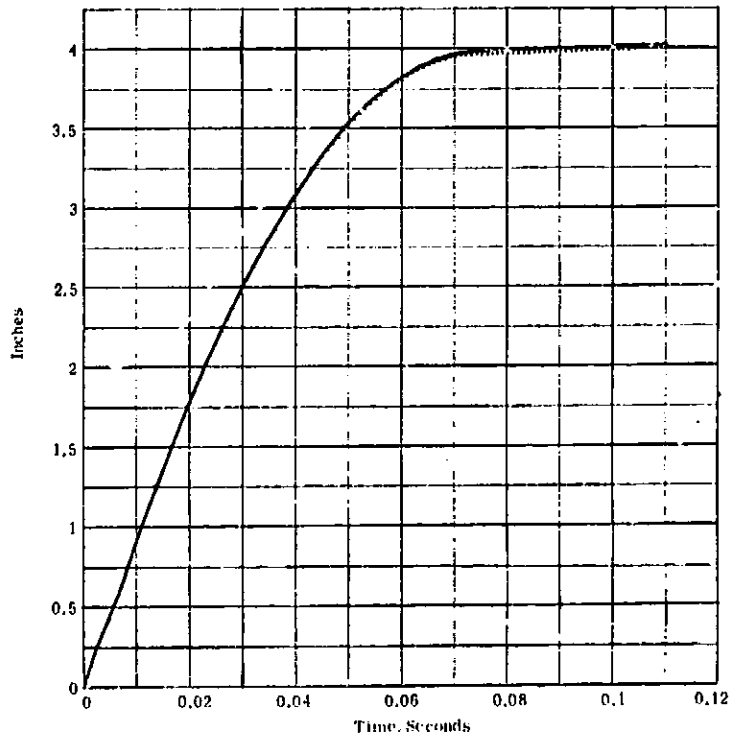

c) Footpad Penetration - d

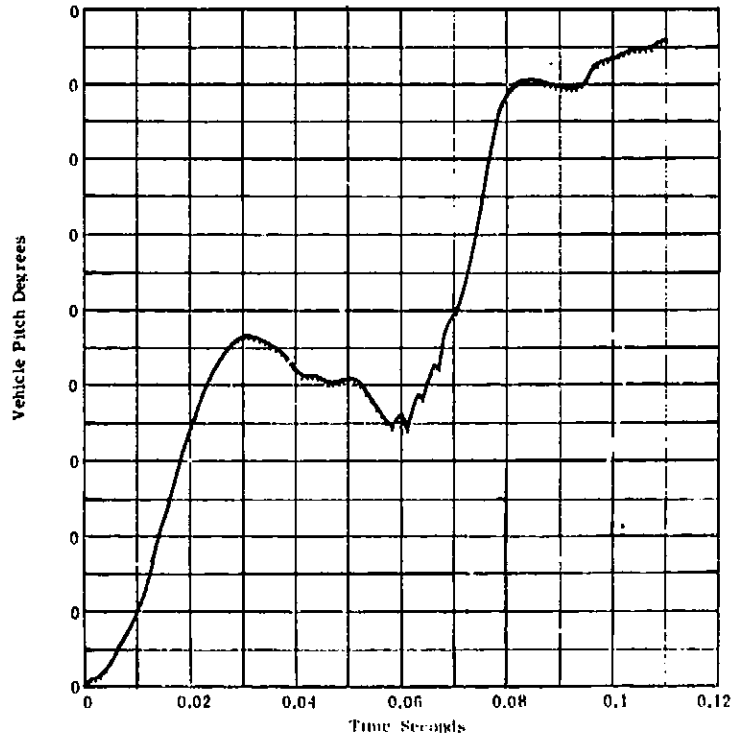

e) Vehicle Pitch Acceleration - Ξ

Figure 6-20. Computer Results For LM Model Drop No. 1 Using High Strut Damping in Computer Simulation (See Figure 6-10 for drop conditions) (Sheet 1 of 4)

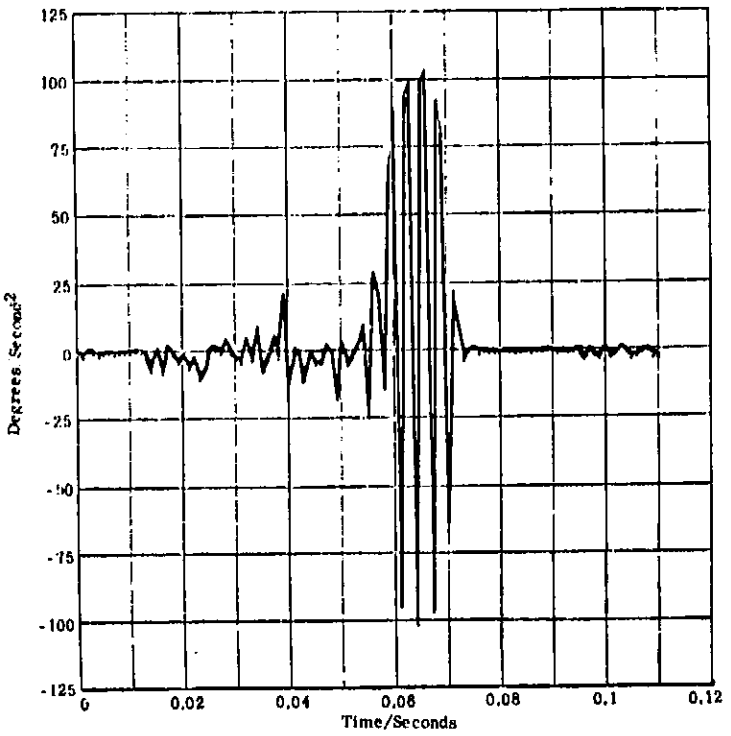

e) Vehicle Pitch Acceleration - $\ddot{\Xi}$

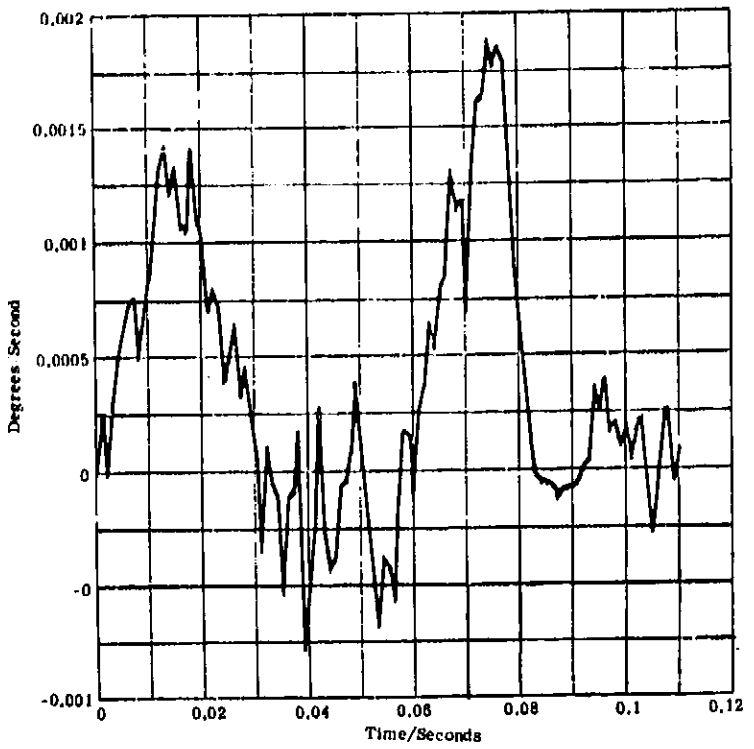

f) Vehicle Pitch Rate - $\dot{\Xi}$

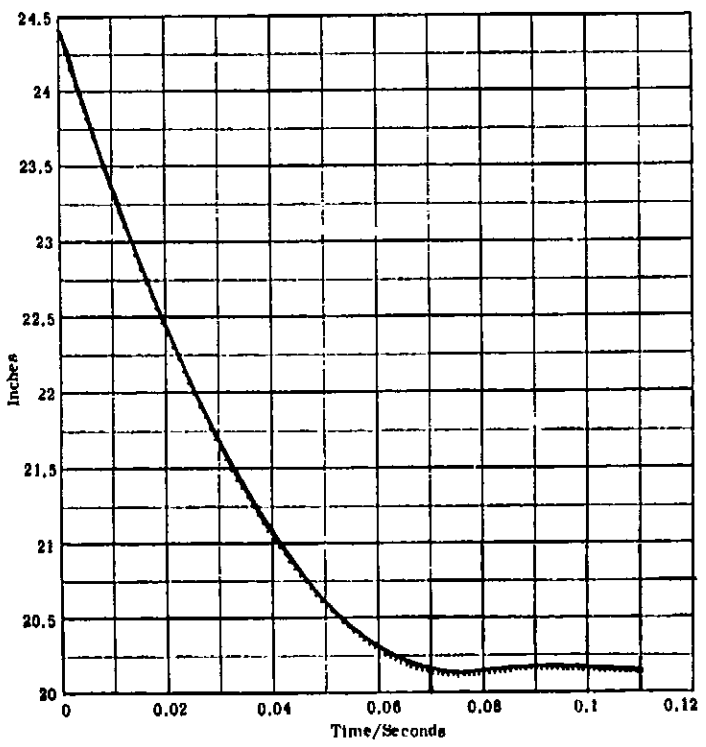

g) Vehicle c.g. Vertical Position - X

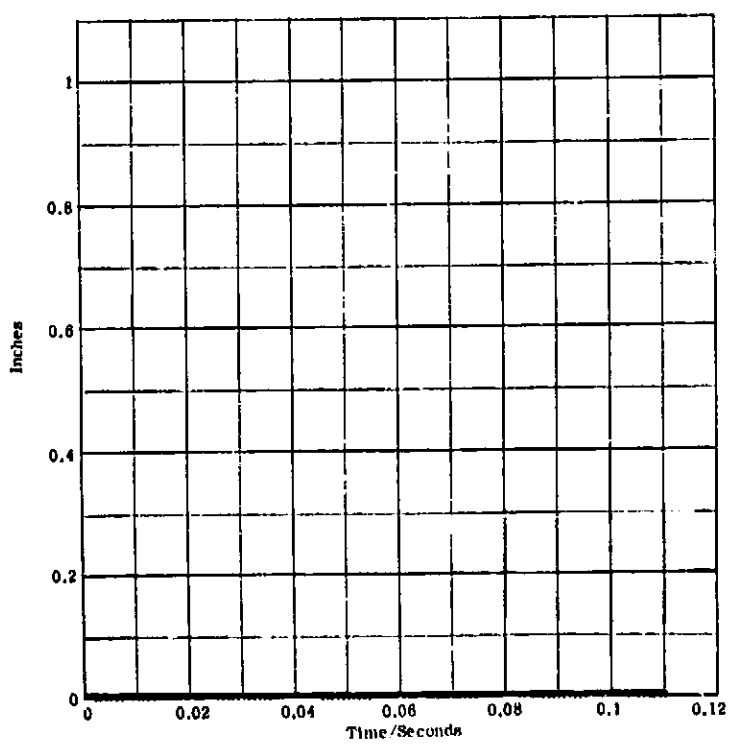

h) Vehicle c.g. Horizontal Position - Y

Figure 6-20. Computer Results For LM Model Drop No. 1 Using High Strut Damping in Computer Simulation (See Figure 6-10 for drop conditions) (Sheet 2 of 4)

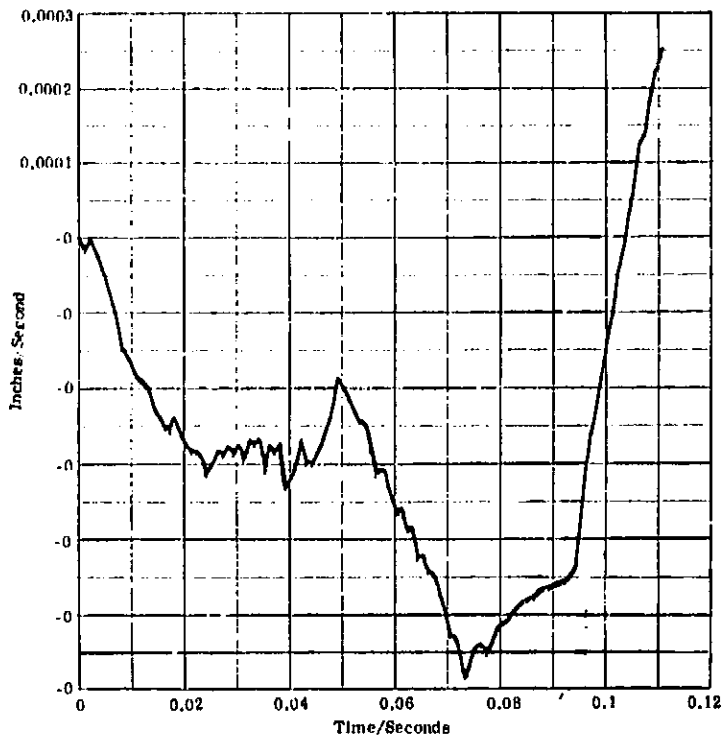

i) Vehicle c.g. Horizontal Velocity - $\dot{Y}$

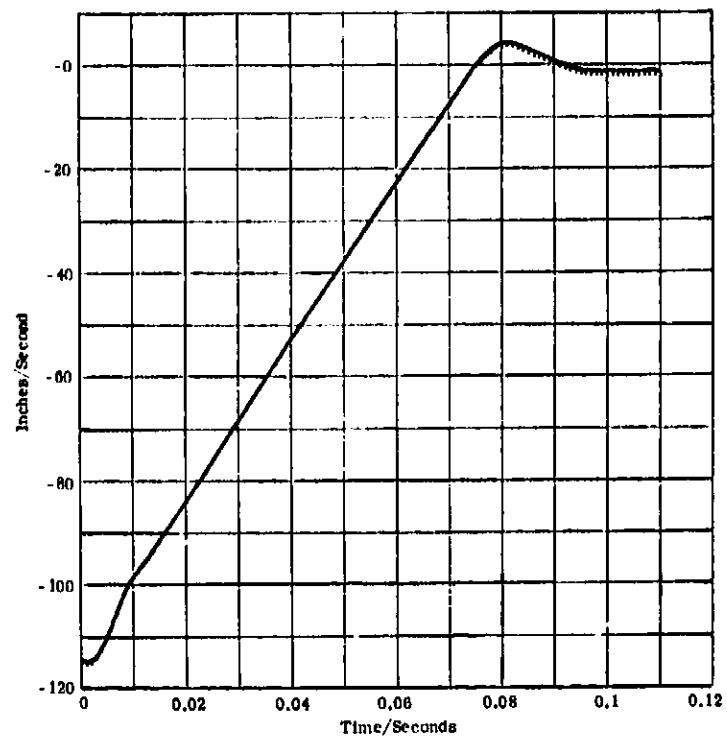

j) Vehicle c.g. Vertical Velocity - $\dot{X}$

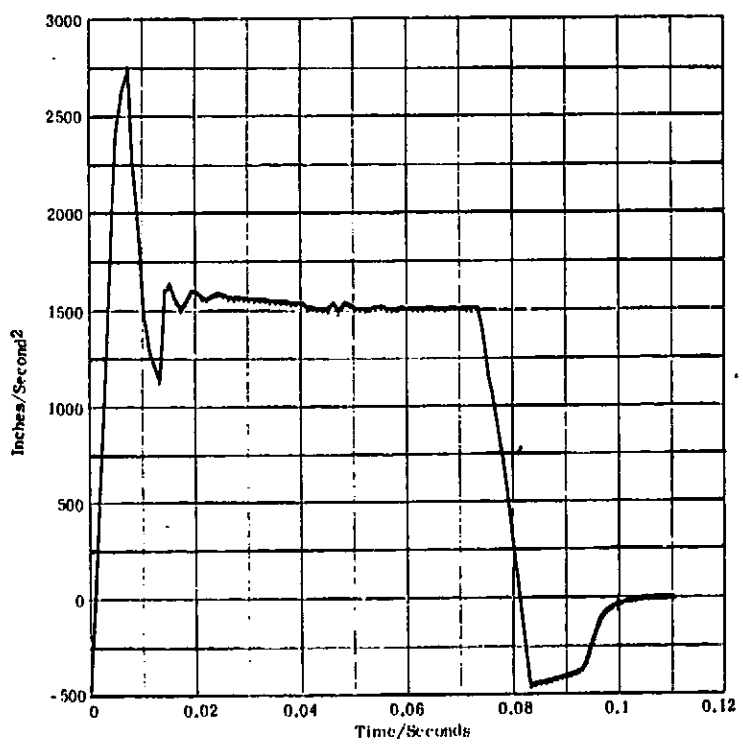

k) Vehicle c.g. Vertical Acceleration - $\ddot{X}$

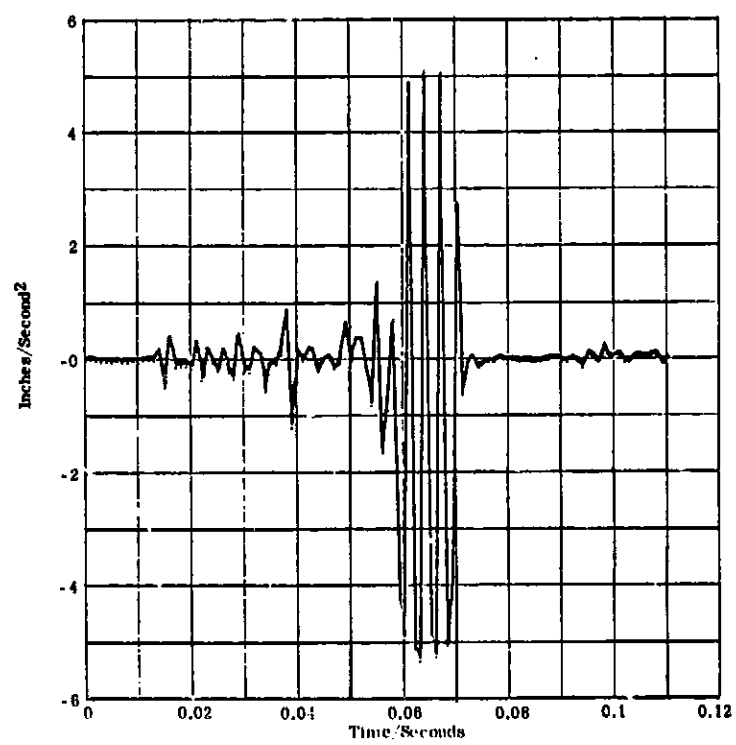

l) Vehicle c.g. Horizontal Acceleration - $\ddot{Y}$

Figure 6-20. Computer Results For LM Model Drop No. 1 Using High Strut Damping in Computer Simulation (See Figure 6-10 for drop conditions) (Sheet 3 of 4)

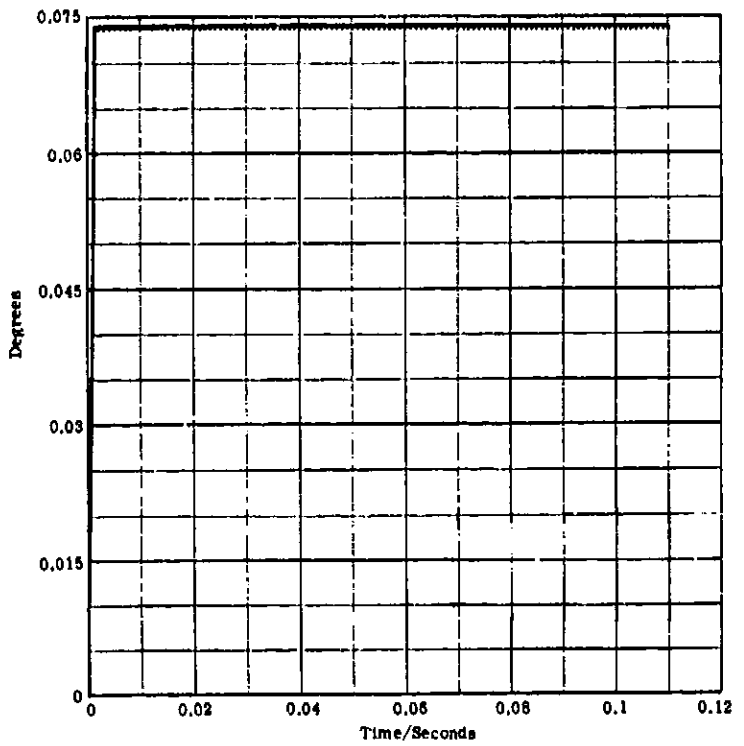

m) Footpad Pitch Angle - α

Figure 6-20. Computer Results For LM Model Drop No. 1 Using High Strut Damping in Computer Simulation (See Figure 6-10 for drop conditions) (Sheet 4 of 4)

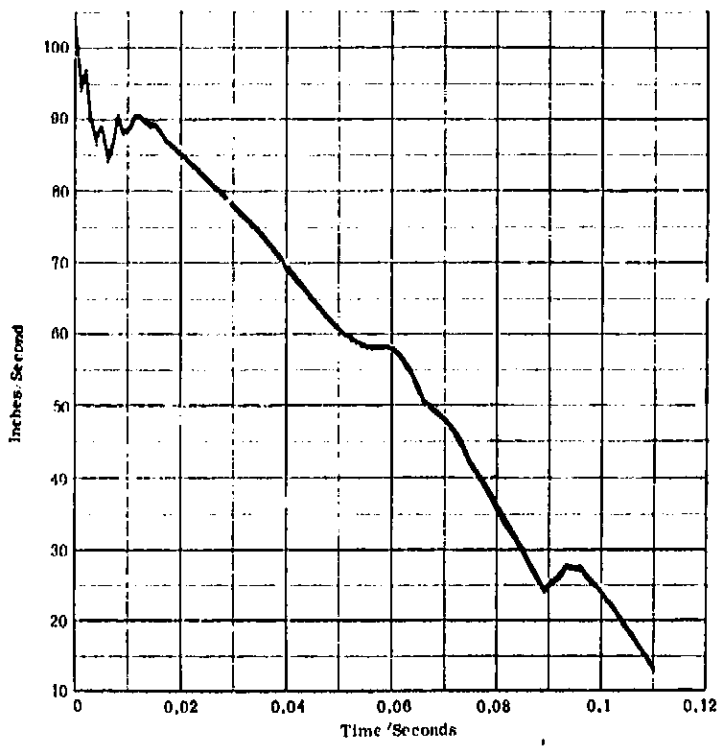

a) Footpad Velocity - V_{ap}

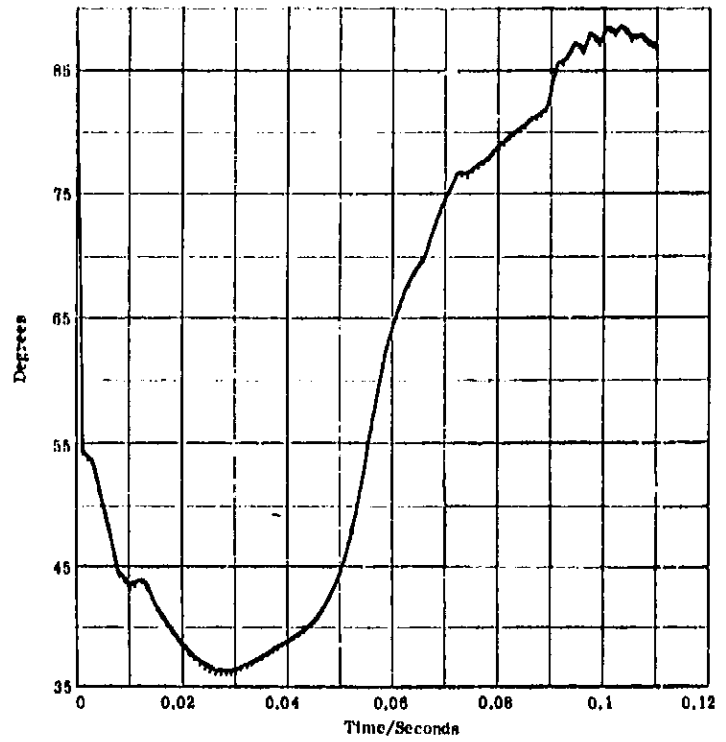

b) Footpad Velocity Angle - θ

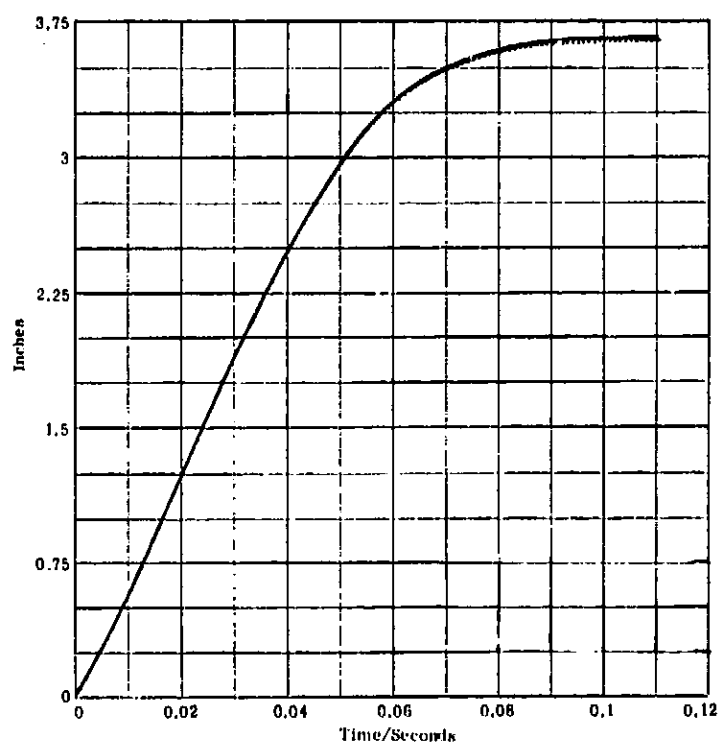

c) Footpad Penetration - d

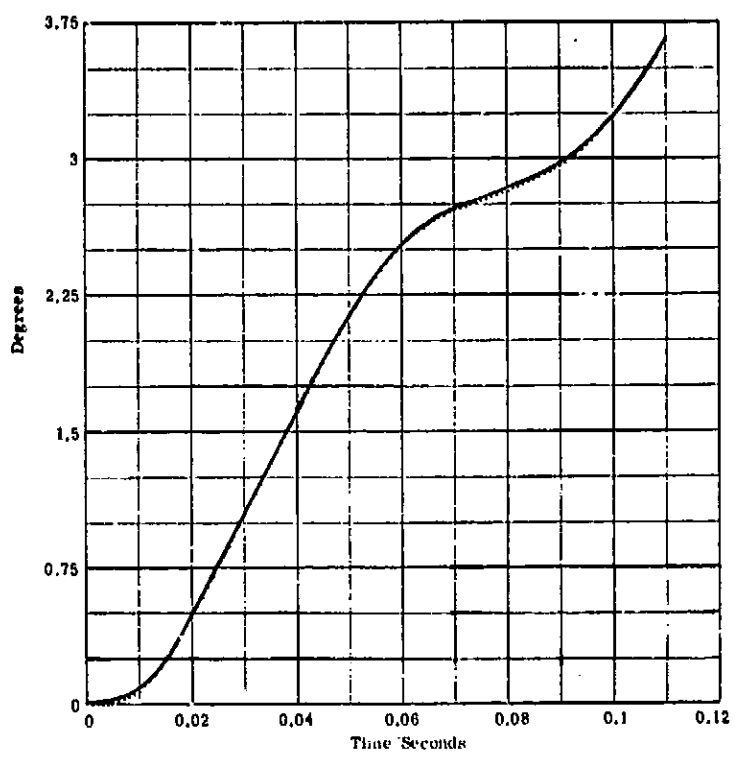

d) Vehicle Pitch Angle - Ξ

Figure 6-21. Computer Results For LM Model Drop No. 3 Using High Strut Damping in Computer Simulation (See Figure 6-10 for drop conditions) (Sheet 1 of 4)

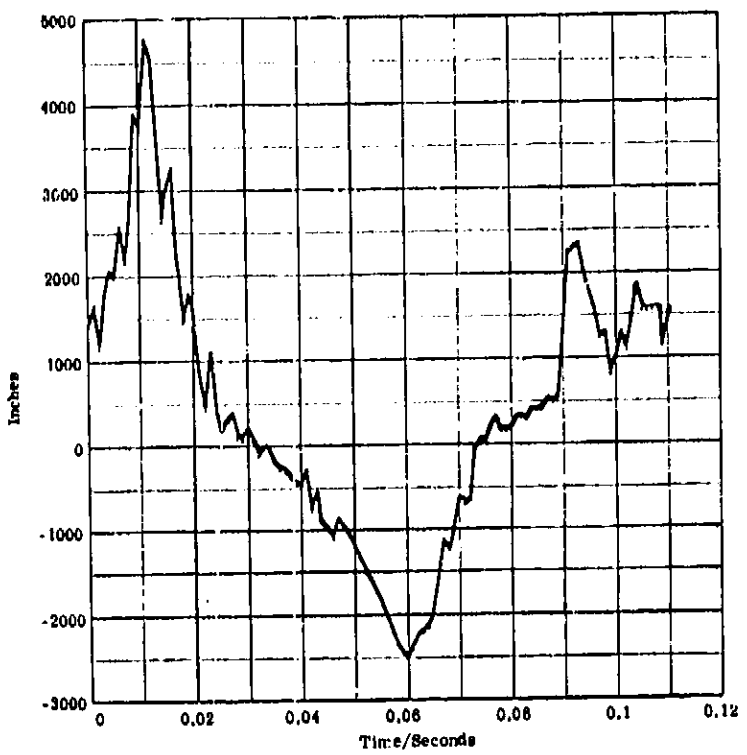

e) Vehicle Pitch Acceleration-$\ddot{\Xi}$

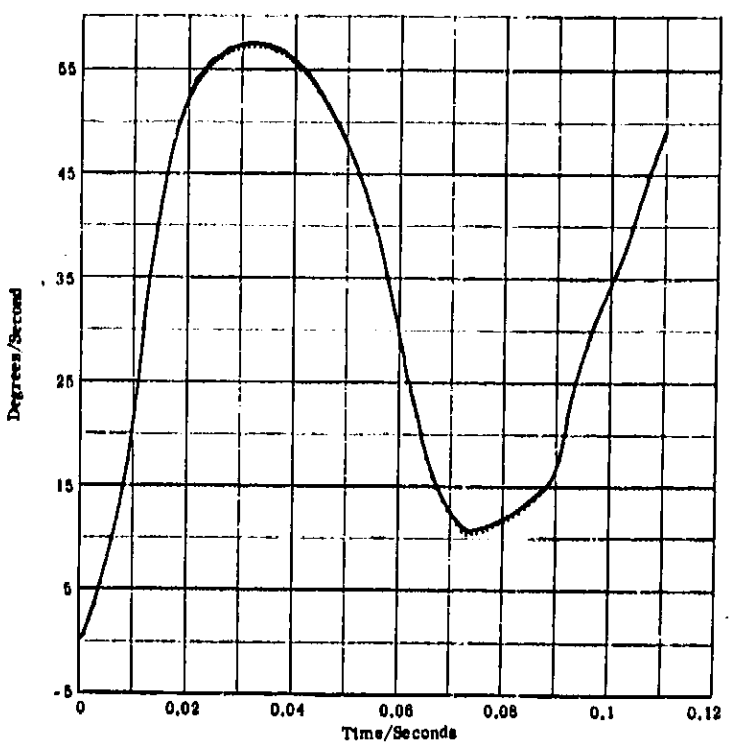

f) Vehicle Pitch Rate -$\dot{\Xi}$

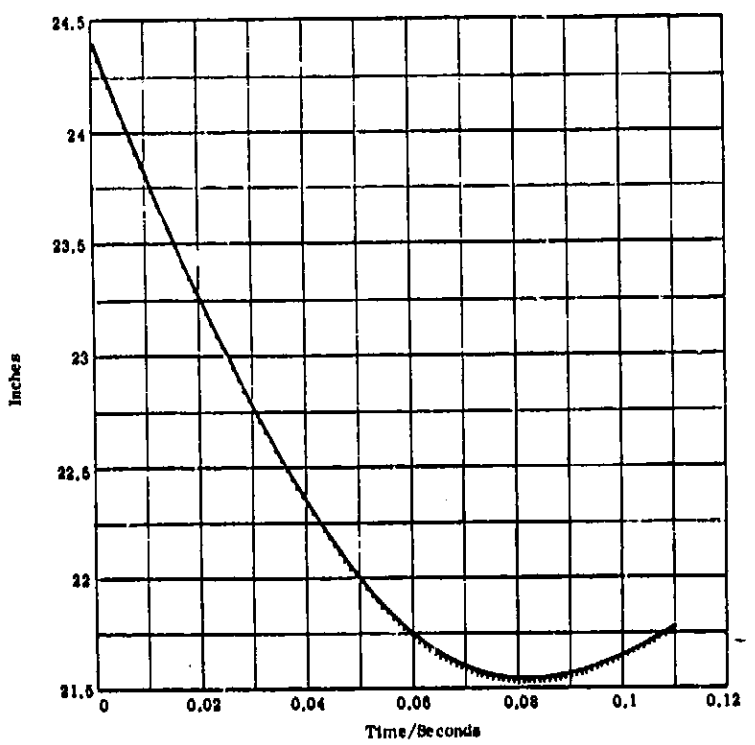

g) Vehicle c.g. Vertical Position - X

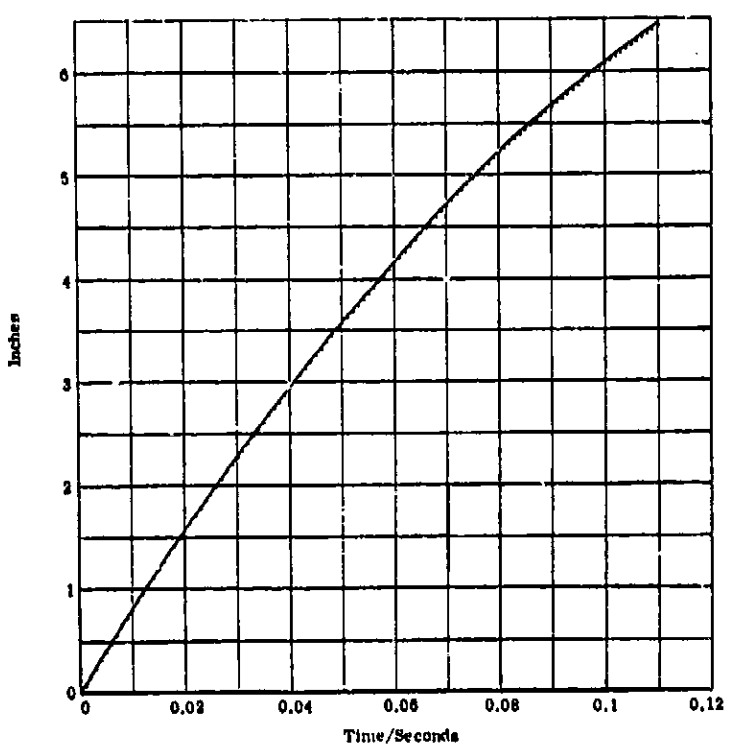

h) Vehicle c.g. Horizontal Position - Y

Figure 6-21. Computer Results For LM Model Drop No. 3 Using High Strut Damping in Computer Simulation (See Figure 6-10 for drop conditions) (Sheet 2 of 4)

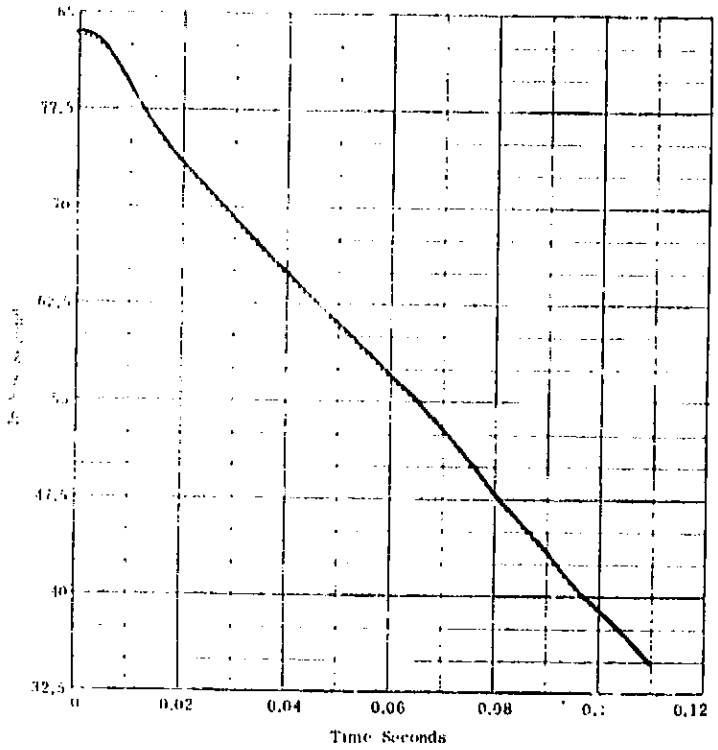

i) Vehicle c.g. Horizontal Velocity - $\dot{Y}$

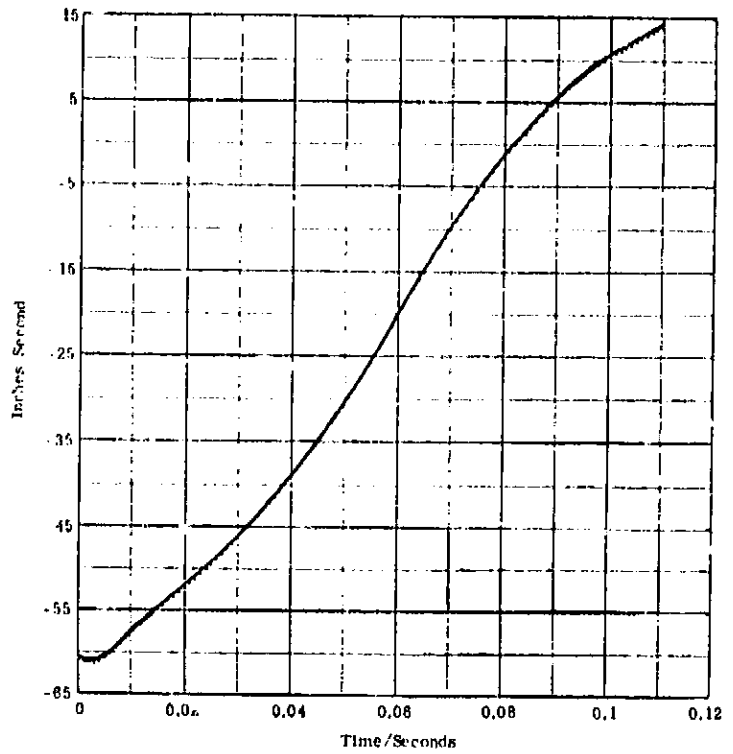

j) Vehicle c.g. Vertical Velocity - $\dot{X}$

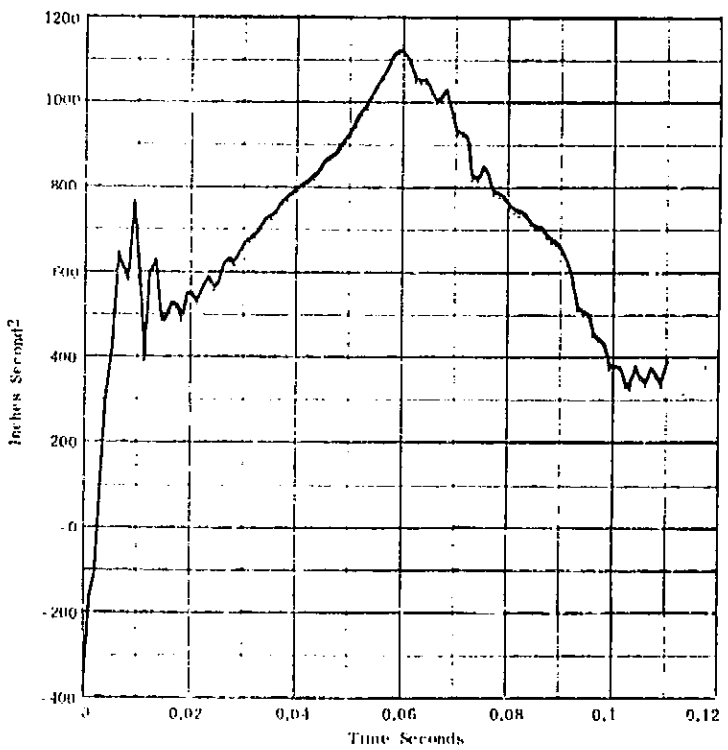

k) Vehicle c.g. Vertical Acceleration - $\ddot{X}$

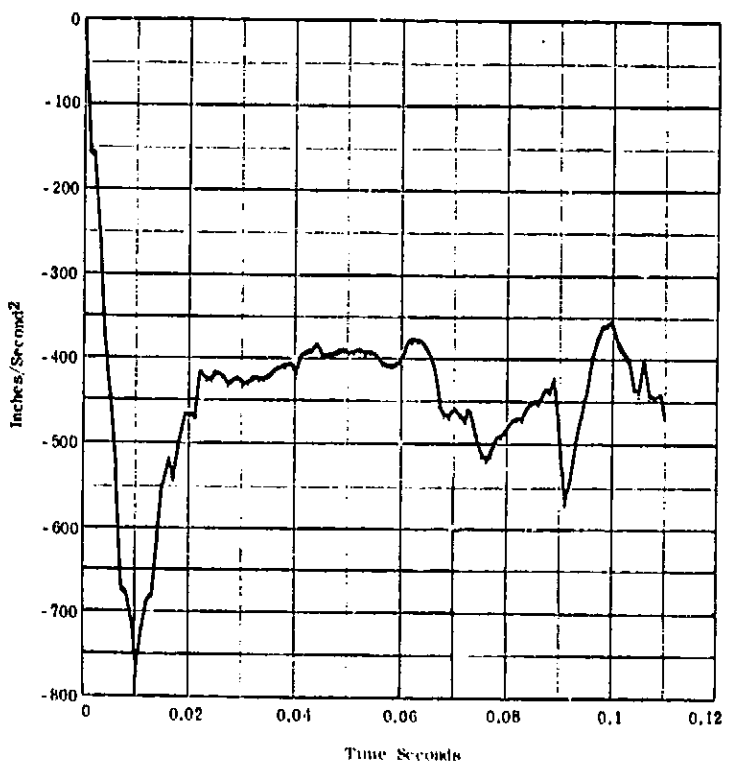

l) Vehicle c.g. Horizontal Acceleration - $\ddot{Y}$

Figure 6-21. Computer Results For LM Model Drop No. 3 Using High Strut Damping in Computer Simulation (See Figure 6-10 for drop conditions) (Sheet 3 of 4)

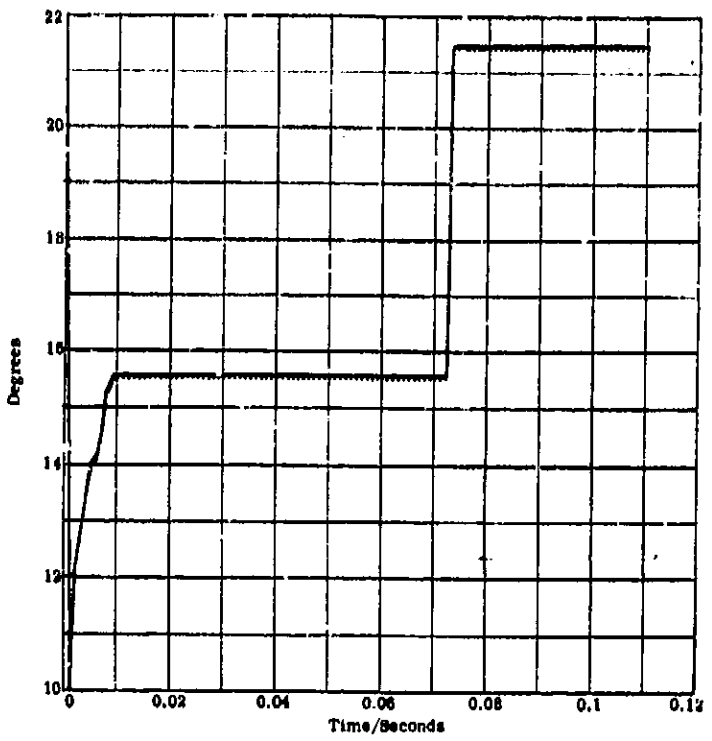

m) Footpad Pitch Angle -α

Figure 6-21. Computer Results For LM Model Drop No. 3 Using High Strut Damping in Computer Simulation (See Figure 6-10 for drop conditions) (Sheet 4 of 4)

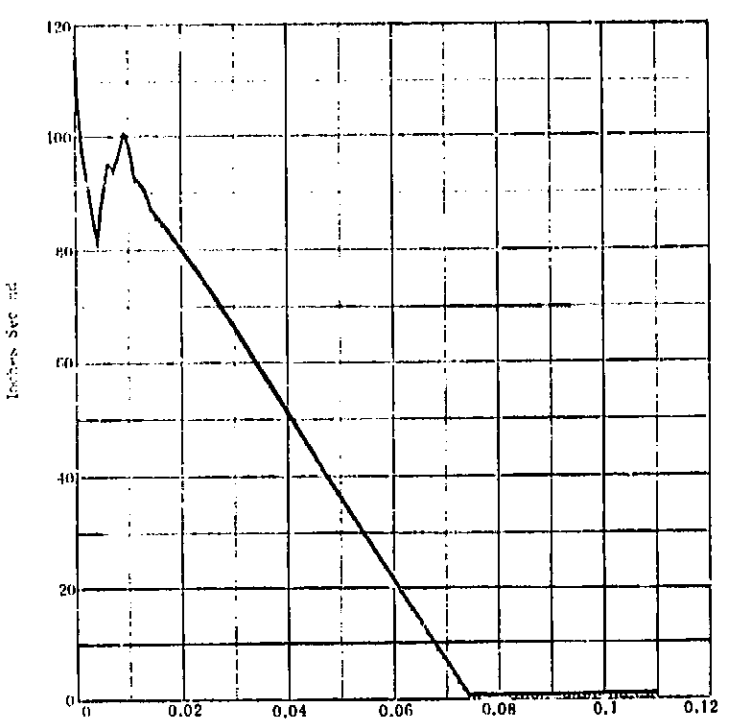

a) Footpad Velocity - V_{ap}

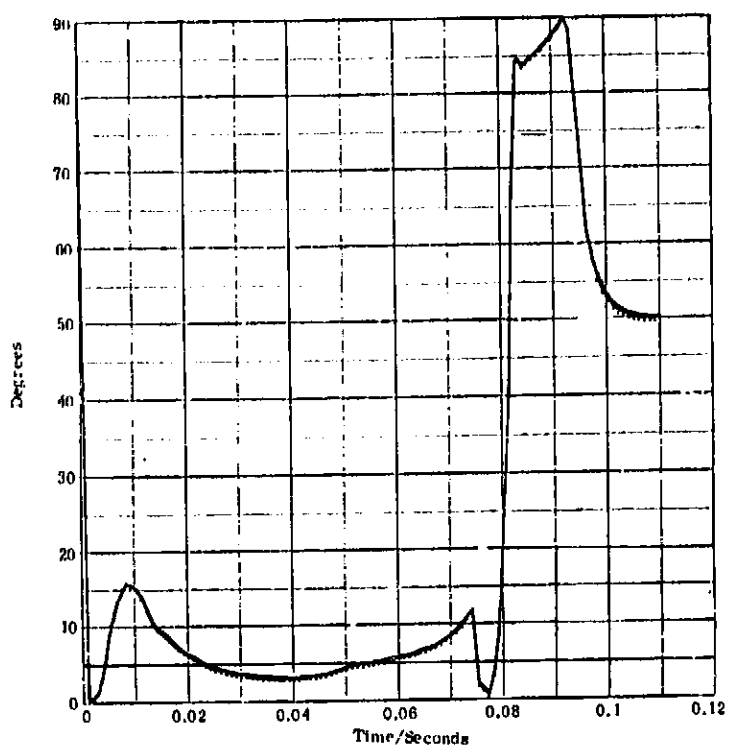

b) Footpad Velocity Angle - θ

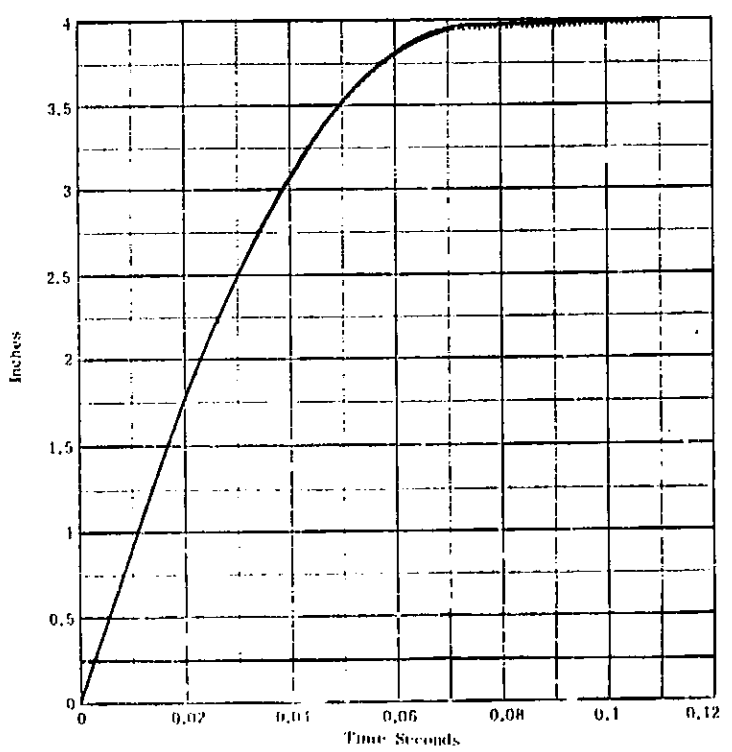

c) Footpad Penetration - d

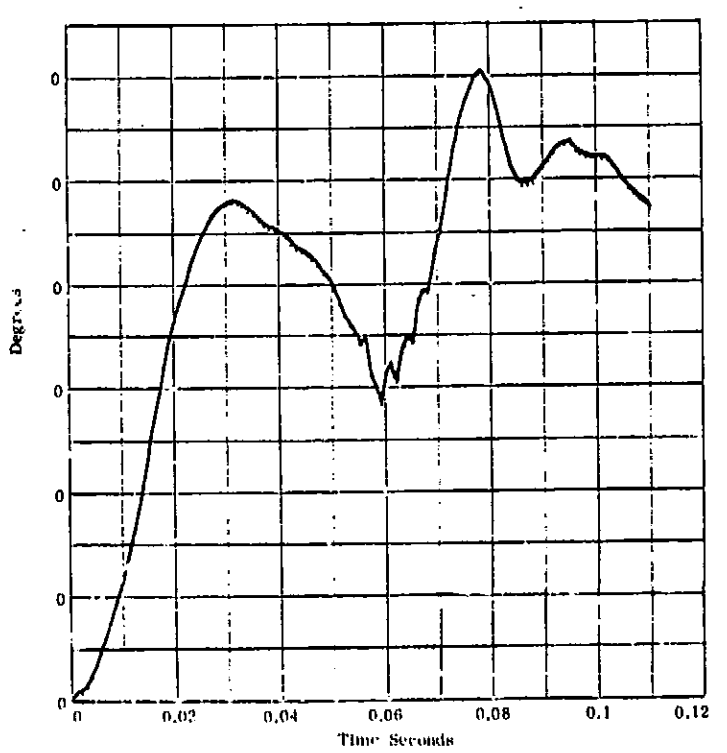

d) Vehicle Pitch Angle - Ξ

Figure 6-22. Computer Results For LM Model Drop No. 4 Using High Strut Damping in Computer Simulation (See Figure 6-10 for drop conditions) (Sheet 1 of 4)

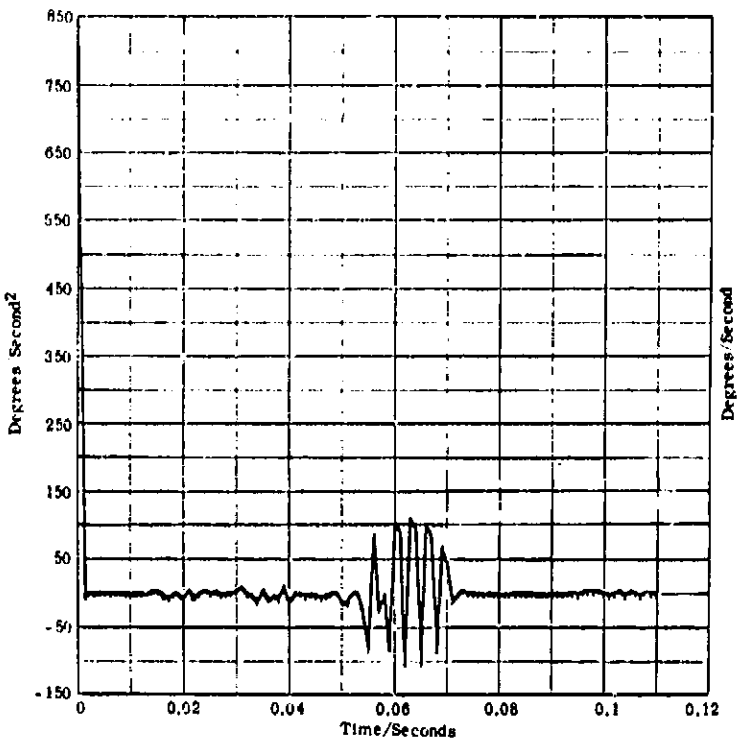

e) Vehicle Pitch Acceleration-$\ddot{\Xi}$

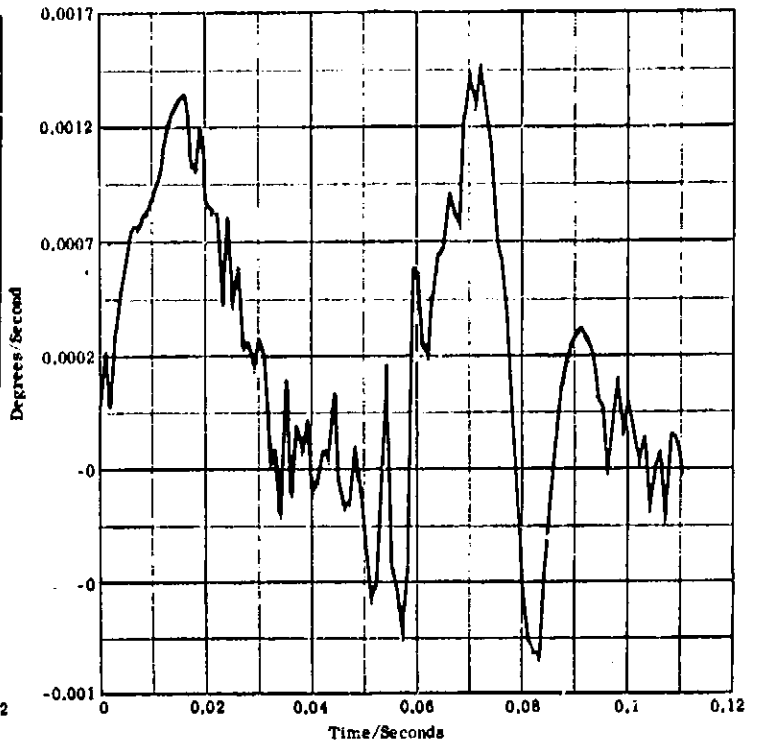

f) Vehicle Pitch Rate - $\dot{\Xi}$

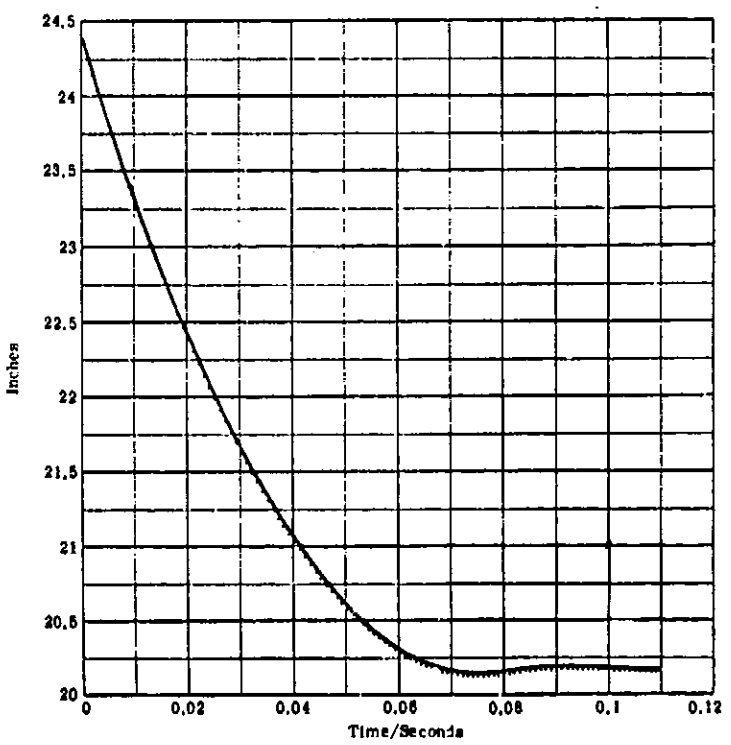

g) Vehicle c.g. Vertical Position - X

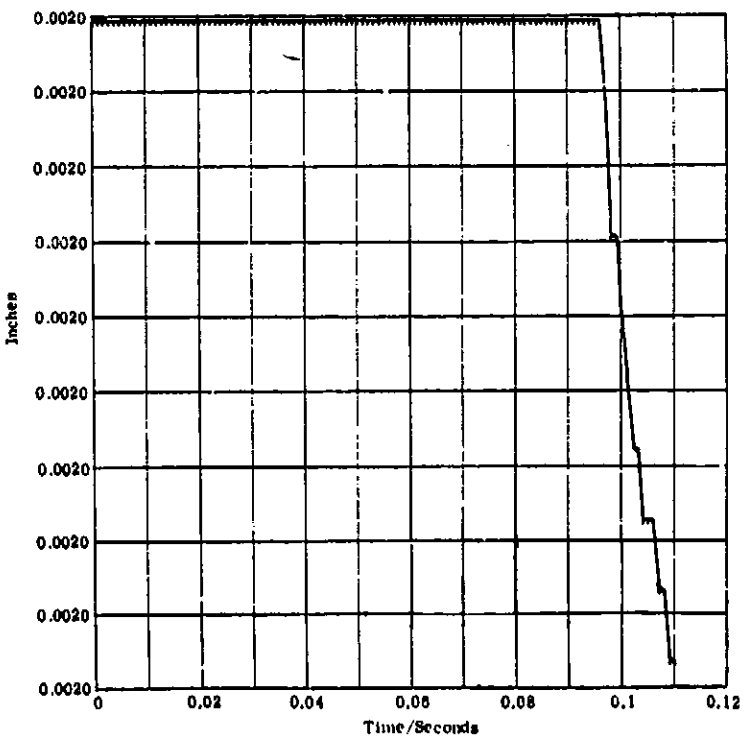

h) Vehicle c.g. Horizontal Position - Y

Figure 6-22. Computer Results For LM Model Drop No. 4 Using High Strut Damping in Computer Simulation (See Figure 6-10 for drop conditions) (Sheet 2 of 4)

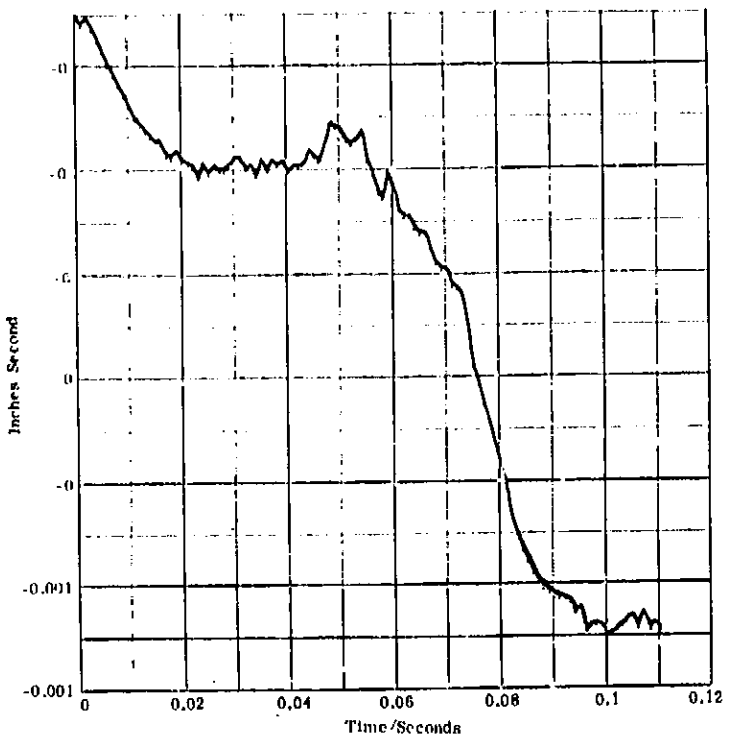

i) Vehicle c.g. Horizontal Velocity - $\dot{Y}$

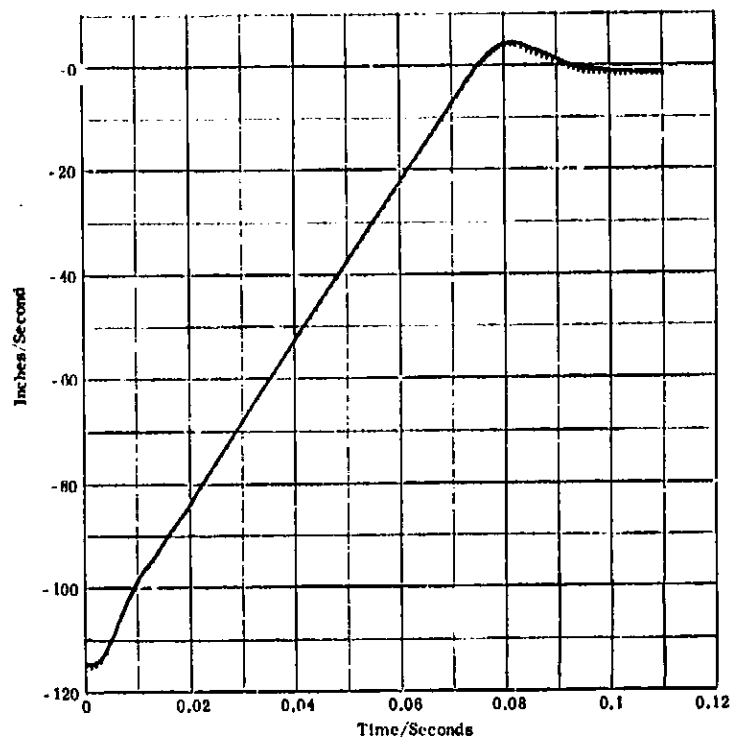

j) Vehicle c.g. Vertical Velocity - $\dot{X}$

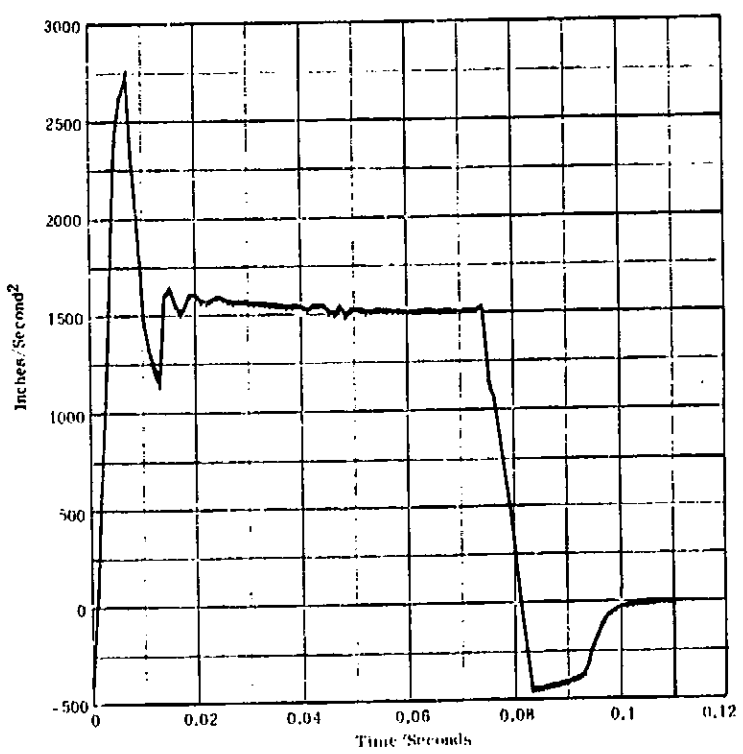

k) Vehicle c.g. Vertical Acceleration - $\ddot{X}$

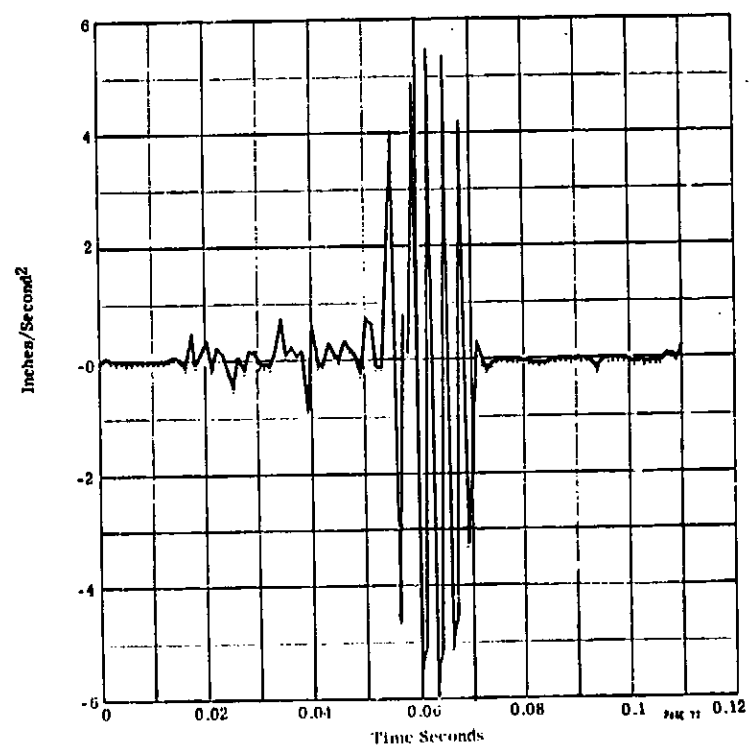

l) Vehicle c.g. Horizontal Acceleration - $\ddot{Y}$

Figure 6-22. Computer Results For LM Model Drop No. 4 Using High Strut Damping in Computer Simulation (See Figure 6-10 for drop conditions) (Sheet 3 of 4)

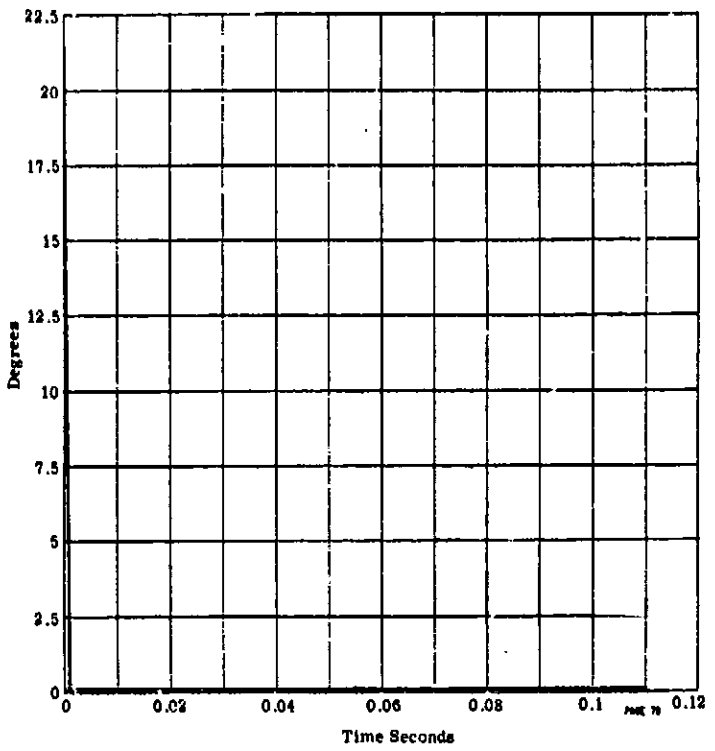

m) Footpad Pitch Angle - α

Figure 6-22. Computer Results For LM Model Drop No. 4 Using High Strut Damping in Computer Simulation (See Figure 6-10 for drop conditions) (Sheet 4 of 4)

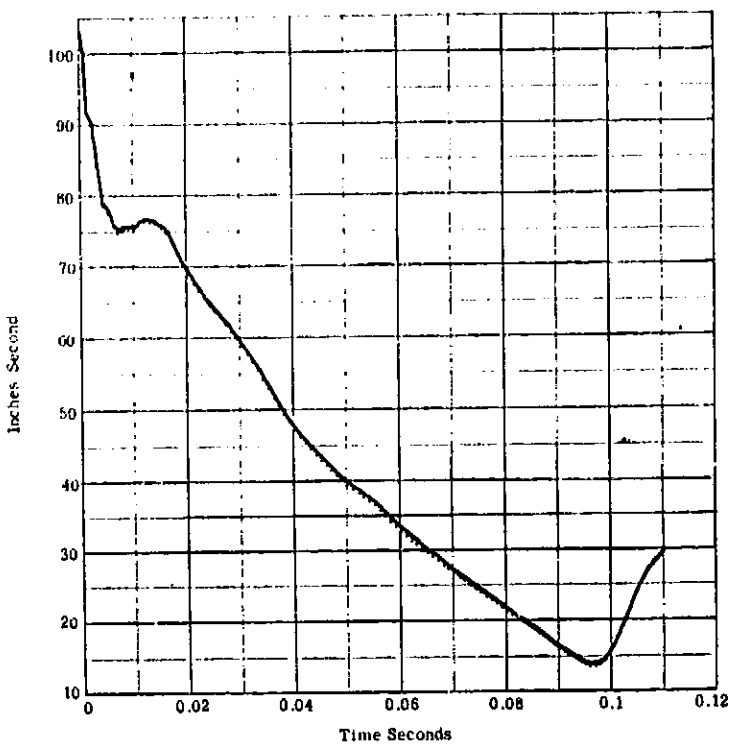

a) Footpad Velocity - V_{ap}

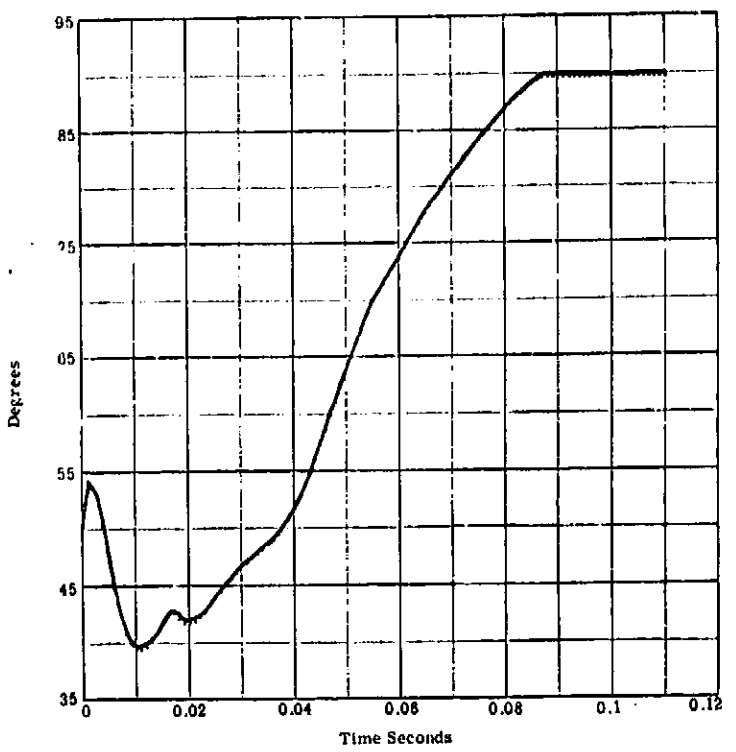

b) Footpad Velocity Angle - θ

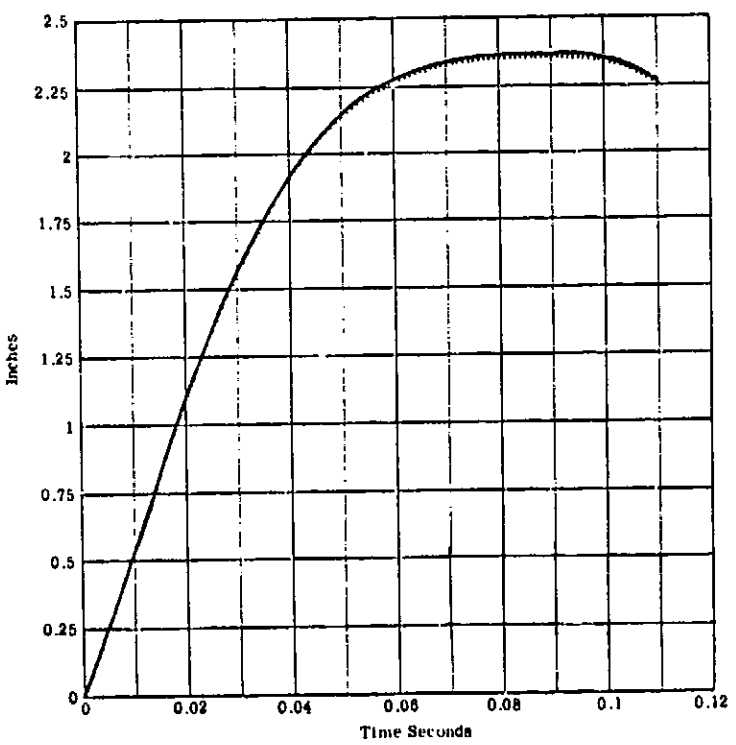

c) Footpad Penetration - d

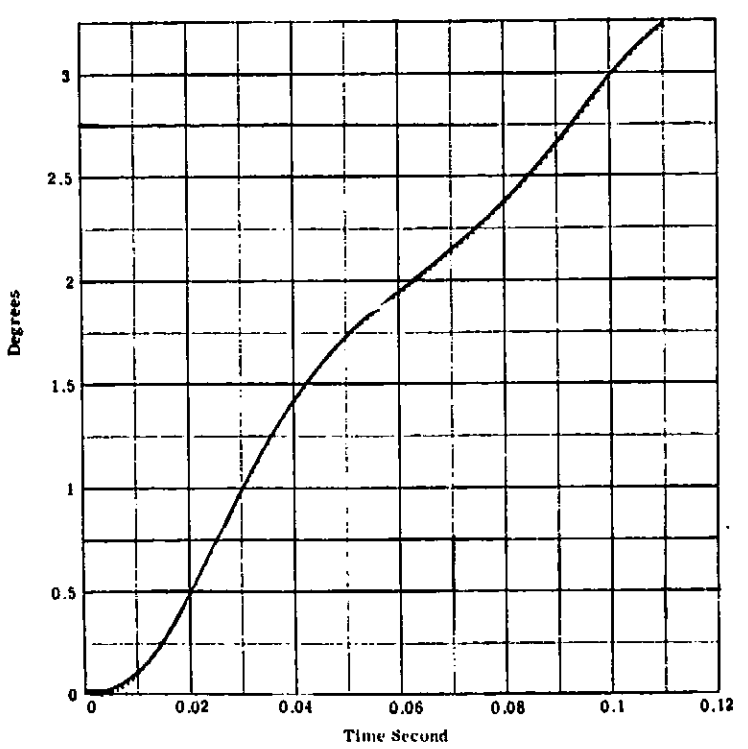

d) Vehicle Pitch Angle - Ξ

Figure 6-23. Computer Results For LM Model Drop No. 5 Using High Strut Damping in Computer Simulation (See Figure 6-10 for drop conditions) (Sheet 1 of 4)

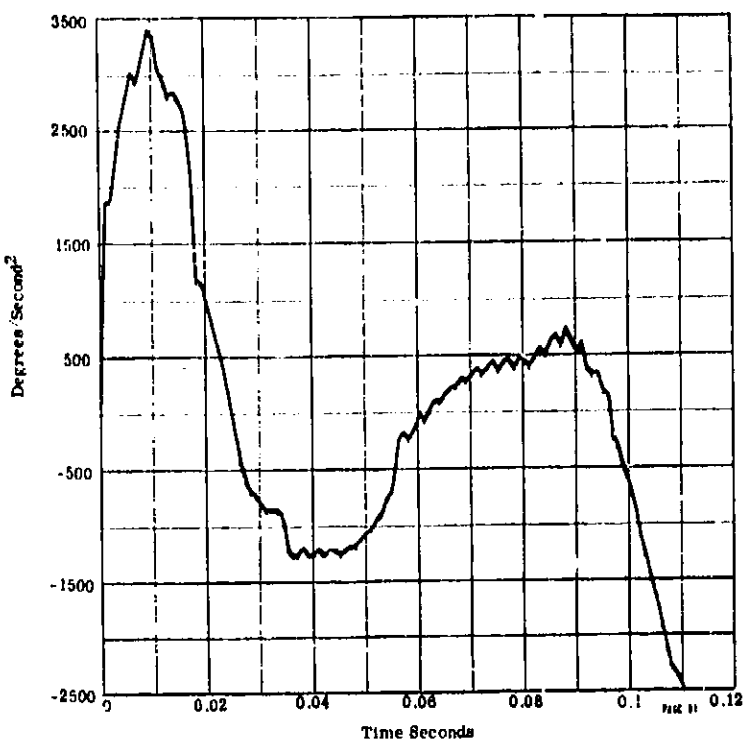

e) Vehicle Pitch Acceleration-$\ddot{\Xi}$

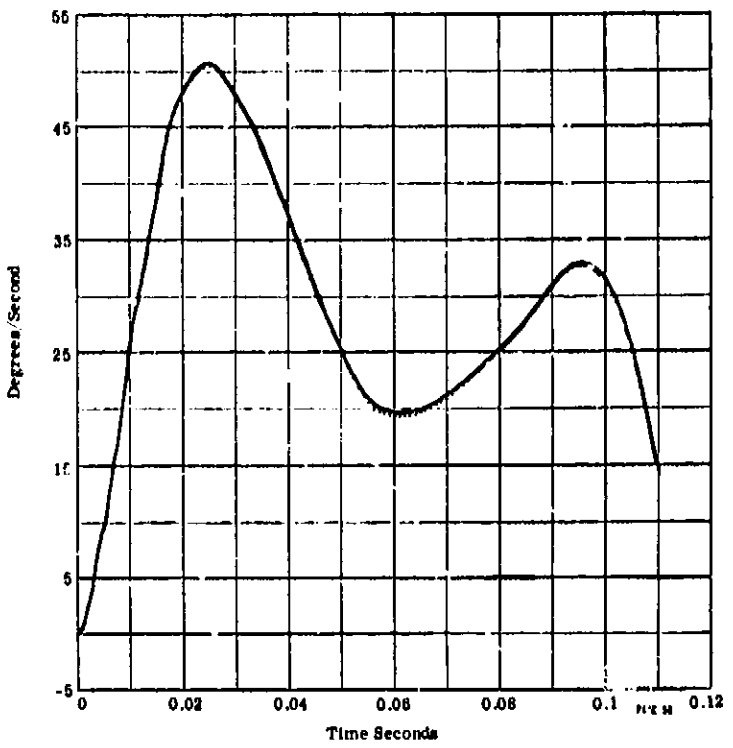

f) Vehicle Pitch Rate - $\dot{\Xi}$

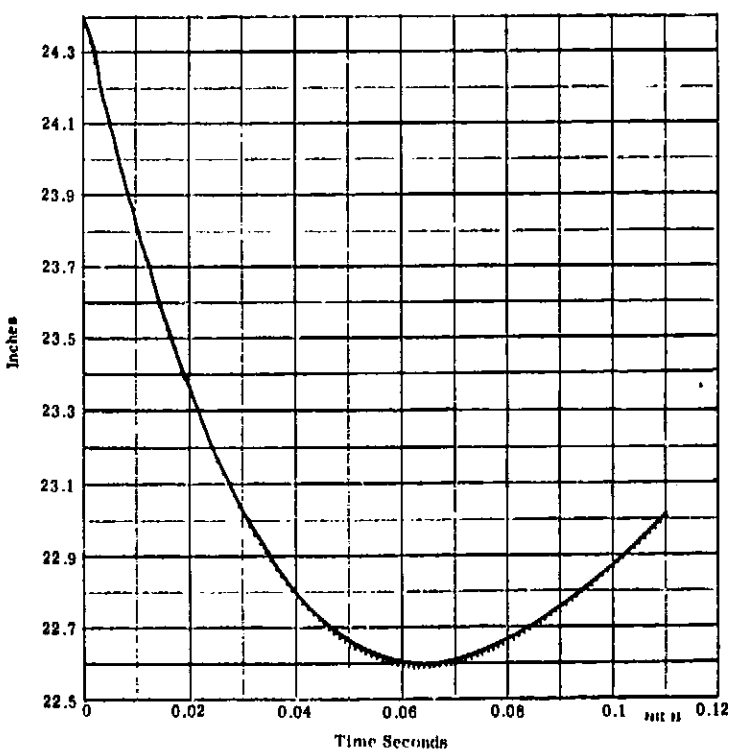

g) Vehicle c.g. Vertical Position - X

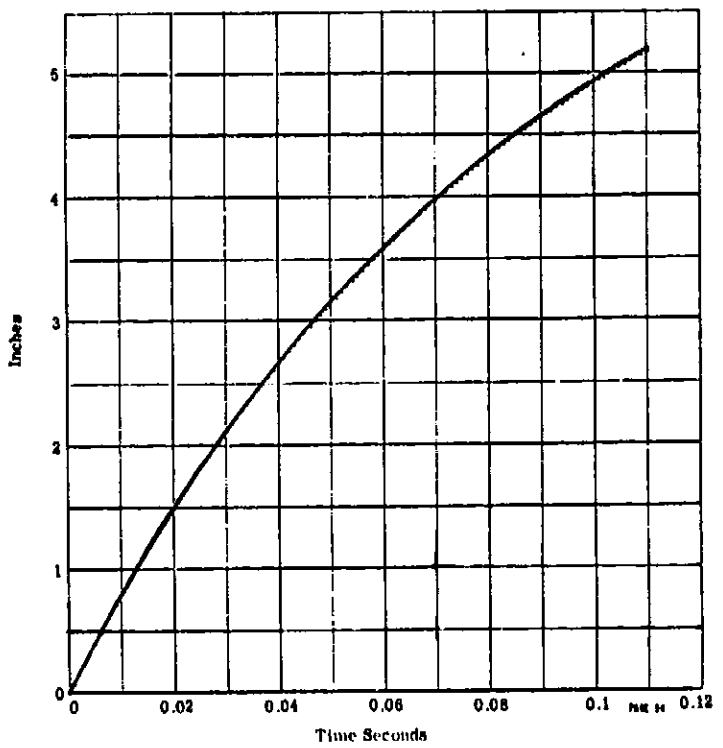

h) Vehicle c.g. Horizontal Position - Y

Figure 6-23. Computer Results For LM Model Drop No. 5 Using High Strut Damping in Computer Simulation (See Figure 6-10 for drop conditions) (Sheet 2 of 4)

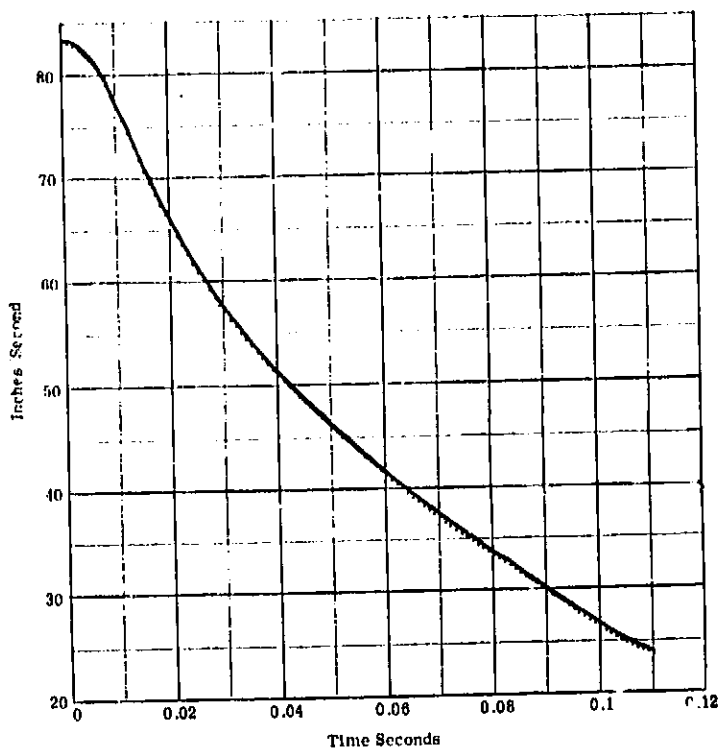

i) Vehicle c.g. Horizontal Velocity - $\dot{Y}$

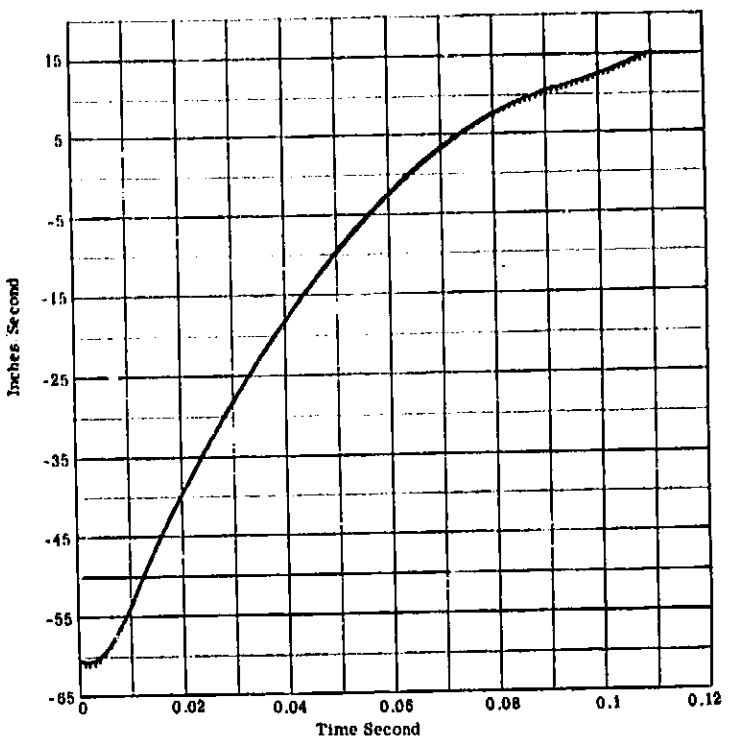

j) Vehicle c.g. Vertical Velocity - $\dot{X}$

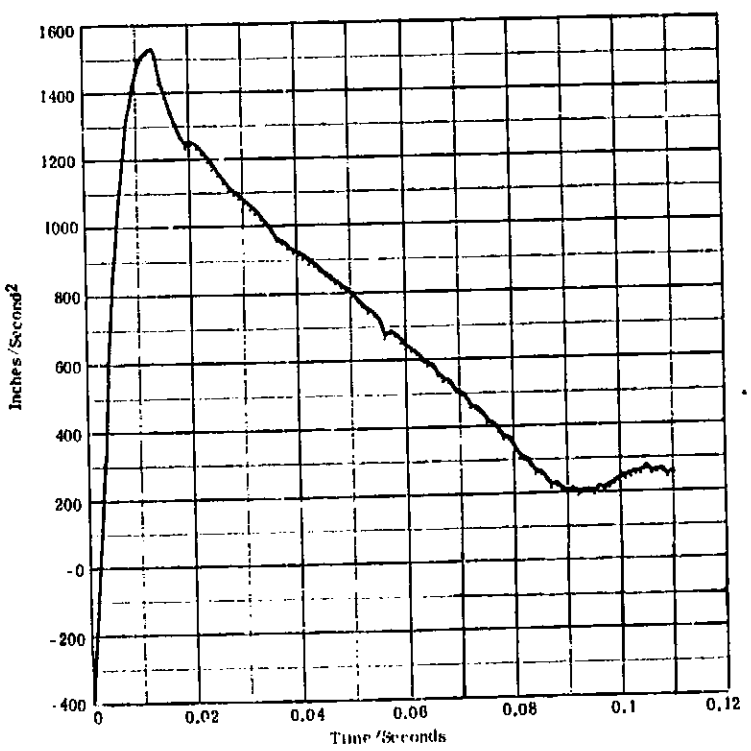

k) Vehicle c.g. Vertical Acceleration - $\ddot{X}$

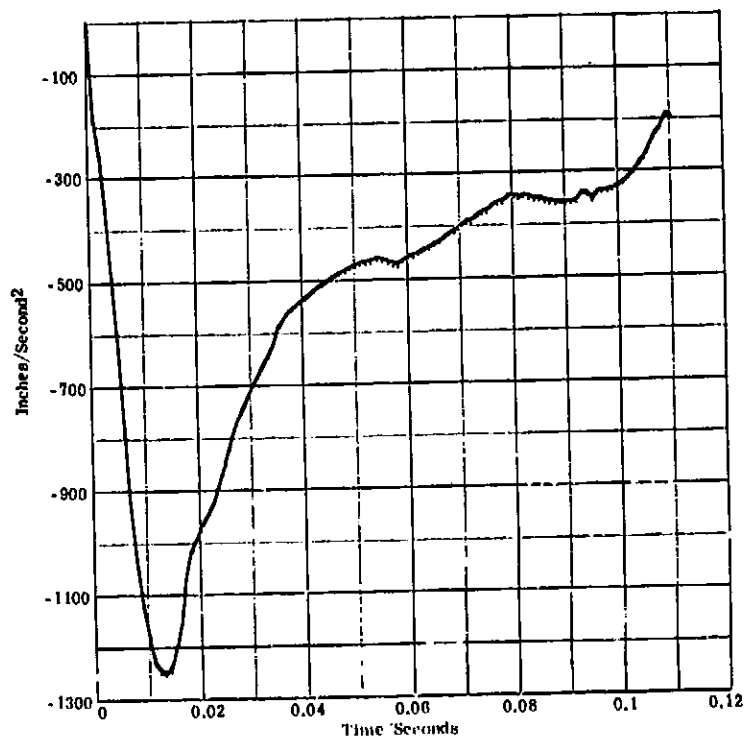

l) Vehicle c.g. Horizontal Acceleration - $\ddot{Y}$

Figure 6-23. Computer Results For LM Model Drop No. 5 Using High Strut Damping in Computer Simulation (See Figure 6-10 for drop conditions) (Sheet 3 of 4)

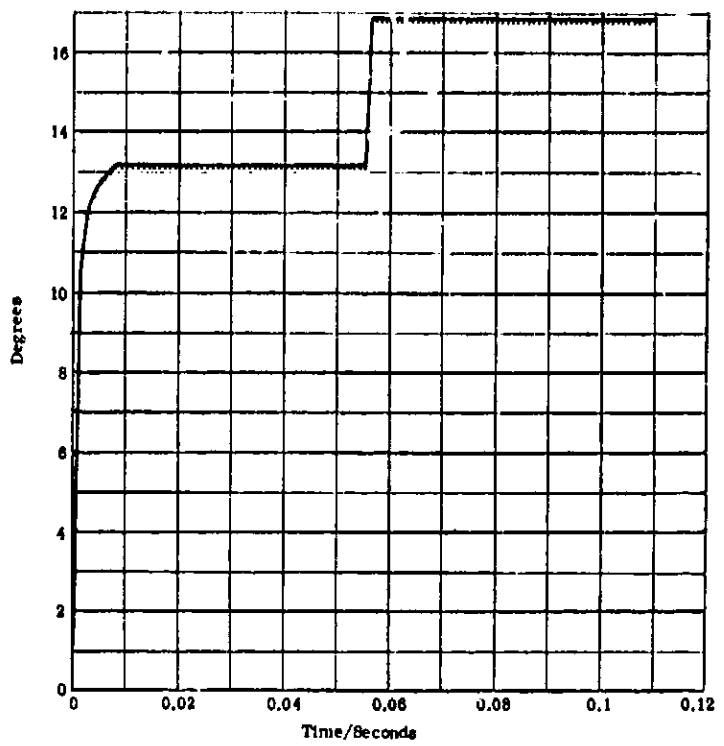

m) Footpad Pitch Angle -α

Figure 6-23. Computer Results For LM Model Drop No. 5 Using High Strut Damping in Computer Simulation (See Figure 6-10 for drop conditions) (Sheet 4 of 4)

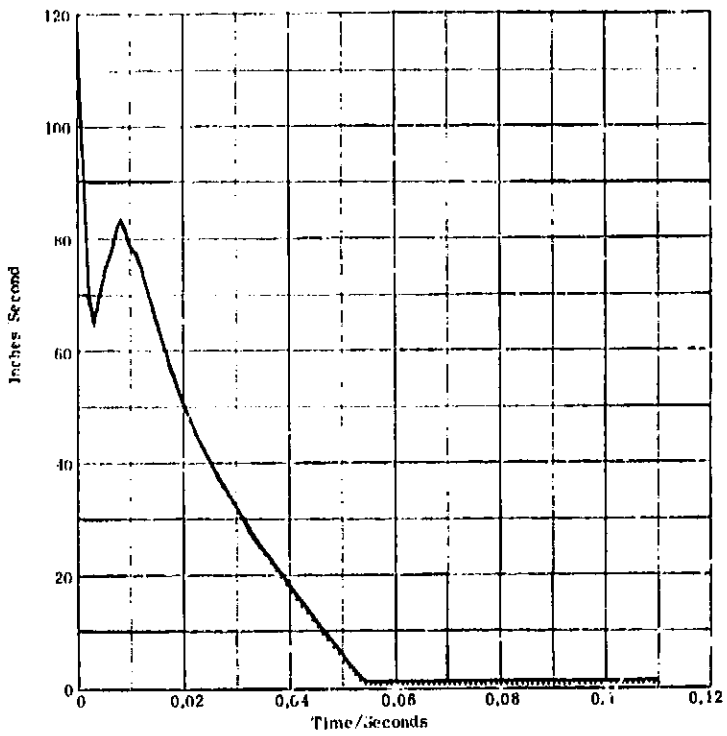

a) Footpad Velocity - Vap

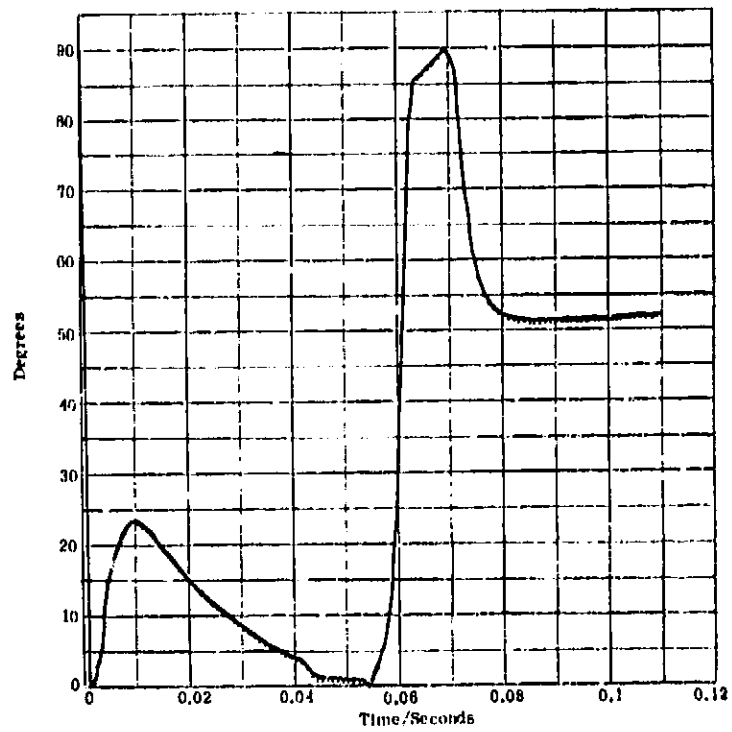

b) Footpad Velocity Angle - θ

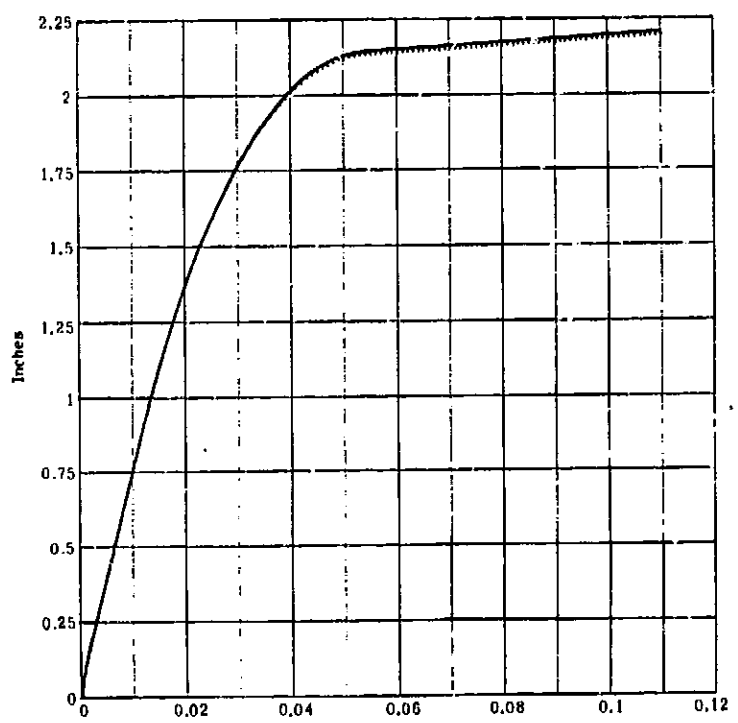

c) Footpad Penetration - d

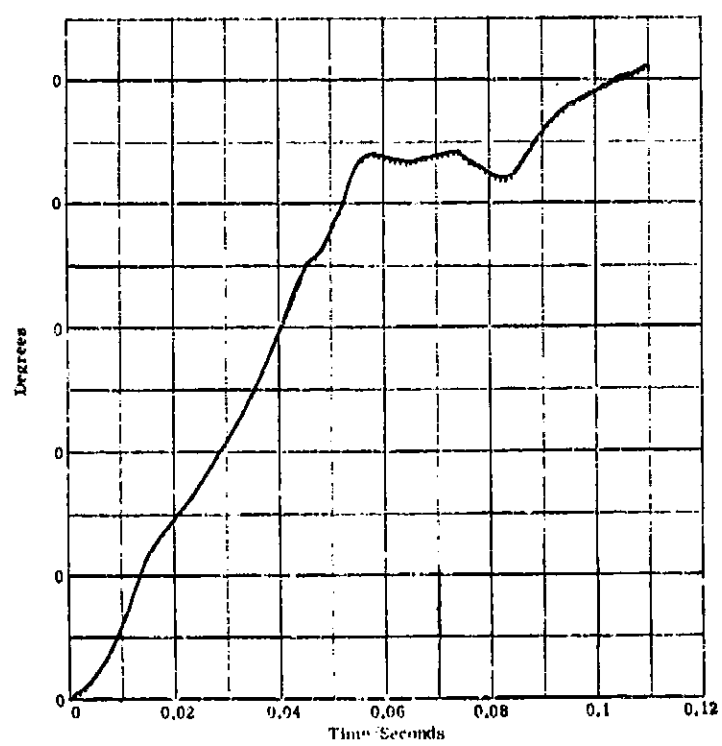

d) Vehicle Piich Angle - Ξ

Figure 6-24. Computer Results For LM Model Drop No. 6 Using High Strut Damping in Computer Simulation (See Figure 6-10 for drop conditions) (Sheet 1 of 4)

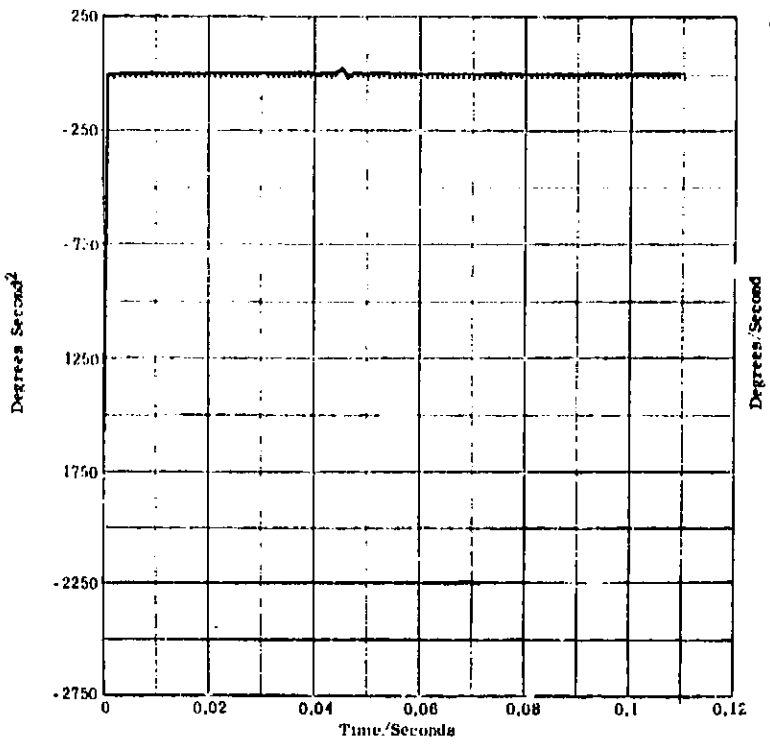

e) Vehicle Pitch Acceleration - $\ddot{\Xi}$

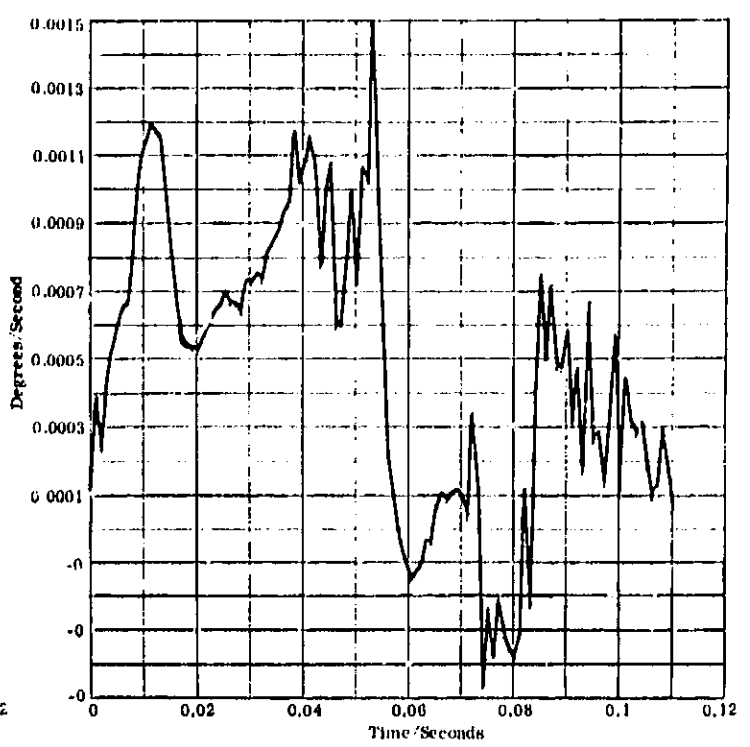

f) Vehicle Pitch Rate - $\dot{\Xi}$

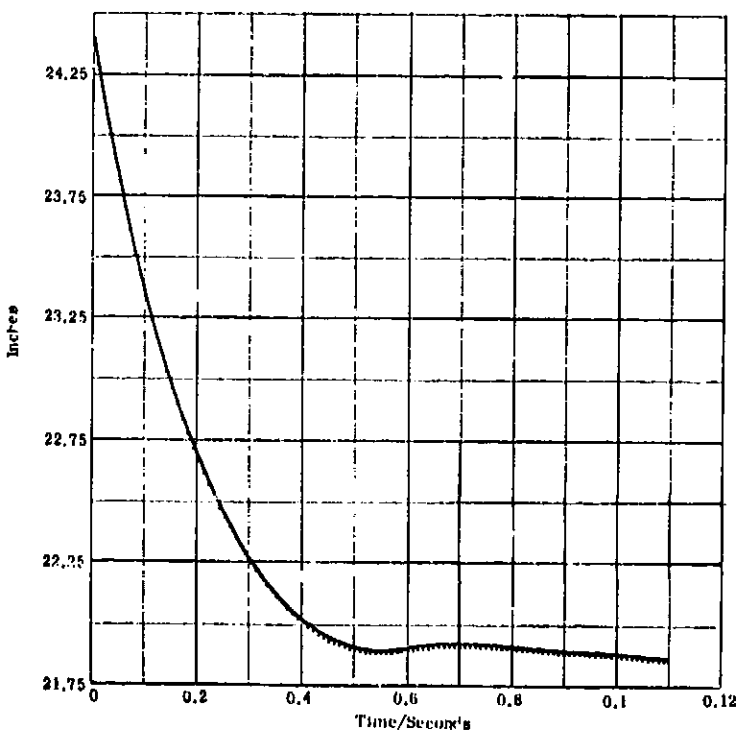

g) Vehicle c.g. Vertical Position - X

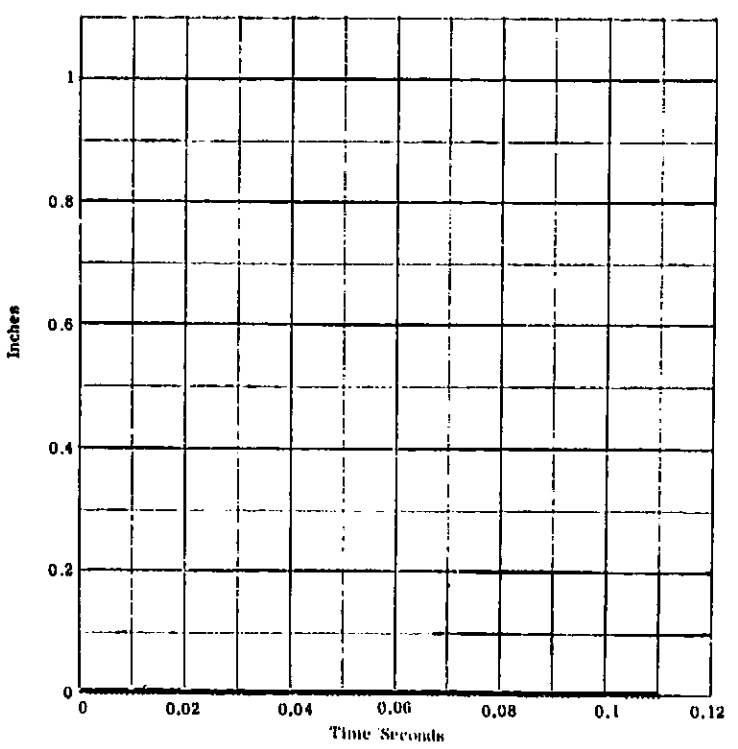

h) Vehicle c.g. Horizontal Position - Y

Figure 6-24. Computer Results For LM Model Drop No. 6 Using High Strut Damping in Computer Simulation (See Figure 6-10 for drop conditions) (Sheet 2 of 4)

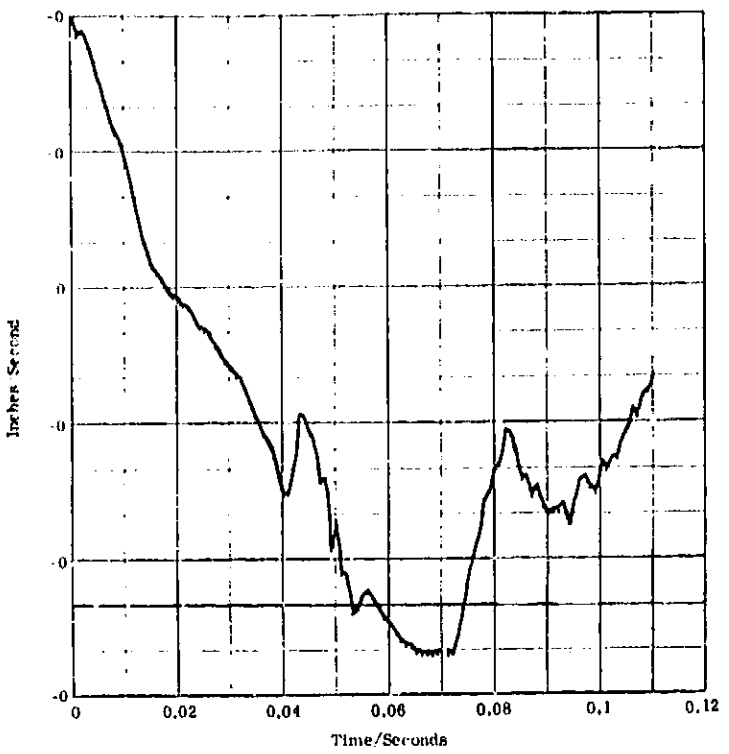

i) Vehicle c.g. Horizontal Velocity - $\dot{Y}$

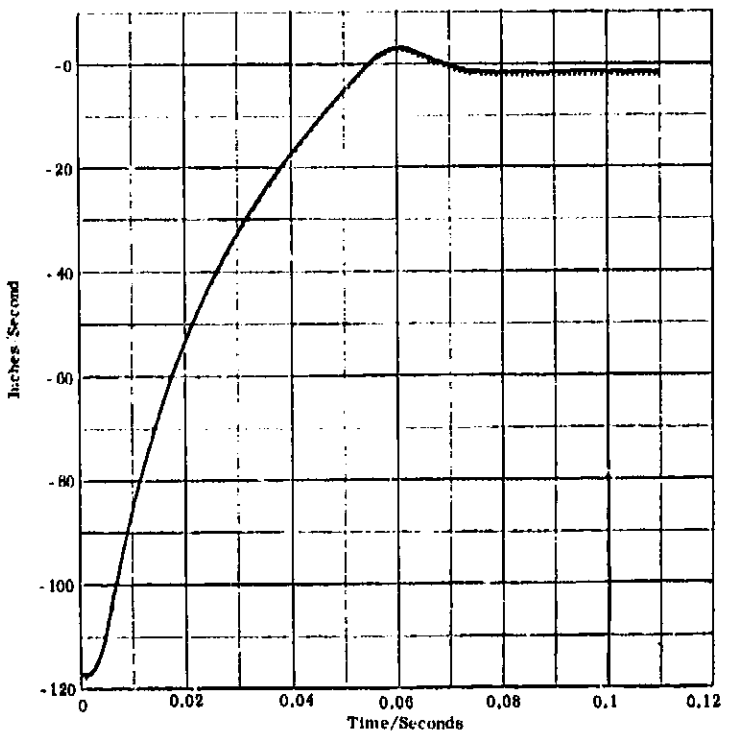

j) Vehicle c.g. Vertical Velocity - $\dot{X}$

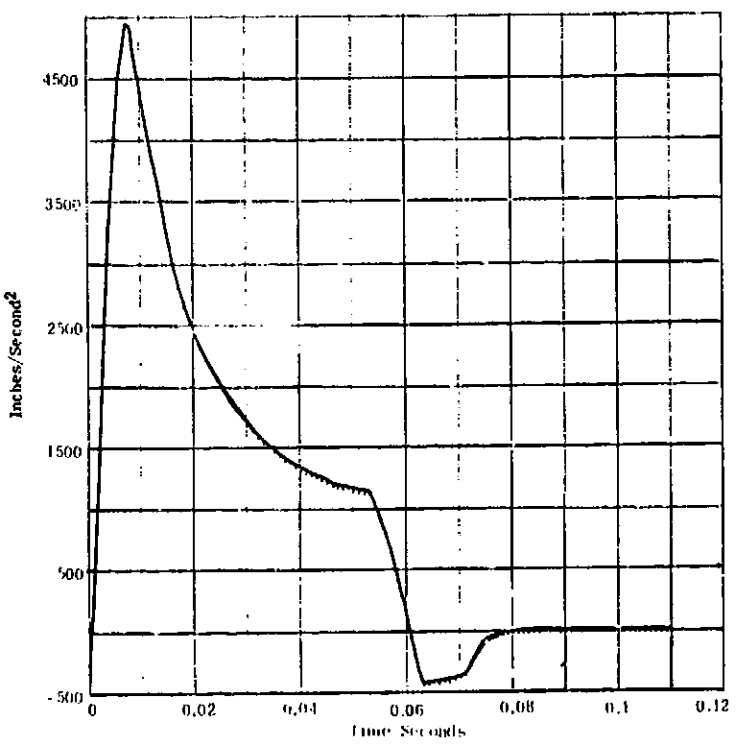

k) Vehicle c.g. Vertical Acceleration - $\ddot{X}$

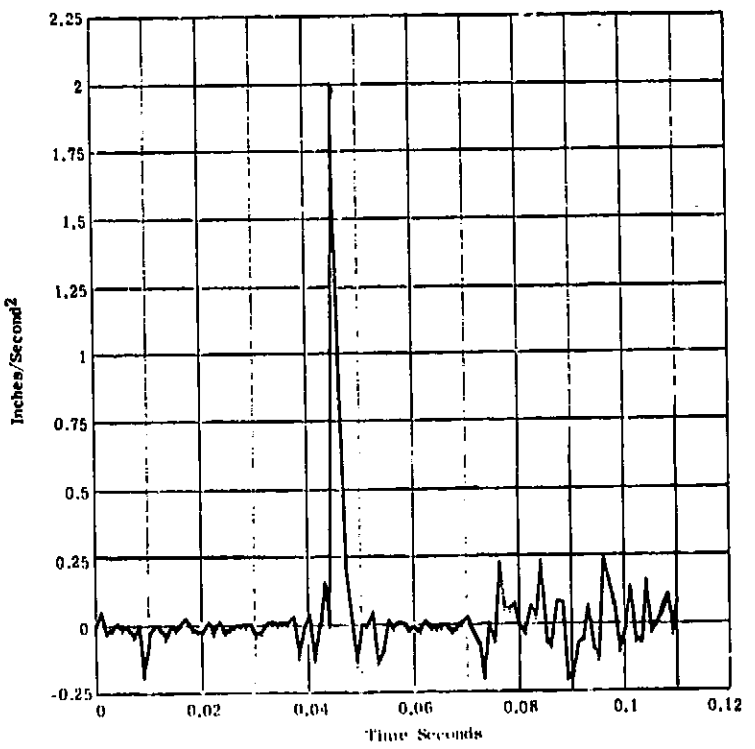

l) Vehicle c.g. Horizontal Acceleration - $\ddot{Y}$

Figure 6-24. Computer Results For LM Model Drop No. 6 Using High Strut Damping in Computer Simulation (See Figure 6-10 for drop conditions) (Sheet 3 of 4)

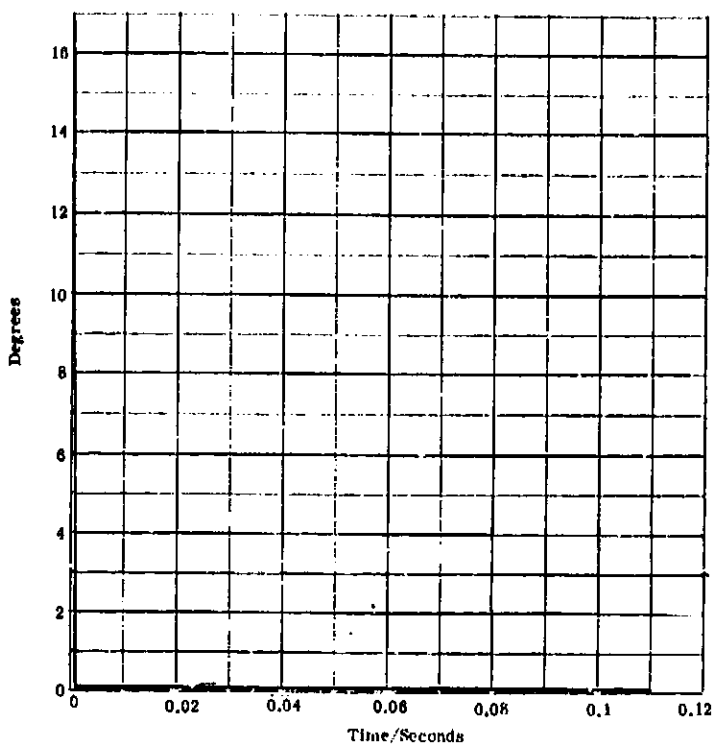

m) Footpad Pitch Angle - α

Figure 6-24. Computer Results For LM Model Drop No. 6 Using High Strut Damping in Computer Simulation (See Figure 6-10 for drop conditions) (Sheet 4 of 4)

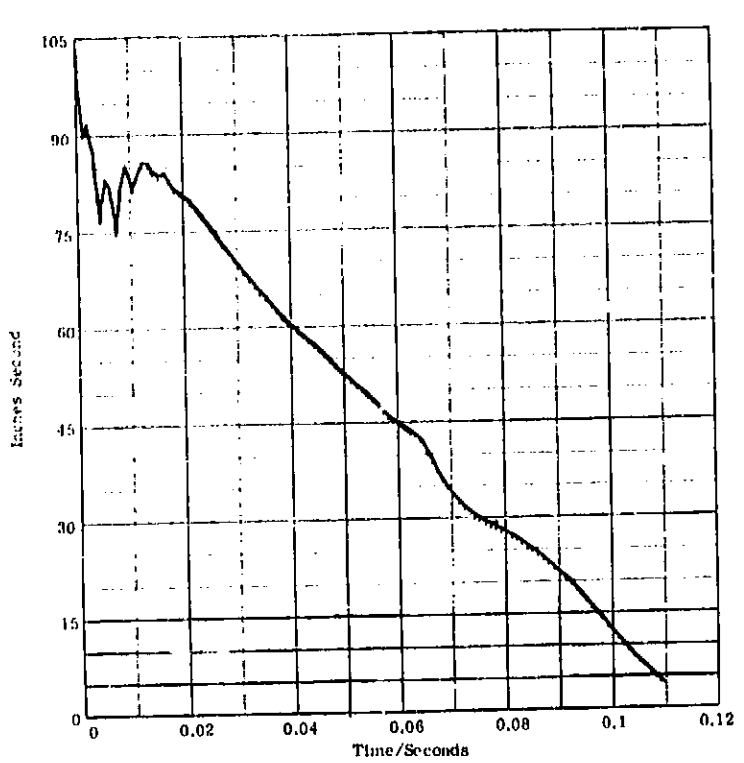

a) Footpad Velocity - V_{ap}

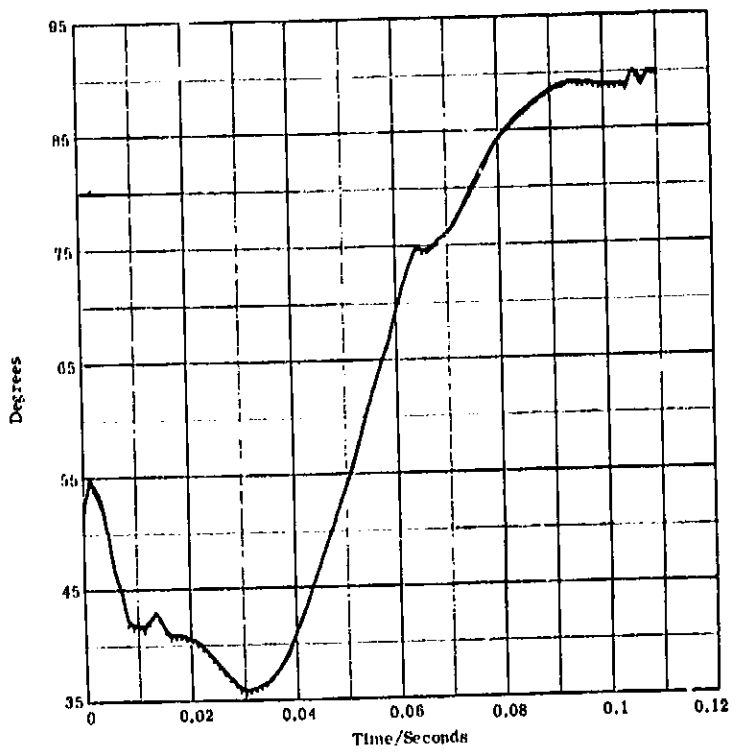

b) Footpad Velocity Angle - θ

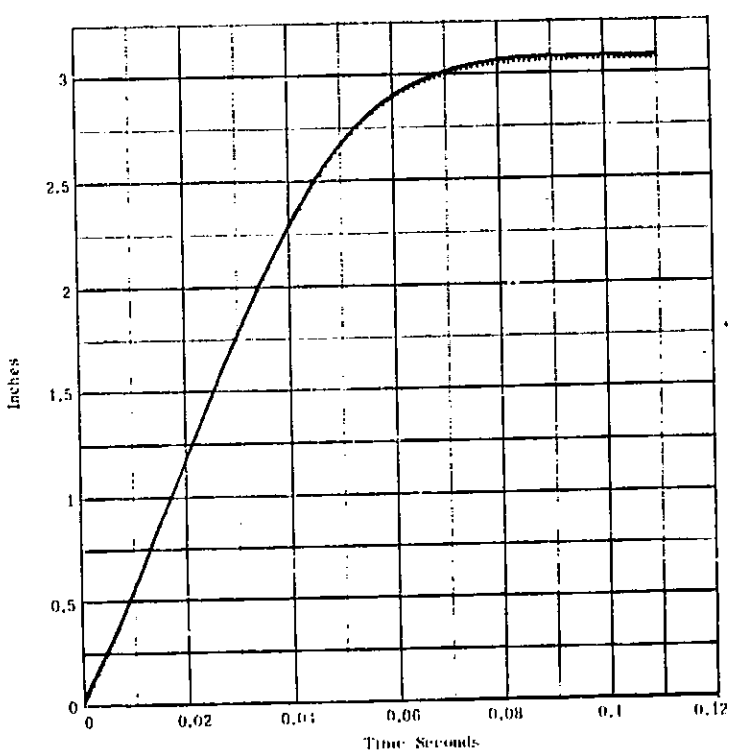

c) Footpad Penetration - d

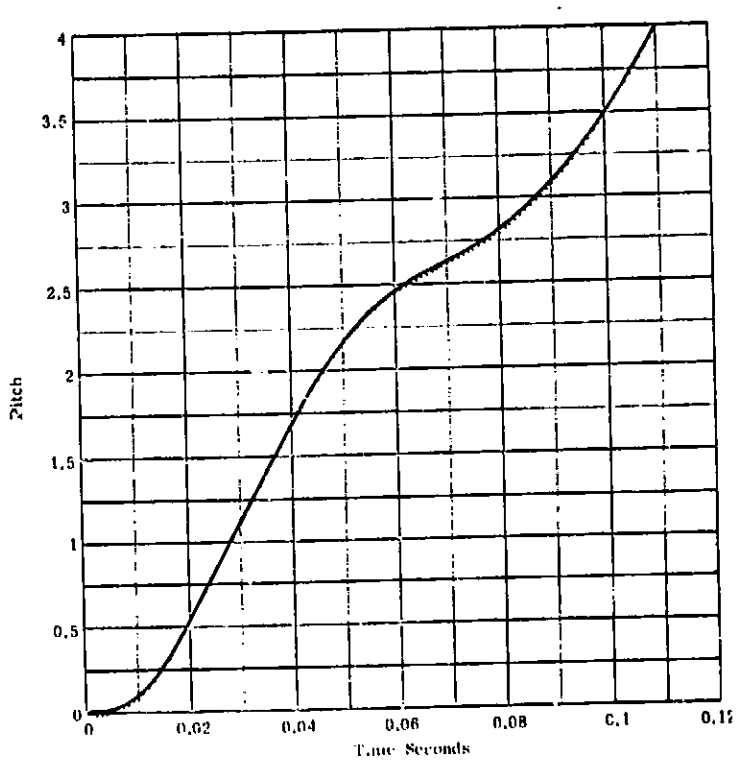

d) Vehicle Pitch Angle - Ξ

Figure 6-25. Computer Results For LM Model Drop No. 7 Using High Strut Damping in Computer Simulation (See Figure 6-10 for drop conditions) (Sheet 1 of 4)

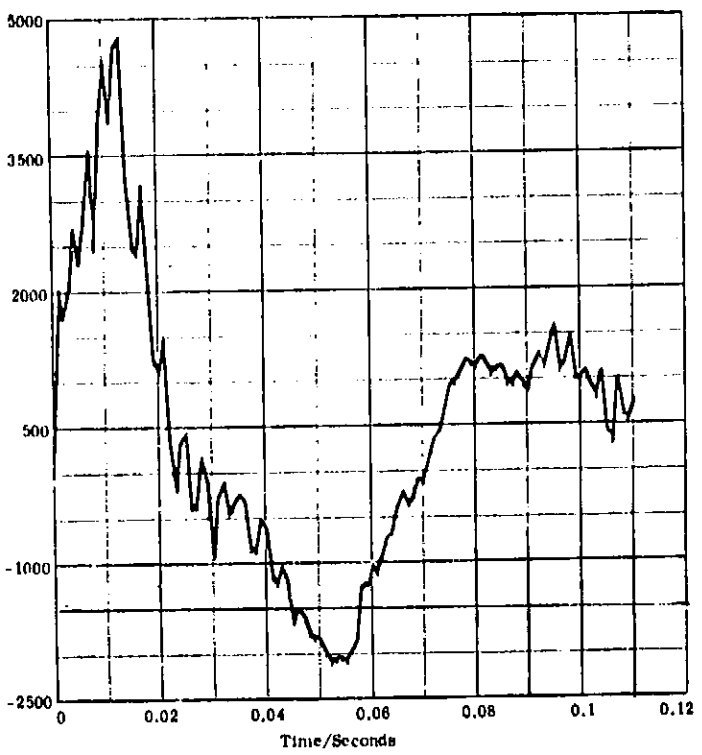

e) Vehicle Pitch Acceleration - $\ddot{\Xi}$

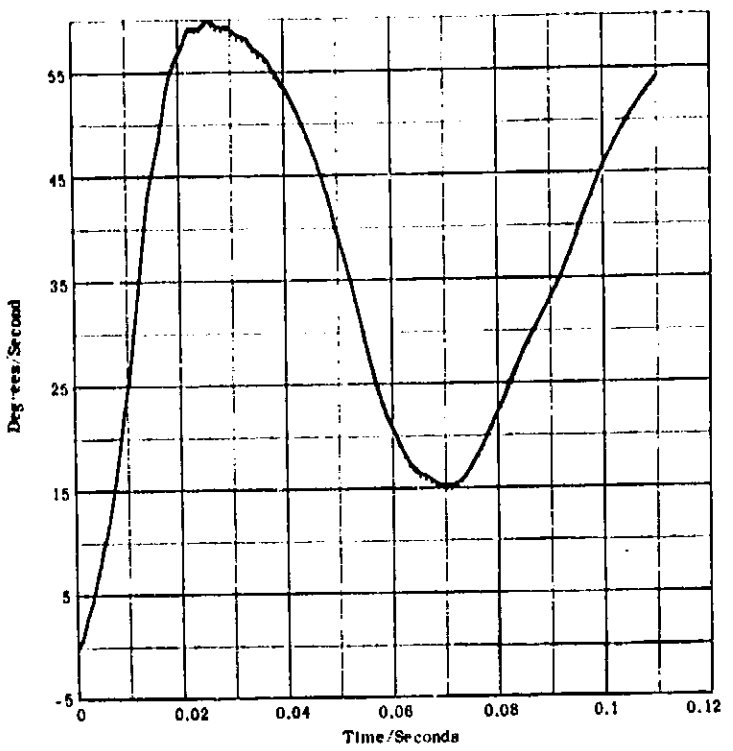

f) Vehicle Pitch Rate - $\dot{\Xi}$

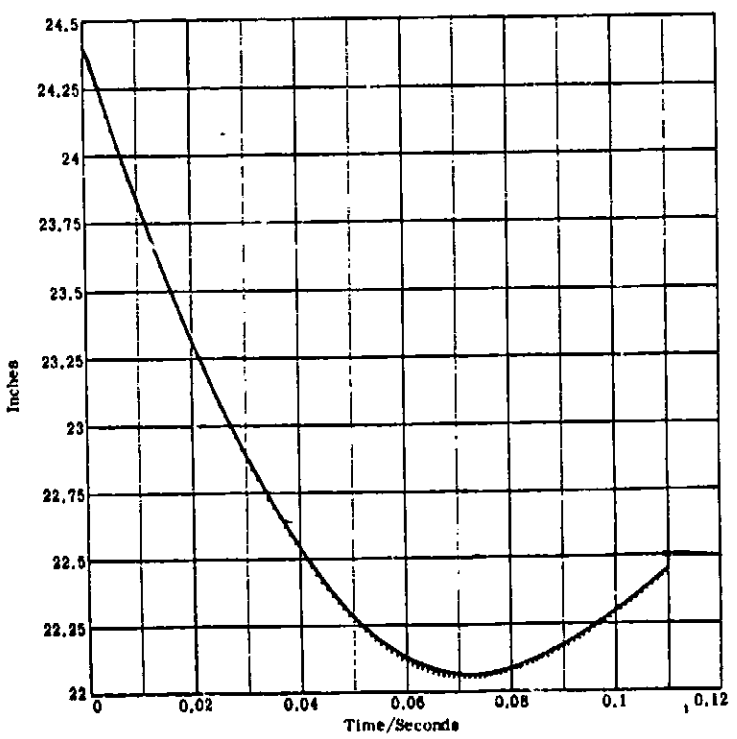

g) Vehicle c.g. Vertical Position - X

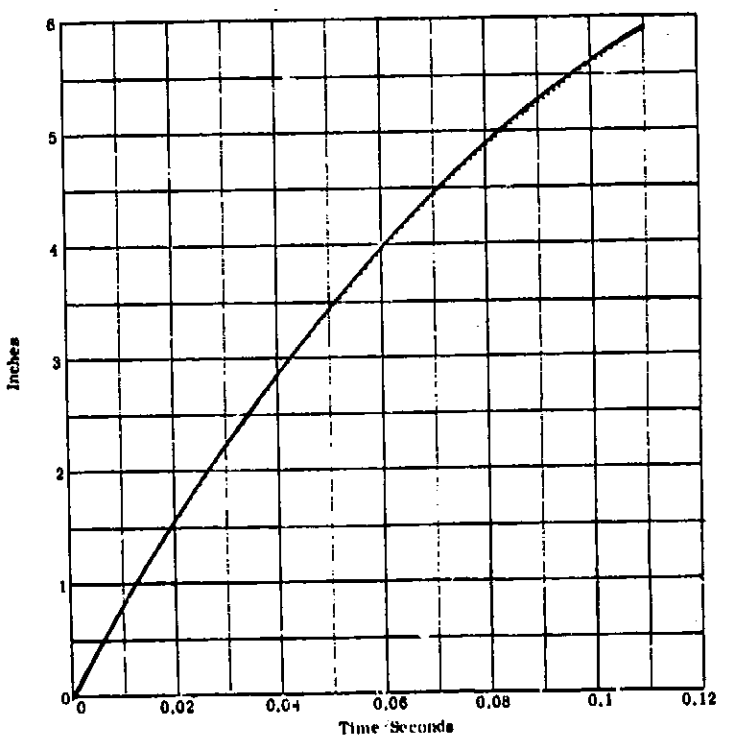

h) Vehicle c.g. Horizontal Position - Y

Figure 6-25. Computer Results For LM Model Drop No. 7 Using High Strut Damping in Computer Simulation (See Figure 6-10 for drop conditions) (Sheet 2 of 4)

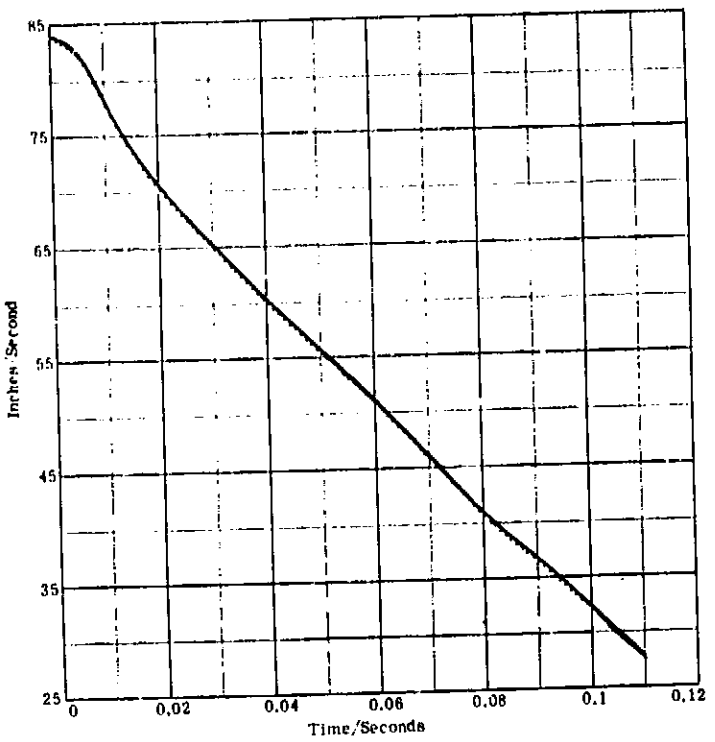

i) Vehicle c.g. Horizontal Velocity - $\dot{Y}$

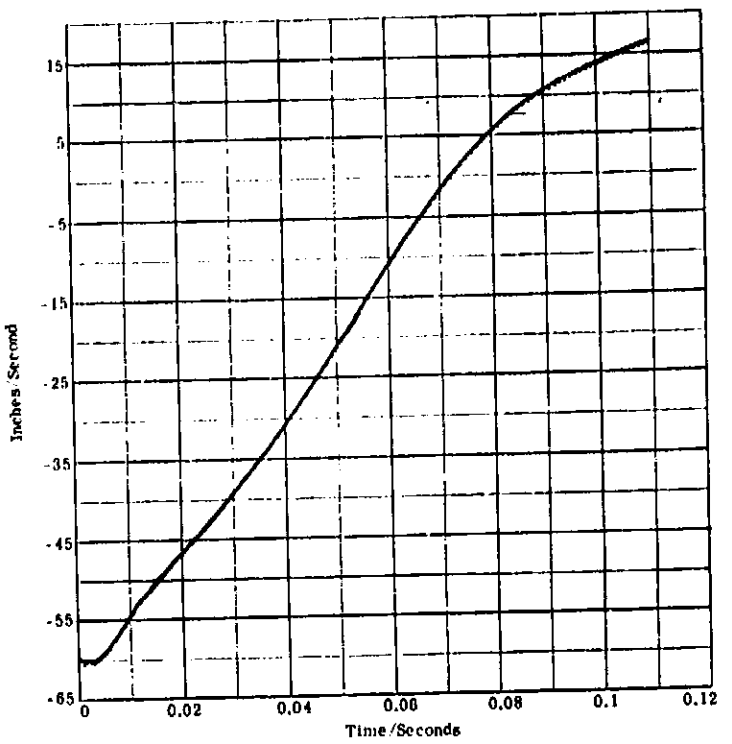

j) Vehicle c.g. Vertical Velocity - $\dot{X}$

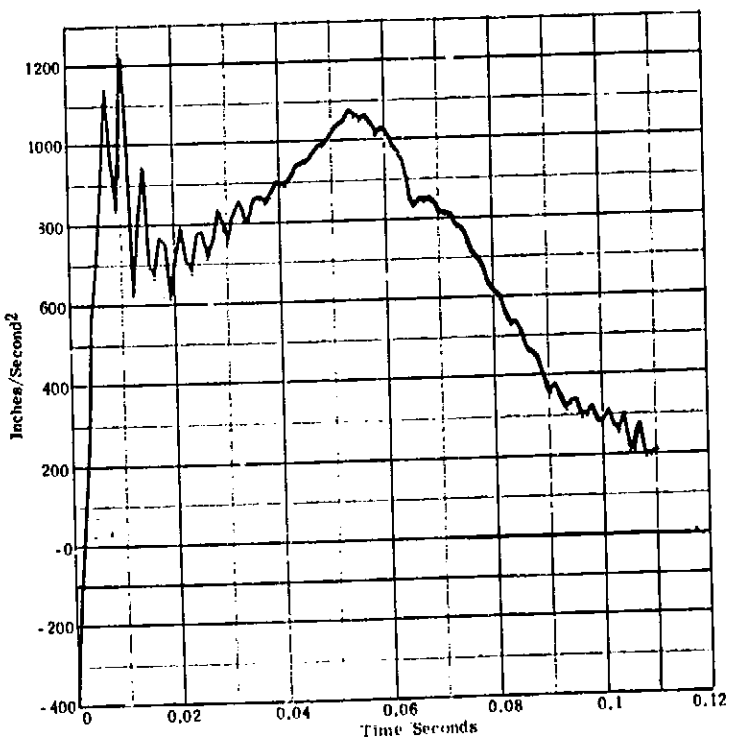

k) Vehicle c.g. Vertical Acceleration - $\ddot{X}$

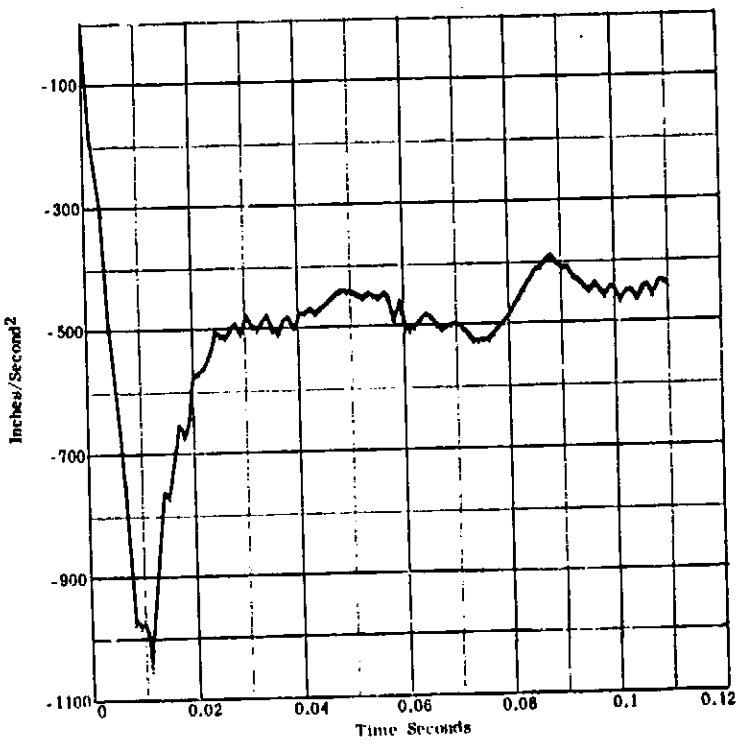

l) Vehicle c.g. Horizontal Acceleration - $\ddot{Y}$

Figure 6-25. Computer Results For LM Model Drop No. 7 Using High Strut Damping in Computer Simulation (See Figure 6-10 for drop conditions) (Sheet 3 of 4)

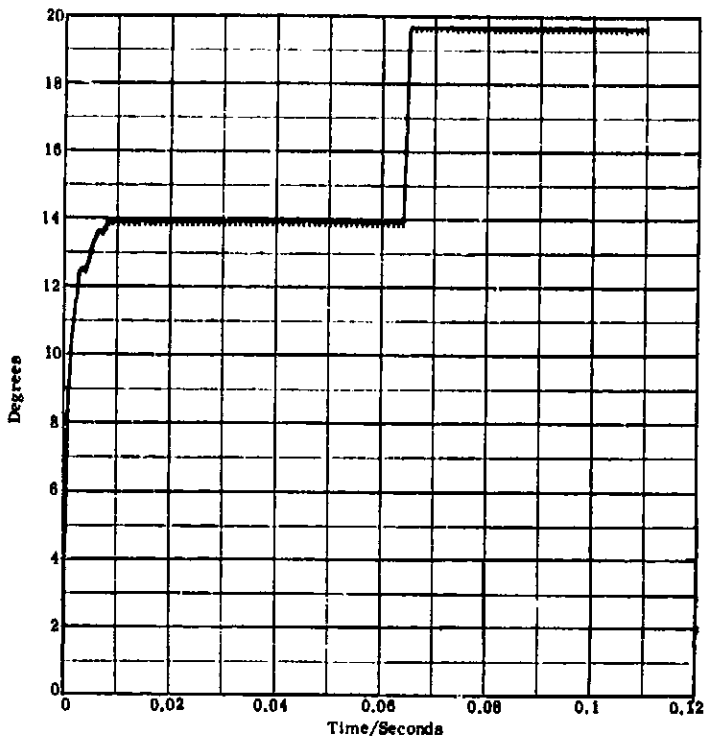

m) Footpad Pitch Angle - α

Figure 6-25. Computer Results For LM Model Drop No. 7 Using High Strut Damping in Computer Simulation (See Figure 6-10 for drop conditions) (Sheet 4 of 4)

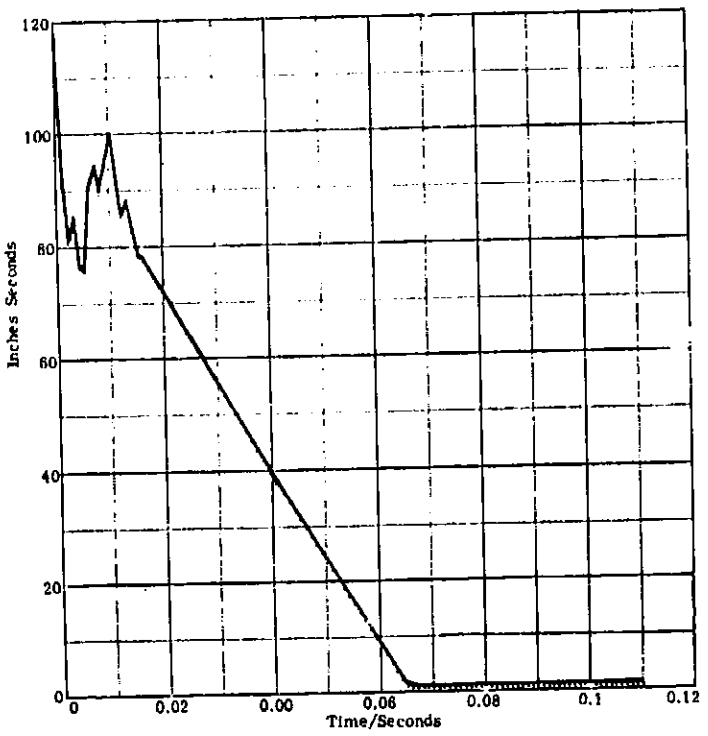

a) Footpad Velocity - Vap

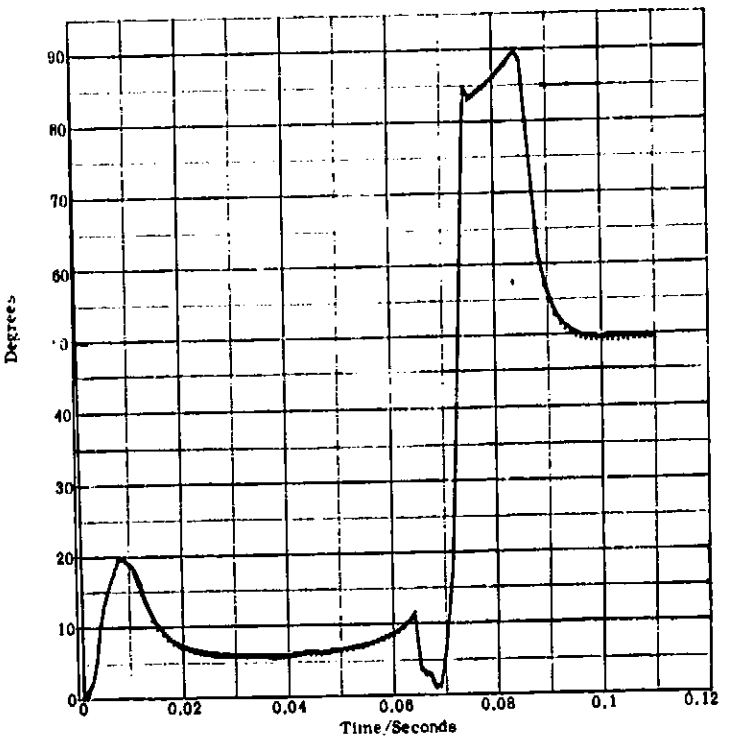

b) Footpad Velocity Angle - θ

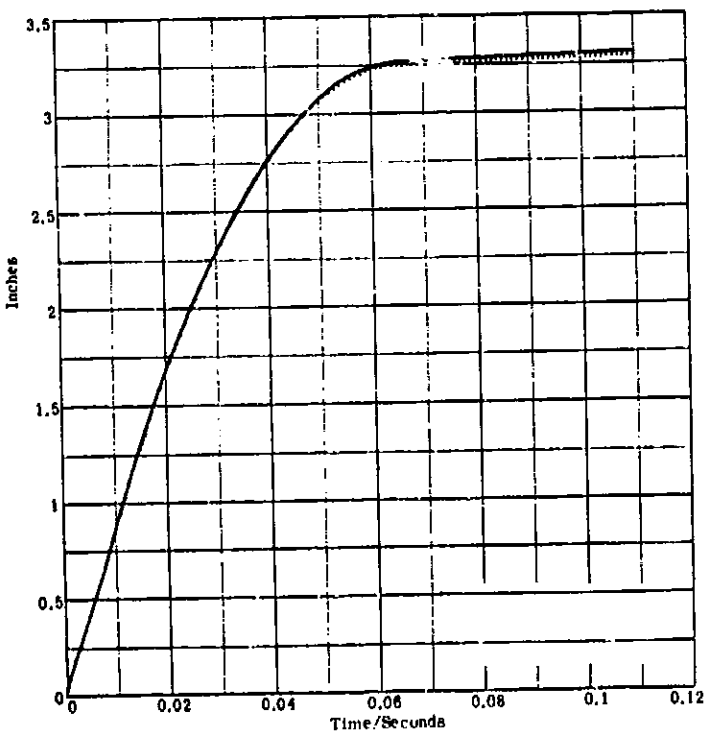

c) Footpad Penetration - d

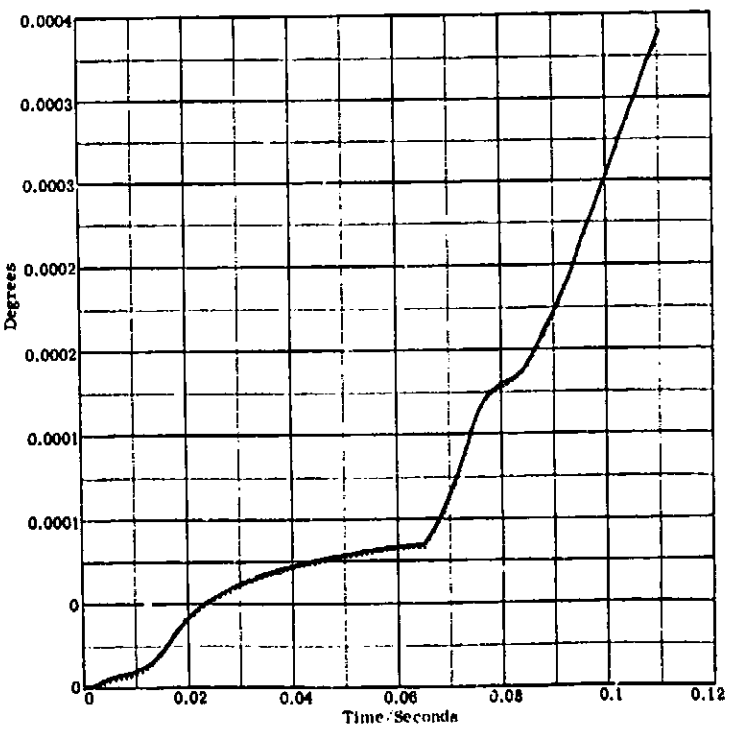

d) Vehicle Pitch Angle - Ξ

Figure 6-26. Computer Results For LM Model Drop No. 8 Using High Strut Damping in Computer Simulation (See Figure 6-10 for drop conditions) (Sheet 1 of 4)

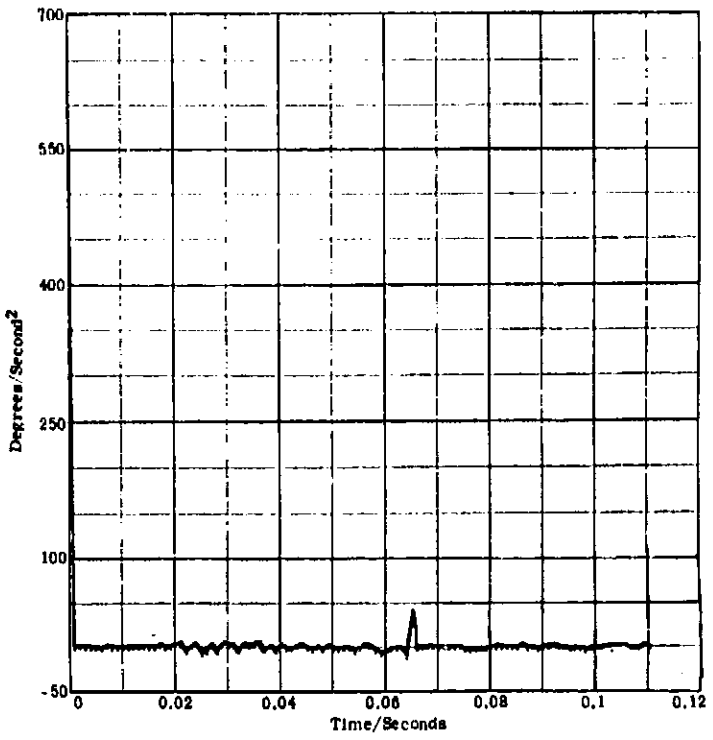

e) Vehicle Pitch Acceleration - $\ddot{\Xi}$

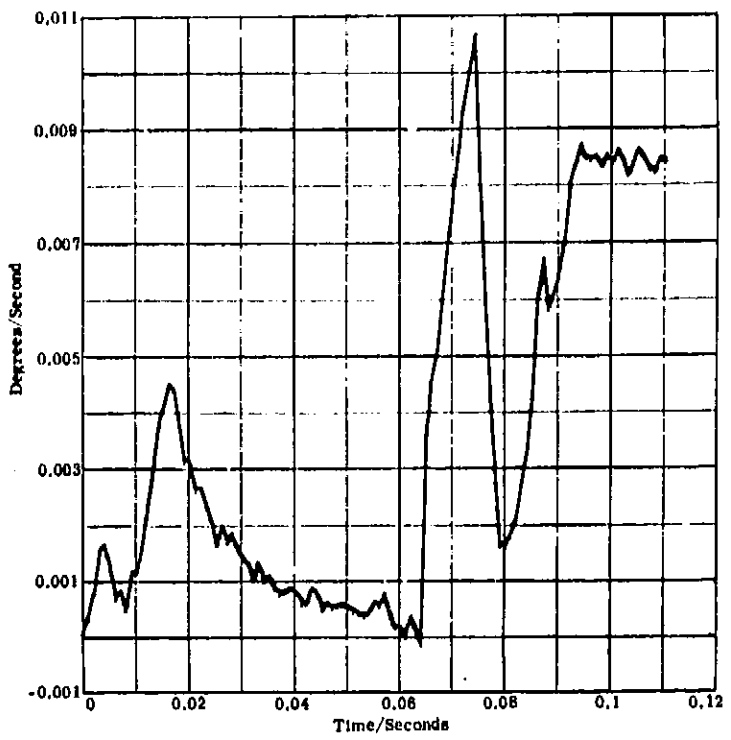

f) Vehicle Pitch Rate - $\dot{\Xi}$

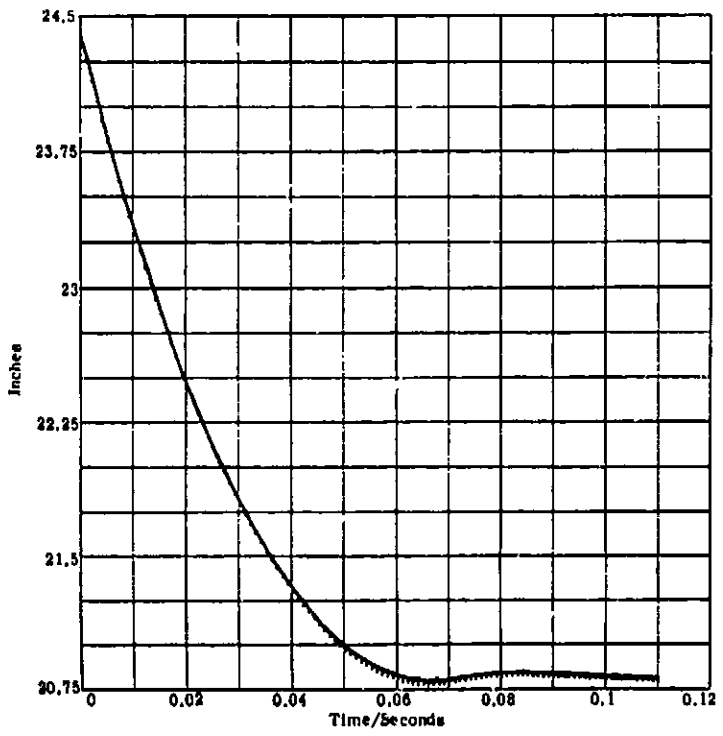

g) Vehicle c.g. Vertical Position - X

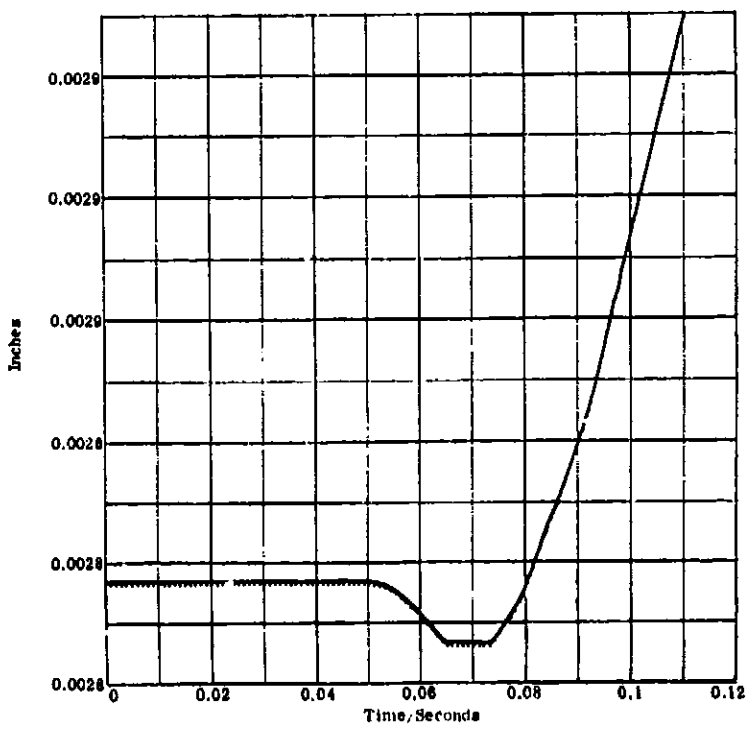

h) Vehicle c.g. Horizontal Position - Y

Figure 6-26. Computer Results For LM Model Drop No. 8 Using High Strut Damping in Computer Simulation (See Figure 6-10 for drop conditions) (Sheet 2 of 4)

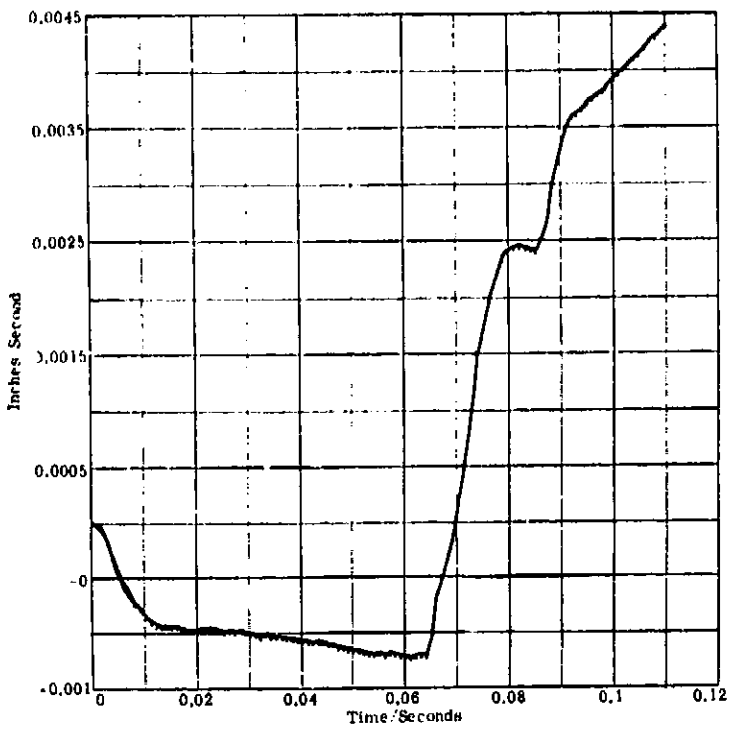

i) Vehicle c.g. Horizontal Velocity - $\dot{Y}$

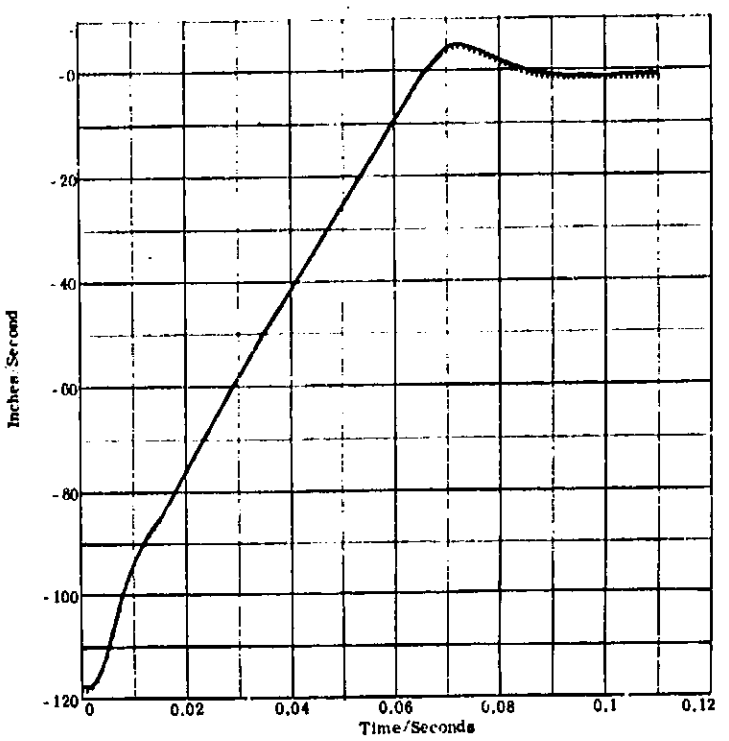

j) Vehicle c.g. Vertical Velocity - $\dot{X}$

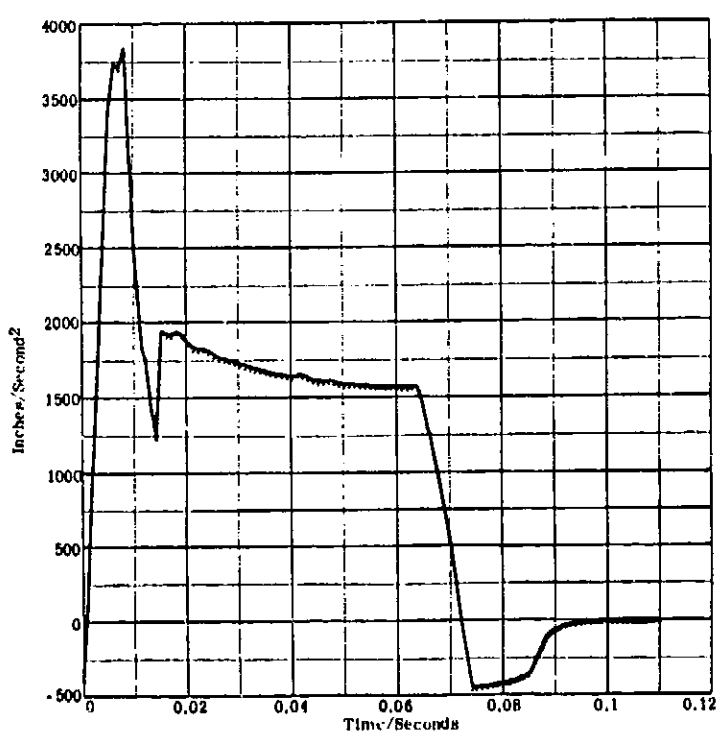

k) Vehicle c.g. Vertical Acceleration - $\ddot{X}$

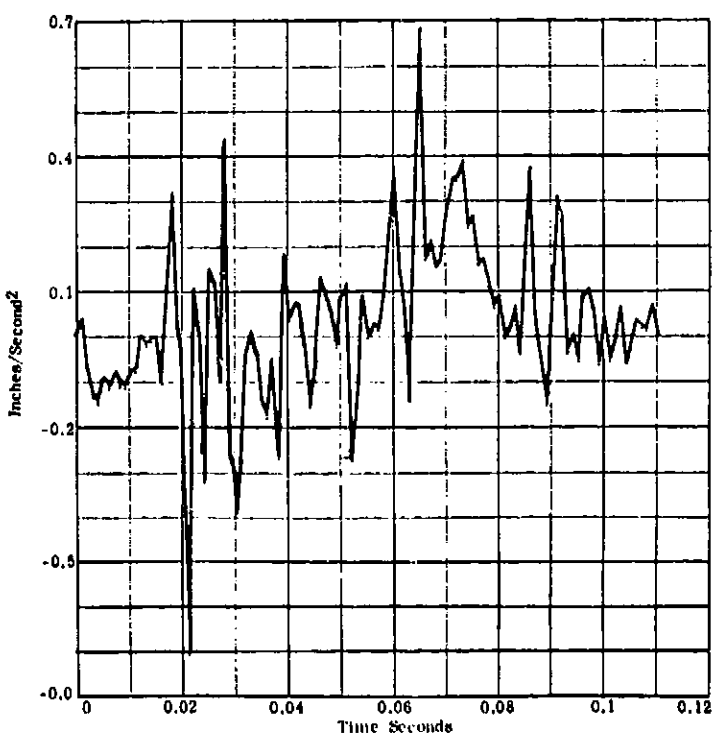

l) Vehicle c.g. Horizontal Acceleration - $\ddot{Y}$

Figure 6-26. Computer Results For LM Model Drop No. 8 Using High Strut Damping in Computer Simulation (See Figure 6-10 for drop conditions) (Sheet 3 of 4)

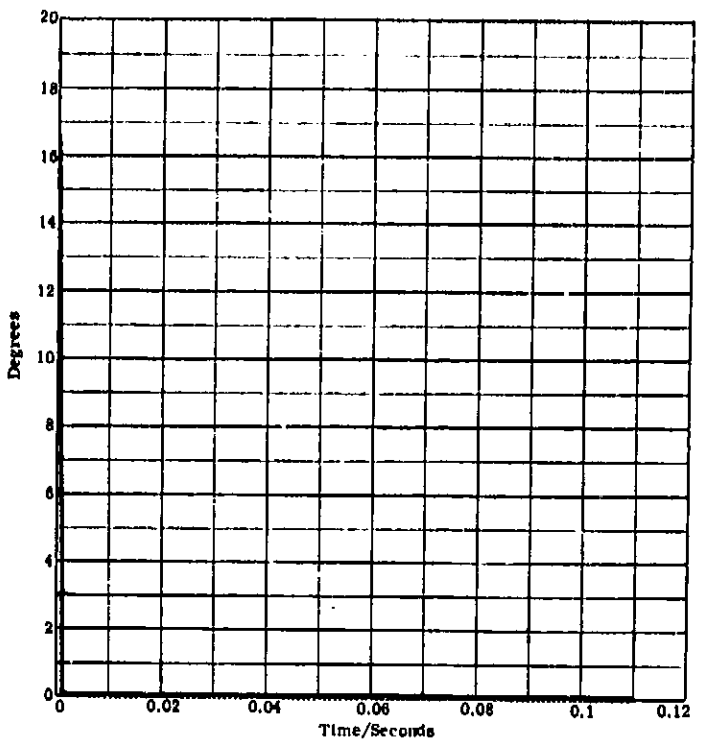

m) Footpad Pitch Angle - α

Figure 6-26. Computer Results For LM Model Drop No. 8 Using High Strut Damping in Computer Simulation (See Figure 6-10 for drop conditions) (Sheet 4 of 4)

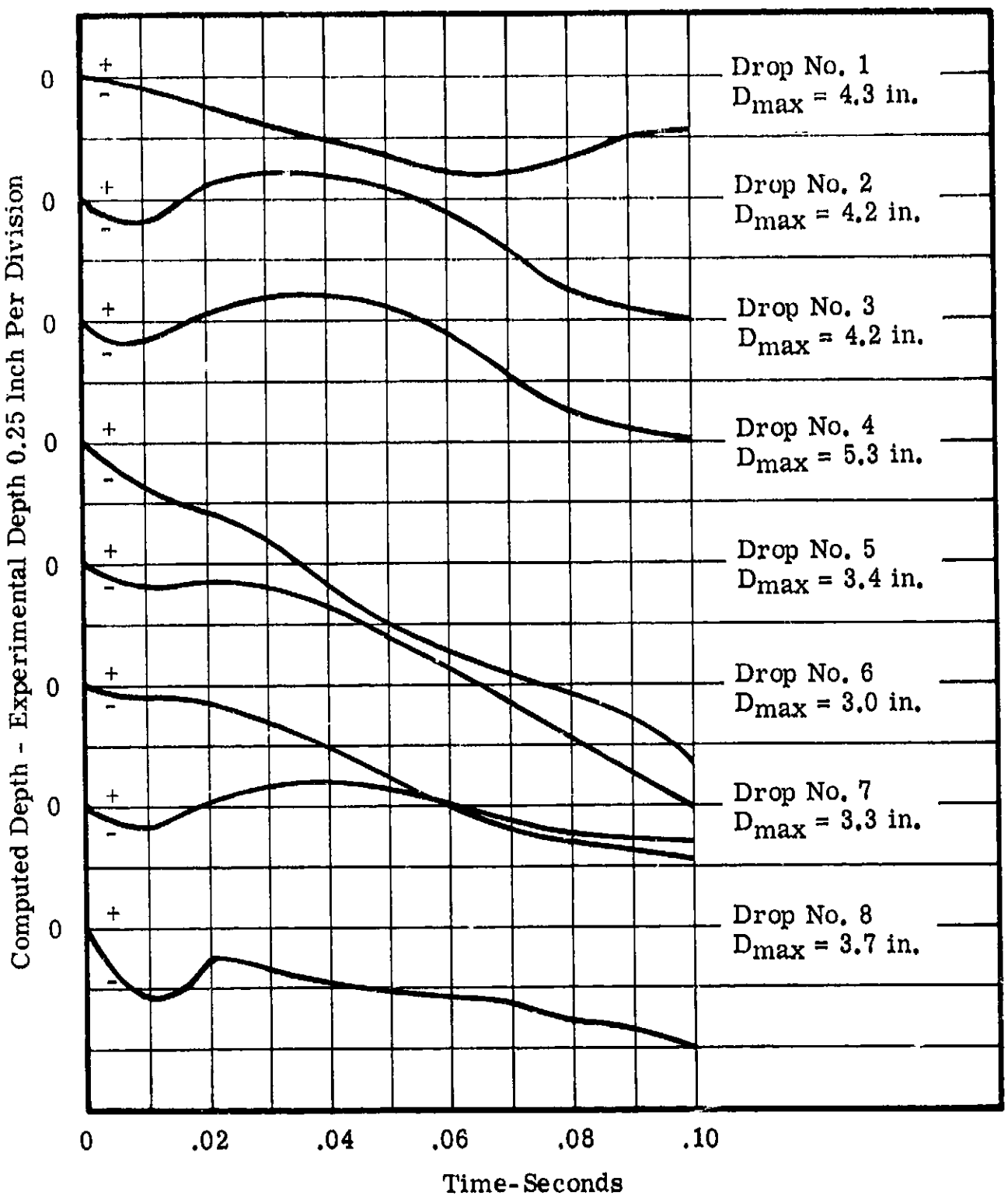

Figure 6-27. Comparison of Computed and Experimental Footpad Penetration Depths

SECTION VII

CONCLUSIONS AND RECOMMENDATIONS

7.1 INTRODUCTION

This section of the report summarizes the main conclusions resulting from the LM Soil Mechanics Study and presents recommendations for what is felt to be effective utilization of the main results of the study for application to investigations of both the present Apollo Lunar Module and possible future refinements of the Lunar Module. Secondary conclusions resulting from the study are also presented. These deal with items such as the development of soil placement and soil-bed control procedures, model testing technology, development and utilization of dynamic controlled motion soil testing equipment, and other facets of the study.

It is difficult to summarize all the important conclusions reached in an extensive and many-phased program such as the LM Soil Mechanics Study. In many cases the importance of a finding can not be initially recognized since the importance depends on future utilizations which can not always be anticipated. In this respect it is hoped that the details of the study, as contained in the previous sections of this report and in the appendices, will supplement considerably the conclusions presented in this section of the report.

7.2 CONCLUSIONS RELATED TO THE SEMI-EMPIRICAL SOIL MODEL

1. The most significant soil properties affecting the dynamic interaction between a dry particulate, cohesionless soil and a penetrator, such as the footpads of the Lunar Module, are: the soil bulk mass density, ρ, the relative density or degree of compactness, D_r, the angle of internal friction, ϕ, and to a lesser degree, the elastic modulus of the soil at a specific confining pressure,

E_S. Grain size and grain size distribution parameters are not directly involved if the atmospheric pressure is low - as of course it would be in lunar applications. For atmospheric pressures equal to that of the earth, fine grain soils (mean grain size less than approximately .30 mm) show changes in strength due to pore gas effects. Grain size and grain size distribution affect strength by changing the angle of internal friction and the minimum-maximum density range for a given soil type. This can be accounted for, however, by using the correct ϕ, γ, D_r and E_S values in the semi-empirical force laws.

The cohesive strength parameter, C, is known to have an effect on strength and the derived force laws would have to be extended with additional terms to account for the force/penetrator interaction of soils having significant cohesive strength.

2. Based on the correlation studies and the properties of the test soils used for the semi-empirical determination of the force laws, the range of the soil properties over which the force laws are applicable are:

   ρ, .3 to 2.0 grams/cubic centimeter

   ϕ, 25° to 50°

   D_r, 0 to .95

   E_S, 4×10^3 to 25×10^3 psi (Sonic modulus at 4 psi confining pressure)

   C, 0 to .05 psi

3. Based on the analysis of the lunar soil as presented in "Surveyor III Mission Report, Part II, Scientific Results" Section IV "Soil Mechanics Surface Sampler: Lunar Surface Tests, Results, and Analysis" by R. F. Scott and F. J. Roberson, the derived soil model is considered to be directly applicable to the lunar soil. While estimates of the upper limits in the soil cohesive strength (.14 psi) would indicate some slight effect on net footpad forces, the accuracy available on the other soil descriptors, coupled with the sensitivity of the spacecraft

motion to minor variations in soil strength parameters, would not warrant the inclusion of any effects from the small cohesive strength of the lunar soil.

As discussed in Section II the soils used in this study were limited to air-dried particulate materials which ordinarily would be classified as cohesionless. To determine accurately the upper limit on applicability of the derived soil force laws to soils having small cohesion would require a detail study using soils with carefully controlled cohesive shear strengths. However, it should also be noted that the cohesive shear strength parameter C is an empirical constant defined as the intercept point on the shear stress axis of a direct shear or triaxial maximum-shear-stress versus normal-stress diagram. By this definition several of the soils in the present study had C values in excess of the upper limit estimate of the lunar soil. Within this range excellent correlation was obtained using an analytical soil model which assumed that the soils were cohesionless.

4. The variable penetration load of the soil obtained under static conditions (penetrations at rates of 4 in./min. or less) is significantly greater than the equivalent, penetration dependent load obtained under dynamic conditions. This factor is accounted for in the derived analytical soil interaction model.

5. The local gravitational field affects both the mechanical strength and the "momentum transfer" portions of the soil dynamic reactive force. The momentum transfer drag coefficient is shown to be made up of two effects. The first is a true momentum transfer effect which results in a drag coefficient in the vicinity of unity. The second is a "soil mobility" effect, i.e. a resistance to flow of the soil away from the penetrating soil wedge. This effect results in a force which is dependent on the soil strength parameters (D_r and ϕ) and the local acceleration of gravity.

6. Within the range of four-inch diameter footpads to thirty-seven-inch diameter footpads, size scaling of footpad reactive forces is accounted for by the dimensional terms (areas, lengths, depths, etc.) contained within the derived force laws.

7. While derived specifically for the footpads of the Lunar Module Spacecraft, the analytical model given here can be applied to other systems. The portions of the force law that apply specifically to the LM footpads are:

   a. Angular orientation of the footpad during "slide-out" - specifically associated with the LM footpad shape and the ball joint construction and location relative to the footpad face.

   b. The ψ function relating axial and normal forces on the LM footpad - specifically associated with the LM footpad shape.

   c. Dimensionless multipliers in the C_D and C_{MS} functions - these are form factors which will vary with footpad shape.

8. The analytical soil model derived in this study yields excellent correlation with both drag test and oblique impact test results over a very wide range of soil properties. Because of the close correlation obtained between the above test results and the analytical prediction the general concept of the soil load-deformation process, as reflected in the soil model, is felt to be a realistic reflection of the actual motion phenomena occurring in the soil during a moderate speed penetrometer impact.

9. The results of the detail correlation study show that the analytical soil model derived in this study - when incorporated into a landing dynamics computer program - can be used to predict realistically the details of the footpad motion and reactive forces during touchdown of the Lunar Module. Specifically, predictions of penetration versus time and maximum footpad penetrations were within $\pm$ 15% of those obtained experimentally. Predictions of instantaneous

footpad velocity in both the horizontal and vertical directions were within $\pm$ 10%. Predictions of shock strut forces versus time, which reflect the footpad reactions, were essentially equal to those computed when both the experimental and theoretical results were filtered of high frequency transients. Correlation of the high frequency transients would apparently require a more detailed analytical model of the leg structure.

10. The results of the stability profile comparison studies indicate that the experimental performance can be bracketed by two different versions of the soil model. The original version of the soil model assumed that during the "slide-out" phase of the footpad's motion the lift force, F_{np}, for θ values greater than 90° (penetration decreasing) could be calculated using the ψ function for $\theta = 90°$. This assumption resulted in the predicted LM Model stability being greater than that obtained experimentally. The modified version of the soil model assumed that the lift force, F_{np}, dropped to zero when θ became greater than 90°. This assumption resulted in the predicted model stability being less than that obtained experimentally. Of the two versions of the soil model the modified version predicted results closer to the experimental results than the original version. On a velocity vector basis the V_V versus V_H stability profile for the modified version of the soil model differed from the experimental profile by approximately 10%.

The best version of the soil model would be one which compromised between the two soil models used in the stability profile correlation study. A suggested compromise which maintains continuity with the ψ function for $\theta < 90°$ is,

$$\psi = .55 \left[A_{pt}/A_{ft}\right]\left[1-(\theta-\pi/2)\Big/(\theta_c-\pi/2)\right], \pi/2 \le \theta \le \theta_c$$

$$= 0 \quad , \qquad \theta > \theta_c$$

with the θ_c value being in the vicinity of $3\pi/4$. Stability profile predictions with such an incorporation should better the results obtained with the above mentioned modified soil model which corresponds to a θ_c value of $\pi/2$. Further drag test studies should

be conducted to establish a precise ψ function for values greater than $\pi/2$ since it is undoubtedly penetration dependent as was the ψ function for θ values less than $\pi/2$.

7.3 RECOMMENDATIONS FOR UTILIZATION OF THE ANALYTICAL SOIL MODEL

As shown by the correlation studies covered in Section VI of this report, the derived soil model can predict with reasonable accuracy the forces acting on and motions of the LM footpad during landings onto a soil of specified density, relative density, and angle of internal friction. For this reason the soil model should be quite valuable for carrying out studies of LM landing performance. Types of studies for which the soil model/landing dynamics program may be used include the following:

1. Studies of the accuracy needed in specification of the lunar soil properties. That is, determination of how accurately the soil properties must be known to predict adequately the performance of the LM spacecraft when it lands on the lunar soil. This would first require a specification of the accuracy desired on various vehicle performance parameters. Once this was determined the landing dynamics computer program with the soil subroutine could be utilized to determine how great a variation in each of the soil properties is necessary before exceeding the specified accuracy on a particular vehicle performance parameter (such as a shock strut maximum stroke).

2. Comparative studies to show, in detail, how hard surface landing performance differs from the landing performance on various soils. While limited experimental and theoretical studies have been carried out in this area, a comprehensive study would be valuable not only in relation to the LM spacecraft but also to yield guidelines for future spacecraft design and analysis. This is particularly important due to the fact that a landing dynamics computer program with a soil subroutine is more complex and requires much longer running times than a simplified rigid surface computer program. A study of the above type might allow rigid surface results to be "corrected" empirically to account for the soil effects.

3. Studies to determine the maximum landing conditions capability of the LM spacecraft - at present the LM spacecraft is limited in landing ability from the standpoint of horizontal and vertical velocities, ground slopes, and vehicle attitude. These limitations are based on the results of landing dynamics investigations using a quite simplified soft surface model which does not reflect the actual forces encountered when landing on a lunar like soil.

   Even if it were never actually utilized in a landing of one of the LM spacecraft, it would be desirable to know the actual landing capabilities of LM. The soil model from this program could be used quite effectively in establishing these operational capabilities.

4. Studies to determine the possible weight savings which could be achieved on an LM spacecraft by taking advantage of the load-deformation characteristics of the lunar soil. The lunar soil is actually a good load-limiting energy absorber. By taking advantage of its energy absorbing ability the size of the shock strut energy absorbers on the LM could be reduced considerably. In addition, since for most situations the softness of the surface reduces toppling stability problems, the spread or size of the landing gear system could conceivably be reduced. While such changes in the system are not anticipated for the first few missions the savings possible in size and weight, coupled with the ability to replace this weight with other payload, could make it an attractive possibility for later utilization on the LM.

   The soil model derived in the present study could be used to establish realistically the above weight savings possibilities. However, studies in this area will first require a considerable amount of experience to be built up in using the landing dynamics computer program with the soil subroutine and possibly additional experimental correlation studies to achieve a high degree of confidence in the accuracy of output information.

5. Studies to determine the optimum footpad size. Since the derived analytical soil/footpad interaction model is applicable for footpads from 4.0 inches diameter to at least 37 inches diameter, studies could be carried out to optimize the size. This could also be carried out in conjunction with the studies suggested in 4, above. Again, as was true for Item 4 above, experience in use of the program and possibly additional correlation studies would be necessary to achieve a high degree of confidence in the accuracy of the output information of such a study.

7.4 SECONDARY CONCLUSIONS AND RECOMMENDATIONS

1. The studies conducted show, as other soil studies have indicated, that it is very important to use extreme care in the soil placement. The hopper method developed in this study results in consistent soil properties for soils having a fairly uniform grain size. It is not effective for soils having a very wide gradation or a very small mean grain size (70 microns or smaller) since, in the air dried state, the fine grain soils tend to clump and do not distribute uniformly.

2. The dynamic penetrometer is recommended for determination of soil properties. It must be used in conjunction with other instruments to yield the properties. It is convenient to use.

3. Additional and/or more precise information on soil properties may be possible from the dynamic penetrometer by using the complete acceleration signature (g's versus time) rather than simply using the peak "g" reading as was done in the present study. The process of signature interpretation could be automated via a digital computer program to facilitate rapid evaluation of a test-bed's properties. Such a computer program would be based upon a simplified version of the soil model developed in the present study.

4. Since footpad velocity information is quite important in interpreting oblique impact test results, it is recommended that improved methods of measuring

the velocity be used in future tests. The present study used both differentiation of a displacement signal from a slide wire potentiometer and, in some cases, integration of a seismic accelerometer signal. Both methods have disadvantages so that a replacement procedure is recommended.

5. Integration of accelerometer signals is not recommended as a method for determining long term vehicle velocities and positions due to the integrated effects of signal drift. This may be overcome by using stabilized amplifiers in the recording circuitry.

6. It is extremely valuable in the testing phase of a program, such as the present one, to be able to examine test data as quickly as possible after the test is run. Long time periods of recording, handling, and data reduction often bring about a situation in which poor data or inconsequential data is not recognized until long after the testing is completed. Immediate availability of the test results allows for redirection of the testing program so that the maximum amount of pertinent information can be gained with a given amount of testing. It is therefore recommended that future testing of this type include careful development of quick data handling procedures which allow the analyst to examine test results immediately after a test is completed.